



# MONASH University

---

## Wavepacket Modelling of Broadband Shock-Associated Noise in Supersonic Shock-Containing Jets

---

Marcus Hoi-Chun Wong

*Supervisors:*

Dr Daniel Edgington-Mitchell (Primary)

Professor Damon Honnery (Associate)

Professor Peter Jordan (External)

*Examination panel:*

Professor Sanjiva Lele

Professor Aniruddha Sinha

*A thesis submitted in partial fulfillment of the requirements  
for the degree of  
Doctor of Philosophy (Engineering)*

Laboratory for Turbulence Research in Aerospace and Combustion

Department of Mechanical and Aerospace Engineering

Monash University, Melbourne, Australia

December, 2020

# **Wavepacket Modelling of Broadband Shock-Associated Noise in Supersonic Shock-Containing Jets**

Copyright © 2021

Marcus Hoi-Chun Wong



When we started our measurements, we realized that the theory of aerodynamic noise could never be checked in detail.

---

Jet Noise and Shear Flow Instability Seen From an Experimenter's Viewpoint

ERIK MOLLO-CHRISTENSEN, 1967

Jet noise prediction is notoriously challenging because only subtle features of the flow turbulence radiate sound.

---

Nozzles, turbulence, and jet noise prediction

JONATHAN B. FREUND, 2019

## Abstract

This thesis reports on the modelling of broadband shock-associated noise (BBSAN) in supersonic shock-containing jets using stability theory. The large-scale coherent structures are modelled as hydrodynamic *wavepackets*. The interaction of wavepackets with the shock-cell structure is assumed to produce BBSAN. The modelling effort is supported by experimentally-derived acoustic data.

To facilitate the experimental side of this investigation, a new jet noise research facility was conceived at the Laboratory for Turbulence Research in Aerospace and Combustion (LTRAC) Shock Laboratory. The new facility involves a jet rig mounted inside an anechoic chamber, ensuring a controlled environment for acoustic measurements. The design strategy is based on the acoustic and flow requirements to study supersonic jet noise; the jet rig is capable of continuous operation up to an ideally-expanded Mach number of 1.7 and the anechoic chamber facilitates the measurement of high amplitude and high-frequency noise over a wide directivity range. The facility is designed and constructed to be amenable to future upgrades and modifications.

A rigorous validation process is performed to test the acoustic characteristics of the new facility. The free-field behaviour of the anechoic chamber, the geometric far-field of the jet, and potential sources of spurious noise are determined by the qualification testing program. Improvement in the quality of acoustic data is demonstrated when compared to past measurements from another, non-anechoic, LTRAC supersonic jet facility.

Following the validation of the new facility, experimental acoustic data of unheated supersonic underexpanded jets at three different Mach numbers are azimuthally decomposed. The relative contribution of successive azimuthal modes to BBSAN is found to be sensitive to the observer angle and jet operating condition; more modes are required to reconstruct the total acoustic signal at higher frequencies and increasing upstream angles. The results demonstrate the need to carefully consider the azimuthal content of BBSAN when comparing acoustic measurements to predictions made by wavepacket models.

Concurrently, to understand the limitations of a wavepacket model for BBSAN, an idealised line-source model is used to test the different source parameters. The two-point source

model uses wavepackets to describe the coherent structures, while the shock-cell structure is approximated by a set of stationary wave-guide modes. An acoustic analogy is used to link the flow-field to the far-field sound. The motivation for using a simple model problem is to test the impact of coherence decay, the signature of an stochastic, or jittering, wavepacket, on the generation of BBSAN. When higher-order shock-cell modes are used to reconstruct the acoustic spectrum at higher frequencies, the inclusion of a jittering wavepacket is necessary to broaden the narrowband peaks observed in previous BBSAN models.

Lastly, having measured the azimuthal structure of BBSAN, and informed by the findings from the two-point line-source model, comparisons are made between experimental data and predictions from a new wavepacket model. While the same modelling framework as the line source is retained, the new model uses a more complete description of the real flow-field. Rather than using the acoustic field to inform source parameters, both the turbulent and shock components are deduced from large-eddy simulation and particle image velocimetry datasets respectively. A link to stability theory is established where wavepackets are also described using solutions to parabolised stability equations. By comparing with azimuthally-decomposed acoustic data over a wide frequency and observation range, excellent agreement is observed at peak frequencies ( $\pm 2\text{dB/St}$ ). The results confirm the critical role of wavepacket jitter in the underlying sound generating mechanism of BBSAN.

**Key words:** aeroacoustics, jet noise, instability

# Publications During Enrolment

## 0.1 Journal Papers

- Wong, M.H., Jordan, P., Maia, I.A., Cavalieri, A.V., Kirby, R., Fava, T.C., & Edgington-Mitchell, D., (in press). Wavepacket Modelling of Broadband Shock-Associated Noise in Supersonic Jets. *Journal of Fluid Mechanics*.
- Wong, M.H., Kirby, R., Jordan, P. and Edgington-Mitchell, D., 2020. Azimuthal decomposition of the radiated noise from supersonic shock-containing jets. *The Journal of the Acoustical Society of America*, 148(4), pp.2015-2027.
- Wong, M.H., Jordan, P., Honnery, D.R., and Edgington-Mitchell, D., 2019. Impact of coherence decay on wavepacket models for broadband shock-associated noise in supersonic jets. *Journal of Fluid Mechanics*, 863, pp.969–993.
- Knast, T., Bell, G., Wong, M., Leb, C.M., Soria, J., Honnery, D.R. and Edgington-Mitchell, D., 2018. Coupling modes of an underexpanded twin axisymmetric jet. *AIAA Journal*, 56(9), pp.3524-3535.

## 0.2 Conference Papers

- Wong, M.H., Edgington-Mitchell, D.M., Honnery, D., Cavalieri, A.V. and Jordan, P., 2019. A Parabolised Stability Equation based Broadband Shock-Associated Noise Model. In 25th AIAA/CEAS Aeroacoustics Conference (p. 2584).
- Wong, M.H., Edgington-Mitchell, D.M., Honnery, D.R., Jordan, P. and Savarese, A., 2018. Kinematic wavepacket model for broadband shock associated noise in underex-

panded supersonic jets. In 24th AIAA/CEAS Aeroacoustics Conference (p. 3465).

- Markesteijn, A.P., Semiletov, V., Karabasov, S.A., Tan, D.J., Wong, M., Honnery, D. and Edgington-Mitchell, D.M., 2017. Supersonic jet noise: an investigation into noise generation mechanisms using large eddy simulation and high-resolution PIV data. In 23rd AIAA/CEAS aeroacoustics conference (p. 3029).
- Tan, D.J., Kalyan, A., Gryazev, V., Wong, M., Honnery, D., Edgington-Mitchell, D.M. and Karabasov, S.A., 2017. On the application of shock-associated noise models to piv measurements of screeching axisymmetric cold jets. In 23rd AIAA/CEAS Aeroacoustics Conference (p. 3028).
- Kalyan, A., Gryazev, V., Karabasov, S.A., Tan, D.J., Wong, M., Honnery, D. and Edgington-Mitchell, D., 2017, December. Improved predictions of broadband shock associated noise in supersonic jets. In INTER-NOISE and NOISE-CON Congress and Conference Proceedings (Vol. 255, No. 6, pp. 1338-1349). Institute of Noise Control Engineering.



## Declaration

I hereby declare that this thesis contains no material which has been accepted for the award of any other degree or diploma at any university or equivalent institution and that, to the best of my knowledge and belief, this thesis contains no material previously published or written by another person, except where due reference is made in the text of the thesis.

This thesis includes two original papers published in peer-reviewed journals, one original paper submitted to a peer-review journal, and two original papers published in conferences. The core theme of the thesis concerns the measurement and modelling of broadband shock-associated noise. The ideas, development, and writing up of all the papers in the thesis were the principal responsibility of myself, the student, working within the Department of Mechanical & Aerospace Engineering under the joint supervision of Dr Daniel Edgington-Mitchell, Professor Peter Jordan and Professor Damon Honnery.

The inclusion of co-authors reflects the fact that the work came from active collaboration between researchers and acknowledges input into team-based research.

In the case of Chapters 5, 6, and 7, and Appendices A, and B, my contribution to the work involved the following:

Title	Status	Student contribution	Co-authors (contribution)	Monash student
Chapter 5				
Azimuthal Decomposition of the Radiated Noise from Supersonic Shock-containing Jets	Published journal paper	60%: Development of ideas, data collection, data analysis, figure preparation, and writing.	1. Kirby, R. (10%: Data collection and input into manuscript.)	1. Yes
			2. Jordan, P. (15%: Input into manuscript.)	2. No
			3. Edgington-Mitchell, D. (15%: Input into manuscript.)	3. No
Chapter 6				
Impact of Coherence Decay on Wavepacket Models for Broadband Shock-Associated Noise in Supersonic Jets	Published journal paper	60%: Development of ideas, data analysis, figure preparation, and writing.	1. Jordan, P. (20%: Input into manuscript.)	1. No
			2. Honnery, D. (5%: Input into manuscript.)	2. No
			3. Edgington-Mitchell, D. (15%: Input into manuscript.)	3. No



Title	Status	Student contribution	Co-authors (contribution)	Monash student
<i>Chapter 7</i>				
Wavepacket Modelling of Broadband Shock-Associated Noise in Supersonic Jets	Accepted journal paper	55%: Development of ideas, data analysis, figure preparation, and writing.	1. Jordan, P. (10%: Input into manuscript.) 2. Maia, I. (5%: Input into manuscript.) 3. Cavalieri, A. (10%: Input into manuscript.) 4. Kirby, R. (5%: Input into manuscript.) 5. Fava, T. (5%: Data analysis.) 6. Edgington-Mitchell, D. (10%: Data collection and input into manuscript.)	1. No 2. No 3. No 4. Yes 5. No 6. No

Title	Status	Student contribution	Co-authors (contribution)	Monash student
<i>Appendix A</i>				
A Parabolised Stability Equation based Broadband Shock-Associated Noise Model	Published conference paper	60%: Development of ideas, data analysis, figure preparation, and writing.	1. Jordan, P. (10%: Input into manuscript.) 2. Cavalieri, A. (10%: Input into manuscript.) 3. Honnery, D. (5%: Input into manuscript.) 4. Edgington-Mitchell, D. (15%: Input into manuscript.)	1. No 2. No 3. No 4. No
<i>Appendix B</i>				
Kinematic Wavepacket Model for Broadband Shock-Associated Noise in Underexpanded Supersonic Jets	Published conference paper	70%: Development of ideas, data analysis, figure preparation, and writing.	1. Jordan, P. (10%: Input into manuscript.) 2. Savarese, A. (5%: Input into manuscript.) 3. Honnery, D. (5%: Input into manuscript.) 4. Edgington-Mitchell, D. (10%: Input into manuscript.)	1. No 2. No 3. No 4. No

I have renumbered sections of submitted or published papers in order to generate a consistent presentation within the thesis.

Candidate's signature:

Date: 02/12/2020

The undersigned hereby certify that the above declaration correctly reflects the nature and extent of the student's and co-authors' contributions to this work. In instances where I am not the responsible author I have consulted with the responsible author to agree on the respective contributions of the authors.

Primary supervisor's signature:

Date: 02/12/2020

# Acknowledgements

*"There is nothing of sham or hypocrisy in it. It is what it is, without an apology."*

— J. E. Lawrence, *Nebraska State Journal* - 1949

While this thesis is signed by yours truly, without the on-going support from those around me, I can wholeheartedly say its completion would not have been possible. I wish to express my deepest gratitude to all those who were on this journey with me over the last 4.5 years.

I am truly fortunate to have had the unwavering support and mentoring from my three immensely knowledgeable and caring supervisors. I am greatly indebted to my primary supervisor Daniel Edgington-Mitchell. Thank you for showing faith in me ever since my undergraduate studies. Your ardent support and encouragement have pushed me to achieve goals which I thought were beyond my reach. Of the many things which I will be forever grateful for, thank you for always having my back. While I have not warmed up to your infatuation of writing JFM papers, I hope the ones in this thesis will suffice.

I would also like to acknowledge the significant contributions of my two additional supervisors Damon Honnery and Peter Jordan. Damon, thank you for your insightful suggestions during the development of the new facility. Your mentorship and sound advice throughout the initial years helped me understand the *actual* purpose of a PhD. Peter, I cannot believe how fortunate I was to be part of your research team and be guided by your expertise. Apart from refining my palate at *Cluricaume*, thank you for introducing me to the rigours of jet noise research and consistently challenging me as a research scientist. You and your family's hospitality, generosity and kindness during my stay in Poitiers was most appreciated.

The construction of the new jet facility would not have been possible without the tireless efforts of several talented tradespeople. I want to acknowledge the excellent workmanship of the Monash Mechanical and Aerospace Technical Services Group, in particular Keith Erbs who was assigned to my project and fabricated the jet rig. Danny Lynch, thank you for sharing your knowledge and doing such a fine job with the anechoic chamber, it will be used for many years to come. Phil, I am truly grateful for your support on and off the ice; if it wasn't for you, this facility would not have been built.

My time at LTRAC had been shaped by the friends and colleagues who I saw daily (pre-2020). Thank you to the 'old hands' - Nick, Dom, Joel, Tom, Graham, Mike - who took me under their wing and showed me, despite the daily grind, there is light at the end of the tunnel. I also wish to express my deepest gratitude to the LTRAC 'Larrikans' - Bhav, Rhiannon, Harry, Anesu Junior ('AJ'), Sean and Keith. Thank you for bringing life and excitement into a PhD. I will miss our banter, camaraderie, the weekly beverage sessions and the debut of 'Navier-Stokes City'. I was very fortunate to have you guys around right until the end. Special thanks must go to Tom, Bhav and AJ for being the patient teachers and providing the manpower required during the set up of the Shock Lab; I now know the difference between a 'pipe' and a 'tube'. Rhiannon, thank you for always making time for my spontaneous questions, requests and discussions; collaborating with you had significantly improved the quality of my work.

I was very humbled and fortunate to have had the opportunity to visit Poitiers twice. Nadia and Yves (le chef) - thank you for your hospitality and having to put up with my horrible/non-existent French. I would like to pay my special regards to the 'Petit zoo' group - Igor, Selene, Matteo, Tamon, Oguzhan, Ugur, Bruno, Eduardo, Marc and Evan - thank you all for welcoming me with open arms and for your laughter, support, and understanding. Igor, thanks mate for coming to my aide on a daily basis and for listening to my frequent vents. It was a pleasure getting to know you as a friend and colleague. Merci beaucoup!

Away from the office, I would like to give a shout out to my family. Thank you for bringing me up to never quit before a job is finished. This unyielding temperament was required on numerous occasions. I hope I did you all proud. I would like to pay my special regards to Samim for the daily (and often free) strong lattes. The peculiarity of completing my thesis in the year 2020 will not be forgotten. Nathan ('Cachia'), cheers mate for not even

batting an eye when I had to take over the living room and having to tolerate my outbursts of profanities late into the night during lockdown.

Finally, but most importantly, is my better half. Vaishali, I have no words to express my gratitude for the sacrifices you made so that we could be together while getting our doctorates. I most definitely would not have accomplished this without you by my side. Thank you Dr. Parkash.

*This research was supported by an Australian Government Research Training Program (RTP) Scholarship and the Endeavour Research Leadership Award - an Australian Government initiative.*

# Contents

<b>Abstract</b>	<b>ii</b>
<b>Publications During Enrolment</b>	<b>iv</b>
0.1 Journal Papers . . . . .	iv
0.2 Conference Papers . . . . .	iv
<b>Declaration</b>	<b>vii</b>
<b>Acknowledgements</b>	<b>xii</b>
<b>List of Figures</b>	<b>xxxii</b>
<b>List of Tables</b>	<b>xxxii</b>
<b>Nomenclature</b>	<b>xxxii</b>
<b>1 Introduction</b>	<b>1</b>
1.1 Motivation . . . . .	1
<b>2 Background</b>	<b>4</b>
2.1 Structure of a Shock-Containing Supersonic Jet . . . . .	4
2.1.1 Shock-Cell Structure . . . . .	5
2.1.2 Models for Shock-Cell Structure . . . . .	7
2.1.3 Turbulent Field and Coherent Structures . . . . .	10
2.1.4 Instability Waves . . . . .	11
2.1.5 Wavepackets and Resolvent Analysis . . . . .	12
2.2 Components of Supersonic Jet Noise . . . . .	14

2.2.1	Turbulent Mixing Noise . . . . .	15
2.2.2	Broadband Shock-Associated Noise . . . . .	16
2.2.3	Screech and Resonance Mechanisms . . . . .	18
2.3	Theory of Aerodynamic Noise . . . . .	19
2.3.1	Lighthill's Acoustic Analogy . . . . .	19
2.3.2	Modelling the Lighthill Stress Tensor . . . . .	22
2.4	Wavepacket Models for Turbulent Jet Noise . . . . .	23
2.4.1	Kinematic Models . . . . .	25
2.4.1.1	Axial Source Structure . . . . .	26
2.4.1.2	Azimuthal Source Structure . . . . .	27
2.4.1.3	Coherence decay . . . . .	28
2.4.1.4	Eduction of Wavepacket Characteristics . . . . .	29
2.4.2	Dynamic Models . . . . .	30
2.4.2.1	Parabolised Stability Equations . . . . .	31
2.4.2.2	Prediction of Far-Field Sound . . . . .	32
2.5	Approaches to Modelling Broadband Shock-Associated Noise . . . . .	33
2.5.1	Harper-Bourne and Fisher - Phased Array Model (1973) . . . . .	34
2.5.2	Morris and Miller - Computational RANS Model (2009) . . . . .	36
2.5.3	Tam - Instability Wave Model (1987) . . . . .	37
2.5.4	Wavepacket Models . . . . .	39
2.6	Summary . . . . .	42
2.6.1	Resumé of Research on BBSAN Modelling . . . . .	42
2.6.2	Organisation of Present Work . . . . .	44
<b>3</b>	<b>Design and Development of the Supersonic Jet Anechoic Facility</b>	<b>46</b>
3.1	Introductory Statement . . . . .	46
3.2	LTRAC Shock Laboratory . . . . .	47
3.3	Design Parameters and Requirements . . . . .	49
3.4	Anechoic Chamber . . . . .	51
3.4.1	Foam Wedges & Chamber Wall . . . . .	53
3.4.2	Dimensions . . . . .	56



3.4.3	Chamber Access . . . . .	57
3.4.4	Inlet & Exhaust . . . . .	58
3.5	Co-axial Jet Rig . . . . .	59
3.5.1	Central Air Supply System . . . . .	60
3.5.2	Jet Ducting System . . . . .	64
3.5.2.1	Settling Chamber . . . . .	64
3.5.2.2	Plenum Chambers . . . . .	65
3.5.2.3	Flow Control & Monitoring . . . . .	66
3.5.2.4	Supporting Structures . . . . .	66
3.5.3	Nozzles . . . . .	67
3.6	Concluding Statement . . . . .	68
<b>4</b>	<b>Anechoic Facility Validation</b>	<b>69</b>
4.1	Introductory Statement . . . . .	69
4.2	Instrumentation, Data Processing & Microphone Corrections . . . . .	70
4.2.1	Instrumentation Details . . . . .	70
4.2.2	Acoustic Data Acquisition & Processing . . . . .	72
4.2.3	Microphone Response Corrections . . . . .	72
4.3	Free-field Calibration . . . . .	73
4.3.1	Acoustic Far-Field . . . . .	75
4.3.2	Geometric Far-Field . . . . .	79
4.4	Rig Noise Analysis . . . . .	81
4.5	Comparison of Jet Acoustic Spectra . . . . .	82
4.6	Comparison with Monash Supersonic Jet Facility . . . . .	85
4.7	Uncertainty & Repeatability . . . . .	87
4.8	Concluding Statement . . . . .	88
<b>5</b>	<b>Azimuthal Structure of Broadband Shock-Associated Noise</b>	<b>90</b>
5.1	Introductory Statement . . . . .	90
5.2	Paper: Introduction . . . . .	92
5.3	Paper: Methodology . . . . .	93
5.3.1	Facility Overview . . . . .	93

5.3.2	Coordinate Systems . . . . .	95
5.3.3	Operating Conditions . . . . .	95
5.3.4	Data Acquisition . . . . .	95
5.3.5	Microphone Array and Azimuthal Decomposition . . . . .	95
5.4	Paper: Experimental Results and Analysis . . . . .	95
5.4.1	Single Microphone Far-field Noise Spectrum . . . . .	95
5.4.2	Azimuthal Modal Analysis of the Midfield . . . . .	96
5.5	Paper: Summary and Outlook . . . . .	99
5.6	Paper: Appendix . . . . .	100
5.7	Paper: References . . . . .	103
5.8	Concluding Statement . . . . .	105
<b>6</b>	<b>Line Source Wavepacket Model for Broadband Shock-Associated Noise</b>	<b>107</b>
6.1	Introductory Statement . . . . .	107
6.2	Paper: Introduction . . . . .	110
6.3	Paper: Mathematical Model . . . . .	114
6.4	Paper: Acoustic Efficiency and Directivity . . . . .	117
6.4.1	Parameters of the Source Model . . . . .	117
6.4.2	Far-field Acoustic Predictions . . . . .	118
6.5	Paper: Interpretation of Sound-Radiation Characteristics . . . . .	121
6.5.1	Fourier Transform into Wavenumber Space . . . . .	121
6.5.2	Nonlinear Interaction Terms . . . . .	123
6.6	Paper: Coherence Decay and Higher-Order shock-cell modes . . . . .	125
6.7	Paper: Conclusions and Perspectives . . . . .	129
6.8	Paper: Appendix . . . . .	129
6.9	Paper: References . . . . .	132
6.10	Concluding Statement . . . . .	135
<b>7</b>	<b>Wavepacket Model for Broadband Shock-Associated Noise</b>	<b>137</b>
7.1	Introductory Statement . . . . .	137
7.2	Paper: Introduction . . . . .	140
7.3	Paper: Mathematical Formulation . . . . .	143

7.3.1	Sound Prediction Using Lighthill's Acoustic Analogy . . . . .	143
7.3.2	Equivalent BBSAN Source Model . . . . .	145
7.4	Paper: Databases . . . . .	146
7.4.1	Numerical Database . . . . .	146
7.4.2	Experimental Database . . . . .	147
7.4.3	Acoustic Database . . . . .	147
7.5	Paper: Construction of Source Variables . . . . .	148
7.5.1	Eduction of Shock-Cell Structure . . . . .	148
7.5.2	Eduction of Wavepacket Component . . . . .	150
7.5.3	Coherence-matched Source Term . . . . .	153
7.5.4	Summary of BBSAN Source Model Construction . . . . .	153
7.6	Paper: Nearfield Predictions and Comparisons . . . . .	155
7.6.1	Shock-cell Component . . . . .	155
7.6.2	Wavepacket Component . . . . .	155
7.7	Paper: Far-field Acoustic Spectra and Comparisons with Experiment . . . . .	159
7.7.1	Directivity Contour Maps . . . . .	159
7.7.2	Far-field Noise Spectra . . . . .	162
7.8	Paper: Source Term Characteristics . . . . .	166
7.9	Paper: Summary and Conclusions . . . . .	169
7.10	Paper: Appendix . . . . .	170
7.11	Paper: References . . . . .	172
7.12	Further Comparisons Between PSE and LES Wavepackets . . . . .	179
7.13	Discussion of the Use of PSE . . . . .	184
7.14	Concluding Statement . . . . .	185
<b>8</b>	<b>Conclusions</b>	<b>187</b>
8.1	Summary of Main Results . . . . .	187
8.2	Open Issues and Future Outlook . . . . .	190
	<b>Bibliography</b>	<b>193</b>

**A Kinematic Wavepacket model for Broadband Shock-Associated Noise in Underex-**  
**panded Supersonic Jets** **210**

A.1 Introductory Statement . . . . . 210

A.2 Conference Paper . . . . . 210

**B A Parabolised Stability Equation Based Broadband Shock-Associated Noise Model**  
**225**

B.1 Introductory Statement . . . . . 225

B.2 Conference Paper . . . . . 225

**C SJAF Design Drawings** **242**

C.1 Introductory Statement . . . . . 242

C.2 Anechoic Chamber Drawings . . . . . 242

C.3 Jet Rig Drawings . . . . . 248

# List of Figures

1.1	Sound radiation from a hot overexpanded supersonic jet. Pressure fluctuations are shown as black and white contours. Colours show temperature fluctuations. Schematic of jet (blue) and observer (green) coordinate systems are overlaid; the azimuthal angle $\phi$ is common between both. Large-eddy simulation figure taken from Brès <i>et al.</i> [8]. . . . .	2
2.1	Colour schlieren of a $NPR = 3.4$ underexpanded supersonic jet measured in the LTRAC supersonic jet facility; mean image (top) and instantaneous snapshot (bottom). Images obtained by R. Kirby. . . . .	5
2.2	Shock-cell structure; schematic adapted from Savarese [19] (upper) and mean schlieren (lower). Schlieren image obtained by R. Kirby. . . . .	6
2.3	Schematic of a shock-cell system bounded by a vortex sheet. Adapted from Tam and Tanna [23] . . . . .	8
2.4	Centreline shock modes from an underexpanded jet. Adapted from Tam <i>et al.</i> [28] . . . . .	9
2.5	Axisymmetric wavepackets detected in subsonic (left) [56] and supersonic (right) [72] turbulent jets at $St = 0.5$ . The pressure and axial velocity components are shown in the upper and lower rows respectively. . . . .	13
2.6	The acoustic spectrum of jet noise measured at $\theta = 110^\circ$ relative to the downstream jet axis (left). Near-field sound pressure map showing the directivity behaviour of different noise components (right). . . . .	15
2.7	Wavy-wall analogy for Mach wave radiation. Taken from Tam [2]. . . . .	16

2.8	Directivity behaviour of different components of $T_{ij}$ ; a) $T_{11}$ b) $T_{12}$ . Taken from Crighton [105]. . . . .	21
2.9	Representative wavepacket line source at different frequencies. Taken from Maia <i>et al.</i> [116] . . . . .	26
2.10	Effect of coherence decay in wavenumber space; sound source with perfect coherence (left) and with coherence decay (right). Squares indicate the radiation criterion for subsonic (red) supersonic (green). Adapted from Cavalieri <i>et al.</i> [14]. . . . .	29
2.11	Different representations of the BBSAN source from; (a) experimental causality analysis performed by Savarese <i>et al.</i> [53], (b) equivalent discrete sources from a RANS-CFD approach [148], (c) unfiltered source map from Ray and Lele [149] and (d) the same source as (c) but with only the radiating component shown. . . . .	34
2.12	Phased array antenna model proposed by Harper-Bourne and Fisher. Adapted from Harper-Bourne [21]. . . . .	35
2.13	Artificial dips observed in Tam's BBSAN similarity model ( $\psi^o = 180^\circ - \theta^o$ ). Taken from Tam [157]. . . . .	39
3.1	Isometric view of the laboratory space housing SJAF (coloured). . . . .	48
3.2	Initial design envelope for jet facility. . . . .	51
3.3	Schematic of the anechoic chamber. . . . .	53
3.4	Estimated transmission loss across single and double panel walls. . . . .	54
3.5	Foam panels and arrangement; isometric (left) and top (right) views. . . . .	55
3.6	Removable window wedge panels (left), floor panels (centre) and door (right) of the anechoic chamber. . . . .	57
3.7	Top and side views showing the proposed laser path (green) and optical equipment set-up for planar PIV experiments. . . . .	59
3.8	Isometric (left) and sectioned-top (right) view of the integration of jet plumbing with anechoic chamber. . . . .	60
3.9	Run time as a function of mass flow rate. Red dashed line indicates a 20 minute run time. . . . .	62

3.10	Run time as a function of nozzle exit diameter for a range of NPR. Red-dashed line indicates a 20 minute run time. . . . .	63
3.11	Run time as a function of NPR for an different nozzle exit areas. . . . .	63
3.12	Cross-section side view schematic of jet rig. . . . .	64
3.13	Spider for core jet centrebody. Tabs not shown. . . . .	67
4.1	Mounting of microphones. . . . .	71
4.2	Corrections for microphone pressure measurements; a) effect of protective grid on microphone pressure readings and b) schematic of manufacturer-specified free-field corrections. Adapted from Ahuja [161]. . . . .	73
4.3	Free-field corrections for G.R.A.S. Type 40BE microphone without protective grid for a range of incident angles. . . . .	74
4.4	Microphone traverse directions as specified by ISO 3745. . . . .	76
4.5	Deviation from the inverse-square law. Tolerances (red-dashed lines) from ISO 3745. . . . .	77
4.6	Microphone directions for jet source measurement. Microphone not shown. .	78
4.7	Deviation from the inverse-square law at three different polar angles for a range of frequencies. Red-dashed lines indicates maximum permissible deviation as specified by ISO 3745. Distance is normalised by jet diameter. . . . .	78
4.8	Deviation from the inverse-square law for $M_j = 0.5$ . . . . .	79
4.9	Deviation from the inverse-square law for $M_j = 0.9$ . . . . .	80
4.10	Deviation from the inverse-square law for $M_j = 1.5$ . . . . .	80
4.11	OASPL as a function of jet velocity for $\theta = 30^\circ$ (left), $\theta = 90^\circ$ (centre) and $\theta = 120^\circ$ (right). . . . .	82
4.12	OASPL as a function of $\beta$ for $\theta = 60^\circ$ (circles) and $\theta = 90^\circ$ (triangles). . . . .	83
4.13	Comparisons with subsonic jet noise measurements from Bridges and Brown [195] (NASA). . . . .	84
4.14	Comparison with one-third octave spectra data from Norum and Seiner [29] for an underexpanded jet at $NPR = 3.67$ . . . . .	85

4.15	Comparison of far-field noise ( $50D$ ) measured in the SJF (left) and in the SJAF (right); $NPR = 2.6$ (upper) and $NPR = 3.4$ (lower). Dashed-lines show predictions from the model of Tam and Tanna [23] (equation 2.13) and contours are in units of dB/St. . . . .	86
4.16	One-third octave spectra repeatability in the SJAF at condition $NPR = 3.67$ for observer position $\theta = 90^\circ$ . Note for case '17-May-2020' the spectra was taken with microphone protective grid on. . . . .	88
5.1	Schematics of facility and experimental setup; (a) sectioned plan and side view schematic of SJAF showing key components of the facility (dimensions in mm), (b) schematic of adopted coordinate system, (c) azimuthal ring set-up (colour Online). . . . .	94
5.2	(Colour Online) Effect of changing NPR at (a) $\theta = 60^\circ$ , (b) $\theta = 90^\circ$ and the dependence on $\beta^4$ as a function of $M_j$ . . . . .	96
5.3	(Colour Online) Directivity contour plots for power spectral density (PSD) in the far-field ( $R = 50D$ ) for NPRs (a) 2.25, (b) 3.10 and (c) 3.67. Polar angles taken with respect to downstream jet axis and contours are in dB/St. Dashed lines indicate peak frequency predictions from Eq.(1). . . . .	97
5.4	(Colour Online) Decomposed acoustic spectra in the mid-field ( $R = 11D$ ) for different NPRs; $NPR = 2.25$ (upper row), 3.10 (middle row) and 3.67 (lower row). Polar angles taken with respect to downstream jet axis; $\theta = 80^\circ$ (left column), $\theta = 95^\circ$ (middle column) and $\theta = 115^\circ$ (right column). . . . .	98
5.5	(Colour Online) Full and decomposed spectra in the mid-field ( $R = 11D$ ) for different conditions; $NPR = 2.25$ (upper row), $NPR = 3.10$ (middle row) and $NPR = 3.67$ (lower row). Polar angles taken with respect to downstream jet axis and contours are in dB/St. Dashed lines indicate peak frequency predictions from Eq.(1). . . . .	99



5.6	(Colour Online) Reconstruction of the acoustic field with modes added successively ( $m = 0, \pm 1, \pm 2 \dots$ ). Top row; $St - \theta$ maps displaying the number of modes required to reconstruct the total acoustic signal to within 1dB/St for $NPR =$ a) 2.25, b) 3.10 and c) 3.67. The 130dB/St contour (red line) identifies the primary BBSAN lobe seen in Fig.5. The vertical dashed lines locate $\theta = 95^\circ$ . Bottom row; Reconstruction of acoustic spectrum at $\theta = 95^\circ$ with increasing number of modes. . . . .	100
5.7	Deviation from the inverse-square law at three different angles for a range of frequencies and polar angles. Red dashed line indicates maximum permissible deviation as specified by ISO 3745. . . . .	102
5.8	Example of an interpolated fit to the $R_{pp}$ two-point data as a function of azimuthal separation for $NPR = 3.67$ at $\theta = 95^\circ$ for a) $St = 0.2$ and b) $St = 0.7$ . . . . .	102
6.1	Contours of sound pressure level (arbitrary dB) as a function of frequency ( $St$ ) and directivity ( $\theta$ ) for a) unit coherence and b) with coherence decay. The jet issues from a converging nozzle ( $M_d = 1.0$ ) at a nozzle pressure ratio of $NPR = 3.4$ which corresponds to a fully-expanded jet Mach number of $M_j = 1.45$ and an off-design parameter of $\beta = 1.04$ . The dashed line indicates the peak frequency as predicted by Harper-Bourne and Fisher [20]. . . . .	119
6.2	Sound pressure level at a distance of $100D$ for a wavepacket frequency of a) $St = 0.3$ and b) $St = 0.6$ as a function of observation angle $\theta$ for a wavepacket with $k_h L = 5$ . . . . .	119
6.3	Power spectrum at a distance of $100D$ through a range of observation angles between $\theta = 60^\circ$ to $\theta = 150^\circ$ measured from the downstream jet axis for a wavepacket with $k_h L = 5$ . Each measurement angle is offset by $\Delta dB = 25$ . NASA experimental data from Norum and Seiner [200]. . . . .	120

- 6.4 The real part of the CSD of the unit coherence (a) and with statistical decay (b) models for  $L_c = 1.0D$ . The diagonal line represents  $y_1 = y_2$ . The corresponding Fourier transformed CSD in wavenumber space of the unit coherence (c) and with statistical decay (d) models. Diagonal line corresponds to  $k_{y1} = -k_{y2}$ . The square represents the acoustic matching criterion  $|k|/k_h = 0.6M_j$ . The amplitude of both models have been normalised to highlight the effect of coherence decay. The wavepacket frequency is  $St = 0.4$  for a jet operating at  $\beta = 1.04$ . . . . . 122
- 6.5 Power spectrum at a distance of  $100D$  through a range of observation angles between  $\theta = 60^\circ$  to  $\theta = 150^\circ$  measured from the downstream jet axis for a wavepacket with  $k_h L = 5$  for multiple shock-cell waveguide modes. Each measurement angle is offset by  $25dB$ . NASA experimental data from Norum and Seiner [200]. . . . . 126
- 6.6 The corresponding Fourier transformed CSD in wavenumber space for  $St = 0.4$  and  $St = 0.6$ . Left-hand side frames ((a) and (c)) correspond to the unit coherence model while the right-hand side ((b) and (d)) are for the two-point model with a coherence decay length  $L_c = 1.0D$ . Diagonal line corresponds to  $k_{y1} = -k_{y2}$ . The square represents the acoustic matching criterion  $|k|/k_h = 0.6M_j$ . The amplitude of both models have been normalised to highlight the effect of coherence decay. The jet is operating at  $\beta = 1.04$ . . . . . 127
- 6.7 Fourier transform of CSD for a)  $St = 0.4$  and b)  $St = 0.6$  extracted along the line  $k_{y1} = -k_{y2}$ . The vertical lines represent different observation angles; dashed line =  $60^\circ$ , dash-dotted line =  $90^\circ$  and dotted line =  $150^\circ$ . Solid (green) vertical lines represent the acoustic matching criterion. . . . . 128
- 6.8 Effect of modelling variables on the acoustic power spectrum when (a) changing convection velocity  $u_c$ , (b) changing amplitude width  $C_2$ , (c) changing wavepacket envelope length scale  $L$ , (d) changing coherence decay length scale  $L_c$  for an observation angle of  $\theta = 150^\circ$  at a distance of  $100D$ . The modelled jet is operating at a nozzle pressure ratio of  $NPR = 3.4$ . . . . . 130

6.9	Contours of sound pressure level (arbitrary dB) as a function of frequency ( $St$ ) and directivity ( $\theta$ ) for a range of $L_c$ and $L$ . Each row corresponds to the two-point model with constant value of $L_c$ ; a)-c) $L_c = 0.5D$ , d)-f) $L_c = 1.0D$ , g)-i) $L_c = \infty$ . Each column corresponds to the two-point model with constant value of $k_h L$ ; $k_h L = 3.0$ (a),d) and g)), $k_h L = 5.0$ (b),e) and h)) and $k_h L = 7.0$ (c),f) and i)). The modelled jet is operating at a nozzle pressure ratio of $NPR = 3.4$ .	131
7.1	Schematic of experimental setup with the prescribed source ( $x, r, \phi$ ) and observer ( $R, \theta, \phi$ ) coordinate systems. . . . .	144
7.2	LES (left) and PIV (right) $x - r$ contour mean fields for ideally-expanded and shock-containing jets respectively; streamwise velocity (top), radial velocity (centre) and density (bottom). Flow quantities are normalised by the ideally-expanded condition. . . . .	147
7.3	Summary of BBSAN model construction; (a) source model with $q_t$ obtained directly from LES data and (b) statistical source model with $q_t$ obtained from PSE solutions. . . . .	154
7.4	$x - r$ contour plots of flow variables $u_x, u_r, \rho$ from PIV experiments (top-plane) and model (bottom-plane). . . . .	156
7.5	Comparison of real parts of $u_x$ between the extracted wavepacket from the first SPOD mode (left column) and PSE predictions (right column) for $m = 0$ . Flow quantities are normalised by the ideally-expanded condition. . . . .	157
7.6	Radial cross-section comparisons of $u_x$ between LES (symbols) and PSE (lines) for $m = 0$ at $x = 4D$ . . . . .	157
7.7	Centreline axial velocity fluctuations from LES (symbols) and PSE (lines) for $m = 0$ . . . . .	158
7.8	Convection velocity as a function of axial position for $m = 0$ . . . . .	159
7.9	$St - \theta$ directivity contour maps of sound pressure level spectra at $R = 11D$ . Contours are in dB/St. . . . .	161
7.10	Comparison of acoustic spectra for total measured signal and reconstructed model using the first three azimuthal modes $m = 0, 1, 2$ . . . . .	163
7.11	Comparison of acoustic spectra for azimuthal mode $m = 0$ . . . . .	164

7.12	Comparison of acoustic spectra for azimuthal mode $m = 1$ . . . . .	165
7.13	Comparison of acoustic spectra for azimuthal mode $m = 2$ . . . . .	166
7.14	$x - r$ contour maps of the reconstructed BBSAN source PSD. Intensity levels are normalised by the maximum value. . . . .	167
7.15	The normalised real components of the CSD of $S_{11}$ for $m = 0$ and frequencies $St = 0.6$ (top row) and $St = 0.8$ (bottom row). The different reconstructed source models are LES (left column), PSE without coherence decay (centre column) and PSE with coherence decay (right column). Contours levels are from -0.5 to 0.5 and normalised by the maximum value. . . . .	168
7.16	Variation in peak BBSAN predictions as predicted by equation (1.2) due to differences in jet parameters for the first three shock-cell modes ( $n_s = 1, 2, 3$ ). For the cold jet, a convection velocity of $u_c = 0.7U_j$ was used for both plots while the relationship in equation (B2) was used for the heated case. . . . .	172
7.17	Radial cross-section comparisons between LES (symbols) and PSE (lines) for $m = 0$ at $x = 4D$ . . . . .	180
7.18	Radial cross-section comparisons between LES (symbols) and PSE (lines) for $m = 1$ at $x = 4D$ . . . . .	181
7.19	Comparison of real parts of $q_t$ between the extracted wavepacket from LES (left column), corresponding first SPOD mode (centre column) and PSE predictions (right column) for $m = 0$ . Flow quantities normalised by the ideally-expanded condition. . . . .	182
7.20	Comparison of real parts of $q_t$ between the extracted wavepacket from LES (left column), corresponding first SPOD mode (centre column) and PSE predictions (right column) for $m = 1$ . Flow quantities normalised by the ideally-expanded condition. . . . .	183
7.21	Alignment metric $\mathcal{B}$ for $m = 0$ (left) and $m = 1$ (right) for a range of frequencies. Circles and triangles represent alignment with full LES signal and the first SPOD mode respectively. . . . .	185

# List of Tables

3.1	Design parameters for the new facility. . . . .	49
3.2	Summary of some anechoic jet noise facilities. . . . .	52
4.1	Maximum deviations allowed for SPL measured in an anechoic chamber. . .	75
5.1	Summary of jet operating conditions. . . . .	95
6.1	Constant values for each parameter used in proposed model. . . . .	130
7.1	Summary of jet operating parameters for each database. . . . .	145
7.2	Summary of LES parameters. . . . .	146
7.3	Summary of source model inputs. . . . .	153

# Nomenclature

## Abbreviations

<i>BBSAN</i>	Broadband shock-associated noise
<i>BOS</i>	Background-oriented schlieren
<i>CSD</i>	Cross spectral density
<i>FFT</i>	Fast fourier transform
<i>K – H</i>	Kelvin Helmholtz
<i>LES</i>	Large-eddy simulation
<i>NPR</i>	Nozzle pressure ratio
<i>NS</i>	Navier Stokes
<i>OASPL</i>	Overall sound pressure level
<i>P – P,PP</i>	Pack & Prandtl
<i>PIV</i>	Particle image velocimetry
<i>PSD</i>	Power spectral density
<i>PSE</i>	Parabolised stability equations
<i>RANS</i>	Reynolds-averaged Navier-Stokes
<i>SJAF</i>	Supersonic Jet Anechoic Facility
<i>SJF</i>	Supersonic Jet Facility
<i>SPL</i>	Sound pressure level
<i>SPOD</i>	Spectral proper orthogonal decomposition
<i>TTR</i>	Total temperature ratio

## Greek symbols

$\beta$	Off-design parameter
$\gamma$	Ratio of specific heats; Coherence function

$\nabla$	Gradient operator
$\omega$	Angular frequency
$\phi$	Azimuthal angle
$\rho$	Density
$\tau$	Viscouss stress
$\theta$	Observer angle measured from downstream jet axis

**Roman symbols**

$q$	Flow variables
$x$	Source coordinates
$y$	Observer coordinates
$v$	Total velocity vector
$\mathcal{A}, A$	Arbitrary source amplitude
$A$	Area
$a$	Speed of sound
$c$	Speed of sound
$D$	Nozzle diameter
$f$	Frequency
$G$	Green's function
$i, j$	Tensor components
$J$	Bessel Function
$k$	Wavenumber
$L$	Characteristic length scale
$M$	Mach number
$m$	Azimuthal mode number
$n$	Shock-cell mode number
$p$	Pressure
$R$	Specific gas constant; Radial distance to observer
$r$	Jet radial direction
$S$	Source term
$St$	Strouhal number

$T$	Temperature
$t$	Time
$T_{ij}$	Lighthill's stress tensor
$U$	Mean jet velocity
$u$	Total jet velocity
$x$	Jet axial direction
$Re$	Reynolds number

### Subscripts

0	Total condition
$\infty$	Ambient condition
$a$	Acoustic component
$c$	Convective condition
$c$	Core nozzle condition
$cf$	Co-flow nozzle condition
$d$	Design condition
$e$	Exit condition
$h$	Hydrodynamic component
$j$	Ideally-expanded condition
$p$	Peak condition
$ref$	Reference condition
$s$	Shock component
$t$	Tank condition
$t$	Turbulence component

### Superscripts

$'$	Fluctuating component
-----	-----------------------





# Chapter 1

## Introduction

### 1.1 Motivation

With the ubiquity of high-bypass turbofan engines on current aircraft, the intense noise radiated from the exhaust, to both the community and those on board, remains an important issue [1]. At cruise conditions, the high thrust requirements result in supersonic jet efflux velocity. As summarised by Tam [2], noise from supersonic jets may be separated into three distinct components. In addition to low-frequency turbulent mixing noise, which is dominant at downstream angles, imperfectly-expanded flows also produce screech and broadband shock-associated noise (BBSAN). Discrete screech tones are generated by a self-reinforcing aeroacoustic feedback loop [3–5]. Non-resonant interaction of jet turbulence with the shock-cells produces BBSAN, which is most intense in the sideline directions. The distinctive sound radiation pattern of a shock-containing jet may be observed in figure 1.1. Interest in BBSAN remains high for both commercial [6] and high-performance military [7] aircraft. This component of supersonic jet noise is the focus of this thesis.

Requirements to meet strict noise regulations [9], protection from hearing loss for civilian and military personnel [10, 11], and on-going interest in supersonic transport [12] are often the primary motivations for studying supersonic jet noise. The goal is to implement noise reduction systems. Such systems may either be achieved by trial and error strategies or directly addressing the problem at the source. The latter approach requires an intimate understanding of the sound generation mechanisms which are often concealed in the jet's turbulent field.

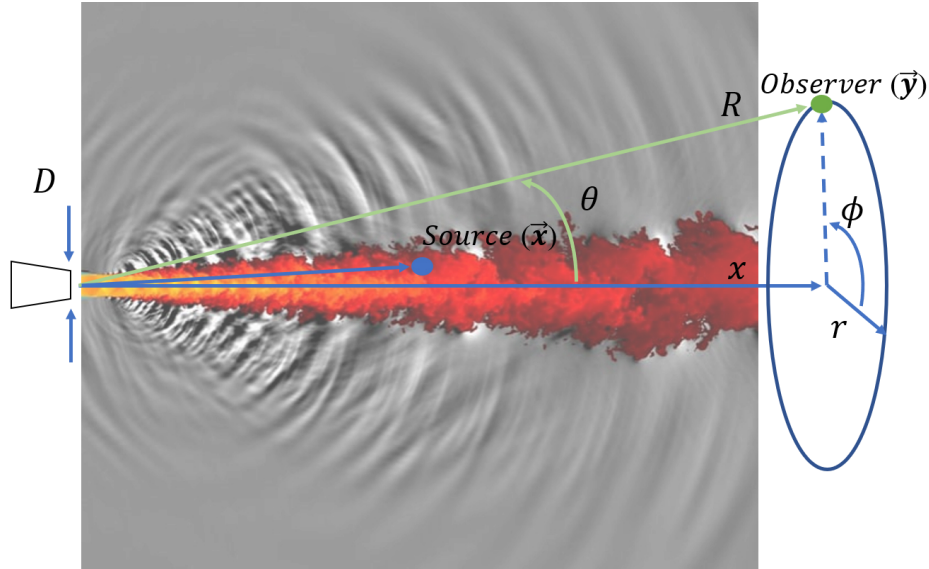


Figure 1.1: Sound radiation from a hot overexpanded supersonic jet. Pressure fluctuations are shown as black and white contours. Colours show temperature fluctuations. Schematic of jet (blue) and observer (green) coordinate systems are overlaid; the azimuthal angle  $\phi$  is common between both. Large-eddy simulation figure taken from Brès *et al.* [8].

The identification of sound sources in turbulent flows falls into the discipline of aeroacoustics; the study of sound generation by unsteady aerodynamic forces. Motivated by the jet noise problem, the mathematical foundations of the field were formally developed by Sir James Lighthill [13] in 1952. Despite the existence of Lighthill's general theory, however, a general consensus in the modelling approach for jet noise has eluded researchers to this day. As highlighted by Cavalieri *et al.* [14] and Freund [15], the *scale-disparity* between the seemingly chaotic turbulent structures and organised acoustic pressure waves poses a significant obstacle in modelling jet noise; the epigraphs of this thesis eloquently summarise this challenge. A cursory observation of the problem (figure 1.1) would suggest that the task is even more daunting in a shock-containing supersonic jet where strong discontinuities exist and non-linear effects dominate.

The body of work by Tam and co-workers (summarised by Tam [2]) in the 1980s suggests BBSAN is generated by instability waves interacting with the repetitive shock-cell structure. His model is successful in recovering many of the spectral and directivity trends. The results implicitly indicate much of the chaotic turbulent motion is acoustically redundant, and only suitable descriptions of the large-scale deterministic structures of the jet are needed to predict BBSAN. Beneath the fine-scale stochastic turbulence, there exist well-defined orderly

structures known as *wavepackets* [14, 16], also referred to as instability waves. In terms of sound generation, despite having lower energies than the aggregate of all stochastic eddies, they possess much of the acoustically-important turbulence motion that drives the relatively weak acoustic field. Being largely determined by the properties of the operator that is obtained by linearising the Navier-Stokes equations about the time average, wavepackets offer insight into underlying dynamic laws. Hence, if successful, wavepacket models may offer a new appreciation of the coveted sound source mechanisms.

Extending the work of Tam, this thesis discusses the use of wavepackets to model the coherent turbulent structures that interact with the shock-cells to generate BBSAN. High-quality acoustic measurements are required to check model predictions. To this end, the first half of the thesis is focused on the design, construction and validation of a new jet noise facility. An experimental acoustic campaign was conducted to measure the azimuthal structure of BBSAN. In parallel, important flow features associated with BBSAN emission were highlighted by using a simple model problem. The findings culminate in the development of a new wavepacket model for BBSAN. The encouraging results offer an explanation to some of the outstanding problems encountered in previous modelling attempts.

The following discussion is aided by introducing the coordinate system for a turbulent jet as depicted in figure 1.1. Unless otherwise specified, the turbulent field is cast in cylindrical coordinates: the  $x$ -axis is aligned with the jet centreline,  $r$  is the radial distance and  $\phi$  the azimuthal angle. For a far-field observer, the azimuthal coordinate of the cylindrical system is used, the polar angle  $\theta$  is defined from the downstream jet axis and  $R$  is the distance from the nozzle exit to the observer.

## Chapter 2

# Background

### 2.1 Structure of a Shock-Containing Supersonic Jet

The generation of BBSAN occurs in jet plumes containing shock cells, and the presence of those shock cells is determined by the jet exit conditions. In both convergent and convergent-divergent nozzles, shock cells may form when the jet is operated at off-design conditions. Despite shocks being a non-isentropic phenomena, an important parameter to consider is the ideally-expanded Mach number  $M_j$  (see section 2.1.1).

For convergent-divergent nozzles, only a single upstream condition permits the flow to isentropically expand to a specific exit velocity greater than the speed of sound. Referred to as the ideally or perfectly-expanded condition, the jet exit pressure is equivalent to the ambient ( $p_e = p_\infty$ ), and the jet velocity  $U_j$  is related to  $M_j$  via,

$$M_j = U_j/c_j, \quad (2.1)$$

where the subscript  $j$  denotes ideally-expanded conditions. The speed of sound  $c_j$  may be evaluated by  $\sqrt{\gamma R T_j}$ , where  $T_j$  is the ideally-expanded temperature of the jet and  $R$  is the gas constant. The ideally-expanded jet Mach number is characterised by the ratio of total pressures between the upstream reservoir  $p_0$  and the quiescent air  $p_\infty$ . Using isentropic relations, the nozzle pressure ratio (NPR) is related to  $M_j$  as,

$$NPR = \frac{p_0}{p_\infty} = \left(1 + \frac{\gamma - 1}{2} M_j^2\right)^{\frac{\gamma}{\gamma - 1}}, \quad (2.2)$$

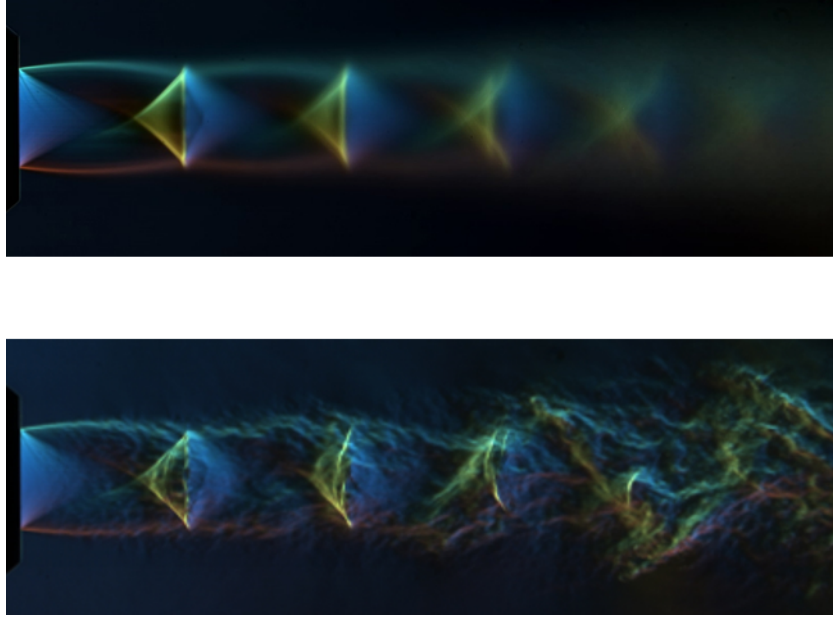


Figure 2.1: Colour schlieren of a  $NPR = 3.4$  underexpanded supersonic jet measured in the LTRAC supersonic jet facility; mean image (top) and instantaneous snapshot (bottom). Images obtained by R. Kirby.

where  $\gamma$  is the specific heat ratio of air. The critical pressure ratio for air is  $NPR = 1.89$ . At this condition, the exit ( $M_e$ ) and ideally-expanded Mach numbers will be equivalent.

A continual increase in  $p_0$  will not increase exit Mach number since the flow is choked. As there is an imbalance in pressures at the exit ( $p_e \neq p_\infty$ ), the jet is said to be imperfectly expanded ( $M_e \neq M_j$ ). In the case of an underexpanded jet ( $p_e > p_\infty$ ), a series of expansion and compression waves exists downstream of the nozzle exit to return the flow to ambient conditions. This results in the formation of shock diamonds or shock cells (figure 2.1). Because of entrainment of the surrounding fluid, the shocks begin to dissipate further downstream as observed in figure 2.1, signalling the end of the jet's potential core [17]. Once ambient conditions are met, the flow field becomes subsonic and mean velocity profiles will emulate the fully-developed region of a subsonic jet.

### 2.1.1 Shock-Cell Structure

For an underexpanded jet, the typical shock-cell structure is shown in figure 2.2. As the pressure at the exit is higher than the ambient, a series of expansion fans form at the nozzle lip, accelerating the flow and causing the jet to initially bulge out. Consequently, the pressure in the region 'R-I' decreases. At the jet boundary (sonic line), the Mach lines of the fans are

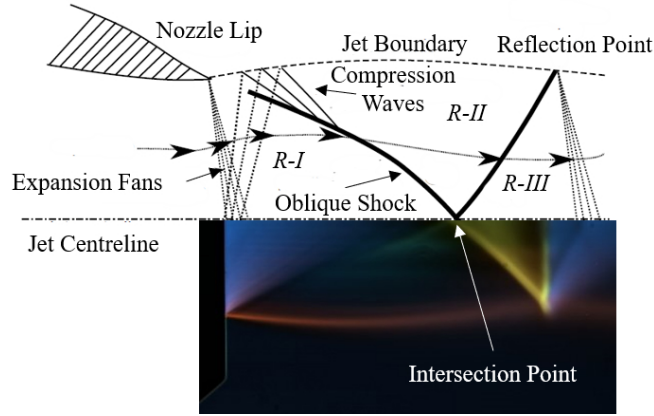


Figure 2.2: Shock-cell structure; schematic adapted from Savarese [19] (upper) and mean schlieren (lower). Schlieren image obtained by R. Kirby.

reflected as compression waves, because of the pressure equilibrium requirement between the side of the high-speed flow and that of the quiescent medium. The curvature of the jet boundary forces the compression waves to coalesce and form an oblique shock. The oblique shocks from the upper and lower half of the jet meet at the intersection point, and force the flow to once again decelerate in the region 'R-III'. Upon reaching the jet boundary at the reflection point, a series of expansion fans ensues ending the first period of the shock-cell structure. The constant acceleration and deceleration of the flow continues until ambient conditions are reached. For a large NPR, a Mach disk will be visible [18].

The properties of the shock structure are largely determined by the operating pressure ratio. An important parameter to consider for an imperfectly-expanded jet is the off-design parameter  $\beta$ ,

$$\beta = \sqrt{M_j^2 - M_d^2}, \quad (2.3)$$

where  $M_d$  is the design Mach number of the nozzle. For convergent nozzles, the design Mach number is always unity, whereas, for convergent-divergent nozzles,  $M_d$  will vary depending on the geometry. The off-design parameter indicates the degree of over- or under-expansion of the jet plume [20]. Since  $M_j$  is only a function of the nozzle pressure ratio (equation 2.2), the pressure imbalance at the nozzle exit may be approximated by

$$\frac{\Delta p}{p_\infty} \propto \beta^2. \quad (2.4)$$

Each shock cell is separated by a distance  $L_s$ . From experiments, Harper-Bourne and Fisher [20] were able to measure and approximate this separation in terms of nozzle diameter ( $D$ )

$$L_s = 1.1D\beta. \quad (2.5)$$

As observed in figure 2.1, however,  $L_s$  decreases with increasing distance from the nozzle exit. Harper-Bourne [21] later suggested that the subsequent spacing ( $L_M$ ) of the  $M^{th}$  shock-cell may be empirically obtained according to

$$L_M = L_1 - (M - 1)\Delta L, \quad \Delta L = \kappa L_1, \quad (2.6)$$

where  $\kappa = 0.06$ . The value of  $\kappa$  changes depending on whether screech is present or not; screech has a significant effect on the shock-cell structure [22]. As shown in figure 2.2, for an underexpanded jet, the expansion fans at the nozzle exit results in the ideally-expanded (or effective) jet diameter  $D_j$  being larger than the exit itself. Tam and Tanna [23] showed the relationship to be

$$\frac{D_j}{D} = \left[ \frac{1 + \frac{1}{2}(\gamma - 1)M_j^2}{1 + \frac{1}{2}(\gamma - 1)M_d^2} \right]^{\frac{\gamma+1}{4(\gamma-1)}} \left( \frac{M_d}{M_j} \right)^{1/2}. \quad (2.7)$$

In reality, the shock cells are not stationary. Several mechanisms (aeroacoustic resonance loops, interaction with turbulent structures) may cause them to fluctuate around the jet centreline [24]. This may be observed in the instantaneous snapshot in figure 2.1; unlike the mean field, the intersection points of the three shock cells do not axially align with each other. The motion of the shocks becomes more violent further downstream. In most BBSAN models, however, they are approximated as stationary.

### 2.1.2 Models for Shock-Cell Structure

Models have been developed to describe the near-periodic shock-cell structure. For weakly imperfectly-expanded jets, the perturbations follow a near sinusoidal behaviour. Thus, it is permissible to idealise the shock-cells as a stationary wave with a characteristic wavelength  $\lambda_s$ . Prandtl [25] assumed the shock cells to be small perturbations about a potential flow



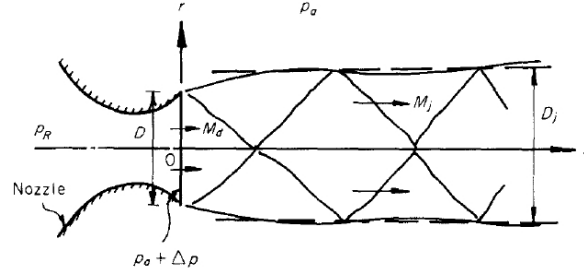


Figure 2.3: Schematic of a shock-cell system bounded by a vortex sheet. Adapted from Tam and Tanna [23]

bounded by a vortex sheet (figure 2.3). Following corrections by Pack [26], the Pack and Prandtl (P-P) shock-cell model was conceived. For an axisymmetric jet, the shock-cell perturbations are now described by a sum of stationary waves, compactly summarised by Tam [27] as

$$\begin{aligned}\frac{p_s}{p_\infty} &= \sum_n A_n J_0\left(\frac{2r\alpha_n}{D}\right) \cos(k_{s_n}x), \\ \frac{u_s}{U_j} &= -\frac{1}{\rho_j U_j} \sum_n A_n J_0\left(\frac{2r\alpha_n}{D}\right) \cos(k_{s_n}x), \\ \frac{v_s}{U_j} &= -\frac{\beta}{\rho_j U_j} \sum_n A_n J_1\left(\frac{2r\alpha_n}{D}\right) \sin(k_{s_n}x),\end{aligned}\tag{2.8}$$

where  $J_0$  and  $J_1$  are Bessel functions of order zero and one respectively, and  $\alpha_n$  denotes the  $n$ -th root of the zeroth-order Bessel function. For each shock-cell mode, the characteristic wavenumber and amplitude  $k_{s_n}$  and  $A_n$  are given by

$$k_{s_n} = \frac{2\alpha_n}{D_j\beta'},\tag{2.9}$$

$$A_n = \frac{2\Delta p}{\alpha_n J_1(\alpha_n) p_\infty}.\tag{2.10}$$

Some important relationships may be deduced from equations 2.8-2.10. Firstly,  $L_s$  is related to the fundamental wavenumber by  $L_s = 2\pi/k_{s_1}$  [23]. The wavenumber is inversely proportional to the off-design parameter which agrees with the observation that shock-cell separation increases with Mach number. By combining equation 2.4 with equation 2.10, the

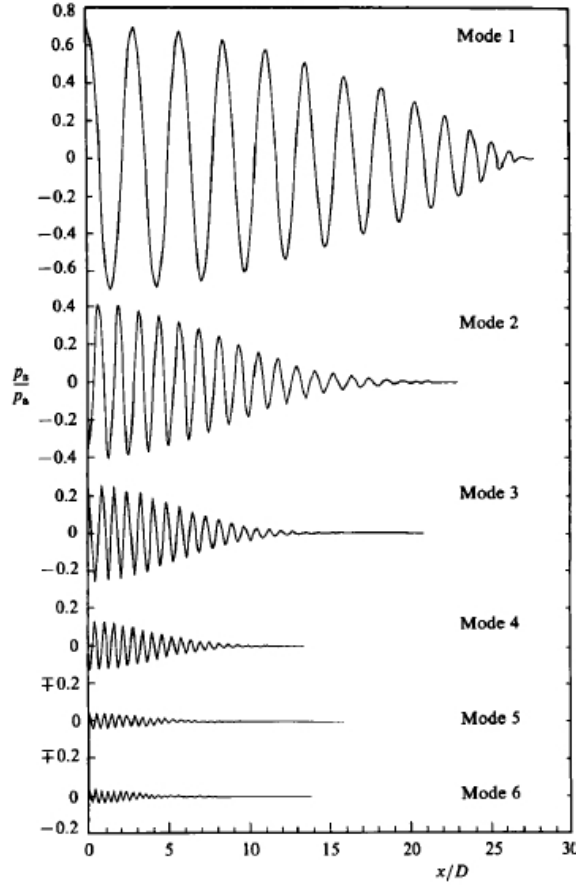


Figure 2.4: Centreline shock modes from an underexpanded jet. Adapted from Tam *et al.* [28]

amplitude  $A_n$  is proportional to  $\beta^2$ .

The simplicity of the P-P model is due to the parallel vortex sheet assumption, which is a valid approximation when wavelengths are large compared to the shear-layer thickness, for instance in regions close to the nozzle exit. Further downstream, however, the vortex sheet approximation fails as the shear layer grows because of entrainment of ambient air. This growth changes the effective width of the jet, shortening the spacing between adjacent shock cells (equation 2.6) and attenuating shock-cell strength (figure 2.2). Hence, the accuracy of equations 2.9-2.10 decreases in the downstream region.

Recognising this shortfall, Tam *et al.* [28] developed a better multiple-scales model for the shock-cell structure. The linearised time-independent mass, momentum and energy equations were solved using a slowly-spreading mean flow. Eddy-viscosity terms were included to capture the effects of turbulence. Compared to axial pressure measurements [29], predictions from the multiple-scales model were better than the inviscid vortex sheet model.

Tam *et al.* [28] also showed that the shock structure towards the end of the potential core is dominated by a single Fourier mode (figure 2.4); higher-order modes are only required to describe the fine-scale shock structures in the initial region of the jet. This result suggests, perhaps unexpectedly, that an adjusted P-P model may be sufficient in describing the downstream shock-cell structure. This finding has important ramifications when it comes to describing the shock structure in BBSAN models (section 2.5).

### 2.1.3 Turbulent Field and Coherent Structures

High-Reynolds-number jet turbulence was once thought to be solely described by stochastic turbulent eddies [30]. As measurement techniques evolved, however, it soon became apparent that there exists underlying organised structures, which persist over much longer spatiotemporal scales than the energetically dominant turbulent eddies themselves. The existence of these coherent structures in jets and shear flows has been confirmed experimentally [31–34]. The resulting flow pattern is reminiscent of an axially-extended wave-like structure [35–38].

Despite their presence, it is difficult to detect these structures in unforced natural jets owing to their small fluctuation energies compared to those of the chaotic eddies. A common approach is to isolate individual frequency-azimuthal modes from near-field pressure and flow measurements. For example, by using a ring of near-field microphones to discern between the axisymmetric and helical modes, axially-extended wave patterns were observed in the images obtained by Moore [39]. These observations were confirmed in more recent near-field measurements performed by Breakey *et al.* [40].

Organised structures are also detected in experimental supersonic flows. The high jet efflux velocity gives rise to several experimental challenges; traditional measurement techniques such as hot-wire anemometry are inappropriate, and global time-resolved flow fields are near-impossible to obtain. A novel solution was proposed by McLaughlin *et al.* [41] to reduce the density of the flow. By using a glow discharge to excite an ideally-expanded jet, both McLaughlin *et al.* [41] and Troutt and McLaughlin [42] observed coherent structures.

Recently, the advancement in experimental techniques and availability of high-fidelity numerical simulation data has offered new insights. The downstream-propagating motion

may be easily visualised using high-speed schlieren [43, 44]. Non-intrusive flow measurements using particle image velocimetry (PIV) in both subsonic [37, 45], ideally-expanded supersonic [46] and shock-containing flows [47, 48] have been successful in quantifying their structure. In flows with a strong natural resonance mechanism (e.g. screech, impingement tones), isolation of coherent structures is relatively straightforward as there is a single dominant frequency. The availability of full flow information from large-eddy simulations (LES) [49] further facilitates the detection of coherent structures in turbulent jets.

Suitable signal-processing techniques are able to extract the coherent turbulent motions. These include conditional sampling strategies such as linear stochastic estimation [50–53] or performing modal analysis [54, 55] on flow data. Spectral proper orthogonal decomposition (SPOD) has recently been shown to be an ideal candidate [56, 57]. Following a Fourier transform in time and azimuth, the application of SPOD filters out fine-scale turbulence, allowing the wave-like characteristics of the underlying structure to be examined. Moreover, recent works [58–60] have shown there exists a theoretical link between SPOD and resolvent analysis (section 2.1.5).

#### 2.1.4 Instability Waves

The detection of wave-like structures motivated the use of instability theory to describe their motion and characteristics, including amplitude, velocity and wavenumber. Instability waves arise from an infinitesimal disturbance of a laminar base flow. The description of the resulting disturbance wave is obtained by solving the linearised version of the Navier-Stokes (N-S) equations. Depending on the nature of the system, the disturbances may either be stable, returning to a laminar state, or unstable where a transition to turbulence occurs. The use of linearised dynamic models in fluid applications is summarised in the monographs of Schmid *et al.* [61] and Criminale *et al.* [62].

The spatial instability of a compressible round jet was obtained by Michalke [63]. Homogeneity in the temporal, axial and azimuthal directions, permits the solutions to be described by a set of orthogonal modes. Cast in cylindrical coordinates (figure 1.1), the normal mode *ansatz* is given by

$$\mathbf{q}(x, r, \theta, t) = \hat{\mathbf{q}}(r)e^{i(\alpha x + m\theta - \omega t)}, \quad (2.11)$$

where  $\hat{\mathbf{q}}(r)$  is the radial shape function and  $\alpha$ ,  $m$ ,  $\omega$  are the axial wavenumber, azimuthal mode and frequency respectively. Substituting this ansatz into the linearised N-S equation, and assuming a 1D-parallel base flow, the modal growth rate and radial shape of the instability wave may be obtained for a specified axial station. Using the measured velocity profile by Crow and Champagne [33] at  $x = 2D$ , the solution obtained by Michalke [63] agreed well with experimental measurements. This was further confirmed by Suzuki and Colonius [35]. Using a caged microphone array, they were able to measure the azimuthally-coherent near-pressure field of an unforced subsonic jet. Measurements agreed favourably with the growth rates predicted from solving the quasi-parallel linear equations at each axial station.

There is a wealth of literature on instability waves in high-speed flows; a review article on the topic is provided by Morris [64]. In particular, the work by Tam and Hu [65] arrived at a major finding on the instability characteristics of supersonic jets. By modelling the jet as a cylindrical vortex sheet, three families of waves were found to exist: the Kelvin-Helmholtz (K-H) instability, the supersonic instability and the subsonic instability. These waves were first detected visually by Oertel *et al.* [66]. The K-H mode describes the amplification of the initial dominant instability and becomes indistinguishable from the supersonic wave above a critical Mach number. The upstream-propagating subsonic wave has been proposed as the key component in closing resonant feedback loops [5]. The effect of shock cells on instability waves has been investigated experimentally for a screeching underexpanded jet [67, 68]. An important conclusion was that the presence of the shock cells does not significantly affect the growth of the K-H instability.

### 2.1.5 Wavepackets and Resolvent Analysis

The justification for using local linear instability models to describe dynamics of a turbulent jet may only be shown *a posteriori*; since in these jets the flow is neither laminar nor parallel and transition to turbulence has already occurred. The quasi-parallel assumption breaks down as the jet begins to diverge. To account for these approximations, instead of using a simple laminar parallel profile, the mean flow field is used as the base flow. By taking into

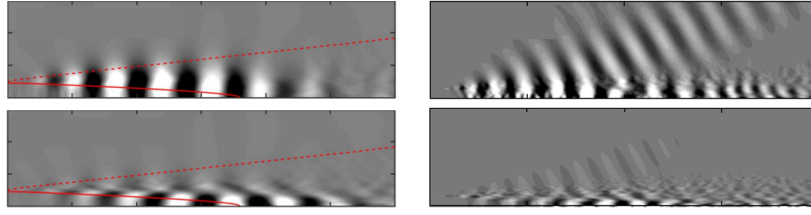


Figure 2.5: Axisymmetric wavepackets detected in subsonic (left) [56] and supersonic (right) [72] turbulent jets at  $St = 0.5$ . The pressure and axial velocity components are shown in the upper and lower rows respectively.

account the divergence of the jet mean flow, instead of the exponential growth observed when using the parallel flow assumption, the instability wave amplitude reaches a maximum and then begins to decay downstream of the point at which the K-H wave becomes locally convectively stable, forming a *wavepacket*. This behaviour was first shown analytically by Crighton and Gaster [69] and subsequent works have confirmed this observation in both subsonic [37, 70] and ideally-expanded supersonic flows [71, 72]. By isolating a given frequency-azimuthal mode, wavepacket solutions show favourable agreement with the dominant spatial structures deduced from experiments [37, 70] and high-quality numerical databases [49, 56, 73]. Examples of wavepackets in turbulent jets are shown in figure 2.5.

The recent application of resolvent analysis in the study of turbulent jets has provided a more complete justification for the use of linear theory and its link to coherent structures [14, 38, 74]. Instead of neglecting the non-linear terms, as in stability theory where a homogeneous model was used (equation 2.28), resolvent analysis considers the exact inhomogeneous model (equation 2.27). The non-linear terms are treated as external forcing to the N-S system. An optimisation problem is solved to obtain the shapes of the forcings that would lead to the maximum growth of disturbances. In other words, the role of non-linearity is revealed. Thus, in lieu of the original *scale-separation* argument where instability waves representing the deterministic large-scale structures are superposed on top of a mean flow established by the fine-scale eddies [69], the resolvent framework treats the most dominant linear responses (wavepackets) as the optimal solutions to some external forcing due to turbulence (non-linear effects).

Previous success of using homogeneous linear models is now attributed to the existence of a large gain separation between the optimal and sub-optimal modes, which reveals a modal behaviour. In these cases, the flow will be dominated by a single wavepacket for each

frequency, and such wavepacket may also be obtained by means of linear stability analysis. These structures are generally associated with a large spatial separation between forcing and response. Hence, with appropriate upstream boundary conditions, the wavepacket derived from homogeneous models, such as linear stability, will correspond closely to the first resolvent mode.

Under certain conditions, the computed response modes from resolvent analysis also have the advantage of being directly equivalent to experimental results. As shown by Towne *et al.* [59], if the non-linear forcing related to a given turbulent flow can be considered as spatial white-noise, resolvent modes should be exactly equal to modes from SPOD. While the forcing in real turbulent flows is not white, the agreement between wavepackets educed from resolvent analysis and SPOD [38, 74, 75] shows that this hypothesis is well supported at higher frequencies and the first few azimuthal modes. The agreement deteriorates for lower frequencies and higher azimuthal modes, where the structure of the forcing starts to become more relevant [75, 76].

Large-scale coherent structures, which can be modelled as wavepackets, are found to be important in the generation of noise in turbulent jets; their role in noise generation is discussed in section 2.4. Unlike subsonic jets, instability waves in supersonic jets were quickly associated with the radiated noise [72, 77]. In shock-containing supersonic jets, the interaction of these downstream-propagating structures with the shock-cells is critical to the generation of BBSAN.

## 2.2 Components of Supersonic Jet Noise

Noise radiated from supersonic shock-containing jets may be separated into shock-associated and non-shock-associated components. In imperfectly-expanded jets, the train of shock-cells interacts with the downstream-travelling turbulent fluctuations, generating strong acoustic waves. This shock-associated noise comprises two components; screech and broadband shock-associated noise. A typical jet noise spectrum is shown in figure 2.6.

Apart from identification using spectral trends, an important distinction between the noise components is also observed in their directivity characteristics (figure 2.6). Turbulent noise, associated with wavepackets, dominates in the aft region, while shock-associated

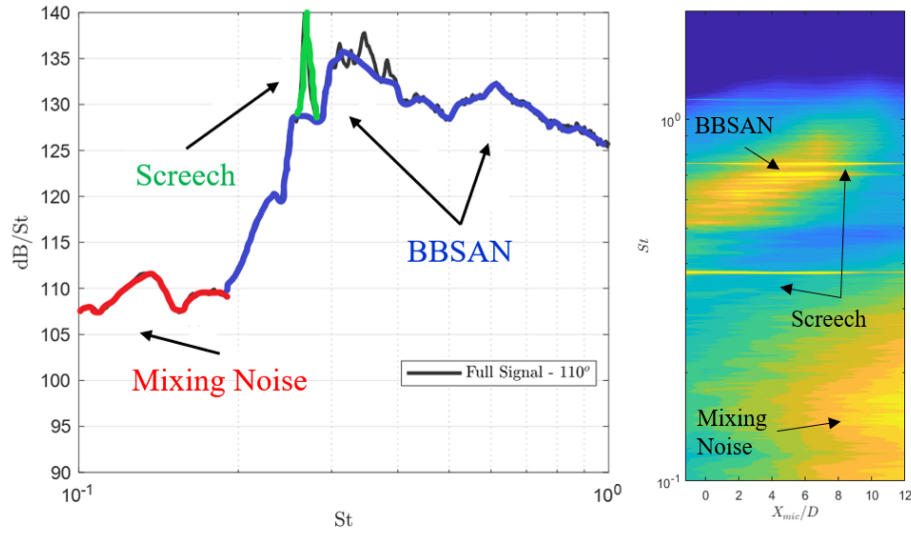


Figure 2.6: The acoustic spectrum of jet noise measured at  $\theta = 110^\circ$  relative to the downstream jet axis (left). Near-field sound pressure map showing the directivity behaviour of different noise components (right).

noise contributes more in the sideline and upstream directions. Their amplitudes also vary significantly, with screech tones being several orders of magnitude louder. While measurement and identification can be performed with relative ease with the correct equipment, predicting directivity and amplitudes for supersonic jet noise spectra remains a challenging problem to this day.

### 2.2.1 Turbulent Mixing Noise

Turbulent mixing noise occurs in both subsonic and supersonic jets. As shown in figure 2.6, this component of jet noise is most dominant at low frequencies and in the downstream direction. The intensity of mixing noise increases with Mach number and temperature. Turbulent-mean flow interactions, driven by some form of non-linear forcing, are the main generation mechanism [14]. In supersonic jets, the peak noise manifests in the form of Mach wave radiation. This occurs when the large-scale turbulence travels at a speed greater than the ambient acoustic velocity [78]. By modelling the coherent structure as an instability wave, Mach wave radiation may be visualised using the wavy-wall analogy in figure 2.7 [2].

Tam and Burton [77] improved on this approach by accounting for the growth and decay of instability waves (i.e., wavepackets). Instead of a single wavenumber, a spread of wavenumbers is obtained, and those with supersonic phase speeds will result in noise



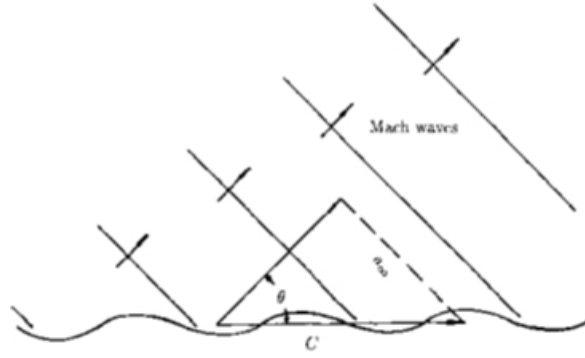


Figure 2.7: Wavy-wall analogy for Mach wave radiation. Taken from Tam [2].

radiation. This was recently confirmed by Sinha *et al.* [72], who propagated the K-H mode from PSE solutions to the far-field and observed excellent agreement with acoustic spectra.

Early on, contributions to mixing noise were separated into two parts [79]: one associated with the random fine-scale turbulence and the other with the large-scale coherent structures. While Mach wave generation is dominant downstream, it was hypothesised that fine-scale turbulence is important in the sideline direction. This artificial split resulted in two similarity spectra for jet noise. Experimental laboratory [80] and full-scale [81] measurements have supported this claim.

Recently, however, the justification for using two similarity spectra has been questioned [16, 82]. Evidence to support the splitting was based on empirical fits to data, and hence the underlying noise generation mechanisms remain hidden. It has been conjectured that turbulent noise may solely be explained by the evolution of large-scale structures. Downstream angles are dominated by low-order azimuthal modes, while higher modes propagate towards the sideline directions. The recent study by Nekkanti and Schmidt [83], for both subsonic and supersonic jets, provides the strongest indication that sideline and upstream mixing noise are associated with the same wavepackets that generate Mach wave radiation.

### 2.2.2 Broadband Shock-Associated Noise

Broadband shock-associated noise (BBSAN) is a high-frequency noise component (figure 2.6) observed in both small-scale laboratory experiments [84] and large-scale applications such as commercial and military jet engines [6, 7]. As its name suggests, BBSAN is characterised by multiple broad peaks in the acoustic spectrum; the main lobe is followed by successive

peaks. It was first studied by Harper-Bourne and Fisher [20] in shock-containing flows. The peak frequencies of BBSAN were found to increase as the observer moves downstream ( $\theta$  decreases) and the noise intensity is maximum perpendicular to the jet flow. The main peak narrows with increasing  $\theta$ . As a result of constructive source interference, the main BBSAN peak frequency  $f_p$  is a function of convection velocity, shock-cell spacing and observer angle. The relationship is expressed as,

$$f_p = \frac{u_c}{L_s(1 - M_c \cos \theta)} \quad (2.12)$$

where  $u_c$  and  $M_c$  are the convection velocity and Mach number respectively. The quasi-periodic shock-cell structure may be decomposed into a set of spatial Fourier modes (equation 2.8). Subsequent spectral peaks are observed because of the interaction of turbulence with the higher-order shock-cell modes [23, 85]. Using this interpretation,  $f_p$  may be re-expressed as

$$f_p = \frac{u_c k_{s_n}}{2\pi(1 - M_c \cos \theta)}, \quad n = 1, 2, 3, \dots, \quad (2.13)$$

where  $n$  is the shock-cell mode. This relationship holds for both over and underexpanded jets.

Using normal shock relations, Harper-Bourne and Fisher [20] also showed that the BBSAN intensity is proportional to the fourth power of the off-design parameter  $\beta$ , which, from equation 2.4, makes it a function only of NPR. Together with the directivity trends, these distinctive signatures have been used to identify and isolate flow components responsible for BBSAN production [86].

The effect of temperature on BBSAN has previously been investigated in both models [87] and experiments [88]. With relevance to peak frequency prediction in equation 2.12, heated jets have lower convection velocities when normalised by  $U_j$  and a shorter potential core. Despite these differences, the measurements of Kuo *et al.* [88] for underexpanded jets show either no change or only a slight increase in peak frequency. This observation is corroborated by the measurements of Wishart [89] who also found that the effect of varying temperature on shock structure is relatively small. Concerning amplitude, Kuo *et al.* [88] and Viswanathan *et al.* [90] found that while heating initially increases BBSAN sound pressure

levels, further increase in temperature does not correspond to a rise in sound amplitude. A mechanistic explanation was offered by Miller [91] who suggested the observed temperature saturation is due to the balance between propagation and source term effects.

Debate regarding the location of BBSAN generation is still ongoing (section 2.5). However, numerous studies [92–95] have independently suggested that the main BBSAN peak is generated at the later shock-cells towards the end of the potential core. This observation is of significance when linked to the axial extent of the different shock-cell modes (figure 2.4). In moderately-strongly underexpanded jets, while the first few shocks form sudden discontinuities, the shock-cell structure further downstream consists of only a single Fourier mode [28]. Thus, shock-cell descriptions using instability theory (such as the P-P model), may be used to adequately predict the primary BBSAN peak frequency.

Unlike in subsonic jet noise or screech, the azimuthal structure of radiated BBSAN is not well documented; only a handful of studies have examined the azimuthal modes of BBSAN in detail. In the far-field, Arroyo and Moreau [95] investigated the azimuthal modes using an LES of a non-screeching underexpanded jet at a single operating condition. Higher-order modes feature more prominently at higher frequencies and at more upstream positions. Suzuki [96] also arrived at similar conclusions by observing the azimuthal modal distributions in an LES of an underexpanded jet. Experimentally, this behaviour was also measured by Vold *et al.* [97] for an overexpanded jet, although the dependence on observer position was not investigated. In the near-field and vortical region, by extracting the upstream-travelling acoustic component, Arroyo and Moreau [95] observed the pressure distributions for each azimuthal mode vary significantly in space and frequency.

### 2.2.3 Screech and Resonance Mechanisms

Screech manifests as high-amplitude discrete tones, arising from a self-reinforcing aeroacoustic feedback loop [3, 4]. Small-scale instabilities from the nozzle lip propagate and grow downstream as a K-H instability. The growing instability then interacts with the downstream shock cells [47, 98], generating strong acoustic waves. While historically the cycle is assumed to be closed by the upstream-propagating acoustic waves, Tam and Ahuja [99] proposed that it is instead due to the upstream-propagating guided acoustic mode of the jet [65]. Recent

experimental and numerical evidence support this claim [100, 101]. A thorough summary on screech and aeroacoustic resonance can be found in the review by Edgington-Mitchell [5].

Screech and BBSAN are intrinsically linked as both arise from turbulence-shock interactions. While the generation process and downstream propagation are common, no feedback loop is present for BBSAN. Interestingly, in the weakest-link feedback model of Tam *et al.* [102], the screech component in shock-containing jets is proposed to be a limiting case of BBSAN as  $\theta$  approaches  $0^\circ$ .

The presence of screech may severely alter the characteristics of BBSAN. In an experimental study performed by André *et al.* [22], the noise characteristics from an untreated nozzle were compared to one with tabs. The tabs were used to suppress screech by disrupting the feedback loop. The presence of screech resulted in a lower BBSAN peak frequency because of attenuation of the shock-cell structure. From a modelling perspective, the presence of screech tones also poses a problem, as it alters the required turbulence length-scales; appropriate treatment is necessary to decouple the broadband and screeching velocity fluctuations [103].

## 2.3 Theory of Aerodynamic Noise

In the previous sections, a broad overview is provided on the flow features and radiated noise of supersonic shock-containing jets. To understand which fluid motions of the jet are responsible for driving the sound field, an acoustic analogy may be used. This section aims to provide a brief summary on the salient features on the acoustic analogy approach. Detailed discussions on the topic can be found in the original works of Lighthill [13, 104] and the monographs by Crighton [105] and Goldstein [106].

### 2.3.1 Lighthill's Acoustic Analogy

Acoustic analogies are an exact manipulation of the N-S equations. By rearranging the continuity and momentum equations, Lighthill [13] was the first to propose such a framework, whereby the problem is separated into the freely-propagating disturbances, the 'acoustic field', and the non-linear 'source' region. Many types of analogies exist, depending on how the source is defined. The following is a summary of Lighthill's acoustic analogy.

The analogy predicts turbulence-induced sound waves, travelling at velocity  $c_\infty$ , into a stationary-homogeneous medium of density  $\rho_0$ . The approach involves linearisation about some uniform mean flow. The difference between the base flow and the full compressible N-S equations is defined as the source. The source drives the base flow which gives rise to the fluctuations responsible for the emitted sound. Lighthill's equation, for density fluctuations  $\rho$ , reads

$$\frac{\partial^2 \rho}{\partial t^2} - c_\infty^2 \nabla^2 \rho = \frac{\partial^2 T_{ij}}{\partial x_i \partial x_j}, \quad (2.14)$$

where  $t$  is time,  $\mathbf{y}$  and  $\mathbf{x}$  are the observer and the source positions respectively. The Lighthill stress tensor  $T_{ij}$  reads

$$T_{ij} = \rho u_i u_j - \tau_{ij} + (p - c_\infty^2 \rho) \delta_{ij}, \quad (2.15)$$

where  $u$  is fluid velocity,  $\tau$  are viscous stresses and  $p$  is pressure. The contribution of  $T_{ij}$  is zero outside of the source volume  $V$ . When no solid boundaries are present, equation 2.14 may be solved using a free-field Green's function,

$$\rho(\mathbf{y}, t) = \frac{1}{4\pi c_\infty^2 r} \int_V \frac{\partial^2 T_{ij}}{\partial x_i \partial x_j} \left( \mathbf{x}, t - \frac{r}{c_\infty} \right) d\mathbf{x}, \quad (2.16)$$

where  $r = |\mathbf{x} - \mathbf{y}|$ . The Green's function may be interpreted as a filtering operation, where only acoustically-matched source components radiate noise to the far-field [82, 105]. Different Green's functions may be used depending on the geometry of the problem [107].

An interpretation of Lighthill's equation is that, in a turbulent jet, noise generated is due to the deformation of compact disorganised eddies convected by the mean flow. The eddies have spatiotemporal scales much smaller than the acoustic waves. From equation 2.14, these sources behave as compact quadrupoles due to the second derivative operating on the stress tensor. The different components of the quadrupole radiate sound in distinctive directions (figure 2.8). For example,  $T_{11}$  radiates predominantly in the downstream direction and is silent in the sideline directions [105]. Following some simplification of the stress tensor and some dimensional analysis, a central result from Lighthill's theory is that the radiated sound power  $P$  is proportional to the eighth-power of jet velocity  $U_0$ ,

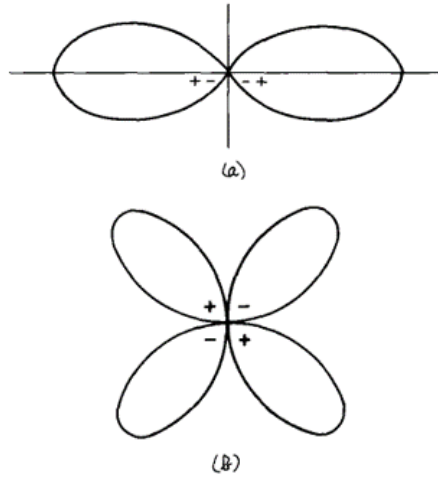


Figure 2.8: Directivity behaviour of different components of  $T_{ij}$ ; a)  $T_{11}$  b)  $T_{12}$ . Taken from Crighton [105].

$$P \sim (\rho_0 U_0^3 D^2) M^5. \quad (2.17)$$

Equation 2.17 is the well-known Lighthill's  $U^8$  law which is often used to validate jet noise measurements (see Chapter 4).

The attractiveness of Lighthill's acoustic analogy is that the sound field, due to some flow disturbance, can readily be obtained by solving the partial differential equation on the left-hand side of equation 2.14. The downside is that this technique requires the user to know, *a priori*, the non-linear source term in full. In real flows such as high-Reynolds number jets, however, the source is near-impossible to obtain. For supersonic shock-containing jets, obtaining the full spatiotemporal information experimentally is not possible with current techniques.

Moreover, as highlighted by Jordan and Gervais [82], the question of what constitutes the 'true' source term, is difficult to answer. The definition of the source term is dependant on how the base flow is defined [16]. For example, Lighthill's analogy does not take into account fluid-acoustic interactions. No distinction is made between self-noise and shear-noise and both are embedded in the description of  $T_{ij}$ . In jets, the refraction of sound waves away from the jet axis has been argued to lead to a 'cone of silence' [108]; an effect which cannot be captured without some modification of the source term. Attempts to address this issue were proposed in the analogies of Phillips [109] and Lilley [110], where linearisation

was performed on an unidirectional transversely-sheared flow, and flow-acoustic effects are included in the wave operator (left-hand side of the equation). By accounting for propagation and refraction effects, however, the solutions to Phillips' and Lilley's equations are much more complex than Lighthill's.

Ultimately, Lighthill's analogy treats the sound sources as embedded in an uniform, quiescent mean flow; effects due to a moving medium and velocity gradients are embedded in the source term, which must be modelled. Even Lighthill himself described the acoustic analogy only as a "*... general procedure for estimating the intensity of the sound produced in terms of the details of the fluid flow...*". Hence, while a supersonic shock-containing jet is far from an 'uniform, quiescent mean flow', provided a sufficiently good model of the source term is obtained, one may recover the far-field sound.

### 2.3.2 Modelling the Lighthill Stress Tensor

As indicated by previous authors [105, 106], appropriate simplifications may be made to the description of  $T_{ij}$  for turbulent jets. For turbulent cold jets, the effects of viscosity and entropic non-uniformity are often deemed negligible. The stress tensor  $T_{ij}$  in equation 2.15 may be approximated as

$$T_{ij} \approx \rho u_i u_j. \quad (2.18)$$

This approximation is made in many reduced-order source models in both subsonic and supersonic jets. The influence of this approximation on the radiated sound field was investigated by Bodony and Lele [111] for an ideally-expanded  $M = 2.0$  jet. Significant cancellation effects between the momentum ( $\rho u_i u_j$ ) and entropic ( $p - c_\infty^2 \rho$ ) terms were observed. The effect is more significant in heated flows. Their findings suggest that simplifications to  $T_{ij}$  should be made with caution.

Even though increasing computational capabilities, in theory, allow the entire space-time structure of the stress tensor to be obtained, the ambiguity in using an acoustic analogy approach remains. Acoustic analogies are used to describe the conversion of energy from a source term, that is a function of the hydrodynamic field, to the acoustic field; exact details of the responsible mechanisms remain hidden. Moreover, the modelling of the source term

is largely dependent on the view of turbulence. For example, early attempts to model the source term used isotropic turbulence to represent the compact stochastic eddies. These attempts are incompatible with the existence of large-scale coherent structures and their role in sound emission.

Instead, by using appropriate models for the source term, an acoustic analogy approach may be used to identify the acoustically important features of the turbulent field. The right-hand side of equation 2.14 may be replaced by an appropriate model function

$$S(\mathbf{x}, t) \approx \frac{\partial^2 T_{ij}(\mathbf{x}, t)}{\partial x_i \partial x_j}. \quad (2.19)$$

To test the hypothesis of sound production by large-scale structures, an equivalent axially-extended source is used [33, 63, 105] in subsonic jets. The subsequent success of using non-compact sources to predict far-field noise strongly suggests that wavepackets are ideal candidates that capture the acoustically-efficient turbulent motions in jets.

## 2.4 Wavepacket Models for Turbulent Jet Noise

Determining the connection between the radiated sound field and the responsible fluid motion is not a straightforward exercise. Wavepacket models offer an avenue to investigate this problem, and have been used extensively to model the noise produced by turbulent subsonic [112] and supersonic [72] jets. As described in section 2.1.3, wavepackets represent the large-scale coherent structures of a turbulent flow and are related to stability mechanisms. Despite having lower fluctuation energies than the fine-scale turbulence, wavepackets are more acoustically-efficient because of their high space-time coherence. While this modelling approach is in stark contrast to the classic view of acoustic sources as compact stochastic eddies [13], wavepackets have in recent years emerged as an ideal source candidate. The appeal lies in the reduced-order framework, agreement with data (both in the hydrodynamic and acoustic field), application to control theory and connection to the underlying physics. A thorough summary of the topic can be found in the reviews by Jordan and Colonius [16] and Cavalieri *et al.* [14].

Noise generation by a wave-like distributed source was first postulated by Mollo-



Christensen [32]. For a given frequency, the volume distribution of sound sources (equation 2.19) may be represented as a wavepacket. Subsequent studies by Michalke [63], Crow and Champagne [33] and Crighton [105] offered deeper insights into the characteristics of the far-field noise generated by axially-extended orderly structures. Michalke [63] found that, by decomposing the source term in equation 2.14 into azimuthal Fourier modes, the most efficient noise generators in an axisymmetric jet are the lower-order modes. In 1984, using the solution to Lighthill's analogy by Michalke and Fuchs [113], Mankbadi and Liu [114] were the first to use a wavepacket-like source to predict the sound field of a fully-turbulent unforced jet. In the same year, Tam and Burton [77] also used instability waves to successfully model the radiated sound from an excited supersonic jet [41, 42]. Ensuing studies have consolidated these findings [72, 112, 115, 116].

Overall, the modelling strategy can be separated into two approaches. The *kinematic* approach requires the construction of an *empirical* sound source in the form of a wavepacket, that is propagated to the far-field using an acoustic analogy [32, 105, 117, 118]. The wavepacket characteristics are deduced from experimental observations or numerical simulations. In contrast, *dynamic* models aim to describe the wavepacket dynamics using stability theory; both the hydrodynamic and acoustic motions are obtained by solving the equations of motion [35, 70, 72]. The former allows one to investigate the important source features for far-field noise generation but, as described previously, the 'inner' flow dynamics cannot be accessed without turning to stability theory.

More recently, resolvent analysis (section 2.1.5) has been shown to be the unifying framework connecting the two approaches [14]. The problem is manipulated into an input-output system, where the operator is known as the resolvent. The non-linearities are treated as external forcing on the mean flow which gives rise to the hydrodynamic wavepackets, and those hydrodynamic wavepackets in turn are responsible for the far-field sound. Unlike the work of Schmidt *et al.* [74] and Lesshafft *et al.* [38] where the output is flow fluctuations, the optimal modes of the acoustic field are now sought (i.e., going from the forcing terms to the acoustic field). In this framework, the connection between the turbulent field and the far-field sound is clearer. Initial results confirm that the source of far-field sound is indeed the well-defined wavepackets, which are forced by the underlying turbulence [58, 119]. Interestingly, the optimal forcing mode of the acoustic response is spatially extended

compared to the forcings of the K-H wavepacket, which is localised near the nozzle exit [38, 74].

Since many of the modelling results for non-shock containing jets are relevant in wavepacket models for BBSAN (Chapters 5-7), a short resumé of the pertinent ideas is warranted.

### 2.4.1 Kinematic Models

For wavepacket models, it is appropriate to re-write Lighthill's acoustic analogy (equation 2.14) in  $\mathbf{x} - \omega$  space

$$\nabla^2 p(\mathbf{y}, \omega) + k_a^2 p(\mathbf{y}, \omega) = S(\mathbf{x}, \omega), \quad (2.20)$$

where a Fourier-transform in time has been performed, producing the Helmholtz equation. The solution to equation (2.20) for the acoustic pressure field in the frequency domain,  $\omega$ , is given by

$$p(\mathbf{y}; \omega) = \int_V S(\mathbf{x}, \omega) G_0(\mathbf{x}, \mathbf{y}; \omega) d\mathbf{x}, \quad (2.21)$$

where an implicit  $\exp(-i\omega t)$  term is assumed. The free-field Green's function  $G_0$  is now defined as

$$G_0(\mathbf{x}, \mathbf{y}, \omega) = \frac{1}{4\pi} \frac{e^{ik_a|\mathbf{x}-\mathbf{y}|}}{|\mathbf{x}-\mathbf{y}|} \quad (2.22)$$

where  $k_a = \omega/c_\infty$  is the acoustic wavenumber.

Fluctuations in turbulent jets, and hence  $T_{ij}$ , are stationary random processes [106]. In the temporal domain, fluctuations may be described by correlation functions. The equivalent expressions in the spectral domain are spectral density functions [120]. The power spectral density (PSD) of the sound field can hence be described using the two-point cross-spectral density (CSD) of the source by multiplying equation 2.21 by its complex conjugate

$$p(\mathbf{y}; \omega) p^*(\mathbf{y}; \omega) = \int_V \int_V \langle S(\mathbf{x}_1, \omega) S^*(\mathbf{x}_2, \omega) \rangle G_0(\mathbf{x}_1, \mathbf{y}) G_0^*(\mathbf{x}_2, \mathbf{y}; \omega) d\mathbf{x}_1 d\mathbf{x}_2, \quad (2.23)$$

where  $\langle \rangle$  represents an ensemble average and  $\mathbf{x}_1$  and  $\mathbf{x}_2$  are two points in the non-zero source region. For a given azimuthal mode, an appropriate two-point wavepacket source is

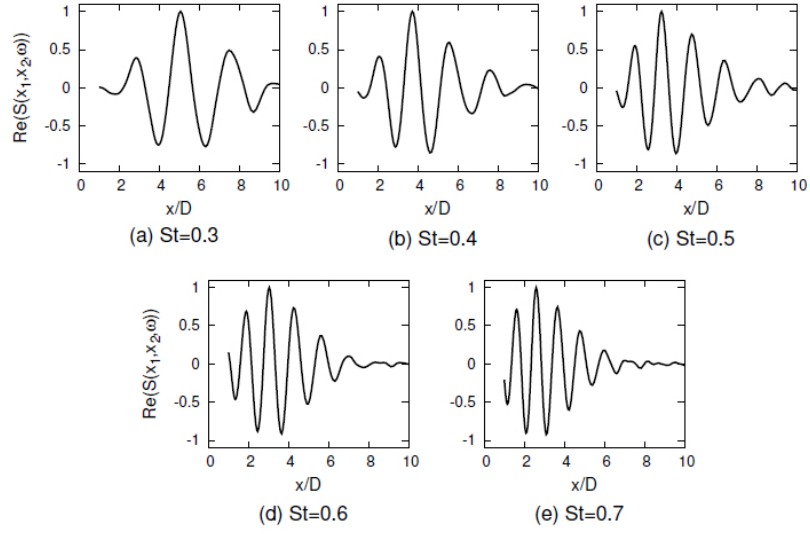


Figure 2.9: Representative wavepacket line source at different frequencies. Taken from Maia *et al.* [116]

$$S(x_1, \omega)S^*(x_2, \omega) = \mathcal{A}e^{ik_h(x_1-x_2)}e^{-x_1^2/L^2-x_2^2/L^2}e^{-(x_1-x_2)^2/L_c^2}, \quad (2.24)$$

where the critical parameters are the amplitude  $\mathcal{A}$ , hydrodynamic wavenumber  $k_h$ , characteristic lengths  $L$  and  $L_c$  for the wavepacket and coherence decay respectively. In general, all parameters are a function of frequency.

Using equation 2.23, the user is able to propagate a model sound source (equation 2.24) to the far-field. Previous works have used this approach to study the axial [121], azimuthal [112], and two-point structure [116] of an equivalent wavepacket source. In chapter 6, the same modelling strategy is used to investigate a two-point wavepacket model for BBSAN.

#### 2.4.1.1 Axial Source Structure

Single-point line source models have previously been used to represent an axially-extended wavepacket [33, 63, 105, 112, 121]. For a given frequency, the wavepacket travels at a phase velocity of  $u_c = \omega/k_h$  and has an axial extent characterised by  $L$ . The growth, saturation and decay behaviour is represented by an envelope which bounds the travelling wave as shown schematically in figure 2.9.

Because of axial source interference, a coherent wavepacket source bounded by a Gaussian envelope (equation 2.24) is capable of describing the axisymmetric *superdirectivity* be-

haviour of subsonic jets. This was confirmed by Cavalieri *et al.* [112] over a wide range of jet velocities and for both the axisymmetric and helical azimuthal modes. Aided by high-fidelity LES data, Maia *et al.* [116] revisited this problem and found an asymmetric Gaussian to be a more faithful representation of the actual wavepacket shape. Improved agreement with data was observed when an asymmetric envelope was used. A similar finding is made in the present work; a Gaussian envelope was initially adopted in the simple model in Chapter 6 but the deduced wavepacket shape from data and stability equations revealed an asymmetric shape (Appendix B).

#### 2.4.1.2 Azimuthal Source Structure

In subsonic jets, Michalke and Fuchs [113] and Cavalieri *et al.* [112] have shown that the near-pressure field is dominated by the first three azimuthal modes. On the other hand, the velocity field is less clear, with the resulting azimuthal spectrum being broader. For example, close to the nozzle exit, Cavalieri *et al.* [37] showed that the most-energetic azimuthal velocity mode is 11 for a  $M = 0.4$  jet. Similar conclusions have been obtained for supersonic jets in both the near-pressure [122] and velocity fields [72, 123].

As demonstrated experimentally by Cavalieri *et al.* [112] and Armstrong *et al.* [124], the far-field noise of a subsonic jet is dominated by the lower-order azimuthal modes. An explanation for this behaviour was deduced by Michalke and Fuchs [113]. Assuming homogeneity in the azimuthal direction and using cylindrical coordinates, the integral for a single-point source reads

$$p(R, \theta, m, \omega) = \int_x e^{ik_a x \cos \theta} \int_r S(x, r, m, \omega) J_m(k_a r \sin \theta) r dr, \quad (2.25)$$

where  $J_m$  denotes a Bessel function of the first kind, and the term  $J_m(k_a r \sin \theta)$  is largest for low values of  $m$ . Physically, while higher-order modes possess greater fluctuation energy, source interference attenuates their propagation to the far-field, leaving the first three azimuthal modes as the most efficient acoustic generators. As highlighted in section 2.2.2, the azimuthal structure of both the acoustic and source field for BBSAN is unclear; the works in Chapters 5 and 7 will address this issue.

### 2.4.1.3 Coherence decay

While linear wavepacket models were found to capture certain features of subsonic jet noise, they fail to predict the sound amplitude by more than an order of magnitude [115, 125]. The mismatch between predictions and measurements may be attributed to the effect of wavepacket *jitter*. As discussed by Cavalieri *et al.* [121], the concept of ‘jitter’ may be described as the randomness of the wavepacket, which may be thought of physically as the space-time desynchronisation of the propagating wavepacket due to the non-linear turbulence effects.

For a statistical two-point source (equation 2.21), wavepacket jitter is modelled as coherence decay. This was first studied by Williams and Kempton [126], who showed that a loss in coherence may amplify the radiated sound. Cavalieri *et al.* [121] showed that this behaviour is critical in subsonic jets but less so in the supersonic case. For wavepacket models in subsonic jets, Cavalieri and Agarwal [125] noted that “...in addition to the amplitudes and phases, the statistical (wavepacket) source should also match the coherence function of the flow fluctuations.”

One way to visualise the impact of wavepacket jitter is to transform the source from physical space to wavenumber space (figure 2.10). As described by Crighton [105], to be an acoustically efficient noise generator, the source needs to be ‘acoustically matched’; it must possess wavenumbers which can couple with the propagating sound waves. For a line source, this condition is compactly expressed by the inequalities

$$\frac{|k_1|}{k_h} \leq M_c, \quad \frac{|k_2|}{k_h} \leq M_c \quad (2.26)$$

where  $k_1$  and  $k_2$  are the wavenumbers at two points  $x_1$  and  $x_2$  respectively. In subsonic jets, the peak of the distribution of wavenumbers for a linear wavepacket is not in the radiating range. Wavepacket jitter is required to ‘stretch’ the source energy into the radiating range. However, Sinha *et al.* [72] found that in a perfectly-expanded  $M = 1.5$  jet the unsteadiness of such wavepackets is unimportant for sound emission. As shown by Cavalieri *et al.* [121] and Cavalieri and Agarwal [125], this is due to the peak wavenumbers of the linear wavepackets satisfying the inequality in equation 2.26. This criterion is analogous to the requirement that only instability waves with supersonic phase velocities can radiate sound; in this instance, two-point statistics (coherence decay) may be of limited relevance.

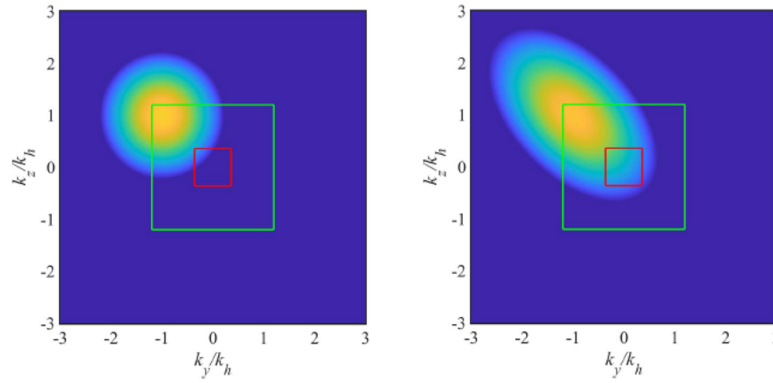


Figure 2.10: Effect of coherence decay in wavenumber space; sound source with perfect coherence (left) and with coherence decay (right). Squares indicate the radiation criterion for subsonic (red) supersonic (green). Adapted from Cavalieri *et al.* [14].

The importance of wavepacket jitter as a function of jet velocity is supported by results from resolvent analysis. Jeun *et al.* [119] found that the optimal flow response in supersonic jets closely resembles that of a linear wavepacket, confirming that non-linearities have minimal effect on far-field sound. In subsonic jets, however, there are non-negligible contributions from suboptimal modes which indicate background forcing of the wavepacket is important [58]. The role of wavepacket jitter in shock-containing flows is analysed in Chapter 6.

#### 2.4.1.4 Eduction of Wavepacket Characteristics

In the kinematic approach, wavepacket characteristics may either be inferred from the far-field sound [112] (i.e., outside-in) or obtained directly from flow data [116] (i.e., inside-out). While indicating what the source parameters may be, the ‘outside-in’ approach is ill-posed, as more than one set of parameters may be found to give satisfactory results. Moreover, the parameters found may not be representative of those observed in a real jet. This was indeed explicitly shown by Maia *et al.* [116] in modelling source characteristics for a subsonic jet. Using an ‘inside-out’ approach, source parameters ( $\mathcal{A}, k_h, L, L_c$  from equation 2.24) were carefully educed directly from a high-fidelity large-eddy simulation (LES) and compared to the parameters previously obtained by Cavalieri *et al.* [112] for the same inverse problem. Parameter values were clearly shown to differ.

As fluctuating flow variables contain both hydrodynamic and acoustic signatures, Un-

Unnikrishnan *et al.* [127] deduced wavepacket parameters by separating the irrotational isentropic acoustic mode from the solenoidal hydrodynamic mode via application of Doak's momentum potential theory (MPT) [128]. Many of the previous modelling results were confirmed, though it was shown that by isolating the acoustic mode, the acoustically-efficient features of the wavepacket were more accurately captured.

Using this approach, the analyses performed by Maia *et al.* [116] and Unnikrishnan *et al.* [127] not only support the use of wavepackets to model the source term in equation 2.19, but also attempts to reveal the exact characteristics of the acoustically-efficient wavepacket. Their work may be thought of as the precursor to dynamic models, where the description of wavepackets is now directly obtained from solving the governing equations.

### 2.4.2 Dynamic Models

By substituting the modal ansatz of equation 2.11 into the governing equations, the problem may be written as

$$\mathcal{L}_{\omega,m}\hat{q}_{\omega,m} = \hat{f}_{\omega,m}, \quad (2.27)$$

where  $\mathcal{L}$  is the operator obtained by linearisation about a time-averaged mean flow and the non-linear Reynolds stresses are contained on the right-hand side. From resolvent analysis, however, the low-rank dynamics of turbulent jets and spatial separation between forcing and optimal flow response allows for the homogeneous case to be studied [38, 74]. Hence, as alluded to in section 2.1.5, the right-hand side of equation 2.27 may be set to zero

$$\mathcal{L}_{\omega,m}\hat{q}_{\omega,m} = 0. \quad (2.28)$$

As highlighted in section 2.1.4, early attempts to describe coherent structures in jets assumed parallel or locally-parallel flows. The disturbance solutions to equation 2.28, however, would result in exponential growth. To obtain the realistic spatial evolution of the wavepacket in a turbulent jet, the parallel flow assumption needs to be relaxed. Methods do exist to deal with the divergence of the jet mean flow: using multiple-scales asymptotic expansions [77, 129], solving global stability equations [56, 130, 131] or the linearised Euler

equations [115, 132]. Compared to the locally-parallel case, however, the computational cost and complexity of these methods often make them prohibitive from a modelling perspective. A suitable compromise can be found by using parabolised stability equations (PSE) [133].

#### 2.4.2.1 Parabolised Stability Equations

In the PSE framework, it is assumed that the set of flow variables  $\mathbf{q}$  may be further decomposed into a slowly and rapidly varying component by using an appropriate multiple-scales ansatz [69]. The slowly-varying part accounts for the slow spread of the turbulent jet. The multiple-scale ansatz is substituted into the governing linearised equations. The resultant matrix system is discretised and solved by streamwise spatial marching. The problem is initiated by the K-H instability at the nozzle exit and the marching scheme tracks this mode's development downstream. The general procedure for using PSE in turbulent jets is described in Gudmundsson and Colonius [70].

The general procedure to compare PSE with measurements involves applying a spatiotemporal filter to the data and scaling the solutions. SPOD has been successfully employed to filter out smaller-scale turbulence to highlight the coherent structures present in the flow [70, 72]. After removing the incoherent fluctuations, PSE is shown to align closely with the resultant wavepacket shape. The indeterminate amplitudes of the PSE solutions require appropriate metrics to be developed for comparison to data. Different approaches to this task have been performed by previous authors [134], ranging from simple scalar multiplications to bi-orthogonal projections of LES data onto PSE wavepackets near the nozzle exit [135]. Some ambiguity remains in this exercise since scaling amplitudes are found to be sensitive to the choice of the matching flow variables, the region of interest, and the axial position [136].

Nevertheless, PSE solutions show good agreement in the turbulent field of both subsonic [37, 70, 137] and supersonic [71, 72, 138, 139] jets. By virtue of the diverging mean flow, instead of predicting exponential growth, the PSE eigenfunctions are shown to match well with the average downstream travelling K-H wavepacket. In the initial region of the jet, the rapid growth rates in the pressure and velocity fields are well described by PSE wavepackets [37, 72]. Past the saturation point, however, discrepancies are observed in the velocity



field because of the increasing dominance of non-linear effects and fluctuations that are uncorrelated with extracted wavepackets. Despite the linear assumption, Sasaki *et al.* [137] showed that even at high frequencies and for higher azimuthal modes, PSE solutions remain robust representations of axially-extended wavepackets. Application to shock-containing flows have been previously performed [140, 141]. The severe departure from the slow spread rate assumption due to strong discontinuities at the shocks, however, could make the solution unstable.

While the PSE technique can provide a global solution of the near-field, the technique does come with caveats [142]. By turning a boundary-value problem into an initial-value one, applications of PSE require regularisation techniques to stabilise the solution by quickly damping out non-dominant modes. Depending on the phase speed of the dominant K-H wavepacket, the PSE framework may cause damping or amplification of the corresponding acoustic wave. At low Mach numbers, the subsonic velocity of the K-H mode leads to significant damping of the acoustic mode and hence a poor prediction of the propagating sound waves in the irrotational near-field. On the other hand, the Mach waves in supersonic jets are reasonably well-captured because of their downstream propagation being insensitive to the imposed marching scheme. This difference between Mach regimes is explicitly shown in the PSE pressure field solutions in figure 2.5. To circumvent this issue, propagation of sound waves to the far-field can be achieved by coupling the PSE solution with an acoustic analogy method [143, 144] or solving a boundary-value problem (Kirchhoff surface) [72, 115]. The choice is often guided by numerical, robustness and/or sensitivity issues.

#### 2.4.2.2 Prediction of Far-Field Sound

Until recently, the role of instability waves in sound radiation was still unclear. Direct numerical simulations of low Reynolds number jets suggested that linear theory lacked some of the pertinent features to adequately describe sound generation [145]. This observation contradicted the largely successful linear wave theory proposed earlier by Tam and Burton [77]. In subsonic jets, Suponitsky *et al.* [146] showed non-linear mechanisms to be critical for sound generation mechanisms. Using PSE solutions from subsonic and supersonic jets, Cheung *et al.* [143] showed noise predictions for the supersonic jet performed better than

subsonic cases.

Using results from both the kinematic and dynamic modelling framework, the above discrepancies can now be addressed. In subsonic flows, despite linear wavepackets exhibiting good agreement with coherent structures, they are inefficient acoustic sources for reasons discussed in section 2.4.1.3. Hence, along with the shortcomings of PSE, early predictions were often incorrect by several orders of magnitude. When non-linearities are appropriately accounted for in the form of coherence decay, an equivalent source using wavepacket solutions recovers the lost sound [115, 144].

Conversely, the application to supersonic flows is more straightforward on account of the supersonic phase velocities being able to couple with the acoustic field. Non-linear effects are less important in terms of sound emission. Thus, sound radiation by supersonic is well predicted by linear wavepackets [77, 147]. This result is supported by the work of Sinha *et al.* [72] where PSE solutions were extrapolated to the far-field using a Kirchhoff surface; good agreement is observed at low polar angles for both cold and hot supersonic jets.

## 2.5 Approaches to Modelling Broadband Shock-Associated Noise

Despite its first detection and characterisation by Harper-Bourne and Fisher [20] nearly 50 years ago, the modelling of BBSAN generation still remains a point of conjecture in the aeroacoustic community. This may partly be attributed to the difference in modelling viewpoints of turbulence: viewing it as stochastic compact eddies (i.e., Lighthill [13]) or as large-scale structures (i.e., wavepackets). Thus, BBSAN sources were classified as either ‘localised’ or ‘distributed’ as seen in figure 2.11.

Lele [150] investigated the differences between the two approaches by rearranging the different sources into ‘phased arrays’. His work followed a kinematic modelling approach (section 2.4.1); different descriptions of the equivalent BBSAN source were propagated to the far-field via Lighthill’s acoustic analogy. Amongst other findings, Lele [150] proposed that despite the different approaches, all models may equivalently be treated as a phased-array of noise sources. This was later supported by Ray and Lele [149] who showed that localised and distributed BBSAN sources are not mutually exclusive (figure 2.11). While source energy may be localised, when only the radiating components are used (those that

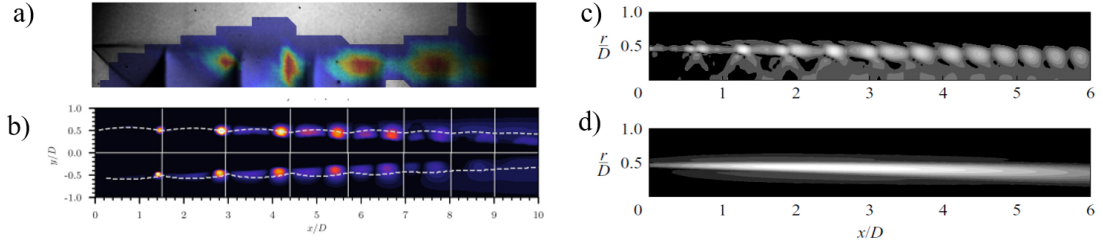


Figure 2.11: Different representations of the BBSAN source from; (a) experimental causality analysis performed by Savarese *et al.* [53], (b) equivalent discrete sources from a RANS-CFD approach [148], (c) unfiltered source map from Ray and Lele [149] and (d) the same source as (c) but with only the radiating component shown.

match the radiating criterion), the same sources are distributed in space. This observation again raises the issue of what constitutes the ‘true’ acoustic source for BBSAN.

In light of the discussion in section 2.4, rather than distinguishing by their source distribution, the subsequent summary of BBSAN models will instead be interpreted from the perspective of *kinematic* and *dynamic* modelling approaches. For the sake of compactness, only modelling of cold shock-containing jets is discussed and source amplitude prefactors are not written out in full and are denoted by the symbol  $\mathcal{A}$  for all models.

### 2.5.1 Harper-Bourne and Fisher - Phased Array Model (1973)

The seminal work by Harper-Bourne and Fisher [20] suggested that the source mechanism of BBSAN may be modelled as a localised phased-array system. The idealised sources are separated by the shock-cell length  $L_s$ , mimicking an eddy traversing the nozzle lip-line, which generates noise as it interacts with each individual shock-reflection point (figure 2.2). The eddy convects with velocity  $u_c$  and decays as it travels downstream. The phase difference between each discrete source captures the time difference it takes for the turbulent eddy to convect downstream and interact with each shock cell. The 3D representation is approximated by a line source as depicted in figure 2.12.

By removing the condition of identical sources, Lele [150] wrote out an equivalent source term for a multi-point array

$$S(x, t) = 2\pi \sum_n \mathcal{A}_n q_n(t - \tau_n) \delta(x_1 - X_n), \quad (2.29)$$

where  $q_n$  is the source emitted at location  $X_n$  with time delay  $\tau_n$ . By applying a Fourier

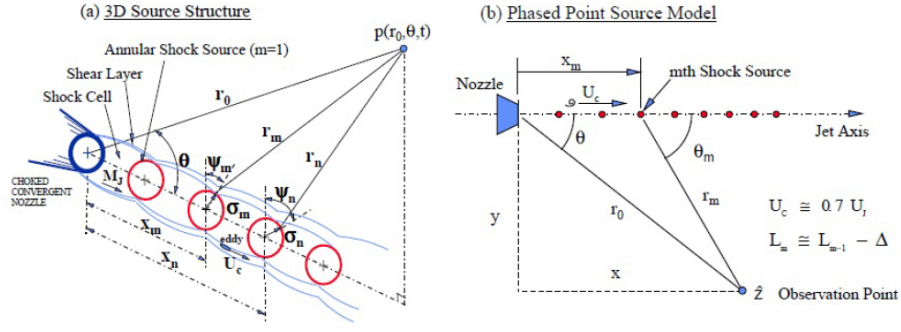


Figure 2.12: Phased array antenna model proposed by Harper-Bourne and Fisher. Adapted from Harper-Bourne [21].

transform and considering the CSD between two sources  $X_m$  and  $X_n$ , the far-field sound PSD is obtained by substituting equation 2.29 into 2.23,

$$p(\mathbf{y}; \omega) p^*(\mathbf{y}, \omega) \approx \mathcal{A} \sum_{m=1}^M \sum_{n=1}^N G_{mn}(\omega) \cos \left( \frac{\omega(x_n - x_m)}{U_c} (1 - M_c \cos \theta) \right) \quad (2.30)$$

where  $G_{mn}$  represents the CSD function between the two sources. It is convenient to introduce the measure of coherence

$$C_{mn} = \frac{|G_{mn}|}{|G_{mm} G_{nn}|^{1/2}} \quad (2.31)$$

where  $G_{mm}$  and  $G_{nn}$  are the auto-spectral densities of each source. When  $C_{mn} = 1$ , the original model of Harper-Bourne and Fisher [20] is recovered. Identical sources result in source pairs with perfect cross-coherence. While this interpretation was able to capture many of the salient features of BBSAN, such as the peak frequency prediction in equation 2.12, it incorrectly predicts the occurrence of many narrow-band peaks in the acoustic spectra. The peaks are due to the constructive and destructive interference between the sources. Discrete sources only make sense when the convecting turbulent structures do not extend over a large streamwise region and the coherence length is less than  $L_s$ ; this is only true close to the nozzle exit. Further downstream, as observed in experiments, the eddies will grow into large-scale coherent structures and interact with multiple shock cells. When coherence is allowed to decay ( $C_{mn} \leq 1$ ), the artificial harmonic peaks are suppressed. This approach was later adopted by Harper-Bourne [21], by using measured coherence of the bulk turbulence.

### 2.5.2 Morris and Miller - Computational RANS Model (2009)

In another approach, a BBSAN model developed by Morris and Miller [151] used solutions of the Reynolds-averaged Navier-Stokes (RANS) equations, requiring only the nozzle geometry and jet operating condition to be specified. The source term is represented as a set of spatial derivatives,

$$S_j^v = -v_{sj} \frac{\partial v_{ti}}{\partial x_j} - v_{tj} \frac{\partial v_{si}}{\partial x_j}. \quad (2.32)$$

where  $v_s$  are the shock-cell induced perturbations and  $v_t$  are the turbulent fluctuations. By relating the source term to shock-cell strength  $p_s$  and solving equation 2.23 via a free-field Green's function, the far-field PSD is given by

$$p(\mathbf{y}; \omega) p^*(\mathbf{y}, \omega) \approx \mathcal{A} \int_{-\infty}^{\infty} \int_{-\infty}^{\infty} \frac{1}{l} p_s(\mathbf{x}) p_s(\mathbf{x} + \boldsymbol{\eta}) R^v(\mathbf{y}, \boldsymbol{\eta}, \tau) e^{i\omega(\tau - \mathbf{y} \cdot \boldsymbol{\eta} / x_{c\infty})} d\tau d\boldsymbol{\eta} d\mathbf{x}. \quad (2.33)$$

where  $R^v(\mathbf{y}, \boldsymbol{\eta}, \tau)$  is the two-point-two-time cross-correlation tensor of the turbulent velocities with spatial and temporal separation  $\boldsymbol{\eta}$  and  $\tau$ . The correlation function is modelled as

$$R^v(\mathbf{y}, \boldsymbol{\eta}, \tau) = R^v(\mathbf{y}, 0, 0) e^{\frac{-|\tau|}{\tau_s}} e^{-\frac{(\epsilon - u_c \tau)^2}{l^2}} e^{-\frac{(\eta^2 + \zeta^2)}{l_\perp^2}}, \quad (2.34)$$

where turbulent lengths ( $l, l_\perp$ ) and time ( $\tau_s$ ) scales are approximated from the RANS-CFD simulations and scaled to match the BBSAN spectrum. Since noise field computations using the reconstructed sources are sensitive to the definition of the integrated scales, efforts have been made to refine their description [148, 152–154]. For example, Kalyan and Karabasov [152] improved the computed BBSAN spectra by incorporating a mixed-scale model to obtain a better estimate of the frequency-dependent length scales. Tan *et al.* [103] provided a method to isolate the BBSAN velocity fluctuations from the effects of screech.

Given appropriate calibration of scaling coefficients, favourable agreement with experimental data is obtained with this 'outside-in' approach. From an engineering perspective, the appeal of these models remains high as they can provide BBSAN computation with reasonable accuracy and fast turnaround times. Provided a RANS-CFD simulation is performed, BBSAN may be computed for any nozzle geometry and operating condition.

Models similar to those of Harper-Bourne and Fisher [20] and Morris and Miller [151] are based on ‘bulk-turbulence’ statistics. The auto-correlation and cross-correlation measures (and their spectral analogues) contain the statistical information required to inform modelling choices. These metrics are dominated by the signatures of energy-containing eddies [155]. While wavepacket models also require two-point information (section 2.4.1), their higher-order statistics differ significantly when compared to the often studied bulk flow. This was shown by Jaunet *et al.* [45] using synchronised dual-plane PIV data of a subsonic turbulent jet. Hence, while two-point BBSAN source models based on bulk-flow statistics [20, 151, 156] do explicitly include two-point coherence or correlation information, they are not directly equivalent to wavepacket models where only the velocity perturbations of the acoustically-efficient lowest-order azimuthal modes are used.

### 2.5.3 Tam - Instability Wave Model (1987)

Unlike the kinematic models above, a more fundamental dynamic approach was first proposed by Tam and Tanna [23], who reasoned that BBSAN arose from the weakly non-linear interactions between large-scale coherent structures and shocks. The interaction between the shocks and instability waves generates disturbances which propagate at supersonic velocities, manifesting as a form of Mach wave radiation. In this model, the coherent structures are represented as instability waves [77, 78], while the periodic shock-cell structure is modelled as a series of time-independent waveguide modes (P-P model). To construct the source, the shock-containing flow quantities  $\chi$  are decomposed as follows

$$\chi = \bar{\chi} + \epsilon_t \chi_t + \epsilon_s \chi_s + \epsilon_s \epsilon_t \chi' \quad (2.35)$$

where  $\epsilon$  denotes a small magnitude and  $\bar{\chi}$  are the mean flow quantities. The disturbances are separated into the turbulence  $\epsilon_t \chi_t$  and shock-cell  $\epsilon_s \chi_s$  components. The non-linear interaction between them,  $\epsilon_s \epsilon_t \chi'$ , is deemed to be the source of BBSAN. The decomposed flow is substituted into the governing equations where only the leading-order interaction terms are retained. The turbulent fluctuations may be represented as a convecting 1-D instability wave,

$$u_t = \mathcal{A}_t e^{i(k_h x - \omega t)} \quad (2.36)$$

where  $k_h$  is the wavelength and  $\mathcal{A}_t$  describes the growth and decay of the wave. Tam's equivalent BBSAN source has the form

$$S(x, t) = u_s \times u_t \approx \sum_n \mathcal{A}_n \left[ e^{-i((k_{sn} - k_h)x - \omega t)} + e^{-i((k_{sn} + k_h)x - \omega t)} \right]. \quad (2.37)$$

The result is two propagating waves; one with subsonic phase velocity which cannot produce acoustic waves and another with supersonic phase velocity that propagates upstream. Provided the properties of the shock are well captured, application of this model recovers the main peak frequencies with a high-degree of accuracy. Equation 2.37 also implies that the total noise spectrum is made up of a superposition of many spectral peaks due to the higher-order shock-cell modes ( $n \geq 1$ ).

The work of Tam and co-authors [23, 28, 102] was consolidated into a stochastic model for BBSAN [157] which was further refined for moderately imperfectly-expanded flows [87]. Because of the prohibitive nature of the extensive numerical computations required, a similarity source model was constructed which, when compared to experimental measurements [29], gave favourable noise spectra predictions over a wide range of jet operating conditions. While motivated by stability theory, the construction of the similarity source model is equivalent to a kinematic approach; apart from the convection velocity and wavenumber, the construction of the source model required two empirical parameters determined from matching to measured far-field sound.

While successful, there are two main issues with Tam's model. Firstly, artificial dips are observed between successive peaks in the far-field spectrum (figure 2.13). Tam corrected this by using an empirical adjustment to broaden the peaks. The adjustment is physically linked to the unsteady motion of the shock cells, which is not captured by the stationary representation. Secondly, as azimuthally-decomposed BBSAN measurements were not available at the time, scaling coefficients were used to match source model predictions, for a single azimuthal mode, to the total signal. Tam [157] assumed that the total acoustic spectrum had a similar shape to the axisymmetric mode.

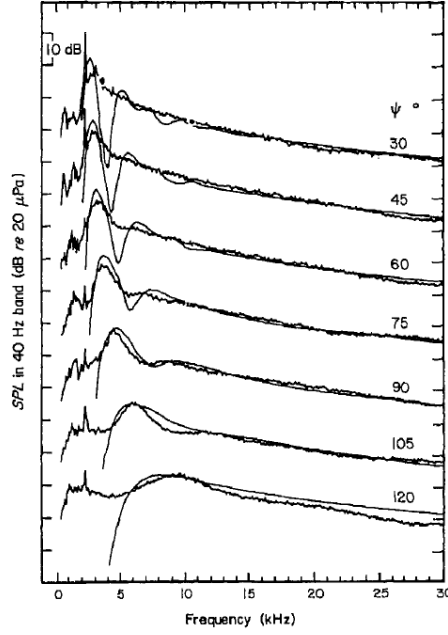


Figure 2.13: Artificial dips observed in Tam’s BBSAN similarity model ( $\psi^o = 180^\circ - \theta^o$ ). Taken from Tam [157].

#### 2.5.4 Wavepacket Models

Building on Tam’s work and motivated by the recent success of wavepacket models in turbulent jets, Lele [150] formulated a kinematic wavepacket source model. This modelling strategy is supported by the findings of Sasidharan Nair *et al.* [158] when MPT was used to segregate the hydrodynamic and acoustic modes in an underexpanded jet; the acoustic mode revealed a wavepacket structure. Lele’s formulation is similar to Tam’s, where the shocks are represented as stationary waves. The turbulent component is now modelled as

$$u_t = \int \sum_m \mathcal{A}_m e^{-\frac{1}{2}(\frac{x_1 - X_0}{L})^2} e^{-\frac{1}{2}(\frac{t - T_0}{T})^2} e^{i(k_h x_1 - \omega_t t)} d\omega, \quad (2.38)$$

where  $u_t$  represents a linear combination of a set of wavepackets at different frequencies. The wavepacket is bounded by a spatial and temporal envelope;  $L$ ,  $T$  are the characteristic length and time scale of the Gaussian envelope and  $X_0$ ,  $T_0$  denote their respective maxima. Equation 2.38 is similar to the kinematic source model representation used by Cavalieri *et al.* [121] for subsonic jets. The source term, for a given frequency and shock-cell mode, thus has the following expression



$$S_{m,n} = \mathcal{A}_{m,n} e^{-\frac{1}{2}(\frac{y_1 - y_0^m}{L})^2} e^{-\frac{1}{2}(\frac{t - t_0^m}{T})^2} \frac{1}{2} \left\{ e^{ik_{sn}x} + e^{-ik_{sn}x} \right\} \left\{ e^{k_h x_1 - \omega_t t} + c.c. \right\}, \quad (2.39)$$

where *c.c.* represents the complex conjugate and *m* denotes a particular ‘realisation’ of the wavepacket with distinct amplitude, spatial and temporal characteristics. Substituting equation 2.39 into equation 2.14, the far-field PSD is found to be

$$p(\mathbf{y}; \omega) p^*(\mathbf{y}, \omega) \approx \sum_m \sum_n \mathcal{A}_{m,n} \int F(\omega, \omega_t, \theta) d\omega_t, \quad (2.40)$$

where

$$F(\omega, \omega_t, \theta) = e^{-\alpha_g^2 \left[ \left( -\frac{\omega}{\omega_t} M_c \cos \theta - \frac{k_{sn}}{k_h} \right)^2 - \frac{\beta_g^2}{\alpha_g^2} \left( -\frac{\omega}{\omega_t} - 1 \right)^2 \right]}. \quad (2.41)$$

The function *F* in equation 2.41 provides insight into the underlying dynamics, i.e. how the far-field BBSAN spectral shape is affected by both the temporal and spatial behaviour of the wavepacket. The properties of the spatial and temporal envelopes, which are modelled as Gaussians in equation 2.39, may be adjusted using  $\alpha_g$  and  $\beta_g$  terms respectively. Savarese [19] investigated the effects of varying the parameters for an individual realisation of the wavepacket and observing the changes on the far-field sound. Larger wavepackets (high  $\alpha_g$  values) were found to interact with multiple shock cells. While producing the well-known BBSAN directivity behaviour, noise was lost at high frequencies. Varying  $\alpha_g$  through a large range of values did change the peak frequency. On the other hand, intermittent behaviour of wavepackets (with small values of  $\beta_g$ ), were found to broaden the spectrum at high frequencies. This is a possible explanation for why Tam’s model predicted a spectrum with narrow peaks when using a time-independent decaying instability wave. Savarese [19] concluded that a set of wavepackets with different characteristics would be required to describe the entire BBSAN spectrum. This was implicitly shown by Tam when the effects of unsteady shock motions were accounted for in his equivalent source term.

More complex descriptions of the wavepacket have been used in BBSAN models. Analogous to the investigation by Maia *et al.* [116] in a subsonic jet, an ‘inside-out’ kinematic approach was attempted by Suzuki [96], where the wavepacket parameters were extracted from the linear hydrodynamic region of an LES database of an underexpanded jet and the shock-cells were represented by several distinct ‘Gaussian humps’. A line source was used

to represent the equivalent near-field pressure of a shock-containing jet. In this instance, coherence information was extracted and fed directly into the model. While the results confirmed modelling assumptions and obtained similar primary BBSAN peak predictions to LES results, poor agreement was found at higher frequencies where the model severely under-predicted sound amplitude.

A dynamic wavepacket model was proposed by Ray and Lele [149] with wavepackets obtained via PSE solutions. While general trends were promising, agreement with experimental data remained poor at high frequencies. Ray and Lele [149] believed the mismatch at high frequencies was due to the breakdown of linear stability theory, but this was not investigated further. Furthermore, motivated by showing that the source wavenumbers arising from the non-primary shock-cell modes lie outside the radiating range [105], only the primary mode was retained. This observation, however, contradicts the notion that high-frequency noise at upstream angles is due to the interaction of the wavepackets with higher-order shock-cell modes [85, 95, 157]. It is worth emphasising that Savarese [19], Ray and Lele [149] and Suzuki [96] all used the equivalent of a single shock-cell mode, with relatively poor agreement observed at high frequencies.

## 2.6 Summary

### 2.6.1 Résumé of Research on BBSAN Modelling

Some pertinent points from the literature review are summarised below.

- BBSAN is generated by the interaction between turbulence and the quasi-stationary shock structure. While easily identifiable, the strategy to model this component of jet noise is less clear, with previous attempts having varying degrees of success. Conventionally, the BBSAN source is separated into the turbulence and shock components; each component is modelled separately before being combined.
- The radiated field suggests the sound source of the main BBSAN peak is strongest towards the end of the potential core. In this region, a single Fourier mode dominates and the shock perturbations emulate a smooth sinusoid. Subsequent BBSAN peaks may be recovered using higher-order shock-cell modes. These observations indicate, for BBSAN prediction, a linear set of stationary waves is an appropriate representation of the shocks.
- Recently, there has been considerable evidence to suggest large-scale organised structures in turbulent jets may be described by *wavepackets*. These are axially-extended, azimuthally-coherent, wave-like structures which are underpinned by stability theory. Wavepackets have been used successfully to predict and describe many important underlying mechanisms relating to sound generation in turbulent jets. Hence, it is a natural progression to use wavepackets to describe the turbulence component in BBSAN models.
- Wavepacket models may be divided into two different but linked classes. *Kinematic* models use an acoustic-analogy to propagate an equivalent sound source to the far-field. The parameters of the equivalent source may be altered to test its characteristics to match the acoustic field. On the other hand, *dynamic* models have sources obtained by solving the linearised governing equations. A kinematic wavepacket model can be used to determine the acoustic relevance of particular flow features, which would in turn inform the modelling choices for a stability-based model.

- Wavepackets are characterised by their frequency, azimuthal and axial wavenumbers. Despite the success of using instability waves in BBSAN models, relatively few measurements of the azimuthal content of the far-field sound are available in the literature. Difficulty exists in comparing and reconciling the differences between prediction and measurements. Consequently, the efficacy of using wavepackets/instability waves for BBSAN prediction is unknown.
- Non-linear effects from background turbulence may cause a perfectly-coherent wavepacket to 'jitter' or become intermittent. This effect is statistically represented as coherence decay. Unlike subsonic jets, wavepacket jitter is unimportant in terms of sound radiation in ideally-expanded supersonic jets. The effect of coherence decay in shock-containing jets, however, has not been investigated. Recent initial findings, however, have pointed to its possible relevance to BBSAN generation. For BBSAN, a perfectly time-periodic wavepacket is shown to produce narrow peaks in the acoustic spectrum because of interaction with multiple discrete shock-cell modes. An intermittent wavepacket can broaden peaks at high frequencies. This suggests coherence decay may indeed be the 'missing ingredient' in stability-based BBSAN models.
- The majority of BBSAN models require an 'outside-in' approach; source parameters are obtained from the acoustic field alone. Despite their relative success, two observations can be made. Firstly, a degree of empiricism (i.e., tuning coefficients) is required to match far-field data; the source parameters are not unique. Secondly, certain features of the BBSAN spectra are still poorly predicted. The mismatch observed in existing models suggests a revisit of the underlying flow dynamics responsible for BBSAN is necessary.

In summary, while BBSAN modelling using wavepackets is promising, there remain deficiencies and questions which need to be addressed. The following research questions were posed to answer the challenges in modelling BBSAN alluded to above:

- What does the azimuthal structure of far-field BBSAN look like?
- What effects do non-linearities, in the form of wavepacket jitter, and higher shock-cell modes play in wavepacket BBSAN models?

- What are the limitations of using a reduced-order wavepacket model to predict the qualitative AND quantitative trends of BBSAN?

To answer the research questions, the following research objectives were proposed:

- Experimentally measure the far-field azimuthal structure of BBSAN from an underexpanded supersonic jet.
- Test the effects of wavepacket jitter by using an analytical two-point kinematic BBSAN wavepacket model.
- Using an 'inside-out' approach, validate the proposed BBSAN wavepacket model by using experimental and numerical data of a shock-containing jet and observe both qualitative and quantitative trends.

### 2.6.2 Organisation of Present Work

The subsequent chapters follow the progression of work required to answer the research questions and objectives outlined above. To perform azimuthal decomposition of the radiated noise from shock-containing jets, a new jet noise facility at Monash University was required. Chapter 3 summarises the design methodology and highlights salient features of the Supersonic Jet Anechoic Facility (SJAF). To replicate free-field behaviour, the jet rig is enclosed by an anechoic chamber. The validation process used to quantify its acoustic performance is addressed in Chapter 4.

Following the successful qualification of the new facility, Chapter 5 describes an experimental campaign to measure the azimuthal structure of far-field BBSAN. Measurements were performed at three underexpanded jet conditions. The relative contribution of successive azimuthal modes to BBSAN was found to be sensitive to the observer angle and jet operating condition. The measurements are used for comparisons in Chapter 7.

Chapter 6 addresses the second research objective by using a kinematic two-point wavepacket model to test the impact of coherence decay on the radiated BBSAN. The results from the study showed conclusively that wavepacket jitter, and its interaction with higher shock-cell modes, is vital for predicting frequencies above the main peak.

Finally, the findings from Chapters 5 and 6 are incorporated into a new wavepacket model for BBSAN in Chapter 7. Favourable agreement is observed between model predictions and experimental measurements for the first three azimuthal modes. The results confirm that the hypothesis that BBSAN is generated by the interaction between large-scale coherent structures and shock-cells is indeed well-founded.

## Chapter 3

# Design and Development of the Supersonic Jet Anechoic Facility

### 3.1 Introductory Statement

The Laboratory for Turbulence Research in Aerospace and Combustion (LTRAC) at Monash University had two operational gas-jet facilities prior to the commencement of this project. However, neither are enclosed in a controlled environment amenable to free-field acoustic measurements. Both reside in a non-anechoic shared laboratory space, where acoustic waves are free to reflect off surrounding surfaces, including walls, other experimental rigs, optical tables, cupboards and storage units. While acoustic measurements have previously been performed in both facilities [47, 152, 159, 160, amongst others], the resulting spectra were primarily used to identify discrete screech and impingement tones. Relative amplitudes, rather than absolute sound pressure level (SPL) values, were reported for the reasons specified above. Hence, comparisons with other jet noise facilities and model predictions were not possible. Furthermore, because of the open nature of both existing facilities, the operator is potentially exposed to high levels of noise for an extended period of time. These limitations were identified as a severe restriction for this project and future jet noise research at LTRAC. As such, a new small-scale anechoic jet facility was conceived.

The new facility provided the designer an opportunity to start from a ‘clean slate’. The goal was to establish a working facility capable of performing high-quality acoustic and flow

measurements within a reasonable time frame and budget. The approach and methodology followed was largely based on the guidelines and principles suggested by Ahuja [161], though design concepts were also adopted from many working jet noise facilities described in literature. The design of the facility can be separated into two components: the anechoic chamber and the jet rig. A critical initial consideration was the required facility size. This was not only determined by the actual constraint of the available laboratory space, but also by the acoustic requirements of the facility.

The desire to obtain simultaneous acoustic and flow measurements forms a challenging requirement for the new facility. Potential optical flow measurement techniques include Background Oriented Schlieren (BOS) and Particle Image Velocimetry (PIV). For PIV specifically, the requirement to seed the surrounding ambient air necessitates a co-flow design. Because of space constraints and the need to protect equipment from the intense radiated noise, optical access into the room is required. Novel design solutions were implemented to achieve this requirement as outlined later in the chapter. While compatibility with optical measurement techniques was an essential design consideration, this project required only the acquisition of acoustic data. Hence, components specific to flow visualisation, such as the PIV seeder system, and optical setup, including laser and camera placement, are not discussed. The implementation of BOS and PIV measurement systems remain as future work.

This chapter discusses the design methodology and development of the new Supersonic Jet Anechoic Facility (SJAF). Following a brief overview of the design parameters and requirements, detailed design features of both the anechoic chamber and the jet rig are highlighted. A set of design drawings for the facility is provided in Appendix C.

## 3.2 LTRAC Shock Laboratory

The new jet noise facility is housed in the Shock Laboratory, together with the TK-1 supersonic wind tunnel [162, 163] and the shock tube facility [164]. The layout of the laboratory space is shown in figure 3.1. The available floor area is  $6.7\text{m} \times 6.5\text{m}$  and the height of the room is  $3.0\text{m}$ . A large mobile exhaust system is mounted via an overhead cantilever arm. In addition to the specific facilities, space is also occupied by optical tables, shelving units and



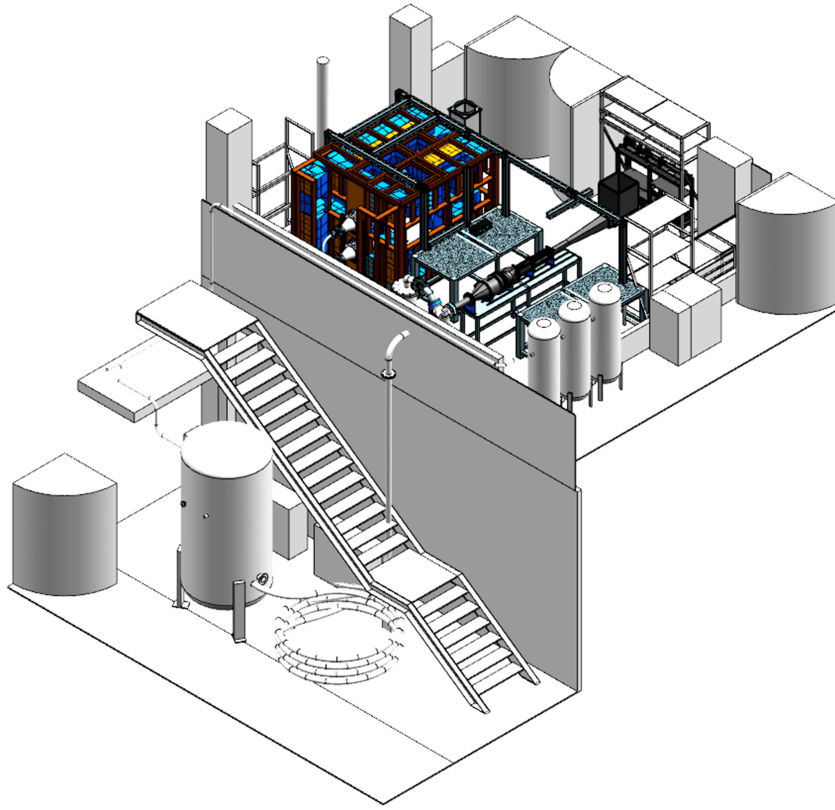


Figure 3.1: Isometric view of the laboratory space housing SJAF (coloured).

workbenches. The laboratory space is located on the mezzanine floor of the building and is not isolated from the rest of the structure. Several components of the air supply system are located external to the laboratory. No heating system is installed, so only unheated jets are able to be studied. A description of the air supply system is provided in section 3.5.1.

Because of limited space and budget constraints, and unlike other facilities which are isolated structures (see examples listed in table 3.2), the design was required to be a 'room-within-a-room'. As discussed by Ahuja [161], and shown in section 3.4.2, the need to measure low-frequency sound requires a large anechoic space. Compromises on size and position were necessary to maximise the acoustic capabilities of the chamber while ensuring that integration with the existing laboratory space was possible. For example, the orientation of the chamber was set by the position of the air supply line, which is shared with the wind tunnel, and the chamber height was limited by the overhead exhaust boom. Based on the physical constraints, safe access to electrical outlets, gas valves and optical tables, it was determined that the total available volume for the anechoic chamber is approximately  $3\text{m} \times 2\text{m} \times 2\text{m}$ . The remainder of this chapter details the design choices for both the anechoic

Table 3.1: Design parameters for the new facility.

Design Parameters	Requirement
Range of Frequencies	$> 500 \text{ Hz}$
Size of Jet Rig	Maximum possible
Jet Exit Velocity Range	$M_j \leq 1.7$
Jet Exit Temperature Condition	Cold (unheated)
Microphone Positions (polar angle from downstream jet axis)	$30^\circ - 120^\circ$
Max. External Dimensions ( $L \times W \times H$ )	$\approx 2.5 \times 2 \times 2\text{m}$
Run Time	Maximum possible

chamber and the accompanying jet rig.

### 3.3 Design Parameters and Requirements

The design process for establishing a jet noise research facility began with a critical examination of the relevant parameters outlined in Ahuja [165]. These parameters include the frequency range of interest for comparison of experimental and modelling data, the size of the nozzle, the jet exit temperature condition, and the range of polar angles where microphones are to be positioned. There were also additional restrictions on available floor space, as well as the need for integration with the existing air supply line. Summarised in table 3.1, these key parameters are all inherently coupled. Together they determine not only the size of the anechoic chamber, but also the diameter of the jet and the specifications of the microphones.

While full-scale engine noise typically spans a frequency range of 20Hz to 10kHz, the primary focus on supersonic jet noise limits the scope of the design problem. BBSAN is the phenomenon of interest for this project, and is known to occur at high frequencies. Acoustic data from a full-scale Pratt and Whitney F135 turbofan engine from a F-35B by Neilsen *et al.* [81] shows BBSAN occurring above 500Hz. For comparisons to laboratory-scale facilities, frequency  $f$  is represented as a non-dimensional Strouhal number  $St$ ,

$$St = \frac{fD_j}{U_j}, \quad (3.1)$$

where  $D_j$  and  $U_j$  are the ideally-expanded diameter and velocity of the jet. To determine the scale of the model, upper and lower frequency bounds must be established based on the diameter of the jet and the desired velocity range. Because of the air supply restrictions discussed in section 3.5.1, an upper limit on jet velocity was imposed at  $M_j = 1.7$ , and only unheated flows were considered. From the narrow-band spectra measured by Viswanathan *et al.* [90], the low-frequency bound for BBSAN was expected to be  $St \approx 0.2$ .

The size of the anechoic chamber also determines the maximum permissible jet diameter. The maximum external width of the box is 2m, due to the location of the TK-1 and optical tables (figure 3.1). For far-field measurements, microphones should ideally be mounted further than 45 jet diameters away from the nozzle [161], to ensure the microphones are in the geometric far-field (section 4.3.2). As an initial example, a 0.02m jet exit diameter demands the microphones be mounted 1m from the nozzle exit if they are to be located a distance of 50 jet diameters perpendicular to the jet axis. The final nozzle size is smaller than this example, however, as the internal chamber width must be narrower than 2m to allow for the chamber walls and foam wedges (section 3.4.2).

While BBSAN extends up to a frequency of  $St \approx 10$ , standard free-field microphone capabilities render it impossible to measure the highest of frequencies produced by such small nozzles. Previous BBSAN measurements [29] had shown that the primary peak occurs below  $St \approx 1.5$ . Thus, an upper limit of  $St = 2$  was deemed a suitable compromise. Higher-frequency secondary BBSAN peaks also occur from the turbulence interaction with higher-order shock-cell modes [157]. At lower Mach numbers and downstream angles, since the BBSAN main peak occurs at higher frequencies [20], subsequent peaks cannot be measured. The highest frequency response of the available free-field microphones is 80kHz (section 4.2.1).

Another important design consideration was the location of the microphones relative to the nozzle exit. Unlike subsonic jets, a significant component of supersonic jet noise (including BBSAN) radiates in the sideline and upstream directions. Hence, any design of the jet facility required the microphones to be mounted upstream of the nozzle exit and not be impeded by upstream plumbing. Lastly, an extended run time is necessary for PIV measurements (section 3.5.1).

In addition to satisfying the requirements outlined in table 3.1, the design of the facility

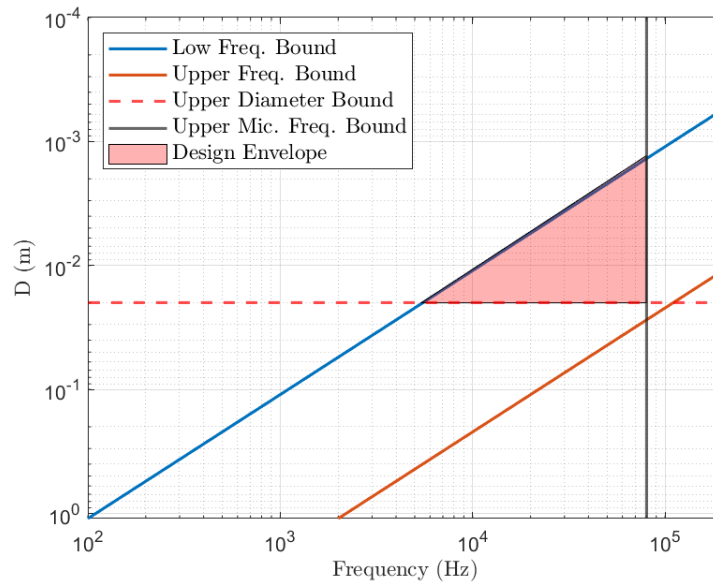


Figure 3.2: Initial design envelope for jet facility.

needed to be flexible. While the primary objective is to measure noise from supersonic jets, the facility should be amenable to future changes and upgrades. The intention is to use the facility to investigate other aeroacoustic phenomena, such as dual stream flows, trailing edge noise and resonant flows. Furthermore, the facility should allow non-intrusive flow measurements to be performed.

By considering these requirements, a preliminary 'design envelope' for the sizing of the facility was established and is shown in figure 3.2. Following an initial sizing, an iterative design process resulted in a 8mm core (primary) jet and an outer (secondary) co-flow with a diameter of  $D = 16\text{mm}$  (section 3.5.3), corresponding to an area ratio between the core jet and co-flow of three. A more in-depth discussion on the design strategy and the final design of the facility follows.

### 3.4 Anechoic Chamber

In general, the anechoic chamber aims to replicate a free-field environment by lining the walls with non-reflective material. The chamber walls provide a barrier to spurious noise that would otherwise enter the room, and also to protect operators from high-intensity noise. The chamber requires an inlet opening, for the jet plenum, and an exhaust port located on

Table 3.2: Summary of some anechoic jet noise facilities.

Facility	Size (wedge-tip to wedge-tip)
SHJAR - NASA [166]	18m radius dome
PNRPU [167]	$11.8 \times 8.2 \times 5.3$ m
University of Mississippi [168]	$5.7 \times 6 \times 2.4$ m
Lockhead-Georgia Tech [169]	$6.7 \times 6 \times 8.5$ m
Syracuse University [170]	$7.9 \times 6 \times 4.2$ m
GDTL - Ohio State [171]	$5.1 \times 4.5 \times 2.5$
HotJet - Florida State [172]	$5 \times 5.7 \times 4.3$ m
Federal University of Santa Clara [173]	$5 \times 2.95 \times 4.05$ m
AeroacouSTic Facility- VKI[174]	$4 \times 3 \times 4$ m
Tohoku University [46]	$3 \times 3 \times 2$ m
SUCRE - PPrime [175, 176]	$3 \times 3 \times 2.5$ m
University of Illinois [177]	$2.1 \times 2.3 \times 2.5$ m

the opposite wall. Large anechoic chambers often have a transparent floor, mounting points for microphones and other instruments and lighting fixtures. Since operational anechoic facilities are not uncommon (table 3.2), the current design incorporates many existing features from current working facilities where possible. A non-exhaustive list of anechoic chambers used for jet noise research is provided in table 3.2.

As discussed in section 3.3, the new anechoic chamber needed to fit into a volume of  $\approx 3\text{m} \times 2\text{m} \times 2\text{m}$ . The differences between the features of small and large facilities is important in terms of access, air-flow management and equipment set up for optical measurements. Many of the design features in large anechoic chambers ( $\geq 50\text{m}^3$ ), were found to be unsuitable or unnecessary. Thus, the current design borrowed concepts from smaller anechoic jet facilities [174, 175, 177]. In particular, the facility at the University of Illinois [177] was of interest, since it shared many of the same design requirements.

The major design considerations associated with a small anechoic chamber relate to qualification and access. As detailed in chapter 4, the new facility has to satisfy the qualifications for anechoic chambers as prescribed in ISO 3745 [178]. The qualification process is more challenging as the acoustic range of interest is at higher frequencies. The limited available space also meant that physical and optical access needed to be carefully considered. For example, optical access into the chamber is required because of the lack of internal space to mount cameras and lasers (section 3.4.3).

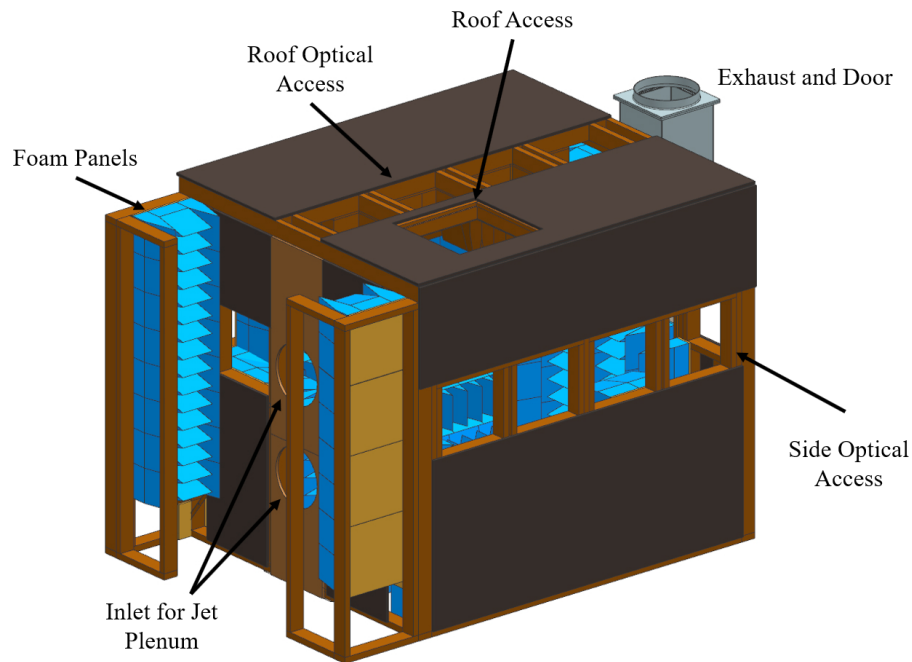


Figure 3.3: Schematic of the anechoic chamber.

The final design of the SJAF anechoic chamber is shown in figure 3.3. The external dimensions of the anechoic chamber are  $2.8\text{m} \times 2.0\text{m} \times 2.0\text{m}$ . The internal surfaces of the chamber are lined with acoustic foam wedges, which along with the acoustically-insulated stud walls, yields internal dimensions, wedge-tip-to-wedge-tip, of  $1.5\text{m} \times 1.2\text{m} \times 1.3\text{m}$ . Access to the anechoic chamber is via a conventional hinged door opposite the openings for the jet plenum. The door contains an opening for the exhaust. For optical access, windows are located on all four walls and the ceiling of the chamber. When not in use, they remain covered with removable foam wedge panels. To replenish entrained air, acoustically-treated inlet slots are incorporated into the upstream wall.

### 3.4.1 Foam Wedges & Chamber Wall

In addition to providing a clean acoustic environment, a key design requirement of the facility is to provide high transmission loss, i.e., good reduction in sound intensity across the walls, to protect the operator outside the anechoic chamber. This is achieved by specifying an appropriate wall thickness, and through the use of acoustic foam. The chamber was constructed in a modular fashion; the four walls and ceiling were constructed as separate pieces before assembly. Each wall panel was constructed as a wooden stud frame and 10mm

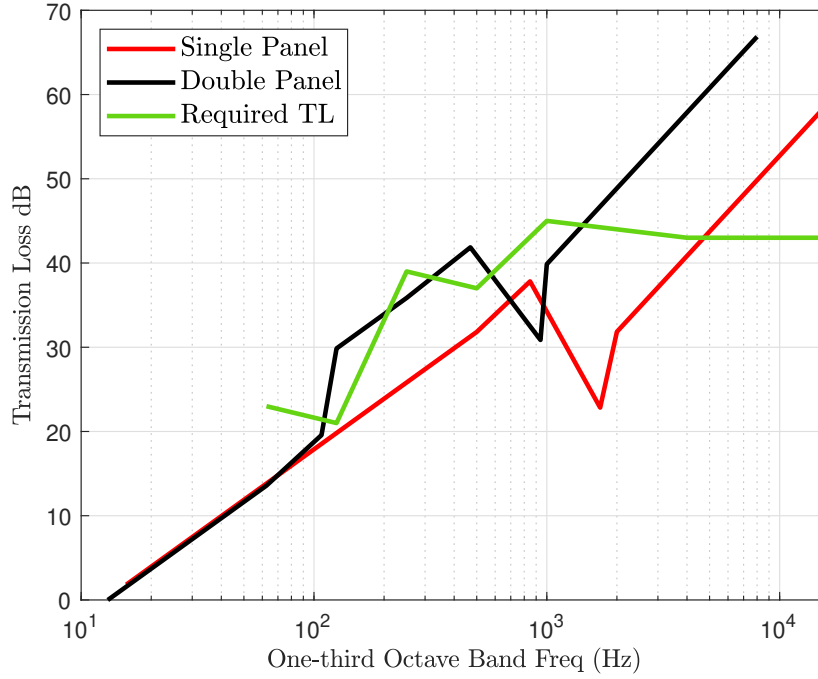


Figure 3.4: Estimated transmission loss across single and double panel walls.

plywood was used to clad the exterior. The space between the walls was filled with insulating rock wool with no air gap. The resulting thickness of the double-layer wall is  $l_w = 0.1\text{m}$ . By approximating the double-layer wall as two isolated isotropic panels separated by an air gap [179], the chamber wall was estimated to provide a 30-40dB noise reduction for frequencies ranging from 100Hz - 10kHz (figure 3.4). A single-layer wall was also considered; while saving space, the required acoustic transmission loss could not be achieved.

One of the most important components of an anechoic chamber is the wall lining material. Chamber walls are usually internally covered with wedges to prevent acoustic reflection. While off-the-shelf options were available, wedges were instead designed specific to the application of this facility. The triangular wedge shape is the most efficient geometry for sound absorption [180, 181]. Upon impingement of the acoustic wave, the energy of the incident wave is dissipated to the surrounding air and contained within the adjacent wedges. An important wedge parameter is its length, which is related to the cut-off frequency (i.e. frequency at which the room is no longer considered to be anechoic). As shown by Duda [182], the relationship between the required length of the wedges  $l_c$  and the wavelength of sound  $\lambda$  corresponding to the cut-off frequency is

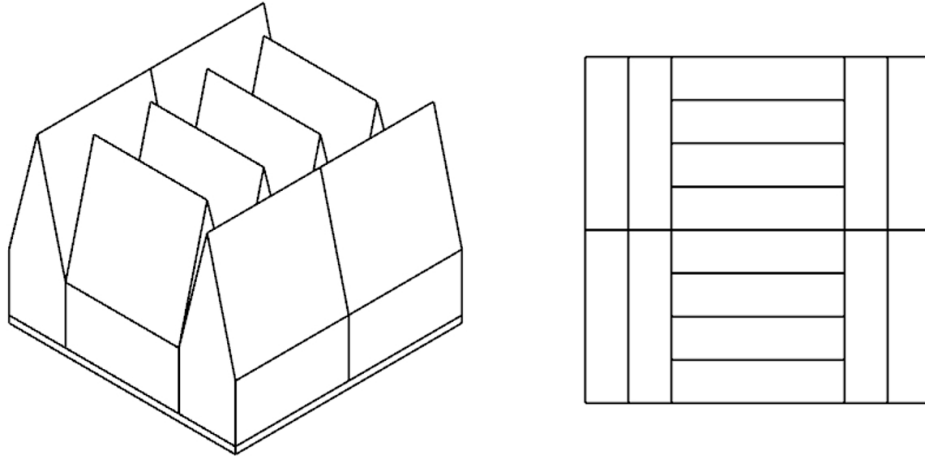


Figure 3.5: Foam panels and arrangement; isometric (left) and top (right) views.

$$l_c \geq \lambda/4. \quad (3.2)$$

For studying BBSAN, the lowest required frequency is  $\approx 4\text{kHz}$  (figure 3.2), which corresponds to a minimum wedge length of  $l_c = 0.02\text{m}$ . However, a lower cut-off frequency might be warranted in future studies. A length of  $l_c = 0.3\text{m}$  was deemed appropriate, corresponding to a nominal cut-off frequency of approximately  $500\text{Hz}$ . Given the length of the wedge base to be  $200\text{mm}$ , the taper angle of the wedges is  $14^\circ$ .

Historically, the wedges would be constructed out of mineral wool. Modern facilities commonly use fibreglass or low-density foam. Fibreglass wedges are used in hot jet facilities because of the flammability of foam. Although the current facility uses an unheated jet, flame retardant properties were still deemed necessary because of the use of a high-powered laser during PIV measurements. Hence, the wedges are made out of low-density flame-retardant polyurethane foam (type S28/70CM) from Joyce Foam Products. The acoustic absorption coefficient of the foam material is above 0.8 for frequencies over  $1000\text{Hz}$ . Burrin and Tanna [169] found that the arrangement of the wedges did not have a significant effect on the sound absorption characteristics. Except at corners and edges, the foam wedges are grouped together into blocks of eight as shown in figure 3.5.

Each wedge combination was attached to plywood boards via an adhesive and screwed onto the stud wall frame. The foam panels are modular and attached to the walls in an alternating fashion. The design also allows them to be removed as required, including those



on the floor and ceiling. The installation and construction methodology allows the anechoic chamber amenable to future upgrades and changes.

### 3.4.2 Dimensions

Given the thickness of the wall and wedge length, a number of factors determined the final inner dimensions of the anechoic chamber.

For far-field measurements, the microphones must be sufficiently far from the jet to be located in the geometric far-field (section 4.3.2). It is generally accepted that the acoustic far-field of a jet begins at 40-50 jet diameters from the nozzle exit [165, 171]. For an 8mm nozzle exit, this corresponds to a minimum radial distance  $R$  of 0.32m-0.4m. This is validated in the measurements shown in Chapter 4. Moreover, the microphones need to be placed a certain distance away from the wedge tips to prevent near-field effects degrading the microphone performance (section 4.3.1). A quarter of the longest acoustic wavelength  $\lambda$  is a sufficient separation distance [178]. Hence, the minimum width of the anechoic chamber is given by

$$D_{width,min} = 2R + \lambda/2 + 2l_c + 2l_w. \quad (3.3)$$

While a larger far-field distance can be achieved by placing the jet in one corner of the room, this was deemed unsuitable for a number of reasons. Apart from construction difficulties, the desire to perform azimuthal decomposition of the radiated sound field meant the microphones would have to be placed at equal radial distances in the azimuthal direction, similar to, for example, the experimental set up of Piantanida *et al.* [183]. An asymmetric alignment of the jet may restrict the microphone placement on the shorter side, and reflections may occur because of the low-angle sound rays grazing the wedge tips [165].

Finally, the length of the chamber must be sufficient to allow microphones to be mounted upstream of the jet exit. This was achieved by extending the length of the plenum chamber to ensure the jet nozzle was well-offset from the rear wall. The jet rig as one unit may also be traversed in the axial direction (section 3.5.2). Since there were no external physical barriers restricting the front and rear walls, the internal length of the chamber was extended to allow for microphone angles as far upstream as  $\approx 150^\circ$ . The height of the anechoic chamber was restricted by the overhead support of the exhaust system and the requirement for optical

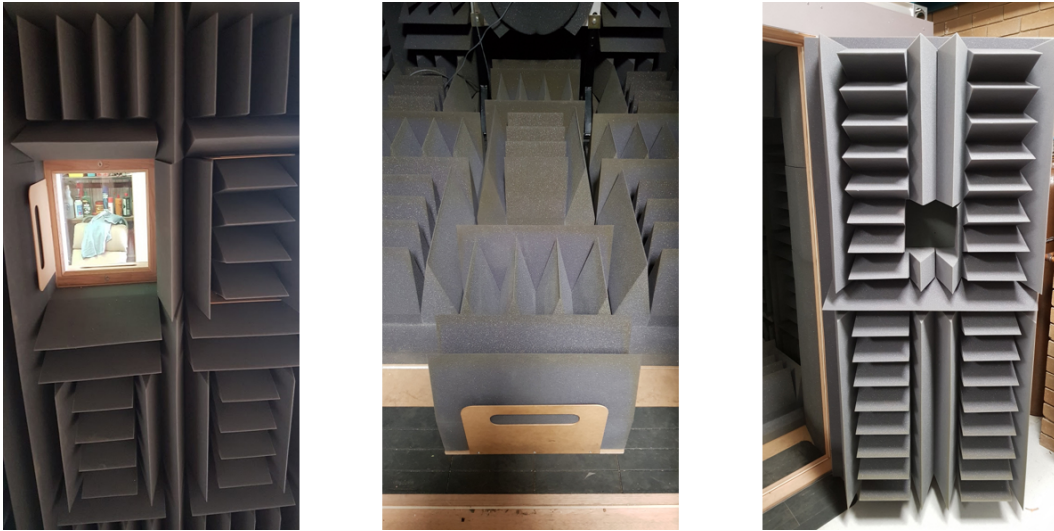


Figure 3.6: Removable window wedge panels (left), floor panels (centre) and door (right) of the anechoic chamber.

equipment to be mounted on the ceiling (section 3.4.3).

### 3.4.3 Chamber Access

The user-access points of a small anechoic chamber must be carefully considered because of limited space and the possibility of interference with flow measurements. These include the main door, ceiling and windows.

The restriction placed on the width of the chamber meant the door was situated on the wall opposing the jet. While not ideal, this location allowed the most efficient use of space. Budget limitations also meant that a sliding double door was not possible, so a conventional hinged timber solid-core door was selected. The dimensions of the door are  $1.8\text{m} \times 0.9\text{m}$  with a thickness of 40mm. Door width was maximised to allow for large items to be brought into the chamber during installation of the jet rig. The inside surface of the door is covered with foam wedges as shown in figure 3.6. The dense composite material in the core of the door offers significant acoustic insulation properties.

A grated floor was deemed unnecessary for the anechoic chamber. Instead, the wedge panels on the floor are simply placed into position. To access the inside of the chamber, the operator must manually remove a small number of wedge panels. Handles are attached to each panel to assist in this process (figure 3.6).

Prolonged exposure to intense radiated noise in an open facility has the potential to cause

damage to sensitive equipment including cameras and lasers. All diagnostic instrumentation is thus isolated from the jet exhaust in this design. Similar to Fontaine *et al.* [177], windows were built into the chamber walls to allow optical access to the jet exhaust. The chamber has 12 windows, each of size  $0.4\text{m} \times 0.4\text{m}$ , across the four chamber walls and along the ceiling. The windows are double glazed to provide additional sound insulation. The windows along the left and right walls are intended to be used for techniques such as planar PIV and BOS, whereas the windows on the front and rear wall are for stereoscopic PIV measurements of cross-stream planes.

An added benefit of this set up is the secure mounting of mirrors, lenses, cameras and lasers on an optical table (figure 3.7). If required, the operator can easily perform alignment of the optical system without having to access the inside of the chamber while the jet operates continuously. The anechoic chamber is surrounded by a frame composed of X95 rails for mounting optical equipment (figure 3.1). The frame is not connected to the anechoic chamber to prevent potential vibrations affecting the optics. As an example, figure 3.7 shows the basic set up for a planar PIV experiment. The laser beam, which is shared with TK-1, is focused and directed using a series of mirrors and lenses, entering from a ceiling window. The camera is to be mounted orthogonal to the direction of the flow. A group of optics, mounted above the chamber ceiling and aligned with the jet centreline, includes a combination of cylindrical and spherical lenses to produce a laser sheet and a  $90^\circ$  right-angle mirror that turns the beam downward. Since access to the roof is required during alignment, the ceiling includes a built-in access hole ( $0.5\text{m} \times 0.5\text{m}$ ), which is covered by a removable panel when the jet is operational.

For purely acoustic experimental campaign, the windows may be covered by dedicated wedge panels as shown in figure 3.6. For ease of removal, these panels are securely attached to the window frames via strong earth magnets. This allows the operator to easily remove selected individual panels without the need for any tools.

#### 3.4.4 Inlet & Exhaust

In order to simulate a free-field environment, air flow into and out of the chamber is critical. High-speed jets entrain large amounts of ambient air which must be replenished from the

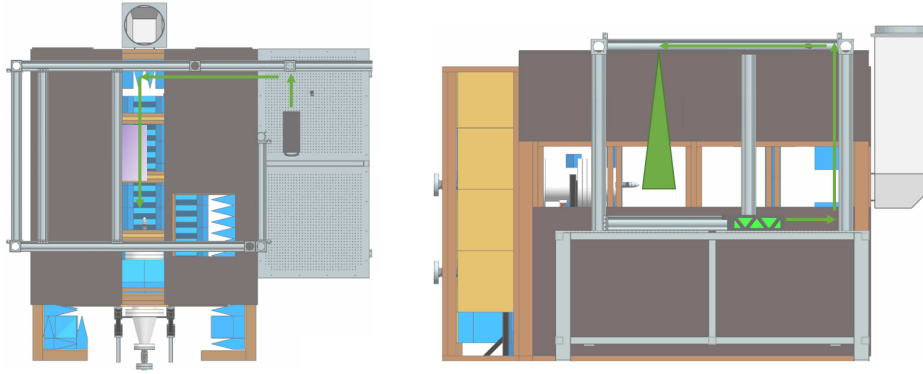


Figure 3.7: Top and side views showing the proposed laser path (green) and optical equipment set-up for planar PIV experiments.

outside. Two inlet slots of size  $0.9\text{m} \times 0.2\text{m}$  were installed and located on the upstream wall of the chamber. The size was determined to minimise the velocity of the incoming air, so as not to disturb the microphones. Inspired by the design of Quartararo and Lauchle [184], to preserve the anechoic performance inside the chamber, a fake wall lined with acoustic wedges was constructed to allow air to flow freely into the chamber while preventing the propagation of sound.

Since the door is directly opposite to the jet, a  $0.2\text{m} \times 0.2\text{m}$  exhaust port was cut out from the door. Unlike other larger facilities [169, 171], a bell-mouth collector was not used. This is because of the small jet diameter and the short distance between the nozzle and the door. For PIV experiments, an exhaust system is also crucial in removing the seeding particles expelled from the nozzle. The square port is connected to the same exhaust system as TK-1, which can be throttled to the appropriate exhaust velocity. For acoustic-only measurements (chapters 4 & 5), the operation of the fan is not required and the jet simply discharges into the exhaust port.

### 3.5 Co-axial Jet Rig

As mentioned in section 3.3, the initial sizing of the jet rig was performed in parallel with the anechoic chamber. The jet rig possesses a modular design which makes it amenable to future changes and upgrades. Small-scale supersonic co-axial jet facilities with PIV capability are uncommon, and incorporating this type of facility into the anechoic chamber was a highly challenging task. Inspiration was drawn from other working facilities [174, 185, 186]. Major

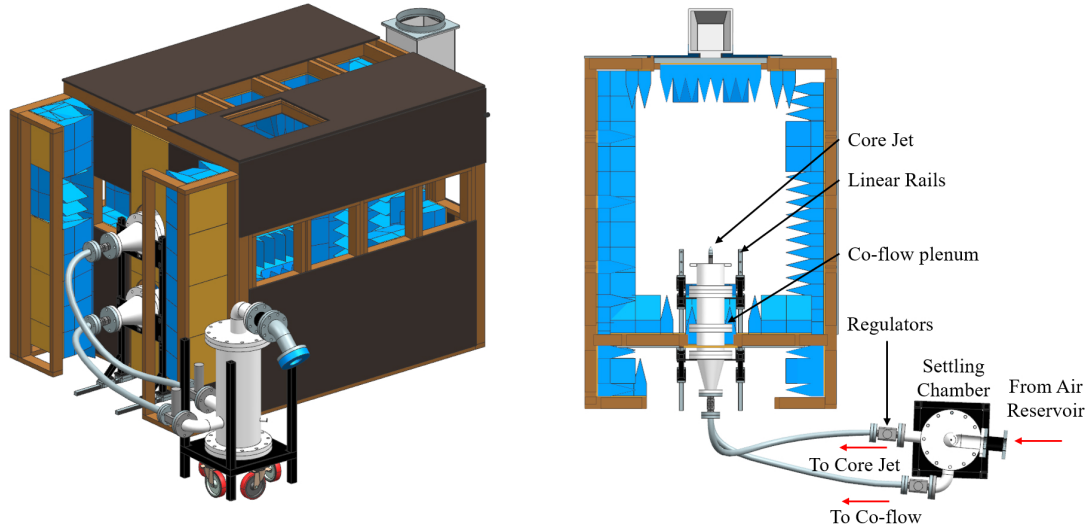


Figure 3.8: Isometric (left) and sectioned-top (right) view of the integration of jet plumbing with anechoic chamber.

design considerations include integration with the central laboratory plumbing system, unification of the core nozzle with the co-flow and limited floor space. Integration of the jet rig with the anechoic chamber is shown in figure 3.8.

### 3.5.1 Central Air Supply System

Since the jet rig uses the same air supply as the recently commissioned supersonic wind tunnel, many of the upstream high-pressure plumbing components were already in place. The maximum pressure limit, storage volume, and recharge rate were determined based on the operational requirements of the tunnel. A detailed description of the system is given in Knast [163] and only key details are reproduced here.

An 11kW scroll compressor is used, capable of compressing air to a maximum of 14 bar. Compressed air is passed through a heatless-desiccant dryer and a single  $0.33\text{m}^3$  wet tank. The dried air is plumbed into two  $0.33\text{m}^3$  storage tanks and connected to the main  $5.12\text{m}^3$  air reservoir outside of the building. The total available air storage volume is  $6.12\text{m}^3$ . The compressed air then passes through a passive-coiled heat exchanger (based on the requirements of TK-1) and into the laboratory via a 100mm pipe. Air flow is controlled by an eccentric rotary plug control valve, which is connected to a DAQ (NI USB-6341 BNC) and monitored using a custom LabVIEW control program. The operator controls the air flow by changing the position of the valve. Manual butterfly valves are used to direct the air into

either the tunnel or the jet settling chamber.

As the air supply system was set, to determine the optimal nozzle exit diameter, mass flow rate calculations were performed to obtain the maximum available run time based on the amount of stored air available. As highlighted in table 3.1, continuous flow for the core jet up to an ideally-expanded Mach number of  $M_j \approx 1.7$  is desired. The jet Mach number is obtained by specifying the nozzle pressure ratio (NPR), which is defined as  $NPR = p_0/p_\infty$ , where  $p_0$  and  $p_\infty$  are the total and ambient pressures, respectively. The relationship between Mach number and NPR is given by

$$M_j = \left[ \frac{2}{\gamma - 1} \left( NPR^{\frac{\gamma-1}{\gamma}} - 1 \right) \right]^{1/2}, \quad (3.4)$$

where  $\gamma$  is the specific heat ratio. Assuming isentropic flow, the theoretical mass flow rate for a supersonic jet issuing from a choked nozzle ( $M_j \geq 1$ ) reads

$$\dot{m} = \frac{p_0 A}{\sqrt{T_0}} \left[ \frac{\gamma}{R} \left( \frac{2}{\gamma + 1} \right)^{\frac{\gamma+1}{\gamma-1}} \right]^{1/2}, \quad (3.5)$$

where  $R$  is the gas constant for air,  $A$  is the exit nozzle area and  $T_0$  is the total temperature. The estimated run time of the jet rig can be found by computing

$$t_r = \frac{V_t}{A} \frac{\sqrt{T_0}}{T_{ti}} \frac{P_{ti}}{p_0} \left( 1 + \frac{\gamma - 1}{2} \right)^{-\frac{\gamma+1}{2(\gamma-1)}} \left[ 1 - \left( \frac{P_{tf}}{P_{ti}} \right)^{1/\gamma} \right] \quad (3.6)$$

where  $T_t$ ,  $P_t$  and  $V_t$  are the temperature, pressure and volume of the tank respectively. The subscripts  $i$  and  $f$  represent the initial and final conditions, i.e., from a full to empty tank. Because of the losses in the system, the final pressure in the storage tanks cannot be equal to the stagnation pressure in the jet plenum. A single conservative safety factor of 1.2 was applied to account for these losses. From the sizing of the anechoic chamber (section 3.4.2), the core nozzle cannot have an exit diameter larger than 15mm.

The expected run time for the jet rig as a function of mass flow rate is shown in figure 3.9. The maximum tank pressure is set by the compressor (14 bar) and, as a conservative estimate, the total tank volume was assumed to be 5m<sup>3</sup>. For a continuous run time of up to 20 minutes (a typical run time for obtaining a set of PIV measurements based on present hardware), the permitted maximum total mass flow rate is approximately 0.3-0.4 kg/s.

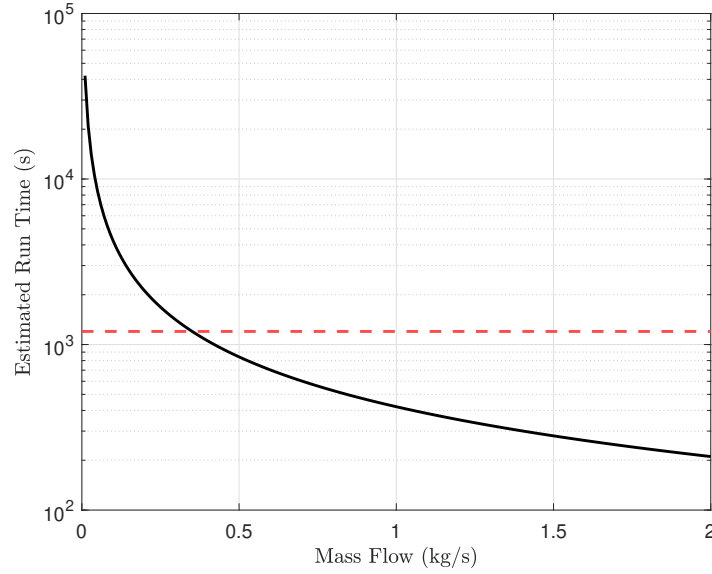


Figure 3.9: Run time as a function of mass flow rate. Red dashed line indicates a 20 minute run time.

Determining the maximum mass flow rate of the facility allows the size of the core nozzle to be found. Figure 3.10 shows the estimated run time as a function of exit diameter for a range of NPR. The condition  $NPR = 5.0$  corresponds to the ideally-expanded jet Mach number of 1.7. The curves show that an exit diameter of 0.01m would satisfy the requirements in table 3.1. Out of an abundance of caution, a conservative diameter of 8mm was selected; the longer run time allows jet conditions to stabilise before measurements are performed. A smaller nozzle also allows for multiple runs without the need for the tanks to be recharged. Nevertheless, depending on the desired velocity of the co-flow, the exit diameter could be increased, provided the mass flow rate and acoustic free-field limitations are respected.

To determine the size of the outer secondary nozzle, the ratio between the co-flow and core nozzle exit areas  $A_{cf}/A_c$  is used. To study the most limiting scenario, it was assumed both the core and co-flow to be operated at the same NPR. For an 8mm core nozzle, figure 3.11 shows expected run time as a function of NPR. It is evident, with an area ratio of  $A_{cf}/A_c = 3$ , the jet can no longer be operated above  $NPR = 3.5$ . For seeding purposes, however, the co-flow will be operated at a much lower velocity compared to the core jet, and an area ratio of three was deemed satisfactory. Furthermore, this sizing allows future experiments on supersonic co-flows to be performed, where common configurations in literature have area ratios between 2 and 5 [187].

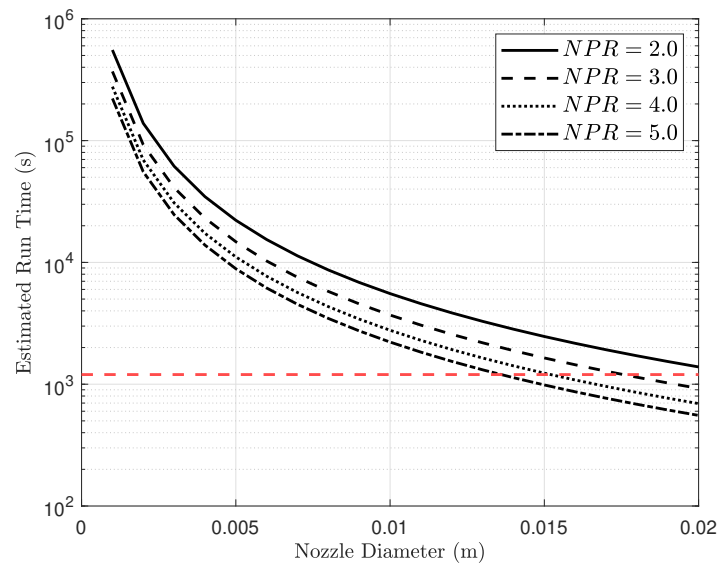


Figure 3.10: Run time as a function of nozzle exit diameter for a range of NPR. Red-dashed line indicates a 20 minute run time.

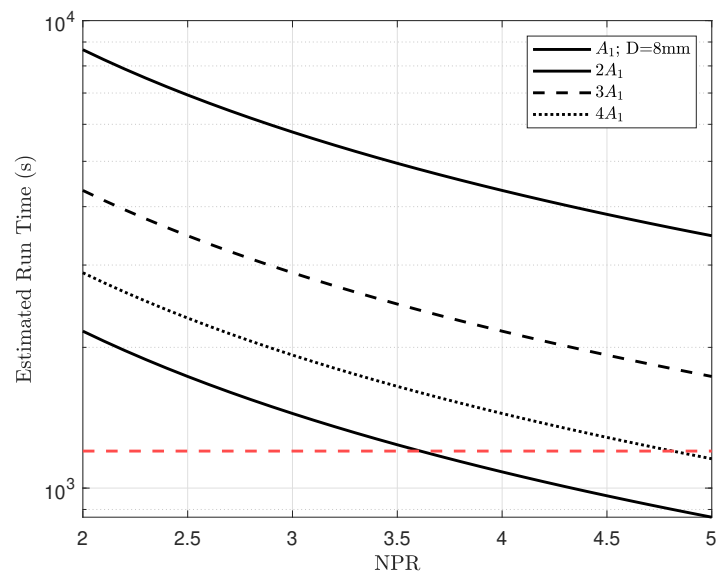


Figure 3.11: Run time as a function of NPR for an different nozzle exit areas.



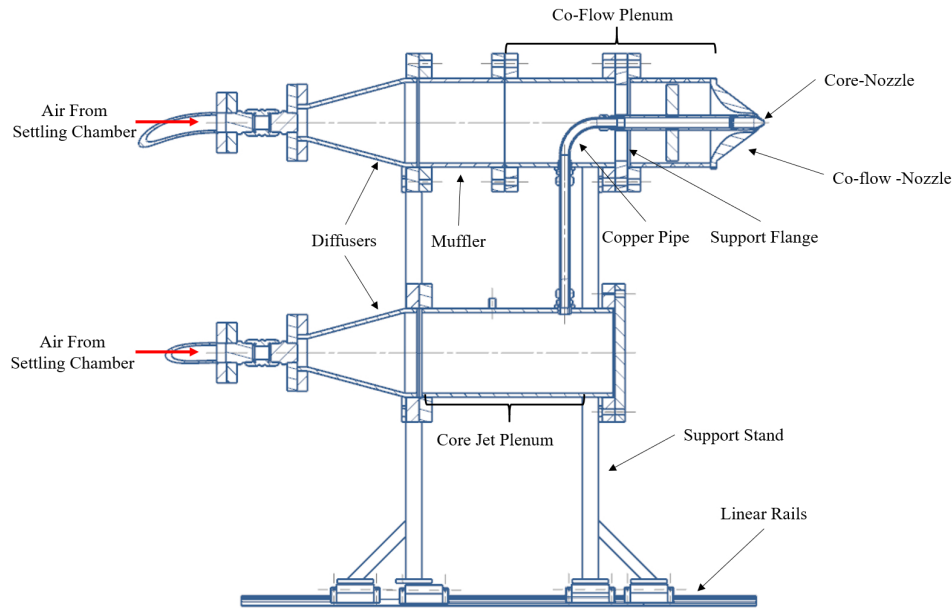


Figure 3.12: Cross-section side view schematic of jet rig.

### 3.5.2 Jet Ducting System

The full assembly of the jet rig is approximately 1.3m in length and the jet axis is 0.8m above the floor wedges. A cross-section of the co-axial jet rig is shown in figure 3.12. All pressurised components were designed to the appropriate ANSI high pressure standards and subsequently underwent and passed a hydrostatic pressure test to a limit of 20 bar, which is well above what the compressor can produce.

#### 3.5.2.1 Settling Chamber

Immediately downstream of the butterfly valve, compressed air flows into a large settling chamber. The role of the settling chamber is two-fold. Firstly, upstream pressure fluctuations (from valves and feed pipes) are damped out by permitting the flow to settle and be isolated from the jet. Secondly, the settling chamber allows PIV seeding to be injected into the flow and controlled by the operator externally. The size of the settling chamber was based on allowing adequate time for the compressed air to be seeded; an estimated suitable settling time is 5-10s [174]. The tank was constructed using a single mild-steel tube with an internal diameter of 280mm and a 600mm flange welded on at either end. Ports for introducing seeding material and measurement probes were also manufactured.

Another reason to have a large settling chamber is it serves as a simple muffler to attenuate

upstream noise. The sudden expansion and contraction at the inlet and outlet respectively causes sound waves to reflect back and interfere with each other. The diameter of a muffler should be made as large as possible and at least an order of magnitude larger than the nozzle exit [161]. The position of the settling chamber should attenuate sound generated by upstream components (compressor, control valve, duct noise). Using the method prescribed in Bies *et al.* [179], the transmission loss of this settling chamber is estimated to be between 5-10dB.

The flow leaving the settling chamber is then split into two streams; one to the core jet and the other to the co-flow. While dual settling chambers are desirable for individual control of both jets, the duplication of equipment in a limited space made this option not feasible. Pressurised air from the settling chamber is then fed into the jet plenums via a flexible wire-braided high-pressure Polytetrafluoroethylene (PTFE) hose. The flexible high-pressure hoses removed potential sharp bends that would generate spurious noise [161].

### 3.5.2.2 Plenum Chambers

The jet is constructed in a modular fashion; each section is made out of mild-steel and joined together via flanged connections. Gaskets are used to seal the gap between each section. The recess and protrusion due to gaskets may produce unwanted internal noise [161], though this may be mostly avoided if the flow velocity is sufficiently low. The low entrance velocity is achieved by expanding the flow through a wide-angle diffuser into a large-diameter plenum. An additional acoustic muffler, of the same diameter as the plenum, is used to attenuate flow noise generated upstream. The muffler walls are lined with acoustic foam.

The core-jet and the co-flow each have their own individual plenum chambers. The diameters of the plenum chambers were chosen to minimise fluid velocity and to provide a large contraction ratio for the nozzles. The core jet plenum sits underneath the main jet axis, with a length of 0.5m and 200mm diameter. The co-flow plenum is in line with the jet axis with a length of 0.7m and an identical diameter. No flow conditioning was performed upstream of either nozzle because of the large contraction ratio, though it may easily be introduced.

The core-jet plenum is connected to the nozzle via a bent copper tube and a straight

steel pipe with a total length of 800mm and a diameter of 25.4mm. The protrusion of the copper tube into the co-flow plenum was deemed to have minimal effect, since the plenum velocity is sufficiently low, the nozzle contraction ratio is large, and the protrusion location is far-upstream relative to the nozzle exit. A similar design was also used in the coannular jet by Cutler and White [185]. Copper was chosen because of the required bend radius of 80mm.

### 3.5.2.3 Flow Control & Monitoring

Pressure probe ports are placed throughout the jet rig; the settling chamber and each of the jet plenums have a single port. All probes are connected to a single LabVIEW control program. To measure stagnation pressure, as used to compute NPR, RS-3100 pressure transducers with a range of 0-10 bar are mounted to each plenum. For the settling chamber, the pressure is measured using the same type of pressure transducer but with a range of 0–20 bar. The stated manufacturer accuracy of the transducer is  $\pm 0.25\%$ , but the variance in measured plenum pressure was approximately  $\pm 1\%$ . In order to manually select the desired NPR for both jets, a pair of Fairchild 100 High-Flow pressure regulator are used for each stream [47], mounted immediately after the settling chamber. The manual option was not only more cost effective, but also simplified the design compared to an automated option.

### 3.5.2.4 Supporting Structures

To ensure its concentricity and structural integrity, the centrebody of the core jet is secured by a 'spider' (support flange with struts) holding it in place (figure 3.13). The spider was cut out of a steel block using a CNC machine, with three struts separated equally in the azimuthal direction. The centrebody is held in place by a circular slot. Bridges *et al.* [188] and Zaman *et al.* [189] found that tones occur because of the coupling between vortex shedding of the supporting struts with various duct acoustic modes. Tabs mounted on the leading edge are therefore used to disrupt this resonance behaviour.

Appropriate supporting structures were manufactured for both the settling and plenum chambers. The large settling chamber is supported by a transportable mild-steel stand mounted on castor wheels, enabling the structure to be easily manoeuvred into place during

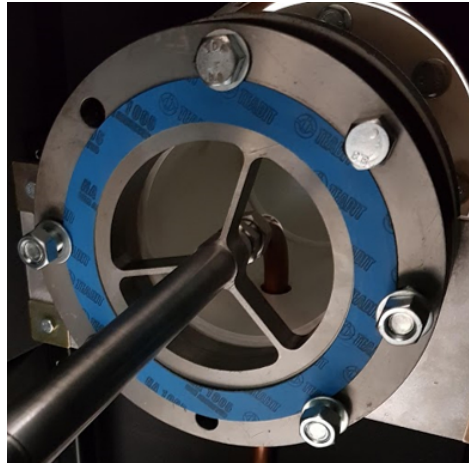


Figure 3.13: Spider for core jet centrebody. Tabs not shown.

installation. The plenums are supported on stainless steel stands that run along linear rails, allowing the whole jet rig to be traversable in the axial direction. This capability is useful for maximising microphone polar angles and small adjustments during optical alignment of the jet. Linear rails also require less force from the operator when moving the heavy steel components. During acoustic measurement campaigns, foam is used to cover any remaining exposed surfaces.

### 3.5.3 Nozzles

The contraction profile of the jet was based on optimal design guidelines [190–192]. Both the core jet and the co-flow undergo a contraction where the profile of the jet follows a fifth-order polynomial, ensuring smooth connection with the plenum sections. The core jet issues from a converging-round nozzle with an exit diameter of 8mm and a lip thickness of 0.5mm. The nozzle body is attached to the straight tube section via a threaded joint. This allows for simple modifications to the nozzle exit if desired. The joint was manufactured such that smooth transitions occur on both the inside and outside surfaces. The resulting contraction ratio is 10.

The co-flow nozzle is required to provide seeding to the ambient flow. The configuration can also be used to study co-axial jets. The co-flow nozzle is constructed from mild-steel and is mounted onto the flanged section. A tailored centering pin was designed and used to ensure the jet axis of the two nozzles are aligned. The protrusion length of the co-flow nozzle can be adjusted using appropriate spacers to change the axial separation between

the nozzle exit planes. When only the core-jet is in operation (see the measurements in Chapter 5 for example), the co-flow nozzle can be removed. This is beneficial since the upstream directivity range is improved for acoustic measurements.

### 3.6 Concluding Statement

This chapter provided a design overview of the new Supersonic Jet Anechoic Facility (SJAF) at Monash University. The purpose of the facility is to provide an acoustically clean environment for fundamental jet noise research, in which acoustic and velocity measurements can be obtained. The anechoic chamber was designed with a number of novel features to allow optical diagnostic measurements to be performed. Located in the same laboratory space, the jet rig shares the same air supply as the supersonic wind tunnel. A challenging aspect of the design process was to fit the facility within the space available, while ensuring acoustic performance was not compromised. It was also designed to be adaptable to future modifications and upgrades.

The first critical step of the design was to determine the size of the anechoic chamber. The final dimensions ( $l \times w \times h$ ) resulted in an internal wedge-tip to wedge-tip distance of  $1.5\text{m} \times 1.2\text{m} \times 1.3\text{m}$  and an external dimension of  $2.8\text{m} \times 2.0\text{m} \times 2.0\text{m}$ . The anechoic chamber is lined with acoustic wedges of length  $0.3\text{m}$  which corresponds to a nominal cut-off frequency of  $500\text{Hz}$ .

The jet rig has a primary core jet and a secondary co-flow with exit diameters  $8\text{mm}$  and  $16\text{mm}$  respectively, corresponding to an area ratio of three. The outer-flow provides seeding material to the ambient air during PIV campaigns, or may be used to investigate dual-stream jets. Appropriate plenums and a settling chamber were incorporated between the nozzles and the main supply line to ensure stable upstream conditions and control of air flow. The jet rig was designed in a modular fashion, allowing modifications in the future as required.

Following the design and construction, prior to undertaking an experimental campaign, the anechoic jet facility must be calibrated to establish its acoustic characteristics. The steps used to validate the facility design are outlined in Chapter 4.

## Chapter 4

# Anechoic Facility Validation

### 4.1 Introductory Statement

First and foremost, a high-quality jet noise research facility should provide an acoustically-clean environment for noise measurements. For the desired frequency range, the anechoic chamber should mimic a free-field environment. While the facility was designed to meet the specifications listed in section 3.3, calibration tests needed to be performed to ensure the chamber is indeed anechoic for the frequency range specified. It is also important to characterise the acoustic performance in light of the potential contamination of measurements by a number of sources including unwanted reflections, rig noise, or valve noise.

General requirements for anechoic chambers are specified in the ISO 3745 engineering standards [178], though the qualification methods described in this section are specific to jet noise research facilities [161, 166]. The validation process may be broken down into three parts: 1) verification of the free-field behaviour of the anechoic chamber, 2) determination of the geometric far-field of the jet and 3) identification of potential sources of spurious noise. To confirm that free-field behaviour is achieved, measured sound intensity should obey the inverse-square law with increasing distance.

It is important to emphasise the present validation process was focused on characterising the facility, and understanding the possible sources of extraneous noise. This exercise was not intended to match measurements to those from other existing ‘validated’ facilities. As pointed out by Bridges and Brown [166], there is no single ‘standard’ set of jet noise measurements; radiated noise is highly sensitive to upstream flow conditions, including

the state of the nozzle exit boundary layer [73], which are often difficult to replicate across different jet rigs. Further, the facility is new, and the nozzle is untested, so there were no historical datasets available for direct comparison. The aim of the qualification process was thus to independently determine the acoustic performance of the facility. In addition, the validation measurements provide a 'baseline' database for the SJAF. Future modifications and upgrades to the facility can be quantified and compared against these measurements. Nevertheless, qualitative comparisons of acoustic results with other facilities are shown to ensure salient jet noise trends are recovered. Specifically, results include comparisons to subsonic 'baseline' noise measurements from NASA's Small Hot Jet Aeroacoustic Rig (SHJAR) [166], far-field acoustics of shock-containing jets from the NASA Langley Jet-Noise Laboratory (LJNL) [29] and the LTRAC Supersonic Jet Facility (SJF) at Monash [84]. Jet noise results of Bridges and Brown [166] and Norum and Seiner [29] were used to identify possible noise sources other than the jet itself. Comparisons to results from the SJF demonstrate the improved acoustic environment of the SJAF, particularly for the detection of BBSAN.

While the initial design is a co-axial jet, all calibration measurements were performed using a single jet stream; there is no co-flow and the outer nozzle was removed. This not only simplifies the validation campaign, but also matches the experimental setup used to obtain the measurements in Chapter 5. For all calibration measurements, window openings were covered with acoustic foam. Flow field characterisation of the facility was not performed, but should be completed in future work.

## **4.2 Instrumentation, Data Processing & Microphone Corrections**

### **4.2.1 Instrumentation Details**

Acoustic measurements were made using G.R.A.S. Type 40BE 1/4" pre-polarised free-field microphones with a flat frequency response between 4Hz-100kHz and a nominal sensitivity of 3.6mV/Pa. The microphone was connected directly to a G.R.A.S. 1/4" CCP Standard Preamplifier and a 12AL 1-Channel CCP Power Module via a 6m BNC cable. The microphone signals were acquired using a National Instruments DAQ (NI USB-6341 16-Bit). The NI-SignalExpress program was used to acquire the measurements. Prior to each daily run, the microphones were calibrated using a G.R.A.S. pistonphone with a standard calibration

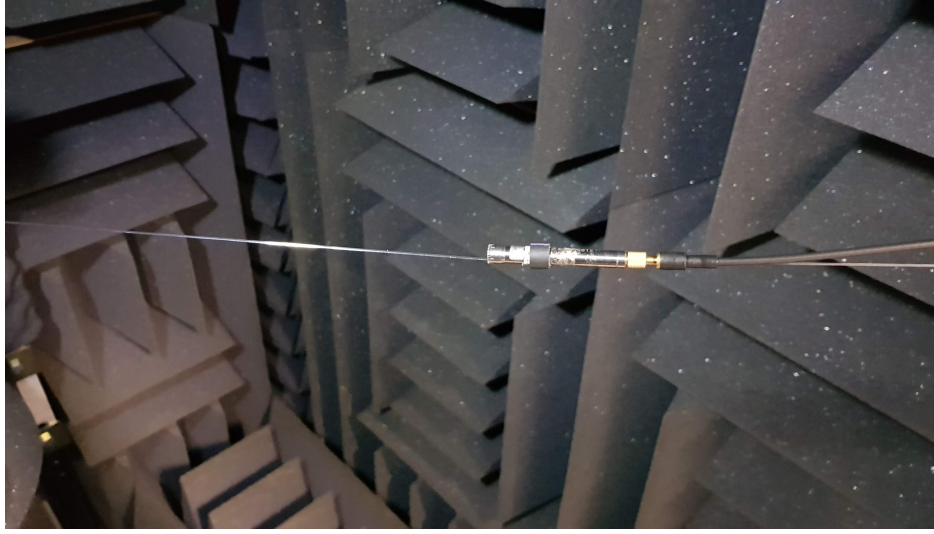


Figure 4.1: Mounting of microphones.

level of 114dB at 1kHz. The reference pressure used for all acoustic measurements was  $P_{ref} = 20\mu\text{Pa}$ . The calibrated microphone sensitivity  $S$  (mV/Pa) is defined as

$$S = \frac{V_0}{P_{ref} \times 10^{L_c/20}} \quad (4.1)$$

where  $V_0$  is the measured output voltage,  $L_c$  is the pistonphone's output sound pressure level (114dB).

The small internal size of the anechoic chamber precluded the incorporation of a custom microphone stand, which if poorly designed, would likely be a source of unwanted acoustic reflections. The microphone supports must have minimal surface area and be readily adjustable for different measurement positions. With this in mind, microphones were mounted on a rubber sleeve attached to taut fishing lines, similar to Hahn [171]. One end of the fishing line was attached to the source (nozzle or speaker), and the other to the foam wedges. The sleeve slides across the length of the string as needed. The radial microphone traverses may be easily adjusted throughout the room as required. No evidence of acoustic reflections was observed using this mounting technique. The microphones were aligned to the source, corresponding to a  $0^\circ$  angle of incidence. For all acoustic measurements, solid surfaces of the jet plenum were covered with acoustic foam.

For the acoustic far-field test in detailed in section 4.3.1, a 45mm diameter speaker with a range of 140-20,000Hz was used to replicate a point source. A Stanford Research Systems



DS345-30 MHz function generator was used to generate the input signal to the speaker.

### 4.2.2 Acoustic Data Acquisition & Processing

Each recording consisted of 400,000 samples and was acquired at a rate of 200kHz at 16-Bit, corresponding to a Nyquist frequency of 100kHz. This equates to a total recording time of two seconds. A low-pass filter was applied during post-processing to remove aliasing effects. Before carrying out the Fast Fourier transforms (FFTs) of the pressure signal, to improve convergence, the time series was separated into data blocks. To suppress side-lobe leakage, a Hanning window was used. The power spectral density (PSD) was computed by applying a FFT on each data block. The sound pressure level (SPL) was then converted to decibel per unit frequency

$$SPL(f) = 10 \log_{10} \left( \frac{PSD(f)}{P_{ref}^2} \right). \quad (4.2)$$

where SPL is presented in units of dB/Hz. For jet noise measurements, the PSD was non-dimensionalised by the factor  $U_j/D_j$ , and frequency is thus defined as  $St = fD_j/U_j$  where  $D_j$  and  $U_j$  are the ideally-expanded diameter and velocity of the jet respectively. The non-dimensionalised SPL has units dB/St. A detailed methodology for the post-processing of acoustic data is presented in section 5.6 of Chapter 5. Unless otherwise specified, the noise data is presented as narrowband power spectral densities (PSDs) and SPLs are in units of dB/Hz or dB/St. The overall sound pressure level (OASPL) in dB may be obtained by integrating over the entire narrowband spectra

$$OASPL = 10 \log_{10} \left( \sum 10^{\frac{SPL(f)}{10}} \right). \quad (4.3)$$

### 4.2.3 Microphone Response Corrections

As alluded to in Chapter 3, the high frequencies of BBSAN ( $\sim 10^5$ Hz) generated by the 8mm nozzle necessitate some corrections to the raw signal. Firstly, at this frequency range, the microphone protective grids have a significant effect on the measured signal as shown in figure 4.2a. Thus, the microphone grids were removed for all measurements.

Microphone pressure response also needs to be adjusted as the acoustic wavelengths

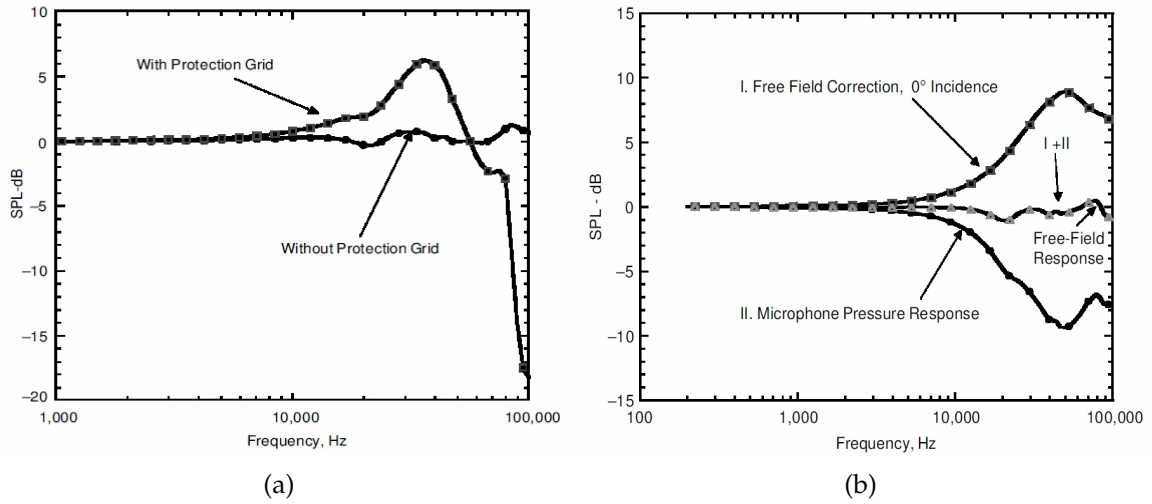


Figure 4.2: Corrections for microphone pressure measurements; a) effect of protective grid on microphone pressure readings and b) schematic of manufacturer-specified free-field corrections. Adapted from Ahuja [161].

become comparable to the size of the microphone; the sound field is disturbed and diffraction can occur. The correction is made by adding the microphone pressure reading to the free-field corrections (figure 4.2b) supplied by the manufacturer (figure 4.3). Without the application of these corrections, the measured signal can be several decibels lower than the true signal. To apply the correction, both the measured pressure response and the free-field corrections were expressed in 1Hz bandwidth (dB/Hz) [161].

Since the internal dimensions of chamber are small, atmospheric corrections were not performed. The background noise was checked to ensure it did not affect the measurements; an appropriate threshold of the signal being 3dB louder than the background was considered [166]. Ambient pressure and temperature were monitored during experiments.

### 4.3 Free-field Calibration

Free-field calibrations of the anechoic chamber were performed to determine if the chamber is indeed anechoic according to the definitions supplied in ISO 3745[178]. An important characteristic of a free-field environment is that sound amplitude should follow the inverse-square law; for every doubling in distance, there is a 6dB decrease in sound intensity. A point source (speaker) and the jet were used to determine the *acoustic* and *geometric* fields respectively.

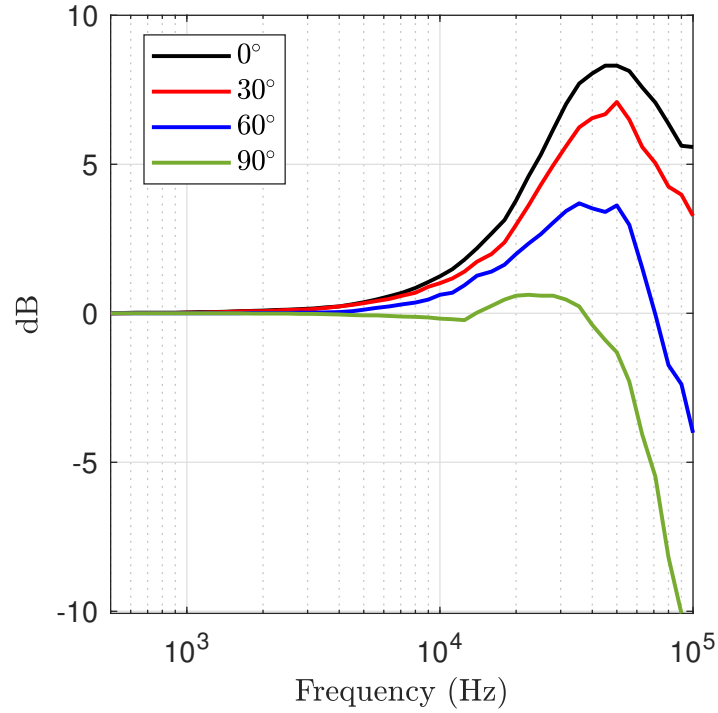


Figure 4.3: Free-field corrections for G.R.A.S. Type 40BE microphone without protective grid for a range of incident angles.

The ‘acoustic’ far-field is defined as the maximum radial distance where the sound field of a point source obeys the inverse-square law, and is not subjected to near-wedge effects and reflections from the chamber walls. In contrast, the ‘geometric’ far-field is bounded by the minimum radial distance for which the inverse-square law is obeyed where the jet exhaust is now the source. For far-field measurements, the microphone should be mounted in both the acoustic and geometric far-field. The qualification tests performed confirmed the limits of both regions, as well as the cut-off frequency of the chamber. All measurements were made with the jet rig in place.

To determine the deviation from the inverse-square law, the method prescribed by Cune-fare *et al.* [193] was used. The theoretical free-field SPL ( $SPL_p$ ) at distance  $r_i$  is given by

$$SPL_p(r_i) = 20 \log_{10} \left[ \frac{a}{r_i - r_0} \right], \quad (4.4)$$

where  $a$  and  $r_0$  are the apparent acoustic source strength, and the offset distance between the physical location of the source and its acoustic centre, respectively. For  $N$  measurements in the radial direction, the values of  $a$  and  $r_0$  are

Table 4.1: Maximum deviations allowed for SPL measured in an anechoic chamber.

Frequency Range (Hz)	Tolerance (dB)
$\leq 630$	$\pm 1.5$
800 - 5000	$\pm 1.0$
$\geq 6300$	$\pm 1.5$

$$a = \frac{(\sum_{i=1}^N r_i)^2 - N \sum_{i=1}^N r_i^2}{\sum_{i=1}^N r_i \sum_{i=1}^N q_i - N \sum_{i=1}^N r_i q_i}, \quad (4.5)$$

$$r_0 = \frac{\sum_{i=1}^N r_i \sum_{i=1}^N r_i q_i - \sum_{i=1}^N r_i^2 \sum_{i=1}^N q_i}{\sum_{i=1}^N r_i \sum_{i=1}^N q_i - N \sum_{i=1}^N r_i q_i}, \quad (4.6)$$

where  $q_i = 10^{-0.05(SPL_{pi})}$ . The discrepancy in dB between the measured  $SPL_{pi}$  and theoretical value at distance  $r_i$  is thus given by

$$\Delta SPL_p(r_i) = SPL_{pi} - SPL_p(r_i). \quad (4.7)$$

As specified in the standard [178], maximum permissible deviation between measured and theoretical sound pressure levels in an anechoic environment is summarised in table 4.1. The tolerances must be satisfied in all directions and at a distance greater than a quarter wavelength away from the chamber wall.

#### 4.3.1 Acoustic Far-Field

For the acoustic far-field test, the speaker was placed facing upwards at the centre of the room (0.7m from the back wall and 0.6m from the side walls). The ISO 3745 standard [178] requires the microphone to be traversed in four principle directions, from the speaker to the upper corners of the chamber, and an additional direction of choice. The direction chosen was directly above the source. Figure 4.4 shows the five directions used for the free-field qualification test.

It has been demonstrated that pure-tone qualifications will always exhibit a higher deviation from free-field performance than if a broadband signal is used [194]. Hence, pure tones were generated to obtain the largest deviation possible. The microphone distance began at

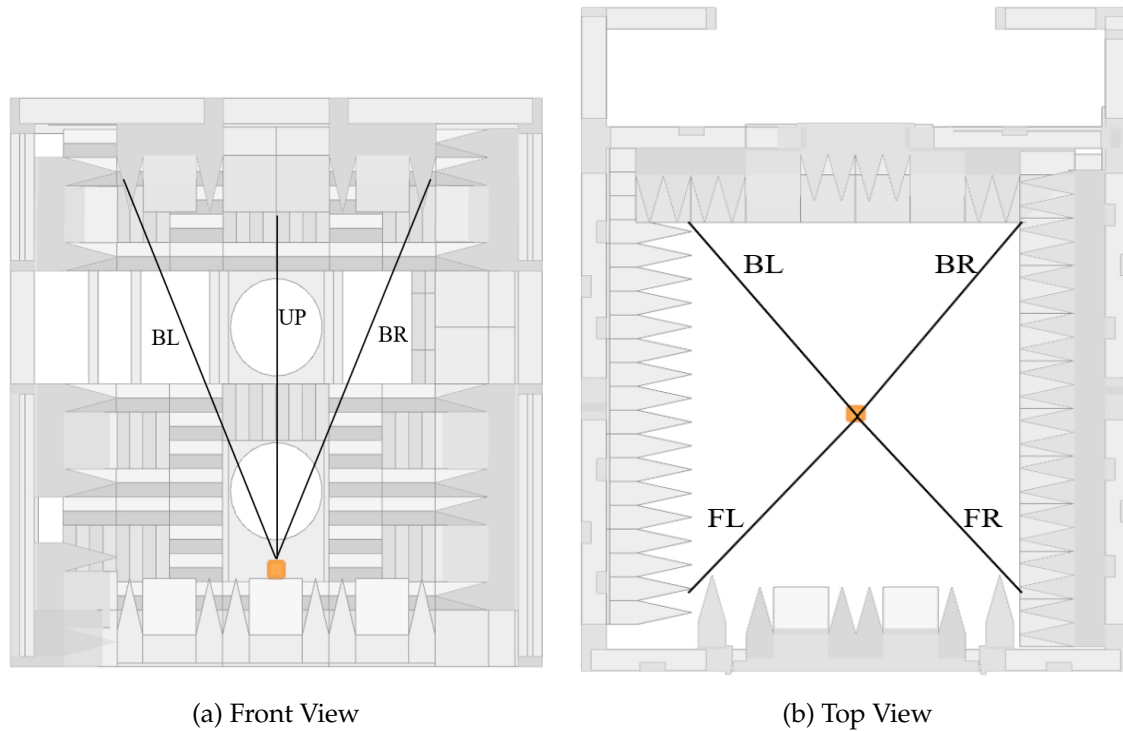


Figure 4.4: Microphone traverse directions as specified by ISO 3745.

0.2m from the source and extended incrementally to the wedge-tip at the wall.

The results from the qualification tests are shown in figure 4.5 for a selection of frequencies. For all directions at 250Hz, the measurements do not obey the inverse-square law and the chamber cannot be deemed anechoic at this low frequency. For the 500Hz signal, the microphone data is contaminated by near-wall effects. This is expected as the nominal design cut-off frequency is 500Hz (section 3.4.1). At higher frequencies, the deviations are within the specified tolerance across all tested directions. Despite the presence of the jet rig, measurements for the rear wall are within tolerance. Evidence of reflections close to the wedge-tips is absent as minimal deviations are observed when distance increases.

In addition to the measurements required by the standard, the speaker was placed along the jet centreline at a position close to the nozzle exit (figure 4.6). The microphone was traversed along three polar angles;  $60^\circ$ ,  $90^\circ$  and  $120^\circ$ , with the speaker position defining the origin. The additional measurements were made to mimic the typical microphone positions used in jet noise experiments.

Figure 4.7 shows that for the frequencies of interest, deviations are within the required tolerance (table 4.1), confirming that the inverse-square law holds for far-field measurements.

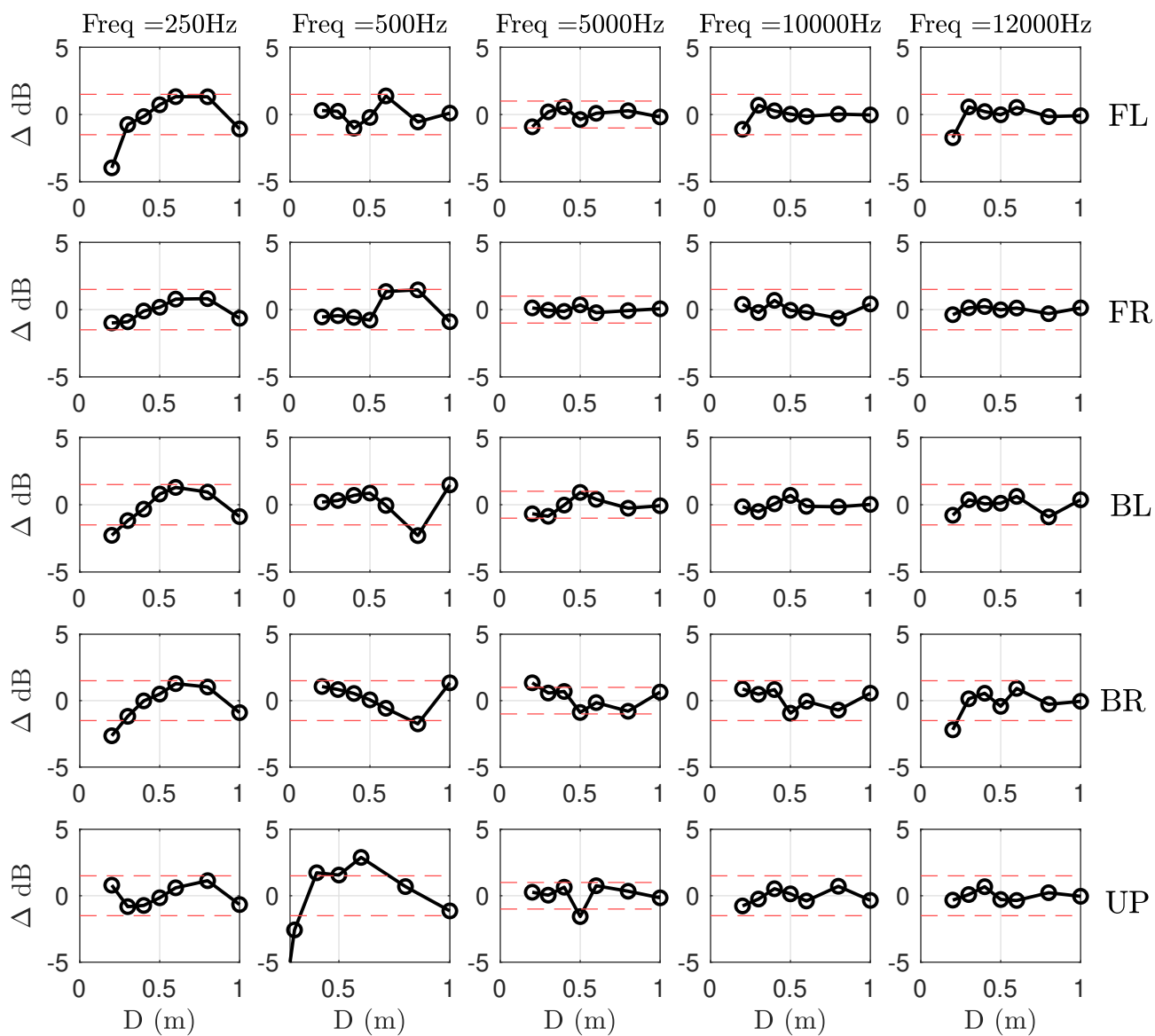


Figure 4.5: Deviation from the inverse-square law. Tolerances (red-dashed lines) from ISO 3745.

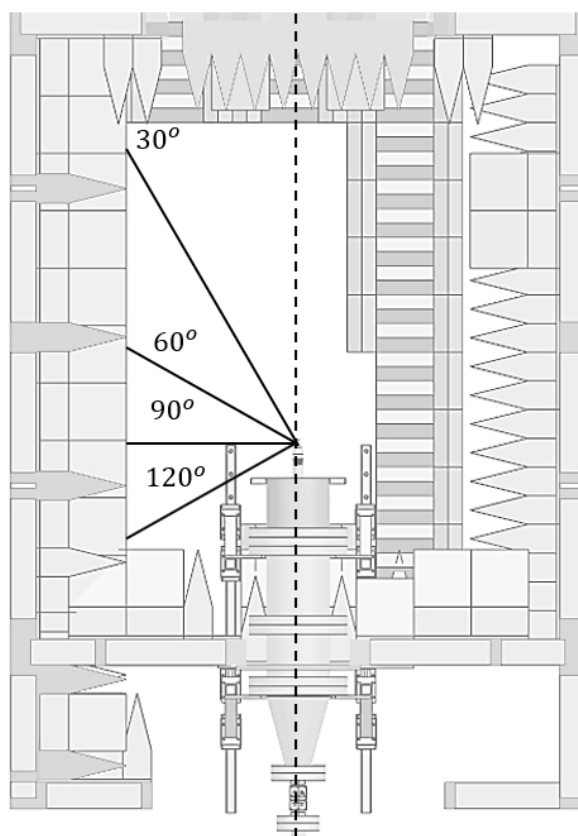


Figure 4.6: Microphone directions for jet source measurement. Microphone not shown.

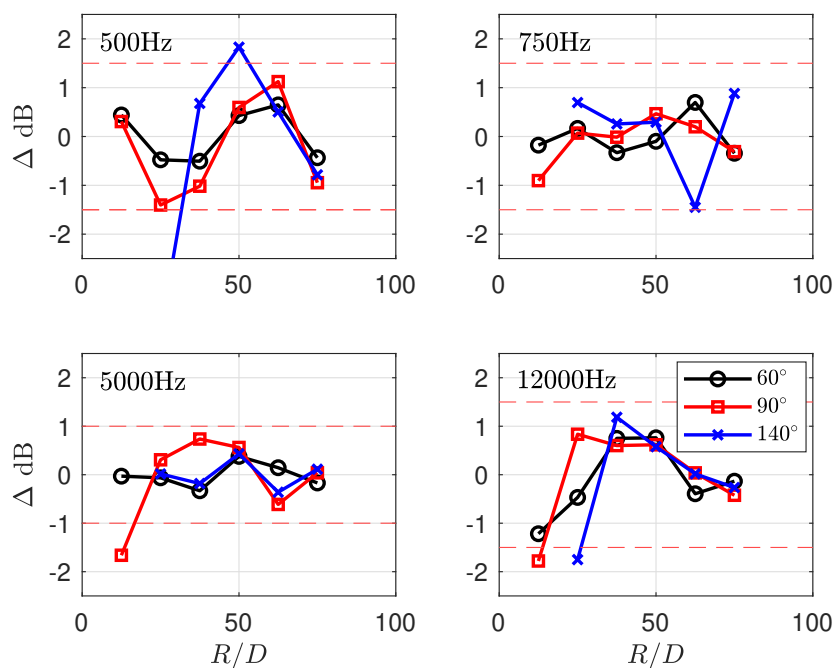


Figure 4.7: Deviation from the inverse-square law at three different polar angles for a range of frequencies. Red-dashed lines indicates maximum permissible deviation as specified by ISO 3745. Distance is normalised by jet diameter.

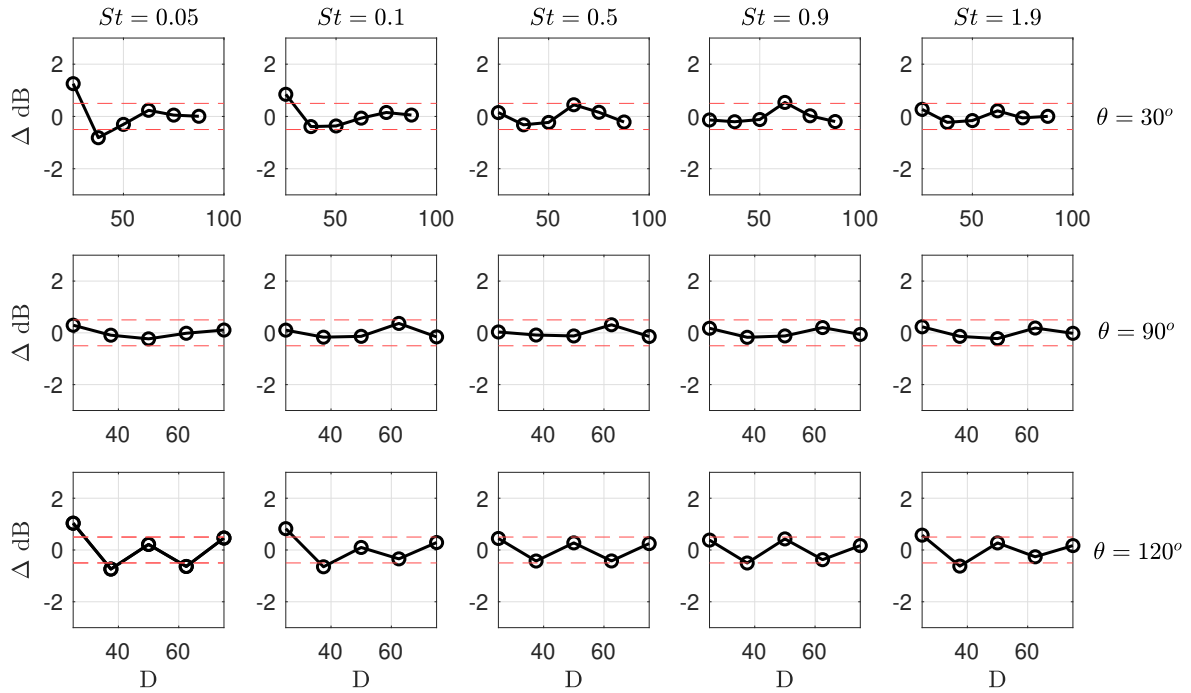


Figure 4.8: Deviation from the inverse-square law for  $M_j = 0.5$ .

Slight deviations are recorded closer to the nozzle at upstream positions ( $\theta = 140^\circ$ ) because of the presence of the jet plenums and support structure.

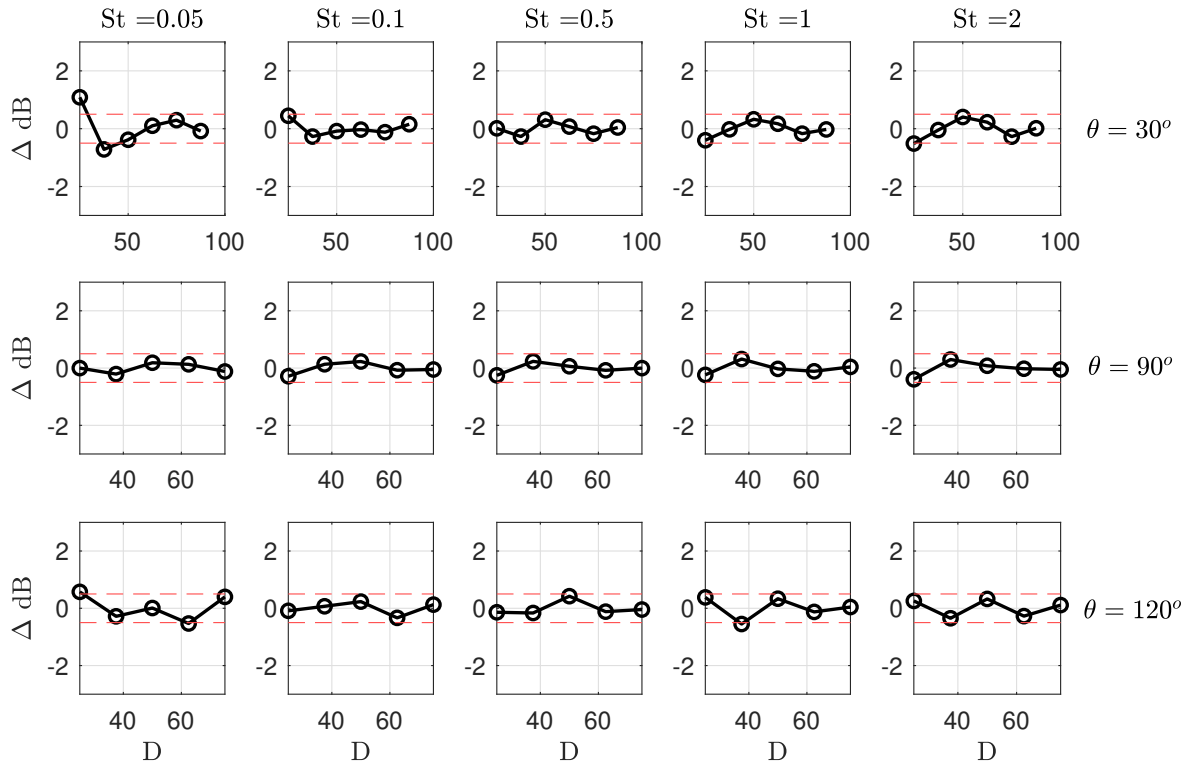
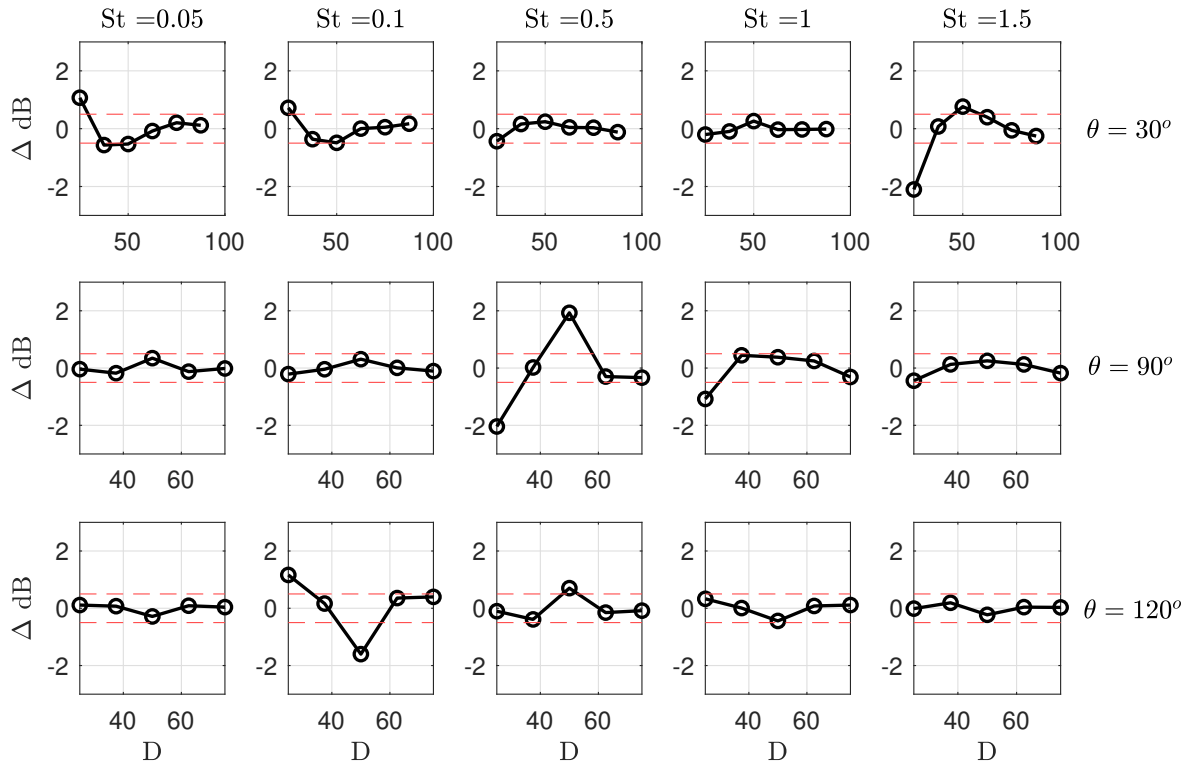
### 4.3.2 Geometric Far-Field

The geometric far-field test were performed using the jet as the sound source. The jet was operated at three exit velocities;  $M_j = 0.5, 0.9$  and  $1.5$ . The measurements were obtained at four polar angles:  $30^\circ, 60^\circ, 90^\circ$  and  $120^\circ$  (figure 4.6). The distance of the microphones was increased from  $0.2\text{m}$  to the wedge-tip at the wall in increments of  $0.1\text{m}$ . This corresponded to a non-dimensional distance of  $25D$  to  $75D$ .

The recorded signals were processed as described in section 4.2.2. The narrowband data were converted to one-third octave bands and the quoted non-dimensional frequencies are the central values of the corresponding band. By performing the analysis in one-third octave bands, the recorded signals are less susceptible to fluctuations that are not due to the acoustic performance of the chamber. A tolerance of  $\pm 0.5\text{dB}$  is shown for reference.

The results in figures 4.8-4.10 confirm the anechoic chamber is large enough for far-field acoustic measurements of turbulent jets to be obtained. The geometric far-field region begins approximately  $40D$  from the nozzle exit. It should be noted that these results only apply for



Figure 4.9: Deviation from the inverse-square law for  $M_j = 0.9$ .Figure 4.10: Deviation from the inverse-square law for  $M_j = 1.5$ .

a jet exit diameter of 8mm. Using a larger nozzle will yield a different geometric far-field limit. Changes in mass flow rate requirements may also alter internal rig noise. Similar tests must be conducted to ensure microphones are indeed in the far-field if larger nozzles are installed.

#### 4.4 Rig Noise Analysis

Ideally, all sources of rig noise should be identified and characterised [166]. Extraneous noise sources may include operation of the exhaust, resonant tones, ambient noise external to the facility, valve noise and duct noise. The behaviour of rig noise might also vary with operating jet conditions and ambient conditions. As explained by Bridges and Brown [195], a systematic and exhaustive approach would be to use insertion loss techniques, where each jet rig component is isolated to independently measure its contribution to the total noise field across the jet's full operational range. The inability to remove certain components (such as the pressure regulator used to set the jet NPR) rendered this method infeasible.

An alternative method is to evaluate the OASPL as a function of jet velocity. Demonstrated by Lighthill [13], acoustic power in subsonic jets follows the  $U^8$  scaling law. Deviations from this relationship indicate contributions from non-aeroacoustic sources. While unable to definitively separate each noise source, this method provides the total contribution and indicates susceptible operational ranges. Measurements were obtained at downstream ( $30^\circ$ ), sideline ( $90^\circ$ ) and upstream ( $120^\circ$ ) angles. The microphone was placed at a constant distance of  $50D$ .

Figure 4.11 shows that there is minimal rig noise for velocities greater than  $M \approx 0.7$ ; sound intensity closely tracks the  $U^8$  scaling law (equation 2.17). The downstream direction displays the best agreement with theory as this is the dominant direction of subsonic jet noise [112]. Similar to the measurements of Craft *et al.* [172], the sideline angle performed slightly worse than the other two directions. At low velocities, discrepancies are evident, especially at the upstream angle.

BBSAN is observed when the ideally-expanded Mach number is greater than unity ( $M_j > 1$ ). The intensity of BBSAN, represented by OASPL, is proportional to  $\beta^4$  [20], for  $\beta^4 > 0.5$ . The off-design parameter  $\beta$ , which represents the degree of underexpansion, is

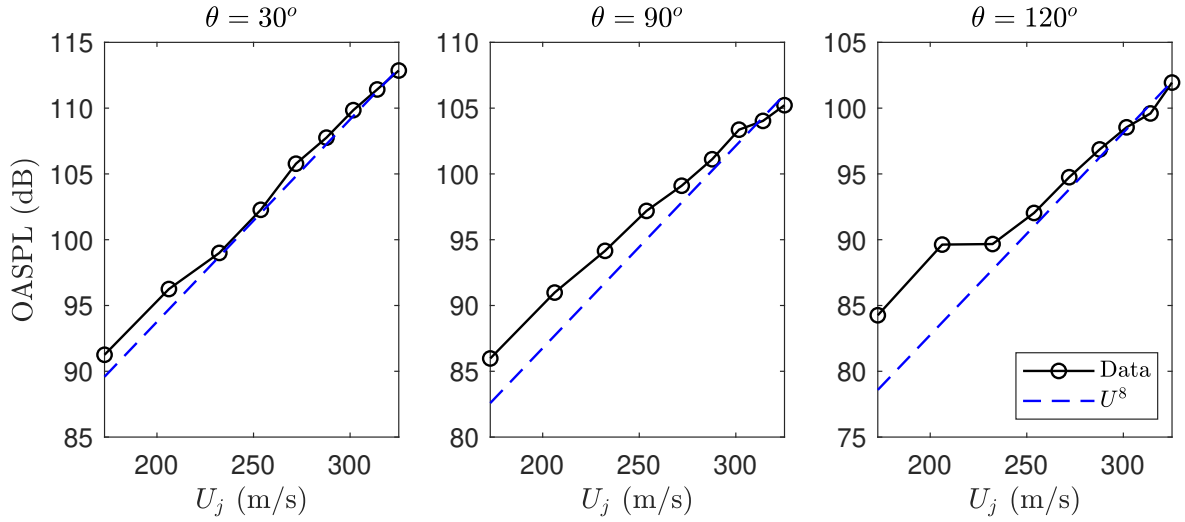


Figure 4.11: OASPL as a function of jet velocity for  $\theta = 30^\circ$  (left),  $\theta = 90^\circ$  (centre) and  $\theta = 120^\circ$  (right).

given by

$$\beta = \sqrt{M_j^2 - 1}. \quad (4.8)$$

Figure 4.12 shows that the measured signal follows this well-known relationship. Again, a larger degree of variation is observed in the sideline direction. At low values of  $\beta$ , the trend is not observed as the BBSAN contribution is small relative to turbulent mixing noise [20]. The results confirm that internal rig noise is not significant for high-subsonic and supersonic flows up to the operational limit of the facility.

## 4.5 Comparison of Jet Acoustic Spectra

To ensure the measured data do not contain spurious trends, another method is to compare it against well-validated jet noise data in literature [161]. High-quality historical data sets exist for both subsonic [195, 196] and supersonic [29, 197] jets. While operating conditions might be identical (within instrumentation uncertainty), comparisons of spectra between different facilities must be made with caution, since jet noise is highly sensitive to the facility itself. Minor differences in upstream flow conditions and the nozzle may affect the radiated noise.

For subsonic jet noise, the state of the boundary layer at the nozzle exit is critical to the radiated noise [198, 199, amongst others]. Given identical exit diameters, Zaman [199]

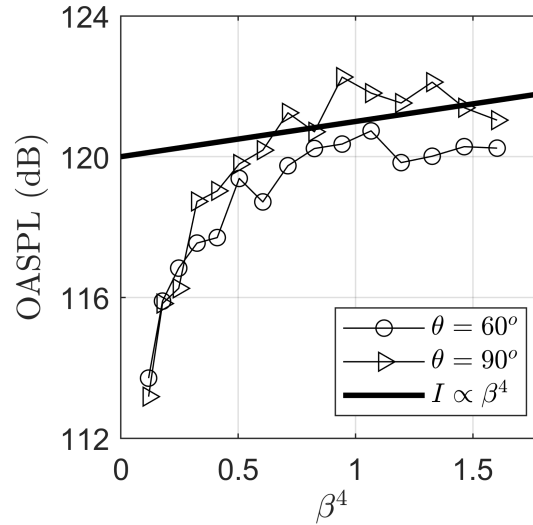


Figure 4.12: OASPL as a function of  $\beta$  for  $\theta = 60^\circ$  (circles) and  $\theta = 90^\circ$  (triangles).

showed that a nozzle with a nominally laminar boundary layer could produce higher sound pressure levels at high frequencies compared to one with a fully-turbulent boundary layer. Because of the large difference between plenum chamber and nozzle exit diameters, which yields a cleaner flow, laboratory-scale jets are usually of the former type [199]. To successfully match acoustic data from two jets, it is critical that the nozzle boundary layer conditions are also matched [73]. Since no boundary layer trip was utilised, and no flow measurements have been conducted to observe the resultant velocity field, it is expected that the new facility should exhibit different characteristics to those in other facilities.

Despite these observations, comparisons may provide a qualitative indication of possible acoustic contamination. Measured spectra in one-third octave bands are shown for  $M_j = 0.5$  and 0.9 and compared to the 'baseline' cold subsonic data from Bridges and Brown [195]. The microphones, mounted at  $30^\circ$  and  $90^\circ$ , were placed at a radial distance of  $50D_j$  and scaled in a lossless manner to  $100D_j$  to match the baseline dataset. It is important to note the nozzles used on the two jet rigs are significantly different.

Good agreement between the current measurements and data from Bridges and Brown [195] is observed in figure 4.13 at both Mach numbers. Some discrepancies are observed at high frequencies and near the peak (up to 5dB at some frequencies). Small oscillations with respect to a moving average across frequency are also visible for the current measurements. While these discrepancies could be the signature of rig noise [171, 177], another explanation

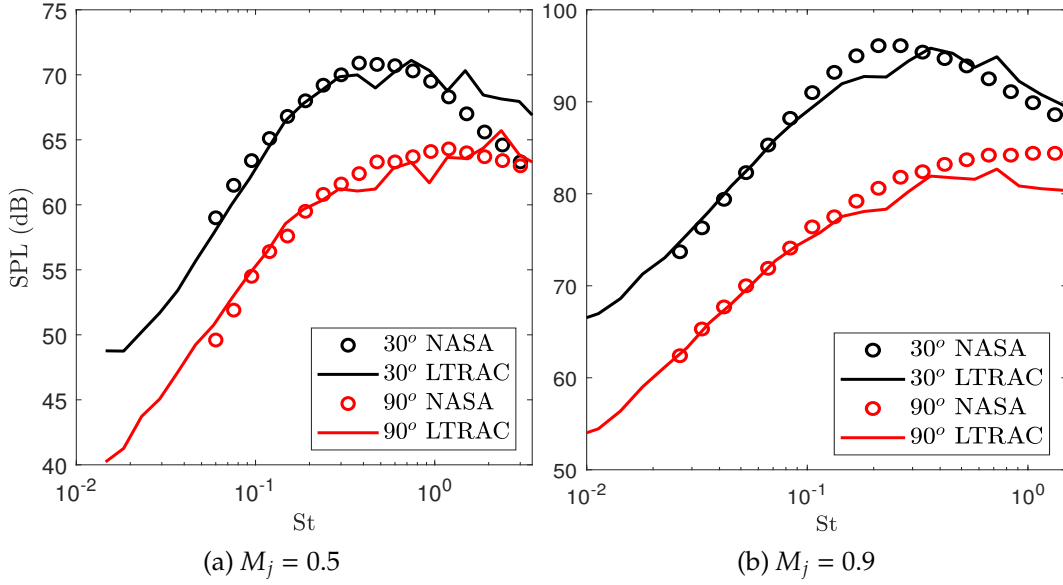


Figure 4.13: Comparisons with subsonic jet noise measurements from Bridges and Brown [195] (NASA).

for the mismatch may be attributed to the different design of the nozzles [195] as alluded to previously.

Comparisons for shock-containing jets are more precarious than the subsonic case. This is due to the presence of screech, which can significantly alter the BBSAN peak frequency and amplitude [22]. In addition to the sensitivities due to the plumbing, the external geometry of the jet rig, such as nozzle lip thickness, upstream flanges and supporting structures, may also have a significant effect on acoustic resonance mechanisms [5, 48]. Nevertheless, one-third octave band 'baseline' measurements from Norum and Seiner [200] were compared to measured data in figure 4.14. The baseline NASA data were obtained for an underexpanded jet at  $NPR = 3.67$  ( $\beta = 1.1$ ) at a radial distance of  $100D_j$ . The SJAF data were scaled in a lossless manner. At low frequencies ( $St < 0.2$ ), the baseline data is consistently louder than the current data by 1-2dB. At the BBSAN peak, however, there is good agreement in amplitude. The peak in the SJAF data at  $St = 0.31$  corresponds to the fundamental screech frequency which does not appear for the baseline case. Similar agreement is observed at other operating conditions, suggesting the SJAF data is sufficiently clean. When compared to figure 4.13, the relative improvement in agreement between the baseline and measured data may be the result of a nominally-turbulent boundary layer at higher Mach numbers [201].

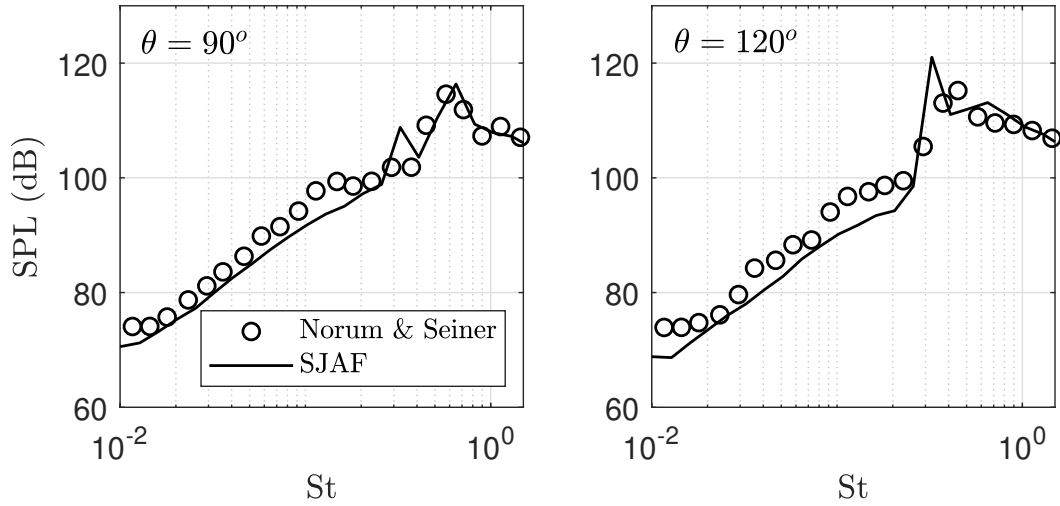


Figure 4.14: Comparison with one-third octave spectra data from Norum and Seiner [29] for an underexpanded jet at  $NPR = 3.67$ .

## 4.6 Comparison with Monash Supersonic Jet Facility

As discussed in the introduction of Chapter 3, one of the main motivations to construct the SJAF was to improve the free-field environment for jet noise measurements at LTRAC. To illustrate this improvement, current measurements are shown alongside historical data acquired in the non-anechoic Supersonic Jet facility (SJF). The comparison is again qualitative in nature since different nozzles were used; SJF used a converging  $D = 15\text{mm}$  nozzle [84]. Two underexpanded jet conditions ( $NPR = 2.6$  and  $3.4$ ) are shown in the  $St - \theta$  directivity maps in figure 4.15. Microphones were mounted in the far-field at a distance of  $50D$  from the nozzle exit. Polar angles ( $\theta$ ) were measured relative to the downstream jet axis. Frequencies and amplitudes have been normalised according to section 4.2.2. To aid in comparison, the dashed lines indicate BBSAN peak frequency predictions from equation 2.13.

There are clear differences between the two spectra. While screech tones (discrete horizontal lines) are detected at the same frequencies, they are broader in the SJF data. Contamination at low frequencies is observed in the SJF ( $St \approx 0.1 - 0.2$ ), particularly over sideline and upstream directions. For the case  $NPR = 3.4$ , there is an unexplained tone at  $St \approx 0.2$ . The main BBSAN lobe in the SJF spectra is also much weaker compared to the SJAF one. When compared to equivalent contour maps in literature [19, 53, 95], it is evident the SJAF spectra are superior in quality compared to those measured in the SJF. Similar conclusions can be made for other jet operating conditions.

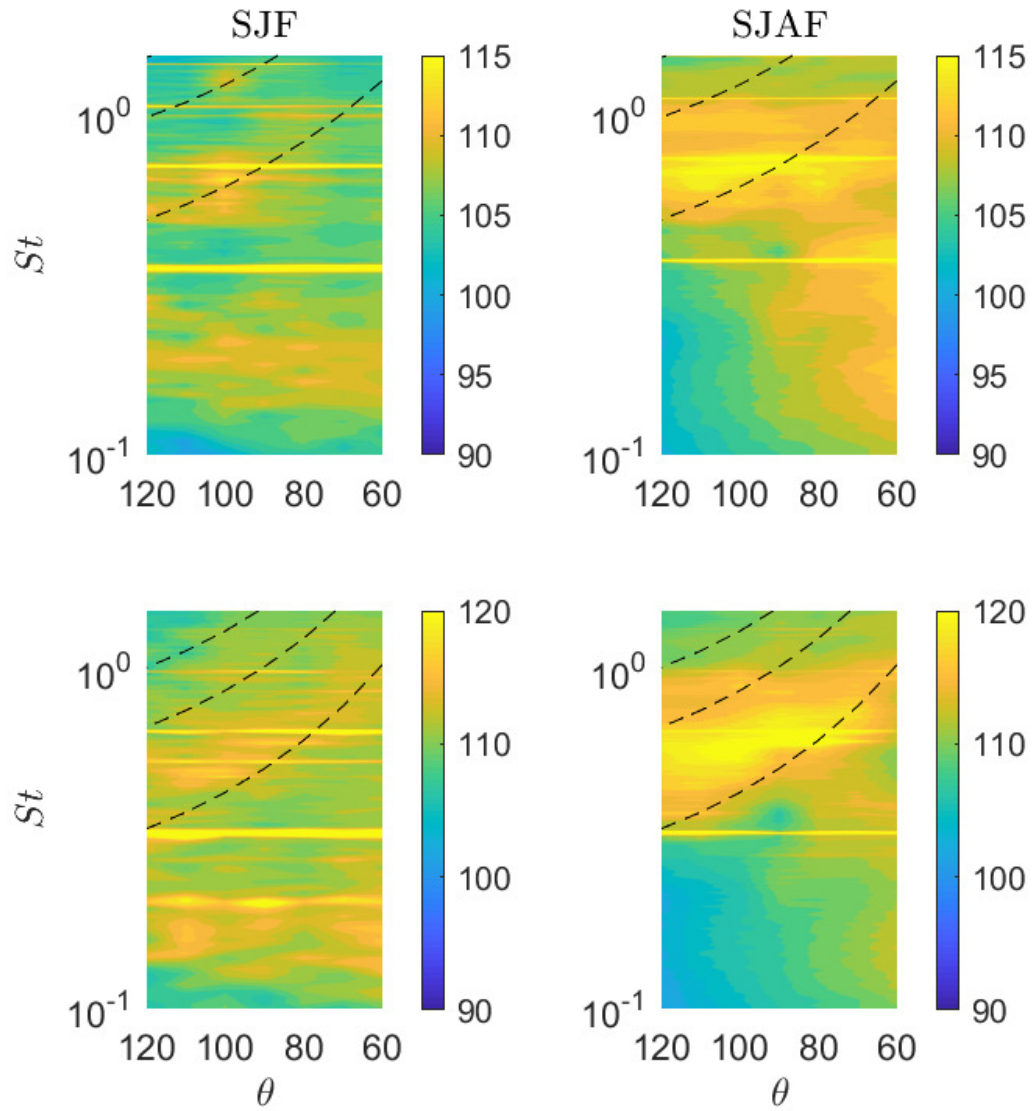


Figure 4.15: Comparison of far-field noise ( $50D$ ) measured in the SJF (left) and in the SJAF (right);  $NPR = 2.6$  (upper) and  $NPR = 3.4$  (lower). Dashed-lines show predictions from the model of Tam and Tanna [23] (equation 2.13) and contours are in units of dB/St.

## 4.7 Uncertainty & Repeatability

Since its completion in early 2019, several calibration and acoustic campaigns have been performed in the SJAF. An important measure of quality is the ability to replicate previous measurements and determination of the expected variability. Apart from variation in ambient conditions, instrumentation error and maintenance of flow conditions affect measurement uncertainty. Ambient temperature and humidity, recorded daily during a test campaign, varied between 15°C – 25°C and 40%-70% respectively.

The pressure sensors are calibrated yearly. The stated manufacturer accuracy of the sensors is  $\pm 0.25\%$ , but the measured plenum pressure range was approximately  $\pm 1\%$ . The microphone was calibrated daily and the pistonphone used has a tolerance of less than  $\pm 0.2\text{dB}$ . Maintaining the desired NPR remains the largest source of uncertainty as the plenum pressure is set and controlled manually by the operator.

A qualitative indication of the repeatability in measured acoustic data is shown in figure 4.16. One-third octave spectra measured at  $\theta = 90^\circ$  from three separate experiment campaigns of the same test case ( $NPR = 3.67$  underexpanded jet) are presented. The two peaks correspond to the bands containing a strong screech tone. Overall, there is good agreement ( $\pm 0.5 \text{ dB/St}$ ) between all datasets, particularly over the range of frequencies where BBSAN dominates. For the test campaign labelled '17-May-2019', degradation in the signal at both low and high frequencies is evident as the microphone protection grid is not removed (section 4.2.3).

Another method to quantify the uncertainty in the measured SPL is to determine the length of measurement time required for a specified confidence interval. The RMS of the measured pressure signal is assumed to follow a Gaussian distribution. A finite recording time results in a quantifiable uncertainty value that depends on the spectral bandwidth  $B$  and the measurement duration  $T$  [120]. The uncertainty  $\mu$  in dB, for a given standard deviation  $\sigma$ , is given by

$$\mu = 20 \log_{10} \left( 1 \pm \frac{\sigma}{2 \sqrt{BT}} \right). \quad (4.9)$$

Alternatively, the minimum time for each measurement  $T_{min}$  can be computed by rearranging equation 4.9,



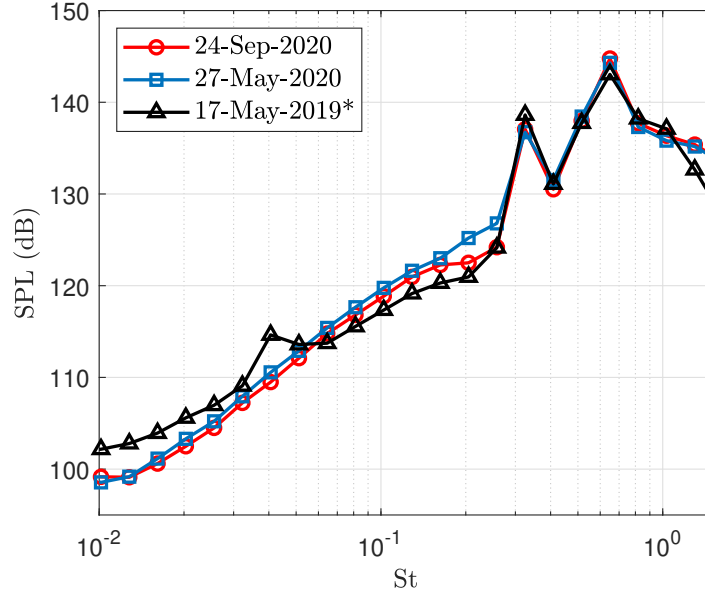


Figure 4.16: One-third octave spectra repeatability in the SJAF at condition  $NPR = 3.67$  for observer position  $\theta = 90^\circ$ . Note for case '17-May-2020' the spectra was taken with microphone protective grid on.

$$T_{min} = \frac{\left( \frac{2 \left( 10^{\frac{\mu}{20}} - 1 \right)}{\sigma} \right)^{-2}}{B}. \quad (4.10)$$

Using the same FFT parameters as section 4.2.2, for a  $1\sigma$  confidence interval and a target uncertainty of  $\pm 0.5\text{dB}$ , the minimum required recording time is 0.6 seconds. Since all acoustic recordings were obtained over a two second recording time, the condition is satisfied.

## 4.8 Concluding Statement

The steps performed to validate the new Supersonic Jet Anechoic Facility (SJAF) were outlined in this chapter. The methodology prescribed by Ahuja [161] was followed, and the requirements specified in ISO 3745 [178] were met. The qualification tests were necessary to determine the acoustic characteristics of the anechoic chamber, and also provided an opportunity to check both the experimental technique and data processing methodology. A large amount of acoustic data were obtained both with and without the jet in operation.

The free-field calibration process was split into two parts; the determination of the acoustic and geometric far-field. The acoustic characteristics satisfy the inverse-square law

within the bounds specified in ISO 3745 [178]. The geometric far-field for the single 8mm nozzle begins at 40-50D. The cut-off frequency of the chamber was found to be 500Hz.

As discussed by previous authors, validation of a facility does not require the reproduction of historical jet noise spectra; facility-specific effects make such an approach problematic. Instead, the objective is to identify reproducible discrepancies between measurements and well-known trends. The validation process identified that the largest source of acoustic contamination is from the jet rig itself; it is most significant at low Mach numbers and at high frequencies. For the study of BBSAN, the measured acoustic signal is deemed to be sufficiently clean.

While a large amount of acoustic data has been presented, continual quality control is required as planned upgrades occur. Results presented here apply only to the current configuration; a single 8mm jet with no eductor, and all chamber walls lined with foam wedges. Acoustic validation of the chamber needs to be repeated following the implementation of the anticipated PIV system, and flow-field characterisation will also be required. The removal of window wedge panels for optical access and operation of the exhaust may affect the acoustic behaviour of the facility. If different nozzles are to be used, validation of the acoustic far-field must be performed again. Ongoing checks with each design modification will be required to ensure data quality is not compromised.

The results presented in this section verify that the facility used for the measurements of this experimental campaign meets all the requirements specified in Chapter 3, and provides confidence in the acoustic data acquired in the SJAF. Subsequent to the validation process, an acoustic campaign was conducted in the facility to measure and azimuthally decompose the acoustic field of a supersonic shock-containing jet. This campaign is detailed in Chapter 5.

## Chapter 5

# Azimuthal Structure of Broadband Shock-Associated Noise

### 5.1 Introductory Statement

In the framework of sound generated by large-scale orderly structures, a decomposition in the azimuthal direction is often used to exploit the inherent symmetries of axisymmetric jets. Decomposition with respect to the azimuthal angle is convenient since, by construction, wavepackets are characterised by their axial and azimuthal structure [16]. Michalke and Fuchs [113] showed analytically that the lower-order azimuthal modes of the source are the most acoustically efficient. This has since been confirmed experimentally in subsonic jets [112, 202]. Furthermore, in a linear problem, an azimuthal component of the source will generate the same azimuthal mode in the sound field [63, 112, 113]; the contribution of a wavepacket source is most clear when compared to its corresponding azimuthal mode in the acoustic field. Thus, it is clear that azimuthally-decomposed mid-field or far-field sound measurements are critical in the assessing the efficacy of wavepacket source models.

Despite their aforementioned importance, few datasets currently exist in literature focusing on the azimuthal content of broadband shock-associated noise. Investigation of azimuthal modes in supersonic jets has historically been concentrated on the more dominant screech component [5]. For BBSAN, the detailed studies using LES data by Arroyo and Moreau [95] and Suzuki [96] provide insight into both far-field and near-field azimuthal

structure, but only at a single Mach number. Overall, there is a lack of data (experimental or numerical) showing the spectral content of each BBSAN azimuthal mode and its variation with Mach number.

The dearth of azimuthally-decomposed BBSAN data has hindered previous BBSAN modelling attempts. Despite the success of Tam's instability wave BBSAN model [157], where the source function involves both axisymmetric ( $m = 0$ ) and higher-order ( $m > 0$ ) azimuthal modes, the dependence on the azimuthal wavenumber was removed and the source was assumed to be solely axisymmetric. Contributions from higher modes were replaced by a similarity model. Similar treatments have been used by subsequent authors [149, 203, 204]. Due to the unavailability of decomposed BBSAN spectra, the exact contributions from each of the source's azimuthal modes are hidden.

To address these issues, and using the new facility described in Chapter 3 and 4, far-field and mid-field measurements are recorded for the noise radiating from an underexpanded jet. Acoustic data are acquired at three conditions ( $M_j = 1.14, 1.38, 1.5$ ) and a range of polar angles ( $60^\circ < \theta < 120^\circ$ ). Azimuthal decomposition is performed using the cross-correlation between a pair of microphones. Apart from filling the identified gap in the literature, the decomposed spectra is used in Chapter 7 for mode-by-mode comparisons with the new wavepacket model.

This chapter is presented as a journal paper published in The Journal of the Acoustical Society of America, "Azimuthal decomposition of the radiated noise from supersonic shock-containing jets", © 2020 Acoustical Society of America. This article may be downloaded for personal use only. Any other use requires prior permission of the author and the Acoustical Society of America. The following article appeared in Wong *et al.* [205] and may be found at [Marcus H. Wong et al, J. Acoust. Soc. Am. 148 2015 \(2020\)](#).

# Azimuthal decomposition of the radiated noise from supersonic shock-containing jets<sup>a)</sup>

Marcus H. Wong,<sup>1,b)</sup> Rhiannon Kirby,<sup>1</sup> Peter Jordan,<sup>2,c)</sup> and Daniel Edgington-Mitchell<sup>1,d)</sup>

<sup>1</sup>Laboratory for Turbulence Research in Aerospace and Combustion (LTRAC), Department of Mechanical and Aerospace Engineering, Monash University, Melbourne, VIC 3800, Australia

<sup>2</sup>Département Fluides, Thermique, Combustion, Institut Pprime, CNRS–Université de Poitiers–ENSMA, Poitiers, 86000, France

## ABSTRACT:

Acoustic measurements of unheated supersonic underexpanded jets with ideally expanded Mach numbers of 1.14, 1.38, and 1.50 are presented. Of the three components of supersonic jet noise, the focus is on the broadband shock-associated noise (BBSAN) component. Motivated by the modelling of BBSAN using the wavepacket framework, a traversable microphone ring is used to decompose the acoustic pressure into azimuthal Fourier modes. Unlike noise radiated downstream, BBSAN is dominated by azimuthal modes 1–3, which are approximately 3–4 dB/St stronger than the axisymmetric component. Crucially, the relative contribution of successive modes to BBSAN is sensitive to the observer angle and jet operating condition. Four azimuthal modes are necessary to reconstruct the total BBSAN signal to within 1 dB/St accuracy for the conditions presented here. The analysis suggests, however, that the number of modes required to maintain this accuracy increases as the peak frequency shifts upward. The results demonstrate the need to carefully consider the azimuthal content of BBSAN when comparing acoustic measurements to predictions made by jet noise models built on instability theory. © 2020 Acoustical Society of America.

<https://doi.org/10.1121/10.0002166>

(Received 17 July 2020; revised 12 September 2020; accepted 22 September 2020; published online 14 October 2020)

[Editor: Tim Colonius]

Pages: 2015–2027

## I. INTRODUCTION

Broadband shock-associated noise (BBSAN) is a high-frequency noise component emanating from shock-containing supersonic jets. Observed in both military (Vaughn *et al.*, 2018) and civilian aircraft (Huber *et al.*, 2014), it is more prominent in the upstream and sideline directions. BBSAN is produced by the interaction of downstream-travelling turbulent structures with the train of shock-cells in the jet plume (Tam, 1995). Unlike the discrete component known as screech (Edgington-Mitchell, 2019; Raman, 1999), where noise is generated by an easily disrupted feedback loop, suppression of BBSAN is not straightforward. The lack of simple noise mitigation strategies means BBSAN remains an important component of jet noise.

The work by Harper-Bourne and Fisher (1973) identified the main features of BBSAN; the sound field is characterised by a broad spectral lobe which varies in frequency as a function of the observer position and the ideally expanded Mach number ( $M_j$ ) of the jet. The distinctive directivity arises from the constructive and destructive interference within the axially extended acoustic source. Using the interpretation of Tam and Tanna (1982), the shock-cell structure

can be represented as a series of waveguide modes with wavenumbers  $k_n$  and the shock-cell length approximated by  $L_1 = 2\pi/k_1$ . Tam and Tanna (1982) also showed that the primary BBSAN peak frequency,  $f_p$ , varies with the observer angle,  $\theta$ , measured from the downstream jet axis, according to

$$f_p = \frac{u_c}{L_n(1 - M_c \cos(\theta))}, \quad n = 1, \quad (1)$$

where  $u_c$  is the convection velocity of the large-scale coherent structures, and  $L_1$  is the shock-cell spacing of the first shock-cell mode  $n = 1$ . Equation (1) can also be used to predict peaks generated by higher-order shock-cell modes ( $n \geq 2$ ). The width of the BBSAN peak narrows as the observer angle increases. The amplitude of BBSAN scales to the fourth power of the off-design parameter, defined as  $\beta = (M_j^2 - M_d^2)^{1/2}$ , where  $M_d$  is the design Mach number of the nozzle.

When studying noise generated from a circular nozzle, it is useful to exploit the symmetry inherent in the flow. By casting the problem in cylindrical coordinates, both the sound field and its underlying source (Lighthill, 1952) can be decomposed in the azimuthal direction and represented as a Fourier series due to circumferential homogeneity. The advantage of using such a decomposition is exemplified in subsonic jets; the sound field is dominated by the lowest-order azimuthal modes at low polar angles (Cavaliere *et al.*, 2012; Michalke and Fuchs, 1975). The acoustic efficiency

<sup>a)</sup>This paper is part of a special issue on Supersonic Jet Noise.

<sup>b)</sup>Electronic mail: marcus.wong@monash.edu, ORCID: 0000-0001-9096-6519.

<sup>c)</sup>ORCID: 0000-0001-8576-5587.

<sup>d)</sup>ORCID: 0000-0001-9032-492X.

of higher-order azimuthal modes is reduced due to azimuthal source interference. The interference is explicitly expressed by the Bessel function term in line-source models (Michalke, 1970). Cavalieri *et al.* (2012) also showed that there exists a direct correspondence between the acoustic source and sound field of the same azimuthal mode. From a reduced-order modelling perspective, this is appealing as the desired azimuthal component of the far-field sound can be obtained by computing only the corresponding sound-producing wavepacket (Cavalieri *et al.*, 2019; Jordan and Colonius, 2013).

While our understanding of the role of wavepackets in subsonic and ideally expanded jets (Sinha *et al.*, 2014) is now relatively mature, their application to model BBSAN is less common. By artificially separating the shock and turbulence components, Tam and Tanna (1982) first proposed the use of spatially extended instability waves to model the downstream-travelling coherent structures. A BBSAN model (Tam, 1987) was developed based on the interaction of these proposed instability waves with stationary shock-cells; experimental sound spectra were reproduced with a high degree of accuracy over a wide range of operating conditions. The model predictions, however, were obtained semiempirically by adopting approximations and scaling arguments. One such simplification was the removal of the dependence on the azimuthal wavenumber, treating the source as effectively axisymmetric. Hence, comparisons were only made with the total sound field (Norum and Seiner, 1982). In their model, Ray and Lele (2007) also made a comparable simplification whereby far-field pressure predictions for only the first three azimuthal modes were combined and scaled to match the total acoustic signal. Recently, wavepacket models for BBSAN have been proposed (Lele, 2005; Wong *et al.*, 2019a; Wong *et al.*, 2019b). Similar to Tam (1987), they have shown fair agreement with experimental spectral shape, but relied on empirical adjustments to match measured amplitudes since no azimuthally decomposed far-field data were available. The validation of BBSAN models, in particular those predicated on instability theory, is hindered by the lack of azimuthally decomposed sound-field data.

While azimuthal decomposition has previously been performed on shock-containing jets, the focus has, until now, been largely on the identification of different screech oscillation modes (Edgington-Mitchell, 2019, and see references therein). Only a handful of studies have examined the azimuthal modes of BBSAN in detail. Arroyo and Moreau (2019) investigated azimuthal modes using a large-eddy simulation (LES) of a non-screeching underexpanded jet at one exit condition. Successive azimuthal modes were found to peak at higher frequencies. Suzuki (2016) also arrived at similar conclusions by observing the azimuthal modal distributions in a LES of an underexpanded jet. An upward shift in the emission angle and frequency led to higher-order modes featuring more prominently. Experimentally, this behaviour was also measured by Vold *et al.* (2012) for an overexpanded jet, although the dependence on the observer

position was not investigated. Of the above studies, only Suzuki (2016) made mode-by-mode comparisons between the decomposed far-field data and BBSAN model predictions, but poor agreement was found. Furthermore, the mentioned studies considered only weakly off-design conditions ( $\beta < 0.8$ ); whether the same observations apply to stronger levels of under- or overexpansion is not known.

The aim of this study is to provide azimuthally decomposed sound-field measurements of shock-containing jets for comparison with models. Specifically, we examine the azimuthal modal composition for BBSAN and its variation with the Mach number and observer position. The findings should better inform future BBSAN models and allow a basis for comparison between model and experiment. The paper is organised as follows. The experimental facility and setup is discussed in Sec. II, which includes the microphone apparatus, acquisition details, and post-processing techniques. In Sec. III, we present both the far-field acoustic results and azimuthally decomposed midfield spectra. A summary of the findings and future perspectives is provided in Sec. IV.

## II. METHODOLOGY

### A. Facility overview

The acoustic measurements were acquired in the Monash University Laboratory for Turbulence Research in Aerospace and Combustion (LTRAC) Supersonic Jet Anechoic Facility (SJAF). The facility is designed for the study of acoustics and flow-fields of cold small-scale supersonic jets in a controlled environment. The key components of the facility are presented below.

#### 1. Anechoic chamber

The jet exhausts into an anechoic chamber designed according to the best practices as suggested by Ahuja (2003). The interior chamber dimensions (wedge-tip to wedge-tip) are 1.5 m  $\times$  1.2 m  $\times$  1.4 m. The anechoic chamber walls are acoustically treated using foam wedges with a depth of 400 mm, corresponding to a nominal cut-on frequency of 500 Hz. The floor of the anechoic chamber is also lined with wedge panels. Entrained and exhausted air is replaced via two open sections along the upstream wall. The rectangular openings are acoustically treated with an overhanging wall to ensure no external noise propagates into the chamber. The acoustic performance of the chamber is provided in Appendix A.

#### 2. Air supply

Compressed air is passed through a heatless-desiccant dryer that is connected to a 5 m<sup>3</sup> air reservoir. The air supply allows for a continuous operation up to a nozzle pressure ratio (NPR) of five. The jet operating condition is determined by the NPR and defined as  $\text{NPR} = P_t/P_\infty$ , where  $P_t$  and  $P_\infty$  are the total and ambient pressures, respectively. Since the facility shares the same air supply as a supersonic

wind tunnel (Knast *et al.*, 2017), a manual butterfly valve is used to direct air into a large mixing chamber. The air flow is controlled by an eccentric rotary plug control valve. In order to manually select the desired NPR, a Fairchild 100 High-Flow Pressure Regulator is used (Edgington-Mitchell *et al.*, 2014). Pressurised air from the mixing chamber is then fed into the jet plenum chamber via a flexible wire-braided high pressure polytetrafluoroethylene (PTFE) hose. The stagnation pressure in the plenum, as used to determine the NPR, was measured using an RS-3100 pressure transducer with a range of 0–10 bar. The stated manufacturer accuracy of the transducer is  $\pm 0.25\%$ , but the measured range in the plenum was approximately  $\pm 1\%$ . The size of the plenum chamber was designed to minimise fluid velocity and provide a large contraction ratio at the nozzle exit plane. No flow conditioning was used upstream of the nozzle exit. A schematic of the facility is shown in Fig. 1(a).

### 3. Nozzle geometry and design

The jet issues from a converging round nozzle that has an exit diameter of  $D = 8$  mm and a lip thickness of 0.5 mm. The mild-steel plenum chambers and nozzles are assembled in a modular fashion via flange connections [Fig. 1(a)]. The modular nature of the jet rig allows for future modifications and upgrades. The jet rig is mounted onto an adjustable steel stand, which traverses linear rails to allow constrained axial motion.

The plenum is connected to the nozzle via a bent and straight circular section with a total length of 800 mm and a diameter of 25.4 mm. The nozzle contour follows a fifth-order polynomial (Morel, 1975), ensuring that a smooth connection with the straight section is achieved. The resulting contraction ratio is ten.

The small nozzle exit diameter is dictated by the restrictions on air supply and the internal dimensions of the anechoic chamber. Using a small nozzle ensures that the jet

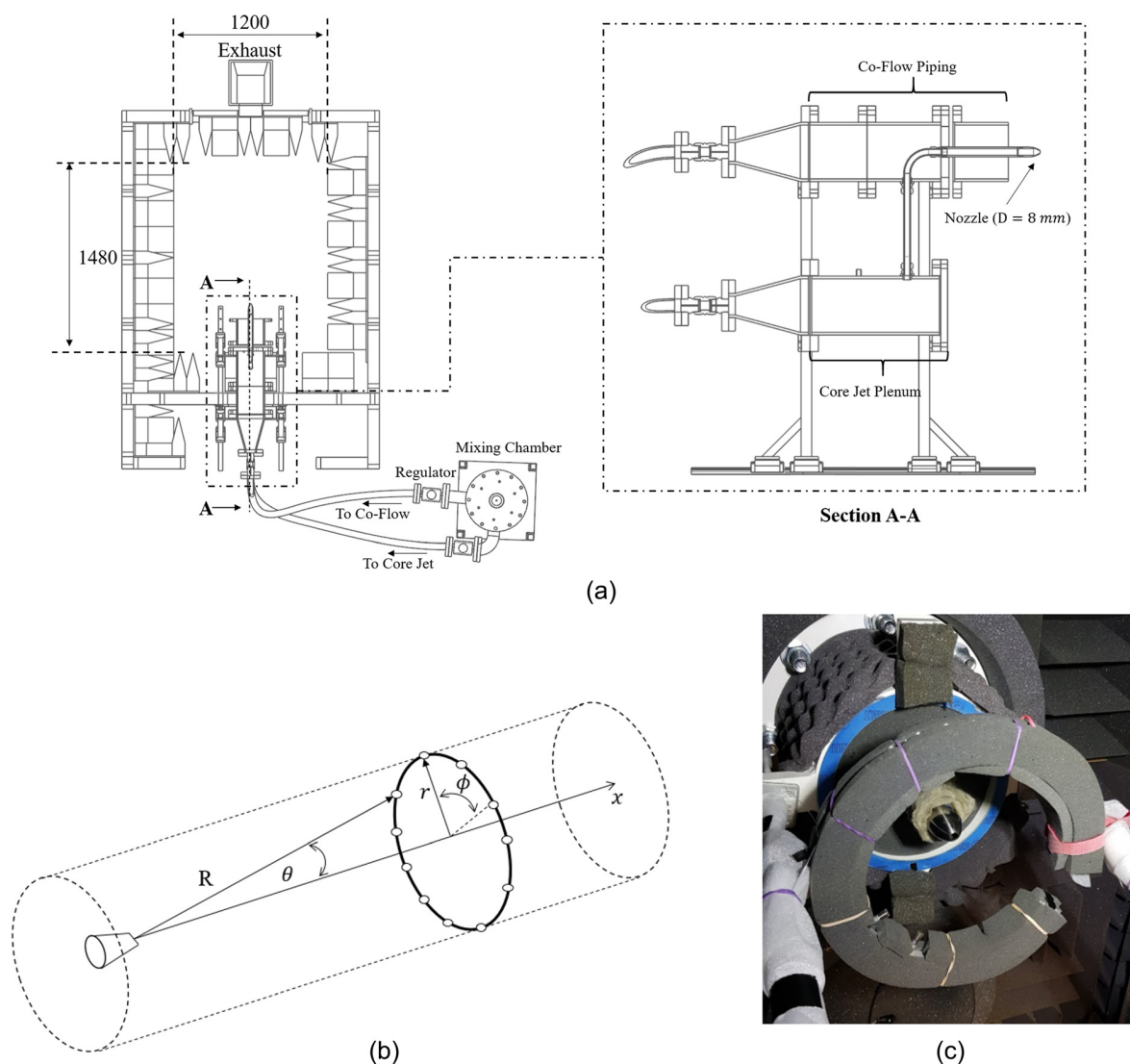


FIG. 1. (Color online) Schematics of facility and experimental setup. (a) Sectioned plan and side view schematic of SJAF, showing key components of the facility (dimensions in mm), (b) schematic of adopted coordinate system, and (c) azimuthal ring setup.



is able to operate continuously even at high NPR. This allows for jet conditions to stabilise and lengthy data acquisition. Importantly, the acoustic frequency range of interest is significantly higher than the cut-on frequency of the anechoic chamber.

## B. Coordinate systems

To facilitate the following discussion, two coordinate systems are used in a similar fashion to those in Cavalieri *et al.* (2012) as shown in Fig. 1(b). The cylindrical coordinate system of the jet is represented by  $(x, r, \phi)$ , where  $x$  is the downstream jet axis,  $r$  is the radial direction, and  $\phi$  is in azimuth. This is overlaid with a spherical coordinate system  $(R, \theta, \Phi)$ , representing the acoustic field, where  $R$  is the distance,  $\theta$  is the polar angle, and  $\Phi$  is the azimuth.

## C. Operating conditions

Acoustic measurements were performed on cold supersonic underexpanded jets. The jet operating conditions are characterised by the NPR and the off-design parameter  $\beta$  (Norum and Seiner, 1982). For a converging nozzle, the design Mach number  $M_d$  is unity, and so  $\beta = (M_j^2 - 1)^{1/2}$ . The Reynolds number at the nozzle exit is on the order of  $10^5$ , based on the assumption of isentropic flow. We note that the Reynolds numbers of all three conditions correspond to the turbulent transition region of a supersonic jet ( $Re \approx 10^5$ ). Therefore, the measured acoustic field may differ from jets at higher Reynolds numbers which have a fully turbulent shear layer at the nozzle exit (Bogey *et al.*, 2012; Ozawa *et al.*, 2020). We define  $D_j$  and  $U_j$  as the ideally expanded diameter (Tam and Tanna, 1982) and jet velocity, respectively. The operating conditions for the midfield measurements are summarised in Table I.

## D. Data acquisition

Acoustic measurements were made using G.R.A.S. Type 46BE 1/4 in. pre-amplified microphones with a frequency range of 4 Hz–100 kHz and a nominal sensitivity of 3.6 mV/Pa. The microphone signals were passed through an amplifier and acquired using a National Instruments DAQ. Each recording consisted of 400 000 samples and was acquired at a rate of 200 kHz, corresponding to a Nyquist frequency of 100 kHz. A low-pass filter was used in the post-processing stage to remove aliasing effects. The microphones were calibrated using a G.R.A.S. pistonphone with a standard calibration level of 114 dB at 1 kHz. The reference pressure used for all acoustic measurements is  $P_{ref} = 20 \mu\text{Pa}$ . The methodology to obtain the acoustic spectra

from measured time signals is presented in Appendix B. To facilitate comparison with acoustic measurements of shock-containing jets in literature, nondimensionalised frequency  $St$  is used. We define the Strouhal number as  $St = fD_j/U_j$ , where  $f$  is the frequency in Hz. For all acoustic measurements, solid surfaces, including the ring, are covered with acoustic foam [Fig. 1(c)].

## E. Microphone array and azimuthal decomposition

We obtain sound pressure level readings at two different distances. At a distance of  $R = 50D$  from the nozzle exit, which we refer to as “far-field,” noise measurements were obtained at a range of polar angles from  $\theta = 60^\circ$ – $120^\circ$ . The aim of performing these simple single-microphone far-field measurements is to validate the new facility against trends in the existing literature.

We then present acoustic measurements using an azimuthal ring at a constant radial distance of  $r = 11D$  from the jet axis. These measurements are performed to interrogate the modal composition of BBSAN. The azimuthal ring setup is shown in Fig. 1(c). The location of the microphone is assumed to be well outside of the hydrodynamic field for a shock-containing supersonic jet (Seiner and Yu, 1984; Suzuki, 2016; Tam, 1987), ensuring that only acoustic fluctuations are detected. These measurements, which we refer to as “midfield,” are used to decompose the acoustic field into azimuthal modes using a methodology similar to Sinha *et al.* (2018).

The methodology involves two microphones, one fixed and the other moved in  $10^\circ$  azimuthal increments. By tracing the cross correlation between the two microphones as a function of the azimuthal separation, the cross-correlation matrix  $R_{pp}$  is constructed and used to obtain the azimuthal decomposition of the radiated acoustic field. The processing steps are detailed in Appendix C. While the process is more time-consuming than for a fixed microphone array (Suzuki and Colonius, 2006), we effectively reproduce the same results with a much smaller microphone count. It was found that sweeping over an azimuthal range of  $180^\circ$  was sufficient for the frequency range of interest. The azimuthal array is traversed in the axial direction in order to obtain measurements at different polar angles. Since the azimuthal ring is at a fixed distance to the jet axis, the radial distance  $R$  between the nozzle and microphone differs for each polar angle.

## III. EXPERIMENTAL RESULTS & ANALYSIS

### A. Single microphone far-field noise spectrum

Before azimuthally decomposing the mid-acoustic field, it is instructive to first look at the far-field behaviour of the jet. Narrowband far-field noise spectra are shown in Fig. 2 at  $\theta = 60^\circ$  and  $90^\circ$  for a range of NPR. Typical BBSAN directivity and amplitude traits are clearly observed; the peak BBSAN frequency decreases as NPR and  $\theta$  increase. Moreover, it can be seen that the intensity of BBSAN, represented by the overall sound pressure level (OASPL), follows

TABLE I. Summary of jet operating conditions.

NPR	$M_j$	$D_j/D$	$\beta$	Re
2.25	1.14	1.01	0.55	$2.8 \times 10^5$
3.10	1.38	1.05	0.95	$3.8 \times 10^5$
3.67	1.50	1.09	1.12	$4.5 \times 10^5$



the well-known  $\beta^4$  proportionality (Harper-Bourne and Fisher, 1973) for  $\beta^4 > 0.5$ . Strong screech peaks are also evident in the acoustic spectra. The presence of screech is known to affect BBSAN, lowering the BBSAN peak frequency for the same operating condition (André *et al.*, 2013) and also modulating the lengthscales of velocity fluctuations in the jet plume (Tan *et al.*, 2017). Since the nozzles were not designed with screech suppression features, comparison with other BBSAN studies in literature where screech was suppressed (André *et al.*, 2013; Norum and Seiner, 1982; Savarese *et al.*, 2013; Viswanathan *et al.*, 2010) was not undertaken.

In Fig. 3, we show the sound pressure level (SPL) as a function of the polar angle ( $60^\circ < \theta < 120^\circ$ ) and frequency ( $0.1 < St < 1.5$ ) at three different NPRs. The BBSAN peak frequency predictions from Eq. (1) are also plotted for comparison. Both NPR = 3.10 and NPR = 3.67, in Figs. 3(b) and 3(c), respectively, display agreement with Eq. (1), where we have defined the convection velocity as  $u_c = 0.7u_j$  and the shock-cell spacing  $L_1$  using the vortex sheet approximation from the Pack and Prandtl (P and P) model (Pack, 1950). The presence of a higher-order shock-cell mode ( $n = 2$ ) is evident as the second BBSAN lobe. There is a slight underprediction of BBSAN frequency for NPR = 2.25 [Fig. 3(a)], possibly due to the mismatch in shock-cell spacing between the P-P model and the experiment. Discrete screech peaks are also observed. Mixing noise is not prominent as this noise component has only a small contribution at sideline and upstream positions (Sinha *et al.*, 2014). The results from far-field measurements are in agreement with well-validated models from the literature and give us confidence in the midfield measurements presented below.

## B. Azimuthal modal analysis of the midfield

Following the method shown in Appendix C, we obtain the azimuthal decomposition of the radiated noise. Due to the microphone array being only  $11D$  from the jet axis, the origin of the polar angle  $\theta$  is now taken at a downstream location of  $x_0 = 5D$ , in similar fashion to Gojon and Bogey (2017). The origin is redefined in an effort to more faithfully capture the origin of the acoustic source and is an indirect

demonstration that BBSAN is generated at the downstream shock-cells (Tam *et al.*, 1985). Sound pressure level measurements are only shown up to  $St = 1.5$  due to the upper frequency limit of the microphones. Hereafter, we shall focus only on the BBSAN component in our discussion.

### 1. Azimuthally decomposed spectra

The acoustic pressure spectra at  $\theta = 80^\circ$ ,  $95^\circ$ , and  $115^\circ$  for the range of NPRs in Table I is shown in Fig. 4. The first four azimuthal modes ( $m = 0, \pm 1, \pm 2, \pm 3$ ) are shown, along with the full signal. For  $m > 0$ , we combine both the negative and positive components [Eq. (C8)] and, hence, drop the “ $\pm$ ” for compactness. The BBSAN lobe is present for all azimuthal modes and follows the known trends as the Mach number and observer location vary. For both NPR = 3.10 and NPR = 3.67, the lobe due to the second shock-cell mode, viewed at the sideline and upstream angles, is clearly present.

We first focus on the relative importance of each azimuthal mode across the frequency range of interest. At low frequencies ( $St \leq 0.6 - 0.7$ ), the single helical mode is dominant. There is a clear distinction between each successive mode ( $m > 1$ ) with decreasing amplitude as the mode number increases. The separation between modes becomes less pronounced as the frequency increases. Figure 4 also clearly shows that  $m = 0$  is not the dominant azimuthal mode for the angles of interest. The sound field of the axisymmetric mode is on average 3–4 dB/St less than the dominant mode(s). This observation is also consistent with subsonic jet noise and source models; higher azimuthal modes ( $m = 1$  and 2) become increasingly important at higher frequencies and for positions further upstream, whereas downstream noise is dominated by mode  $m = 0$  (Jordan and Colonius, 2013).

At  $St \approx 0.6 - 0.7$ , the distinction between nonzero azimuthal modes is absent and we observe an approximately equal contribution from modes  $m = 1, 2$ , and 3. This trend is observed at all three NPRs shown and continues as mode number increases (not shown for brevity). The increasing contribution from successive modes as the frequency increases is consistent with the findings of Kuo *et al.* (2013)

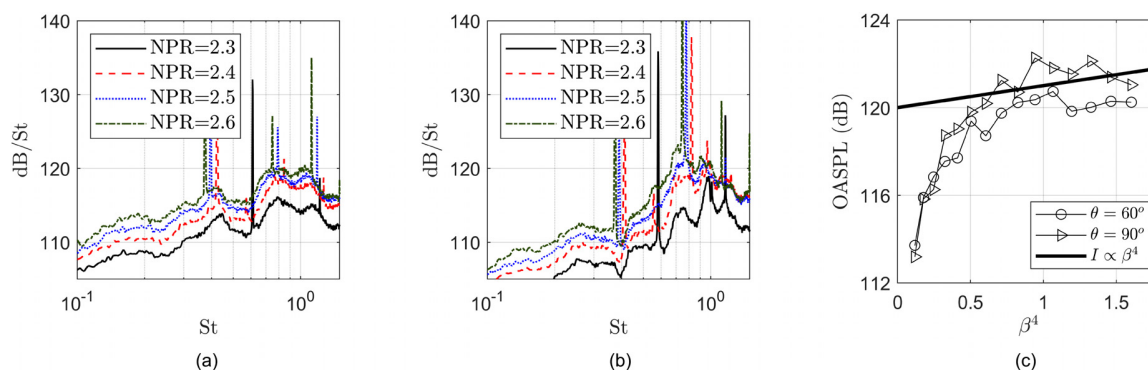


FIG. 2. (Color online) Effect of changing NPR at (a)  $\theta = 60^\circ$ , (b)  $\theta = 90^\circ$ , and the dependence on  $\beta^4$  as a function of  $M_j$ .

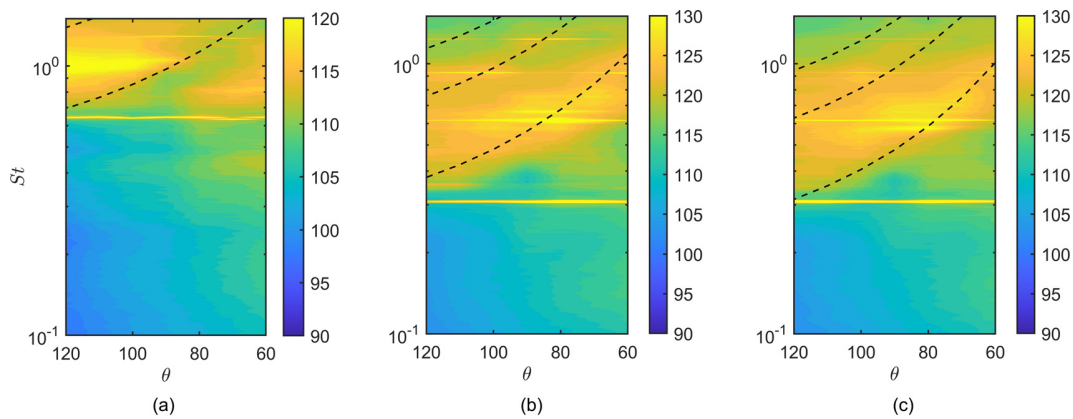


FIG. 3. (Color online) Directivity contour plots for power spectral density (PSD) in the far-field ( $R = 50D$ ) for NPRs (a) 2.25, (b) 3.10, and (c) 3.67. Polar angles taken with respect to downstream jet axis and contours are in dB/St. Dashed lines indicate peak frequency predictions from Eq. (1).

and Vold *et al.* (2012), who measured the same behaviour in both ideally expanded and overexpanded jets.

By comparing these results against well-known BBSAN trends, we arrive at some observations of interest. Depending on the frequencies of the BBSAN lobe, the relative contribution of each azimuthal mode varies. For instance, looking at the NPR = 2.25 jet at  $\theta = 80^\circ$ , the  $m = 1, 2$ , and 3 azimuthal modes are of similar strength for the BBSAN lobe, while those same modes are distinct (with  $m = 1$  being the strongest) at the lobe for the NPR = 3.67 case at  $\theta = 115^\circ$ . A similar trend is also observed when comparing the azimuthal content of higher frequency secondary lobes ( $n = 2$ ) to the primary one ( $n = 1$ ).

The trends observed in Fig. 4 are shown in a more comprehensive manner in the  $St$ – $\theta$  contour diagrams in Fig. 5. Decomposed acoustic spectra up to  $m = 4$  are shown between  $50^\circ < \theta < 125^\circ$ . For both NPR = 3.10 and NPR = 3.67 jets, the BBSAN directivity of the primary ( $n = 1$ ) and secondary ( $n = 2$ ) peaks agrees favourably with Eq. (1) (dashed lines). For NPR = 2.25, the experimental peak frequency is higher than that suggested by Eq. (1) as expected from the far-field data in Fig. 3(a). The same inputs as in Sec. III A were used in Eq. (1) for all azimuthal modes. This suggests that the instability waves associated with each azimuthal mode convect at a similar velocity.

From Eq. (1), the BBSAN lobe shifts upward as the Mach number decreases and observer position moves downstream. Therefore, as  $\theta$  and NPR decrease, the azimuthal content of BBSAN becomes increasingly multi-modal. Figure 5 illustrates this trend. At low Mach numbers (NPR = 2.25), since the BBSAN lobe is above  $St \approx 0.7$ , there is largely an equal contribution from the first four nonzero modes. At higher Mach numbers, the BBSAN lobe shifts down and we see a difference in modal behaviour. At NPR = 3.67, BBSAN that peaks at sideline and upstream angles ( $\theta > 90^\circ$ ) is dominated by  $m = 0, 1$ , and 2. However, at lower emission angles ( $\theta < 90^\circ$ ), the BBSAN lobe shifts to higher frequencies and the contribution from modes  $m = 3$  and 4 is non-negligible. Similar behaviour is also seen for NPR = 3.1. This trend is in agreement with Arroyo

and Moreau (2019) in which LES of a non-screaching underexpanded jet with an ideally expanded Mach number of  $M_j = 1.15$  was investigated. Although the experimental measurements of this study are conducted in the presence of screech, this does not seem to affect the frequency dependence of the azimuthal modes that contribute to BBSAN.

In regions where the difference between the azimuthal modes is pronounced (low-frequency, upstream angles), the acoustic field exhibits low-rank behaviour. Here, “low-rank” is referred to as a rank- $N$  truncation of the azimuthal Fourier basis, which provides an approximate description of the sound field to within 1 dB/St precision of the full-rank data. The connection between BBSAN directivity and variation in the azimuthal modal quality is further explored in Sec. IIIB 2.

## 2. Acoustic field reconstruction

To investigate the relevance of subsequent lower-order azimuthal modes to the full BBSAN signal as a function of  $\theta$  and NPR, we perform reconstructions of the acoustic field using an increasing number of azimuthal modes [Eq. (C6)]. The upper row of Fig. 6 contains rank maps showing the number of modes required to attain 1 dB/St precision for the total signal. The modes are added successively. The solid red contour provides a visual aid for the position of the BBSAN lobe. As expected from Fig. 4, a single-mode ( $m = 0$ ) representation of the acoustic field is insufficient. At low frequencies ( $St \lesssim 0.6$ – $0.7$ ), apart from some inconsistencies for the NPR = 3.10 case, low-rank behaviour is observed with the combination of 2–3 modes, sufficient to recover the full signal. Comparing this trend with the position of the BBSAN lobes, we, hence, observe low-rank behaviour for NPR = 3.10 and NPR = 3.67; 2–3 modes, again, provide a sufficient approximation for BBSAN. As alluded to in Sec. IIIB 1, however, at lower emission angles, the number of required modes increases. For example, at NPR = 3.10, five modes are required at  $\theta = 70^\circ$ , while only three modes are used at  $\theta = 100^\circ$  to obtain the same precision. The latter observation, however, does not apply at

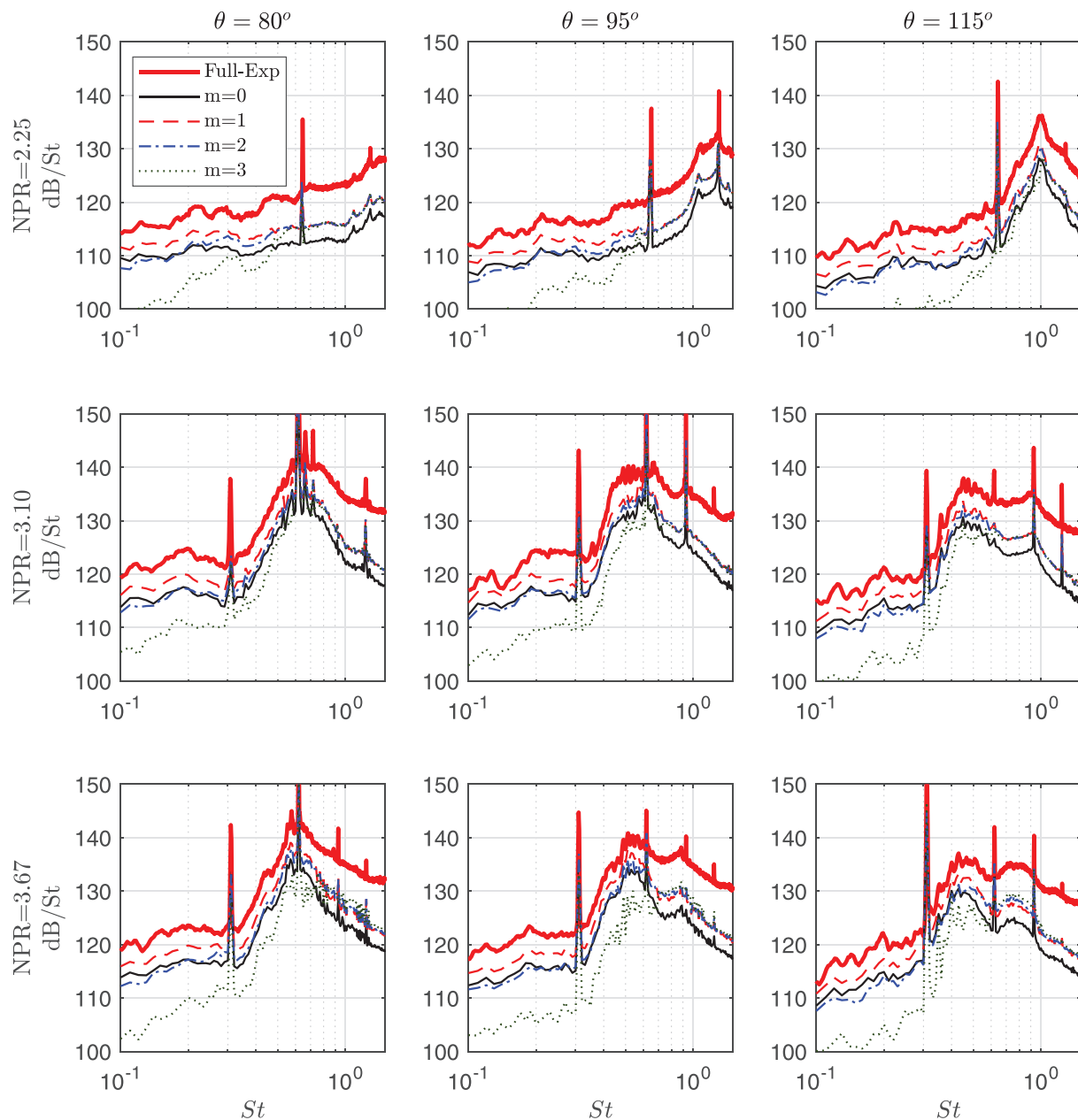


FIG. 4. (Color online) Decomposed acoustic spectra in the midfield ( $R = 11D$ ) for different NPRs; NPR = 2.25 (upper row), NPR = 3.10 (middle row), and NPR = 3.67 (lower row). Polar angles taken with respect to downstream jet axis;  $\theta = 80^\circ$  (left column),  $\theta = 95^\circ$  (middle column), and  $\theta = 115^\circ$  (right column).

NPR = 2.25, where the higher-frequency lobe consistently requires 4–5 modes to capture the total BBSAN amplitude.

To further illustrate this behaviour, reconstructed acoustic spectra at  $\theta = 95^\circ$  are shown in the lower row of Fig. 6. The corresponding position on the rank maps is indicated by the vertical dashed line. While convergence is rapid at low frequencies, the low-rank approximation deteriorates as frequency increases. Consequently, we observe that the secondary lobe is of increased modal complexity relative to the primary lobe [Figs. 6(b) and 6(c)]. To summarise, BBSAN can be approximated by an azimuthally low-rank approximation. As the peak frequency varies, the exact number of

modes required for reconstruction of the total sound field will depend on both the operating condition of the jet and the observer position with an increasing number of modes required at higher frequency.

These observations suggest that previous instability wave BBSAN models neglected some relevant features. For example, the removal of azimuthal dependence by Tam (1987) does not adequately address the multi-modal behaviour at high frequencies. Similarly, we might infer that the truncation of modes to  $m \leq 2$  by Ray and Lele (2007) likely contributed to the observed “missing sound” at high frequencies. These approximations may explain why such

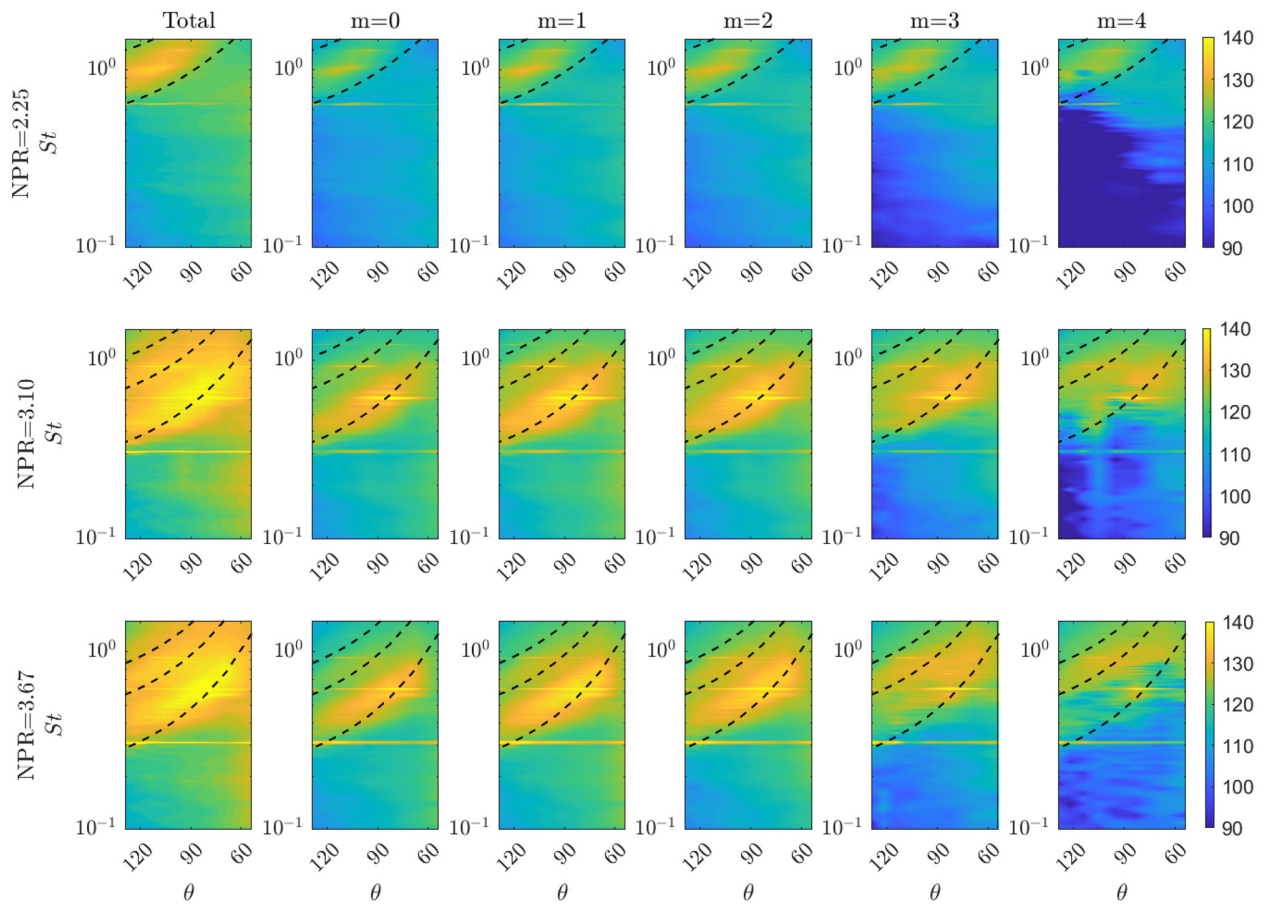


FIG. 5. (Color online) Full and decomposed spectra in the mid-field ( $R = 11D$ ) for different conditions;  $NPR = 2.25$  (upper row),  $NPR = 3.10$  (middle row), and  $NPR = 3.67$  (lower row). Polar angles taken with respect to downstream jet axis, and contours are in dB/St. Dashed lines indicate peak frequency predictions from Eq. (1).

models either had poor amplitude predictions at high frequencies or resorted to empiricism to match the total measured sound field. A more insightful means of validating such models may be to undertake azimuthal mode-by-mode comparisons, similar to the process of Cavalieri *et al.* (2012) for subsonic jets.

#### IV. SUMMARY AND OUTLOOK

Acoustic measurements were obtained from an under-expanded jet operating at three conditions. Far-field single microphone measurements were acquired to validate measurements from the new facility. Using two microphones mounted on a traversable array, the sound field was decomposed for the purposes of exploring the modal composition of BBSAN.

The single microphone measurements were in agreement with previous observations. Strong screech peaks were observed and the well-known BBSAN directivity shape was recovered, in agreement with Tam and Tanna (1982). The BBSAN amplitude was also found to follow the  $\beta^4$  scaling.

Using a similar methodology to Sinha *et al.* (2018), azimuthally decomposed acoustic spectra were obtained. It was

found that, unlike in subsonic and ideally expanded jets where the dominant sound radiation is in the downstream direction, the axisymmetric mode is not the dominant contribution to BBSAN in the acoustic field. Rather, the  $m = 1$  mode is the most important for  $St \leq 0.7$ . Further, we show that modes  $m > 1$  are increasingly important for higher frequencies. Successive reconstructions of the acoustic field demonstrate that approximately 3–5 azimuthal modes are required to recover the total BBSAN signal; the minimum number of requisite modes varies depending on the peak frequency. When correlated with the known directivity of BBSAN, we arrive at an interesting corollary; the total BBSAN sound field becomes progressively low-rank in azimuth as polar angle and Mach number increase. For the secondary lobe, at frequencies higher than the primary frequency, we clearly see higher-rank behaviour.

From a modelling perspective, the findings are consistent with the predictions made by wavepacket BBSAN models. In such models, the shock-cells are axisymmetric and assumed to be stationary, whereas the frequency and azimuthal characteristics are solely defined by the wavepacket. It is well-known that the source location shifts toward the nozzle as the frequency increases (Suzuki, 2016). Previous parabolised stability equation (PSE) calculations of



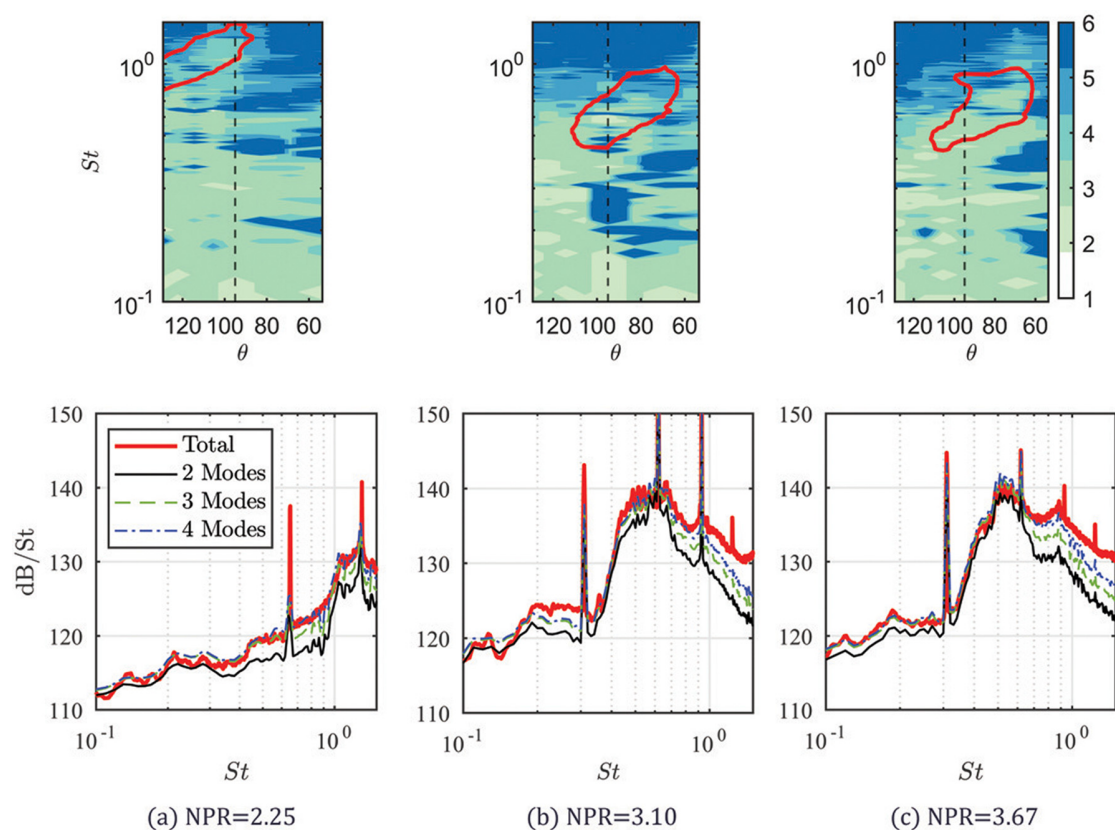


FIG. 6. (Color online) Reconstruction of the acoustic field with modes added successively ( $m = 0, \pm 1, \pm 2, \dots$ ). (Top row)  $St$ - $\theta$  maps displaying the number of modes required to reconstruct the total acoustic signal to within 1 dB/St for (a)  $NPR = 2.25$ , (b)  $NPR = 3.10$ , and (c)  $NPR = 3.67$ . The 130 dB/St contour (red line) identifies the primary BBSAN lobe seen in Fig. 5. The vertical dashed lines locate  $\theta = 95^\circ$ . (Bottom row) Reconstruction of the acoustic spectrum at  $\theta = 95^\circ$  with an increasing number of modes.

hydrodynamic wavepackets in supersonic jets (Ray and Lele, 2007; Rodríguez *et al.*, 2015) have shown that the spatial extent of wavepackets contracts as the azimuthal mode number increases, shifting the peak of the envelope closer to the nozzle exit. Hence, only for the high-frequency BBSAN components can wavepackets of higher-order modes be acoustically efficient. Ray and Lele (2007) also found that the energy is more evenly distributed across azimuthal modes of instability waves as the frequency increases, in accordance with our findings here.

The nontrivial contribution of higher-order azimuthal modes to the full spectrum necessitates that wavepacket models for BBSAN should be able to accurately predict their evolution, particularly for higher frequencies, as confidently as for the lower-order modes. Sasaki *et al.* (2017) have demonstrated the validity of wavepacket models up to a Strouhal number of  $St = 4.0$  and azimuthal wavenumber  $m = 4$  for an  $M = 0.9$  jet. This suggests wavepackets are well-placed to model the large-scale structures over the BBSAN spectral range. While outside the scope of the present study, there is clear motivation for future work on the construction and refinement of these wavepacket models for shock-containing jets.

The results presented not only directly address the issue of the lack of azimuthally decomposed acoustic data, but also

shed light on the relative contribution of each azimuthal mode to the full BBSAN signature. The importance of higher-order modes, including their relevance in shaping overall BBSAN directivity, should be addressed in future models.

## ACKNOWLEDGMENTS

This research is supported by an Australian Government Research Training Program (RTP) Scholarship and the Endeavour Research Leadership Award—an Australian Government initiative. The authors also received funding from the Australian Research Council through the Discovery Projects scheme. M.H.W. would also like to thank Mr. Danny Lynch and Mr. Phil Nicholson and acknowledge the support of the Monash Mechanical and Aerospace Technical Services Group in the construction of SJAF.

## APPENDIX A

The method of Ahuja (2003) is used to calibrate the anechoic chamber and determine its acoustic “cleanliness.” For a point source, the measured sound amplitude should obey the inverse-square law as the distance increases in any direction. Apart from the removal of the nozzle and

azimuthal ring, no further modifications were made inside the chamber. A 45 mm diameter speaker with a range of 140–20 000 Hz is placed along the jet centreline at the same position as the nozzle exit. The same G.R.A.S. Type 46BE 1/4 in. microphones were used and mounted on a traverse line at different directions from the source. To determine the deviation from the inverse-square law, the method prescribed by [Cunefare et al. \(2003\)](#) was used. The theoretical free-field SPL ( $SPL_p$ ) at distance  $r_i$  is given by

$$SPL_p(r_i) = 20 \log_{10} \left[ \frac{a}{r_i - r_0} \right], \quad (A1)$$

where  $a$  and  $r_0$  are the apparent acoustic source strength and the offset distance between the physical location of the source and its acoustic centre, respectively. For  $N$  number of measurements in the radial direction, the values of  $a$  and  $r_0$  are given, respectively, as

$$a = \frac{\left( \sum_{i=1}^N r_i \right)^2 - N \sum_{i=1}^N r_i^2}{\sum_{i=1}^N r_i \sum_{i=1}^N q_i - N \sum_{i=1}^N r_i q_i}, \quad (A2)$$

$$r_0 = \frac{\sum_{i=1}^N r_i \sum_{i=1}^N r_i q_i - \sum_{i=1}^N r_i^2 \sum_{i=1}^N q_i}{\sum_{i=1}^N r_i \sum_{i=1}^N q_i - N \sum_{i=1}^N r_i q_i}, \quad (A3)$$

where  $q_i = 10^{-0.05(SPL_{pi})}$ . The deviation in dB between the measured  $SPL_{pi}$  and theoretical value at distance  $r_i$  is, therefore, given by

$$\Delta SPL_p(r_i) = SPL_{pi} - SPL_p(r_i). \quad (A4)$$

The curves in Fig. 7 show that the frequencies of interest are within the required tolerance as specified in [ISO 3745 \(2012\)](#) and confirms that the inverse-square law holds for far-field measurements. Some slight deviations are seen closer to the nozzle at upstream positions ( $\theta = 140^\circ$ ) due to the presence of upstream piping.

## APPENDIX B

The following outlines the steps required to process microphone data to obtain the ensemble-averaged power spectral density (PSD) spectra shown in Sec. III. All acoustic data were acquired at a sample rate of 200 kHz for 2 s, giving a total of  $N_t = 4 \times 10^5$  sample points  $P(t)$ . The signal is checked for spurious trends and noise spikes, and a low-pass filter is applied at 80 kHz. The mean of the signal is removed and then de-trended using a linear regression line  $\tilde{P}(t)$

$$p(t) = \left( P(t) - \frac{1}{N_t} \sum_{n=1}^{N_t} P(t) \right) - \tilde{P}(t). \quad (B1)$$

Before carrying out the fast Fourier transforms (FFTs) of  $p(t)$  to improve convergence, we separate the time signal into  $N_B$  blocks of data each containing  $N_{fft} = 2048$  points. To suppress side-lobe leakage, a Hanning window  $H_0(t)$  is used. The FFT of each block  $p_k(t)$  is then given by

$$p_k(f) = \frac{\sqrt{8/3}}{N_{fft}} (\text{FFT}(H_0(t)p_k(t))). \quad (B2)$$

The PSD is computed by

$$\text{PSD}(f) = \frac{1}{N_B} \sum_{k=1}^K p_k(f)p_k^*(f), \quad (B3)$$

where the signal has been averaged over  $N_B = 974$  blocks and “\*” denotes the complex conjugate. We convert the PSD into the SPL using the classic definition and a reference pressure of  $P_{ref} = 20 \mu\text{Pa}$  giving

$$SPL(f) = 10 \log_{10} \left( \frac{\text{PSD}(f)}{P_{ref}^2} \right). \quad (B4)$$

The presented SPL is in units of dB/St because the PSD is nondimensionalised by the factor  $U_j/D_j$ , and the frequency is, thus, defined as  $\text{St} = fD_j/U_j$ .

## APPENDIX C

We present the methodology used to compute the two-point cross correlation matrix  $R_{pp}(\phi_1, \phi_2)$ . The Fourier-transformed signals from the two microphones [Eq. (B2)], are used to compute the cross spectrum,

$$R_{pp}(\phi_1, \phi_2; f) = \frac{1}{N_B} \sum_{k=1}^K p_k(\phi_1; f)p_k^*(\phi_2; f), \quad (C1)$$

where  $\psi = \phi_2 - \phi_1$ , and we drop the  $x$  and  $r$  coordinates for compactness as both microphones are on the same circumferential plane. The azimuthal homogeneity of the round jet allows  $R_{pp}$  to only depend on  $\psi$ .

The increment in  $\phi$  is fixed at  $10^\circ$ , but a finer discretisation is desired for our analysis. We employ interpolation to reconstruct  $R_{pp}$  for each desired St. We note that  $R_{pp}$ , from Eq. (C1), is a complex quantity and can be separated into the synchronous (real) and asynchronous (imaginary) component,

$$R_{pp}(\psi; f) = a(\psi; f) + ib(\psi; f). \quad (C2)$$

The real component,  $a(\psi; f)$  is a symmetric function and, hence, a sinc function was found to be an appropriate fit for a wide range of frequencies. For the imaginary component,  $b(\psi; f)$  is antisymmetric along the diagonal. The derivative of the sinc function was used to fit the imaginary component well. The interpolated fits are summarised as

$$a(\psi; f) \approx A \text{sinc}(B\psi), \quad (C3)$$

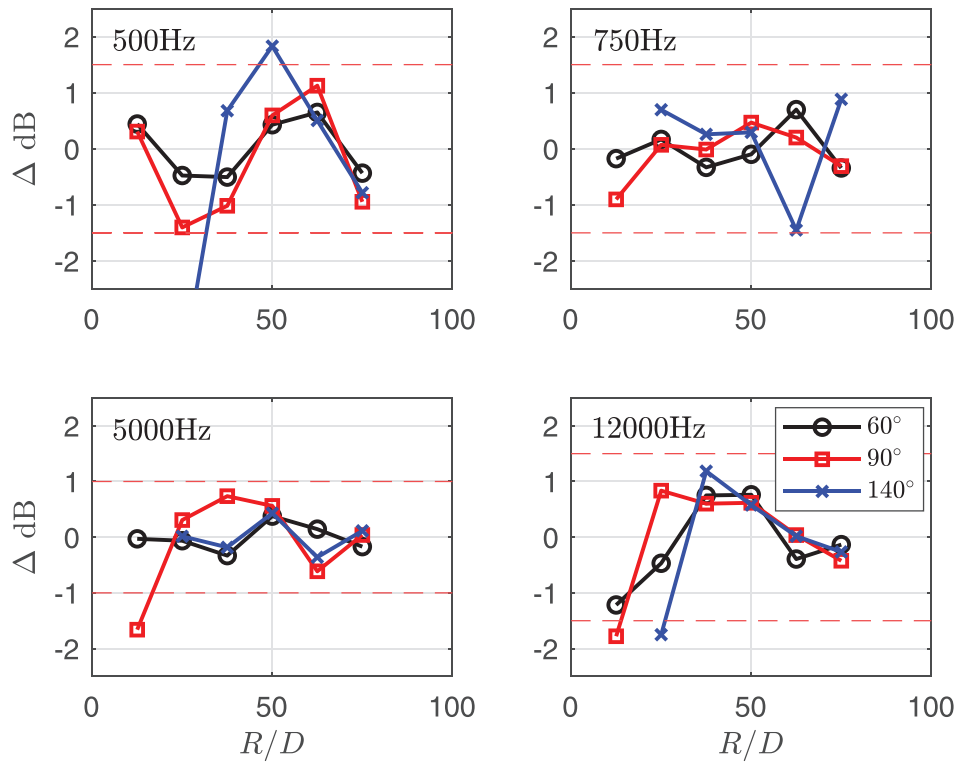


FIG. 7. (Color online) Deviation from the inverse-square law at three different angles for a range of frequencies and polar angles. The red dashed line indicates the maximum permissible deviation as specified by ISO 3745.

$$b(\psi; f) \approx \frac{(C(D\psi \cos(D\psi) - \sin(D\psi)))}{D\psi^2}, \quad (C4)$$

where  $A$ ,  $B$ ,  $C$ , and  $D$  are fitting parameters. An example of the raw data  $R_{pp}$  with an interpolated fit  $\tilde{R}_{pp}$  is shown in Fig. 8. Where a sinc function was found to be inappropriate, the values at the grid points are connected with a linear fit. We note, here, that the goal is to have a curve that is faithful

to the measured data rather than to infer physical meaning from the fit itself.

Using the interpolated fits  $\tilde{R}_{pp}$ , the  $m$ th azimuthal Fourier mode is obtained by performing a Fourier transform in azimuth, giving

$$\tilde{R}_{pp}(f, m) = \frac{1}{2\pi} \int_{-\pi}^{\pi} \tilde{R}_{pp}(\phi_1, \phi_2; f) e^{-im\psi} d\psi, \quad (C5)$$

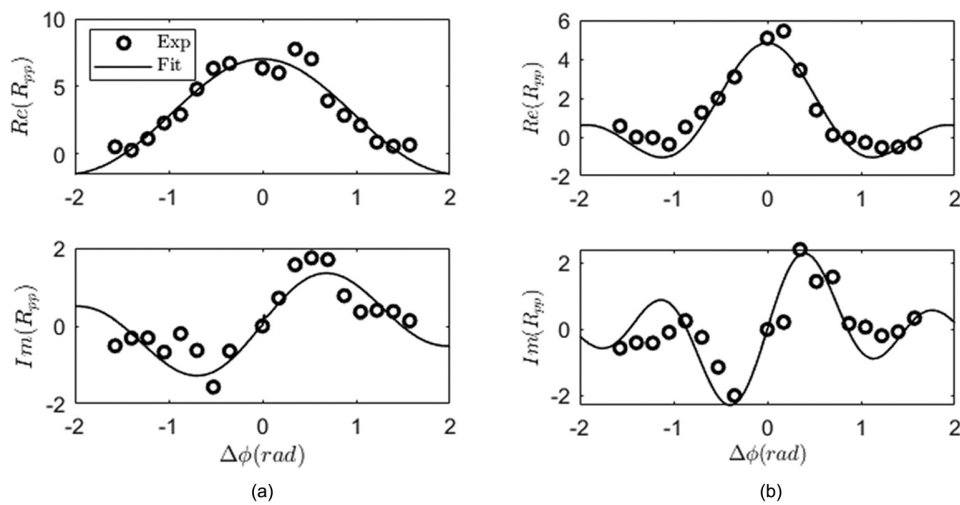


FIG. 8. Example of an interpolated fit to the  $R_{pp}$  two-point data as a function of the azimuthal separation for  $NPR = 3.67$  at  $\theta = 95^\circ$  for (a)  $St = 0.2$  and (b)  $St = 0.7$ .

and its reconstruction is given by

$$\tilde{R}_{pp}(\psi; f) = \sum_{m=-\infty}^{\infty} \tilde{R}_{pp}(f, m). \quad (C6)$$

where for the axisymmetric mode ( $m = 0$ ),

$$\tilde{R}_{pp,0}(\psi; f) = \tilde{R}_{pp}(f, m = 0), \quad (C7)$$

and for  $m \geq 1$ ,

$$\tilde{R}_{pp,m}(\psi; f) = \tilde{R}_{pp}(f, m) + \tilde{R}_{pp}(f, -m). \quad (C8)$$

Using the circumferential isotropy and homogeneity properties (Michalke and Fuchs, 1975), the Fourier coefficients of  $\tilde{R}_{pp}$  are equivalent to the PSDs of pressure fluctuations when  $\psi = 0$ , which gives

$$\text{PSD}(f) = \tilde{R}_{pp}(\psi = 0; f), \quad (C9)$$

and, thus, the amplitude  $|\tilde{R}_{pp,m}(\psi = 0; f)|$  is substituted into Eq. (B4) to compute the power spectrum for each azimuthal mode.

- Ahuja, K. (2003). "Designing clean jet-noise facilities and making accurate jet-noise measurements," *Int. J. Aeroacoust.* **2**(3), 371–412.
- André, B., Castelain, T., and Bailly, C. (2013). "Broadband shock-associated noise in screeching and non-screeching underexpanded supersonic jets," *AIAA J.* **51**(3), 665–673.
- Arroyo, C. P., and Moreau, S. (2019). "Azimuthal mode analysis of broadband shock-associated noise in an under-expanded axisymmetric jet," *J. Sound Vib.* **449**, 64–83.
- Bogey, C., Marsden, O., and Bailly, C. (2012). "Effects of moderate Reynolds numbers on subsonic round jets with highly disturbed nozzle-exit boundary layers," *Phys. Fluids* **24**(10), 105107.
- Cavaliere, A. V., Jordan, P., Colonius, T., and Gervais, Y. (2012). "Axisymmetric superdirectivity in subsonic jets," *J. Fluid Mech.* **704**, 388–420.
- Cavaliere, A. V., Jordan, P., and Lesshafft, L. (2019). "Wave-packet models for jet dynamics and sound radiation," *Appl. Mech. Rev.* **71**(2), 020802.
- Cunefare, K. A., Biesel, V. B., Tran, J., Rye, R., Graf, A., Holdhusen, M., and Albanese, A.-M. (2003). "Anechoic chamber qualification: Traverse method, inverse square law analysis method, and nature of test signal," *J. Acoust. Soc. Am.* **113**(2), 881–892.
- Edgington-Mitchell, D. (2019). "Aeroacoustic resonance and self-excitation in screeching and impinging supersonic jets—a review," *Int. J. Aeroacoust.* **18**(2-3), 118–188.
- Edgington-Mitchell, D., Oberleithner, K., Honnery, D. R., and Soria, J. (2014). "Coherent structure and sound production in the helical mode of a screeching axisymmetric jet," *J. Fluid Mech.* **748**, 822–847.
- Gojon, R., and Bogey, C. (2017). "Numerical study of the flow and the near acoustic fields of an underexpanded round free jet generating two screech tones," *Int. J. Aeroacoust.* **16**(7-8), 603–625.
- Harper-Bourne, M., and Fisher, M. (1973). "The noise from shock waves in supersonic jets," *AGARD-CP-131* **11**, 1–13.
- Huber, J., Fleury, V., Bulté, J., Laurendeau, E., and Sylla, A. A. (2014). "Understanding and reduction of cruise jet noise at aircraft level," *Int. J. Aeroacoust.* **13**(1-2), 61–84.
- ISO 3745. (2012). *ISO 3745: Acoustics—Determination of Sound Power Levels and Sound Energy Levels of Noise Sources Using Sound Pressure—Precision Methods for Anechoic Rooms and Hemi-Anechoic Rooms* (International Organization for Standardization, Geneva, CH, 2012).
- Jordan, P., and Colonius, T. (2013). "Wave packets and turbulent jet noise," *Annu. Rev. Fluid Mech.* **45**, 173–195.
- Knast, T., and Edgington-Mitchell, D. (2017). "Design of a supersonic wind tunnel facility," in *17th Australian International Aerospace Congress: AIAC 2017*, Engineers Australia, Royal Aeronautical Society, p. 516.
- Kuo, C.-W., Buisson, Q., McLaughlin, D. K., and Morris, P. J. (2013). "Experimental investigation of near-field pressure fluctuations generated by supersonic jets," in *19th AIAA/CEAS Aeroacoustics Conference*, p. 2033.
- Lele, S. (2005). "Phased array models of shock-cell noise sources," in *11th AIAA/CEAS Aeroacoustics Conference*, p. 2841.
- Lighthill, M. J. (1952). "On sound generated aerodynamically. I. General theory," *Proc. R. Soc. London, Ser. A* **211**, 564–587.
- Michalke, A. (1970). "A wave model for sound generation in circular jets," Technical Report (Deutsche Forschungs- und Versuchsanstalt für Luft- und Raumfahrt, eV).
- Michalke, A., and Fuchs, H. (1975). "On turbulence and noise of an axisymmetric shear flow," *J. Fluid Mech.* **70**(1), 179–205.
- Morel, T. (1975). "Comprehensive design of axisymmetric wind tunnel contractions," *J. Fluids Eng.* **97**(2), 225–233.
- Norum, T., and Seiner, J. (1982). "Measurements of mean static pressure and far field acoustics of shock containing supersonic jets," Technical Report (TM 84521, NASA, 1982).
- Ozawa, Y., Nonomura, T., Oyama, A., and Asai, K. (2020). "Effect of the Reynolds number on the aeroacoustic fields of a transitional supersonic jet," *Phys. Fluids* **32**(4), 046108.
- Pack, D. (1950). "A note on Prandtl's formula for the wave-length of a supersonic gas jet," *Q. J. Mech. Appl. Math.* **3**(2), 173–181.
- Raman, G. (1999). "Supersonic jet screech: Half-century from Powell to the present," *J. Sound Vib.* **225**(3), 543–571.
- Ray, P., and Lele, S. K. (2007). "Sound generated by instability wave/shock-cell interaction in supersonic jets," *J. Fluid Mech.* **587**, 173–215.
- Rodríguez, D., Cavaliere, A. V., Colonius, T., and Jordan, P. (2015). "A study of linear wavepacket models for subsonic turbulent jets using local eigenmode decomposition of PIV data," *Eur. J. Mech. B Fluids* **49**, 308–321.
- Sasaki, K., Cavaliere, A. V., Jordan, P., Schmidt, O. T., Colonius, T., and Brès, G. A. (2017). "High-frequency wavepackets in turbulent jets," *J. Fluid Mech.* **830**, R2.
- Savarese, A., Jordan, P., Girard, S., Collin, E., Porta, M., and Gervais, Y. (2013). "Experimental study of shock-cell noise in underexpanded supersonic jets," in *19th AIAA/CEAS Aeroacoustics Conference*, p. 2080.
- Seiner, J. M., and Yu, J. C. (1984). "Acoustic near-field properties associated with broadband shock noise," *AIAA J.* **22**(9), 1207–1215.
- Sinha, A., Rodríguez, D., Brès, G. A., and Colonius, T. (2014). "Wavepacket models for supersonic jet noise," *J. Fluid Mech.* **742**, 71–95.
- Sinha, A., Towne, A., Colonius, T., Schlinker, R. H., Reba, R., Simonich, J. C., and Shannon, D. W. (2018). "Active control of noise from hot supersonic jets," *AIAA J.* **56**(3), 933–948.
- Suzuki, T. (2016). "Wave-packet representation of shock-cell noise for a single round jet," *AIAA J.* **54**(12), 3903–3917.
- Suzuki, T., and Colonius, T. (2006). "Instability waves in a subsonic round jet detected using a near-field phased microphone array," *J. Fluid Mech.* **565**, 197–226.
- Tam, C. (1987). "Stochastic model theory of broadband shock associated noise from supersonic jets," *J. Sound Vib.* **116**(2), 265–302.
- Tam, C. (1995). "Supersonic jet noise," *Annu. Rev. Fluid Mech.* **27**(1), 17–43.
- Tam, C., Jackson, J., and Seiner, J. (1985). "A multiple-scales model of the shock-cell structure of imperfectly expanded supersonic jets," *J. Fluid Mech.* **153**, 123–149.
- Tam, C., and Tanna, H. (1982). "Shock associated noise of supersonic jets from convergent-divergent nozzles," *J. Sound Vib.* **81**(3), 337–358.
- Tan, D., Soria, J., Honnery, D., and Edgington-Mitchell, D. (2017). "Novel method for investigating broadband velocity fluctuations in axisymmetric screeching jets," *AIAA J.* **55**(7), 2321–2334.
- Vaughn, A. B., Neilsen, T. B., Gee, K. L., Wall, A. T., Micah Downing, J., and James, M. M. (2018). "Broadband shock-associated noise from a high-performance military aircraft," *J. Acoust. Soc. Am.* **144**(3), EL242–EL247.
- Viswanathan, K., Alkisslar, M., and Czech, M. (2010). "Characteristics of the shock noise component of jet noise," *AIAA J.* **48**(1), 25–46.



- Vold, H., Shah, P., Morris, P., Du, Y., and Papamoschou, D. (2012). "Axisymmetry and azimuthal modes in jet noise," in *18th AIAA/CEAS Aeroacoustics Conference (33rd AIAA Aeroacoustics Conference)*, p. 2214.
- Wong, M. H., Edgington-Mitchell, D. M., Honnery, D., Cavalieri, A. V., and Jordan, P. (2019a). "A parabolised stability equation based broadband shock-associated noise model," in *25th AIAA/CEAS Aeroacoustics Conference*, p. 2584.
- Wong, M. H., Jordan, P., Honnery, D. R., and Edgington-Mitchell, D. (2019b). "Impact of coherence decay on wavepacket models for broadband shock-associated noise in supersonic jets," *J. Fluid Mech.* **863**, 969–993.

## 5.8 Concluding Statement

To the authors' knowledge, this is the first time the azimuthal decomposition of mid-field BBSAN has been performed over a range of Mach numbers. The findings from this investigation offer new insight into BBSAN modelling by shedding light on the relative contribution of each azimuthal mode to the full BBSAN signature.

The contribution of each azimuthal mode is found to be closely linked to the directivity behaviour of BBSAN. Unlike subsonic and ideally-expanded jets, the axisymmetric mode ( $m = 0$ ) is not the dominant contributor to the mid-field BBSAN signature. Instead, the  $m = 1$  mode is the most important for  $St = 0.7$ . Successive modes become more important as frequency increases. When correlated with the known directivity of BBSAN, it can be observed that the total BBSAN sound field becomes progressively lower-rank in azimuth as polar angle and Mach number increase. For the secondary BBSAN peak at frequencies higher than the primary frequency, high-rank behaviour is observed.

The results from this experimental study also highlight the dangers of comparing stability-based BBSAN models to the full acoustic spectrum. The assumptions made by previous authors [149, 157] may lead to erroneous conclusions due to the roll-off at high frequencies differing significantly between the total signal and that of each mode. For example, using only the axisymmetric mode shape (c.f. Tam [157]) will underpredict the amplitude of the second BBSAN peak. Likewise, combining only the first three azimuthal modes (c.f. Ray and Lele [149]) leads to a mismatch since more than 4-5 modes are required to reconstruct the total signal at high frequencies ( $St > 0.8$ ). Hence, when using stability-type models for BBSAN, mode-by-mode comparisons should be made between models and experiment. The spectra in this chapter are used for comparisons to model predictions in Chapter 7.

It should be highlighted that the results presented in this chapter applies to mid-field acoustic measurements; the jet should be treated as an extended source rather than a point source. Hence, extrapolation to the far-field should be made with care as differences in directivity and modal energy distributions may be observed [206]. While no azimuthal decomposition measurements were performed in the far-field, the current results could be compared to the predictions computed by Arroyo and Moreau [95] for a  $M = 1.15$  under-expanded jet. By comparing near-field and far-field measurements, Arroyo and Moreau

[95] observed that the primary ( $n = 1$ ) BBSAN peak frequency did not change across the first three azimuthal modes. For peaks associated with higher-order shock modes ( $n > 1$ ), however, small shifts in frequencies were observed. In terms of distribution of modal energy, a qualitative comparison of the  $NPR = 2.25$  jet suggests an even distribution in SPL across the first three azimuthal modes in the mid-field; this is different to the results of Arroyo and Moreau [95]. For example, Arroyo and Moreau [95] predicted at upstream angles,  $m = 2$  is the most dominant mode in the far-field while current mid-field spectra show the first four modes having very similar amplitude. A similar observation was made by Brown and Bridges [207] when comparing mid-field microphone measurements to the far-field data collected by Juve *et al.* [208] for a subsonic jet from a chevron nozzle. The distribution of the modal energy of the acoustic field was more uniform in the mid-field measurements compared to the far-field. In future studies, it will be ideal to perform the same azimuthal decomposition of the acoustic far-field to confirm these trends for BBSAN.

With the availability of azimuthally-decomposed data, the focus now pivots to investigating the characteristics of a wavepacket BBSAN source model.

## Chapter 6

# Line Source Wavepacket Model for Broadband Shock-Associated Noise

### 6.1 Introductory Statement

The previous chapter offered insights into the azimuthal structure of BBSAN and also provided a database for comparison to model predictions. The isolation of each azimuthal mode allows a fair evaluation of a wavepacket BBSAN source; there is no requirement to reconstruct the signal using a truncated set of source modes. Before blindly constructing the equivalent wavepacket source, however, it is essential to determine what the important sound-generating flow features are. To this end, the *kinematic* modelling framework is utilised; source characteristics are varied and propagated to the far-field via an acoustic analogy.

The deficiencies observed in previous BBSAN stability-type models provide the initial motivation. While the main peak is well predicted, all models exhibit some mismatch at higher frequencies. The models of Ray and Lele [149] and Suzuki [96] severely under-predict noise above the main peak, while Tam's model [157] predicts artificial narrow-band peaks. Those results suggest the previous equivalent BBSAN source is incomplete and requires refinement.

A plausible explanation for the missing high-frequency sound observed in the predictions by Ray and Lele [149] and Suzuki [96] is the neglect of higher-order shock-cell modes. The

shock-cell structure may be decomposed into a set of Fourier waveguide modes [23]; stability-type BBSAN models is built on the premise that interaction between wavepackets and the fundamental mode is responsible for the primary BBSAN peak [23, 28]. Higher-order shock modes generate subsequent BBSAN peaks [85, 157]. In contrast, Ray and Lele [149] only used a single Fourier mode while Suzuki [96] modelled the shocks as ‘Gaussian humps’.

On the issue of narrow-band peaks, Lele [150] first suggested using an unsteady wavepacket to rectify the problem. The localised temporal changes of the wavepacket may lead to broader spectral widths at high frequencies [19]. Temporal changes in the wavepacket envelope and phase are known as jitter [125]. In ideally-expanded jets, intermittent wavepacket behaviour is less important when considering the radiated sound field [72]. The interplay between a jittering wavepacket and higher-order shock modes for BBSAN, however, remains an open question.

In this chapter, a model problem is considered to test the hypothesis that a jittering wavepacket may resolve the mismatch at high frequencies. In this model, the source for BBSAN is represented by the multiplication of the turbulence and shock components [2]. The shock-cell structure is described by a Pack and Prandtl model. For the turbulence component, the two-point wavepacket model by Cavalieri and Agarwal [125] is used as it permits independent variation of the different wavepacket source parameters which are associated with measurable flow quantities [45, 116]. The jittering wavepacket is represented statistically as coherence decay; a two-point model is required since a single-point model results in unit coherence. To simplify the problem, a line source is adopted and only a single component of the  $T_{ij}$  stress tensor is computed. The power spectral density (PSD) of the sound field is obtained by the convolution of the two-point cross-spectral density with the free-field Green’s function. The simple model allows rapid computations of the far-field sound to be performed. For brevity, only a single jet operating condition was considered.

Nominal values are used for the wavepacket parameters: envelope length, convection velocity, spectral dependence and coherence length; the exact values in a shock-containing jet are an unknown. A parametric study is performed to observe the effect of these parameters on the far-field spectra. The interaction between the wavepacket and a single shock-cell mode, or multiple modes, is investigated. The influence of coherence decay is tested by changing the value of the coherence length parameter. The sound-generation process is

visualised by Fourier-transforming the source CSD into wavenumber space [115, 125]. In this problem, the nozzle geometry is not considered and the observer is assumed to be in the far-field. Computed model spectra are scaled to match the amplitudes of the measurements from [29]. To avoid confusion, it should be highlighted that the position nomenclature used in this chapter is different to the one specified in figure 1.1;  $x$  represents the observer position while  $y$  denotes the source location.

The results from this chapter should be interpreted with the following points in mind. Firstly, the importance of source correlation/coherence decay has been recognised in previous BBSAN models [20, 85]. The measurements were based on bulk-turbulence statistics rather than the individual azimuthal modes. The experimental measurements by Jaunet *et al.* [45], however, show that there is a clear demarcation between the two. Thus, the investigation into the effects of coherence decay of wavepackets on far-field BBSAN, rather than the bulk-turbulence, is a novel contribution of this work. Secondly, it is important to emphasise that the exercise is not to develop a prediction scheme, but rather to highlight the pertinent features of a wavepacket BBSAN source. The effect of source parameters on the shape of the spectrum will inform future modelling efforts. Ultimately, the structure of the source CSD is the primary interest; identifying, understanding and modelling the flow behaviour responsible for that structure is the goal.

This chapter is presented as a journal paper published in The Journal of Fluid Mechanics [203]. This article is reprinted with permission from Cambridge University Press: Journal of Fluid Mechanics, "Impact of coherence decay on wavepacket models for broadband shock-associated noise in supersonic jets", Wong, Marcus H, et al. © 2019. Development of the mathematical framework and preliminary results were presented in a paper for the 24th AIAA/CEAS Aeroacoustics Conference (Appendix A).

# Impact of coherence decay on wavepacket models for broadband shock-associated noise in supersonic jets

Marcus H. Wong<sup>1,†</sup>, Peter Jordan<sup>2</sup>, Damon R. Honnery<sup>1</sup>  
and Daniel Edgington-Mitchell<sup>1</sup>

<sup>1</sup>Laboratory for Turbulence Research in Aerospace and Combustion,  
Department of Mechanical and Aerospace Engineering, Monash University,  
Melbourne, VIC 3800, Australia

<sup>2</sup>Département Fluides, Thermique, Combustion, Institut Pprime,  
CNRS – Université de Poitiers – ENSMA, 86000 Poitiers, France

(Received 25 May 2018; revised 27 November 2018; accepted 1 December 2018;  
first published online 29 January 2019)

Motivated by the success of wavepackets in modelling the noise from subsonic and perfectly expanded supersonic jets, we apply the wavepacket model to imperfectly expanded supersonic jets. Recent studies with subsonic jets have demonstrated the importance of capturing the ‘jitter’ of wavepackets in order to correctly predict the intensity of far-field sound. Wavepacket jitter may be statistically represented using a two-point coherence function; accurate prediction of noise requires identification of this coherence function. Following the analysis of Cavalieri & Agarwal (*J. Fluid Mech.*, vol. 748, 2014, pp. 399–415), we extend their methodology to model the acoustic sources of broadband shock-associated noise in imperfectly expanded supersonic jets using cross-spectral densities of the turbulent and shock-cell quantities. The aim is to determine the relationship between wavepacket coherence-decay and far-field broadband shock-associated noise, using the model as a vehicle to explore the flow mechanisms at work. Unlike the subsonic case where inclusion of coherence decay amplifies the sound pressure level over the whole acoustic spectrum, we find that it does not play such a critical role in determining the peak sound amplitude for shock-cell noise. When higher-order shock-cell modes are used to reconstruct the acoustic spectrum at higher frequencies, however, the inclusion of a jittering wavepacket is necessary. These results suggest that the requirement for coherence decay identified in prior broadband shock-associated noise (BBSAN) models is in reality the statistical signature of jittering wavepackets. The results from this modelling approach suggest that nonlinear jittering effects of wavepackets need to be included in dynamic models for broadband shock-associated noise.

**Key words:** absolute/convective instability, aeroacoustics, jet noise

## 1. Introduction

When a supersonic jet is operating at off-design conditions, a train of quasi-periodic shock cells appears. Compared to subsonic or perfectly expanded supersonic jets,

<sup>†</sup> Email address for correspondence: [marcus.wong@monash.edu](mailto:marcus.wong@monash.edu)

these shock cells lead to an additional kind of aerodynamic noise. Shock-cell noise is comprised of discrete tones (known as screech) and a broadband component. The generation of screech is due to a self-sustaining feedback loop (Powell 1953) and is believed to be produced between the second and fourth shock cells (Edgington-Mitchell *et al.* 2014). The production of broadband shock-associated noise (hereafter BBSAN) follows a similar process (Tam, Seiner & Yu 1986), but without the resonant feedback loop.

The broadband component is generated by the interaction of downstream-travelling flow structures with the shock cells (Harper-Bourne & Fisher 1973). This interaction produces sound waves that propagate to the far field, whose maximum intensity is in a direction perpendicular to the jet axis. In the far field, BBSAN is characterised by a broad spectral peak whose peak frequency is a function of the nozzle pressure ratio (NPR), convection velocity and observer location. The amplitude of BBSAN is dependent on the off-design parameter  $\beta = \sqrt{M_j^2 - M_d^2}$  where  $M_j$  and  $M_d$  are the perfectly expanded and design Mach numbers of the jet, respectively.

Models for BBSAN were initially developed based on experimental observations, such as the empirical model of Harper-Bourne & Fisher (1973) which is based on a phased array of localised sources along the jet centreline. The directivity of BBSAN is proposed to be due to the relative phasing between the sources, where the time delay in acoustic emission between adjacent sources is a function of the convection velocity of the convecting flow structures. While the model is capable of reproducing many of the acoustic far-field features, it incorrectly predicts the occurrence of harmonically related peaks, nor does it account for azimuthal modes other than the axisymmetric mode.

More recently semi-empirical hybrid models have been developed. With the increase in computational power available in recent times, hybrid models are now being used to model BBSAN for different nozzle geometries (Miller & Morris 2010; Morris & Miller 2010) with reasonable success. These models use Reynolds averaged Navier–Stokes (RANS) mean-flow solutions to provide input for acoustic-analogy source terms which link flow-field fluctuations to the propagation of sound waves in the far field (Lighthill 1952). Mixed-scale models (Kalyan & Karabasov 2017; Tan *et al.* 2017), using frequency-dependent length scales, have been shown to improve agreement with data over a larger range of frequencies compared to Morris and Miller's original model. The acoustic source models are based on measured bulk two-point turbulence correlations. Such hybrid models are now capable of enabling large parametric studies with fast turnaround times. These semi-empirical models require accurate source descriptions based on turbulence statistics and their construction for a given flow is a non-trivial task. This difficulty motivates the development of simplified reduced-order descriptions of the noise-producing flow features. One such approach involves modelling organised flow structures as hydrodynamic instability waves, or wavepackets as they are now more often called.

The use of wavepackets to represent large-scale coherent structures (Crow & Champagne 1971) is well documented. Mollo-Christensen (1967) was the first to propose their use to model jet noise and many experiments have been performed that indicate the validity of the approach (Suzuki & Colonius 2006; Gudmundsson & Colonius 2011; Cavalieri *et al.* 2012, 2013) for subsonic jets. The growth, saturation and decay behaviour of wavepackets emulates the downstream evolution of large-scale structures as the jet mean profile spreads. The presence of these acoustically non-compact structures has already been confirmed in the hydrodynamic



field of subsonic jets (Suzuki & Colonius 2006; Gudmundsson & Colonius 2011; Cavalieri *et al.* 2013). The reduced-order velocity field deduced from particle image velocimetry (PIV) measurements matches well with the predictions of linear stability models. These models also predict the axisymmetric superdirectivity and lower-order azimuthal character of jet noise, consistent with measured results (Cavalieri *et al.* 2012). A comprehensive summary of subsonic jet-noise modelling using wavepackets can be found in the review of Jordan & Colonius (2013).

Wavepacket models have also been used for supersonic jet noise (Léon & Brazier 2013; Sinha *et al.* 2014). The idea of incorporating large-scale structures for modelling BBSAN was first proposed by Tam. In a series of papers by Tam and co-workers (Tam & Tanna 1982; Tam 1987), a dynamic model for BBSAN has been proposed wherein noise is produced via weak nonlinear interactions between shock cells and turbulent structures in the shear layer. The turbulent structures are represented as a superposition of instability waves at different frequencies. As these instability waves convect downstream, they interact with the shock cells which are represented as a series of stationary waveguide modes. The stochastic description of the model arises from the random fluctuations of the instability waves. Tam's model was found to match well with experimental data although it suffered at upstream angles close to the nozzle exit where non-physical narrow-banded peaks are predicted.

The same observations that motivate dynamic modelling approaches based on stability theory can also be used to construct kinematic models for shock-associated noise in supersonic jets. Unlike dynamic models where the instability modes of the jet and the acoustic field are obtained simultaneously via solution of the linearised flow equations, kinematic sound-source models (Morris & Miller 2010; Kalyan & Karabasov 2017) obtain the radiated sound field via an acoustic analogy. Rather than using the bulk-turbulence statistics to construct the source term (Harper-Bourne & Fisher 1973; Morris & Miller 2010), however, a wavepacket description consistent with the results of dynamic modelling is here used for the source term (Lele 2005). The wavepacket source term parameters can be deduced from carefully planned experiments (Jaunet, Jordan & Cavalieri 2017; Maia *et al.* 2017), where the modelled fluctuating components are first decomposed into azimuthal modes and in frequency. A kinematic model for broadband shock-associated noise, using a wavepacket representation, was first proposed by Lele (2005). Similar to Tam *et al.* (1986), Lele hypothesised that the sources are associated with the nonlinear interaction of instability waves with the stationary shock-cell modes, represented as a sum of standing waves (Pack 1950). The suitability of using wavepackets to model sound sources in shock-containing flows was confirmed by the laser-Doppler velocimetry (LDV) measurements of Savarese *et al.* (2013).

An important element for wavepacket modelling in subsonic jets is the two-point coherence of the associated azimuthal modes. Wavepacket fluctuations in a jet will exhibit coherence decay with distance due to the action of turbulence. For subsonic jets, its neglect can lead to discrepancies in the far field of several orders of magnitude (Baqui *et al.* 2013; Breakey *et al.* 2013; Suzuki 2013; Jordan *et al.* 2014; Zhang *et al.* 2014). By including this phenomenon in their kinematic source model, Cavalieri *et al.* (2011) were able to demonstrate that wavepacket jitter can indeed dramatically increase sound-radiation efficiency in subsonic jets. The impact of coherence decay in wavepacket models in predicting far-field noise is discussed in depth by Cavalieri & Agarwal (2014) who show that a two-point kinematic model with coherence decay is required in subsonic jets in order to match the far-field sound pressure level. By

matching the coherence behaviour to turbulent subsonic jets, Baqui *et al.* (2015) used a linear stability model to show how sensitive far-field predictions are to coherence decay.

For ideally expanded supersonic flows, however, this jittering behaviour has been shown to be less important, since the main hydrodynamic wavelengths are already acoustically ‘matched’ (Crighton 1975) and thus able to radiate to the far field efficiently (Cavalieri *et al.* 2014; Sinha *et al.* 2014). This is further supported by the finding of Cheung & Lele (2009) where nonlinear parabolic stability equations (PSE) accurately predicted the far-field acoustics of a supersonic two-dimensional mixing layer but failed in the subsonic case.

It is well recognised that some form of coherence/correlation decay is a controlling parameter in jet noise. This recognition is evident in the significant effort which has been expended to measure the bulk two-point statistics in turbulent jets (Harper-Bourne 2002; Freund 2003; Kerhervé *et al.* 2004; Jordan & Gervais 2005; Morris & Zaman 2010; Pokora & McGuirk 2015, amongst others). The measurements (typically dominated by the energy-containing eddies), guided the construction of the two-point coherence and correlation function in BBSAN-modelling schemes such as Harper-Bourne & Fisher (1973) and Morris & Miller (2010) respectively. In shock-containing flows, Lele (2005) demonstrated the effect of coherence decay by introducing it into a localised phased-array model similar to that of Harper-Bourne & Fisher. Coherence decay of the bulk turbulence, was found to be effective in controlling the harmonic peaks produced when using a perfectly coherent source pair. The degree of suppression of the higher-order peaks is dependent on the extent to which the cross-coherence decays between sources. These harmonic peaks were also observed in Tam’s dynamic instability wave model.

In the kinematic framework, however, a clear distinction needs to be made between previous BBSAN sound-source models and the proposed wavepacket model. Jaunet *et al.* (2017) have shown considerable difference between two-point bulk statistics, obtained from point measurements, on one hand, and, on the other, two-point statistics of individual azimuthal modes using dual-plane PIV data of a subsonic turbulent jet. The majority of the fluctuating turbulent energy is contained in scales which correspond to higher-order azimuthal modes. These modes, however, have been shown to be acoustically inefficient (Michalke 1970; Cavalieri *et al.* 2012). Hence, while two-point BBSAN source models based on bulk-flow statistics (Harper-Bourne & Fisher 1973; Morris & Miller 2010) do explicitly include two-point coherence or correlation information, they are not directly equivalent to wavepacket models where only the velocity perturbations of the acoustically efficient lowest-order azimuthal modes are used. Throughout the paper, coherence decay will refer to the two-point coherence behaviour of wavepackets, and not that of bulk turbulence as studied previously such as Harper-Bourne & Fisher (1973) and Morris & Miller (2010).

The importance of wavepacket jitter in shock-containing supersonic flows is less clear. Using a model where the turbulence fluctuations are modelled by wavepackets and the shock-cell noise sources as a collection of empirical Gaussian humps, Suzuki (2016) deduced the source parameters from azimuthally decomposed large-eddy simulation (LES) near-field pressure data. The acoustic signature of the source was extracted by solving the boundary-value problem using the pressure field on a surface surrounding the jet as a boundary for the wave equation. By modelling this acoustic signature in the frequency domain, the coherence-decay behaviour was matched for the cases studied. Good agreement at the BBSAN peak frequencies was achieved between the model and data for a range of frequencies. The effect of coherence decay, however, was not discussed.

A further clue to the importance of the aforementioned nonlinear jittering effect, however, can be seen in the results of Ray & Lele (2007) who extended Tam's dynamic broadband shock-associated noise model. The small-amplitude disturbances were decomposed into azimuthal modes and represented as instability waves. For a cold underexpanded jet, they found good agreement at low frequencies but highlighted that their instability model was unable to capture higher frequencies, which they attributed to 'some combination of nonlinear and non-modal effects'. This suggests that, at higher frequencies, the nonlinear effect of wavepacket jitter may play an important role.

In order to develop accurate dynamic models, it is crucial to determine whether coherence decay is important in a given flow. Using kinematic models to 'test' the impact of coherence decay can provide valuable information regarding the forcing term that is required in the dynamic modelling framework (Towne *et al.* 2015).

In this paper, encouraged by the results of Ray & Lele (2007) and Suzuki (2016), we extend the model of Cavalieri & Agarwal (2014) to the study of broadband shock-associated noise. We propose a two-point kinematic model for BBSAN in order to understand the effect of coherence decay in shock containing flows, where the source terms for both the turbulent and shock-cell components are derived from linearised flow equations. The departure point is the single-point wavepacket model (equation (4.4.1) from Lele (2005)) that we modify by replacing the time dependence with a term that models the two-point coherence.

The remainder of the paper is structured as follows. The mathematical formulation of the two-point wavepacket model is first presented in §2. In §3, we highlight the effect of coherence decay on the far-field sound-radiation properties predicted by the model. By comparing to historical experimental data, we specifically look at the acoustic efficiency and directivity for wavepackets interacting with a single shock-cell mode. The interpretation of sound radiating characteristics of the model is then discussed in §4. The effect of coherence decay on the more general model of multiple shock-cell modes is presented in §5 with conclusions and future perspectives provided in §6.

## 2. Mathematical model

The kinematic wavepacket sound-source model is based on Lighthill's acoustic analogy, where the fluctuating sound pressure,  $p$ , is given by the inhomogeneous wave equation

$$\nabla^2 p - \frac{1}{c_0^2} \frac{\partial^2 p}{\partial t^2} = S(\mathbf{y}, t), \quad (2.1)$$

where  $\mathbf{y}$  are the source coordinates,  $c_0$  is the ambient speed of sound,  $t$  is time and  $S(\mathbf{y}, t)$  is the source term expressed as the double divergence of Lighthill's stress tensor along the jet axis. The Helmholtz equation can be obtained via a Fourier transform of (2.1) to arrive at

$$\nabla^2 p + k^2 p = S(\mathbf{y}, \omega), \quad (2.2)$$

where  $k = \omega/c_0$ .

Using a free-field Green's function  $G(\mathbf{x}, \mathbf{y}, \omega)$ , the integral solution to the Helmholtz equation (2.2) is,

$$p(\mathbf{x}, \omega) = \int_V S(\mathbf{y}, \omega) G(\mathbf{x}, \mathbf{y}, \omega) d\mathbf{y}, \quad (2.3)$$

where the integration is carried out over the region  $V$  where  $S \neq 0$  and  $\mathbf{x}$  are the observer coordinates.

As proposed by Tam (1990) and Lele (2005), the full three-dimensional source term for BBSAN can be represented as a one-dimensional multiplicative combination of the shock-cell  $u_s$  and turbulent  $u_t$  velocity fluctuations

$$S(\mathbf{y}, t) \simeq \hat{S}(\mathbf{y}, t) = u_s(\mathbf{y})u_t(\mathbf{y}, t), \quad (2.4)$$

where  $\hat{S}(\mathbf{y}, t)$  is a line-source model (azimuthal and radial dependences are not considered). The coordinate vector  $\mathbf{y}$  is now replaced by the axial position coordinate  $y$ . This modelling of acoustic sources along a line thus only accounts for axisymmetric wavepacket fluctuations.

One approach to model the disturbances due to the quasi-periodic train of shock cells is to regard the jet mixing layer as a waveguide (Prandtl 1904; Pack 1950). By approximating the mixing layer of the jet as a vortex sheet, the disturbances due to the shock cells can be decomposed into a set of spatially periodic functions. Each of these periodic functions can be thought of as a waveguide mode of the jet. In one dimension, the velocity fluctuations related to the shock-cell waveguide modes along the axial direction,  $u_s(y)$ , is represented as (Prandtl 1904; Pack 1950)

$$u_s(y) = U_s \sum_n c_{s_n} \frac{1}{2} \{e^{ik_{s_n}y} + e^{-ik_{s_n}y}\}. \quad (2.5)$$

The shock-cell waveguide modes are described by the wavenumbers  $k_{s_n}$  and the amplitude terms  $c_{s_n}$  where we adopt the expression from Prandtl & Pack's vortex sheet model,

$$k_{s_n} = \frac{2\sigma_n}{D_j(M_j^2 - M_d^2)^{1/2}}, \quad n = 1, 2, 3, \dots, \quad (2.6)$$

$$c_{s_n} = \frac{2\Delta p}{\sigma_n p_\infty}, \quad n = 1, 2, 3, \dots, \quad (2.7)$$

where  $\sigma_n$  is the  $n$ th zero crossing of the zeroth-order Bessel function,  $D_j$  and  $M_j$  are respectively, the ideally expanded diameter and Mach number of the jet.  $M_d$  is the design Mach number which is equal to unity for a convergent nozzle. The amplitude term  $c_{s_n}$  is the ratio between the pressure imbalance  $\Delta p$  at the throat of the nozzle and the ambient pressure  $p_\infty$ . The amplitude decay of the shock modes over axial distance as seen in experimental measurements, however, is not calculated or accounted for. The overall scaling amplitude of the shock cells is represented by  $U_s$ . The complete solution for the vortex sheet shock-cell model can be found in Pack (1950).

To model  $u_t$ , Lele (2005) used a wavepacket whose amplitude is modulated in both space and time. The wavepacket, at a given axial position  $y$ , is defined by its envelope length scale  $L$ , hydrodynamic wavenumber  $k_h$  and frequency  $\omega$ ; the two latter quantities being related by the convection velocity  $k_h = \omega/U_c$ . The explicit single-point form of  $u_t$  with amplitude  $U_t$  is,

$$u_t(y, t) = U_t e^{-(y/L)^2} e^{i(k_h y - \omega t)}. \quad (2.8)$$

To model the jitter of the wavepackets, Lele introduced a temporal modulation term involving stochastic realisations. The work of Cavalieri & Agarwal (2014), however,

established that coherence decay can provide an alternative statistical representation of jitter. Therefore, rather than including a temporal dependence, we use two-point statistics to model the wavepacket's stochastic behaviour. After taking the Fourier transform of the proposed source model  $\hat{S}(y, \omega)$ , the source term at a single point  $y$  is now given by

$$\hat{S}(y, \omega) = A(\omega) e^{-(y/L(\omega))^2} \{e^{ik_h(\omega)y}\} \sum_n c_{s_n} \{e^{ik_{s_n}y} + e^{-ik_{s_n}y}\}, \quad (2.9)$$

where an implicit factor of  $\exp(-i\omega t)$  is assumed and the  $U_s$  and  $U_t$  amplitude terms in (2.5) and (2.8) have been absorbed into the amplitude term  $A(\omega)$ .

While equation (2.9) allows direct computation of the fluctuating pressure field, the Fourier transform that would provide the source term  $S(y, \omega)$  cannot be evaluated as it involves an integrand that is not square integrable (Landahl & Mollo-Christensen 1992; Cavalieri & Agarwal 2014). Fluctuations in a turbulent jet comprise a stationary random process, and are best described through statistical metrics such as variance, autocorrelation and cross-correlation. In the frequency domain, a particularly rich statistical metric is the cross-spectral density, which is the Fourier transform of the cross-correlation, but which can also be defined as the expected value  $\mathcal{E}(\hat{u}\hat{u}^*)$ , where  $\hat{u}$  is the Fourier transform taken for a given realisation, and  $\mathcal{E}$  is the expected-value operator, which is the asymptotic limit of an ensemble average. Using power-spectral densities (PSDs) and cross-spectral densities (CSDs), the Fourier transforms of the autocorrelation and cross-correlation functions, respectively, we express the far-field sound pressure level (SPL) as

$$\langle p(\mathbf{x}, \omega) p^*(\mathbf{x}, \omega) \rangle \approx \int_V \int_V \langle S(y_1, \omega) S^*(y_2, \omega) \rangle G(\mathbf{x}, y_1, \omega) G^*(\mathbf{x}, y_2, \omega) dy_1 dy_2, \quad (2.10)$$

where both PSDs and CSDs are obtained by multiplying by the complex conjugate between position  $y_1$  and  $y_2$  and the hats have been dropped for convenience. The free-field Green's function is

$$G(\mathbf{x}, \mathbf{y}, \omega) = \frac{1}{4\pi} \frac{e^{ik|\mathbf{x}-\mathbf{y}|}}{|\mathbf{x}-\mathbf{y}|}. \quad (2.11)$$

To obtain the two-point source term with unit coherence at position  $y_1$ , we multiply equation (2.9) by its complex conjugate at position  $y_2$

$$\begin{aligned} S(y_1, \omega) S^*(y_2, \omega) &= A^2(\omega) e^{-(y_1/L(\omega))^2} e^{-(y_2/L(\omega))^2} \{e^{ik_h(\omega)(y_1-y_2)}\} \\ &\times \sum_n c_{s_n} \{e^{ik_{s_n}y_1} + e^{-ik_{s_n}y_1}\} \sum_m c_{s_m} \{e^{ik_{s_m}y_2} + e^{-ik_{s_m}y_2}\}. \end{aligned} \quad (2.12)$$

We now define the coherence function between points  $y_1$  and  $y_2$  as

$$\gamma^2(y_1, y_2, \omega) = \frac{|\langle S(y_1, \omega) S^*(y_2, \omega) \rangle|^2}{\langle |S(y_1, \omega)|^2 \rangle \langle |S(y_2, \omega)|^2 \rangle} \quad (2.13)$$

modelled as a Gaussian function following Cavalieri & Agarwal (2014),

$$\gamma^2(y_1, y_2, \omega) = \exp\left(-2 \frac{(y_1 - y_2)^2}{L_c^2(\omega)}\right). \quad (2.14)$$



The coherence decay between points  $y_1$  and  $y_2$  is now defined by the characteristic coherence length scale  $L_c$ . Introducing this effect by multiplying equations (2.12) and (2.14), we arrive at the CSD of the two-point source model for broadband shock-associated noise

$$S(y_1, \omega)S^*(y_2, \omega) = A^2(\omega)e^{-(y_1/L(\omega))^2}e^{-(y_2/L(\omega))^2}\{e^{ik_h(\omega)(y_1-y_2)}\}e^{-(y_1-y_2)^2/L_c(\omega)^2} \\ \times \sum_n c_{s_n}\{e^{ik_{s_n}y_1} + e^{-ik_{s_n}y_1}\} \sum_m c_{s_m}\{e^{ik_{s_m}y_2} + e^{-ik_{s_m}y_2}\}. \quad (2.15)$$

For a given pair of points  $(y_1, y_2)$ , the source term is described by two wavepacket envelope terms  $\exp(-y_1/L(\omega))^2$  and  $\exp(-y_2/L(\omega))^2$  at the two points respectively. The term  $\exp[ik_h(\omega)(y_1 - y_2)]$  describes the phase difference between  $y_1$  and  $y_2$  while the coherence decay is modelled by  $\exp[-(y_1 - y_2)^2/L_c^2(\omega)]$ . Finally this is multiplied by the shock-cell modes at points  $y_1$  and  $y_2$  by the expression  $\sum[\exp(ik_{s_n}y_1) + \exp(-ik_{s_n}y_1)] \sum[\exp(ik_{s_m}y_2) + \exp(-ik_{s_m}y_2)]$ . The frequency dependence notation of  $k_h$ ,  $L$  and  $L_c$ , while implied, is now hereafter omitted for convenience.

Similar to Cavalieri & Agarwal (2014), the model is now governed by two characteristic length scales. The first length scale,  $L$ , characterises the wavepacket amplitude envelope. The second,  $L_c$ , is the coherence length scale which characterises the decay of coherence between two points along the axial direction. It should be noted that as  $L_c \rightarrow \infty$ , the two-point model (2.15) reduces to the unit-coherence model (2.12).

The far-field sound pressure for both models can now be found by inserting equations (2.15) and (2.12) into equation (2.10). Using the usual Fraunhofer far-field approximation where  $|\mathbf{x} - \mathbf{y}| \approx |\mathbf{x}| - \hat{\mathbf{x}} \cdot \mathbf{y}$  (Crighton 1975; Howe 2003), we arrive at the expression

$$\langle p(\mathbf{x}, \omega)p^*(\mathbf{x}, \omega) \rangle \approx \frac{A^2(\omega)}{4\pi x^2} \int \int \langle S(y_1, \omega)S^*(y_2, \omega) \rangle e^{ik \cos \theta (y_1 - y_2)} dy_1 dy_2, \quad (2.16)$$

where  $\theta$  is taken as the angle from the downstream jet axis. Due to the line-source approximation for this model, the double volume integral reduces to a double integral in the streamwise direction.

### 3. Acoustic efficiency and directivity

#### 3.1. Parameters of the source model

Our objective here is to study the impact of coherence decay on BBSAN in a model problem. To do so, we must first specify values of the hydrodynamic terms ( $k_h$ ,  $A(\omega)$ ,  $L$ ) in (2.16). The coherence length term  $L_c$  must also be specified. The chosen modelling parameters are listed in table 1 and given in appendix A; the justification of these values is discussed below.

The first parameter,  $k_h$  is the hydrodynamic wavenumber of the wavepacket defined as  $k_h = \omega/u_c$ . We consider the average convection velocity of the wavepackets to be  $u_c \approx 0.6U_j$ , consistent with the literature (Harper-Bourne & Fisher 1973; Lau 1980; Troutt & McLaughlin 1982; Kerhervé, Fitzpatrick & Jordan 2006; Morris & Zaman 2010).

The second term  $A(\omega)$  represents the wavepacket amplitude. While there is no theoretical form for shock-containing flows, it has been previously measured in experimental campaigns (Bridges & Wernet 2008; Savarese *et al.* 2013). More

recently, Antonialli *et al.* (2018) were able to determine the frequency dependence of wavepacket amplitudes in a subsonic Mach 0.9 jet by comparing large-eddy simulation data of Brès *et al.* (2017) to the fluctuation fields predicted from the parabolised stability equations model of Sasaki *et al.* (2017b). We therefore model the wavepacket amplitude term using an energy-spectrum function as proposed by Antonialli *et al.* (2018)

$$A(\omega) = C_1 e^{-C_2 \omega}, \quad (3.1)$$

where terms  $C_1$  and  $C_2$  are fitting parameters with values  $3.4 \times 10^{-7}$  and 0.58 respectively. The value of  $C_2$  has been normalised based on the Strouhal number of  $St = fD/U_j$ . A similar exponential decay spectrum was also used by Suzuki (2016). The numerical value of  $A(\omega)$  is obtained by fitting the model (3.1) to the measured velocity spectra (Savarese *et al.* 2013) obtained along the shear layer at an axial position  $y/D \approx 3$  for a jet operating at  $NPR = 2.5$ . The amplitude term is normalised to yield a source strength of unity at the peak frequency.

As we do not have at our disposal the wavepacket length scales  $L$  and  $L_c$  for supersonic jets, we adopt values from previous work on subsonic flows. The objective of this study is not to develop a predictive capability but rather to determine the impact of coherence decay in a model problem. Hence, in the same spirit as Cavalieri & Agarwal (2014) who used average values independent of frequency, we evaluate the source term in (2.16) for  $L = 1.0D$  and  $k_h L = 5$ . From the two-point measurements of Jaunet *et al.* (2017) for a  $M = 0.4$  jet, it is evident that coherence lengths have a frequency and axial position dependence. However, without prior measurements of this dependence in shock-containing flows, we adopt for this study an average value of  $L_c = 1.0D$  similar to Cavalieri & Agarwal (2014) and Baqui *et al.* (2015). It should be noted, however, that Suzuki (2016) did extract the coherence length of the near-field pressure in an underexpanded supersonic jet. An approximately constant coherence length scale was found over a range of frequencies, further suggesting that an average value is suitable for the purposes of this study. The sensitivity of the modelling choices have been investigated with some results presented in appendix A.

### 3.2. Far-field acoustic predictions

The far-field sound is obtained by numerical evaluation of (2.16). Figure 1 shows the variation of far-field SPL as a function of emission angle and frequency for an underexpanded jet operating at  $NPR = 3.4$ . The modelled jet issues from a convergent nozzle, which corresponds to an off-design parameter of  $\beta = 1.04$ . In comparing the case between unit coherence and coherence decay, all tuning parameters as specified in § 3.1 with the exception of  $L_c$  are kept constant. The far-field sound pressure contours were obtained using the first ten shock-cell modes ( $n = 10$ ). The use of the number of modes is justified in § 5. It is clear from figure 1 that coherence decay has a significant effect on the BBSAN spectrum. Consistent with experimental observations, both plots comprise a peak frequency that increases with decreasing observation angle; though the effect is more evident in the unit-coherence case.

The first stage of the analysis considers cases involving a single shock-cell mode ( $n = 1$ ); the centreline pressure fluctuations in a moderately underexpanded jet are reasonably well represented by a single mode (Tam, Jackson & Seiner 1985; Ray & Lele 2007). Figure 2 shows the directivity for far-field SPL at  $St = 0.3$  and  $St = 0.6$  for the same conditions as figure 1 but with only the fundamental shock-cell mode ( $n = 1$ ) included. The Strouhal number is defined as  $St = fD/U_j$ . Models with unit coherence and coherence decay are plotted on the same figure for comparison. At  $St = 0.3$ , both

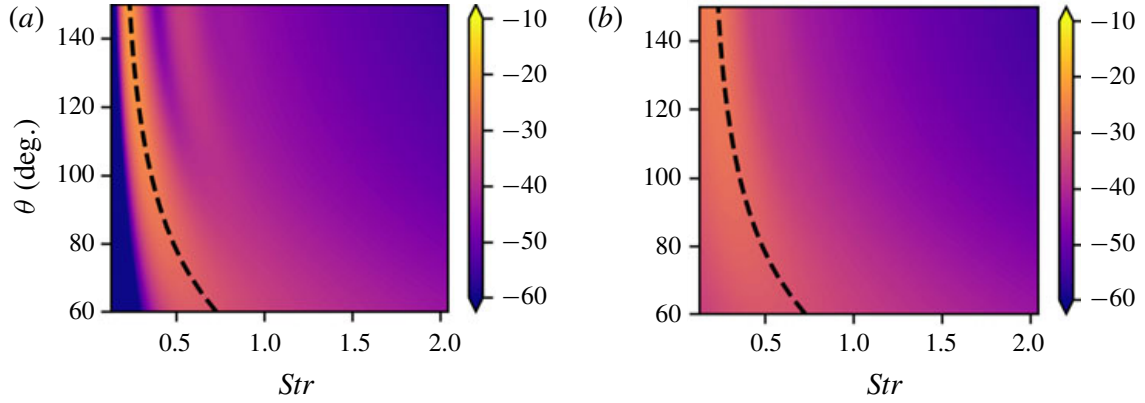


FIGURE 1. (Colour online) Contours of sound pressure level (arbitrary dB) as a function of frequency ( $St$ ) and directivity ( $\theta$ ) for (a) unit coherence and (b) with coherence decay. The jet issues from a converging nozzle ( $M_d = 1.0$ ) at a nozzle pressure ratio of  $NPR = 3.4$  which corresponds to a fully expanded jet Mach number of  $M_j = 1.45$  and an off-design parameter of  $\beta = 1.04$ . The dashed line indicates the peak frequency as predicted by Harper-Bourne & Fisher (1973).

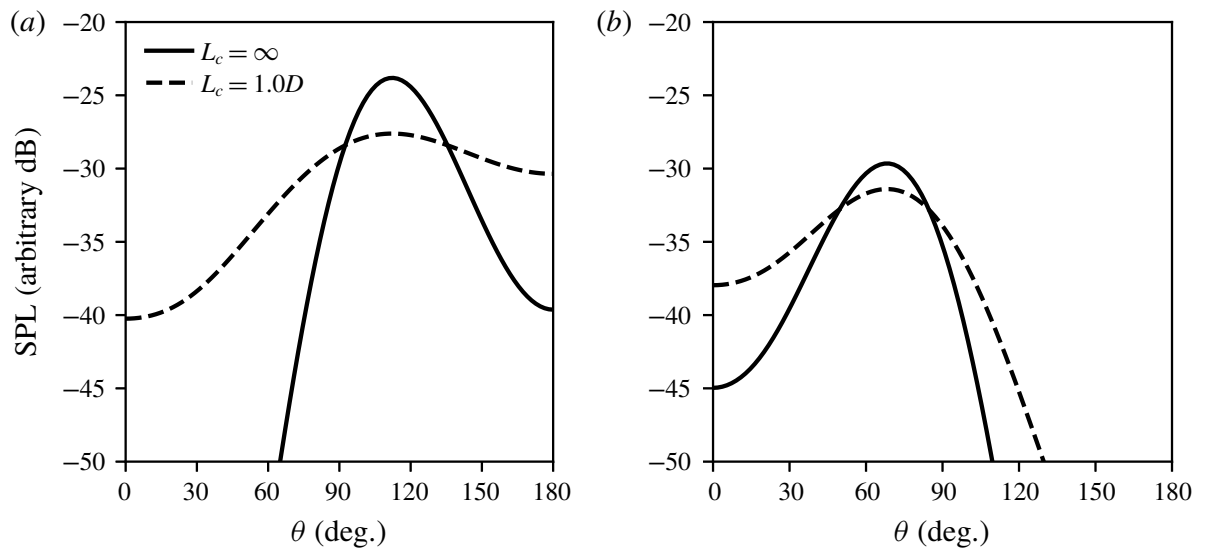


FIGURE 2. Sound pressure level at a distance of  $100D$  for a wavepacket frequency of (a)  $St = 0.3$  and (b)  $St = 0.6$  as a function of observation angle  $\theta$  for a wavepacket with  $k_h L = 5$ .

models predict the highest amplitude of radiation in the direction slightly upstream of perpendicular, consistent with previous findings. At  $St = 0.6$ , the BBSAN peaks shift downstream but with a smaller sound amplitude. With all other terms equal, the introduction of coherence decay broadens the radiation lobe, increasing the SPL in the downstream direction (low  $\theta$  values). Contrary to the subsonic jet case (Cavaleri *et al.* 2011; Baqui *et al.* 2015, amongst others), however, the introduction of coherence decay reduces the peak amplitude by approximately 2–5 dB. The reason for this behaviour will be further explored in § 4. It is also evident, from the peak frequency trends in figures 1 and 2, that the current wavepacket model agrees with the predictions made by localised phased-array models such as Harper-Bourne & Fisher (1973).



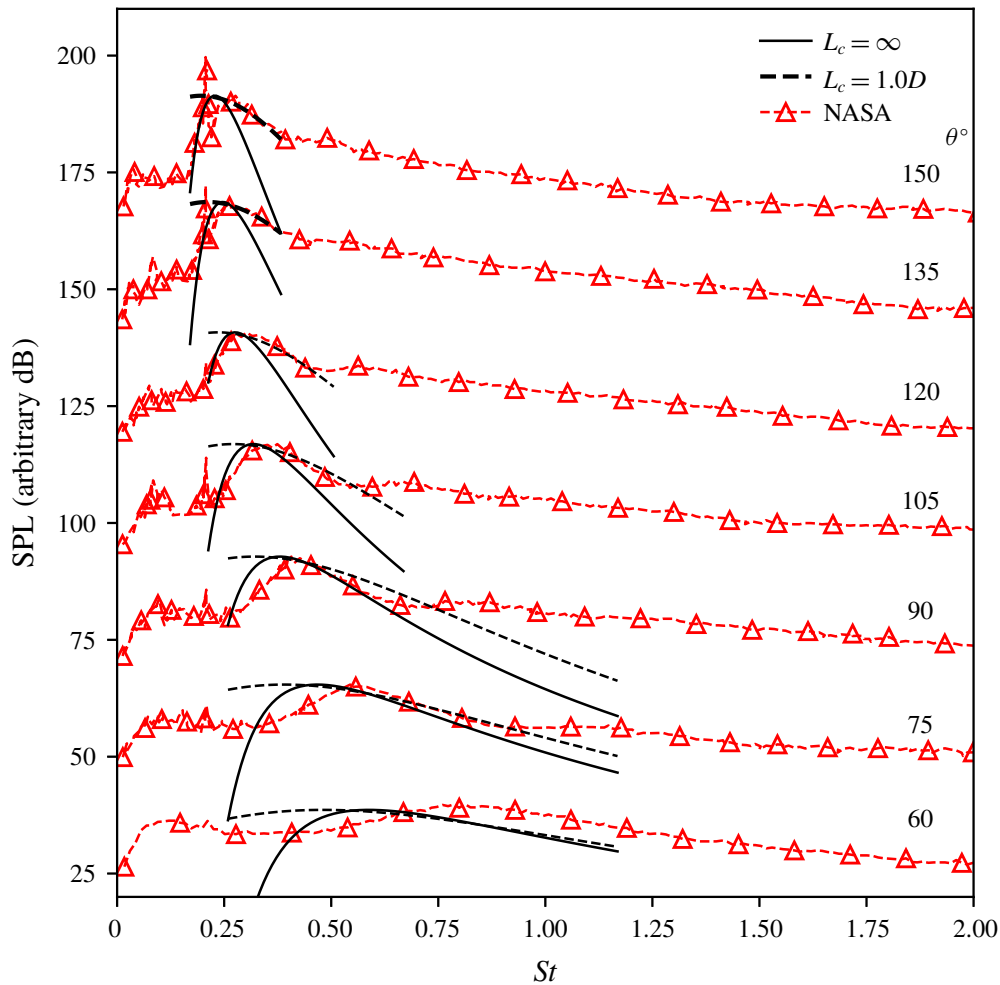


FIGURE 3. (Colour online) Power spectrum at a distance of  $100D$  through a range of observation angles between  $\theta = 60^\circ$  and  $\theta = 150^\circ$  measured from the downstream jet axis for a wavepacket with  $k_h L = 5$ . Each measurement angle is offset by  $\Delta dB = 25$ . NASA experimental data from Norum & Seiner (1982).

Figure 3 shows a comparison of the noise spectra between the two models and experimental data for an underexpanded jet operating at  $NPR = 3.4$  (Norum & Seiner 1982). The modelled peak amplitudes are adjusted to match experimental data in order to facilitate comparison of the spectral shape. As can be seen, while there is reasonable agreement between the two models and the measured data in terms of the peak frequency, the overall agreement between the two models and the data is moderate. Both the unit-coherence and coherence-decay models capture the BBSAN peak frequency dependence and the narrowing of the spectral peak with increasing angle. With the inclusion of coherence decay, however, the BBSAN spectral peak width broadens leading to a more favourable agreement for frequencies greater than the peak. Below  $\theta = 75^\circ$ , both models fail to capture the correct peak frequency. A possible explanation for this disagreement in peak frequency at downstream angles could be due to the choice of the  $u_c$  and  $L$  modelling variables, as discussed in appendix A, or the dominance of jet mixing noise close to the jet axis.

It is evident from figure 3 that the jitter of wavepackets, modelled by coherence decay, broadens the acoustic spectrum. The model suggests, however, that coherence decay does not have a major impact on the sound amplitude. Unlike in subsonic flows, it provides little contribution to the peak SPL. This is also consistent with the results

presented by Sinha *et al.* (2014) for isothermal fully expanded supersonic jets, where it was found that the far-field noise spectrum at downstream observation angles is well captured even without considering the jitter of wavepackets. The reason for this is because in supersonic ideally expanded flows, wavepackets propagate downstream with supersonic phase velocities. As a result, noise in the form of Mach wave radiation is generated efficiently (Tam 1995) in the downstream direction. On the other hand, in shock-containing flows, the presence of shock cells generates an additional component which travels upstream. The effect of jittering, on both upstream- and downstream-travelling components, is discussed in more detail in § 4.

Using a single shock-cell waveguide mode, both wavepacket models show reasonable agreement with the peak of the measured spectrum. However, they suffer from the same issue discussed by Ray & Lele (2007) where the high-frequency sound at upstream angles is ‘missing’. In their study, for a  $M_j = 1.22$  isothermal jet, the frequency range of interest was restricted to  $St < 1$  due to the assumed breakdown of linear theory at high frequencies. More recently, however, it has been shown by Sasaki *et al.* (2017a) that linear theory still yields good agreement for frequencies up to  $St = 4$ . Therefore, we argue here that the drop off in high frequency is not due to the breakdown of linear theory but rather neglecting to include higher-order shock-cell modes. This is further supported by Suzuki’s wavepacket model where a similar underestimation of high-frequency SPL was observed when using an empirical representation of the shock cells. The effect of including higher-order modes is discussed in § 5.

## 4. Interpretation of sound-radiation characteristics

### 4.1. Fourier transform into wavenumber space

In order to explore how coherence affects the source structure and sound-radiation characteristics, the CSD of the models with and without coherence decay are transformed to wavenumber space. This transformation is achieved with the double Fourier transform,

$$\mathcal{F}(k_{y_1}, k_{y_2}) = \frac{1}{(\sqrt{2\pi})^2} \int_{-\infty}^{\infty} \int_{-\infty}^{\infty} F(y_1, y_2) e^{ik_{y_1}y_1} e^{ik_{y_2}y_2} dy_1 dy_2, \quad (4.1)$$

where  $F(y_1, y_2)$  is the two-point expression of the CSD. If we take coherence as unity for the entire domain by inserting (2.12) into (4.1), the Fourier transform for the perfectly coherent model for a single shock-cell mode is

$$\begin{aligned} \mathcal{F}(k_{y_1}, k_{y_2}) = & \frac{1}{(\sqrt{2\pi})^2} \int_{-\infty}^{\infty} \int_{-\infty}^{\infty} A_{n=1}^2(\omega) e^{-(y_1/L)^2} e^{-(y_2/L)^2} \{e^{ik_s y_1} + e^{-ik_s y_1}\} \\ & \times \{e^{ik_s y_2} + e^{-ik_s y_2}\} \{e^{ik_h(y_1 - y_2)}\} e^{ik_{y_1}y_1} e^{ik_{y_2}y_2} dy_1 dy_2. \end{aligned} \quad (4.2)$$

Evaluating the above integral gives

$$\begin{aligned} \mathcal{F}(k_{y_1}, k_{y_2}) = & \frac{A_{n=1}^2(\omega)}{8} (e^{-(1/4)(k_h - k_s + k_{y_1})^2 L^2} + e^{-(1/4)(k_h + k_s + k_{y_1})^2 L^2}) \\ & \times (e^{-(1/4)(k_h + k_s - k_{y_2})^2 L^2} + e^{-(1/4)(-k_h + k_s + k_{y_2})^2 L^2}) L^2, \end{aligned} \quad (4.3)$$

which is the wavenumber spectrum of the perfectly coherent source CSD. Likewise, by inserting (2.15) into (4.1) and evaluating the resulting integral, the Fourier-transformed

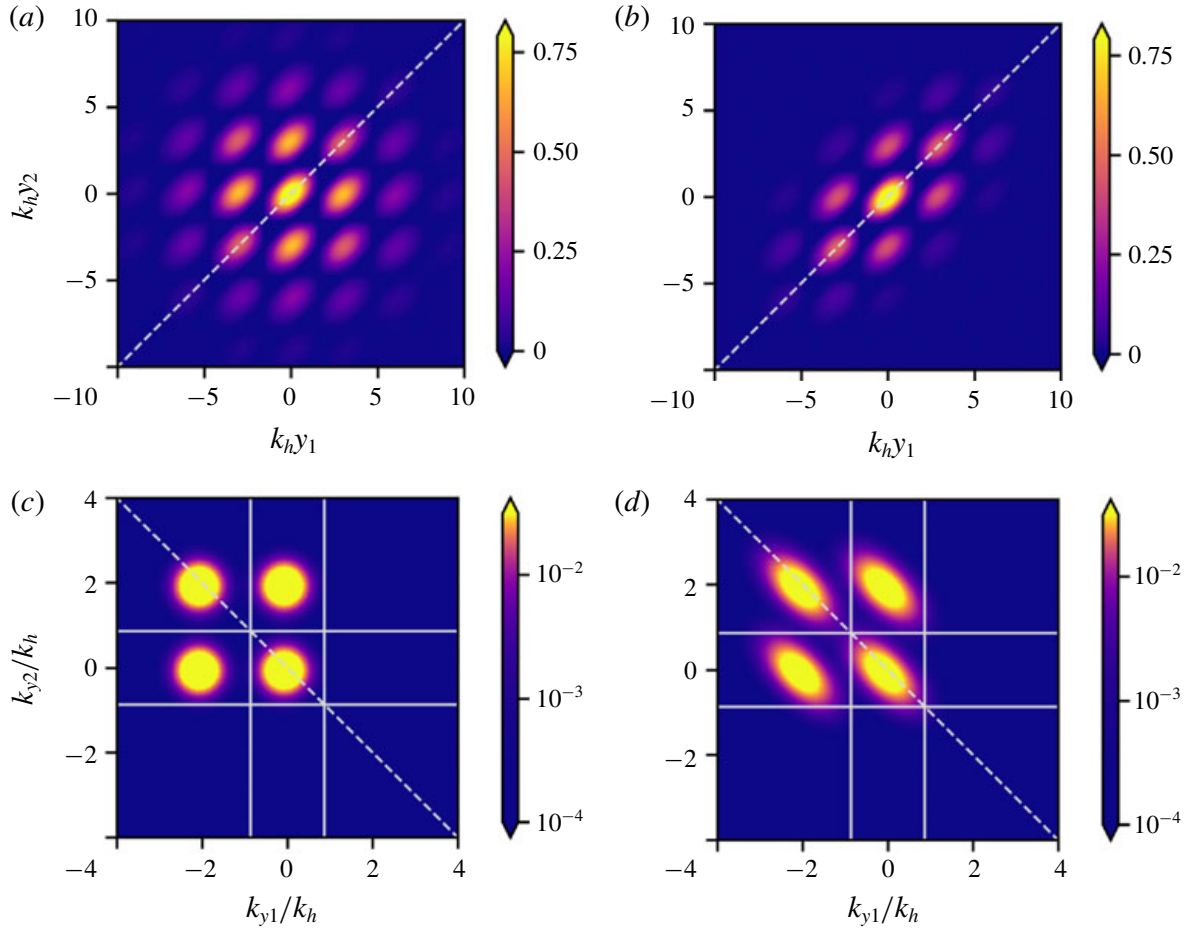


FIGURE 4. (Colour online) The real part of the CSD of the unit coherence (a) and with statistical decay (b) models for  $L_c = 1.0D$ . The diagonal line represents  $y_1 = y_2$ . The corresponding Fourier-transformed CSD in wavenumber space with the unit-coherence (c) and statistical decay (d) models. Diagonal line corresponds to  $k_{y1} = -k_{y2}$ . The square represents the acoustic matching criterion  $|k|/k_h = 0.6M_j$ . The amplitudes of both models have been normalised to highlight the effect of coherence decay. The wavepacket frequency is  $St = 0.4$  for a jet operating at  $\beta = 1.04$ .

CSD of the coherence decay model can also be obtained (the solution is presented in appendix B). Equation (4.3) is obtained from (B 1) by taking the limit  $L_c \rightarrow \infty$ .

Both source CSD models in physical space are shown in figure 4(a,b). In this model problem, the jet nozzle is not present and the sources are simply centred at the origin and extended in both positive and negative directions along the jet axis. The peaks in the contour map are similar to the freckled appearance seen in the two-point pressure correlations obtained by Suzuki (2016). As noted by Suzuki, the spacing between the peaks on the diagonal approximately correspond to the shock-cell spacings. The off-diagonal peaks correspond to the wavepacket interacting with adjacent shock cells. The introduction of coherence decay concentrates the sources in space; along the axis  $y_1 = y_2$ . This behaviour is also seen in the non-shock-containing case, as found by Cavalieri & Agarwal (2014).

A comparison of the models' Fourier-transformed CSDs as given by (4.3) and (B 1) is shown in figure 4(c,d) respectively. The contour scale is logarithmic and both axes are normalised by the hydrodynamic wavenumber of the wavepacket  $k_h$ . The source term in both cases produces four distinct lobes. The existence and ramifications of

these are discussed in detail in § 4.2. The introduction of coherence decay stretches the lobes parallel to the  $k_{y1} = -k_{y2}$  axis. This is consistent with what has been observed in subsonic jets (Cavalieri & Agarwal 2014; Jaunet *et al.* 2017).

As noted by Crighton (1975), only certain spectral components of the source term corresponding to supersonic phase speeds can contribute to far-field noise. In order to isolate only the radiating wavenumbers of the source term, the following conditions need to be met

$$\frac{|k_{y1}|}{k_h} \leq M_c \quad (4.4a)$$

$$\frac{|k_{y2}|}{k_h} \leq M_c, \quad (4.4b)$$

where  $M_c = \omega/(k_h c_0)$  is the convective Mach number. These conditions in wavenumber space are represented by the squares in figure 4(c,d). Source energy that lies outside the square does not contribute to the far-field sound. Unlike the subsonic jet case, where the unit-coherence source lies completely outside the radiation square, the supersonic shock-containing case already has a source lobe satisfying the radiation criterion. This is similar to what is observed in ideally expanded supersonic jets (Cavalieri & Agarwal 2014; Sinha *et al.* 2014). The other three lobes are silent as they lie outside the radiation square.

When coherence decay is introduced we see that the stretching of the radiation lobe actually removes a small portion of the source energy from the radiating region. Unlike the subsonic case, where jittering of the wavepacket causes the source energy to be stretched into the radiation square, coherence decay removes energy in the BBSAN case. This explains why the introduction of coherence decay decreases the peak SPL compared to the unit-coherence case as seen in figure 2.

The Fourier transform contour plots can also be used to explain the directivity behaviour observed in figure 2. For a given value of  $\theta$ , the Fourier-transformed wavenumbers  $k_{y1}$  and  $k_{y2}$  are given by

$$\left( \frac{k_{y1}}{k_h}, \frac{k_{y2}}{k_h} \right) = (-M_c \cos \theta, M_c \cos \theta). \quad (4.5)$$

Therefore, for  $\theta$  values corresponding to the perpendicular direction, the relevant part of the Fourier transform is close to the origin. Moving away from the origin along this axis will correspond to angles upstream and downstream of the jet axis respectively. Hence, the stretching of the source lobe along the  $k_{y1} = -k_{y2}$  axis also broadens the directivity of the jet as depicted in figure 2. This broadening is due to the source energy being stretched in both directions from the origin within the radiation square. To summarise, coherence decay is not a sound amplifier as found in the subsonic case but rather broadens the directivity of BBSAN. This broadening will be seen to be even more important when we consider higher-order shock-cell modes in § 5.

#### 4.2. Nonlinear interaction terms

By transforming the CSD from physical space to wavenumber space, it has been demonstrated that not all wavelengths of the line-source model are responsible for sound generation. The source lobes seen in wavenumber space are due to the

nonlinear interactions present in this BBSAN model. As previously mentioned, only source components corresponding to supersonic phase speeds relative to the ambient speed of sound can be effective BBSAN noise generators. In order to test whether the acoustically matched source component is supersonic, we aim to identify the phase speeds of the four source lobes in wavenumber space.

Recall that the kinematic model comprises the multiplicative combination of the wavepacket and the shock-cell structure as described in (2.4). Using the unit-coherence case for simplicity, after expanding the shock-cell components, the source term in (2.12) can be written as

$$S(y_1, \omega)S^*(y_2, \omega) = \sum_n \{e^{ik_s(y_1+y_2)} + e^{ik_s(y_1-y_2)} + e^{ik_s(-y_1+y_2)} + e^{ik_s(-y_1-y_2)}\} \{e^{ik_h(y_1-y_2)}\}, \quad (4.6)$$

where we have ignored the amplitude and wavepacket envelope terms for this analysis. Expanding again we obtain four terms defined as

$$S(y_1, \omega)S^*(y_2, \omega) = A_{1,2}^+ + A_{1,2}^- + B_{1,2}^+ + B_{1,2}^-, \quad (4.7)$$

where the terms are shown to be

$$A_{1,2}^+ = e^{i(y_1-y_2)(k_h+k_s)}, \quad (4.8a)$$

$$A_{1,2}^- = e^{i(y_1-y_2)(k_h-k_s)}, \quad (4.8b)$$

$$B_{1,2}^+ = e^{iy_1(k_s+k_h)+iy_2(k_s-k_h)}, \quad (4.8c)$$

$$B_{1,2}^- = e^{iy_1(-k_s+k_h)+iy_2(-k_s-k_h)}. \quad (4.8d)$$

By grouping the terms in this manner, we see that the  $A_{1,2}^+$  and  $A_{1,2}^-$  terms, which are respectively the sum and difference nonlinear wave interactions, have phase velocities

$$v^+ = \frac{\omega}{k_h + k_s}, \quad (4.9a)$$

$$v^- = \frac{\omega}{k_h - k_s}. \quad (4.9b)$$

Since  $\omega/(k_h) > \omega/(k_h + k_s)$ , the  $A_{1,2}^+$  component travels slower than the ambient speed of sound and is not acoustically matched. It corresponds to the top left lobe in figure 4(c,d) along the diagonal. Conversely, the term  $A_{1,2}^-$  is capable of either subsonic or supersonic phase speeds and is represented by the bottom right lobe in figure 4(c,d). This explains why only the  $A_{1,2}^-$  component of the total source term is capable of generating far-field noise and is consistent with previous findings (Tam & Tanna 1982).

The terms  $B_{1,2}^+$  and  $B_{1,2}^-$ , on the other hand, involve combined effects of the sum and difference interaction and are a complex conjugate pair. These terms, however, lie off the  $k_{y1} = -k_{y2}$  axis and outside the radiation square and therefore do not contribute to the far-field sound. A similar depiction of these off-diagonal lobes are observed in the Fourier-transformed CSD maps of Baqui *et al.* (2015) and nonlinear wavenumber interactions in low Reynolds number subsonic jets as discussed by Sandham, Morfey & Hu (2006).



## 5. Coherence decay and higher-order shock-cell modes

We now focus on the more general model where higher-order shock-cell modes are included. It has been demonstrated that these additional shock-cell modes do make significant contributions to high frequency sound in the upstream directions (Tam *et al.* 1985; Ray & Lele 2007). We here test the effect of coherence decay when these higher-order shock-cell modes are included.

Tam *et al.* (1985) have argued that it should only be necessary to include the first four shock-cell modes and any higher modes are unnecessary to describe the shock-cell structure. Ray & Lele (2007), on the other hand, justified the use of only the fundamental shock-cell mode as source activity associated with higher-order modes lie outside the range of radiating wavenumbers. This is true when coherence decay is not accounted for.

The sensitivity of the acoustic spectrum to the addition of higher-order shock-cell modes was investigated for the current source model. It was found that the far-field spectrum and source structure did not change significantly beyond the first ten modes. Hence only the first ten shock-cell modes, as defined by (2.6), were used for this study.

By including higher-order modes, as shown by figure 5, an improvement in spectral shape is observed for all observation angles. Higher waveguide modes are required to describe the acoustic spectra for frequencies greater than the broadband peak, consistent with Tam *et al.* (1985). While there are still discrepancies for the downstream angle at  $\theta = 60^\circ$ , both models predict the peak frequency with reasonable accuracy, although the case with coherence decay slightly underpredicts the peak frequency compared to the data. The spectral peak shape predicted when coherence decay is included is more accurate than the case with perfect coherence. For the perfectly coherent wavepacket, oscillations start to occur at higher Strouhal numbers resulting in ‘narrow-banded’ secondary peaks. This deficiency of the perfectly coherent model at higher frequencies for upstream angles agrees with Ray & Lele (2007) where it was found that the linear model (unit coherence by construction) becomes ‘increasingly suspect at higher frequencies’.

Conversely, the two-point model with coherence decay ‘smooths’ out these narrow-banded peaks. This observation is consistent with Ray & Lele’s (2007) assertion that nonlinear effects can rectify these artificial peaks introduced from the instability wave interacting with the higher-order shock-cell modes. This finding is also consistent with the effect of coherence decay when using localised acoustic sources (Lele 2005). We turn to the Fourier-transformed CSD maps to gain an insight into this behaviour.

The Fourier-transformed CSD maps are computed for two frequencies,  $St = 0.4$  (figure 6a,b) and  $St = 0.6$  (figure 6c,d) where we have now included the first ten shock-cell waveguide modes. Compared to the previous single-mode ( $n = 1$ ) case, additional lobes are now visible throughout the wavenumber domain. The additional source-energy lobes are due to the wavepackets interacting with the higher-order Fourier shock-cell modes.

For the unit-coherence case (figure 6a,c), the far-field sound radiation is still dominated by the wavepacket interaction with the  $n = 1$  waveguide mode. For  $St = 0.4$ , interaction with the second mode does not contribute to the far-field radiation as the source energy from this interaction lies outside the radiation square. This is what was observed by Ray & Lele (2007) and it was the reason modes higher than the fundamental were not considered in their study. At a higher frequency ( $St = 0.6$ ), however, the Fourier lobes become more compact and the  $n = 2$  modes migrate into the radiation square as seen in figure 6(c). This is consistent with the behaviour

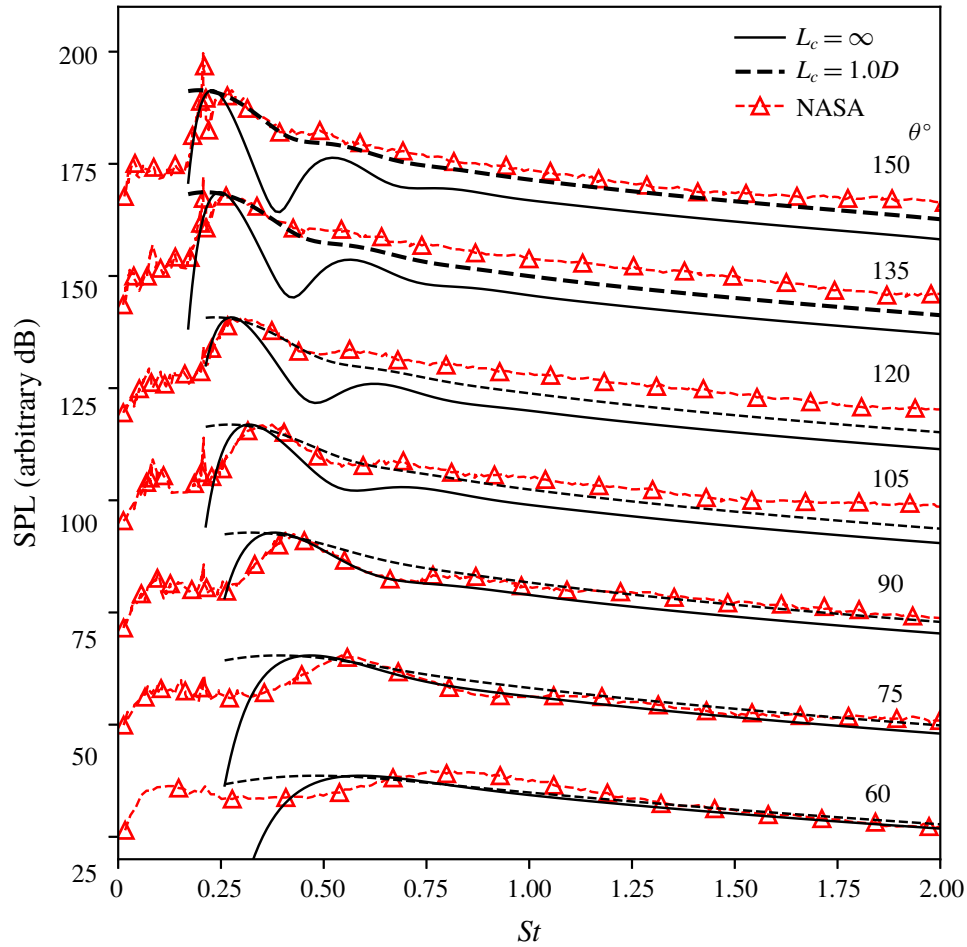


FIGURE 5. (Colour online) Power spectrum at a distance of  $100D$  through a range of observation angles between  $\theta = 60^\circ$  and  $\theta = 150^\circ$  measured from the downstream jet axis for a wavepacket with  $k_h L = 5$  for multiple shock-cell waveguide modes. Each measurement angle is offset by 25 dB. NASA experimental data from Norum & Seiner (1982).

seen in the far-field acoustic spectrum of figures 3 and 5. For frequencies below the broadband peak, we do not see an increase in SPL when higher-order shock modes are added.

For the model where coherence decay is taken into account (figure 6*b,d*), we observe once again a stretching of the source lobes parallel to the  $k_{y1} = -k_{y2}$  line. The stretching causes the fundamental ( $n = 1$ ) mode to merge with the second mode and spreads the source energy within the radiating square. In contrast to the unit-coherence case, the  $n = 2$  shock-cell mode is now also responsible for far-field sound production. This means that coherence decay, which accounts for stochastic effects, can rectify the ‘missing sound’ at higher frequencies in the upstream direction seen in figure 3. It is clear, when compared to the perfectly coherent wavepacket, coherence decay ‘spreads and smooths’ the source energy in wavenumber space. This leads to a more uniform far-field spectrum for all observation angles and, indeed, a smoother directivity also results. This levelling effect in both directivity and frequency is evident when comparing the SPL contour plots in figure 1(*a,b*). Nevertheless, the overprediction in SPL for frequencies below the spectral peak is still present for all observation angles. The overprediction at low frequencies is most likely a result of the *ad hoc* constant coherence length assumption.

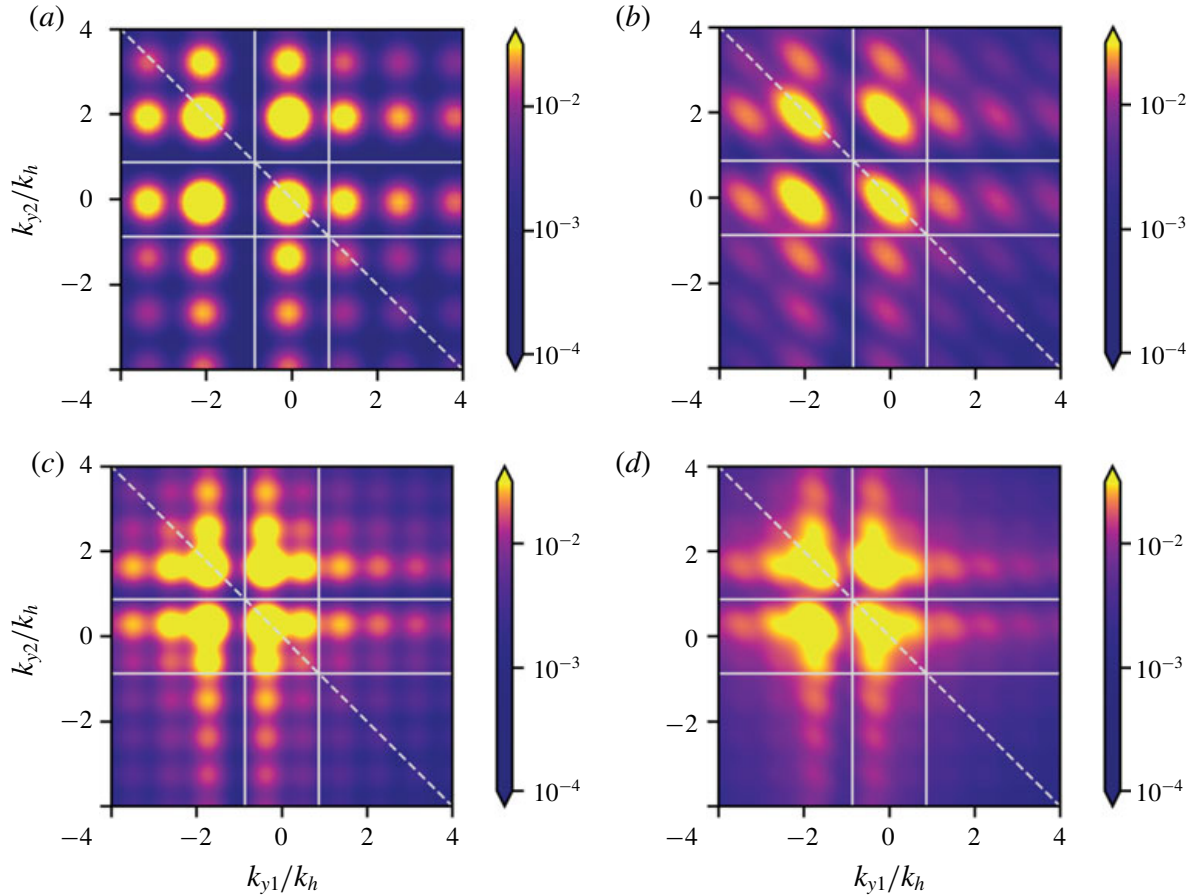


FIGURE 6. (Colour online) The corresponding Fourier-transformed CSD in wavenumber space for  $St = 0.4$  and  $St = 0.6$ . (a,c) Correspond to the unit-coherence model while (b,d) are for the two-point model with a coherence-decay length  $L_c = 1.0D$ . Diagonal line corresponds to  $k_{y1} = -k_{y2}$ . The square represents the acoustic matching criterion  $|k|/k_h = 0.6M_j$ . The amplitude of both models has been normalised to highlight the effect of coherence decay. The jet is operating at  $\beta = 1.04$ .

Suzuki (2016) has also incorporated the effect of coherence decay of wavepackets into his model. However, the empirical treatment of the shock cells as Gaussian humps does not allow the previously discussed effects of coherence decay to be observed. Similar to Ray & Lele (2007), the loss of high-frequency sound can be attributed to the lack of representation of the higher-order shock-cell modes. The predictions from both Suzuki's and Ray & Lele's models are closer to those of figure 3 and hence lack the same agreement to experimental data as other phased-array models such as Harper-Bourne & Fisher (1973) and Morris & Miller (2010).

To show the impact of coherence decay on noise directivity more clearly, the Fourier-transformed points along the  $k_{y1} = -k_{y2}$  line are extracted and shown as dashed lines in figure 7(a,b). Vertical lines corresponding to different radiation directions as specified by (4.5) are also shown for reference. For frequencies slightly greater than the BBSAN peak ( $St = 0.4$ ), coherence decay amplifies the radiated sound in the upstream direction and smooths out the artificial peaks seen in the perfectly coherent case. On the other hand, for higher frequencies ( $St = 0.6$ ), the second shock-cell mode is now also contributing to the far-field sound and the effect of coherence decay is minimal. Comparing this to linear instability model results from Ray & Lele (2007), the impact of coherence decay on higher frequencies is now apparent.



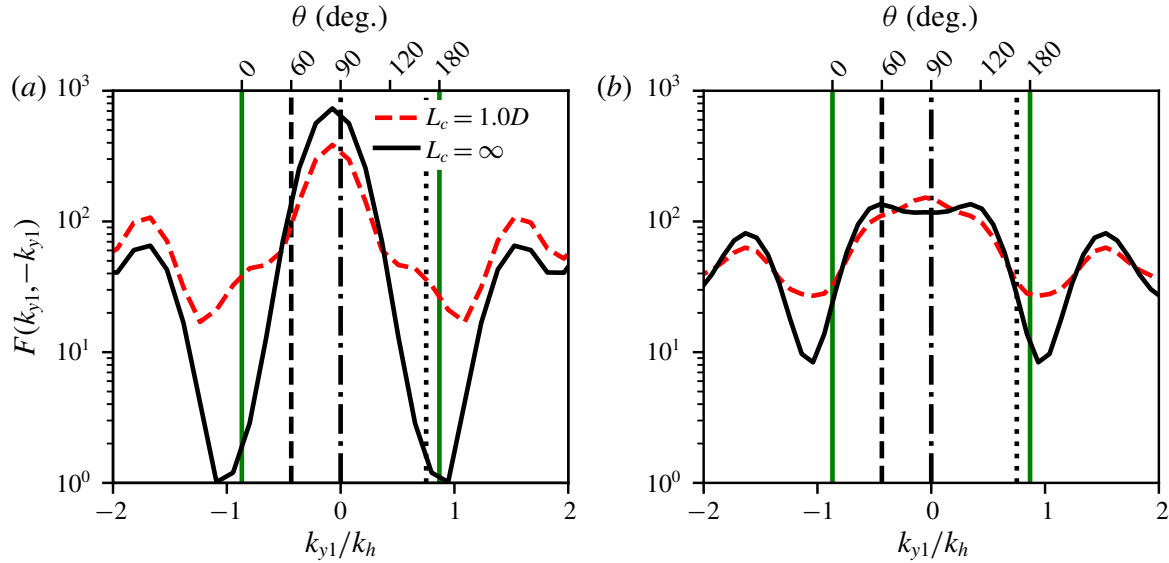


FIGURE 7. (Colour online) Fourier transform of CSD for (a)  $St = 0.4$  and (b)  $St = 0.6$  extracted along the line  $k_{y1} = -k_{y2}$ . The vertical lines represent different observation angles; dashed line =  $60^\circ$ , dash-dotted line =  $90^\circ$  and dotted line =  $150^\circ$ . Solid (green) vertical lines represent the acoustic matching criterion.

Due to the *ad hoc* nature of fixing the modelling parameters to constant values, it is important to establish that changing the combinations and values does not lead to different conclusions. This is done in appendix A. We find, amongst other effects, that the suppression of the narrow-banded peaks cannot be accounted for by the tuning of  $u_c$ ,  $A(\omega)$  and  $L$  within values realistic for supersonic underexpanded jets. We conclude that the inclusion of coherence decay, in the wavepacket framework, is thus imperative. In order to improve predictions at higher frequencies for BBSAN, not only do we need high-order shock modes but also the stochastic forcing term, which in the kinematic model is represented by coherence decay.

The importance of coherence in BBSAN source modelling has been well recognised since Harper-Bourne & Fisher's original model. Using the present BBSAN wavepacket model, however, we suggest that the overall two-point coherence contains much non-acoustically efficient information and that only the coherence decay of the low-order azimuthal modes (wavepackets) is critical in predicting far-field sound. This further suggests a mechanistic explanation for coherence decay in these systems: the coherence decay across sound sources of existing BBSAN models results from the jittering of wavepackets (Williams & Kempton 1978; Cavalieri *et al.* 2011).

## 6. Conclusions and perspectives

Motivated by the pioneering work of Tam (1987), the BBSAN models proposed by Ray & Lele (2007) and Suzuki (2016) indicate the suitability of using wavepackets for this component of jet noise. While successful in predicting many of the known features, the simplified models could not accurately capture the high-frequency sound produced at upstream angles. This is in contrast to the largely accurate predictions made by wavepacket models for supersonic ideally expanded flows (Sinha *et al.* 2014). Wavepacket modelling of subsonic jets suggest that coherence decay of the large-scale structures is critical in those flows. Previous BBSAN models (Harper-Bourne & Fisher 1973; Morris & Miller 2010) have demonstrated the importance of two-point

coherence (or correlation), but only considered it in the context of bulk-turbulent statistics. By constructing a two-point wavepacket model, using the same methodology as Cavalieri & Agarwal (2014), we test the impact of wavepacket coherence decay in shock-containing flows.

The semi-empirical kinematic model presented here provides physical insights into the underlying flow physics: the demonstration that wavepacket jitter is central to the sound generation process in shock-containing flows. The model allows us to test the hypothesis of the suitability in using low-order azimuthal structures with coherence decay to predict BBSAN.

By transforming the single-point model of Lele (2005) into a two-point framework, we show that coherence decay may be crucial in predicting higher-frequency noise in the upstream direction. Unlike in subsonic jets, the inclusion of coherence decay for BBSAN decreases the acoustic efficiency of wavepackets at peak frequency, but spreads source energy over a greater directivity range.

More significantly, however, is the finding that wavepacket jitter is vital for predicting frequencies above the peak. By capturing this jitter as coherence decay, clear improvements in prediction accuracy are made, especially in the upstream and sideline directions where BBSAN dominates. As exemplified in the results of § 5, coherence decay enables sound generation from higher-order shock-cell modes by stretching the source energy into the radiating square.

In addition to offering insight into the physical mechanisms of shock noise, these results also suggest directions for future modelling efforts. The combined effect of coherence decay and higher-order shock-cell modes need to be incorporated into a dynamic modelling approach that obtains wavepackets and shock-cell modes from linear stability calculations. We show that such calculations would need to be forced stochastically, to produce jittering solutions with coherence decay, and they would be required to include multiple shock-cell modes. The findings from this study are expected to help guide both future kinematic and dynamic wavepacket models of BBSAN.

## Acknowledgements

This work was supported by the Australian Government via a Research Training Program (RTP) Scholarship and the Australian Research Council through the Discovery Projects scheme. The authors would also like to thank Ms R. Kirby for her diligent checking of the mathematical formulation.

## Appendix A. Parametric study of model parameters

In this appendix we present results from a short parametric study on the impact of the different model parameters as listed in § 3.1. In order to evaluate each of its effects on the far-field acoustic spectrum, we adjust each parameter individually. When not varied, each parameter is kept constant with the values used equivalent to those stated in § 3.1 and summarised in table 1. The value of  $C_1$  from (3.1) was kept constant as this would only affect the overall amplitude of the noise generated. We show in figure 8 the results for an observation angle  $\theta = 150^\circ$ .

As expected, we notice that varying the values of each modelling parameter changes the shape of the acoustic spectrum produced. Increasing the convection velocity  $u_c$  shifts the peak frequency to higher Strouhal values as shown in figure 8(a). The rapid drop-off at high Strouhal values from increasing  $C_2$  in figure 8(b) corresponds to the

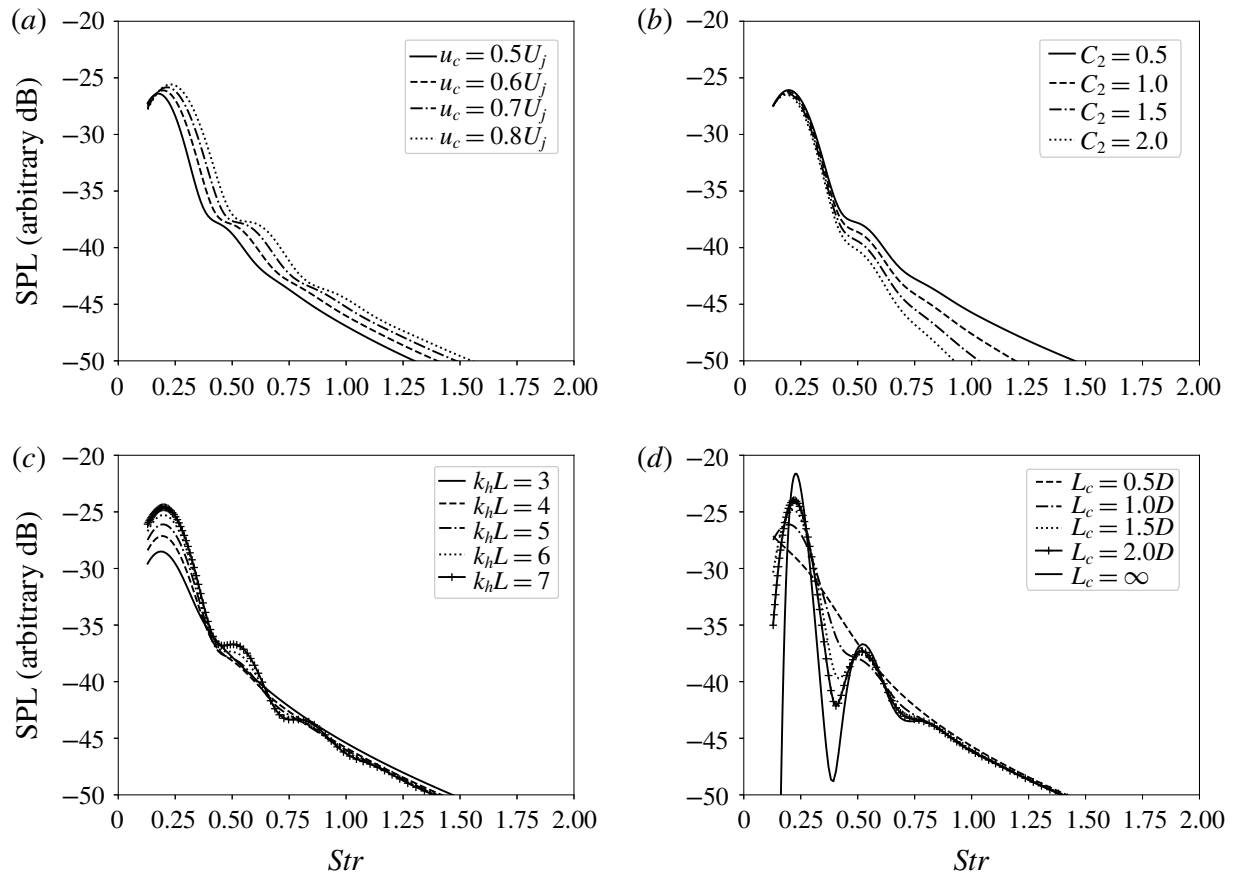


FIGURE 8. Effect of modelling variables on the acoustic power spectrum when (a) changing convection velocity  $u_c$ , (b) changing amplitude width  $C_2$ , (c) changing wavepacket envelope length scale  $L$ , (d) changing coherence-decay length scale  $L_c$  for an observation angle of  $\theta = 150^\circ$  at a distance of  $100D$ . The modelled jet is operating at a nozzle pressure ratio of  $NPR = 3.4$ .

Parameter	Value
$NPR$	3.4
$u_c$	$0.6U_j$
$C_2$	0.58
$k_h L$	5.0
$L_c$	$1.0D$

TABLE 1. Constant values for each parameter used in proposed model.

growing exponential decay as  $C_2$  increases. While it can be seen that  $u_c$  and  $C_2$  do alter the far-field sound spectrum, their effects on the harmonic peaks remain minimal.

We note, however, the two length scales characterising the wavepacket do have a more significant effect on the higher-order peaks. From figure 8(c,d), neither  $L$  nor  $L_c$  alters the peak frequency predicted. We note that for a large spatial wavepacket envelope ( $L$ ) the peak sound amplitude increases but the artificial peaks become more apparent. As we decrease the value of  $L$ , the peaks are suppressed; similar to the impact we see with using a finite value of  $L_c$  in figure 8(d).

To further investigate the relationship between  $L$  and  $L_c$  and their effect with respect to directivity, a set of sound pressure contours is presented in figure 9. The

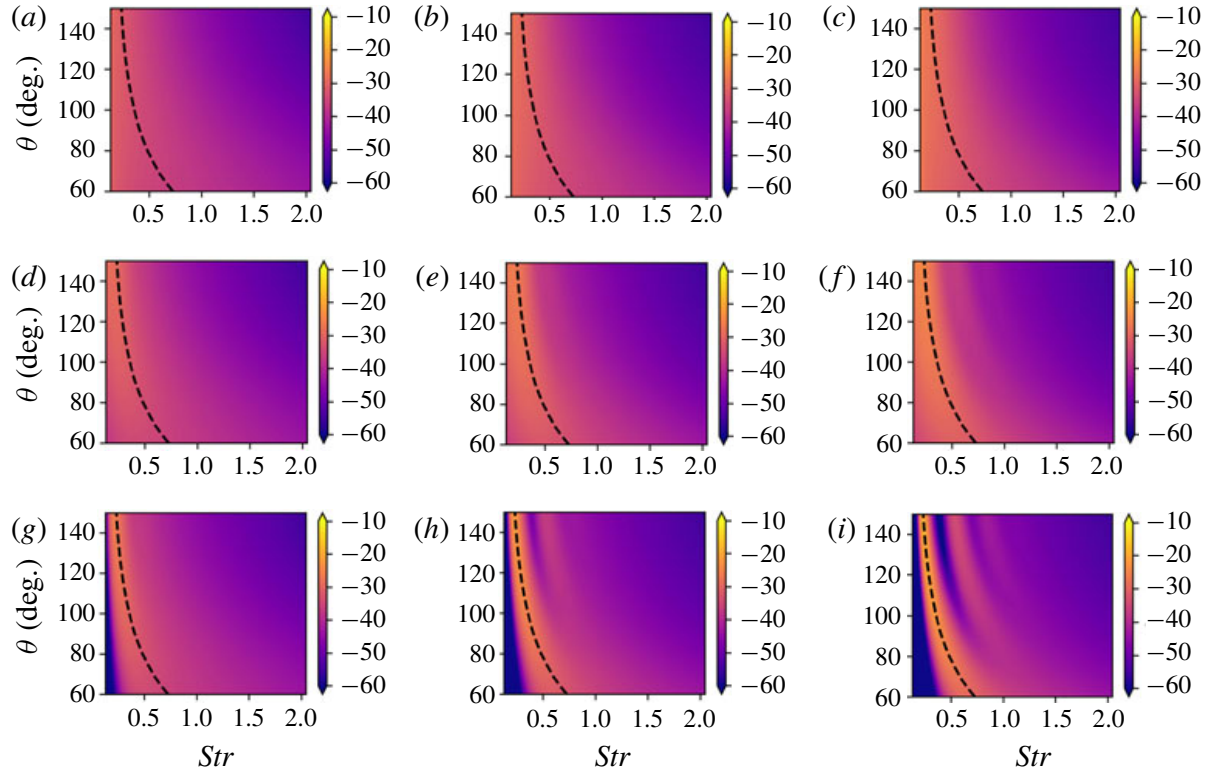


FIGURE 9. (Colour online) Contours of sound pressure level (arbitrary dB) as a function of frequency ( $Str$ ) and directivity ( $\theta$ ) for a range of  $L_c$  and  $L$ . Each row corresponds to the two-point model with constant value of  $L_c$ ; (a–c)  $L_c = 0.5D$ , (d–f)  $L_c = 1.0D$ , (g–i)  $L_c = \infty$ . Each column corresponds to the two-point model with constant value of  $k_h L$ ;  $k_h L = 3.0$  (a,d,g),  $k_h L = 5.0$  (b,e,h) and  $k_h L = 7.0$  (c,f,i). The modelled jet is operating at a nozzle pressure ratio of  $NPR = 3.4$ .

dependency of peak frequency on directivity is lost for small values of  $L$  and  $L_c$ . Increasing  $L$  seems to make the BBSAN peak more prominent for all directivity angles and is consistent with previous findings on the effect of spatial modulation of wavepackets (Cavalieri *et al.* 2011, 2012). The non-compact nature of wavepackets explains, for example, the axisymmetric superdirective radiation of low Mach number turbulent jets (Laufer 1983). In supersonic flows, this can be seen in the directivity dependence of the peak sound-emission frequency.

As found by Cavalieri *et al.* (2012), for superdirectivity to occur, the wavepacket source must not be compact; the condition of  $k_h L \gg 1$  must be met. For BBSAN, the peak frequency also exhibits a directivity dependence (Harper-Bourne & Fisher 1973). Hence, even though by decreasing the value of  $L$  we get the same effect as including coherence decay, we find that the values which would be found in supersonic shock-containing jets will not be small. Using two-point correlations of near-field pressure from LES data, Suzuki (2016) also found that the axial extent of wavepackets extended over several jet diameters.

While narrow wavepacket spatial envelopes have been shown in figure 8(c) to suppress the higher-order peaks, the loss of peak frequency directivity (figure 9) and results from previous studies demonstrate that these small, narrow wavepacket envelopes are not plausible. In shock-containing flows, wavepackets are non-compact. Instead, as discussed in § 5, we propose that coherence decay is responsible for smoothing out these higher-order peaks.

## Appendix B. Fourier transform of two-point CSD

We present below the result from carrying out the double Fourier transform of equation (2.15):

$$\begin{aligned} \mathcal{F}(k_{y_1}, k_{y_2}) = & \frac{1}{8\sqrt{\frac{1}{L^2} + \frac{1}{L_c^2}} \sqrt{\frac{2L^2 + L_c^2}{L^4 + L^2L_c^2}}} \\ & \times \left( e^{-L^2(k_z^2L^2 + 2k_h^2L_c^2 - 2k_hk_zL_c^2 + k_z^2L_c^2 + k_y^2(L^2 + L_c^2) + 2k_s^2(2L^2 + L_c^2) - 2k_s(k_y + k_z)(2L^2 + L_c^2) + 2k_y(k_zL^2 + k_hL_c^2))/4(2L^2 + L_c^2)} \right. \\ & + e^{-L^2(k_z^2L^2 + 2k_h^2L_c^2 - 2k_hk_zL_c^2 + k_z^2L_c^2 + k_y^2(L^2 + L_c^2) + 2k_s^2(2L^2 + L_c^2) + 2k_s(k_y + k_z)(2L^2 + L_c^2) + 2k_y(k_zL^2 + k_hL_c^2))/4(2L^2 + L_c^2)} \\ & + e^{-L^2(2(k_h - k_s)^2L_c^2 + 2(-k_h + k_s)k_zL_c^2 + k_y^2(L^2 + L_c^2) + k_z^2(L^2 + L_c^2) + 2k_y(k_zL^2 + (k_h - k_s)L_c^2))/4(2L^2 + L_c^2)} \\ & \left. + e^{-L^2(2(k_h + k_s)^2L_c^2 - 2(k_h + k_s)k_zL_c^2 + k_y^2(L^2 + L_c^2) + k_z^2(L^2 + L_c^2) + 2k_y(k_zL^2 + (k_h + k_s)L_c^2))/4(2L^2 + L_c^2)} \right). \end{aligned} \quad (\text{B } 1)$$

## REFERENCES

- ANTONIALI, L. A., CAVALIERI, A. V., SCHMIDT, O. T., COLONIUS, T., JORDAN, P., TOWNE, A., BRÉS, G. & AGARWAL, A. 2018 Amplitude scaling of turbulent-jet wavepackets. In *2018 AIAA/CEAS Aeroacoustics Conference*, p. 2978. AIAA.
- BAQUI, Y. B., AGARWAL, A., CAVALIERI, A. V. G. & SINAYOKO, S. 2013 Nonlinear and linear noise source mechanisms in subsonic jets. In *19th AIAA/CEAS Aeroacoustics Conference*, p. 2087. AIAA.
- BAQUI, Y. B., AGARWAL, A., CAVALIERI, A. V. G. & SINAYOKO, S. 2015 A coherence-matched linear source mechanism for subsonic jet noise. *J. Fluid Mech.* **776**, 235–267.
- BREAKEY, D. E., JORDAN, P., CAVALIERI, A. V. G. & LÉON, O. 2013 Near-field wavepackets and the far-field sound of a subsonic jet. In *19th AIAA/CEAS Aeroacoustics Conference*, p. 2083. AIAA.
- BRÉS, G. A., HAM, F. E., NICHOLS, J. W. & LELE, S. K. 2017 Unstructured large-eddy simulations of supersonic jets. *AIAA J.* **55** (4), 1164–1184.
- BRIDGES, J. & WERNET, M. P. 2008 Turbulence associated with broadband shock noise in hot jets. In *14th AIAA/CEAS Aeroacoustics Conference*, p. 2834. AIAA.
- CAVALIERI, A. V. G. & AGARWAL, A. 2014 Coherence decay and its impact on sound radiation by wavepackets. *J. Fluid Mech.* **748**, 399–415.
- CAVALIERI, A. V. G., JORDAN, P., AGARWAL, A. & GERVAIS, Y. 2011 Jittering wave-packet models for subsonic jet noise. *J. Sound Vib.* **330** (18), 4474–4492.
- CAVALIERI, A. V. G., JORDAN, P., COLONIUS, T. & GERVAIS, Y. 2012 Axisymmetric superdirectivity in subsonic jets. *J. Fluid Mech.* **704**, 388–420.
- CAVALIERI, A. V. G., JORDAN, P., WOLF, W. R. & GERVAIS, Y. 2014 Scattering of wavepackets by a flat plate in the vicinity of a turbulent jet. *J. Sound Vib.* **333** (24), 6516–6531.
- CAVALIERI, A. V. G., RODRÍGUEZ, D., JORDAN, P., COLONIUS, T. & GERVAIS, Y. 2013 Wavepackets in the velocity field of turbulent jets. *J. Fluid Mech.* **730**, 559–592.
- CHEUNG, L. C. & LELE, S. K. 2009 Linear and nonlinear processes in two-dimensional mixing layer dynamics and sound radiation. *J. Fluid Mech.* **625**, 321–351.
- CRIGHTON, D. G. 1975 Basic principles of aerodynamic noise generation. *Prog. Aerosp. Sci.* **16** (1), 31–96.
- CROW, S. C. J. & CHAMPAGNE, F. H. 1971 Orderly structure in jet turbulence. *J. Fluid Mech.* **48** (3), 547–591.
- EDGINGTON-MITCHELL, D., OBERLEITHNER, K., HONNERY, D. R. & SORIA, J. 2014 Coherent structure and sound production in the helical mode of a screeching axisymmetric jet. *J. Fluid Mech.* **748**, 822–847.



- FREUND, J. B. 2003 Noise-source turbulence statistics and the noise from a mach 0.9 jet. *Phys. Fluids* **15** (6), 1788–1799.
- GUDMUNDSSON, K. & COLONIUS, T. 2011 Instability wave models for the near-field fluctuations of turbulent jets. *J. Fluid Mech.* **689**, 97–128.
- HARPER-BOURNE, M. 2002 On modelling the near-field noise of the high-speed jet exhausts of combat aircraft. In *8th AIAA/CEAS Aeroacoustics Conference & Exhibit*, p. 2424. AIAA.
- HARPER-BOURNE, M. & FISHER, M. J. 1973 The noise from shock waves in supersonic jets. *AGARD CP* **11**, 1–13.
- HOWE, M. S. 2003 *Theory of Vortex Sound*, vol. 33. Cambridge University Press.
- JAUNET, V., JORDAN, P. & CAVALIERI, A. V. G. 2017 Two-point coherence of wave packets in turbulent jets. *Phys. Rev. Fluids* **2** (2), 024604.
- JORDAN, P. & COLONIUS, T. 2013 Wave packets and turbulent jet noise. *Annu. Rev. Fluid Mech.* **45**, 173–195.
- JORDAN, P., COLONIUS, T., BRES, G. A., ZHANG, M., TOWNE, A. & LELE, S. K. 2014 Modeling intermittent wavepackets and their radiated sound in a turbulent jet. In *Proceedings of the Summer Program*, p. 241. Center for Turbulence Research, Stanford University.
- JORDAN, P. & GERVAIS, Y. 2005 Modelling self- and shear-noise mechanisms in inhomogeneous, anisotropic turbulence. *J. Sound Vib.* **279** (3–5), 529–555.
- KALYAN, A. & KARABASOV, S. A. 2017 Broad band shock associated noise predictions in axisymmetric and asymmetric jets using an improved turbulence scale model. *J. Sound Vib.* **394**, 392–417.
- KERHERVÉ, F., FITZPATRICK, J. & JORDAN, P. 2006 The frequency dependence of jet turbulence for noise source modelling. *J. Sound Vib.* **296** (1–2), 209–225.
- KERHERVÉ, F., JORDAN, P., GERVAIS, Y., VALIERE, J. C. & BRAUD, P. 2004 Two-point laser doppler velocimetry measurements in a mach 1.2 cold supersonic jet for statistical aeroacoustic source model. *Exp. Fluids* **37** (3), 419–437.
- LANDAHL, M. T. & MOLLO-CHRISTENSEN, E. 1992 *Turbulence and Random Processes in Fluid Mechanics*. Cambridge University Press.
- LAU, J. C. 1980 Laser velocimeter correlation measurements in subsonic and supersonic jets. *J. Sound Vib.* **70** (1), 85–101.
- LAUFER, J. Y. T. C. 1983 Noise generation by a low-mach-number jet. *J. Fluid Mech.* **134**, 1–31.
- LELE, S. K. 2005 Phased array models of shock-cell noise sources. In *11th AIAA/CEAS Aeroacoustics Conference*, p. 2841. AIAA.
- LÉON, O. & BRAZIER, J. P. 2013 Investigation of the near and far pressure fields of dual-stream jets using an Euler-based PSE model. In *19th AIAA/CEAS Aeroacoustics Conference*, p. 2280. AIAA.
- LIGHTHILL, M. J. 1952 On sound generated aerodynamically. I. General theory. *Proc. R. Soc. Lond. A* **211**, 564–587.
- MAIA, I. A., JORDAN, P., JAUNET, V. & CAVALIERI, A. V. G. 2017 Two-point wavepacket modelling of jet noise. In *23rd AIAA/CEAS Aeroacoustics Conference*, p. 3380. AIAA.
- MICHALKE, A. 1970 A wave model for sound generation in circular jets. *Tech. Rep.*, Deutsche Luft- und Raumfahrt.
- MILLER, S. A. E. & MORRIS, P. J. 2010 The prediction of broadband shock-associated noise from dualstream and rectangular jets using RANS CFD. In *16th AIAA/CEAS Aeroacoustics Conference*, p. 3730. AIAA.
- MOLLO-CHRISTENSEN, E. 1967 Jet noise and shear flow instability seen from an experimenter's viewpoint. *J. Appl. Mech.* **34** (1), 1–7.
- MORRIS, P. J. & MILLER, S. A. E. 2010 Prediction of broadband shock-associated noise using Reynolds-averaged Navier–Stokes computational fluid dynamics. *AIAA J.* **48** (12), 2931–2944.
- MORRIS, P. J. & ZAMAN, K. B. M. Q. 2010 Velocity measurements in jets with application to noise source modeling. *J. Sound Vib.* **329** (4), 394–414.
- NORUM, T. D. & SEINER, J. M. 1982 Measurements of mean static pressure and far field acoustics of shock containing supersonic jets. *Tech. Rep.* TM 84521. NASA.

- PACK, D. C. 1950 A note on Prandtl's formula for the wave-length of a supersonic gas jet. *Q. J. Mech. Appl. Maths* **3** (2), 173–181.
- POKORA, C. D. & MCGUIRK, J. J. 2015 Stereo-PIV measurements of spatio-temporal turbulence correlations in an axisymmetric jet. *J. Fluid Mech.* **778**, 216–252.
- POWELL, A. 1953 On the mechanism of choked jet noise. *Proc. Phys. Soc. B* **66** (12), 1039.
- PRANDTL, L. 1904 *Über die stationären Wellen in einem Gasstrahl*. Hirzel.
- RAY, P. K. & LELE, S. K. 2007 Sound generated by instability wave/shock-cell interaction in supersonic jets. *J. Fluid Mech.* **587**, 173–215.
- SANDHAM, N. D., MORFEY, C. L. & HU, Z. W. 2006 Nonlinear mechanisms of sound generation in a perturbed parallel jet flow. *J. Fluid Mech.* **565**, 1–23.
- SASAKI, K., CAVALIERI, A. V. G., JORDAN, P., SCHMIDT, O. T., COLONIUS, T. & BRÈS, G. A. 2017a High-frequency wavepackets in turbulent jets. *J. Fluid Mech.* **830**, R2.
- SASAKI, K., PIANTANIDA, S., CAVALIERI, A. V. G. & JORDAN, P. 2017b Real-time modelling of wavepackets in turbulent jets. *J. Fluid Mech.* **821**, 458–481.
- SAVARESE, A., JORDAN, P., GIRARD, S., ROYER, A., FOURMENT, C., COLLIN, E., GERVAIS, Y. & PORTA, M. 2013 Experimental study of shock-cell noise in underexpanded supersonic jets. In *19th AIAA/CEAS Aeroacoustics Conference*, p. 2080. AIAA.
- SINHA, A., RODRÍGUEZ, D., BRÈS, G. A. & COLONIUS, T. 2014 Wavepacket models for supersonic jet noise. *J. Fluid Mech.* **742**, 71–95.
- SUZUKI, T. 2013 Coherent noise sources of a subsonic round jet investigated using hydrodynamic and acoustic phased-microphone arrays. *J. Fluid Mech.* **730**, 659–698.
- SUZUKI, T. 2016 Wave-packet representation of shock-cell noise for a single round jet. In *23rd AIAA/CEAS Aeroacoustics Conference*, p. 4047. AIAA.
- SUZUKI, T. & COLONIUS, T. 2006 Instability waves in a subsonic round jet detected using a near-field phased microphone array. *J. Fluid Mech.* **565**, 197–226.
- TAM, C. K. W. 1987 Stochastic model theory of broadband shock associated noise from supersonic jets. *J. Sound Vib.* **116** (2), 265–302.
- TAM, C. K. W. 1990 Broadband shock-associated noise of moderately imperfectly expanded supersonic jets. *J. Sound Vib.* **140** (1), 55–71.
- TAM, C. K. W. 1995 Supersonic jet noise. *Annu. Rev. Fluid Mech.* **27** (1), 17–43.
- TAM, C. K. W., JACKSON, J. A. & SEINER, J. M. 1985 A multiple-scales model of the shock-cell structure of imperfectly expanded supersonic jets. *J. Fluid Mech.* **153**, 123–149.
- TAM, C. K. W., SEINER, J. M. & YU, J. C. 1986 Proposed relationship between broadband shock associated noise and screech tones. *J. Sound Vib.* **110** (2), 309–321.
- TAM, C. K. W. & TANNA, H. K. 1982 Shock associated noise of supersonic jets from convergent-divergent nozzles. *J. Sound Vib.* **81** (3), 337–358.
- TAN, D. J., KALYAN, A., GRYAZEV, V., WONG, M., HONNERY, D., EDGINGTON-MITCHELL, D. M. & KARABASOV, S. A. 2017 On the application of shock-associated noise models to piv measurements of screeching axisymmetric cold jets. In *23rd AIAA/CEAS Aeroacoustics Conference*, p. 3028. AIAA.
- TOWNE, A., COLONIUS, T., JORDAN, P., CAVALIERI, A. V. G. & BRÈS, G. A. 2015 Stochastic and nonlinear forcing of wavepackets in a mach 0.9 jet. In *21st AIAA/CEAS Aeroacoustics Conference*, p. 2217. AIAA.
- TROUTT, T. R. & MCLAUGHLIN, D. K. 1982 Experiments on the flow and acoustic properties of a moderate-Reynolds-number supersonic jet. *J. Fluid Mech.* **116**, 123–156.
- WILLIAMS, J. E. F. & KEMPTON, A. J. 1978 The noise from the large-scale structure of a jet. *J. Fluid Mech.* **84** (4), 673–694.
- ZHANG, M. Q., JORDAN, P., LEHNASCH, G., CAVALIERI, A. V. G. & AGARWAL, A. 2014 Just enough jitter for jet noise? In *20th AIAA/CEAS Aeroacoustics Conference*, p. 3061. AIAA.

## 6.10 Concluding Statement

This paper makes two key novel contributions; providing an explanation for why coherence decay is important in BBSAN models and revealing the physical mechanism by which coherence decay affects the far-field sound. Coherence decay in the wavepacket framework is the statistical representation of wavepacket jitter [125]; postulated to be due to the forcing of wavepackets by turbulence. The inclusion of correlation/coherence decay in previous BBSAN studies is now associated with a specific ‘physical’ mechanism. The effect of coherence decay on the far-field sound is investigated using a simple kinematic model. This investigation demonstrates the importance of both the coherence decay of instability waves and the inclusion of higher-order shock-cell modes in a BBSAN wavepacket source. Unlike in subsonic jets, coherence decay does not amplify the radiated sound but rather broadens the spectral peak. Consequently, its inclusion will suppress and smooth out the artificial narrow-band peaks at higher-frequencies in the upstream direction predicted by unit coherence sources similar to Tam [157]. Thus, these results explain the deficiencies observed in previous stability-type BBSAN models.

The relationship between coherence decay and higher-order shock cell modes is most evident in the Fourier-transformed representations of the source CSD. In wavenumber space, the inclusion of a coherence decay spreads source energy between the lobes generated by successive shock-cell modes, resulting in a change in BBSAN directivity. The results suggest the intuition by Ray and Lele [149] is correct; the loss of high-frequency sound is indeed due to non-linear effects, which manifest as the jittering of wavepackets. The findings from the short parametric study also support this view.

Previously, Tam [157] hypothesised that shock-cell unsteadiness could be responsible for broadening the artificial peaks. The results of this study, however, lead to an alternative explanation of the smoothing of the acoustic spectra. This line-source model suggests that wavepacket jitter, rather than shock-cell unsteadiness alone, may broaden the narrow high-frequency peaks. Presently, the effect of shock-cell unsteadiness is not included as the shock-cells are explicitly assumed to be stationary in time (represented as zero-frequency waves). This point will be further discussed in the subsequent chapters.

As stated in sections 6.1 and 6.4.1, the model is not a predictive tool; many of the source



parameters are unknown for shock-containing supersonic jets, and estimates from subsonic jets are used. Apart from the amplitude term, a single set of parameters was used across the directivity range examined. A detailed study of the model sensitivity to the chosen parameters is discussed in section 6.8. It is important to emphasise here that the line source model only applies to the axisymmetric case. For higher-order azimuthal modes ( $m \neq 0$ ), the radial structure will have a significant role and the exact nature will have an influence on the result of the volume source integral. Hence, the findings presented in this chapter cannot be directly applied to modes other than the axisymmetric case. Such limitations will be addressed in the next chapter where realistic sound source parameters are instead deduced from numerical and experimental flow data.

## Chapter 7

# Wavepacket Model for Broadband Shock-Associated Noise

### 7.1 Introductory Statement

The importance of wavepacket jitter and higher-order shock-cell modes is elucidated in the previous chapter; a successful wavepacket BBSAN model must adequately describe both phenomena. To confirm the conclusions from Chapter 6, a natural extension of the proposed modelling framework is to instead use realistic inputs observed in turbulent jets.

For a more physical representation, some of the simplifications to the source term made in Chapter 6 are removed. The line source approximation is no longer applicable and a volume source is used instead, thus retaining radial source interference effects. All components of the Lighthill stress tensor are computed. The double divergence of the stress tensor is retained but passed onto the Green's function.

To evaluate the efficacy of the proposed wavepacket BBSAN model, an 'inside-out' approach is adopted. Whereas previous BBSAN models inferred source parameters from the sound field, both wavepackets and shock-cell structure, including their amplitudes, are obtained directly from flow data. Wavepackets and coherence information are extracted from an ideally-expanded  $M_j = 1.5$  LES jet, while the shock-cell structure is adjusted using PIV measurements of an underexpanded  $M_j = 1.45$  jet. In this instance, no calibration of the source term is performed.

While full flow information is available from the LES data, the appeal of a reduced-order model should not be ignored. One objective of this study is to link the large-scale structures to the underlying dynamics. The success of the rather simple model in Chapter 6 suggests that a reduced-order description of the turbulence component is adequate; the LES data contains redundant information not important to sound generation. Hence, the wavepackets are also described by solutions to parabolised stability equations (PSE). The use of PSE also allows the generation of BBSAN to be linked to the governing equations. In the hydrodynamic field, good agreement is observed between PSE solutions and those deduced from the LES data as expected from previous calculations in literature [71, 72, 138].

Sound predictions using both LES and PSE wavepacket descriptions of the source are computed for the first three azimuthal modes. The spectra are compared to the acoustic measurements shown in Chapter 5, over a range of observer angles and frequencies. The source structure of the current model is also investigated, and explanations for the observed features are offered.

Initial PSE results and noise predictions were included in a paper for the *25th AIAA/CEAS Aeroacoustics Conference* (Appendix B). This work has been accepted (April 2021) at the *Journal of Fluid Mechanics*.

# Wavepacket Modelling of Broadband Shock-Associated Noise in Supersonic Jets

Marcus H. Wong<sup>1†</sup>, Peter Jordan<sup>2</sup>, Igor A. Maia<sup>2</sup>, André V. G. Cavalieri<sup>3</sup>, Rhiannon Kirby<sup>1</sup>, Thales C. L. Fava<sup>4</sup> and Daniel Edgington-Mitchell<sup>1</sup>

<sup>1</sup>Laboratory for Turbulence Research in Aerospace and Combustion, Department of Mechanical and Aerospace Engineering, Monash University, Melbourne, VIC 3800, Australia

<sup>2</sup>Departement Fluides, Thermique, Combustion, Institut PPRIME, CNRS - Université de Poitiers - ENSMA, 86036 Poitiers, France

<sup>3</sup>Divisão de Engenharia Aeronáutica, Instituto Tecnológico de Aeronáutica, Instituto Tecnológico de Aeronáutica, São José dos Campos, SP, 12228-900, Brazil

<sup>4</sup>KTH Royal Institute of Technology, Linné FLOW Centre, Department of Mechanics, SE-10044, Stockholm, Sweden

(Received xx; revised xx; accepted xx)

We present a two-point model to investigate the underlying source mechanisms for broadband shock-associated noise (BBSAN) in shock-containing supersonic jets. In the model presented, the generation of BBSAN is assumed to arise from the nonlinear interaction between downstream-propagating coherent structures with the quasi-periodic shock cells in the jet plume. The turbulent perturbations are represented as axially-extended wavepackets and the shock cells are modelled as a set of stationary waveguide modes. Unlike previous BBSAN models, the physical parameters describing the hydrodynamic components are not scaled using the acoustic field. Instead, the source characteristics of both the turbulent and shock components are extracted from the hydrodynamic region of large-eddy simulation and particle image velocimetry datasets. Apart from using extracted data, a reduced-order description of the wavepacket structure is obtained using parabolised stability equations. The validity of the model is tested by comparing far-field sound pressure level predictions to azimuthally-decomposed experimental acoustic data from a cold Mach 1.5 underexpanded jet. At polar angles and frequencies where BBSAN dominates, encouraging comparisons of the radiated noise spectra for the first three azimuthal modes, in both frequency and amplitude ( $\pm 2\text{dB/St}$  at peak frequency), reinforce the suitability of using reduced-order wavepacket sources for predicting BBSAN peaks. On the other hand, wavepacket jitter is found to have a critical role in recovering sound amplitude at inter-peak frequencies. The paper presents a quantitative demonstration that the wavepacket-shock interaction, carefully reconstructed by extracting components from data or linearised models, contains the correct essential flow physics that accounts for most features of the far-field BBSAN spectra.

**Key words:** Aeroacoustics; jet noise; instability

---

† Email address for correspondence: marcus.wong@monash.edu

## 1. Introduction

The intense noise radiated by high-bypass turbofan engines to both the community and those on board remains an important issue. At cruise conditions, the jet exit velocity of the bypass flow in many modern turbofans is supersonic. As summarised by Tam (1995), noise from supersonic jets can be separated into three distinct components: turbulent mixing noise, screech and broadband shock-associated noise (BBSAN). Discrete screech tones are generated by a self-reinforcing feedback loop (Powell 1953; Raman 1999; Edgington-Mitchell 2019). Non-resonant interaction of jet turbulence with the shock cells produces BBSAN, which is most intense in the sideline directions. At aft angles, the contribution of BBSAN is small compared to turbulent mixing noise (Tam 1995; Viswanathan *et al.* 2010). Interest in BBSAN remains high for both commercial (Huber *et al.* 2014) and high-performance military (Vaughn *et al.* 2018) aircraft. This component of supersonic jet noise is the focus of this paper.

As demonstrated by Harper-Bourne & Fisher (1973), the broadband noise component is easily identifiable by its directivity and amplitude trends. At higher frequencies, BBSAN is observed to be more dominant than turbulent mixing noise, and its intensity is proportional to the fourth power of the off-design parameter  $\beta$ , defined as

$$\beta^2 = M_j^2 - M_d^2 \quad (1.1)$$

where the ideally-expanded and design Mach numbers are  $M_j$  and  $M_d$  respectively. The peak frequency of BBSAN also increases as an observer moves downstream. By modelling the interaction of turbulence with the train of shock cells as a phased array, this frequency trend was successfully reproduced by Harper-Bourne & Fisher (1973). Their prediction for BBSAN peak frequency  $f_p$  is given by

$$f_p = \frac{u_c}{L_s(1 - M_c \cos \theta)} \quad (1.2)$$

where  $u_c$  and  $M_c$  are the convection velocity and Mach number of the turbulent structures,  $L_s$  is the shock-spacing, and  $\theta$  is the angle of observation from the downstream jet axis. The early success of this model substantiated the claim that many features of BBSAN could be explained by the interaction of jet turbulence with the quasi-periodic shock-cell structure.

BBSAN modelling approaches nonetheless vary. The model developed by Morris & Miller (2010) uses solutions of the Reynolds-averaged Navier-Stokes (RANS) equations, requiring only the nozzle geometry and jet operating condition to be specified. Based on an acoustic analogy (Lighthill 1952), construction of the equivalent sources requires turbulent length and time scales which are approximated using the RANS CFD simulations. As the equivalent source behaviour is sensitive to these scales, efforts have been made to refine their description to improve predictions (Kalyan & Karabasov 2017; Markesteijn *et al.* 2017; Tan *et al.* 2017, 2019). Within the same framework and by using BBSAN scaling arguments, a different equivalent source term based on decomposing the Navier-Stokes equations was identified by Patel & Miller (2019). Reasonable agreement can be obtained with experiments provided the models are calibrated to match the acoustic field.

Rather than focusing on modelling bulk-turbulent statistics, a more fundamental approach was proposed by Tam & Tanna (1982) on the basis that BBSAN arises from the nonlinear interaction between large-scale coherent structures and shocks. The propagating coherent disturbances, resembling the Kelvin-Helmholtz instability in transitional shear layers, motivated the use of linear stability theory (Tam 1972; Crighton & Gaster

1976). Hence, the turbulent structures are represented as instability waves (Crighton & Gaster 1976; Tam & Chen 1979; Tam & Burton 1984), while the periodic shock-cell structure is modelled as a series of time-independent waveguide modes, with wavenumbers  $k_n$  and a corresponding shock-cell length approximated by  $L_s = 2\pi/k_1$  (Tam & Tanna 1982). Using this interpretation,  $f_p$  can be re-written as

$$f_p = \frac{u_c k_n}{2\pi(1 - M_c \cos \theta)}, \quad n = 1, 2, 3, \dots, \quad (1.3)$$

where  $n$  is the shock-cell mode. Equation (1.3) can also be used to predict peaks generated by higher-order shock-cell modes ( $n \geq 2$ ). The work of Tam and co-workers was consolidated into a stochastic model for BBSAN (Tam 1987). Due to the prohibitive cost of the extensive numerical computations required, a similarity source model was constructed which, when compared to experimental measurements (Norum & Seiner 1982), gave favourable noise spectra predictions over a wide range of jet operating conditions. As azimuthally-decomposed BBSAN measurements were not available at the time, scaling coefficients were used to match source model predictions for a single azimuthal mode to the total signal.

Recently, turbulent mixing noise generation mechanisms in jets have been associated with spatiotemporally coherent structures known as wavepackets. These axially-extended structures have been used extensively for predicting noise radiated from subsonic (Reba *et al.* 2010; Cavalieri *et al.* 2012; Unnikrishnan *et al.* 2019), supersonic (Tam & Burton 1984; Wu 2005; Sinha *et al.* 2014) and installed (Piantanida *et al.* 2016) jet flows. A thorough summary on the topic can be found in the review by Jordan & Colonius (2013), and the relationship to resolvent modes is discussed in detail by Cavalieri *et al.* (2019). The detection of these coherent structures in real flows (Suzuki & Colonius 2006; Kopiev *et al.* 2006; Cavalieri *et al.* 2013; Lesshafft *et al.* 2019), and our ability to describe them in linearised dynamic models (Schmid *et al.* 2002; Criminale *et al.* 2018), make them ideal candidates to represent the turbulent component of the BBSAN source. The flow properties of large-scale coherent structures, now depicted as wavepackets, may be obtained directly from data (Maia *et al.* 2019), or alternatively, using solutions to linearised equations with the mean field as a base flow (Cavalieri *et al.* 2013; Schmidt *et al.* 2018). The success of previous studies in using wavepackets to predict far-field noise (Lele 2005) motivates their use to model BBSAN.

Grounded in stability theory, wavepacket models are well posed and have been used to investigate the underlying sound generation mechanisms for BBSAN. While peak directivity trends were recovered, previous instability wave models for BBSAN offered poor agreement at frequencies above the primary BBSAN peak where sound amplitudes were severely underpredicted (Ray & Lele 2007) or artificial dips in the spectra were observed (Tam 1987). The two-point wavepacket model proposed by Wong *et al.* (2019b) offered an explanation. It was shown that, along with higher-order shock-cell modes, coherence decay (Cavalieri & Agarwal 2014) is essential to broaden the spectral peaks at high frequencies. The inclusion of coherence decay removed the ‘dips’ observed in the predicted acoustic spectra. In Wong *et al.* (2019a), an equivalent BBSAN source was constructed using parabolised stability equations (PSE) to model the wavepackets, along with two-point coherence information derived from an large-eddy simulation (LES) database. While a single amplitude scaling coefficient was required to match experimental data, recovery of the spectral shape at high frequencies was encouraging.

In the BBSAN models described above, the ‘inverse’ approach of determining source parameters from the radiated field is ill-posed, as more than one set of parameters

may be found to give satisfactory results. Moreover, the parameters found may not be representative of those observed in a real jet. A more direct approach is to use information from direct numerical simulation (DNS) or large-eddy simulation (LES) computations to educe or fit model parameters of the acoustic source terms (Freund 2003; O’Hara *et al.* 2004; Karabasov *et al.* 2010, amongst others). Improvement in using this type of approach was explicitly shown by Maia *et al.* (2019) for a subsonic jet. Using an ‘inside-out’ approach, source parameters, including amplitude, were carefully educed directly from a high-fidelity LES of a turbulent jet and compared to the parameters previously obtained by Cavalieri *et al.* (2012) for the same inverse problem. Parameter values were clearly shown to differ. An ‘inside-out’ approach was also attempted by Suzuki (2016) for BBSAN where wavepacket parameters were extracted from the linear hydrodynamic region of an LES database of an underexpanded jet and the shock cells were represented by a number of distinct ‘Gaussian humps’. The results confirmed modelling assumptions and obtained similar peak predictions to LES results, though agreement at high frequencies remained poor. From these observations, it is evident that a discord remains between the mechanistic insights provided by wavepacket model problems and their ability to accurately predict BBSAN.

Unlike previous work which already have shown high-fidelity LES can provide excellent agreement in the far-field (Shur *et al.* 2011; Brès *et al.* 2017; Arroyo & Moreau 2019), this work instead aims to identify the relevant source mechanisms by extending previous wavepacket-type BBSAN models and examining the predicted frequency and amplitude trends. This is achieved by using an ‘inside-out’ approach to construct the equivalent source from experimental and numerical flow databases. We adopt the same interpretation of the BBSAN source as Tam & Tanna (1982) and use Lighthill’s acoustic analogy to evaluate the far-field noise. To test the efficacy of the proposed model, sound predictions are compared to the azimuthally-decomposed acoustic data of a target jet case. The source is composed of shock and turbulent components; the shocks are modelled as stationary waveguide modes based on experimental particle image velocimetry (PIV) data. To test which turbulent features are important for sound generation, three descriptions of the wavepackets are obtained, each with an increasing level of complexity. It will be shown that reduced-order linear wavepackets, requiring only a jet mean flow field and a single amplitude parameter, can be used to accurately predict BBSAN peaks across a wide-directivity range. Inclusion of two-point coherence information does indeed recover the ‘missing sound’ at high frequencies. The study we perform is intended to explore the strengths and limitations associated with the use of large-scale coherent structures in BBSAN modelling. The proposed approach should not be viewed in the same light as direct computation of the acoustic field using near-field surface integration techniques for acoustic propagation (e.g. Ffowcs Williams-Hawkings (FW-H), Kirchhoff), but rather, as an attempt to elucidate the critical parts of the source responsible for BBSAN generation.

The paper is presented as follows. The mathematical framework for the model is explained in § 2 and the key details of the databases used are outlined in § 3. We discuss the steps to educe source parameters in § 4 and § 5 shows comparisons between simplified flow models with those from the databases for both the shock and turbulent components. We present far-field BBSAN predictions in § 6 and source characteristics in § 7. Some conclusions and perspectives are offered in § 8.

## 2. Mathematical formulation

### 2.1. Sound prediction using Lighthill's Acoustic Analogy

The fluctuating sound pressure,  $p$ , in the acoustic field can be computed using Lighthill's acoustic analogy (Lighthill 1952)

$$\frac{1}{c_\infty^2} \frac{\partial^2 p}{\partial t^2} - \nabla^2 p = \frac{\partial^2 T_{ij}}{\partial x_i \partial x_j}, \quad (2.1)$$

where  $t$  is time,  $c_\infty$  is the ambient speed of sound,  $x$  are the source co-ordinates and  $T_{ij}$  is the Lighthill stress tensor

$$T_{ij} = \rho u_i u_j - \tau_{ij} + (p - c_\infty^2 \rho) \delta_{ij}, \quad (2.2)$$

where  $u$  is fluid velocity,  $\tau$  are viscous stresses and  $\rho$  is density. In high-Reynolds number flows, viscous contributions are minimal (Freund 2001) and can hence be neglected. The term  $(p - c_\infty^2 \rho) \delta_{ij}$  represents noise generation due to entropic inhomogeneity. Bodony & Lele (2008) have shown that there is significant cancellation between the entropic term and the momentum component ( $\rho u_i u_j$ ) at downstream observer angles in an ideally-expanded supersonic jet. This cancellation, however, is negligible at sideline directions where we expect BBSAN to dominate. This view is also echoed by Freund (2003) who found that sideline ( $\theta = 90^\circ$ ) noise is dominated by Lighthill source terms that are largely independent of the entropic term. For BBSAN specifically, evidence also exists which suggests the contribution of the entropic term is negligible compared to the momentum terms in unheated shock-containing jets (Ray & Lele 2007; Morris & Miller 2010). From these observations, we choose to neglect the entropic term as a first approximation, as it greatly simplifies the model. The stress tensor is hence approximated by

$$T_{ij} \approx \rho u_i u_j. \quad (2.3)$$

A solution to equation (2.1) for the acoustic pressure field in the frequency domain,  $\omega$ , is given by

$$p(\mathbf{y}; \omega) = \int_V \frac{\partial^2 \hat{T}_{ij}(\mathbf{x}; \omega)}{\partial x_i \partial x_j} G_0(\mathbf{x}, \mathbf{y}; \omega) d\mathbf{x}, \quad (2.4)$$

where  $\hat{T}_{ij}$  is the time Fourier-transformed quantity of  $T_{ij}$ . An implicit  $\exp(-i\omega t)$  dependence on  $t$  is assumed. The observer  $\mathbf{y}$  and the source  $\mathbf{x}$  positions are in spherical and cylindrical coordinates respectively as shown in figure 1. The prescribed cylindrical coordinate system  $(x, r, \phi)$  has the x-axis aligned with the jet centreline,  $r$  is the radial separation and  $\phi$  the azimuthal angle. For the observer coordinates  $(R, \theta, \phi)$ , the same azimuthal coordinate of the cylindrical system is used, the polar angle  $\theta$  is defined from the downstream jet axis and  $R$  is the distance from the origin. The integration is carried out in the volume  $V$  where the source is non-zero. We define  $G_0$  as the free-field Green's function

$$G_0(\mathbf{x}, \mathbf{y}, \omega) = \frac{1}{4\pi} \frac{e^{ik_a |\mathbf{x} - \mathbf{y}|}}{|\mathbf{x} - \mathbf{y}|}, \quad (2.5)$$

where  $k_a = \omega/c_\infty$  is the acoustic wavenumber. We also transfer the second derivative of  $T_{ij}$  onto the Green's function by applying the divergence theorem and assuming the resulting surface integral to be negligible (Goldstein 1976). This makes evaluation of the integral less sensitive to spurious fluctuations in the stress tensor due to numerical noise.



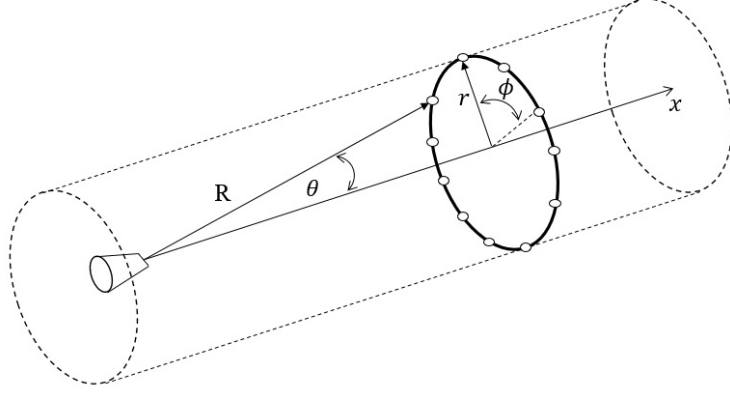


Figure 1: Schematic of experimental setup with the prescribed source  $(x, r, \phi)$  and observer  $(R, \theta, \phi)$  coordinate systems.

Acoustic sources embedded in high-speed flows may also be subjected to propagation effects such as refraction (Tam & Auriault 1998). For predicting far-field BBSAN from an unheated single-stream shock-containing jet, at polar angles  $50^\circ \leq \theta \leq 130^\circ$ , Miller & Morris (2012) show that a free-field Green's function provides adequate results when compared to predictions which included propagation effects.

Equation (2.4) is appropriate for time-periodic  $\hat{T}_{ij}$ , or for a  $T_{ij}$  that may be Fourier transformed in time. Since flow fluctuations are not square-integrable functions, as required for the application of a Fourier transform, one cannot obtain the sound field through direct application of equation (2.4), as the computation of a Fourier transform in this case would require windowing in time. One way to circumvent this issue (Landahl *et al.* 1989; Cavalieri & Agarwal 2014; Baqui *et al.* 2015) is to compute the power spectral density (PSD) of the acoustic field. For a given frequency  $\omega$ , the PSD  $\langle p(\mathbf{y}, \omega) p^*(\mathbf{y}, \omega) \rangle$  is given by

$$\langle p(\mathbf{y}; \omega) p^*(\mathbf{y}; \omega) \rangle = \int_V \int_V \langle T_{ij}(\mathbf{x}_1; \omega) T_{ij}^*(\mathbf{x}_2; \omega) \rangle \frac{\partial^2 G_0(\mathbf{x}_1, \mathbf{y}; \omega)}{\partial x_i \partial x_j} \frac{\partial^2 G_0^*(\mathbf{x}_2, \mathbf{y}; \omega)}{\partial x_i \partial x_j} d\mathbf{x}_1 d\mathbf{x}_2, \quad (2.6)$$

where  $\langle \rangle$  denotes an expected value, the quantity  $\langle T_{ij}(\mathbf{x}_1, \omega) T_{ij}^*(\mathbf{x}_2, \omega) \rangle$  is the cross-spectral density (CSD) of the stress tensor for a pair of points  $\mathbf{x}_1$  and  $\mathbf{x}_2$ ,  $*$  denotes the complex conjugate and we have dropped the hats for convenience. We exploit axisymmetry by expanding  $T_{ij}$  as a series of azimuthal modes (Michalke & Fuchs 1975); noting that there is a direct correspondence between the azimuthal mode of the source and that of the sound field (Michalke 1970; Cavalieri *et al.* 2012). By taking a Fourier transform of the source in azimuth, we can compute azimuthal mode  $m$  of the far-field pressure to be

$$\langle p(R, \theta; m, \omega) p^*(R, \theta; m, \omega) \rangle = \int_V \int_V \langle S_{ij}(m, \omega) \rangle \frac{\partial^2 G_{0,1}(m, \omega)}{\partial x_i \partial x_j} \frac{\partial^2 G_{0,2}^*(m, \omega)}{\partial x_i \partial x_j} d\mathbf{x}_1 d\mathbf{x}_2, \quad (2.7)$$

where we have dropped the spatial coordinates of the source for compactness,  $G_{0,1}$  and  $G_{0,2}$  represent the Green's functions at source location  $\mathbf{x}_1$  and  $\mathbf{x}_2$  respectively, and  $S_{ij}$

represents the CSD of the stress tensor

$$S_{ij}(x_1, r_1, x_2, r_2; m, \omega) = T_{ij}(x_1, r_1; m, \omega) T_{ij}^*(x_2, r_2; m, \omega). \quad (2.8)$$

## 2.2. Equivalent BBSAN source model

The proposed BBSAN model is based on the idea that the source only involves fluctuations associated with interactions between the turbulent component ( $\mathbf{q}_t$ ) and shock perturbations ( $\mathbf{q}_s$ ). This assumption has been made by a number of authors (Tam & Tanna 1982; Lele 2005; Ray & Lele 2007; Wong *et al.* 2019b), where different descriptions of  $\mathbf{q}_t$  and  $\mathbf{q}_s$  were investigated. We follow this approach and, similar to Wong *et al.* (2019b), adopt a two-point description of the source.

As performed by Tam (1987), we decompose the flow variables according to

$$\mathbf{q} = \bar{\mathbf{q}} + \mathbf{q}_t + \mathbf{q}_s, \quad (2.9)$$

where  $\bar{\mathbf{q}}$ ,  $\mathbf{q}_t$ ,  $\mathbf{q}_s$  are the mean, turbulent and shock-cell disturbance components respectively. We take the mean component to be the time-averaged flow of an ideally-expanded jet. The vector  $\mathbf{q}$  refers to the dependent flow variables of interest,  $\mathbf{q} = [u_x, u_r, u_\phi, T, \rho]^T$ , where  $u_x$ ,  $u_r$  and  $u_\phi$  are the axial, radial and azimuthal velocity components respectively. The thermodynamic variables include  $T$  and  $\rho$  which are the temperature and the density of the fluid respectively. The decomposition in equation (2.9) is substituted into the stress tensor in equation (2.3)

$$T_{ij} \approx (\bar{\rho} + \rho_s + \rho_t)(\bar{u}_i + u_{i,t} + u_{i,s})(\bar{u}_j + u_{j,t} + u_{j,s}). \quad (2.10)$$

Assuming that BBSAN is generated by turbulence-shock interaction, the expression for  $T_{ij}$ , as shown in appendix A, can be simplified to

$$T_{ij} \approx \bar{\rho}(u_{i,t}u_{j,s} + u_{i,s}u_{j,t}) + \rho_s(\bar{u}_i u_{j,t} + \bar{u}_j u_{i,t}) + \rho_t(\bar{u}_i u_{j,s} + \bar{u}_j u_{i,s}). \quad (2.11)$$

Here we highlight some characteristics of equation (2.11). Firstly, this representation of  $T_{ij}$  does not account for turbulent mixing noise since only turbulence-shock interaction terms are retained (appendix A). This is justified by the minimal contribution of mixing noise at the frequencies and polar positions where BBSAN is dominant (Viswanathan 2006; Viswanathan *et al.* 2010). Agreement with measured acoustic data at low frequencies and downstream polar angles would therefore not be expected. Secondly, unlike previous wavepacket models in subsonic jets (Cavaliere *et al.* 2011; Piantanida *et al.* 2016; Maia *et al.* 2019), we retain all velocity components of  $T_{ij}$  in order to improve predictions in the sideline direction. We also note that while equation (2.11) is similar to the source term derived by Lele (2005), we retain the double-divergence and have discarded the entropic term.

The BBSAN sound field can be obtained using equations (2.7) and (2.11). Unlike previous two-point wavepacket modelling work (Maia *et al.* 2019; Wong *et al.* 2019b), we choose to relax the line-source simplification and work with a full volumetric source instead. The  $\mathbf{q}_t$  and  $\mathbf{q}_s$  parts of  $T_{ij}$  are each computed using numerical and experimental databases, respectively, as shown in § 4, before being combined according to equation (2.11). The source domain extends from  $0 \leq x \leq 25D$  and  $0 \leq r \leq 2D$  in the axial and radial directions respectively. An appropriate window function, summarised further in § 5.1, is used to ensure no artificial overprediction of the acoustic field (Obrist & Kleiser 2007; Martínez-Lera & Schram 2008).

---

Database	$M_j$	$M_d$	$NPR$	$T_j/T_\infty$	$D_j/D$	$Re$	$\beta$
LES	1.50	1.5	3.67	1.0	1.0	$1.76 \times 10^6$	0
PIV	1.45	1.0	3.40	0.70	1.07	$8.51 \times 10^5$	1.05
Acoustic	1.50	1.0	3.67	0.69	1.09	$4.50 \times 10^5$	1.12

---

Table 1: Summary of jet operating parameters for each database.

### 3. Databases

To explore the sound source mechanisms, far-field acoustic spectra predictions are computed and compared to experimental measurements. The goal is to build an equivalent source appropriate for describing the sound field for a target jet operating condition. The model is based on a decomposition of the flow field into  $\bar{\mathbf{q}}$ ,  $\mathbf{q}_t$  and  $\mathbf{q}_s$  components (equation (2.9)).

We obtain this data from different databases; wavepackets are deduced from an ideally-expanded jet, while the modelling of the shock disturbances is based on an underexpanded jet. Ideally, the exit conditions of these jets ( $NPR$ ,  $M_j$ ,  $Re$ ,  $T_j$ ) should be as close as possible to the target case.

The flow-field databases are summarised in § 3.1-3.2 while the acoustic measurements of the target jet are described in § 3.3. A summary of the jet operating conditions is provided in table 1. We note that the databases do not correspond to identical operation conditions. They are here only used to inform our modelling choices such that the descriptions of  $\mathbf{q}_t$  and  $\mathbf{q}_s$  align closely with a realistic jet. Given the small discrepancies between the databases, we perform a short sensitivity study to assess how these may impact BBSAN peak frequency and amplitude. This is provided in appendix B.

#### 3.1. Numerical database: Large-eddy simulation of $M_j = 1.5$ ideally-expanded jet

The turbulent flow quantities  $\mathbf{q}_t$  are extracted from a large-eddy simulation (LES) of an isothermal ideally-expanded  $M_j = 1.5$  supersonic jet. An extension to the previous LES by Brès *et al.* (2017), this simulation was performed using the compressible flow solver “Charles”, developed at Cascade Technologies, on an unstructured adapted grid with 40 million cells. The jet issues from a round converging-diverging nozzle. The Reynolds number based on nozzle exit conditions is  $Re = \rho_j U_j D / \mu_j = 1.76 \times 10^6$ , matching the experiment carried out at the United Technologies Research Center (UTRC) anechoic jet facility (Schlinker *et al.* 2009). Near-wall adaptive mesh refinement is employed on the internal nozzle surface to closely model the boundary layer inside the nozzle, leading to turbulent boundary layer profiles at the exit (Brès *et al.* 2018). A slow co-flow of  $M_{co} = 0.1$  is also included in the simulation to match the UTRC experimental conditions. As the LES jet is shock-free, direct computation of the BBSAN sound field via an FW-H surface is not possible.

To facilitate post-processing and analysis, the LES data is interpolated from the original unstructured LES grid onto a structured cylindrical grid with uniform spacing in azimuth. The three-dimensional cylindrical grid is defined over  $0 \leq x/D \leq 30$ ,  $0 \leq r/D \leq 6$ , with  $(n_x, n_r, n_\theta) = (698, 136, 128)$ , where  $n_x$ ,  $n_r$  and  $n_\theta$  are the number of grid points in the streamwise, radial and azimuthal direction, respectively. The simulation time step, in acoustic time units, is  $\Delta t c_\infty / D = 0.0004$  and the database is sampled every  $\Delta t c_\infty / D = 0.1$ . Snapshots are therefore recorded every 250 time steps, corresponding to a cutoff (Nyquist) frequency of  $St = \Delta f D / U_j = 3.33$ . The simulation parameters are

---

$[n_x, n_r, n_\theta]$	Sim. Duration	Sampling Period	Nyquist Freq.	Num. Snapshots
698, 136, 128	1000	0.1	3.33	10000

---

Table 2: Summary of LES parameters.

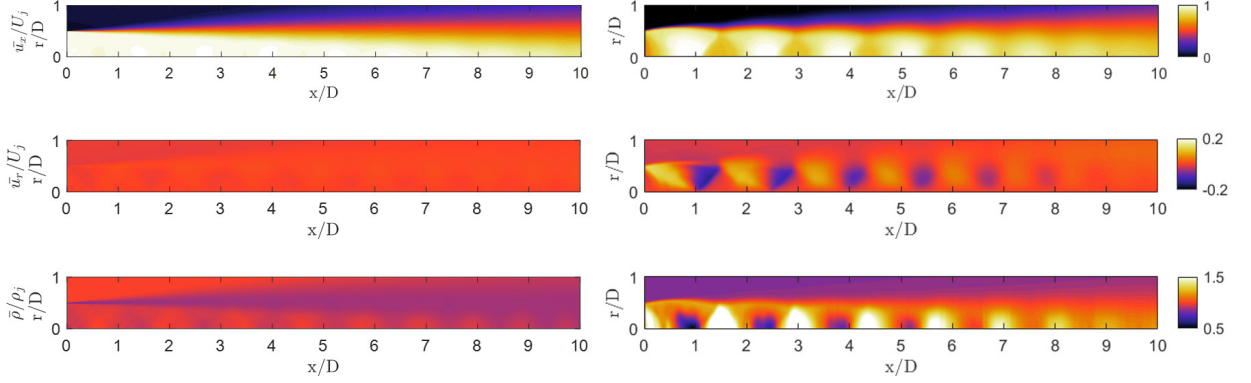


Figure 2: LES (left) and PIV (right)  $x - r$  contour mean fields for ideally-expanded and shock-containing jets respectively; streamwise velocity (top), radial velocity (centre) and density (bottom). Flow quantities are normalised by the ideally-expanded condition.

summarised in table 2. Further details on the numerical strategy can be found in Brès *et al.* (2017).

### 3.2. Experimental database: Particle image velocimetry of $M_j = 1.45$ underexpanded jet

For the description of  $\mathbf{q}_s$ , we resort to high spatial resolution 2D 2C particle image velocimetry (PIV) measurements of a cold screeching underexpanded supersonic jet with an ideally-expanded Mach number of  $M_j = 1.45$ . The data was previously acquired at the supersonic jet facility at the Laboratory for Turbulence Research in Aerospace and Combustion (LTRAC) (Edgington-Mitchell *et al.* 2014a). The facility has been used extensively in previous experimental studies of shock-containing supersonic jets (Edgington-Mitchell *et al.* 2014b; Weightman *et al.* 2019). The facility is not anechoic and noise measurements were not conducted.

The final field of view of the images is  $10D$  and  $2.2D$ , with  $(N_x, N_y) = (1000, 75)$ , in the axial and radial directions respectively. The optical resolution of the images is  $0.001D/px$ . Full details of the experimental set-up and post-processing techniques are described in Edgington-Mitchell *et al.* (2014b). Mean axial and radial velocity fields from both the LES and PIV data are shown in figure 2.

### 3.3. Acoustic database: Far-field acoustic measurements $M_j = 1.5$ underexpanded jet

The acoustic measurements were performed at the Supersonic Jet Anechoic Facility (SJAF) at Monash University. This is a different facility to the jet rig used to acquire the PIV measurements in § 3.2. Most importantly, the jet is mounted inside a fully-enclosed anechoic chamber. The chamber walls are treated with 400mm foam wedges, corresponding to a cut-off frequency of 500Hz. The interior chamber dimensions (wedge-tip-to-wedge-tip) are  $1.5\text{m} \times 1.2\text{m} \times 1.4\text{m}$ . The jet exits out of a converging-round nozzle with an exit diameter of  $D = 8\text{mm}$ . Unheated compressed air is supplied to the jet at  $NPR = 3.67$ , corresponding to the same  $M_j$  as the LES case.

Acoustic measurements were performed using an azimuthal ring of radius  $11D$  and a schematic of the experimental setup is shown in figure 1. The CSD of pressure, as a function of azimuthal separation, was obtained using a pair of G.R.A.S. Type 46BE 1/4" pre-amplified microphones with a frequency range of 4Hz-100kHz, one fixed and the other moving in the azimuthal direction. Using the post-processing methodology detailed in Wong *et al.* (2020), the measured sound fields were azimuthally decomposed. The azimuthal array is traversed axially to acquire measurements at different polar angles over a cylindrical surface. The radial distance  $r = 11D$  is therefore constant, while observer distance  $R$  changes. A detailed description of the experimental setup can be found in Wong *et al.* (2020).

The motivation for using azimuthally-decomposed data is twofold. Firstly, the measurements of previous authors (Suzuki 2016; Arroyo & Moreau 2019; Wong *et al.* 2020) suggest the spectrum of each azimuthal mode differs from the total sound field; an increasing number of modes is required to reconstruct the total signal at high frequencies and for upstream angles. Secondly, in a linear acoustic problem such as this, Michalke & Fuchs (1975) demonstrated there exists a direct correspondence between the acoustic source  $S_{ij}$  and the far-field sound of the same azimuthal mode.

#### 4. Construction of source variables

This section details the procedures used to compute the source variables in equation (2.9) using the databases described in the preceding section. Each source variable ( $\bar{q}$ ,  $\mathbf{q}_t$  and  $\mathbf{q}_s$ ) is either obtained via direct substitution of LES data or constructed using models informed by flow information from the LES and PIV databases.

##### 4.1. Eduction of shock-cell component

Similar to Tam & Tanna (1982) and Lele (2005), we adopt the Pack and Prandtl (Prandtl 1904; Pack 1950) approximation of the shock-cell structure. The shocks are modelled as small disturbances superimposed over an ideally-expanded jet. The model assumes the jet to be bounded by a vortex sheet, allowing the periodic shock-cell structure to be represented by a sum of zero-frequency waves. Good agreement is found close to the nozzle exit, where the shear layer is thin, but worsens downstream as the shear layer thickens, invalidating the vortex sheet assumption (Tam *et al.* 1985). With increasing distance from the nozzle exit, the model therefore fails to predict the decay in shock strength and the accompanying contraction in shock-cell spacing. Since the BBSAN source is reported to extend several jet diameters downstream (Seiner & Norum 1980; Gojon & Bogey 2017), any disagreement between the vortex sheet model and measured jet characteristics is likely to lead to incorrect peak frequency predictions.

While the shock-cell disturbances may be extracted from data (e.g. PIV) or computed by solving linear locally-parallel stability equations (Tam *et al.* 1985), the shock perturbations have a smooth and nearly sinusoidal variation towards the end of the potential core. The Pack and Prandtl (P-P) model therefore remains an attractive simplified approach for capturing the mean shock structure; indeed, source models adopting the approximation are able to reproduce the main features of BBSAN, including higher-order BBSAN peaks (Tam & Tanna 1982; Wong *et al.* 2019b). To remedy the shortfalls of the vortex sheet assumption, we use the PIV database to modify the P-P solution in order to arrive at a more realistic model.

The jet is modelled as a cylindrical vortex sheet (Lessen *et al.* 1965), and the normal mode Ansatz is introduced

$$\mathbf{q}_{s,vortex}(x, r, \theta, t) = \sum_{\omega} \sum_{k_s} \sum_{m_s} \hat{\mathbf{q}}_s(r) e^{i\omega_s t - ik_s x - im_s \phi}, \quad (4.1)$$

where  $\omega_s$  is frequency,  $k_s$  and  $m_s$  are axial and azimuthal wavenumbers. By assuming the shock-cell disturbances are stationary ( $\omega_s = 0$ ) and axisymmetric ( $m_s = 0$ ), we obtain for each dependent variable of interest  $\mathbf{q}_s$ ,

$$q_{s,vortex}(x, r) = \sum_{n=1}^{\infty} A_n J_0(\alpha_n r) e^{-ik_{s_n} x}, \quad (4.2)$$

where  $A_n$  is the amplitude of each shock-cell mode  $n$ ,  $k_{s_n}$  are the axial wavenumbers and  $J_0$  is the zeroth-order Bessel function of the first kind. The boundary condition for constant velocity on the jet boundary (Pack 1950) requires that the values of  $\alpha_n$  satisfy

$$J_0(\alpha_n) = 0, \quad (4.3)$$

and from the dispersion relation, we obtain the sequence of axial wavenumbers to be

$$k_{s_n} = \frac{\alpha_n}{\sqrt{M_j^2 - 1}}. \quad (4.4)$$

In real jets,  $A_n$  and  $k_{s_n}$  are functions of  $x$ , as the underlying evolution of the mean flow modifies each Fourier component. This variation is not captured in the P-P model due to the parallel vortex-sheet assumption. Hence, we wish to obtain a modified version of the vortex sheet model,  $\mathbf{q}_{s,mod}$ , which more closely resembles measured shock-containing jet characteristics. A realistic representation of  $\mathbf{q}_s$  is obtained by subtracting the ideally-expanded flow quantities of the LES dataset from the shock-containing quantities of the PIV dataset

$$\mathbf{q}_s \approx \mathbf{q}_{PIV} - \mathbf{q}_{LES}, \quad (4.5)$$

where we have assumed the quantity  $\mathbf{q}_{LES}$  contains both the mean and turbulent contribution in (2.9). While the PIV data provides axial and radial velocities, the mean shock-associated density modulation ( $\rho_s$ ) is estimated using the ideal gas law, with reconstructed temperatures and pressures obtained by the method of Tan *et al.* (2018). Good agreement is observed between the reconstructed densities and mean background-oriented schlieren (BOS) measurements (Tan *et al.* 2015). LES quantities are then interpolated onto the lower-resolution PIV grid.

To adjust  $k_{s_n}$ , a Fourier transform of  $\mathbf{q}_s$  is performed downstream of the nozzle exit to capture the variation of shock-cell spacing, similar to Morris & Miller (2010). The axial wavenumber from the vortex-sheet approximation is adjusted empirically, using a linear fit to match the PIV data

$$k_{s_n,mod} = 0.79 \times k_{s_n,vortex} + 1.02. \quad (4.6)$$

To determine the axial variation in  $A_n$ , we assume there exists a relationship between the vortex sheet model  $\mathbf{q}_{s,vortex}$  and the adjusted values  $\mathbf{q}_{s,mod}$

$$\mathbf{q}_{s,mod}(x, r; n) = b(x; n) \mathbf{q}_{s,vortex}(x, r; n), \quad (4.7)$$

where the factor  $b(x; n)$  is determined by using the experimentally-deduced values  $\mathbf{q}_s$ ,

$$b(x; n) = \frac{\langle \mathbf{q}_{s,vortex}(x, r; n), \mathbf{q}_s(x, r) \rangle}{\|\mathbf{q}_{s,vortex}(x, r; n)\|^2}, \quad (4.8)$$

and the inner-product is defined as

$$\langle \mathbf{q}_{s,vortex}(x, r; n), \mathbf{q}_s(x, r) \rangle = \int_0^R \mathbf{q}_{s,vortex}(x, r'; n) \mathbf{q}_s^*(x, r') \mathbf{W}(x, r') r' dr', \quad (4.9)$$

where the orthogonality of Bessel functions is exploited. The matrix  $\mathbf{W}$  is solely used to assign null weights to the temperature component, since we are only concerned with the density and velocity components that contribute to the BBSAN source term in (2.11). The integration limit  $R$  is taken to be the maximum radius of the PIV measurement domain.

Unlike Ray & Lele (2007), higher-order modes ( $n > 1$ ) are included in our shock-cell description. Wong *et al.* (2019b) used a line-source wavepacket model, incorporating the effects of coherence decay, to demonstrate the importance of higher-order modes at high frequencies, despite the fact they possess wavenumbers which lie outside the radiating range (Ray & Lele 2007). The final shock-cell structure is reconstructed using three modes ( $n = 1, 2, 3$ ), as this was deemed suitable for predicting the far-field BBSAN over the frequency range of interest.

#### 4.2. *Eduction of wavepacket component*

Two methods are used to obtain the turbulent (wavepacket) component of the source  $T_{ij}$ . The first method involves the direct substitution of post-processed LES data, representing the most ‘complete’ prediction possible for the proposed BBSAN model as it encapsulates the full range of resolved spatial and temporal turbulent scales. The second utilises solutions to parabolised stability equations (PSE), which have previously been shown to be appropriate reduced-order representations of the large-scale perturbations in turbulent jets (Gudmundsson & Colonius 2011; Cavalieri *et al.* 2013; Sinha *et al.* 2014).

##### 4.2.1. *LES database*

The LES data contains a broad range of temporal and spatial scales. To handle this, extraction of coherent wavepackets is performed in a similar fashion to previous studies (Sinha *et al.* 2014; Schmidt *et al.* 2017; Maia *et al.* 2019), assuming the jet to be periodic in azimuth ( $\phi$ ) and statistically stationary. The fluctuating turbulence variables  $\mathbf{q}_t$  are decomposed using the following ansatz,

$$\mathbf{q}_t(x, r, \phi, t) = \sum_{\omega} \sum_m \hat{\mathbf{q}}_t(x, r) e^{-i\omega t + im\phi}, \quad (4.10)$$

where  $\omega$  is angular frequency and  $m$  is azimuthal wavenumber of the wavepacket. Using this decomposition, the LES data is Fourier-transformed in both azimuth and time. For each azimuthal mode  $m \neq 0$ , the contribution from the positive mode  $+m$  is combined with the complex conjugate of that from the negative mode  $-m$ , since the jet has no swirl. Prior to the temporal Fourier transform, the time series is divided into data blocks of  $N_{fft} = 128$  sample points and a Hann window is applied to suppress spectral leakage. The final number of blocks is  $N_B = 310$ , with a 75% overlap, was sufficient to ensure statistical convergence. The resulting frequency bin width is  $\Delta St = 0.052$ , which was considered to be sufficient to resolve the frequency content of BBSAN ( $St > 0.4$  in the present database). For a given  $\omega$  and  $m$ , the  $\mathcal{J}^{th}$  block of the Fourier-transformed

flow field  $\mathbf{q}_{m,\omega}^{(\mathcal{J}^{th})}$  is obtained and substituted directly into the  $\mathbf{q}_t$  part of  $T_{ij}$  in (2.11). Fluctuations extracted from the LES data do not undergo any additional processing. The  $\mathbf{q}_t$  (from LES) and  $\mathbf{q}_s$  (from PIV) parts are then combined to produce the BBSAN source term, given by

$$S_{ij,LES}(\mathbf{x}_1, \mathbf{x}_2; m, \omega) = \frac{1}{N_B} \sum_{\mathcal{J}=1}^{\mathcal{J}=N_B} T_{ij}^{(\mathcal{J})}(\mathbf{x}_1; m, \omega) T_{ij}^{*(\mathcal{J})}(\mathbf{x}_2; m, \omega). \quad (4.11)$$

#### 4.2.2. Parabolised stability equations

The use of PSE to model wavepackets has been well studied in both subsonic (Gudmundsson & Colonius 2011; Cavalieri *et al.* 2013) and supersonic (Sinha *et al.* 2014; Rodríguez *et al.* 2015; Kleine *et al.* 2017) turbulent jets where the mean flow is assumed to be slowly diverging. The PSE approach has also been used to model the turbulent component in previous BBSAN models (Ray & Lele 2007; Wong *et al.* 2019a).

The PSE system follows the same non-dimensionalisation and ansatz (4.10) used to decompose the LES data. It is assumed that  $\mathbf{q}_t(x, r, \phi, t)$  may further be decomposed into a slowly and rapidly varying component. The appropriate multiple-scales ansatz, proposed by Bouthier (1972), Saric & Nayfeh (1975) and Crighton & Gaster (1976), can be written

$$\mathbf{q}_t(x, r, \phi, t) = \hat{\mathbf{q}}_t(x, r) e^{i \int \alpha(x') dx'} e^{-i\omega t} e^{im\phi}, \quad (4.12)$$

where the rapidly and slowly-varying parts are described by the exponential term  $e^{i \int \alpha(x') dx'}$ , and the modal shape function  $\hat{\mathbf{q}}_t$ , respectively. The integrand  $\alpha(x')$  is the complex-valued hydrodynamic wavenumber that varies with axial position. Equation (4.12) can be substituted into the governing inviscid linearised equations. The resultant matrix system is recast into the following compact form

$$\mathbf{A} \hat{\mathbf{q}}_t + \mathbf{C} \frac{\partial \hat{\mathbf{q}}_t}{\partial x} + \mathbf{D} \frac{\partial \hat{\mathbf{q}}_t}{\partial r} = 0, \quad (4.13)$$

where the left-hand side is the linear operator acting on a given  $(m, \omega)$  shape function  $\hat{\mathbf{q}}_t$ . Full expressions for operators  $\mathbf{A}$ ,  $\mathbf{C}$  and  $\mathbf{D}$  can be found in Fava & Cavalieri (2019). To find  $\alpha(x)$  and  $\hat{\mathbf{q}}_t$ , the system is discretised and solved by streamwise spatial marching. Chebyshev polynomials are used to discretise the radial domain and first-order finite differences to approximate the axial derivatives. The axial step-size  $\Delta x$  is limited by the numerical stability condition specified by Li & Malik (1997)

$$\Delta x \geq \frac{1}{|Re \{ \alpha_{m,\omega}(x) \}|}. \quad (4.14)$$

As discussed by Herbert (1997) and Cavalieri *et al.* (2013), there remains an ambiguity in the PSE decomposition, since the spatial growth of  $\mathbf{q}_t$  is shared by both the shape function  $\hat{\mathbf{q}}_t$  and the complex amplitude  $e^{i \int \alpha(x') dx'}$ . A normalisation condition is introduced to remove this ambiguity

$$\int_0^\infty \hat{\mathbf{q}}_t^* \frac{\partial \hat{\mathbf{q}}_t}{\partial x} r dr = 0. \quad (4.15)$$

Dirichlet boundary conditions are used as  $r \rightarrow \infty$  and the condition along the jet centreline follows the treatment prescribed in Mohseni & Colonius (2000) using parity



functions. A complete description of the procedure is provided by Gudmundsson & Colonius (2011) and a good summary can be found in Sasaki *et al.* (2017b).

The PSE solutions are computed using the the mean flow of the ideally-expanded jet LES. The LES mean flow is linearly interpolated onto the PSE grid, and for each frequency, the PSE is solved on its own axial grid given by the minimum step-size specified in equation (4.14). To initiate the marching procedure, initial flow conditions at the nozzle exit plane are provided by the eigenfunction of the Kelvin-Helmholtz (KH) instability mode, obtained by solving the locally-parallel stability problem.

Wavepacket amplitudes are undefined, as PSE solves a linear problem. For meaningful comparisons, PSE solutions must be scaled to experimental results. Different approaches to the task have been performed by previous authors and a summary is provided by Rodríguez *et al.* (2015). Method complexity ranges from a simple scalar multiplication, to more robust bi-orthogonal projections of LES data onto PSE wavepackets near the nozzle exit (Rodríguez *et al.* 2013). While PSE scaling approximately follows an exponential trend with frequency (Antoniali *et al.* 2021), scaling amplitudes are found to be sensitive to the choice of the matching flow variables, region of interest and the axial position.

A scaling method compatible with the goal of this study, that is, to develop a BBSAN model that does not require calibration from far-field acoustic data, demands that the amplitude of the source term must be obtained directly from the flow information. This requires the PSE solution to be scaled to the same amplitude as the extracted LES fluctuations. The most stringent method obtains the PSE amplitudes based solely on flow-field quantities of the LES data at a single given axial station  $x_0$ . We define the source-based inner product of the PSE solutions  $\mathbf{q}_{t,PSE}$  and the  $\mathcal{J}^{th}$  block of the processed LES data  $\mathbf{q}_{t,LES}^{(\mathcal{J}^{th})}$  as

$$\langle \mathbf{q}_{t,PSE}(x, r; m, \omega), \mathbf{q}_{t,LES}^{(\mathcal{J}^{th})}(x, r; m, \omega) \rangle = \int_0^R \mathbf{q}_{t,PSE}(x, r; m, \omega) \mathbf{q}_{t,LES}^{(\mathcal{J}^{th})*}(x, r; m, \omega) \mathbf{W}(x, r') r' dr', \quad (4.16)$$

where we have again assigned null weights to the temperature component, and  $R$  is determined by the outer bound of the LES data. We assume the LES flow variables may be expressed in the form

$$\mathbf{q}_{t,LES}^{(\mathcal{J}^{th})}(x, r; m, \omega) = \mathcal{A}(x; m, \omega) \mathbf{q}_{t,PSE}(x, r; m, \omega), \quad (4.17)$$

where the value  $\mathcal{A}$  is evaluated for every  $\mathcal{J}^{th}$  block according to

$$\mathcal{A}^{(\mathcal{J}^{th})}(x; m, \omega) = \frac{\langle \mathbf{q}_{t,PSE}(x, r; m, \omega), \mathbf{q}_{t,LES}^{(\mathcal{J}^{th})}(x, r; m, \omega) \rangle}{\|\mathbf{q}_{t,PSE}(x, r; m, \omega)\|^2}. \quad (4.18)$$

For each frequency-azimuth pair, the axial scaling location is chosen to be the peak of the PSE wavepacket  $x_0$ ;  $\mathcal{A}(x_0; m, \omega)$  becomes the PSE scaling factor. The wavepacket peak is chosen as  $x_0$  as there is good alignment between PSE solutions and those extracted from LES data at this location (Sasaki *et al.* 2017a; Antoniali *et al.* 2021). Each value of  $\mathcal{A}$  is averaged over the total number of blocks  $N_B$ . The scaled PSE solutions are then substituted into the turbulent part of equation (2.11) and a statistical, perfectly-coherent BBSAN source,  $\check{S}_{ij}$ , is given by

$$\check{S}_{ij,PSE}(\mathbf{x}_1, \mathbf{x}_2; m, \omega) = \check{T}_{ij}(\mathbf{x}_1; m, \omega) \check{T}_{ij}^*(\mathbf{x}_2; m, \omega). \quad (4.19)$$

---

	$\mathbf{q}_s$	$\mathbf{q}_{t,LES}$	$\mathbf{q}_{t,PSE}$
Original dataset/ model	P-P	LES	PSE
Matching dataset	PIV	N/A	LES
Number of empirical parameters	2 ( $k_s, b$ )	0	1 ( $\mathcal{A}$ )
Scaling location	Throughout domain	N/A	Wavepacket peak ( $x_0$ )

---

Table 3: Summary of source model inputs.

#### 4.3. Coherence-matched source term

For a BBSAN line-source model, Wong *et al.* (2019b) demonstrated that the use of wavepacket solutions from PSE gives rise to non-physical dips in the far-field sound spectrum. This is due to the PSE-derived wavepackets, and hence the statistical source  $\tilde{S}_{ij}$ , having unit coherence between any pair of points (Cavalieri & Agarwal 2014). Instead, two-point coherence information of the flow field, which represents randomness in wavepacket phase statistically (Cavalieri *et al.* 2011), smooths out higher-order BBSAN peaks and results in the recovery of missing sound at upstream angles. To reproduce the original source  $S_{ij}$ , in addition to amplitude and phase velocity, two-point coherence of the source must also be matched (Cavalieri & Agarwal 2014; Maia *et al.* 2019). The CSD of  $S_{ij}$  becomes

$$\langle T_{ij}(\mathbf{x}_1; m, \omega) T_{ij}^*(\mathbf{x}_2; m, \omega) \rangle = \gamma^2(\mathbf{x}_1, \mathbf{x}_2; m, \omega) \tilde{T}_{ij}(\mathbf{x}_1; m, \omega) \tilde{T}_{ij}^*(\mathbf{x}_2; m, \omega), \quad (4.20)$$

where  $\gamma$  is the coherence between two points  $\mathbf{x}_1$  and  $\mathbf{x}_2$ . Unlike previous studies (Baqui *et al.* 2015; Maia *et al.* 2019), we do not model the coherence envelope but, rather compute it directly from the LES data. The coherence profile of  $S_{ij,LES}$  (equation (4.11)) is computed between all sets of points in the source region, given by

$$\gamma^2(\mathbf{x}_1, \mathbf{x}_2; m, \omega) = \frac{|\langle S_{ij,LES}(\mathbf{x}_1, \mathbf{x}_2; m, \omega) \rangle|^2}{\langle |S_{ij,LES}(\mathbf{x}_1)|^2 \rangle \langle |S_{ij,LES}(\mathbf{x}_2)|^2 \rangle}. \quad (4.21)$$

#### 4.4. Summary of BBSAN source model construction

An overview of the BBSAN source assembly is shown in figure 3 with model inputs summarised in table 3. The stationary nature of the shock-cell component  $\mathbf{q}_s$  means that the parameters of the Pack and Prandtl model may be deduced from the time-averaged PIV fields and thus temporal fluctuations (hydrodynamic or acoustic) will have zero amplitude. In all the reconstructed sources,  $\mathbf{q}_s$  is informed by the PIV data set alone as the LES and PSE flow fields are shock-free. From here, we shall refer to the ‘LES model’ where wavepacket fluctuations are extracted directly from LES data (figure 3a) and the ‘PSE model’ for wavepackets described by PSE solutions (figure 3b). For the PSE model, we will present both cases with and without coherence decay. As the shock cells are assumed to be axisymmetric and stationary, the frequency and azimuthal dependence are described solely by the properties of the wavepacket.

The three descriptions of  $\mathbf{q}_t$  have varying levels of complexity. In the simplest description, the perfectly-coherent PSE model only requires a jet mean flow profile and a single parameter to fix the free amplitude of the linear solution. This reduced-order representation should confirm the results of Tam (1987). As suggested by Wong *et al.* (2019b), and confirmed in § 6, a linear model is unable to capture certain features of

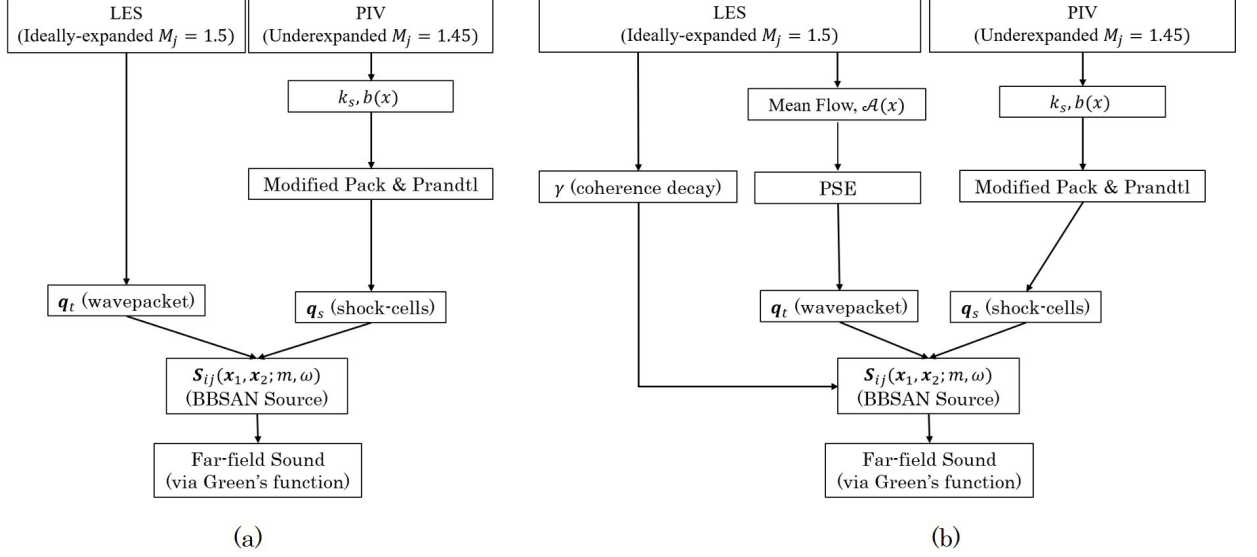


Figure 3: Summary of BBSAN model construction; (a) source model with  $q_t$  obtained directly from LES data and (b) statistical source model with  $q_t$  obtained from PSE solutions.

the BBSAN spectrum and a description of the nonlinearities in the form of coherence decay is thus imposed on the linear wavepackets. The two simplified cases are compared to the wavepacket obtained from LES data alone, which represents the most accurate description of the current BBSAN model.

We would also like to highlight the sensitivities of the far-field sound predictions to the parameters  $b$ ,  $\mathcal{A}$  and  $\gamma$ . Since the components of  $q_t$  and  $q_s$  are multiplied together (equation 2.11), the factors  $b$  and  $\mathcal{A}$  will be combined into a single amplitude factor. As this is a linear factor, changes to both parameters would only affect the overall amplitude of noise generated; for example, a 10% increase in both  $b$  and  $\mathcal{A}$  would result in a increase of 1.65dB/St. On the other hand, the  $\gamma$  parameter is deduced directly from the LES. A detailed study of the sensitivity to  $\gamma$  is presented in (Wong *et al.* 2019b).

Clearly, a shortcoming of this BBSAN source interpretation (Tam 1987; Lele 2005; Ray & Lele 2007) is, by construction, the artificial separation of the shock disturbances from the wavepacket. The evolution and dynamics of the wavepacket are assumed independent of the presence of shocks in the jet. Hence, the properties of the deduced wavepackets (e.g. convection velocity, phase, amplitude) may differ from those in a shock-containing flow. While there is evidence to suggest that wavepacket dynamics are not affected by weak shocks (Edgington-Mitchell *et al.* 2019), it remains unknown whether this extends to highly underexpanded jets, such as that studied here. Despite PSE having been attempted on a shock-containing base flow (Ansaldi *et al.* 2016), that approach is not pursued here, due to the breakdown of the slowly-diverging mean flow assumption in the vicinity of the shocks.

The complexity of the current approach may be attributed to the requirement to carefully extract the source parameters from the flow field. This is crucial for accurate sound pressure level predictions using an ‘inside-out’ approach. While direct computation of the sound field may be more straightforward, provided a shock-containing LES jet is available, the authors would like to reiterate that the present goal is to shed light on the BBSAN generation mechanisms and not simply to obtain the far-field sound. By constructing three source models with increasing complexity, this approach also allows the role of non-linearity to be partially revealed.

## 5. Nearfield predictions and comparisons

### 5.1. Shock-cell component: Comparison of PIV data and modified P-P model

Comparisons between the modified P-P model and experimental PIV data for the shock-cell disturbances are shown in figure 4. The  $x - r$  contour maps show good agreement for each of the flow variables  $[u_x, u_r, \rho]_s$  in phase and amplitude. The axial decay in the strength of the shock-cell structure is also well-captured by the model. There is poor agreement in the shear layer region as expected; the model uses a vortex-sheet approximation which is non-physical along the nozzle lip line. While there remain differences between model and experimental data, figure 4 illustrates that the salient qualitative features of  $\mathbf{q}_s$  are preserved by the model. Furthermore, we expect these small discrepancies to have minimal impact on the far-field noise as they are dwarfed by other effects, as discussed in appendix B.

As alluded to in section 2.2, a spatial Hann window is used to smoothly truncate the source domain in the axial direction. For the axial source domain of length  $L$ , the window function  $w_x$  is given by

$$w_x(x) = \begin{cases} 1 & x < x_w, \\ \frac{1}{2} \left[ 1 + \cos \left( \frac{\pi}{L_w} (x - x_w) \right) \right] & x_w \leq x \leq L, \end{cases} \quad (5.1)$$

where  $x_w$  and  $L_w$  are the start and length of the window respectively. As the experimental shock-cell disturbances are weak by  $x = 10D$ , and since the equivalent source is the product of  $\mathbf{q}_s$  and  $\mathbf{q}_t$  (equation (2.11)), contributions to the BBSAN source at locations  $x > 10D$  are negligible. Hence, the value of  $x_w = 15$  was found to be suitable and  $L_w$  was chosen to ensure zero amplitude at the boundary of the integration domain.

### 5.2. Wavepacket component: Comparison of PSE and LES

We compare the PSE predictions with the wavepackets extracted from LES data for a selection of frequencies and the first azimuthal mode ( $m = 0$ ). The PSE solver used in this study has previously been validated for supersonic flows (Kleine *et al.* 2017). The aim of this section is not to show in-depth comparisons, but rather to highlight key similarities and differences which may impact the BBSAN source composition. Detailed investigations have previously been carried out by Cavalieri *et al.* (2013) and Sinha *et al.* (2014) for subsonic and supersonic jets respectively. Thus, for brevity, only comparisons for axial velocity fluctuations are shown; a similar degree of agreement is obtained for the remaining components of  $\mathbf{q}_t$ .

It is well known that PSE solutions produce poor agreement with LES data for  $St \leq 0.3$ , as a weaker KH growth rate becomes comparable with the Orr mechanism induced by nonlinear interactions (Tissot *et al.* 2017a; Schmidt *et al.* 2018; Pickering *et al.* 2020). Discrepancies at low frequencies, however, do not affect the results presented in § 6, since BBSAN dominates at higher frequencies. Hence, comparisons are only shown for  $St > 0.4$ .

For comparison of wavepacket structure, Spectral Proper Orthogonal Decomposition (SPOD) is also performed on the LES data. SPOD decomposes the flow into an orthogonal basis optimally ranked by energy content. The smaller-scale turbulence will be filtered out, highlighting the coherent structures present in the flow. SPOD has been used to show an acceptable degree of fidelity between PSE predictions and SPOD-filtered LES data for the  $M = 1.5$  jet (Rodriguez *et al.* 2013; Sinha *et al.* 2014). For a given azimuthal mode and frequency, we define the spectral eigenvalue problem (Towne *et al.* 2018)

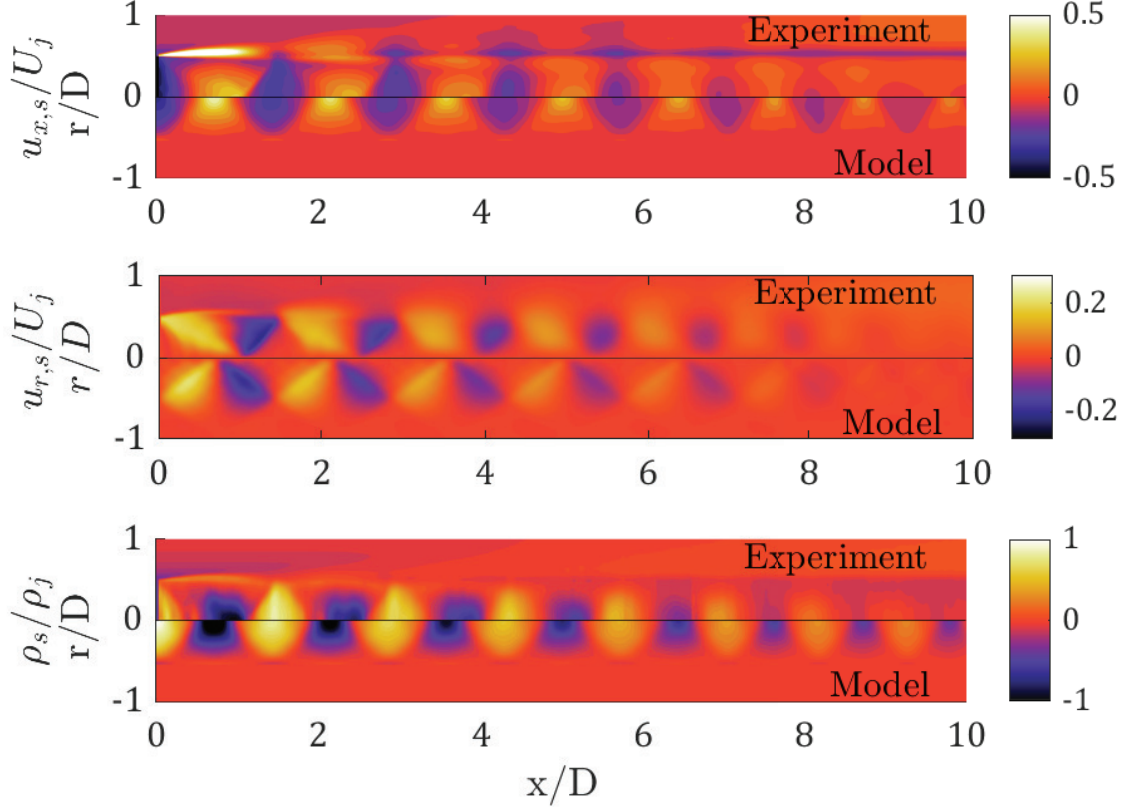


Figure 4:  $x - r$  contour plots of flow variables  $u_x, u_r, \rho$  from PIV experiments (top-plane) and model (bottom-plane).

$$\int \mathcal{Q}_{ij}(\mathbf{x}_1, \mathbf{x}_2; m, \omega) \Psi(\mathbf{x}_2; m, \omega) d\mathbf{x}_2 = \lambda(m, \omega) \Psi(\mathbf{x}_1; m, \omega), \quad (5.2)$$

where  $\mathcal{Q}_{ij}$  is the cross-spectral density matrix of the flow variable of interest,  $\lambda$  and  $\Psi$  are the eigenvalues and a set of linearly-independent spatial eigenfunctions respectively. Both eigenfunctions and eigenvalues are obtained using the snapshot method described in Towne *et al.* (2018).

Figure 5 shows the real component of axial velocity for the axisymmetric mode  $m = 0$ . For each frequency, the PSE solutions (right column) are scaled using the averaged  $\mathcal{A}$  constant. The contour maps show the PSE predictions are able to capture both the near-field fluctuations and the propagating Mach wave radiation. As frequency increases, the axial location of the wavepacket peak ( $x_0$ ) shifts upstream and the spatial wavelength decreases. As expected, the mode shapes, wavelength and phase of the PSE and the leading SPOD (left column) fields exhibit good agreement.

Success in amplitude matching between PSE and LES fields is observed in the radial shapes at the axial station  $x = 4D$  in figure 6. For the PSE solutions, the drop in amplitude of  $u_x$  near the lip line is due to the phase jump either side of the mixing layer in a perfectly-coherent wavepacket (Cavalieri *et al.* 2013). This is not observed in the LES data due to the jitter of the coherent wavepackets (Cavalieri *et al.* 2013; Baqui *et al.* 2015). By comparing the spatial structure of the shock disturbances shown in figure 4 with the wavepacket radial profiles, the distributed nature of the BBSAN source is apparent. The wavepacket has non-zero support within the jet potential core, allowing

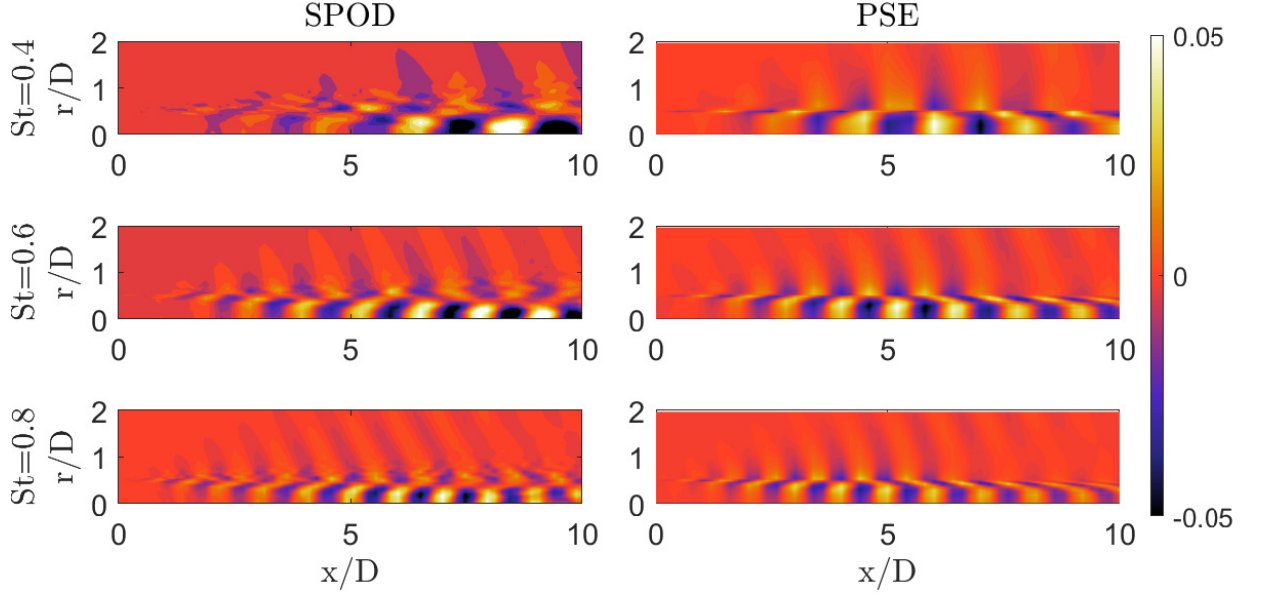


Figure 5: Comparison of real parts of  $u_x$  between the extracted wavepacket from the first SPOD mode (left column) and PSE predictions (right column) for  $m = 0$ . Flow quantities are normalised by the ideally-expanded condition.

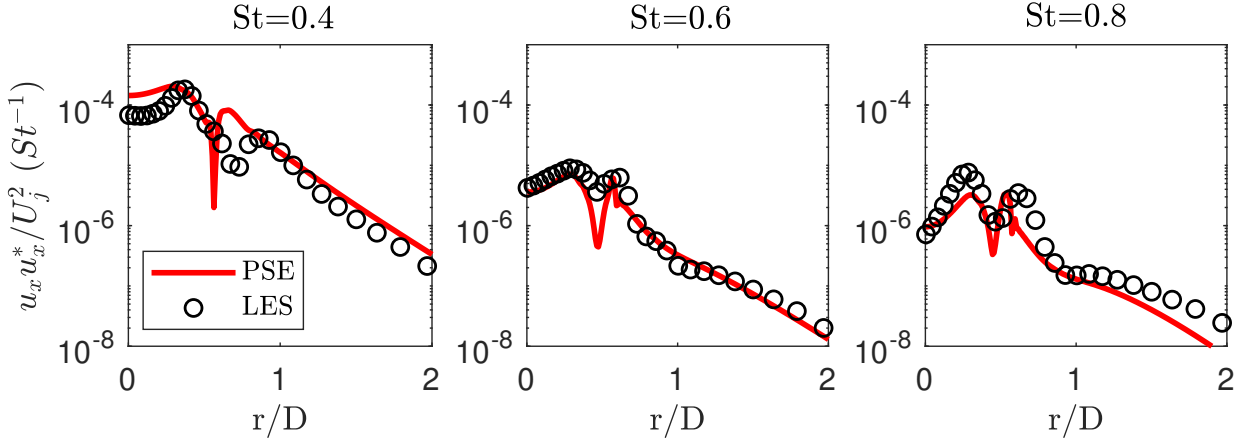


Figure 6: Radial cross-section comparisons of  $u_x$  between LES (symbols) and PSE (lines) for  $m = 0$  at  $x = 4D$ .

it to interact with the shock-cell structure and generate BBSAN. This will be shown in the source maps presented in § 7.

The centreline axial velocity fluctuations in figure 7 increase in energy by approximately four orders of magnitude between the nozzle exit and the location of the peak value ( $x_0 \approx 5D$ ). This amplification is also observed in hot-wire measurements in subsonic jets (Cavalieri *et al.* 2013). As the matching location is at the wavepacket peak, we observe disagreements close to the nozzle exit similar to previous studies (Cavalieri *et al.* 2013; Antonialli *et al.* 2021). This mismatch would have minimal effect on the BBSAN prediction since much of the reconstructed source energy exists further downstream (figure 14). There is ongoing work to investigate the excitation mechanisms of the shear layer at the nozzle and how this affects the wavepacket downstream (Kaplan *et al.* 2020). We also observe that, relative to the LES data, PSE underestimates amplitudes in the downstream portion of the jet ( $x > 6D$ ). This well-known inconsistency has previously been attributed to the dominance of nonlinear effects, and fluctuations that

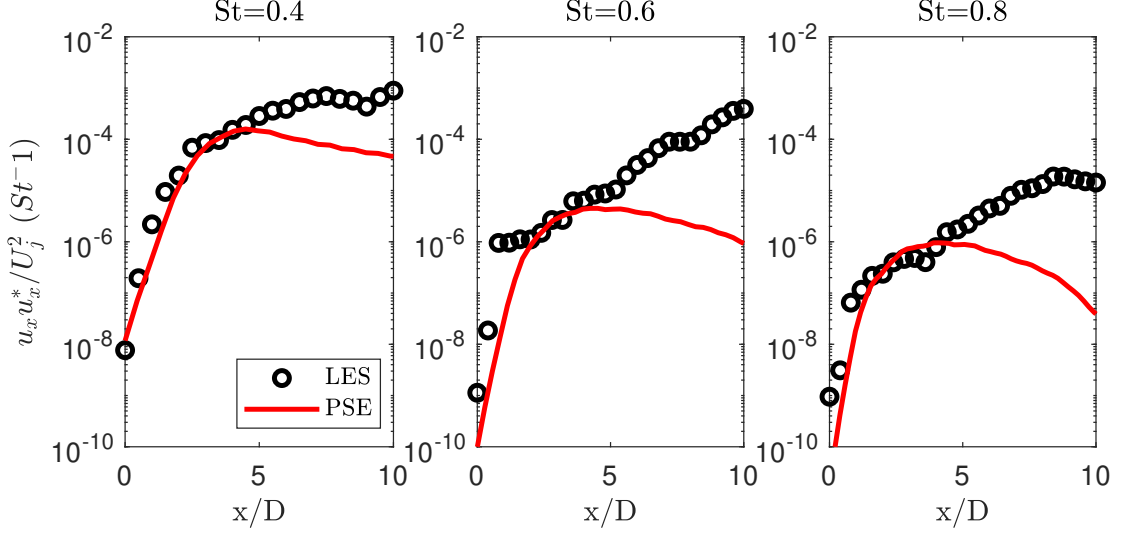


Figure 7: Centreline axial velocity fluctuations from LES (symbols) and PSE (lines) for  $m = 0$ .

are uncorrelated with the extracted wavepackets (Suzuki & Colonius 2006; Gudmundsson & Colonius 2011; Cavalieri *et al.* 2013). Since shock fluctuations remain significant past  $x = 5D$  (figure 4), the discrepancy in turbulent intensity may lead to differences in BBSAN prediction between the LES and PSE model. A more detailed discussion of this issue can be found in § 7.

Lastly, from equation (1.3), it is evident that the BBSAN peak frequency strongly depends on the convection velocity of the large-scale structures. The convection velocity is related to the hydrodynamic wavenumber  $k_h$ , which is extracted from the PSE solution as the real component of the eigenvalue  $\alpha_{m,\omega}$

$$u_c(x_1) = \frac{\omega}{k_h} = \frac{2\pi St}{Re(\alpha_{m,\omega}(x_1))}. \quad (5.3)$$

For the LES case,  $u_c$  can be computed using the argument  $\phi$  of the CSD (Maia *et al.* 2019),

$$u_c(x_1) = \frac{\omega}{k_h} = \omega \left( \frac{\partial \phi}{\partial x_2} \right)^{-1}. \quad (5.4)$$

Figure 8 shows the extracted  $m = 0$  phase velocities for PSE predictions (equation (5.3)) and the LES results (equation (5.4)). Over a range of frequencies,  $u_c$  is estimated as  $\approx 0.7 - 0.8U_j$  over much of the flow domain. Despite disagreements within the first diameter, agreement improves further downstream. This result suggests that both PSE and LES-based sources should predict comparable BBSAN peak frequencies according to equation (1.3).

We have shown that many of the wavepacket features extracted from LES are reproducible with PSE. In line with previous studies (Rodriguez *et al.* 2013; Sinha *et al.* 2014; Sasaki *et al.* 2017a), good agreement is also observed at higher azimuthal wavenumbers. We reiterate that our goal is not to find optimal agreement between PSE model and LES data, but rather, to compute an appropriate scaling parameter for the indeterminate PSE amplitude.



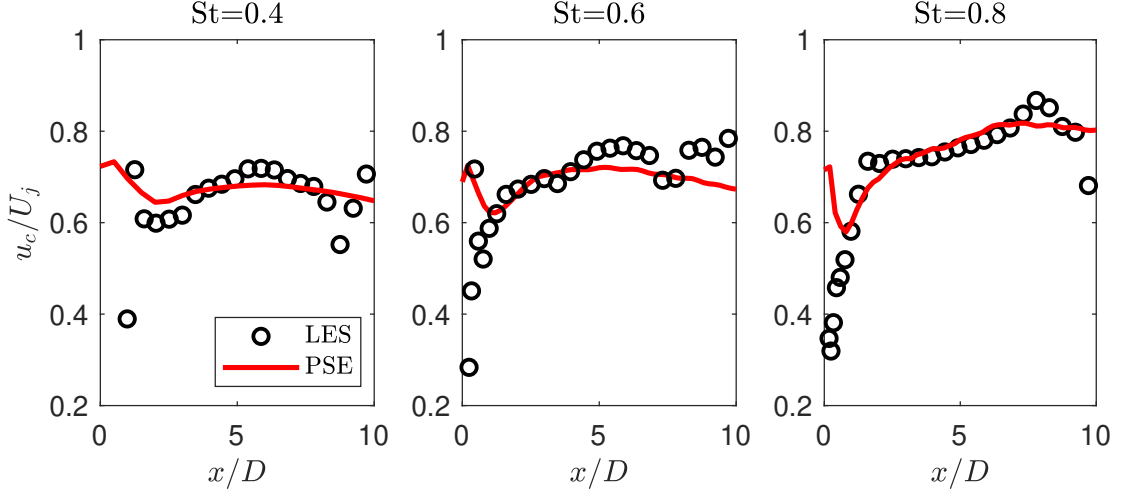


Figure 8: Convection velocity as a function of axial position for  $m = 0$ .

## 6. Far-field acoustic spectra and comparisons with experiment

Far-field acoustic predictions based on the BBSAN source models are examined in comparison with the experimental far-field noise measurements detailed in section § 3.3. There are some points to be highlighted in the presentation of these results. Firstly, we reiterate that, apart from the modifications to the P-P shock-cell model and scaling of the PSE to the LES data, the source is entirely built from flow information alone. The shock-cell representation used for both PSE and LES-based models is identical.

As shown in figure 1, the polar angle  $\theta$  is nominally taken from the downstream jet axis. Since the acoustic measurements are taken along a cylindrical surface at a moderate distance of  $R = 11D$  from the jet centreline, the origin of the polar angle is moved to  $X_o = 5D$  instead of the nozzle exit. This modification enables comparison with directivity results from other far-field jet databases in literature, where microphones are placed much further from the jet, and also provides a small correction in predictions of peak frequency which is consistent with equation (1.3).

After computing the far-field PSD from equation (2.7), the sound pressure level (SPL) is defined by

$$SPL = 10 \log_{10} \left( \frac{\langle pp^* \rangle}{p_{ref}^2} \right) \quad (6.1)$$

where  $p_{ref} = 20 \mu Pa$  and SPL is in units of dB/St.

### 6.1. Directivity contour maps

To observe the spectra and directivity trends of BBSAN, we first present  $St - \theta$  contour maps in figure 9, from experimental data and model predictions. Unlike Tam (1987) and Ray & Lele (2007), who compared predictions to the full acoustic signal, we retain the dependence on azimuthal wavenumber and show results for the first three modes ( $m = 0, 1$  and  $2$ ). To highlight the theoretical BBSAN peak locations, peak frequencies computed using equation (1.3) are also indicated as dashed lines for the first three shock-cell modes ( $n = 1, 2$  and  $3$ ), where we have assumed the convection velocity to be  $u_c = 0.7U_j$ .

As expected in the first column of figure 9, the experimentally measured BBSAN lobe is visible for  $St > 0.4$  between  $65^\circ < \theta < 120^\circ$ , and peak frequency increases as observer position moves downstream. Screech peaks are clearly discernible as discrete frequencies, with the fundamental located at  $St = 0.31$ . The BBSAN primary lobe agrees largely with the theoretical peak frequency prediction at sideline and downstream positions,



though some discrepancy develops at more upstream angles ( $\theta > 110^\circ$ ). This could be due to the measurements not being performed in the ‘true’ far-field, or may arise from the variation in convection velocity as a function of frequency. The frequency of the second shock-cell mode ( $n = 2$ ) peak is consistently higher than theory, which may arise from the mismatch in Mach numbers (and hence shock-cell spacing), between the PIV and acoustic databases (see figure 16a).

To accompany the measured acoustics, figure 9 provides predictions based on the BBSAN source models of § 4. We present three models for the reconstructed BBSAN source, each with a different description of  $\mathbf{q}_t$ . The LES model is presented in the second column of figure 9, while those described by PSE solutions with unit coherence or with coherence decay are shown in columns three and four respectively. We note that discrete peaks do not feature in either of the LES or PSE model predictions, as the screech mechanism is not modelled; the LES database is of an ideally-expanded jet and hence cannot produce screech while on-going works exist looking at the screech problem using a global framework instead of PSE (Beneddine *et al.* 2015; Edgington-Mitchell *et al.* 2020). In addition, significant underprediction occurs at low frequencies ( $St < 0.4$ ), as expected; the source term in equation (2.11) includes only the high-frequency BBSAN component.

Far-field noise predictions using the LES model exhibit fair agreement with measured data across a wide frequency and directivity range. The best agreement is in the sideline direction for both amplitude and peak frequency predictions; the LES model matches the experimental measurements to within  $\pm 2\text{dB/St}$ . The model follows the theoretical BBSAN peak from equation (1.3), even at upstream angles where the peak half-width narrows. This is unsurprising since equation (1.3) assumes that BBSAN is produced by the interaction of an instability wave with the stationary shock-cell structure, with the resulting difference waves effectively behaving as the source of the far-field noise. In addition, the convection velocity of the extracted LES wavepacket (figure 8) is approximately  $0.7U_j$ . The narrowing of the BBSAN lobe at upstream angles is also observed in the acoustic measurements of Norum & Seiner (1982).

Nevertheless, there remain key differences between the LES model and measurements. At slightly downstream angles, overprediction occurs at high frequencies ( $St \approx 1$ ). The overprediction in sound amplitude results in the BBSAN lobe being broader in directivity than the experimental spectra for all three azimuthal modes. The mismatch could be related to the simplification of the Lighthill stress tensor  $T_{ij}$ , where cancellation between different components is known to occur over regions away from the sideline direction (Freund 2003). Bodony & Lele (2008) found, for a  $M_j = 2.0$  ideally-expanded jet, that using only the momentum term ( $\rho u_i u_j$ ) overpredicts the sound amplitude by over  $20\text{dB/St}$  at high frequencies. Since we retain the momentum term alone (2.3), cancellation effects due to entropic and higher-order terms of the equivalent BBSAN source are not accounted for. The definition and simplicity of the present model prevents an investigation into the relevance of this potential phenomenon. Future investigation on the role of the entropic term in shock-containing flows, as a function of frequency and for various observer locations, would be valuable as previous studies only investigated the role of entropic inhomogeneity for a limited set of polar angles in non shock-containing flows (Freund 2003; Uzun *et al.* 2004; Bodony & Lele 2008).

Despite the simplicity, predictions based on the reduced-order PSE model are also encouraging. The primary BBSAN lobe is well-predicted and has similar trends to that of the LES model. This indicates that the proposition of Tam & Tanna (1982), that BBSAN is generated as a result of the interaction between the quasi-periodic shocks and large-scale turbulent structures, is indeed well-founded. Agreement in both peak frequency and amplitude in the present results further substantiates the applicability

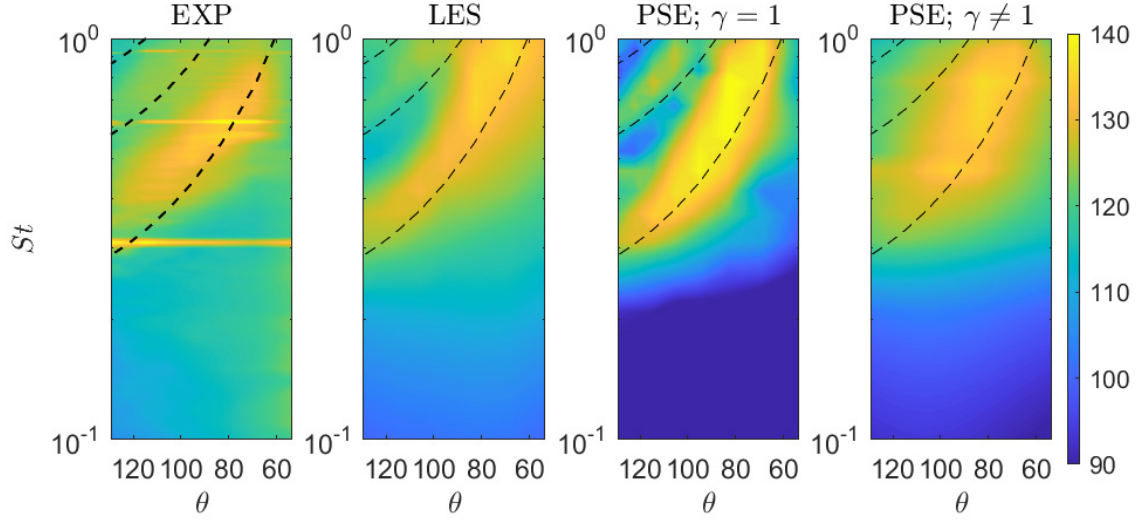
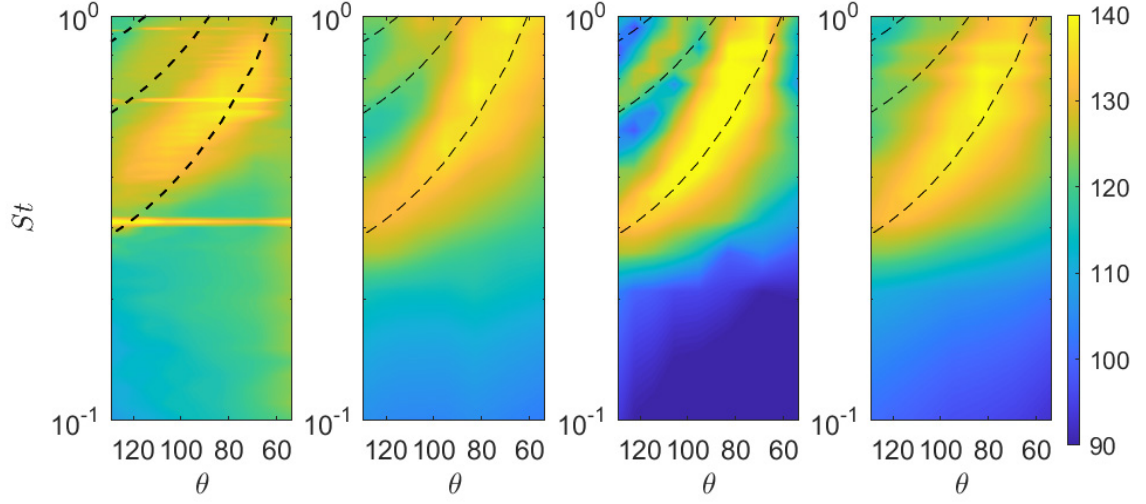
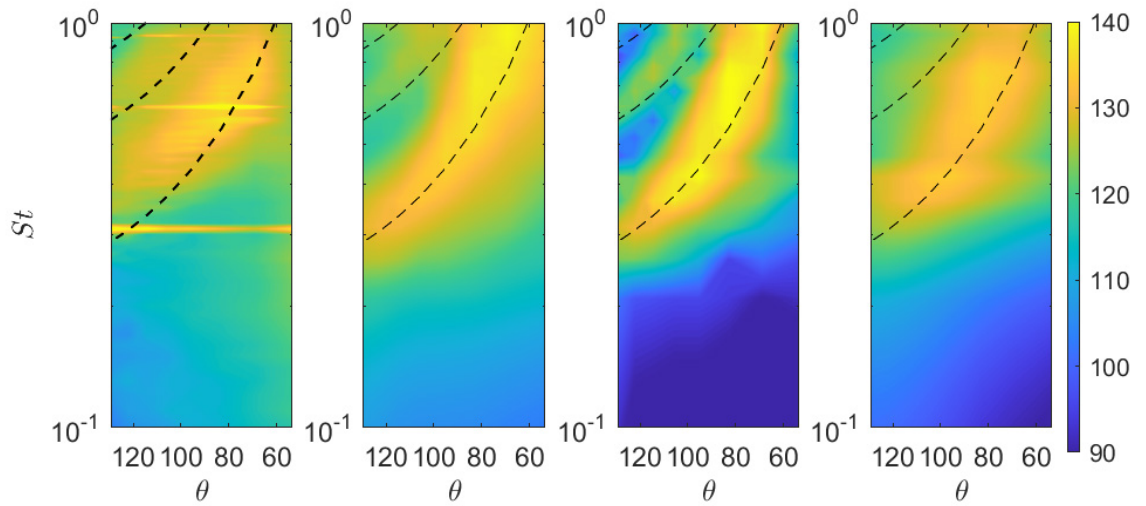
(a)  $m=0$ .(b)  $m=1$ .(c)  $m=2$ .

Figure 9:  $St - \theta$  directivity contour maps of sound pressure level spectra at  $R = 11D$ . Contours are in dB/St.

of the interpretation of Tam & Tanna (1982). For upstream angles, the assumption of perfectly-coherent wavepackets is found to result in overprediction of peak intensity, as well as marked dips in the spectra between primary and secondary shock-cell mode signatures. When coherence decay is incorporated, however, the directivity map is smoothed and the dips are reduced. This effect was reported by Wong *et al.* (2019b) for a simple equivalent line-source model. Directivity changes occur as the source energy is spread in wavenumber space between shock-cell modes. By comparing the predictions from both PSE and LES-based models with experimental measurements, it is clear that a linear wavepacket model requires modification to account for nonlinearities (e.g. wavepacket jitter) in order to successfully predict BBSAN amplitude. The effects of coherence decay are examined in § 6.2.

### 6.2. Far-field noise spectra

Before showing azimuthally-decomposed spectra, the total measured sound-field is presented along with reconstructed model predictions using the first three azimuthal modes in figure 10 at different polar angles. For each observer position, predictions from both the LES (blue squares) and PSE models are shown, along with the full (solid red) acoustic spectra. The PSE predictions are further distinguished by either unit coherence (maroon circles) or coherence decay (green crosses). As shown in the contour directivity plots in figure 9, the models miss the peak BBSAN frequency at upstream angles. Nevertheless, excellent agreement in peak amplitude is observed ( $\pm 2\text{dB/St}$ ) for the primary ( $n = 1$ ) peak across the directivity range. Even with a small number of inputs, the simplified PSE model with perfect coherence performs particularly well in capturing peak amplitudes, though large dips are observed as either the polar angle or frequency increases. There is less success in predicting the secondary lobe ( $n = 2$ ) due to its increased azimuthal modal complexity, requiring 4-5 modes to reconstruct the total signal (Wong *et al.* 2020).

To explore the similarities and differences between experimental and model spectra in further detail, figures 11-13 provide spectra for each of the azimuthal modes. In addition to the total signal, azimuthally-decomposed data (solid black) is shown. In terms of peak frequency and amplitude, we observe fair agreement between models and experiment for both the primary and secondary BBSAN peaks. Peak amplitudes are within  $\pm 2\text{dB/St}$  accuracy and predicted peak half-width is most faithful to the measured spectra in the sideline direction ( $\theta = 95^\circ$ ).

Previous studies have compared stability-based BBSAN models to the total acoustic signal (similar to figure 10). Ambiguity in amplitude of model predictions has led to the azimuthal dependence being dropped; Ray & Lele (2007) assumed a ‘white noise’ spectrum while Tam (1987) assumed the equivalent source to be solely axisymmetric. The spectra of the equivalent source models are then fitted to experimental acoustic data. The ill-posed nature of such ‘outside-in’ approaches may lead to the deduction of source parameters not observed in the jet. Indeed, the azimuthally-decomposed acoustic spectra provided in figures 11-13 and the recent measurements performed by Wong *et al.* (2020) indicate that these assumptions are invalid. For instance, the roll-off at high frequencies of individual azimuthal modes is steeper than the total signal (c.f. Ray & Lele 2007), and the spectral shape of each azimuthal mode is not identical (c.f. Tam 1987).

Using a direct ‘inside-out’ approach, inconsistencies in previous BBSAN amplitude predictions are now nullified. Examination of each individual azimuthal mode suggests that the proposed model can correctly capture the important flow dynamics related to BBSAN. Along with the findings from Wong *et al.* (2019b), the results also offer a convincing explanation for the ‘missing sound’ at high frequencies, as observed by both

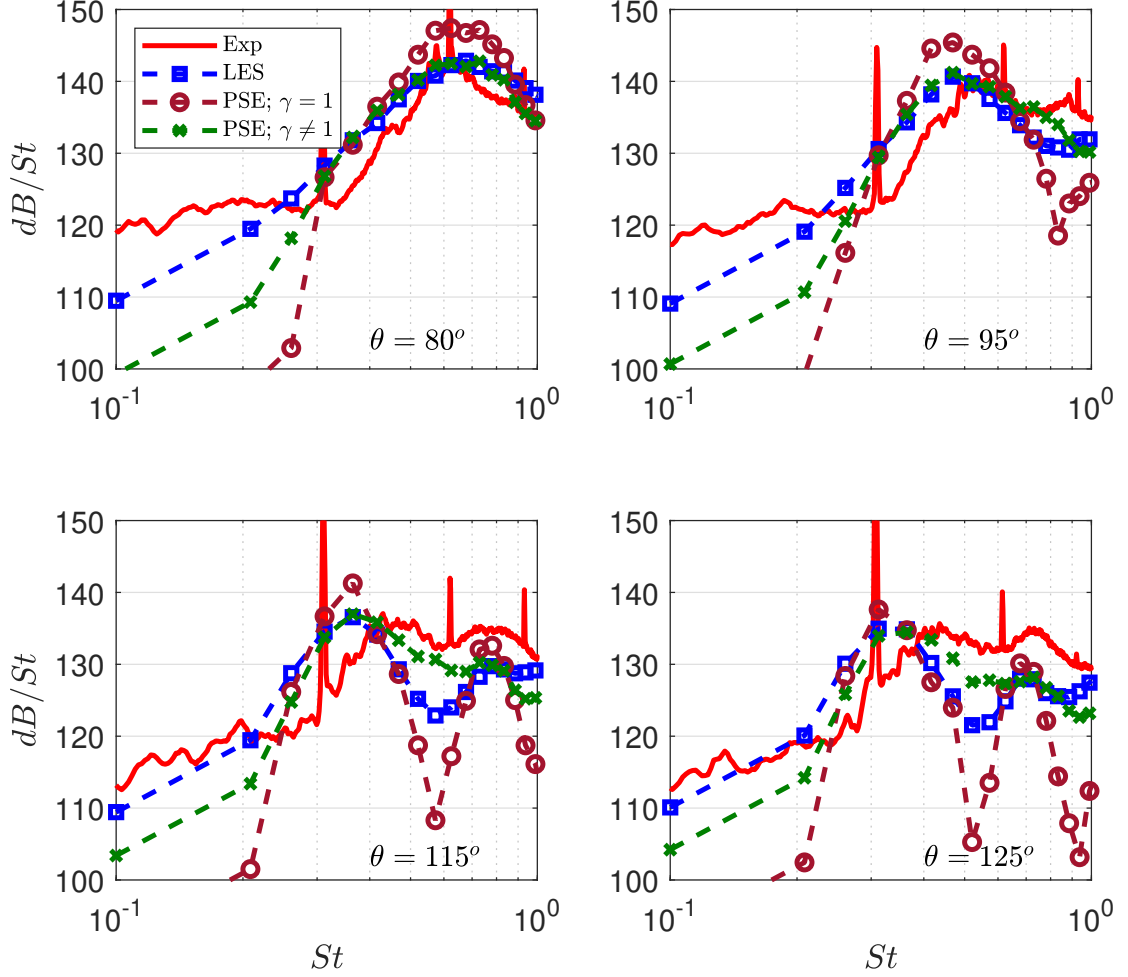


Figure 10: Comparison of acoustic spectra for total measured signal and reconstructed model using the first three azimuthal modes  $m = 0, 1, 2$ .

Suzuki (2016) and Ray & Lele (2007) at upstream angles. It is clear that the secondary BBSAN peak is due to the interaction of the wavepacket with the second shock-cell mode which was not accounted for in either study.

As alluded to in § 6.1, there are regions where the models perform poorly. At upstream angles ( $\theta = 115^\circ$  and  $125^\circ$ ), while the agreement in peak amplitude is within  $\pm 2\text{dB/St}$ , peak frequency is underpredicted. At slightly downstream positions ( $\theta = 80^\circ$ ), the predicted half-width of the primary BBSAN peak is larger than measured. As well as the overprediction at high frequencies, the second harmonic of the screech tone coinciding with the BBSAN peak may explain why the models predict higher peak frequencies ( $St_p \approx 0.6$ ) than the experiment ( $St_p \approx 0.55$ ). The presence of screech is known to attenuate the axial extent of downstream shock cells (André *et al.* 2013). Currently, this cannot be verified as flow measurements are not available to supplement the acoustic database.

We turn our focus to comparing the efficacy of our models. With minimal inputs, the reduced-order model using a perfectly coherent ( $\gamma = 1$ ) wavepacket source does a respectable job in predicting the primary and secondary BBSAN peaks ( $n = 1, 2$ ). This is a confirmation of the modelling approach first proposed by Tam & Tanna (1982); BBSAN is generated by the interaction between large-scale coherent structures and the shock-cell system. In terms of peak noise in the far-field, it is clear that second-order statistics of

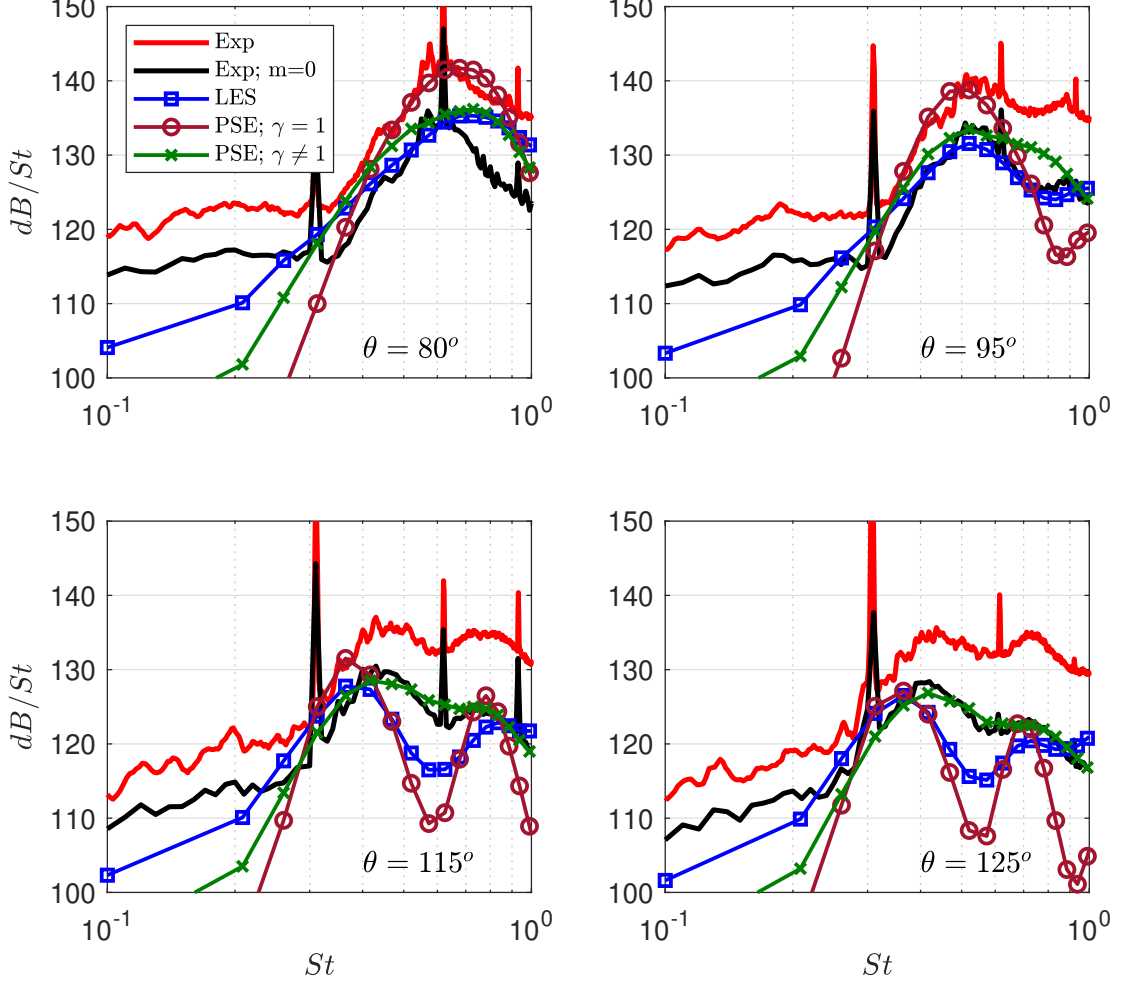


Figure 11: Comparison of acoustic spectra for azimuthal mode  $m = 0$ .

the flow are unimportant. The ability for a simple model to capture both amplitude and peak frequency renders it a promising candidate for future predictive schemes.

Away from the peaks, however, the linear wavepacket source presents some drawbacks. In particular, the ‘dips’ mentioned previously are evident; the discrepancy is more severe at upstream angles, reaching up to 20dB/St less than the measured spectra. The amplitude prediction of the primary peak also becomes questionable over downstream angles (by up to 10dB/St). Agreement in SPL is recovered with the inclusion of two-point coherence information. The improvement was predicted using a model line-source problem (Wong *et al.* 2019b), which included coherence information to represent the jittering of wavepackets due to the action of background turbulence (Zhang *et al.* 2014; Tissot *et al.* 2017b). Together with the LES model, which is the most complete representation of the source CSD, figures 11-13 demonstrate the appropriateness the proposed BBSAN modelling framework.

The dips in figures 11-13 are similar to those observed by Tam (1987), attributed in that study to shock-cell unsteadiness due to interaction with turbulence. It was suggested that the fluctuating motion of the shocks could lead to further peak broadening, with the maximum shock-cell unsteadiness located near the end of the potential core. A quantitative measure for shock-cell unsteadiness was not available at the time and an empirical adjustment to the source structure was made to account for this effect. We show, however, that in fact most of the broadening is instead attributable to wavepacket jitter; nonlinear effects acting on the linear wavepackets are deduced from the LES data as

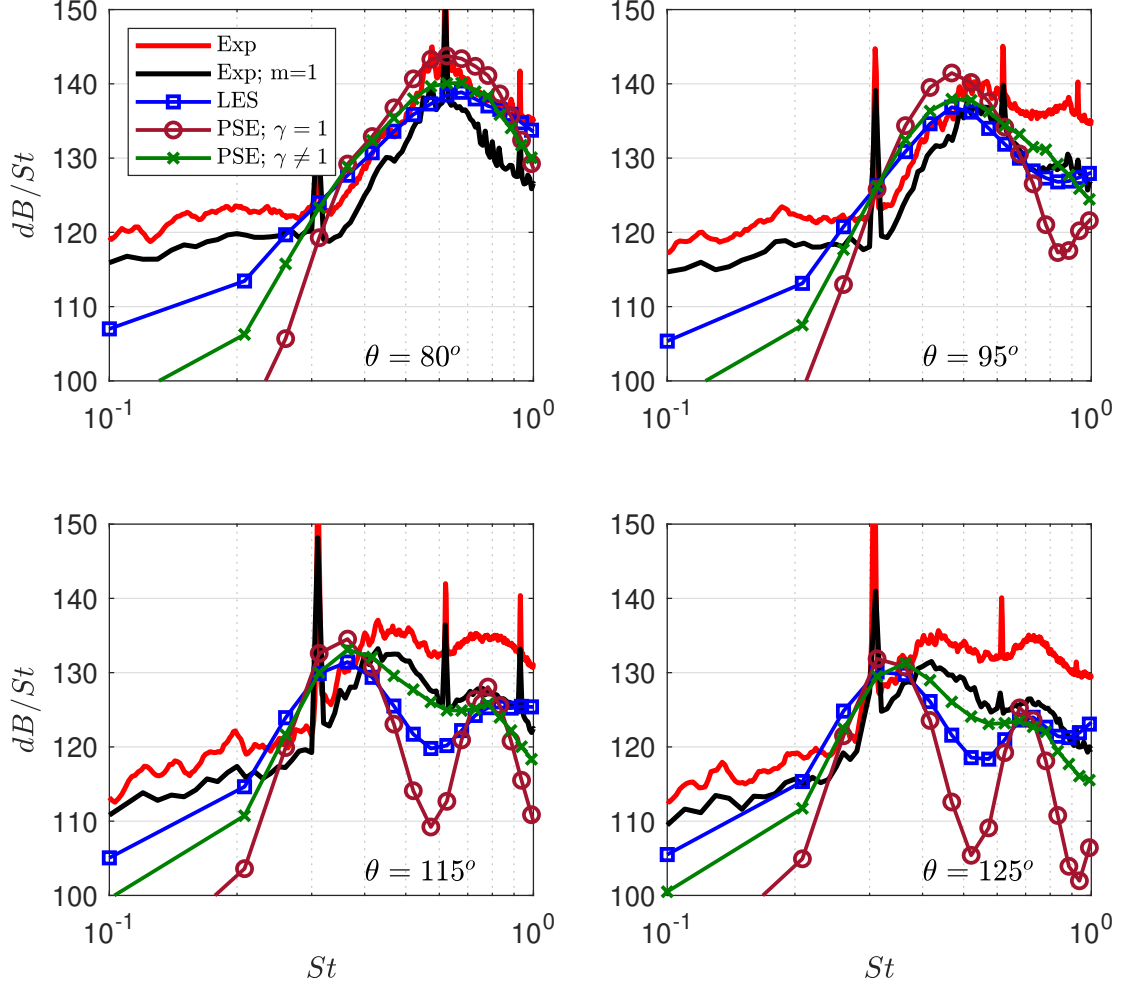


Figure 12: Comparison of acoustic spectra for azimuthal mode  $m = 1$ .

coherence decay and imposed onto the PSE model. While a large portion of the ‘missing sound’ can be attributed to wavepacket jitter (up to 15dB/St), the dips are not entirely eliminated in the LES model spectra (e.g.  $St = 0.6$  for  $\theta = 115^\circ$ ). In reality, the shock structure is unsteady and this phenomenon is not captured by the model (§ 4.4) since the shocks are modelled as zero-frequency waves. The application of  $\mathbf{q}_s$  and  $\mathbf{q}_t$  as distinct variables in our model further restricts the ability to describe how turbulence affects the shocks, and vice-versa. In addition, apart from unsteadiness due to large-scale structures (Tam 1987), periodic shock oscillations in a screeching jet (such as the one used presently) could be attributed to the passage of upstream-travelling acoustic waves (Panda 1998; Edgington-Mitchell *et al.* 2018) or coupling between the shock cells. Due to the current modelling framework, the effects of shock unsteadiness on BBSAN remains unknown.

Based on the above observations, we might hypothesise that the prevailing discrepancies evident in figures 11-13 indicate that both wavepacket jitter (modelled as coherence decay deduced from an ideally-expanded jet) and shock unsteadiness are essential to the composition of an equivalent BBSAN source. Another possibility is that the measure of coherence in a shock-containing jet differs nontrivially to that of an ideally-expanded jet. Investigation into such a coupling between wavepacket dynamics and the shock structure is outside the scope of this study, but ought to be considered in future work. A possible avenue to explore will be to perform resolvent analysis (Schmidt *et al.* 2018; Lesshafft *et al.* 2019) on a shock-containing jet. Since the artificial separation of  $\mathbf{q}_t$  and  $\mathbf{q}_s$  may be avoided, by looking at the relevant forcing modes, resolvent analysis may shed light



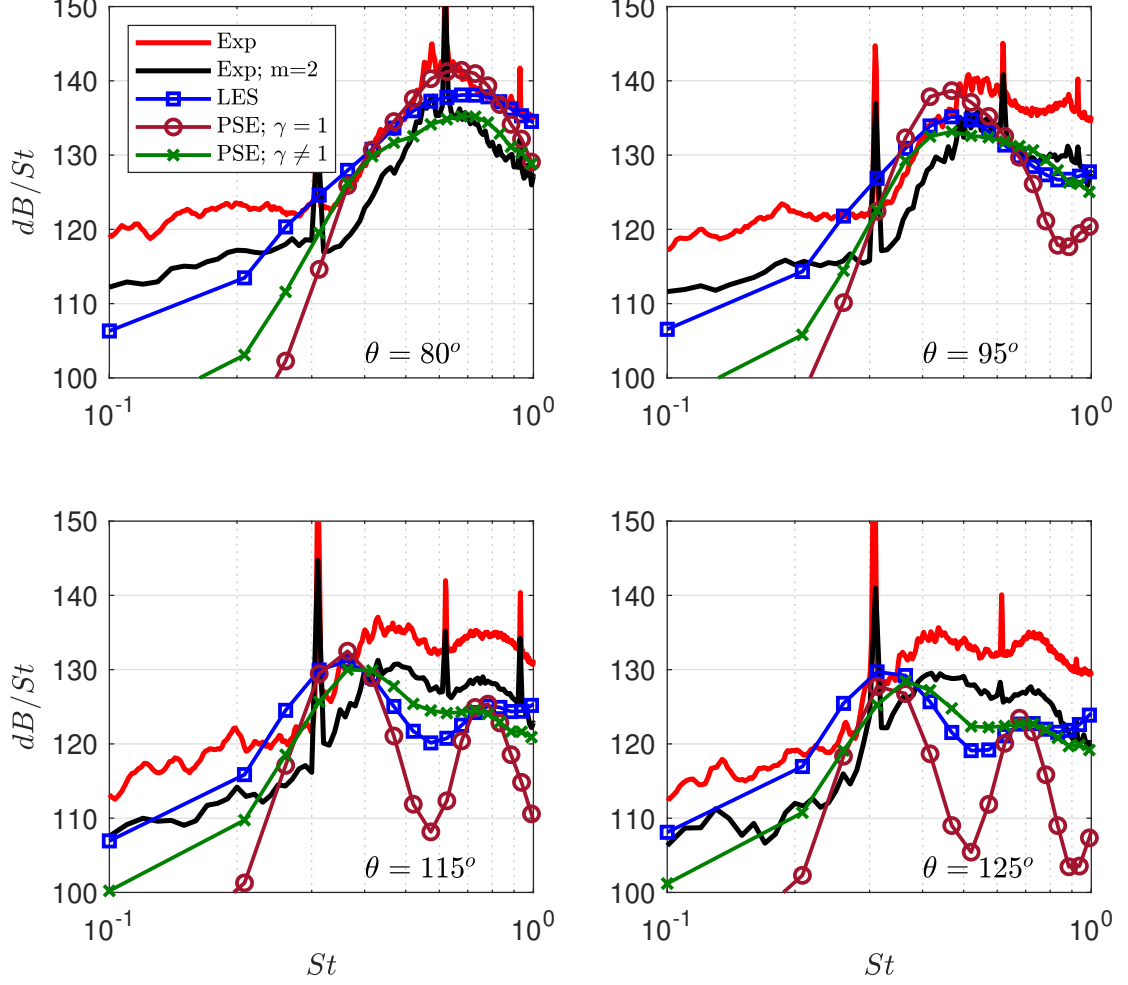


Figure 13: Comparison of acoustic spectra for azimuthal mode  $m = 2$ .

on the exact roles of both wavepacket jitter and shock-cell unsteadiness in relation to BBSAN generation.

At upstream angles ( $\theta = 115^\circ$  and  $125^\circ$ ), we also observe that the PSE model with coherence decay (green crosses) gives more favourable predictions than the LES model when compared to the measured spectra. This is somewhat unexpected since for the LES model, flow variables are directly substituted into the source CSD, while the PSE solution only provides the statistical wavepacket. From equation (4.21), an adequate description of the original acoustic source requires matching of not only average amplitude and phases of wavepackets (provided by the PSE), but also a correct description of the two-point coherence function. A mismatch in the description of any one of these physical traits will translate into disagreement in the predicted acoustic field. We explore this inconsistency in § 7 by inspecting the reconstructed BBSAN sources.

## 7. Source term characteristics

This sections aims to highlight the differences between the reconstructed sources using the various descriptions for  $\mathbf{q}_t$  (LES, PSE with and without coherence decay). For brevity, we will only show the  $S_{11}$  component for the  $m = 0$  azimuthal mode at frequencies  $St = 0.6$  and  $0.8$ . The other source term components and azimuthal modes display similar behaviour.

Figure 14 shows the reconstructed BBSAN sources for both the LES and PSE cases.

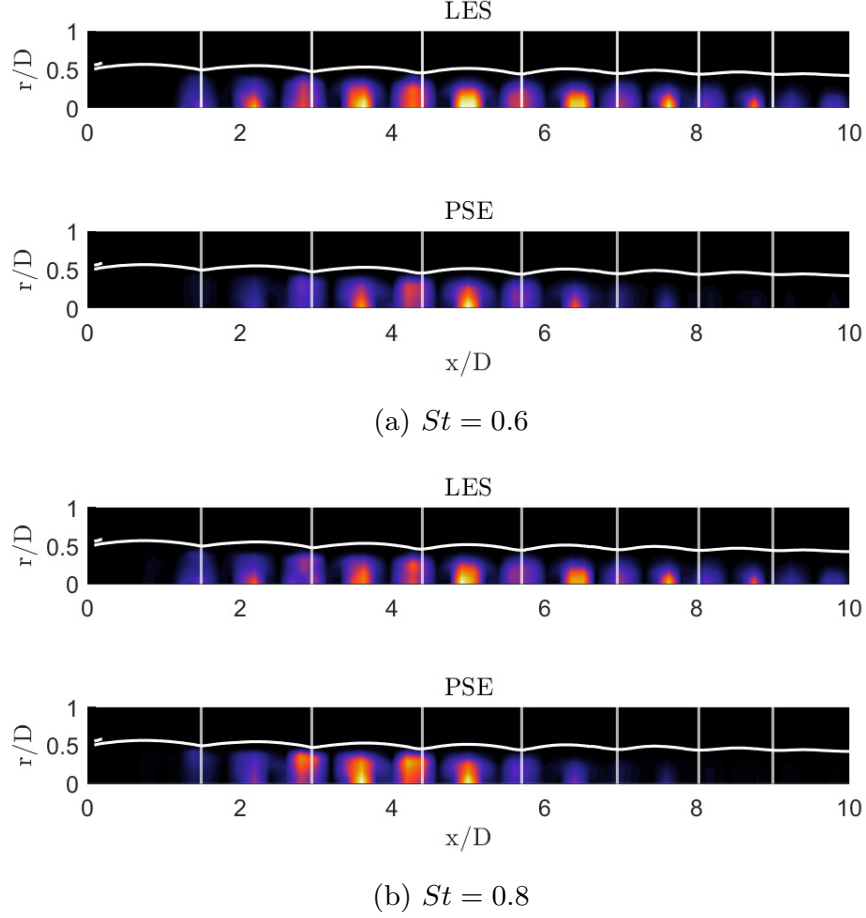


Figure 14:  $x - r$  contour maps of the reconstructed BBSAN source PSD. Intensity levels are normalised by the maximum value.

At each radial station, the PSD of the source in equation 2.8 is plotted by setting  $x_1 = x_2$ . The sources of the two PSE cases ( $\gamma = 1$  and  $\gamma \neq 1$ ) are identical, since the inclusion of coherence decay does not affect the PSD. To aid in visualisation of the shock positions, the sonic line of the jet plume and the shock-reflection points from the PIV data are shown. Contour levels are normalised by the maximum level. Unlike subsonic jets (Maia *et al.* 2019), we do not observe a smooth asymmetric Gaussian envelope. Due to the interaction with the shocks, the source is semi-distributed in both axial and radial directions. For each shock cell, there are two source locations; just upstream of the compression-wave focus and before the shock reflection points. Unlike the source maps of Kalyan & Karabasov (2017) and Tan *et al.* (2018) which are focused on the sonic line in the shear layer, the source exists inside the jet plume. The present distributions are supported by other models (Ray & Lele 2007; Shen *et al.* 2021) and also experimental measurements (Savarese *et al.* 2013). Source intensity is apparent between  $2D \leq x \leq 8D$  downstream, and most intense between the third and fifth shock cells. This is slightly upstream compared to those measured by Norum & Seiner (1980) and Seiner & Yu (1984) for underexpanded jets operating at similar conditions. As frequency increases, the wavepacket contracts (figure 5) and hence the source shifts towards the nozzle, in line with previous modelling efforts (Ray & Lele 2007; Suzuki 2016; Patel & Miller 2019).

Evidently, the LES description has source intensity extending past  $x = 8D$  while the PSE models do not. This is due to the differences between the LES and PSE description of the wavepacket; the PSE solution is unable to capture the downstream



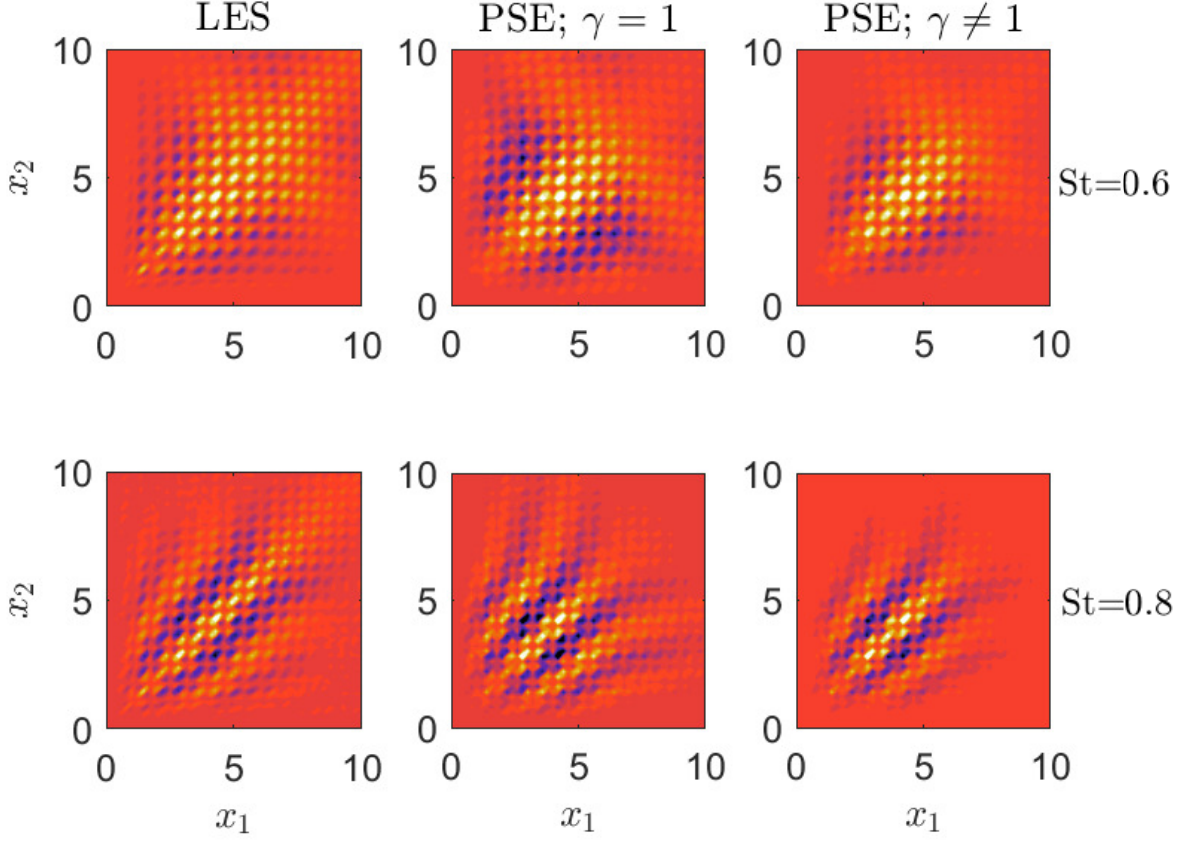


Figure 15: The normalised real components of the CSD of  $S_{11}$  for  $m = 0$  and frequencies  $St = 0.6$  (top row) and  $St = 0.8$  (bottom row). The different reconstructed source models are LES (left column), PSE without coherence decay (centre column) and PSE with coherence decay (right column). Contours levels are from -0.5 to 0.5 and normalised by the maximum value.

incoherent fluctuations as discussed in § 5.2, and as shown in figure 7. This observation may explain the difference in far-field predictions between the LES and PSE with coherence decay ( $\gamma \neq 1$ ) case. As mentioned in § 6.2 and by Cavalieri & Agarwal (2014), agreement between the original and statistical source requires the coherence, in addition to both average amplitude and phase, of wavepackets to be the same. Since two-point coherence information imposed on the PSE model is extracted directly from LES data, any difference in the far-field will arise from a mismatch in the average wavepacket envelope shape.

We also note that the effect of coherence decay is not apparent in figure 14, even though it has significant effect on the far-field sound. To observe the effect of coherence decay, we present radially-integrated source CSDs as defined by equation (2.8), which are equivalent to a line-source approximation (Maia *et al.* 2019; Wong *et al.* 2019b). Amplitudes are normalised for qualitative comparisons. The radially-integrated CSD of the LES source is shown in the left column in figure 15. The freckled appearance is consistent with the CSD of the nearfield pressure of a shock-containing jet (Suzuki 2016; Wong *et al.* 2019b). Discrete peaks are present as the wavepacket interacts with the periodic shock-cell structure. A perfectly-coherent source (centre column) results in a spatially-broader CSD since the wavepacket is coherent over larger lengthscales. When coherence decay (right column) is incorporated into the source description, it narrows the

CSD as expected (Cavalieri & Agarwal 2014; Wong *et al.* 2019b). The effect of coherence decay is to make the perfectly-coherent CSD more compact, and hence more similar to the LES model.

## 8. Summary and conclusions

We present a two-point model for investigating the sound-source mechanisms of broadband shock-associated noise where Lighthill's acoustic analogy (Lighthill 1952) is used to compute the sound field. The flow variables of the source term ( $T_{ij}$ ) are decomposed into the mean, turbulence and shock-cell components as proposed by Tam (1987). Using the same interpretation as Tam & Tanna (1982), we assume BBSAN to be produced by the non-linear interaction of shocks and jet turbulence. To build the equivalent source term, each component is either extracted or modelled from appropriate datasets. We use a modified Pack and Prandtl vortex-sheet model, informed by particle image velocimetry data of a shock-containing jet, to represent the quasi-periodic shock-cell structure. The turbulent component, on the other hand, is modelled as a wavepacket. A large-eddy simulation of an ideally-expanded supersonic jet is used to extract the wavepacket structure. To highlight the links to the underlying physical mechanisms, solutions to parabolised stability equations are also used to describe the statistical wavepacket shape. The same LES data is employed to provide the mean flow and the amplitudes of the PSE solutions. Unlike previous models for BBSAN, the source parameters are solely determined by the turbulent flow field of the shock-containing jet. Acoustic measurements are not used to calibrate or alter the source.

In practical applications where accurately determining the sound field is the sole aim, it is evident that the current approach is unsatisfactory compared to the direct computation of the sound field using LES of a shock-containing jet coupled with integral acoustic methods (Ffowcs Williams-Hawkings (FW-H) or Kirchhoff) (Shur *et al.* 2011; Brès *et al.* 2017; Arroyo & Moreau 2019). On the other hand, successful reproduction of far-field sound is not the present objective; we rather seek to understand the BBSAN generation mechanism. To this end, the acoustic analogy framework is deemed a suitable approach to connect the inner turbulent motions to the radiated sound, and the hypothesis of Tam & Tanna (1982) is the adopted starting point. The efficacy of the current approach should be evaluated from a modelling perspective rather than from the accuracy of far-field sound predictions.

Two major conclusions may be drawn from the results of § 6. Firstly, we have shown that a reduced-order representation of the equivalent source can provide largely accurate frequency and amplitude far-field predictions for BBSAN. This applies over a wide directivity range. Provided that shock-cell and mean flow profiles are available, only a single empirical constant is required to adjust the free amplitude of the linear PSE solutions. The efficacy of the simpler PSE-based approach is corroborated by agreement with the sound field features of the more complex, but complete, model using the LES CSD ( $\pm 2\text{dB/St}$  at peak frequency). Examination of the results is aided by the availability of azimuthally-decomposed acoustic data. The encouraging comparisons between measurements and model predictions further support the BBSAN generation mechanism proposed by Tam & Tanna (1982).

Secondly, the results also provide some answers to the shortfalls of previous BBSAN models. As predicted by the line-source model of Wong *et al.* (2019b), the inclusion of the effects of wavepacket jitter and higher shock-cell modes is integral to predictive ability at higher frequencies and regions between the BBSAN peaks. We demonstrate the importance of these effects by directly quantifying and incorporating them into the

description of the equivalent source. It seems clear that the ‘missing sound’ observed at high frequencies by both Ray & Lele (2007) and Suzuki (2016) is due to the absence of higher shock-cell modes. The results also extend the work of Tam and co-workers. Unlike the assumption made by Tam (1987), where spectral broadening was solely attributed to shock-cell unsteadiness, we show that nonlinearity, in the form of jittering wavepackets, is instead responsible for recovering a large portion of the lost sound between the BBSAN peaks.

The artificial separation of the source into turbulent and shock components, however, means the effects of their interaction cannot be accounted for. Compelled by the modelling framework,  $\mathbf{q}_t$  and  $\mathbf{q}_s$  were both deduced from separate ideally-expanded and shock-containing jets respectively. This may contribute to why, even with exact coherence information, the BBSAN predictions between the first and second peak at upstream angles underpredict the measured data. As hypothesised by Tam (1987), the discrepancy may be due to the inability for the model to capture shock-cell unsteadiness further downstream. This interaction between the two components should be investigated in future work.

## Acknowledgements

The authors would like to thank Dr. Guillaume Brès at Cascade Technologies for providing the simulation database. The LES work was supported by ONR, with computational resources provided by DoD HPCMP. The research benefited from the Multi-modal Australian ScienceS Imaging and Visualisation Environment (MASSIVE) HPC facility, provided through the National Computational Merit Allocation Scheme. M.H.W., R.K. and D.E.M received funding from the Australian Research Council through the Discovery Projects scheme. M.H.W. is further supported by an Australian Government Research Training Program (RTP) Scholarship and the Endeavour Research Leadership Award – an Australian Government initiative.

## Declaration of interests

The authors report no conflict of interest.

## Appendix A. Approximation of $T_{ij}$ for BBSAN

The substitution of the decomposed flow variables into  $T_{ij}$  (equation (2.10)) is rewritten below

$$T_{ij} = (\bar{\rho} + \rho_s + \rho_t)(\bar{u}_i + u_{i,t} + u_{i,s})(\bar{u}_j + u_{j,t} + u_{j,s}). \quad (\text{A } 1)$$

By expanding out the terms we obtain,

$$\begin{aligned} T_{ij} = & \bar{\rho}\bar{u}_i\bar{u}_j + \bar{\rho}\bar{u}_i u_{j,t} + \bar{\rho}\bar{u}_i u_{j,s} + \bar{\rho}\bar{u}_j u_{i,t} + \\ & \bar{\rho}u_{i,t}u_{j,t} + \bar{\rho}u_{i,t}u_{j,s} + \bar{\rho}\bar{u}_j u_{i,s} + \bar{\rho}u_{i,s}u_{j,t} + \bar{\rho}u_{i,s}u_{j,s} + \\ & \rho_s\bar{u}_i\bar{u}_j + \rho_s\bar{u}_i u_{j,t} + \rho_s\bar{u}_i u_{j,s} + \rho_s\bar{u}_j u_{i,t} + \\ & \rho_s u_{i,t}u_{j,t} + \rho_s u_{i,t}u_{j,s} + \rho_s\bar{u}_j u_{i,s} + \rho_s u_{i,s}u_{j,t} + \rho_s u_{i,s}u_{j,s} + \\ & \rho_t\bar{u}_i\bar{u}_j + \rho_t\bar{u}_i u_{j,t} + \rho_t\bar{u}_i u_{j,s} + \rho_t\bar{u}_j u_{i,t} + \\ & \rho_t u_{i,t}u_{j,t} + \rho_t u_{i,t}u_{j,s} + \rho_t\bar{u}_j u_{i,s} + \rho_t u_{i,s}u_{j,t} + \rho_t u_{i,s}u_{j,s}. \end{aligned}$$

To proceed, only the leading-order fluctuation terms are retained and higher-order ones are discarded. Furthermore, we only retain the interaction terms between turbulence and shocks (as these contribute to BBSAN). By only retaining the interaction terms, turbulent mixing noise such as Mach wave radiation is not modelled. Thus, we can simplify the above expression such that

$$T_{ij} \approx \bar{\rho}(u_{i,t}u_{j,s} + u_{i,s}u_{j,t}) + \bar{\rho}_s(\bar{u}_i u_{j,t} + \bar{u}_j u_{i,t}) + \bar{\rho}_t(\bar{u}_i u_{j,s} + \bar{u}_j u_{i,s}) + \underbrace{\{\bar{\rho}\bar{u}_i\bar{u}_j + \bar{u}_i\bar{u}_j\rho_s + \rho_s(\bar{u}_i u_{j,s} + \bar{u}_j u_{i,s})\}}_{\text{non-fluctuating}} \quad (\text{A } 2)$$

The terms in the under-brace in equation (A 2) can be ignored because they are non-fluctuating and hence by definition cannot generate noise. We hence arrive at the approximated expression for the BBSAN stress tensor term

$$T_{ij} \approx \bar{\rho}(u_{i,t}u_{j,s} + u_{i,s}u_{j,t}) + \rho_s(\bar{u}_i u_{j,t} + \bar{u}_j u_{i,t}) + \rho_t(\bar{u}_i u_{j,s} + \bar{u}_j u_{i,s}). \quad (\text{A } 3)$$

## Appendix B. Discussion on jet database parameters

The effects on model predictions due to the variations between the databases is discussed in this appendix. Discrepancies, summarised in table 1, include exit velocity, operating temperature (isothermal in LES, cold in experiments), Reynolds number and nozzle geometry. We again note that the LES and PIV flow fields are only used to inform the modelling choices in order to predict far-field BBSAN SPLs. No acoustic information is directly obtained or used from either of these databases.

As discussed in § 2.1, the non-shock-containing components ( $\bar{q}$  and  $\bar{q}_t$ ) of the shock-containing jet should be obtained from the ideally-expanded case at the same  $M_j$ . To show the effect of using different values of  $M_j$  on frequency, the non-dimensional form of equation (1.2) is

$$St_p = \frac{u_c D_j}{U_j} \left( \frac{1}{L_s(1 - u_c/u_j \cos \theta)} \right), \quad L_s \approx 1.3\beta, \quad (\text{B } 1)$$

where peak frequency is given by Strouhal  $St_p$ . Assuming a constant convection velocity of  $u_c = 0.7U_j$ , the only variable controlling the peak is the shock spacing  $L_s$ , which is approximately proportional to the off-design parameter  $\beta$  (equation 1.1). The shock spacing of a  $M_j = 1.45$  jet is approximately 5% shorter than that for  $M_j = 1.5$ . The variation in the peak prediction is shown in figure 16a, where we observe only a slight difference for the primary peak. For BBSAN intensity, which scales with  $\beta^4$  (Harper-Bourne & Fisher 1973), the mismatch in  $M_j$  results in a 1-2dB/St difference in sound pressure level.

The effect of temperature on BBSAN generation has previously been investigated in models (Tam 1990) and experiments (Kuo *et al.* 2015). With relevance to peak frequency prediction in (1.2), heated jets have lower convection velocities and a shorter potential core. Despite these differences, the measurements of Kuo *et al.* (2015) for underexpanded jets show either no change or a only a slight increase in peak frequency. This minor change is supported by the  $St - \theta$  plot in figure 16b. The convection velocity, as a function of temperature, is taken to be (Tam 1990)

$$u_c/U_j = 0.7 - 0.025(TTR - 1), \quad (\text{B } 2)$$

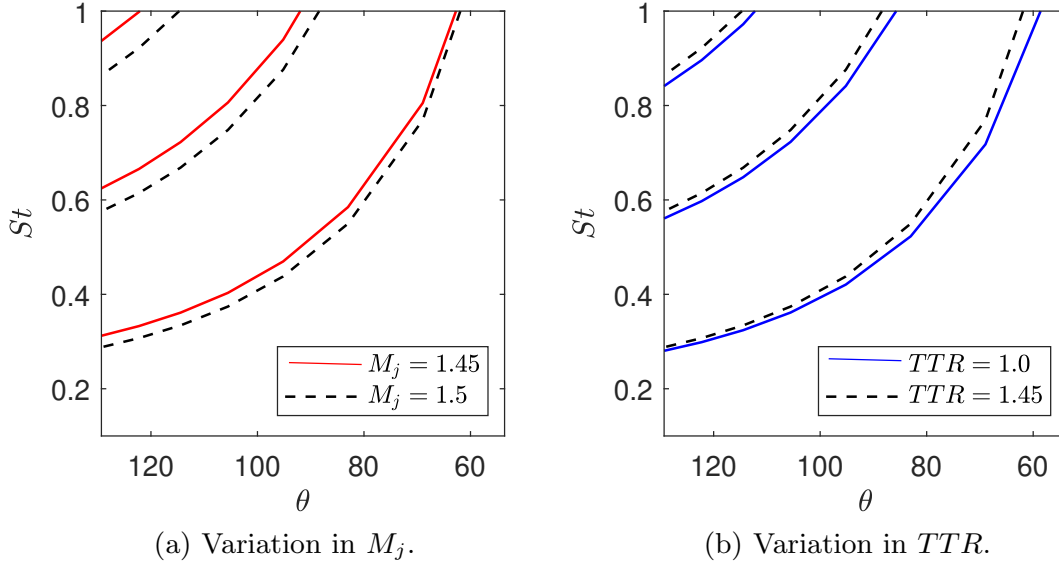


Figure 16: Variation in peak BBSAN predictions as predicted by equation (1.3) due to differences in jet parameters for the first three shock-cell modes ( $n_s = 1, 2, 3$ ). For the cold jet, a convection velocity of  $u_c = 0.7U_j$  was used for both plots while the relationship in equation (B 2) was used for the heated case.

where TTR represents the total temperature ratio, which is equal to 1.45 for the isothermal case and unity for a cold jet. This observation is corroborated by the measurements of Wishart (1995) who also found that the effect of varying temperature on shock structure is relatively small.

We note that all three databases are of fully-turbulent jets with  $Re > 400,000$ , which Viswanathan (2002) deems an appropriate threshold to avoid Reynolds number effects on the radiated sound field. Previous studies have also shown  $Re$  having minimal effect on shock spacing and wavelengths (Tam *et al.* 1985). Similarly, Hu & McLaughlin (1990) found that the evolution of large-scale structures at  $Re = 8000$  is similar to those in underexpanded jets at high Reynolds number. These observations give us some confidence that BBSAN may be considered independent of  $Re$  for the databases investigated here.

Lastly, experimental studies have shown that nozzle geometry can strongly affect screech and resonant characteristics of a supersonic jet (Edgington-Mitchell 2019). Screech is known to significantly influence the decay of the shock-cell structure and hence affects the production of BBSAN (André *et al.* 2013). Since both the acoustic and PIV databases use nozzles without screech suppression features, the intensity and frequency of BBSAN peaks are likely affected by the presence of screech. When interpreting the predictions of § 6, it must be noted that the model does not account for such effects, which will remain a source of error.

While there remain tangible differences across the three databases, our goal is not to match predictions with a particular experiment, but rather to identify the underlying sound source mechanisms. Despite the minor mismatches, the results confirm the suitability of using these databases to inform our flow modelling choices.

## REFERENCES

- ANDRÉ, BENOÎT, CASTELAIN, THOMAS & BAILLY, CHRISTOPHE 2013 Broadband shock-associated noise in screeching and non-screeching underexpanded supersonic jets. *AIAA Journal* **51** (3), 665–673.
- ANSALDI, TOBIAS, AIRIAU, CHRISTOPHE, PÉREZ ARROYO, CARLOS & PUIGT, GUILLAUME 2016

- PSE-based sensitivity analysis of turbulent and supersonic single stream jet. In *22nd AIAA/CEAS Aeroacoustics Conference*, p. 3052.
- ANTONIALI, LUIGI A, CAVALIERI, ANDRÉ VG, SCHMIDT, OLIVER T, COLONIUS, TIM, JORDAN, PETER, TOWNE, AARON & BRÈS, GUILLAUME A 2021 Amplitude scaling of wave packets in turbulent jets. *AIAA Journal* **59** (2), 559–568.
- ARROYO, CARLOS PÉREZ & MOREAU, STÉPHANE 2019 Azimuthal mode analysis of broadband shock-associated noise in an under-expanded axisymmetric jet. *Journal of Sound and Vibration* **449**, 64–83.
- BAQUI, YAMIN B, AGARWAL, ANURAG, CAVALIERI, ANDRÉ VG & SINAYOKO, SAMUEL 2015 A coherence-matched linear source mechanism for subsonic jet noise. *Journal of Fluid Mechanics* **776**, 235–267.
- BENEDDINE, SAMIR, METTOT, CLÉMENT & SIPP, DENIS 2015 Global stability analysis of underexpanded screeching jets. *European Journal of Mechanics-B/Fluids* **49**, 392–399.
- BODONY, DANIEL J & LELE, SANJIVA K 2008 Low-frequency sound sources in high-speed turbulent jets. *Journal of Fluid Mechanics* **617**, 231–253.
- BOUTHER, M 1972 Stabilité linéaire des écoulements presque parallèles. *Journal de Mécanique* **11**, 599–621.
- BRÈS, GUILLAUME A, HAM, FRANK E, NICHOLS, JOSEPH W & LELE, SANJIVA K 2017 Unstructured large-eddy simulations of supersonic jets. *AIAA Journal* **55** (4), 1164–1184.
- BRÈS, GUILLAUME A, JORDAN, PETER, JAUNET, VINCENT, LE RALLIC, MAXIME, CAVALIERI, ANDRÉ VG, TOWNE, AARON, LELE, SANJIVA K, COLONIUS, TIM & SCHMIDT, OLIVER T 2018 Importance of the nozzle-exit boundary-layer state in subsonic turbulent jets. *Journal of Fluid Mechanics* **851**, 83–124.
- CAVALIERI, ANDRÉ VG & AGARWAL, ANURAG 2014 Coherence decay and its impact on sound radiation by wavepackets. *Journal of Fluid Mechanics* **748**, 399–415.
- CAVALIERI, ANDRÉ VG, JORDAN, PETER, AGARWAL, ANURAG & GERVAIS, YVES 2011 Jittering wave-packet models for subsonic jet noise. *Journal of Sound and Vibration* **330** (18-19), 4474–4492.
- CAVALIERI, ANDRÉ VG, JORDAN, PETER, COLONIUS, TIM & GERVAIS, YVES 2012 Axisymmetric superdirectivity in subsonic jets. *Journal of fluid Mechanics* **704**, 388–420.
- CAVALIERI, ANDRÉ VG, JORDAN, PETER & LESSHAFFT, LUTZ 2019 Wave-packet models for jet dynamics and sound radiation. *Applied Mechanics Reviews* **71** (2), 020802.
- CAVALIERI, ANDRÉ VG, RODRÍGUEZ, DANIEL, JORDAN, PETER, COLONIUS, TIM & GERVAIS, YVES 2013 Wavepackets in the velocity field of turbulent jets. *Journal of fluid mechanics* **730**, 559–592.
- CRIGHTON, DG & GASTER, M 1976 Stability of slowly diverging jet flow. *Journal of Fluid Mechanics* **77** (2), 397–413.
- CRIMINALE, WILLIAM O, JACKSON, THOMAS LUTHER & JOSLIN, RONALD DOUGLAS 2018 *Theory and computation in hydrodynamic stability*. Cambridge University Press.
- EDGINGTON-MITCHELL, DANIEL 2019 Aeroacoustic resonance and self-excitation in screeching and impinging supersonic jets—a review. *International Journal of Aeroacoustics* **18** (2-3), 118–188.
- EDGINGTON-MITCHELL, DANIEL, HONNERY, DAMON R & SORIA, JULIO 2014a The underexpanded jet Mach disk and its associated shear layer. *Physics of Fluids* **26** (9), 1578.
- EDGINGTON-MITCHELL, DANIEL, JAUNET, VINCENT, JORDAN, PETER, TOWNE, AARON, SORIA, JULIO & HONNERY, DAMON 2018 Upstream-travelling acoustic jet modes as a closure mechanism for screech. *Journal of Fluid Mechanics* **855**.
- EDGINGTON-MITCHELL, DANIEL, OBERLEITHNER, KILIAN, HONNERY, DAMON R & SORIA, JULIO 2014b Coherent structure and sound production in the helical mode of a screeching axisymmetric jet. *Journal of Fluid Mechanics* **748**, 822–847.
- EDGINGTON-MITCHELL, DANIEL, WANG, TIANYE, NOGUEIRA, PETRONIO, SCHMIDT, OLIVER, JAUNET, VINCENT, DUKE, DANIEL, JORDAN, PETER & TOWNE, AARON 2020 Waves in screeching jets. *arXiv preprint arXiv:2008.09756*.
- EDGINGTON-MITCHELL, DANIEL M, DUKE, DANIEL, HARRIS, DANIELLE, WANG, TIANYE, SCHMIDT, OLIVER T, JAUNET, VINCENT, JORDAN, PETER & TOWNE, AARON

- 2019 Modulation of downstream-propagating waves in jet screech. In *AIAA/CEAS Aeroacoustics Conference 2019*. American Institute of Aeronautics and Astronautics.
- FAVA, THALES C & CAVALIERI, ANDRÉ V 2019 Propagation of acoustic waves in ducts with axially-varying parameters using the parabolized stability equations. In *25th AIAA/CEAS Aeroacoustics Conference*, p. 2447.
- FREUND, JONATHAN B 2001 Noise sources in a low-Reynolds-number turbulent jet at Mach 0.9. *Journal of Fluid Mechanics* **438**, 277–305.
- FREUND, JONATHAN B 2003 Noise-source turbulence statistics and the noise from a Mach 0.9 jet. *Physics of Fluids* **15** (6), 1788–1799.
- GOJON, ROMAIN & BOGEY, CHRISTOPHE 2017 Numerical study of the flow and the near acoustic fields of an underexpanded round free jet generating two screech tones. *International Journal of Aeroacoustics* **16** (7-8), 603–625.
- GOLDSTEIN, MARVIN E 1976 *Aeroacoustics*. New York .
- GUDMUNDSSON, KRISTJAN & COLONIUS, TIM 2011 Instability wave models for the near-field fluctuations of turbulent jets. *Journal of Fluid Mechanics* **689**, 97–128.
- HARPER-BOURNE, M & FISHER, MJ 1973 The noise from shock waves in supersonic jets. *AGARD-CP-131* **11**, 1–13.
- HERBERT, THORWALD 1997 Parabolized stability equations. *Annual Review of Fluid Mechanics* **29** (1), 245–283.
- HU, TIEH-FENG & McLAUGHLIN, DENNIS K 1990 Flow and acoustic properties of low Reynolds number underexpanded supersonic jets. *Journal of Sound and Vibration* **141** (3), 485–505.
- HUBER, JÉRÔME, FLEURY, VINCENT, BULTÉ, JEAN, LAURENDEAU, ESTELLE & SYLLA, AMADOU ANDRÉ 2014 Understanding and reduction of cruise jet noise at aircraft level. *International Journal of Aeroacoustics* **13** (1-2), 61–84.
- JORDAN, PETER & COLONIUS, TIM 2013 Wave packets and turbulent jet noise. *Annual Review of Fluid Mechanics* **45**, 173–195.
- KALYAN, ANUROOPA & KARABASOV, SERGEY A 2017 Broad band shock associated noise predictions in axisymmetric and asymmetric jets using an improved turbulence scale model. *Journal of Sound and Vibration* **394**, 392–417.
- KAPLAN, OĞUZHAN, JORDAN, PETER, CAVALIERI, ANDRÉ & BRÈS, GUILLAUME A 2020 Nozzle dynamics and wavepackets in turbulent jets. *arXiv preprint arXiv:2007.00626* .
- KARABASOV, SA, AFSAR, MZ, HYNES, TP, DOWLING, AP, McMULLAN, WA, POKORA, CD, PAGE, GJ & MCGUIRK, JJ 2010 Jet noise: acoustic analogy informed by large eddy simulation. *AIAA journal* **48** (7), 1312–1325.
- KLEINE, VITOR G, SASAKI, KENZO, CAVALIERI, ANDRÉ V, BRÈS, GUILLAUME A & COLONIUS, TIM 2017 Evaluation of PSE as a model for supersonic jet using transfer functions. In *23rd AIAA/CEAS Aeroacoustics Conference*, p. 4194.
- KOPIEV, VICTOR, CHERNYSHEV, SERGEY, ZAITSEV, M & KUZNETSOV, V 2006 Experimental validation of instability wave theory for round supersonic jet. In *12th AIAA/CEAS Aeroacoustics Conference (27th AIAA Aeroacoustics Conference)*, p. 2595.
- KUO, CHING-WEN, McLAUGHLIN, DENNIS K, MORRIS, PHILIP J & VISWANATHAN, K 2015 Effects of jet temperature on broadband shock-associated noise. *AIAA Journal* **53** (6), 1515–1530.
- LANDAHL, MÅRTEN T, MOLLO-CHRISTENSEN, ERIC & KORMAN, MURRAY S 1989 Turbulence and random processes in fluid mechanics.
- LELE, SANJIVA 2005 Phased array models of shock-cell noise sources. In *11th AIAA/CEAS aeroacoustics conference*, p. 2841.
- LESSEN, M, FOX, JA & ZIEN, HM 1965 The instability of inviscid jets and wakes in compressible fluid. *Journal of Fluid Mechanics* **21** (1), 129–143.
- LESSHAFFT, LUTZ, SEMERARO, ONOFRIO, JAUNET, VINCENT, CAVALIERI, ANDRÉ VG & JORDAN, PETER 2019 Resolvent-based modeling of coherent wave packets in a turbulent jet. *Physical Review Fluids* **4** (6), 063901.
- LI, FEI & MALIK, MUJEEB R 1997 Spectral analysis of parabolized stability equations. *Computers & fluids* **26** (3), 279–297.
- LIGHTHILL, MICHAEL JAMES 1952 On sound generated aerodynamically. i. general theory. In *Proceedings of the Royal Society of London A: Mathematical, Physical and Engineering Sciences*, , vol. 211, pp. 564–587. The Royal Society.

- MAIA, IGOR A, JORDAN, PETER, CAVALIERI, AVG & JAUNET, V 2019 Two-point wavepacket modelling of jet noise. *Proceedings of the Royal Society A* **475** (2227), 20190199.
- MARKESTEIJN, ANTON P, SEMILETOV, VASILY, KARABASOV, SERGEY A, TAN, DOMINIC J, WONG, MARCUS, HONNERY, DAMON & EDGINGTON-MITCHELL, DANIEL M 2017 Supersonic jet noise: an investigation into noise generation mechanisms using large eddy simulation and high-resolution PIV data. In *23rd AIAA/CEAS Aeroacoustics Conference*, p. 3029.
- MARTÍNEZ-LERA, PAULA & SCHRAM, CHRISTOPHE 2008 Correction techniques for the truncation of the source field in acoustic analogies. *The Journal of the Acoustical Society of America* **124** (6), 3421–3429.
- MICHALKE, ALFONS 1970 A wave model for sound generation in circular jets. Technical report.
- MICHALKE, A & FUCHS, HV 1975 On turbulence and noise of an axisymmetric shear flow. *Journal of Fluid Mechanics* **70** (1), 179–205.
- MILLER, STEVEN AE & MORRIS, PHILIP J 2012 The prediction of broadband shock-associated noise including propagation effects. *International Journal of Aeroacoustics* **11** (7-8), 755–781.
- MOHSENI, KAMRAN & COLONIUS, TIM 2000 Numerical treatment of polar coordinate singularities. *Journal of Computational Physics* **157** (2), 787–795.
- MORRIS, PHILIP J & MILLER, STEVEN AE 2010 Prediction of broadband shock-associated noise using Reynolds-averaged Navier-Stokes computational fluid dynamics. *AIAA Journal* **48** (12), 2931–2944.
- NORUM, T & SEINER, J 1980 Location and propagation of shock associated noise from supersonic jets. In *6th Aeroacoustics Conference*, p. 983.
- NORUM, TD & SEINER, JM 1982 Measurements of mean static pressure and far field acoustics of shock containing supersonic jets. *Tech. Rep.*.
- OBRIST, DOMINIK & KLEISER, LEONHARD 2007 The influence of spatial domain truncation on the prediction of acoustic far-fields. In *13th AIAA/CEAS Aeroacoustics Conference (28th AIAA Aeroacoustics Conference)*, p. 3725.
- O’HARA, D, ANDERSSON, N, JORDAN, P, BILLSON, M, ERIKSSON, L & DAVIDSON, L 2004 A hybrid analysis methodology for improved accuracy in low-cost jet noise modelling. In *33rd International Congress and Exposition on Noise Control Engineering INTERNOISE 2004*.
- PACK, DC 1950 A note on prandtl’s formula for the wave-length of a supersonic gas jet. *The Quarterly Journal of Mechanics and Applied Mathematics* **3** (2), 173–181.
- PANDA, J 1998 Shock oscillation in underexpanded screeching jets. *Journal of Fluid Mechanics* **363**, 173–198.
- PATEL, TRUSHANT K & MILLER, STEVEN AE 2019 Statistical sources for broadband shock-associated noise using the Navier-Stokes equations. *The Journal of the Acoustical Society of America* **146** (6), 4339–4351.
- PIANTANIDA, SELENE, JAUNET, VINCENT, HUBER, JÉRÔME, WOLF, WILLIAM R, JORDAN, PETER & CAVALIERI, ANDRÉ VG 2016 Scattering of turbulent-jet wavepackets by a swept trailing edge. *The Journal of the Acoustical Society of America* **140** (6), 4350–4359.
- PICKERING, ETHAN M, TOWNE, AARON, JORDAN, PETER & COLONIUS, TIM 2020 Resolvent-based jet noise models: a projection approach. In *AIAA Scitech 2020 Forum*, p. 0999.
- POWELL, ALAN 1953 On the mechanism of choked jet noise. *Proceedings of the Physical Society. Section B* **66** (12), 1039.
- PRANDTL, LUDWIG 1904 *Über die stationären Wellen in einem Gasstrahl*. Hirzel.
- RAMAN, GANESH 1999 Supersonic jet screech: half-century from powell to the present. *Journal of Sound and Vibration* **225** (3), 543–571.
- RAY, PRASUN & LELE, SANJIVA K 2007 Sound generated by instability wave/shock-cell interaction in supersonic jets. *Journal of fluid mechanics* **587**, 173–215.
- REBA, RAMONS, NARAYANAN, SATISH & COLONIUS, TIM 2010 Wave-packet models for large-scale mixing noise. *International Journal of Aeroacoustics* **9** (4-5), 533–557.
- RODRÍGUEZ, DANIEL, CAVALIERI, ANDRÉ VG, COLONIUS, TIM & JORDAN, PETER 2015 A study of linear wavepacket models for subsonic turbulent jets using local eigenmode decomposition of PIV data. *European Journal of Mechanics-B/Fluids* **49**, 308–321.
- RODRIGUEZ, DANIEL, SINHA, ANIRUDDHA, BRES, GUILLAUME A & COLONIUS, TIM 2013



- Acoustic field associated with parabolized stability equation models in turbulent jets. In *19th AIAA/CEAS Aeroacoustics Conference*, p. 2279.
- RODRÍGUEZ, DANIEL, SINHA, ANIRUDDHA, BRES, GUILLAUME A & COLONIUS, TIM 2013 Inlet conditions for wave packet models in turbulent jets based on eigenmode decomposition of large eddy simulation data. *Physics of Fluids* **25** (10), 105107.
- SARIC, WILLIAM S & NAYFEH, ALI HASAN 1975 Nonparallel stability of boundary-layer flows. *The Physics of Fluids* **18** (8), 945–950.
- SASAKI, KENZO, CAVALIERI, ANDRÉ VG, JORDAN, PETER, SCHMIDT, OLIVER T, COLONIUS, TIM & BRÈS, GUILLAUME A 2017a High-frequency wavepackets in turbulent jets. *Journal of Fluid Mechanics* **830**, R2.
- SASAKI, KENZO, PIANTANIDA, SELENE, CAVALIERI, ANDRÉ VG & JORDAN, PETER 2017b Real-time modelling of wavepackets in turbulent jets. *Journal of Fluid Mechanics* **821**, 458.
- SAVARESE, ALESSANDRO, JORDAN, PETER, GIRARD, STEVE, COLLIN, ERWAN, PORTA, MAURO & GERVAIS, YVES 2013 Experimental study of shock-cell noise in underexpanded supersonic jets. In *19th AIAA/CEAS Aeroacoustics Conference*, p. 2080.
- SCHLINKER, ROBERT, SIMONICH, JOHN, SHANNON, DAN, REBA, RAMONS, COLONIUS, TIM, GUDMUNDSSON, KRISTJAN & LADEINDE, FOLUSO 2009 Supersonic jet noise from round and chevron nozzles: experimental studies. In *15th AIAA/CEAS Aeroacoustics Conference (30th AIAA Aeroacoustics Conference)*, p. 3257.
- SCHMID, PETER J, HENNINGSON, DAN S & JANKOWSKI, DF 2002 Stability and transition in shear flows. applied mathematical sciences, vol. 142. *Appl. Mech. Rev.* **55** (3), B57–B59.
- SCHMIDT, OLIVER T, TOWNE, AARON, COLONIUS, TIM, CAVALIERI, ANDRÉ VG, JORDAN, PETER & BRÈS, GUILLAUME A 2017 Wavepackets and trapped acoustic modes in a turbulent jet: coherent structure eduction and global stability. *Journal of Fluid Mechanics* **825**, 1153–1181.
- SCHMIDT, OLIVER T, TOWNE, AARON, RIGAS, GEORGIOS, COLONIUS, TIM & BRÈS, GUILLAUME A 2018 Spectral analysis of jet turbulence. *Journal of Fluid Mechanics* **855**, 953–982.
- SEINER, JM & NORUM, TD 1980 *Aerodynamic aspects of shock containing jet plumes*. American Institute of Aeronautics and Astronautics.
- SEINER, JOHN M & YU, JAMES C 1984 Acoustic near-field properties associated with broadband shock noise. *AIAA Journal* **22** (9), 1207–1215.
- SHEN, WEIQI, PATEL, TRUSHANT K & MILLER, STEVEN AE 2021 A time domain approach for shock noise prediction with decomposition analyses of large-scale coherent turbulent structures in jets. *Journal of Sound and Vibration* p. 115996.
- SHUR, MICHAEL L, SPALART, PHILIPPE R & STRELETS, MICHAEL KH 2011 Noise prediction for underexpanded jets in static and flight conditions. *AIAA journal* **49** (9), 2000–2017.
- SINHA, ANIRUDDHA, RODRÍGUEZ, DANIEL, BRÈS, GUILLAUME A & COLONIUS, TIM 2014 Wavepacket models for supersonic jet noise. *Journal of Fluid Mechanics* **742**, 71–95.
- SUZUKI, TAKAO 2016 Wave-packet representation of shock-cell noise for a single round jet. *AIAA Journal* **54** (12), 3903–3917.
- SUZUKI, TAKAO & COLONIUS, TIM 2006 Instability waves in a subsonic round jet detected using a near-field phased microphone array. *Journal of Fluid Mechanics* **565**, 197–226.
- TAM, CHRISTOPHER KW 1972 On the noise of a nearly ideally expanded supersonic jet. *Journal of Fluid Mechanics* **51** (1), 69–95.
- TAM, CHRISTOPHER KW 1987 Stochastic model theory of broadband shock associated noise from supersonic jets. *Journal of Sound and Vibration* **116** (2), 265–302.
- TAM, CHRISTOPHER KW 1990 Broadband shock-associated noise of moderately imperfectly expanded supersonic jets. *Journal of Sound and Vibration* **140** (1), 55–71.
- TAM, CHRISTOPHER KW 1995 Supersonic jet noise. *Annual Review of Fluid Mechanics* **27** (1), 17–43.
- TAM, CHRISTOPHER KW & AURIAULT, LAURENT 1998 Mean flow refraction effects on sound radiated from localized sources in a jet. *Journal of Fluid Mechanics* **370**, 149–174.
- TAM, CHRISTOPHER KW & BURTON, DALE E 1984 Sound generated by instability waves of supersonic flows. part 2. axisymmetric jets. *Journal of Fluid Mechanics* **138**, 273–295.
- TAM, CHRISTOPHER KW & CHEN, KC 1979 A statistical model of turbulence in two-dimensional mixing layers. *Journal of Fluid Mechanics* **92** (2), 303–326.

- TAM, CHRISTOPHER KW, JACKSON, JAY A & SEINER, JM 1985 A multiple-scales model of the shock-cell structure of imperfectly expanded supersonic jets. *Journal of Fluid Mechanics* **153**, 123–149.
- TAM, CHRISTOPHER KW & TANNA, HK 1982 Shock associated noise of supersonic jets from convergent-divergent nozzles. *Journal of Sound and Vibration* **81** (3), 337–358.
- TAN, DOMINIC J, EDGINGTON-MITCHELL, DANIEL & HONNERY, DAMON 2015 Measurement of density in axisymmetric jets using a novel background-oriented schlieren (BOS) technique. *Experiments in Fluids* **56** (11), 204.
- TAN, DOMINIC J, HONNERY, DAMON, KALYAN, ANUROOPA, SEMILETOV, VASILY, KARABASOV, SERGEY A & EDGINGTON-MITCHELL, DANIEL 2018 Equivalent shock-associated noise source reconstruction of screeching underexpanded unheated round jets. *AIAA Journal* **57** (3), 1200–1214.
- TAN, DOMINIC J, HONNERY, DAMON, KALYAN, ANUROOPA, SEMILETOV, VASILY, KARABASOV, SERGEY A & EDGINGTON-MITCHELL, DANIEL 2019 Correlation analysis of high-resolution particle image velocimetry data of screeching jets. *AIAA Journal* **57** (2), 735–748.
- TAN, DOMINIC J, KALYAN, ANUROOPA, GRYAZEV, VASILY, WONG, MARCUS, HONNERY, DAMON, EDGINGTON-MITCHELL, DANIEL M & KARABASOV, SERGEY A 2017 On the application of shock-associated noise models to PIV measurements of screeching axisymmetric cold jets. In *23rd AIAA/CEAS Aeroacoustics Conference*, p. 3028.
- TISSOT, GILLES, LAJÚS JR, FRANCISCO C, CAVALIERI, ANDRÉ VG & JORDAN, PETER 2017a Wave packets and orr mechanism in turbulent jets. *Physical Review Fluids* **2** (9), 093901.
- TISSOT, GILLES, ZHANG, MENGQI, LAJÚS, FRANCISCO C, CAVALIERI, ANDRÉ VG & JORDAN, PETER 2017b Sensitivity of wavepackets in jets to nonlinear effects: the role of the critical layer. *Journal of Fluid Mechanics* **811**, 95–137.
- TOWNE, AARON, SCHMIDT, OLIVER T & COLONIUS, TIM 2018 Spectral proper orthogonal decomposition and its relationship to dynamic mode decomposition and resolvent analysis. *Journal of Fluid Mechanics* **847**, 821–867.
- UNNIKRISHNAN, SASIDHARAN, CAVALIERI, ANDRÉ VG & GAITONDE, DATTA V 2019 Acoustically informed statistics for wave-packet models. *AIAA Journal* **57** (6), 2421–2434.
- UZUN, ALI, LYRINTZIS, ANASTASIOS S & BLAISDELL, GREGORY A 2004 Coupling of integral acoustics methods with LES for jet noise prediction. *International Journal of Aeroacoustics* **3** (4), 297–346.
- VAUGHN, AARON B, NEILSEN, TRACIANNE B, GEE, KENT L, WALL, ALAN T, MICAH DOWNING, J & JAMES, MICHAEL M 2018 Broadband shock-associated noise from a high-performance military aircraft. *The Journal of the Acoustical Society of America* **144** (3), EL242–EL247.
- VISWANATHAN, KRISHNAMURTHY 2002 Aeroacoustics of hot jets. In *8th AIAA/CEAS Aeroacoustics Conference & Exhibit*, p. 2481.
- VISWANATHAN, KRISHNA 2006 Scaling laws and a method for identifying components of jet noise. *AIAA Journal* **44** (10), 2274.
- VISWANATHAN, KRISHNA, ALKISLAR, MB & CZECH, MJ 2010 Characteristics of the shock noise component of jet noise. *AIAA Journal* **48** (1), 25–46.
- WEIGHTMAN, JOEL L, AMILI, OMID, HONNERY, DAMON, EDGINGTON-MITCHELL, DANIEL & SORIA, JULIO 2019 Nozzle external geometry as a boundary condition for the azimuthal mode selection in an impinging underexpanded jet. *Journal of Fluid Mechanics* **862**, 421–448.
- WISHART, DAVID PAUL 1995 The structure of a heated supersonic jet operating at design and off-design conditions. *PhDT* .
- WONG, MARCUS H, EDGINGTON-MITCHELL, DANIEL M, HONNERY, DAMON, CAVALIERI, ANDRÉ V & JORDAN, PETER 2019a A parabolised stability equation based broadband shock-associated noise model. In *25th AIAA/CEAS Aeroacoustics Conference*, p. 2584.
- WONG, MARCUS H, JORDAN, PETER, HONNERY, DAMON R & EDGINGTON-MITCHELL, DANIEL 2019b Impact of coherence decay on wavepacket models for broadband shock-associated noise in supersonic jets. *Journal of Fluid Mechanics* **863**, 969–993.
- WONG, MARCUS H., KIRBY, RHIANNON, JORDAN, PETER & EDGINGTON-MITCHELL, DANIEL

- 2020 Azimuthal decomposition of the radiated noise from supersonic shock-containing jets. *The Journal of the Acoustical Society of America* **148** (4), 2015–2027.
- WU, XUESONG 2005 Mach wave radiation of nonlinearly evolving supersonic instability modes in shear layers. *Journal of Fluid Mechanics* **523**, 121.
- ZHANG, MENGQI, JORDAN, PETER, LEHNASCH, GUILLAUME, CAVALIERI, ANDRÉ V & AGARWAL, ANURAG 2014 Just enough jitter for jet noise? In *20th AIAA/CEAS Aeroacoustics Conference*, p. 3061.

## 7.12 Further Comparisons Between PSE and LES Wavepackets

A more comprehensive set of comparisons is shown between the PSE predictions and the wavepackets educed from the LES data. Cases are at three different frequencies ( $St = 0.4, 0.6, 0.8$ ) for the flow variables  $u_x, u_r$  and  $\rho$  and the first two azimuthal modes ( $m = 0, 1$ ).

Radial shapes at the axial station  $x = 4D$  for  $m = 0$  are shown in figure 7.17. The PSE and LES wavepackets are in good agreement for both velocity and density fluctuations. The drop in amplitude close to the lip line for  $u_x$  is due to the phase jump either side of the mixing layer in a perfectly-coherent wavepacket [37]. The differences in radial profiles between azimuthal modes can be explained by the boundary condition imposed along the centreline. The axial velocity component and density are non-zero at the jet centreline for  $m = 0$  (figure 7.17), whereas radial velocity is finite at  $r = 0$  for  $m = 1$  (figure 7.18). For  $m > 1$ , all variables should be zero along the jet centreline.

Figure 7.19 depicts the visual comparisons of the nearfield. For each flow variable, the real parts of a short-time Fourier transform (left column), the leading SPOD mode (centre column), and the PSE solution (right column) are presented for the frequencies under consideration. As expected from the results of Sinha *et al.* [72], similarities exist between all cases. Improved agreement is observed between the PSE solution and the leading SPOD mode, showing that the model correctly captures the structure of the coherent K-H wavepacket. The small-scale jittering behaviour of wavepackets is contained in higher SPOD modes. The signature of Mach wave radiation is visible in both the axial velocity and density fluctuation plots. Similar observations are found for  $m = 1$  helical mode shown in figure 7.20.

To quantify the agreement between the PSE solution and unfiltered LES data, the alignment metric is computed

$$\mathcal{B}^{(\mathcal{J}^{th})} = \frac{\langle \mathbf{q}_{t,PSE}(x, r; m, \omega), \mathbf{q}_{t,LES}^{(\mathcal{J}^{th})}(x, r; m, \omega) \rangle}{\|\mathbf{q}_{t,PSE}(x, r; m, \omega)\| \|\mathbf{q}_{t,LES}^{(\mathcal{J}^{th})}(x, r; m, \omega)\|}, \quad (7.1)$$

where the inner product is defined in equation 4.16 of the paper and a value of  $\mathcal{B} = 1$  corresponds to a perfect agreement. The metric only represents alignment in the radial shapes of  $u_x, u_r$  and  $\rho$  of the wavepacket. The average streamwise variation of  $\mathcal{B}$ , for a range

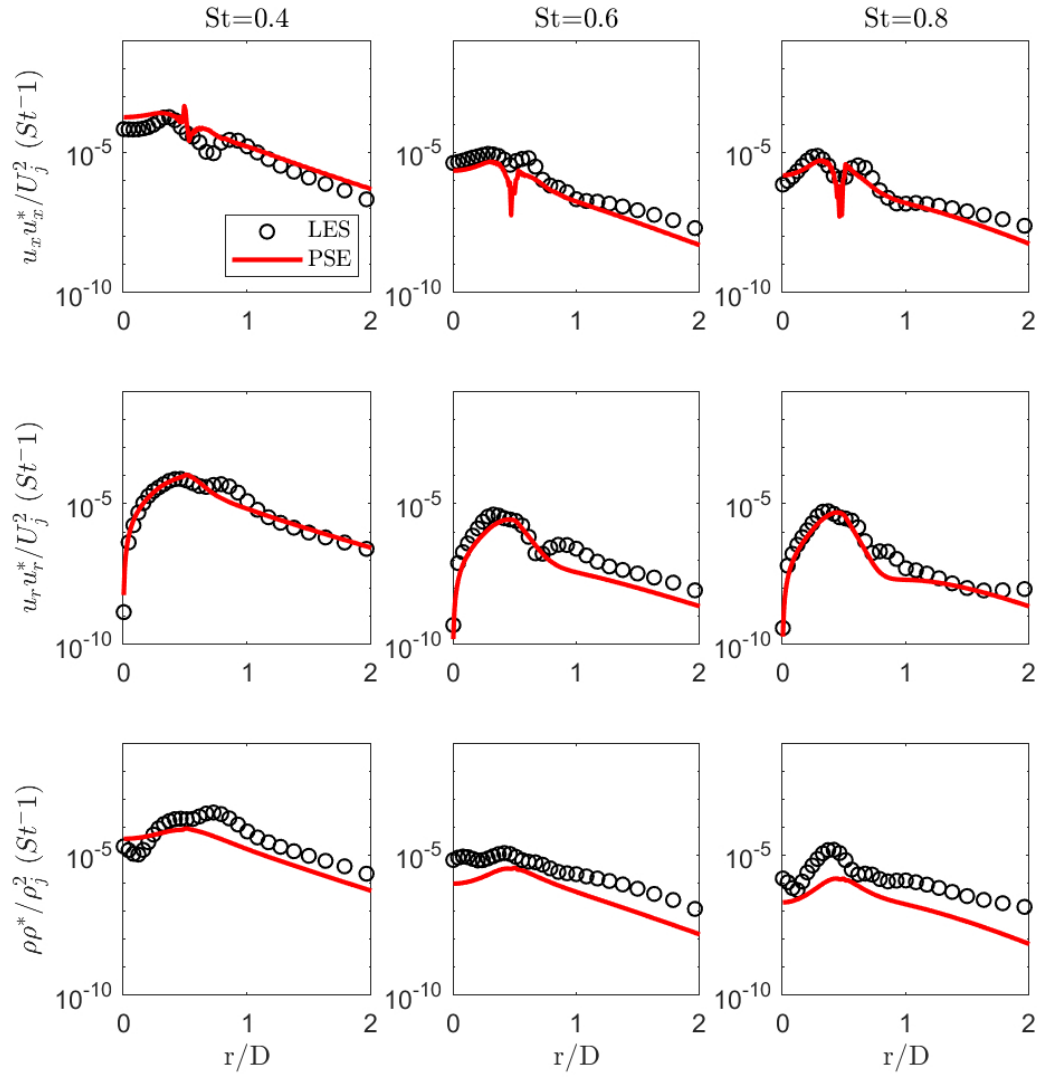


Figure 7.17: Radial cross-section comparisons between LES (symbols) and PSE (lines) for  $m = 0$  at  $x = 4D$ .

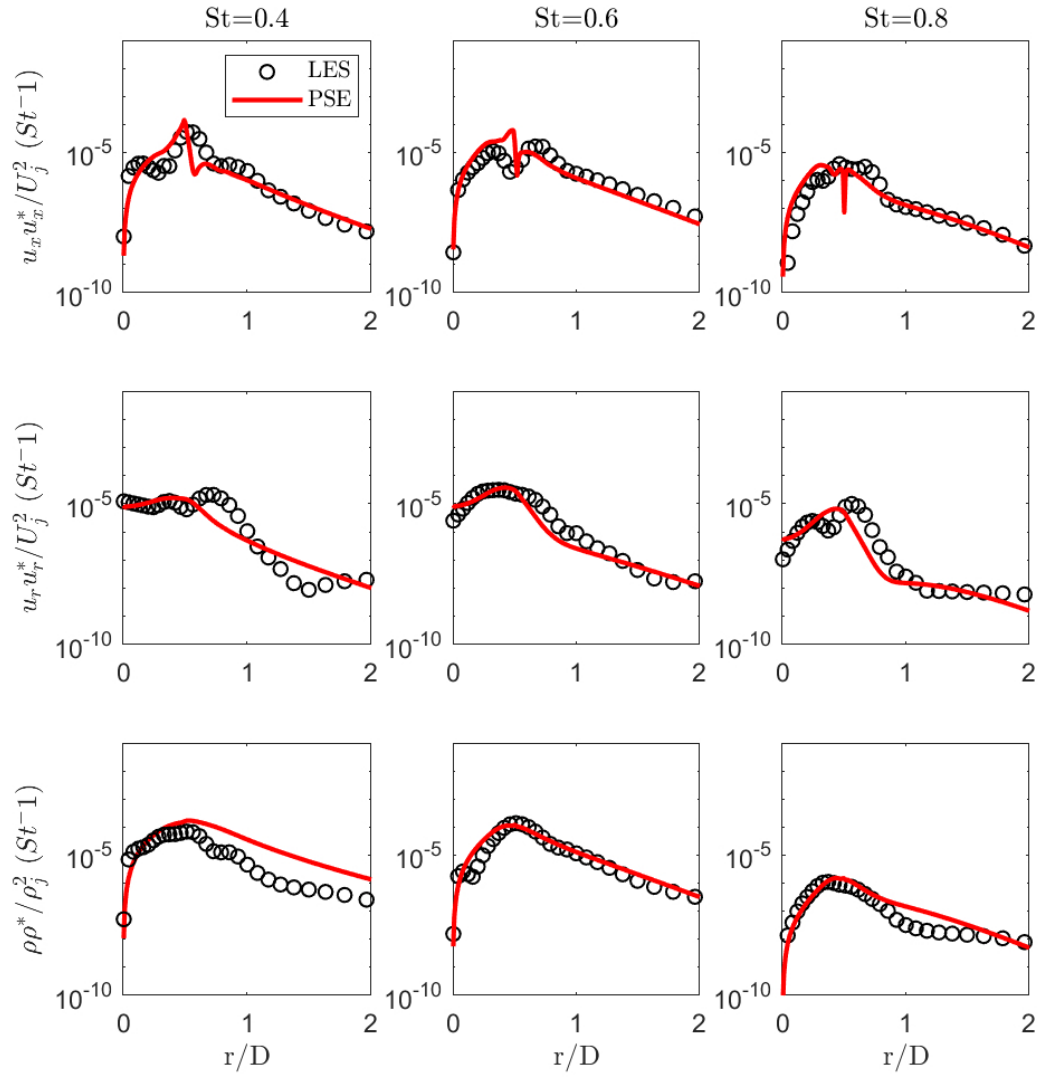


Figure 7.18: Radial cross-section comparisons between LES (symbols) and PSE (lines) for  $m = 1$  at  $x = 4D$ .

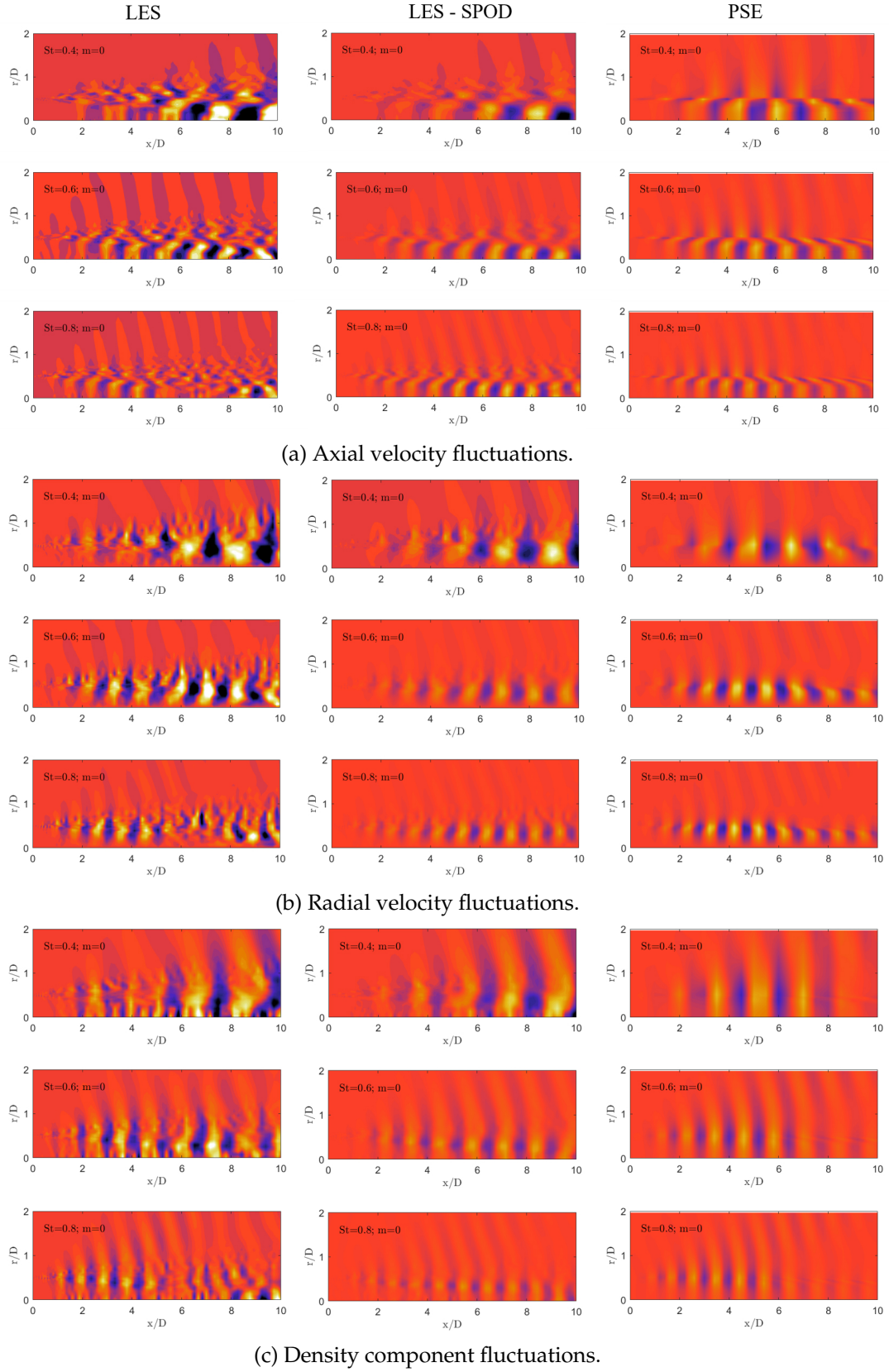


Figure 7.19: Comparison of real parts of  $q_t$  between the extracted wavepacket from LES (left column), corresponding first SPOD mode (centre column) and PSE predictions (right column) for  $m = 0$ . Flow quantities normalised by the ideally-expanded condition.

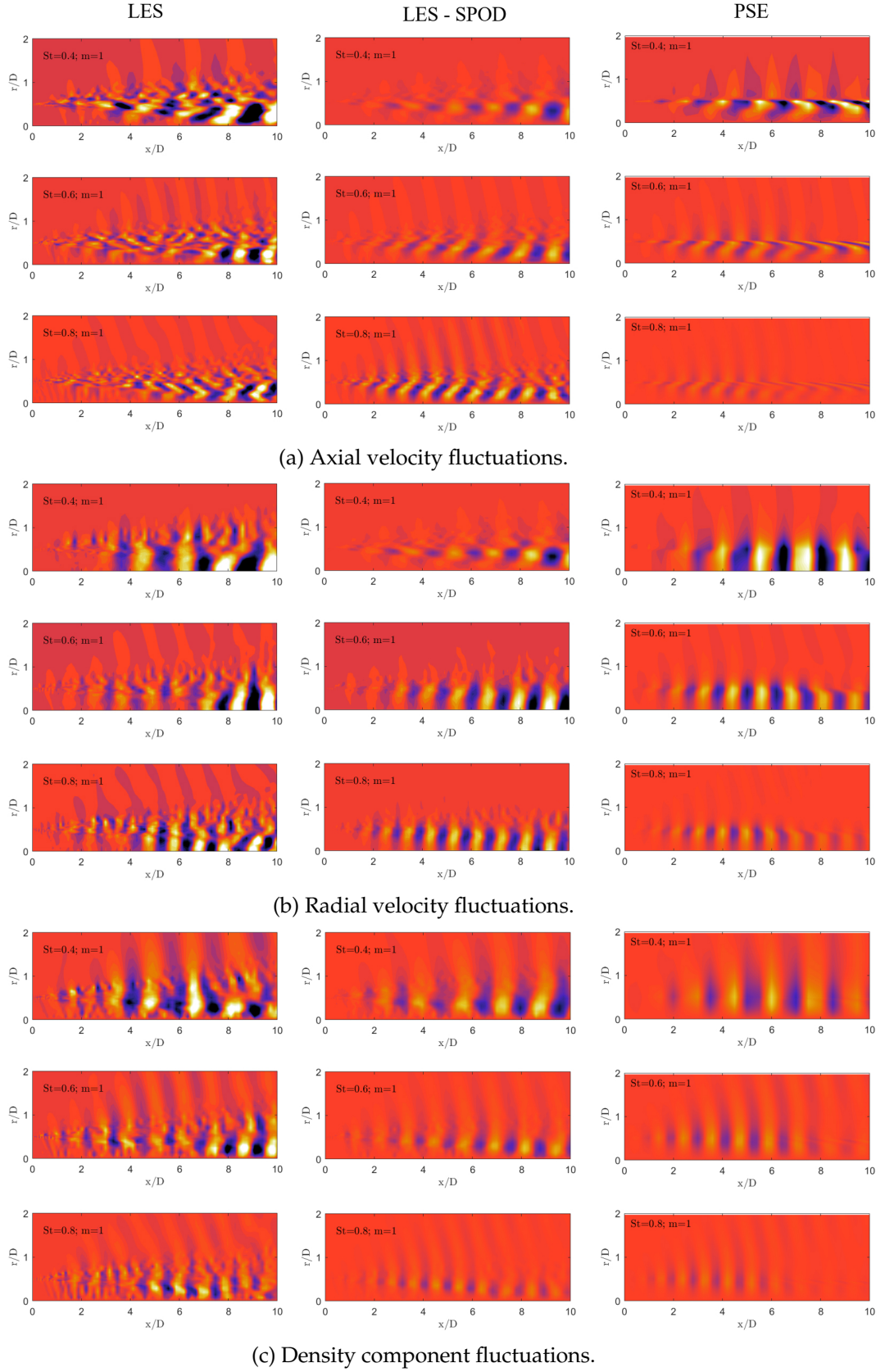


Figure 7.20: Comparison of real parts of  $q_t$  between the extracted wavepacket from LES (left column), corresponding first SPOD mode (centre column) and PSE predictions (right column) for  $m = 1$ . Flow quantities normalised by the ideally-expanded condition.



of frequencies from  $0 \leq x/D \leq 10$ , is shown in figure 7.21. For the axisymmetric mode, when using unfiltered LES data, agreement between the PSE and LES is acceptable ( $0.5 < \mathcal{B} < 0.6$ ). The alignment in radial profile is a maximum at  $x = 2D$ . The value of  $\mathcal{B}$  decreases further downstream, with higher frequencies yielding slightly lower agreement. The agreement is poorer for the helical mode, for which the trend with frequency is less clear.

The metric for alignment between the PSE solutions and the first SPOD mode is also shown (triangle markers). A similar procedure was performed by Sinha *et al.* [72] for a different inner-product norm (pressure and velocity components were computed separately). An improved alignment is found across all frequencies and azimuthal mode as expected, confirming the visualisations in figures 7.19-7.20. This improvement is due to the PSE solution representing the most unstable K-H mode which corresponds to the optimal SPOD mode. In contrast, the full LES signal contains many modes, and a decrease in alignment is expected when the sub-optimal SPOD modes become more important further downstream [38, 59, 74]. On average, there is better agreement for the axisymmetric mode compared to the helical mode.

Figure 7.21 supports the results from previous studies on subsonic [37] and ideally-expanded supersonic jets [72]. In addition, both Sinha *et al.* [72] and Rodriguez *et al.* [138] have shown there exists good alignment between PSE near-field pressure predictions, and the first SPOD mode extracted from the same jet LES used here. For velocity components, however, the alignment is weaker, which may be due to multi-modal mechanisms or the presence of residual shocks; neither phenomenon are captured by PSE.

### 7.13 Discussion of the Use of PSE

As alluded to earlier in section 2.4.2.1, while PSE is a suitable candidate to describe the coherent structures in a turbulent jet, there are limitations to this method as discussed by Towne *et al.* [142]. Using PSE in flows which have multiple unstable modes, or strong acoustic fluctuations in the nearfield, has yielded mixed results. In supersonic jets, in addition to the K-H mode, there exists other modal instabilities which give rise to upstream and downstream-travelling pressure modes [65]. Rodriguez *et al.* [71] show that while these pressure modes have non-negligible amplitudes near the nozzle exit, the PSE will converge

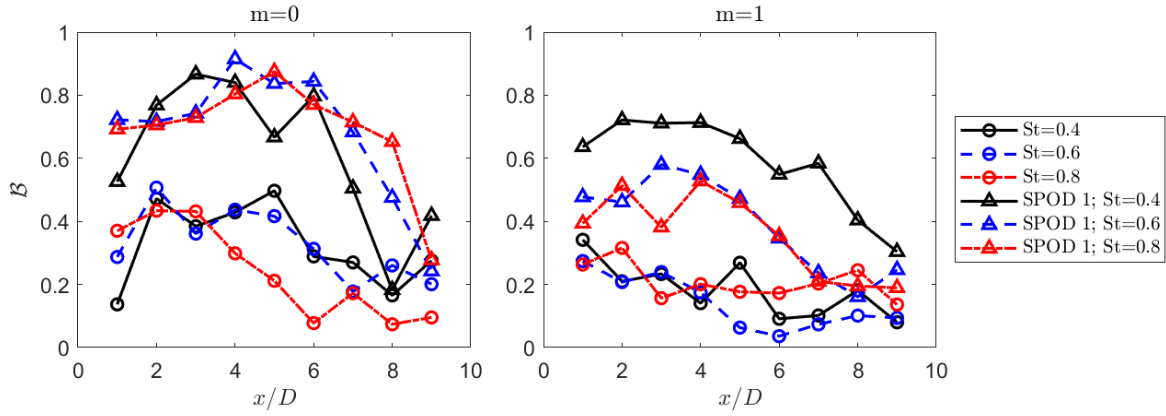


Figure 7.21: Alignment metric  $\mathcal{B}$  for  $m = 0$  (left) and  $m = 1$  (right) for a range of frequencies. Circles and triangles represent alignment with full LES signal and the first SPOD mode respectively.

on the most dominant K-H mode further downstream. The upstream-propagating modes will also be damped out by the parabolic marching scheme. Hence, the PSE model considers only the K-H mode assumed to be that which interacts with the shocks to produce BBSAN. Furthermore, while PSE is successful in describing both the hydrodynamic and near-acoustic field of the unheated ideally-expanded supersonic jet, it should be emphasised that only the flow field fluctuations are used as input to the source model.

## 7.14 Concluding Statement

The results presented in this chapter offer several compelling conclusions and also future directions. On one hand, this source construction supports the BBSAN modelling viewpoint first proposed by Tam and Tanna [23]. This wavepacket model extends the work of Tam [157] by educating the source parameters directly from flow data alone. It is evident that many BBSAN features are reproduced. Encouraging amplitude predictions over a wide spectral and directivity range are obtained based on flow information alone; a  $\pm 2\text{dB/St}$  agreement is observed at the primary peak frequency.

The limits of a purely linear model (PSE with no coherence decay) are now apparent. There is a slight over-prediction in amplitude at sideline directions, and narrowband peaks are present. With the inclusion of non-linearity, in the form of coherence decay, the improved agreement at higher frequencies supports the important role that wavepacket jitter plays in shock-containing flows.

On the other hand, the slight mismatches in the inter-peak regions possibly indicate that further refinement of the source description is required. The observation may be explained by the variation in coherence decay behaviour between shock-containing and shock-free jets. Another possibility is that the periodic oscillations of the shock-cells were not taken into account by the present model.

Together with the findings from the simplified line source model presented in Chapter 6, this modelling approach has shown how the different components of the source function affect the predicted BBSAN sound field. The frequency of the BBSAN peaks are largely governed by the wavenumbers of the wavepacket and shock-cells ( $k_t - k_s$ ). This has been known since the work of Tam and Tanna [23], who showed a slight change in shock-cell spacing will indeed alter the predicted peak frequency. This could be the reason why the predicted BBSAN peak, while derived from PIV data, do not match the measured acoustic measurements for which flow data was unavailable. For correct SPL predictions, however, not only do the amplitudes of both the wavepacket and shocks have to be accurately captured, the jittering nature of the wavepacket needs to be accounted for. The effect of shocks on the evolution of the wavepacket may also depend on the shock strength, and hence operating condition of the jet; this was not taken into account in this current work. It is clear from the results and discussion in this chapter, that more work needs to focus on refining this component of the BBSAN source function.

To summarise, the results not only confirm BBSAN is generated by the interaction of large-scale structures with the shock-cells, but also quantitatively shows the role non-linearity plays in the noise spectra of shock-containing jets. Possible future work and perspectives are outlined in Chapter 8.

## Chapter 8

# Conclusions

### 8.1 Summary of Main Results

This thesis combines experimental acoustic results and modelling strategies to investigate the generation of broadband shock-associated noise in shock-containing jets. For mitigation of jet noise, it is important to identify, understand and model the underlying source mechanisms. Recently, much of the acoustically-important turbulent motion has been associated with wavepackets. Owing to their success and inherent link to the governing equations, these same structures are used in the composition of a new wavepacket model for BBSAN.

The need for high-quality clean acoustic data prompted the design and validation of a new jet noise facility at Monash University, where existing jet rigs operate in a non-anechoic environment. Chapter 3 focuses on the design of the Supersonic Jet Anechoic Facility (SJAF). The facility was conceived not only to support the present research program but also to support a wide range of future aeroacoustic experiments. The jet expels into an enclosed anechoic chamber and uses the same air supply as the existing supersonic wind tunnel. Novel design features of the facility allow for simultaneous acoustic and flow measurements. Careful consideration was given to balancing the acoustic requirements with the size of the chamber and jet. A set of design drawings is provided in Appendix C.

As with all new jet noise facilities, verification of acoustic performance was required. The validation process, reported in Chapter 4, was separated into three distinct campaigns; 1) verification of the free-field behaviour of the anechoic chamber, 2) determination of the geometric far-field of the jet and 3) identification of potential sources of spurious noise.

The adopted methodology largely follows that specified by Ahuja [161], also drawing on experiences reported by other jet noise laboratories. The requirements of the anechoic chamber, as detailed in ISO3745 guidelines [178], were met. The validation process was not about replicating measurements from other facilities but rather to obtain clarity on the performance characteristics and limitations of the new facility. From the qualification tests performed, the original specifications of SJAF were either met or exceeded. Thus, the microphone measurements obtained may be considered acoustically clean.

The subsequent chapters aim to address the research questions raised at the end of Chapter 2. The successful development and validation of SJAF allowed measurements on the azimuthal structure of BBSAN to be performed as detailed in Chapter 5. The experimental campaign was driven by two objectives. Firstly, there is a lack of existing data in literature that describe the variation of far-field BBSAN azimuthal modes as a function of jet Mach number. Secondly, by representing the far-field sound as a function of frequency and azimuthal modes, the sound field may be directly associated with a given wavepacket. By using a pair of microphones, the BBSAN spectra of the first four azimuthal modes were measured over a range of observer angles for three underexpanded conditions. Unlike noise radiated downstream, BBSAN is dominated by azimuthal modes 1–3. Crucially, because of the directivity behaviour of BBSAN, the relative contribution of successive modes to BBSAN is sensitive to the observer angle and jet operating condition; higher modes become increasingly important at higher frequencies. The results highlight the difference in spectral shape between the total signal and the spectra of each azimuthal mode, suggesting that care must be taken when comparing predictions from instability wave models, which are usually characterised by  $(\omega, m)$  pairs, to experimental data. Decomposed spectra were also used in Chapter 7 for comparison to model predictions.

The inability of stability-based BBSAN models to accurately predict high-frequency noise suggested an investigation into the source description was warranted. Previous authors have postulated the importance of non-linearities and higher-order shock-cell modes in BBSAN models. In recent years, coherence decay has been shown to be essential for understanding and modelling noise in subsonic jets, with a relatively small impact in perfectly-expanded supersonic jets. Chapter 6 is devoted to investigating the impact of coherence decay in shock-containing supersonic jets. A kinematic line source model was used to test the effect

of inclusion and omission of coherence decay in a BBSAN source. The inclusion of coherence decay broadened the spectral peak widths, smoothing out the artificial narrow-band peaks observed in previous BBSAN stability models. The results demonstrated that the modelling of BBSAN requires an adequate description of both coherence decay and higher-order shock-cell modes. The qualitative insights obtained from this investigation served as a stepping stone to a more complete BBSAN model in Chapter 7.

The findings from Chapters 5 and 6 were employed in Chapter 7 where a more complete wavepacket BBSAN source was developed. While a more robust multiple-scales approximation of the shock structure could have been computed, a modified Pack and Prandtl model was used as it is more amenable to changes in shock-cell description. The ease of implementing the P&P model also allowed rapid evaluation and testing of the sensitivity of the far-field sound to the shock-cell structure. To obtain a quantitatively accurate model, a volumetric source description was used, where source parameters were deduced from numerical and experimental datasets in an 'inside-out' approach; the acoustic field was not used to scale any modelling variables. Informed by the line source model problem in Chapter 6, two-point coherence information and higher-order shock-cell modes were included in the source description. To form a link to the underlying flow dynamics, solutions to parabolised stability equations were also used to describe wavepackets. Hence, two equivalent BBSAN source models were obtained; one from the direct substitution of numerical data and the other from PSE solutions. For a  $M_j = 1.5$  jet, far-field predictions using the model sources were compared against experimental spectra measured in Chapter 5 for the same azimuthal mode. Encouraging comparisons of the radiated noise spectra, in both frequency and amplitude, were observed for the first three azimuthal modes. Apart from agreement in acoustic spectra, the results also quantitatively confirmed the conclusions from Chapter 6; the inclusion of wavepacket jitter is critical for high-frequency prediction of BBSAN.

Overall, the results in this thesis support the notion that the interaction of shock-cells with the large-scale coherent structures, modelled as wavepackets, is the acoustic generation process for broadband shock-associated noise in supersonic shock-containing jets. The methodology adopted also demonstrates the benefit of using both kinematic and dynamic modelling approaches; a simple reduced-order model may be used to infer which flow features of the jet are critical to the dynamics of sound generation.

## 8.2 Open Issues and Future Outlook

As alluded to in Chapter 1, the understanding and reduction of jet noise can be achieved either via practical engineering strategies (i.e., trial and error, parametric studies) or an inspection of the underlying flow physics at the source level. The scientific contributions of the modelling work in this thesis may be looked at from both perspectives.

Practical jet noise prediction tools with fast turnaround times are valuable for aircraft designers; they can be used to test over a wide range of operating conditions and the results may inform design choices. As jet noise is sensitive to many factors including nozzle exit conditions [73], without resorting to time-consuming numerical simulations, accurate amplitude predictions are often difficult to achieve. Moreover, nearly all existing BBSAN models require some degree of calibration using the acoustic field: calibration coefficients are used to adjust the computed spectral shape and amplitude to match acoustic measurements. This may not be possible from a practical standpoint.

The equivalent source model using PSE solutions in Chapter 7 provides an alternative. Provided that shock-cell and mean flow profiles are available, only a single empirical constant is required to adjust the free amplitude of the linear PSE solutions to obtain a  $\pm 2\text{dB/St}$  accuracy at the main peak. Critically, no calibration is required. Mean profiles may be obtained from experiments (e.g. planar PIV measurements) or numerical simulations (RANS). Amplitude information may be obtained using single-point laser-doppler velocimetry measurements [19, 53]. An immediate next step would be to apply this BBSAN wavepacket model for a single-stream jet over a wider range of Mach numbers.

With some modification, this ‘inside-out’ approach may also be applied to more complex configurations common in real turbofan engines such as non-circular (i.e. elliptical, rectangular, or corrugated) nozzles, dual-stream flows and hot flows. The modal shock-cell description may be obtained for a jet with arbitrary cross-sectional geometry via eigenmode expansion [209]. The implementation of PSE in jets issued from non-circular nozzles [210] and hot jets [211] was successful. The dual-stream jet configuration does, however, require careful consideration. Since two shear layers are present, multiple relevant instability modes exist. The enforced PSE regularisation would lead to their evolution being incorrectly captured [142]. In this instance, one-way Navier-Stokes (OWNS) solutions may be more suitable

[212]. Such investigations will be beneficial to both the academic and industrial community.

While the current results for BBSAN are encouraging, a more complete prediction across a wider directivity range is still unavailable. At angles towards the jet axis, mixing noise will dominate over BBSAN and refraction effects cannot be ignored. Future work looking at modelling mixing noise using wavepackets will be beneficial to the development of a reduced-order supersonic jet noise model.

The results from Chapter 7 raise more questions regarding the BBSAN generating mechanisms. The clear demonstration of the role that non-linearity plays in BBSAN naturally leads to an examination of its form and origin. Presently, non-linearity may lead to wavepacket jitter or the unsteady motion of the shock cells. While previously discussed qualitatively and empirically modelled by Tam [157], the effect of shock-cell unsteadiness on BBSAN has not been quantified. The oscillation of shocks may be attributed to several factors [24]; 1) pressure perturbations from the passage of upstream-propagating sound waves, 2) coupling motion within the shock-cell structure, 3) distortion at the shear-layer interface due to passing vortices, and 4) interaction with large-scale coherent structures. A quantitative model capturing all of these phenomena is as yet unavailable. Furthermore, the artificial separation of the shock-cell perturbations from the wavepacket fluctuations of the present model prohibits the investigation of points 3) and 4). One approach to investigate this problem is to empirically model the effect of shock-cell unsteadiness, similar to Tam [157], and use a line source model problem to observe its relative effect on far-field BBSAN along with coherence decay.

On the other hand, the unifying resolvent analysis framework [14] may provide a more complete picture. By computing the resolvent for a shock-containing jet, the non-linear effects acting on the wavepackets are observed in the forcing term [74]. The artificial separation between the shock and turbulence components may be entirely avoided. An indication on the importance of non-linearity may be observed in the SPOD performed on shock-containing jets. Initial observations show, except at screech frequencies, there is minimal separation between the optimal and suboptimal modes [213, 214], suggesting that non-modal and non-linear mechanisms are important. This observation is consistent with the modelling conclusion that some form of non-linearity, manifested as wavepacket jitter or otherwise, is required in the prediction of high-frequency BBSAN. By looking at the relevant forcing



modes, resolvent analysis may shed light on the exact roles of both wavepacket jitter and shock-cell unsteadiness.

# Bibliography

- [1] S. Morrell, R. Taylor and D. Lyle, "A review of health effects of aircraft noise," *Australian and New Zealand journal of public health*, vol. 21, no. 2, pp. 221–236, 1997.
- [2] C. K. Tam, "Supersonic jet noise," *Annual Review of Fluid Mechanics*, vol. 27, no. 1, pp. 17–43, 1995.
- [3] A. Powell, "On the mechanism of choked jet noise," *Proceedings of the Physical Society. Section B*, vol. 66, no. 12, p. 1039, 1953.
- [4] G. Raman, "Supersonic jet screech: Half-century from powell to the present," *Journal of Sound and Vibration*, vol. 225, no. 3, pp. 543–571, 1999.
- [5] D. Edgington-Mitchell, "Aeroacoustic resonance and self-excitation in screeching and impinging supersonic jets—a review," *International Journal of Aeroacoustics*, vol. 18, no. 2-3, pp. 118–188, 2019.
- [6] J. Huber, V. Fleury, J. Bulté, E. Laurendeau and A. A. Sylla, "Understanding and reduction of cruise jet noise at aircraft level," *International Journal of Aeroacoustics*, vol. 13, no. 1-2, pp. 61–84, 2014.
- [7] A. B. Vaughn, T. B. Neilsen, K. L. Gee, A. T. Wall, J. Micah Downing and M. M. James, "Broadband shock-associated noise from a high-performance military aircraft," *The Journal of the Acoustical Society of America*, vol. 144, no. 3, EL242–EL247, 2018.
- [8] G. Brès, J. Nichols, S. Lele, F. Ham, R. Schlinker, R. Reba and J. Simonich, "Unstructured large eddy simulation of a hot supersonic over-expanded jet with chevrons," in *18th AIAA/CEAS Aeroacoustics Conference (33rd AIAA Aeroacoustics Conference)*, 2012, p. 2213.
- [9] S. Martens, J. T. Spyropoulos and Z. Nagel, "The effect of chevrons on crackle: Engine and scale model results," in *Turbo Expo: Power for Land, Sea, and Air*, vol. 54617, 2011, pp. 315–326.
- [10] N. R. A. Committee *et al.*, "Report on jet engine noise reduction," URL: [http://www.nrac.navy.mil/docs/2009\\_FINAL\\_Jet\\_Noise\\_Report\\_4-26-09.pdf](http://www.nrac.navy.mil/docs/2009_FINAL_Jet_Noise_Report_4-26-09.pdf), 2009.

- [11] W. Bowes, D. Rumpf, D. Bowler, R. Carnes, P. Fratarangelo, W. Heiser, D. Hu, P. Moin and W. Voorhees, "Report on jet engine noise reduction," *Tech. Rep.*, 2009.
- [12] D. L. Huff, B. S. Henderson, J. J. Berton and J. A. Seidel, "Perceived noise analysis for offset jets applied to commercial supersonic aircraft," in *54th AIAA aerospace sciences meeting*, 2016, p. 1635.
- [13] M. J. Lighthill, "On sound generated aerodynamically. i. general theory," in *Proceedings of the Royal Society of London A: Mathematical, Physical and Engineering Sciences*, The Royal Society, vol. 211, 1952, pp. 564–587.
- [14] A. V. Cavalieri, P. Jordan and L. Lesshafft, "Wave-packet models for jet dynamics and sound radiation," *Applied Mechanics Reviews*, vol. 71, no. 2, p. 020 802, 2019.
- [15] J. B. Freund, "Nozzles, turbulence, and jet noise prediction," *Journal of Fluid Mechanics*, vol. 860, pp. 1–4, 2019.
- [16] P. Jordan and T. Colonius, "Wave packets and turbulent jet noise," *Annual Review of Fluid Mechanics*, vol. 45, pp. 173–195, 2013.
- [17] R. S. Snedeker *et al.*, "A study of free jet impingement. part 1. mean properties of free and impinging jets," *Journal of fluid Mechanics*, vol. 45, no. 2, pp. 281–319, 1971.
- [18] D. Edgington-Mitchell, D. R. Honnery and J. Soria, "The underexpanded jet mach disk and its associated shear layer," *Physics of Fluids*, vol. 26, no. 9, p. 1578, 2014.
- [19] A. Savarese, "Experimental study and modelling of shock-cell noise," Ph.D. dissertation, L'UNIVERSITÉ DE POITIERS, 2014.
- [20] M. Harper-Bourne and M. Fisher, "The noise from shock waves in supersonic jets," *AGARD-CP-131*, vol. 11, pp. 1–13, 1973.
- [21] M. Harper-Bourne, "On modelling the near-field noise of the high-speed jet exhausts of combat aircraft," in *8th AIAA/CEAS Aeroacoustics Conference & Exhibit*, 2002, p. 2424.
- [22] B. André, T. Castelain and C. Bailly, "Broadband shock-associated noise in screeching and non-screeching underexpanded supersonic jets," *AIAA journal*, vol. 51, no. 3, pp. 665–673, 2013.
- [23] C. K. Tam and H. Tanna, "Shock associated noise of supersonic jets from convergent-divergent nozzles," *Journal of Sound and Vibration*, vol. 81, no. 3, pp. 337–358, 1982.
- [24] J. Panda, "Shock oscillation in underexpanded screeching jets," *Journal of Fluid Mechanics*, vol. 363, pp. 173–198, 1998.

- [25] L. Prandtl, *Über die stationären Wellen in einem Gasstrahl*. Hirzel, 1904.
- [26] D. Pack, "A note on prandtl's formula for the wave-length of a supersonic gas jet," *The Quarterly Journal of Mechanics and Applied Mathematics*, vol. 3, no. 2, pp. 173–181, 1950.
- [27] C. K. Tam, "On the noise of a nearly ideally expanded supersonic jet," *Journal of Fluid Mechanics*, vol. 51, no. 1, pp. 69–95, 1972.
- [28] C. K. Tam, J. A. Jackson and J. Seiner, "A multiple-scales model of the shock-cell structure of imperfectly expanded supersonic jets," *Journal of Fluid Mechanics*, vol. 153, pp. 123–149, 1985.
- [29] T. Norum and J. Seiner, "Measurements of mean static pressure and far field acoustics of shock containing supersonic jets," Tech. Rep., 1982.
- [30] J. C. Laurence, "Intensity, scale, and spectra of turbulence in mixing region of free subsonic jet," 1956.
- [31] P. Bradshaw, D. H. Ferriss and R. Johnson, "Turbulence in the noise-producing region of a circular jet," *Journal of Fluid Mechanics*, vol. 19, no. 4, pp. 591–624, 1964.
- [32] E. Mollo-Christensen, "Jet noise and shear flow instability seen from an experimenter's viewpoint," *Journal of Applied Mechanics*, vol. 34, no. 1, pp. 1–7, 1967.
- [33] S. C. Crow and F. Champagne, "Orderly structure in jet turbulence," *Journal of Fluid Mechanics*, vol. 48, no. 3, pp. 547–591, 1971.
- [34] G. L. Brown and A. Roshko, "On density effects and large structure in turbulent mixing layers," *Journal of Fluid Mechanics*, vol. 64, no. 4, pp. 775–816, 1974.
- [35] T. Suzuki and T. Colonius, "Instability waves in a subsonic round jet detected using a near-field phased microphone array," *Journal of Fluid Mechanics*, vol. 565, pp. 197–226, 2006.
- [36] V. Kopiev, S. Chernyshev, M. Zaitsev and V. Kuznetsov, "Experimental validation of instability wave theory for round supersonic jet," in *12th AIAA/CEAS Aeroacoustics Conference (27th AIAA Aeroacoustics Conference)*, 2006, p. 2595.
- [37] A. V. Cavalieri, D. Rodriguez, P. Jordan, T. Colonius and Y. Gervais, "Wavepackets in the velocity field of turbulent jets," *Journal of fluid mechanics*, vol. 730, pp. 559–592, 2013.
- [38] L. Lesshafft, O. Semeraro, V. Jaunet, A. V. Cavalieri and P. Jordan, "Resolvent-based modeling of coherent wave packets in a turbulent jet," *Physical Review Fluids*, vol. 4, no. 6, p. 063 901, 2019.
- [39] C. Moore, "The role of shear-layer instability waves in jet exhaust noise," *Journal of Fluid Mechanics*, vol. 80, no. 2, pp. 321–367, 1977.

- [40] D. Breakey, P. Jordan, A. Cavalieri and O. Léon, "Near-field wavepackets and the far-field sound of a subsonic jet," in *19th AIAA/CEAS aeroacoustics conference*, 2013, p. 2083.
- [41] D. K. McLaughlin, G. L. Morrison and T. R. Troutt, "Experiments on the instability waves in a supersonic jet and their acoustic radiation," *Journal of Fluid Mechanics*, vol. 69, no. 1, pp. 73–95, 1975.
- [42] T. Troutt and D. K. McLaughlin, "Experiments on the flow and acoustic properties of a moderate-reynolds-number supersonic jet," *Journal of Fluid Mechanics*, vol. 116, pp. 123–156, 1982.
- [43] D. M. Mitchell, D. R. Honnery and J. Soria, "The visualization of the acoustic feedback loop in impinging underexpanded supersonic jet flows using ultra-high frame rate schlieren," *Journal of visualization*, vol. 15, no. 4, pp. 333–341, 2012.
- [44] M. Akamine, K. Okamoto, S. Teramoto and S. Tsutsumi, "Conditional sampling analysis of high-speed schlieren movies of mach wave radiation in a supersonic jet," *The Journal of the Acoustical Society of America*, vol. 145, no. 1, EL122–EL128, 2019.
- [45] V. Jaunet, P. Jordan and A. Cavalieri, "Two-point coherence of wave packets in turbulent jets," *Physical Review Fluids*, vol. 2, no. 2, p. 024 604, 2017.
- [46] Y. Ozawa, T. Nonomura, A. Oyama and K. Asai, "Effect of the reynolds number on the aeroacoustic fields of a transitional supersonic jet," *Physics of Fluids*, vol. 32, no. 4, p. 046 108, 2020.
- [47] D. Edgington-Mitchell, K. Oberleithner, D. R. Honnery and J. Soria, "Coherent structure and sound production in the helical mode of a screeching axisymmetric jet," *Journal of Fluid Mechanics*, vol. 748, pp. 822–847, 2014.
- [48] J. L. Weightman, O. Amili, D. Honnery, D. Edgington-Mitchell and J. Soria, "Nozzle external geometry as a boundary condition for the azimuthal mode selection in an impinging underexpanded jet," *Journal of Fluid Mechanics*, vol. 862, pp. 421–448, 2019.
- [49] G. A. Brès and S. K. Lele, "Modelling of jet noise: A perspective from large-eddy simulations," *Philosophical Transactions of the Royal Society A*, vol. 377, no. 2159, p. 20 190 081, 2019.
- [50] R. J. Adrian, "Stochastic estimation of conditional structure: A review," *Applied scientific research*, vol. 53, no. 3-4, pp. 291–303, 1994.
- [51] C. Picard and J. Delville, "Pressure velocity coupling in a subsonic round jet," *International Journal of Heat and Fluid Flow*, vol. 21, no. 3, pp. 359–364, 2000.

- [52] F. Kerherve, P. Jordan, A. Cavalieri, J. Delville, C. Bogey and D. Juvé, "Educing the source mechanism associated with downstream radiation in subsonic jets," *Journal of Fluid Mechanics*, vol. 710, pp. 606–640, 2012.
- [53] A. Savarese, P. Jordan, S. Girard, E. Collin, M. Porta and Y. Gervais, "Experimental study of shock-cell noise in underexpanded supersonic jets," in *19th AIAA/CEAS Aeroacoustics Conference*, 2013, p. 2080.
- [54] K. Taira, S. L. Brunton, S. T. Dawson, C. W. Rowley, T. Colonius, B. J. McKeon, O. T. Schmidt, S. Gordeyev, V. Theofilis and L. S. Ukeiley, "Modal analysis of fluid flows: An overview," *Aiaa Journal*, vol. 55, no. 12, pp. 4013–4041, 2017.
- [55] K. Taira, M. S. Hemati, S. L. Brunton, Y. Sun, K. Duraisamy, S. Bagheri, S. T. Dawson and C.-A. Yeh, "Modal analysis of fluid flows: Applications and outlook," *AIAA journal*, vol. 58, no. 3, pp. 998–1022, 2020.
- [56] O. T. Schmidt, A. Towne, T. Colonius, A. V. Cavalieri, P. Jordan and G. A. Brès, "Wavepackets and trapped acoustic modes in a turbulent jet: Coherent structure eduction and global stability," *Journal of Fluid Mechanics*, vol. 825, pp. 1153–1181, 2017.
- [57] A. Towne, O. T. Schmidt and T. Colonius, "Spectral proper orthogonal decomposition and its relationship to dynamic mode decomposition and resolvent analysis," *Journal of Fluid Mechanics*, vol. 847, pp. 821–867, 2018.
- [58] A. Towne, T. Colonius, P. Jordan, A. V. Cavalieri and G. A. Bres, "Stochastic and nonlinear forcing of wavepackets in a mach 0.9 jet," *AIAA paper*, vol. 2217, p. 2015, 2015.
- [59] A. Towne, O. T. Schmidt and T. Colonius, "Spectral proper orthogonal decomposition and its relationship to dynamic mode decomposition and resolvent analysis," *arXiv preprint arXiv:1708.04393*, 2017.
- [60] O. Semeraro, L. Lesshafft, V. Jaunet and P. Jordan, "Modeling of coherent structures in a turbulent jet as global linear instability wavepackets: Theory and experiment," *International Journal of Heat and Fluid Flow*, vol. 62, pp. 24–32, 2016.
- [61] P. J. Schmid, D. S. Henningson and D. Jankowski, "Stability and transition in shear flows. applied mathematical sciences, vol. 142," *Appl. Mech. Rev.*, vol. 55, no. 3, B57–B59, 2002.
- [62] W. O. Criminale, T. L. Jackson and R. D. Joslin, *Theory and computation in hydrodynamic stability*. Cambridge University Press, 2018.
- [63] A. Michalke, "A wave model for sound generation in circular jets," Technical Report, 1970.

- [64] P. J. Morris, "The instability of high speed jets," *International Journal of Aeroacoustics*, vol. 9, no. 1-2, pp. 1–50, 2010.
- [65] C. K. Tam and F. Q. Hu, "On the three families of instability waves of high-speed jets," *Journal of Fluid Mechanics*, vol. 201, pp. 447–483, 1989.
- [66] H. Oertel *et al.*, "Mach wave radiation of hot supersonic jets investigated by means of the shock tube and new optical techniques," in *Proceedings of the 12th International Symposium on Shock-Tubes and Waves, Israel*, 1980.
- [67] D. M. Edgington-Mitchell, D. Duke, D. Harris, T. Wang, O. T. Schmidt, V. Jaunet, P. Jordan and A. Towne, "Modulation of downstream-propagating waves in jet screech.," in *AIAA/CEAS Aeroacoustics Conference 2019*, American Institute of Aeronautics and Astronautics, 2019.
- [68] D. Edgington-Mitchell, T. Wang, P. Nogueira, O. Schmidt, V. Jaunet, D. Duke, P. Jordan and A. Towne, "Waves in screeching jets," *arXiv preprint arXiv:2008.09756*, 2020.
- [69] D. Crighton and M. Gaster, "Stability of slowly diverging jet flow," *Journal of Fluid Mechanics*, vol. 77, no. 2, pp. 397–413, 1976.
- [70] K. Gudmundsson and T. Colonius, "Instability wave models for the near-field fluctuations of turbulent jets," *Journal of Fluid Mechanics*, vol. 689, pp. 97–128, 2011.
- [71] D. Rodriguez, A. Sinha, G. A. Brès and T. Colonius, "Acoustic field associated with parabolized stability equation models in turbulent jets," in *19th AIAA/CEAS Aeroacoustics Conference*, 2013, p. 2279.
- [72] A. Sinha, D. Rodriguez, G. A. Brès and T. Colonius, "Wavepacket models for supersonic jet noise," *Journal of Fluid Mechanics*, vol. 742, pp. 71–95, 2014.
- [73] G. A. Brès, P. Jordan, V. Jaunet, M. Le Rallic, A. V. Cavalieri, A. Towne, S. K. Lele, T. Colonius and O. T. Schmidt, "Importance of the nozzle-exit boundary-layer state in subsonic turbulent jets," *Journal of Fluid Mechanics*, vol. 851, pp. 83–124, 2018.
- [74] O. T. Schmidt, A. Towne, G. Rigas, T. Colonius and G. A. Brès, "Spectral analysis of jet turbulence," *Journal of Fluid Mechanics*, vol. 855, pp. 953–982, 2018.
- [75] E. M. Pickering, A. Towne, P. Jordan and T. Colonius, "Resolvent-based jet noise models: A projection approach," in *AIAA Scitech 2020 Forum*, 2020, p. 0999.
- [76] E. M. Pickering, G. Rigas, D. Sipp, O. T. Schmidt and T. Colonius, "Eddy viscosity for resolvent-based jet noise models," in *25th AIAA/CEAS Aeroacoustics Conference*, 2019, p. 2454.

- [77] C. K. Tam and D. E. Burton, "Sound generated by instability waves of supersonic flows. part 2. axisymmetric jets," *Journal of Fluid Mechanics*, vol. 138, pp. 273–295, 1984.
- [78] C. K. Tam and K. Chen, "A statistical model of turbulence in two-dimensional mixing layers," *Journal of Fluid Mechanics*, vol. 92, no. 2, pp. 303–326, 1979.
- [79] C. Tam, M. Golebiowski and J. Seiner, "On the two components of turbulent mixing noise from supersonic jets," in *Aeroacoustics conference*, 1996, p. 1716.
- [80] C. K. Tam, K. Viswanathan, K. Ahuja and J. Panda, "The sources of jet noise: Experimental evidence," *Journal of Fluid Mechanics*, vol. 615, pp. 253–292, 2008.
- [81] T. B. Neilsen, A. B. Vaughn, K. L. Gee, S. H. Swift, A. T. Wall, J. M. Downing and M. M. James, "Three-way spectral decompositions of high-performance military aircraft noise," *AIAA Journal*, vol. 57, no. 8, pp. 3467–3479, 2019.
- [82] P. Jordan and Y. Gervais, "Subsonic jet aeroacoustics: Associating experiment, modelling and simulation," *Experiments in Fluids*, vol. 44, no. 1, pp. 1–21, 2008.
- [83] A. Nekkanti and O. T. Schmidt, "Modal analysis of acoustic directivity in turbulent jets," *AIAA Journal*, pp. 1–12, 2020.
- [84] D. J. Tan, A. Kalyan, V. Gryazev, M. Wong, D. Honnery, D. M. Edgington-Mitchell and S. A. Karabasov, "On the application of shock-associated noise models to piv measurements of screeching axisymmetric cold jets," in *23rd AIAA/CEAS Aeroacoustics Conference*, 2017, p. 3028.
- [85] P. J. Morris and S. A. Miller, "Prediction of broadband shock-associated noise using reynolds-averaged navier-stokes computational fluid dynamics," *AIAA journal*, vol. 48, no. 12, pp. 2931–2944, 2010.
- [86] T. K. Patel and S. A. Miller, "Statistical sources for broadband shock-associated noise using the navier-stokes equations," *The Journal of the Acoustical Society of America*, vol. 146, no. 6, pp. 4339–4351, 2019.
- [87] C. K. Tam, "Broadband shock-associated noise of moderately imperfectly expanded supersonic jets," *Journal of Sound and Vibration*, vol. 140, no. 1, pp. 55–71, 1990.
- [88] C.-W. Kuo, D. K. McLaughlin, P. J. Morris and K. Viswanathan, "Effects of jet temperature on broadband shock-associated noise," *AIAA journal*, vol. 53, no. 6, pp. 1515–1530, 2015.
- [89] D. P. Wishart, "The structure of a heated supersonic jet operating at design and off-design conditions," *PhDT*, 1995.



- [90] K. Viswanathan, M. Alkislar and M. Czech, "Characteristics of the shock noise component of jet noise," *AIAA Journal*, vol. 48, no. 1, pp. 25–46, 2010.
- [91] S. A. Miller, "The scaling of broadband shock-associated noise with increasing temperature," *International Journal of Aeroacoustics*, vol. 14, no. 1-2, pp. 305–326, 2015.
- [92] T. Norum and J. Seiner, "Location and propagation of shock associated noise from supersonic jets," in *6th Aeroacoustics Conference*, 1980, p. 983.
- [93] J. Seiner and T. Norum, "Experiments of shock associated noise of supersonic jets," 1979.
- [94] R. Gojon and C. Bogey, "Numerical study of the flow and the near acoustic fields of an under-expanded round free jet generating two screech tones," *International Journal of Aeroacoustics*, vol. 16, no. 7-8, pp. 603–625, 2017.
- [95] C. P. Arroyo and S. Moreau, "Azimuthal mode analysis of broadband shock-associated noise in an under-expanded axisymmetric jet," *Journal of Sound and Vibration*, vol. 449, pp. 64–83, 2019.
- [96] T. Suzuki, "Wave-packet representation of shock-cell noise for a single round jet," *AIAA Journal*, vol. 54, no. 12, pp. 3903–3917, 2016.
- [97] H. Vold, P. Shah, P. Morris, Y. Du and D. Papamoschou, "Axisymmetry and azimuthal modes in jet noise," in *18th AIAA/CEAS Aeroacoustics Conference (33rd AIAA Aeroacoustics Conference)*, 2012, p. 2214.
- [98] T. Suzuki and S. K. Lele, "Shock leakage through an unsteady vortex-laden mixing layer: Application to jet screech," *Journal of Fluid Mechanics*, vol. 490, pp. 139–167, 2003.
- [99] C. K. Tam and K. Ahuja, "Theoretical model of discrete tone generation by impinging jets," *Journal of Fluid Mechanics*, vol. 214, pp. 67–87, 1990.
- [100] D. Edgington-Mitchell, V. Jaunet, P. Jordan, A. Towne, J. Soria and D. Honnery, "Upstream-travelling acoustic jet modes as a closure mechanism for screech," *Journal of Fluid Mechanics*, vol. 855, 2018.
- [101] R. Gojon, C. Bogey and M. Mihaescu, "Oscillation modes in screeching jets," *AIAA Journal*, vol. 56, no. 7, pp. 2918–2924, 2018.
- [102] C. Tam, J. Seiner and J. Yu, "Proposed relationship between broadband shock associated noise and screech tones," *Journal of sound and vibration*, vol. 110, no. 2, pp. 309–321, 1986.

- [103] D. J. Tan, J. Soria, D. Honnery and D. M. Edgington-Mitchell, "Novel method for investigating broadband velocity fluctuations in axisymmetric screeching jets," *AIAA Journal*, vol. 55, no. 7, pp. 2321–2334, 2017.
- [104] M. Lighthill, "On sound generated aerodynamically. ii. turbulence as a source of sound," in *Proceedings of the Royal Society of London A: Mathematical, Physical and Engineering Sciences*, The Royal Society, vol. 222, 1954, pp. 1–32.
- [105] D. Crighton, "Basic principles of aerodynamic noise generation," *Progress in Aerospace Sciences*, vol. 16, no. 1, pp. 31–96, 1975.
- [106] M. E. Goldstein, "Aeroacoustics," *New York, McGraw-Hill International Book Co.*, 1976. 305 p., 1976.
- [107] J. F. Williams and L. Hall, "Aerodynamic sound generation by turbulent flow in the vicinity of a scattering half plane," *Journal of fluid mechanics*, vol. 40, no. 4, pp. 657–670, 1970.
- [108] H. S. Ribner, "Effects of jet flow on jet noise via an extension to the lighthill model," *Journal of Fluid Mechanics*, vol. 321, pp. 1–24, 1996.
- [109] O. M. Phillips, "On the generation of sound by supersonic turbulent shear layers," *Journal of Fluid Mechanics*, vol. 9, no. 1, pp. 1–28, 1960.
- [110] G. M. Lilley, "On the noise from jets," 1974.
- [111] D. J. Bodony and S. K. Lele, "Low-frequency sound sources in high-speed turbulent jets," *Journal of Fluid Mechanics*, vol. 617, pp. 231–253, 2008.
- [112] A. Cavalieri, P. Jordan, T. Colonius and Y. Gervais, "Axisymmetric superdirectivity in subsonic jets," *Journal of fluid Mechanics*, vol. 704, pp. 388–420, 2012.
- [113] A. Michalke and H. Fuchs, "On turbulence and noise of an axisymmetric shear flow," *Journal of Fluid Mechanics*, vol. 70, no. 1, pp. 179–205, 1975.
- [114] R. Mankbadi and J. Liu, "Sound generated aerodynamically revisited: Large-scale structures in a turbulent jet as a source of sound," *Philosophical Transactions of the Royal Society of London. Series A, Mathematical and Physical Sciences*, vol. 311, no. 1516, pp. 183–217, 1984.
- [115] Y. B. Baqui, A. Agarwal, A. V. Cavalieri and S. Sinayoko, "A coherence-matched linear source mechanism for subsonic jet noise," *Journal of Fluid Mechanics*, vol. 776, pp. 235–267, 2015.
- [116] I. A. Maia, P. Jordan, A. Cavalieri and V. Jaunet, "Two-point wavepacket modelling of jet noise," *Proceedings of the Royal Society A*, vol. 475, no. 2227, p. 20 190 199, 2019.

- [117] S. Crow and F. Champagne, "Orderly structure in jet turbulence," *Journal of Fluid Mechanics*, vol. 48, no. 3, pp. 547–591, 1971.
- [118] D. Crighton and P. Huerre, "Shear-layer pressure fluctuations and superdirective acoustic sources," *Journal of Fluid Mechanics*, vol. 220, pp. 355–368, 1990.
- [119] J. Jeun, J. W. Nichols and M. R. Jovanović, "Input-output analysis of high-speed axisymmetric isothermal jet noise," *Physics of Fluids*, vol. 28, no. 4, p. 047 101, 2016.
- [120] J. S. Bendat and A. G. Piersol, *Random data: analysis and measurement procedures*. John Wiley & Sons, 2011, vol. 729.
- [121] A. V. Cavalieri, P. Jordan, A. Agarwal and Y. Gervais, "Jittering wave-packet models for subsonic jet noise," *Journal of Sound and Vibration*, vol. 330, no. 18-19, pp. 4474–4492, 2011.
- [122] C.-W. Kuo, Q. Buisson, D. K. McLaughlin and P. J. Morris, "Experimental investigation of near-field pressure fluctuations generated by supersonic jets," in *19th AIAA/CEAS aeroacoustics conference*, 2013, p. 2033.
- [123] A. Alomar, A. Nicole, D. Sipp, V. Rialland and F. Vuillot, "Reduced-order model of a reacting, turbulent supersonic jet based on proper orthogonal decomposition," *Theoretical and Computational Fluid Dynamics*, pp. 1–29, 2020.
- [124] R. R. Armstrong, A. Michalke and H. V. Fuchs, "Coherent structures in jet turbulence and noise," *AIAA J*, vol. 15, no. 7, pp. 1011–1017, 1977.
- [125] A. V. Cavalieri and A. Agarwal, "Coherence decay and its impact on sound radiation by wavepackets," *Journal of Fluid Mechanics*, vol. 748, pp. 399–415, 2014.
- [126] J. F. Williams and A. Kempton, "The noise from the large-scale structure of a jet," in *Structure and mechanisms of turbulence II*, Springer, 1978, pp. 265–272.
- [127] S. Unnikrishnan, A. V. Cavalieri and D. V. Gaitonde, "Acoustically informed statistics for wave-packet models," *AIAA Journal*, vol. 57, no. 6, pp. 2421–2434, 2019.
- [128] P. Doak, "Momentum potential theory of energy flux carried by momentum fluctuations," *Journal of sound and vibration*, vol. 131, no. 1, pp. 67–90, 1989.
- [129] C. K. Tam and P. J. Morris, "The radiation of sound by the instability waves of a compressible plane turbulent shear layer," *Journal of Fluid Mechanics*, vol. 98, no. 2, pp. 349–381, 1980.
- [130] J. W. Nichols and S. K. Lele, "Global modes and transient response of a cold supersonic jet," *Journal of Fluid Mechanics*, vol. 669, p. 225, 2011.
- [131] L. Lesshafft, P. Huerre, P. Sagaut and M. Terracol, "Nonlinear global modes in hot jets," 2006.

- [132] P. Jordan, T. Colonius, G. Bres, M. Zhang, A. Towne and S. Lele, "Modeling intermittent wavepackets and their radiated sound in a turbulent jet," in *Proceedings of the Summer Program*, Center for Turbulence Research, Stanford University, 2014, p. 241.
- [133] T. Herbert, "Parabolized stability equations," *Annual Review of Fluid Mechanics*, vol. 29, no. 1, pp. 245–283, 1997.
- [134] D. Rodriguez, A. V. Cavalieri, T. Colonius and P. Jordan, "A study of linear wavepacket models for subsonic turbulent jets using local eigenmode decomposition of piv data," *European Journal of Mechanics-B/Fluids*, vol. 49, pp. 308–321, 2015.
- [135] D. Rodriguez, A. Sinha, G. A. Bres and T. Colonius, "Inlet conditions for wave packet models in turbulent jets based on eigenmode decomposition of large eddy simulation data," *Physics of Fluids*, vol. 25, no. 10, p. 105 107, 2013.
- [136] L. A. Antonialli, A. V. Cavalieri, O. Schmidt, T. Colonius, A. Towne, G. A. Brès and P. Jordan, "Amplitude scaling of turbulent-jet wavepackets," in *2018 AIAA/CEAS Aeroacoustics Conference*, 2018, p. 2978.
- [137] K. Sasaki, A. V. Cavalieri, P. Jordan, O. T. Schmidt, T. Colonius and G. A. Brès, "High-frequency wavepackets in turbulent jets," *Journal of Fluid Mechanics*, vol. 830, R2, 2017.
- [138] D. Rodriguez, A. Sinha, G. Brès and T. Colonius, "Parabolized stability equation models in turbulent supersonic jets," in *18th AIAA/CEAS Aeroacoustics Conference (33rd AIAA Aeroacoustics Conference)*, 2012, p. 2117.
- [139] L. Cheung and S. Lele, "Acoustic radiation from subsonic and supersonic mixing layers with nonlinear pse," in *42nd AIAA Aerospace Sciences Meeting and Exhibit*, 2004, p. 363.
- [140] T. Ansaldi, C. Airiau, C. Pérez Arroyo and G. Puigt, "Pse-based sensitivity analysis of turbulent and supersonic single stream jet," in *22nd AIAA/CEAS Aeroacoustics Conference*, 2016, p. 3052.
- [141] M.-R. Choi and S. Lele, "Prediction of shock-cell structure using parabolized stability equations," in *39th Aerospace Sciences Meeting and Exhibit*, 2001, p. 744.
- [142] A. Towne, G. Rigas and T. Colonius, "A critical assessment of the parabolized stability equations," *Theoretical and Computational Fluid Dynamics*, vol. 33, no. 3-4, pp. 359–382, 2019.
- [143] L. Cheung, D. Bodony and S. Lele, "Noise radiation predictions from jet instability waves using a hybrid nonlinear pse-acoustic analogy approach," in *13th AIAA/CEAS Aeroacoustics Conference (28th AIAA Aeroacoustics Conference)*, 2007, p. 3638.

- [144] L. C. Cheung and S. K. Lele, "Linear and nonlinear processes in two-dimensional mixing layer dynamics and sound radiation," *Journal of Fluid Mechanics*, vol. 625, pp. 321–351, 2009.
- [145] K. Mohseni, T. Colonius and J. B. Freund, "An evaluation of linear instability waves as sources of sound in a supersonic turbulent jet," *Physics of fluids*, vol. 14, no. 10, pp. 3593–3600, 2002.
- [146] V. Saponitsky, N. D. Sandham and C. L. Morfey, "Linear and nonlinear mechanisms of sound radiation by instability waves in subsonic jets," *Journal of Fluid Mechanics*, vol. 658, pp. 509–538, 2010.
- [147] M. Malik, C.-L. Chang, M. Malik and C.-L. Chang, "Pse applied to supersonic jet instability," in *35th Aerospace Sciences Meeting and Exhibit*, 1997, p. 758.
- [148] D. J. Tan, D. Honnery, A. Kalyan, V. Semiletov, S. A. Karabasov and D. Edgington-Mitchell, "Equivalent shock-associated noise source reconstruction of screeching underexpanded unheated round jets," *AIAA Journal*, vol. 57, no. 3, pp. 1200–1214, 2018.
- [149] P. Ray and S. K. Lele, "Sound generated by instability wave/shock-cell interaction in supersonic jets," *Journal of fluid mechanics*, vol. 587, pp. 173–215, 2007.
- [150] S. Lele, "Phased array models of shock-cell noise sources," in *11th AIAA/CEAS aeroacoustics conference*, 2005, p. 2841.
- [151] P. Morris and S. Miller, "The prediction of broadband shock-associated noise using rans cfd," in *15th AIAA Aeroacoustics Conference*, vol. 15, 2009, pp. 49–56.
- [152] A. Kalyan and S. A. Karabasov, "Broad band shock associated noise predictions in axisymmetric and asymmetric jets using an improved turbulence scale model," *Journal of Sound and Vibration*, vol. 394, pp. 392–417, 2017.
- [153] D. J. Tan, D. Honnery, A. Kalyan, V. Semiletov, S. A. Karabasov and D. Edgington-Mitchell, "Correlation analysis of high-resolution particle image velocimetry data of screeching jets," *AIAA journal*, vol. 57, no. 2, pp. 735–748, 2019.
- [154] A. P. Markesteijn, V. Semiletov, S. A. Karabasov, D. J. Tan, M. Wong, D. Honnery and D. M. Edgington-Mitchell, "Supersonic jet noise: An investigation into noise generation mechanisms using large eddy simulation and high-resolution piv data," in *23rd AIAA/CEAS aeroacoustics conference*, 2017, p. 3029.
- [155] P. J. Morris and K. B. Zaman, "Velocity measurements in jets with application to noise source modeling," *Journal of sound and vibration*, vol. 329, no. 4, pp. 394–414, 2010.

- [156] U. Michel and B. S. Noise, "Theory vis-a-vis experimental results," in *First Joint CEAS/AIAA Aeroacoustics Conference (16 th AIAA Aeroacoustics Conference)*, 1995, p. 545.
- [157] C. K. Tam, "Stochastic model theory of broadband shock associated noise from supersonic jets," *Journal of Sound and Vibration*, vol. 116, no. 2, pp. 265–302, 1987.
- [158] U. Sasidharan Nair, K. Goparaju and D. Gaitonde, "Energy-dynamics resulting in turbulent and acoustic phenomena in an underexpanded jet," *Aerospace*, vol. 5, no. 2, p. 49, 2018.
- [159] J. L. Weightman, O. Amili, D. Honnery, J. Soria and D. Edgington-Mitchell, "An explanation for the phase lag in supersonic jet impingement," *Journal of Fluid Mechanics*, vol. 815, 2017.
- [160] T. Knast, G. Bell, M. Wong, C. M. Leb, J. Soria, D. R. Honnery and D. Edgington-Mitchell, "Coupling modes of an underexpanded twin axisymmetric jet," *AIAA Journal*, vol. 56, no. 9, pp. 3524–3535, 2018.
- [161] K. Ahuja, "Designing clean jet-noise facilities and making accurate jet-noise measurements," *International Journal of Aeroacoustics*, vol. 2, no. 3, pp. 371–412, 2003.
- [162] T. Knast and D. Edgington-Mitchell, "Design of a supersonic wind tunnel facility," in *17th Australian International Aerospace Congress: AIAC 2017*, Engineers Australia, Royal Aeronautical Society, 2017, p. 516.
- [163] T. Knast, "The effect of jet exit pressure on jets in supersonic crossflow," Ph.D. dissertation, Monash University.
- [164] B. S. Thethy, M. Rezay Haghdooost, C. O. Paschereit, D. Honnery, D. M. Edgington-Mitchell and K. Oberleithner, "Redistribution of transient shock waves using shock dividers," in *AIAA Scitech 2020 Forum*, 2020, p. 0925.
- [165] K. Ahuja, "Designing clean jet-noise facilities and making accurate jet-noise measurements," *International Journal of Aeroacoustics*, vol. 2, no. 3, pp. 371–412, 2003.
- [166] J. Bridges and C. Brown, "Validation of the small hot jet acoustic rig for aeroacoustic research," in *11th AIAA/CEAS aeroacoustics conference*, 2005, p. 2846.
- [167] V. Kopiev, V. Palchikovskiy, Y. V. Bersenev, S. Y. Makashov, I. Belyaev, I. Korin, E. Sorokin, I. Khramtsov and O. Y. Kustov, "Design and qualification of an anechoic facility in pnrpu," *Procedia Engineering*, vol. 176, pp. 264–272, 2017.
- [168] M. Ponton, J. Seiner, L. Ukeiley and B. Jansen, "A new anechoic chamber design for testing high-temperature jet flows," *AIAA Paper*, vol. 2190, p. 2001, 2001.

- [169] R. Burrin and H. Tanna, "The lockheed-georgia coannular jet research facility," *The Journal of the Acoustical Society of America*, vol. 65, no. S1, S44–S44, 1979.
- [170] C. Tinney, M. Glauser, T. Coughlin, L. Ukeiley and A. Hall, "Designing an anechoic chamber for the experimental study of high speed heated jets," in *42nd AIAA Aerospace Sciences Meeting and Exhibit*, 2004, p. 10.
- [171] C. B. Hahn, "Design and validation of the new jet facility and anechoic chamber," Ph.D. dissertation, The Ohio State University, 2011.
- [172] J. Craft, P. Upadhyay, T. J. Worden and F. S. Alvi, "Characterization and validation of an anechoic facility for high-temperature jet noise studies," in *46th AIAA fluid dynamics conference*, vol. 3800, 2016.
- [173] L. P. Bastos, C. J. Deschamps, A. R. da Silva, J. A. Cordioli, J. R. Siroto, I. A. Maia, E. L. Coelho and R. L. Queiroz, "Development, validation and application of a newly developed rig facility for investigation of jet aeroacoustics," *Journal of the Brazilian Society of Mechanical Sciences and Engineering*, vol. 40, no. 4, p. 171, 2018.
- [174] D. Guariglia, C. Schram and F. Stella, "Design of a facility for shock-cell noise investigation on a subsonic/supersonic coaxial jet," in *PhD VKI Symposium*, 2015.
- [175] V. Jaunet, M. Mancinelli, P. Jordan, A. Towne, D. M. Edgington-Mitchell, G. Lehnasch and S. Girard, "Dynamics of round jet impingement," in *25th AIAA/CEAS Aeroacoustics Conference*, 2019, p. 2769.
- [176] M. Mancinelli, V. Jaunet, P. Jordan and A. Towne, "Screech-tone prediction using upstream-travelling jet modes," *Experiments in Fluids*, vol. 60, no. 1, p. 22, 2019.
- [177] R. A. Fontaine, B. Bobbitt, G. S. Elliott, J. M. Austin and J. B. Freund, "Design and demonstration of a new small-scale jet noise experiment," *AIAA*, 2012.
- [178] "Iso 3745: Acoustics — determination of sound power levels and sound energy levels of noise sources using sound pressure — precision methods for anechoic rooms and hemi-anechoic rooms," International Organization for Standardization, Geneva, CH, Standard, Mar. 2012.
- [179] D. A. Bies, C. Hansen and C. Howard, *Engineering noise control*. CRC press, 2017.
- [180] M. Delany and E. Bazley, "The high frequency performance of wedge-lined free field rooms," *Journal of Sound and Vibration*, vol. 55, no. 2, pp. 195–214, 1977.
- [181] L. L. Beranek and H. P. Sleeper Jr, "The design and construction of anechoic sound chambers," *The Journal of the Acoustical Society of America*, vol. 18, no. 1, pp. 140–150, 1946.

- [182] J. Duda, "Basic design considerations for anechoic chambers," *Noise Control Engineering Journal*, vol. 9, pp. 60–67, 1977.
- [183] S. Piantanida, V. Jaunet, J. Huber, W. R. Wolf, P. Jordan and A. V. Cavalieri, "Scattering of turbulent-jet wavepackets by a swept trailing edge," *The Journal of the Acoustical Society of America*, vol. 140, no. 6, pp. 4350–4359, 2016.
- [184] L. R. Quartararo and G. C. Lauchle, "Inlet wall design for high-volume flow subsonic anechoic chambers," *Noise Control Engineering Journal*, vol. 24, no. 3, pp. 86–94, 1985.
- [185] A. Cutler and J. White, "An experimental and cfd study of a supersonic coaxial jet," 2001.
- [186] B. Callender, E. Gutmark and R. Dimicco, "The design and validation of a coaxial nozzle acoustic test facility," in *40th AIAA Aerospace Sciences Meeting & Exhibit*, 2002, p. 369.
- [187] C. Pérez Arroyo, G. Puigt, C. Airiau and J.-F. Boussuge, "Large eddy simulation of shock-cell noise from a dual stream jet," in *22nd AIAA/CEAS Aeroacoustics Conference*, 2016, p. 2798.
- [188] J. Bridges, A. Fagan, K. Zaman and C. Miller, "Tones encountered with a coannular nozzle and a method for their suppression," 2017.
- [189] K. Zaman, J. E. Bridges, A. F. Fagan and C. J. Miller, "Tones encountered with a coannular nozzle and a method for their suppression," *AIAA Journal*, vol. 56, no. 5, pp. 1922–1929, 2018.
- [190] M. Mikhail, "Optimum design of wind tunnel contractions," *AIAA J*, vol. 17, no. 5, pp. 471–477, 1979.
- [191] T. Morel, "Comprehensive design of axisymmetric wind tunnel contractions," *Journal of Fluids Engineering*, vol. 97, no. 2, pp. 225–233, 1975.
- [192] R. D. Mehta and P. Bradshaw, "Design rules for small low speed wind tunnels," *The Aeronautical Journal*, vol. 83, no. 827, pp. 443–453, 1979.
- [193] K. A. Cunefare, V. B. Biesel, J. Tran, R. Rye, A. Graf, M. Holdhusen and A.-M. Albanese, "Anechoic chamber qualification: Traverse method, inverse square law analysis method, and nature of test signal," *The Journal of the Acoustical Society of America*, vol. 113, no. 2, pp. 881–892, 2003.
- [194] K. A. Cunefare, J. Badertscher and V. Wittstock, "On the qualification of anechoic chambers; issues related to signals and bandwidth," *The Journal of the Acoustical Society of America*, vol. 120, no. 2, pp. 820–829, 2006.
- [195] J. Bridges and C. A. Brown, "Validation of the small hot jet acoustic rig for jet noise research," *NASA*, 2005.



- [196] K. Viswanathan, "Quality of jet noise data: Issues, implications and needs," *AIAA Paper*, vol. 365, 2002.
- [197] H. Tanna, "An experimental study of jet noise part ii: Shock associated noise," *Journal of Sound and Vibration*, vol. 50, no. 3, pp. 429–444, 1977.
- [198] R. Fontaine, "Very near-nozzle shear-layer turbulence and jet noise," Ph.D. dissertation, University of Illinois at Urbana-Champaign, 2015.
- [199] K. Zaman, "Effect of initial boundary-layer state on subsonic jet noise," *AIAA journal*, vol. 50, no. 8, pp. 1784–1795, 2012.
- [200] T. Norum and J. Seiner, "Broadband shock noise from supersonic jets," *AIAA journal*, vol. 20, no. 1, pp. 68–73, 1982.
- [201] C. Brown and J. Bridges, "Small hot jet acoustic rig validation," 2006.
- [202] D. Juve, M. Sunyach and G. Comte-Bellot, "Filtered azimuthal correlations in the acoustic far field of a subsonic jet," *AIAA Journal*, vol. 17, no. 1, pp. 112–113, 1979.
- [203] M. H. Wong, P. Jordan, D. R. Honnery and D. Edgington-Mitchell, "Impact of coherence decay on wavepacket models for broadband shock-associated noise in supersonic jets," *Journal of Fluid Mechanics*, vol. 863, pp. 969–993, 2019.
- [204] M. H. Wong, D. M. Edgington-Mitchell, D. Honnery, A. V. Cavalieri and P. Jordan, "A parabolised stability equation based broadband shock-associated noise model," in *25th AIAA/CEAS Aeroacoustics Conference*, 2019, p. 2584.
- [205] M. H. Wong, R. Kirby, P. Jordan and D. Edgington-Mitchell, "Azimuthal decomposition of the radiated noise from supersonic shock-containing jets," *The Journal of the Acoustical Society of America*, vol. 148, no. 4, pp. 2015–2027, 2020.
- [206] G. A. Faranosov, I. V. Belyaev, V. F. Kopiev, M. Y. Zaytsev, A. A. Aleksentsev, Y. V. Bersenev, V. A. Chursin and T. A. Viskova, "Adaptation of the azimuthal decomposition technique to jet noise measurements in full-scale tests," *AIAA Journal*, vol. 55, no. 2, pp. 572–584, 2017.
- [207] C. Brown and J. Bridges, "Acoustic efficiency of azimuthal modes in jet noise using chevron nozzles," in *12th AIAA/CEAS Aeroacoustics Conference (27th AIAA Aeroacoustics Conference)*, 2006, p. 2645.
- [208] D. Juve, M. Sunyach and G. Comte-Bellot, "Filtered azimuthal correlations in the acoustic far field of a subsonic jet," *AIAA Journal*, vol. 17, no. 1, pp. 112–113, 1979.

- [209] C. Tam, "The shock-cell structures and screech tone frequencies of rectangular and non-axisymmetric supersonic jets," *Journal of Sound and Vibration*, vol. 121, no. 1, pp. 135–147, 1988.
- [210] A. Sinha, K. Gudmundsson, H. Xia and T. Colonius, "Parabolized stability analysis of jets from serrated nozzles," *Journal of Fluid Mechanics*, vol. 789, pp. 36–63, 2016.
- [211] E. Piot, G. Casalis, F. Muller and C. Bailly, "Investigation of the pse approach for subsonic and supersonic hot jets. detailed comparisons with les and linearized euler equations results," *International Journal of Aeroacoustics*, vol. 5, no. 4, pp. 361–393, 2006.
- [212] A. Towne and T. Colonius, "One-way spatial integration of hyperbolic equations," *Journal of Computational Physics*, vol. 300, pp. 844–861, 2015.
- [213] S. Karami and J. Soria, "Analysis of coherent structures in an under-expanded supersonic impinging jet using spectral proper orthogonal decomposition (spod)," *Aerospace*, vol. 5, no. 3, p. 73, 2018.
- [214] W. Shen, T. K. Patel and S. A. Miller, "Extraction of large-scale coherent structures from large eddy simulation of supersonic jets for shock-associated noise prediction," in *AIAA Scitech 2020 Forum*, 2020, p. 0742.
- [215] M. H. Wong, D. M. Edgington-Mitchell, D. R. Honnery, P. Jordan and A. Savarese, "Kinematic wavepacket model for broadband shock associated noise in underexpanded supersonic jets," in *2018 AIAA/CEAS Aeroacoustics Conference*, 2018, p. 3465.
- [216] G. A. Brès, F. E. Ham, J. W. Nichols and S. K. Lele, "Unstructured large-eddy simulations of supersonic jets," *AIAA journal*, vol. 55, no. 4, pp. 1164–1184, 2017.

## **Appendix A**

# **Kinematic Wavepacket model for Broadband Shock-Associated Noise in Underexpanded Supersonic Jets**

### **A.1 Introductory Statement**

This conference paper [215] was prepared for the *24th AIAA/CEAS Aeroacoustics Conference* and contains the preliminary developmental work for the journal paper contained in Chapter 6. Motivated by the model problem of Cavalieri and Agarwal [125], a two-point kinematic wavepacket model for BBSAN was constructed. The effect of coherence decay, modelled as a Gaussian, was used to test its effect on far-field BBSAN spectrum. The noise predictions from the model were compared to the data from Norum and Seiner [29].

### **A.2 Conference Paper**

# Kinematic Wavepacket Model for Broadband Shock Associated Noise in Underexpanded Supersonic Jets

Marcus H. Wong<sup>\*</sup>, Damon Honnery<sup>†</sup> and Daniel Edgington-Mitchell<sup>‡</sup>

*Laboratory for Turbulence Research in Aerospace and Combustion (LTRAC), Department of Mechanical and Aerospace Engineering, Monash University, Melbourne, VIC 3800, Australia*

Alessandro Savarese<sup>§</sup>

*Airbus Operation S.A.S. - Institut PPrime*

Peter Jordan<sup>¶</sup>

*Institut PPrime CNRS - Université de Poitiers - ENSMA, Poitiers, 86036, France*

Motivated by the success of wavepackets in modelling the noise from subsonic and perfectly-expanded supersonic jets, we apply the wavepacket model to imperfectly expanded supersonic jets. Previous work by Savarese et al. [1] adopted a kinematic single-point wavepacket model first formulated by Lele [2]. Recent studies with subsonic jets, however, have demonstrated the importance of capturing the ‘jittering’ of wavepackets in order to correctly predict the intensity of far-field sound. Following the analysis of Cavalieri and Agarwal [3], we extend their methodology to model the acoustic sources of broadband shock-associated noise in imperfectly-expanded supersonic jets using cross-spectral densities of the turbulent and shock-cell velocity quantities. We model the downstream propagating vortices as wavepackets, with the aim of determining the relationship between coherence decay, the statistical representation of jitter, and broadband shock-associated noise. Unlike the subsonic case where inclusion of coherence decay amplifies sound pressure level over the whole acoustic spectrum, we find that it does not play a critical role in increasing sound amplitude for shock-cell noise. When higher-order shock-cell modes are used to capture high frequency noise, however, the inclusion of a jittering wavepacket is necessary.

## Nomenclature

$\alpha_T$	=	scaling factor for transverse velocity terms
$\gamma(y_1, y_2, \omega)$	=	two point coherence function
$\omega$	=	acoustic frequency
$\omega_h$	=	wavepacket frequency
$\rho$	=	fluctuating density
$\theta$	=	observation angle relative to downstream jet axis
$a_m(\omega_h)$	=	amplitude of the m-th wavepacket at the frequency $\omega_h$
$c_0$	=	far-field speed of sound
$c_{s_n}$	=	amplitude coefficient of the shock cells of $n^{th}$ mode
$L$	=	longitudinal extent of wavepacket
$L_c$	=	coherence decay length scale
$k$	=	acoustic wavenumber
$k_{s_n}$	=	shock cell wavenumber $n^{th}$ mode

<sup>\*</sup>PhD Student, Laboratory for Turbulence Research in Aerospace and Combustion (LTRAC), Department of Mechanical and Aerospace Engineering, Monash University, Melbourne, VIC 3800, Australia

<sup>†</sup>Professor, Laboratory for Turbulence Research in Aerospace and Combustion (LTRAC), Department of Mechanical and Aerospace Engineering, Monash University, Melbourne, VIC 3800, Australia

<sup>‡</sup>Senior Lecturer, Laboratory for Turbulence Research in Aerospace and Combustion (LTRAC), Department of Mechanical and Aerospace Engineering, Monash University, Melbourne, VIC 3800, Australia

<sup>§</sup>CIFRE PhD student, Institut PPrime - Airbus Operation S.A.S., France.

<sup>¶</sup>Institute PPrime, CNRS - Université de Poitiers - ENSMA, UPR 3346, 43 Rue de l'Aérodrome, 86036 Poitiers, France

$k_h$	=	wavenumber of wavepacket
$k_y$	=	positional wavenumber
$M_c$	=	convective Mach number
$p$	=	fluctuating pressure
$S$	=	acoustic source term
$t$	=	time
$T_0$	=	centred time of wavepacket
$T_g$	=	existence time of wavepacket
$u_s(y)$	=	shock cell velocity fluctuation
$u_t(y, t)$	=	linear combination of a set of wavepackets at different frequencies.
$U_c$	=	convective velocity
$U_t$	=	scaling factor for turbulence fluctuations
$U_s$	=	scaling factor for shock cell fluctuations
$V$	=	integration volume
$\mathbf{x}$	=	observer cartesian co-ordinate system
$\mathbf{y}$	=	jet cylindrical co-ordinate system
$Y_0$	=	position of maximum amplitude of wavepacket

## I. Introduction

SUPERSONIC jet noise can be separated into shock associated or non-shock associated noise. In supersonic imperfectly expanded jets, shock-cells exist in order to return the flow back to ambient pressure. This train of expansion and compression waves interacts with the turbulent fluctuations in the jet shear layer, generating strong acoustic waves. This shock associated noise is composed of two components; broad-band shock associated noise and screech. Broad-band shock associated noise (hereafter referred to as BBSAN) is generated via an interaction between shock cells and turbulence instabilities in the shear layer, however, there is no feedback loop present. BBSAN, as its name suggests, is characterised by having a broad peak in its acoustic spectrum. It was first studied in depth by Harper-Bourne and Fisher [4] who conducted an experimental study in shock containing flows. The peak frequency of BBSAN was found to increase as the observer moves downstream towards the jet axis while the noise intensity increased to a maximum in a perpendicular direction to the jet flow. The review paper by Tam [5] provides an in-depth overview of the salient characteristics of BBSAN.

In order to model the noise sources from turbulent jets, Lighthill [6] provided the initial framework known as the acoustic analogy. Acoustic analogies are based on the recasted Navier-Stokes (NS) equations. The flow is decomposed and substituted into the NS equations where only the leading order linear terms are kept. This leads to the inhomogeneous equation

$$\frac{\partial^2 \rho}{\partial t^2} - c_0^2 \nabla^2 \rho = S \quad (1)$$

where  $\rho$  is the fluctuating density,  $c_0$  is the far-field speed of sound and  $S$  is the source term. The source term, or the non-linearities, drive the fluctuations in the base flow. The far-field pressure can be obtained analytically using the Green's function method.

$$p(\mathbf{x}, t) = \frac{1}{4\pi} \int S(\mathbf{y}, t) \frac{dV(\mathbf{y})}{|\mathbf{x} - \mathbf{y}|} \quad (2)$$

While the interpretation and formulation of the source term varies between different kinematic sound-source models [7], it has nevertheless been used as the foundation of many BBSAN models [4, 8–10]. The construction of the fully developed source terms for a given flow is a non-trivial task. The difficulty has therefore prompted research into developing simplistic reduced-order descriptions of the noise-producing flow features. A reduced-order approach which is currently being explored is modelling using wavepackets or hydrodynamic instability waves.

The notion of using wavepackets to represent large-scale coherent structures [11] is well documented. Mollo-Christensen [12] was the first to hypothesise the use of wavepackets to model jet noise and experiments have been performed which indicate the success of such a reduced-order approach [13]. The growth, saturation and decay behaviour of wavepackets emulates the downstream decay of large-scale structures as the jet mean profile diverges.

A comprehensive review of subsonic jet noise modelling using wavepackets can be found in the paper by Jordan and Colonius [7].

The idea of using instability waves to model BBSAN in imperfectly expanded supersonic jets was first proposed by Tam. In a series of papers by Tam and co-workers [8, 14, 15], a more physical dynamic model for BBSAN has been proposed wherein noise is produced via weak non-linear interactions between shock-cells and instability waves in the shear layer. The turbulent structures are represented as a superposition of instability waves at different frequencies. As these instability waves convect downstream, they interact with the shock-cells which are represented as a series of stationary waveguide modes. Tam's physical model was found to match well with experimental data though it suffered at upstream angles close to the nozzle exit where narrow-banded peaks are observed [2].

The success of dynamic models based on stability theory thus suggests the suitability of using wavepackets within the kinematic modelling framework. A wavepacket description, consistent with the results from dynamic modelling, is now imposed on the source term of an acoustic analogy to assess the far-field sound generated. The source term's parameters can be deduced from carefully planned experiments [16, 17]. A kinematic wavepacket model for BBSAN was first proposed by Lele [2]. Lele, similar to Tam et al. [18], hypothesised that the sources are associated with the non-linear interaction of instability waves with the stationary shock-cell modes, represented as a sum of standing waves [19]. Single-point statistics obtained by Savarese et al. [1] confirmed the model's predictive capabilities.

An important element for wavepacket modelling in subsonic jets is the coherence decay. This coherence decay, the statistical signature of a jittering wavepacket, is thought to arise from the wavepackets being non-linearly forced by turbulence [20–22]. While having success in capturing the axial evolution of the acoustic power-spectral density of turbulent jets, predictions made by linear wavepacket models fail as one moves past the end of the potential core. It has been shown previously [3, 23] that linear wavepacket models, which have unit coherence by construct, do not capture the two-point statistics required to correctly account for the coherence decay seen in the flow. The neglect to consider this phenomenon can lead to discrepancies in the far-field sound pressure level of several orders of magnitude [24, 25]. As shown by Cavalieri and Agarwal [3], it is not sufficient to match the average amplitude and phases in the hydrodynamic field of the jet. One must also match the two-point coherence of the source for linear models to agree with the far-field sound pressure field of a turbulent subsonic jet.

For ideally expanded supersonic flows, however, this jittering behaviour has been shown to be less important, since the main hydrodynamic wavelengths are already acoustically 'matched' [26] and thus able to radiate to the far-field efficiently [3, 27, 28]. The importance of wavepacket jitter in shock-containing supersonic flows is less clear. Using a dynamic modelling approach grounded in linear stability theory, Ray and Lele [29] extended Tam's instability wave broadband shock associated noise model. For the cold underexpanded jet case, they found good agreement at low frequencies but highlighted that their instability model was unable to capture higher frequencies attributed to 'some combination of non-linear and non-modal effects'. In the wavepacket modelling framework, we propose that this 'non-linear' effect could be due to the stochastic forcing of turbulence which would be statistically represented by coherence decay. We test this hypothesis by developing a two-point kinematic wavepacket model for BBSAN.

The rest of the paper is organised as follows; the mathematical formulation of the two-point model is shown in § II. The effect of coherence decay on the directivity and spectral behaviour of BBSAN is shown in § III for single shock-cell mode case. The interpretation of sound radiating characteristics of the model is then discussed in § IV and a presentation of the model with coherence decay using multiple shock-cell modes is shown in § V.

## II. Mathematical Model

The kinematic wavepacket sound source model is based on Lighthill's acoustic analogy. The Helmholtz equation can be obtained via a temporal Fourier transform of equation (1) to arrive at

$$\nabla^2 p(\mathbf{x}, \omega) + k^2 p(\mathbf{x}, \omega) = S(\mathbf{y}, \omega), \quad (3)$$

where  $k = \omega/c_0$ .

Using a free-field Green's function  $G(\mathbf{x}, \mathbf{y}, \omega)$ , the integral solution to the Helmholtz equation (3) is,

$$p(\mathbf{x}, \omega) = \int_V S(\mathbf{y}, \omega) G(\mathbf{x}, \mathbf{y}, \omega) d\mathbf{y}, \quad (4)$$

where the integration is carried out over the region  $V$  where  $S \neq 0$ .

As proposed by Tam [30] and Lele [2], the full three-dimensional source term for BBSAN is represented as a multiplicative combination of the shock-cell  $u_s$  and turbulent  $u_t$  fluctuations

$$S(y, t) \simeq \hat{S}(y, t) = u_s(y)u_t(y, t), \quad (5)$$

where  $\hat{S}(y, t)$  is a line source model. This modelling of acoustic sources along a line thus only accounts for axisymmetric fluctuations which are known to be the most acoustically efficient azimuthal mode in subsonic jets [31].

The velocity fluctuation related to the shock-cell waveguide modes,  $u_s(y)$ , is represented as a series of spatially periodic functions [19, 32]

$$u_s(y) = U_s \sum_n c_{s_n} \frac{1}{2} \{ e^{ik_{s_n}y} + e^{-ik_{s_n}y} \}. \quad (6)$$

The Fourier decomposition of the shock-cell structure into the eigenmodes of the mean flow is based off the inviscid solution of a vortex sheet model. The shock-cell waveguide modes are described by the wavenumber  $k_{s_n}$  and the amplitude term  $c_{s_n}$  where we adopt the expression from Prandtl & Pack's vortex sheet model. The amplitude decay of the shock modes over axial distance as seen in experimental measurements, however, is not calculated nor accounted for.

To represent  $u_t$ , Lele [2] used a wavepacket whose amplitude is modulated in both space and time. The wavepacket, at a given axial position  $y$ , is defined by its envelope lengthscale  $L$ , hydrodynamic wavenumber  $k_h$  and frequency  $\omega_t$ , related via the convection velocity  $k_h = \omega_h/U_c$ .

$$u_t(y, t) = U_t \int \sum_m \frac{1}{2} a_m(\omega_h) e^{-\frac{1}{2}(\frac{y-Y_0}{L})^2} e^{-\frac{1}{2}(\frac{t-T_0}{T_g})^2} e^{i(k_h y - \omega_h t)} d\omega_h \quad (7)$$

To capture the intermittency of the wavepackets, Lele introduced a temporal modulation term with stochastic realisations  $\exp[-((t - T_0)^2/(2T_g)^2)]$ . From the work of Cavalieri and Agarwal [3] however, we know that coherence decay is just the statistical representation of jittering wavepackets. Hence, instead of including a temporal dependence, we use two-point statistics to model the wavepacket's intermittent behaviour. After taking the Fourier transform of equation (7), the source term at a single point  $y$  is now given by

$$\hat{S}(y, \omega) = A(\omega) e^{-(\frac{y}{L})^2} \{ e^{ik_h y} \} \sum_n c_{s_n} \{ e^{ik_{s_n}y} + e^{-ik_{s_n}y} \} \quad (8)$$

where an implicit factor of  $\exp(-i\omega t)$  is assumed and  $A(\omega)$  is some amplitude term as a function of frequency.

While equation (8) allows direct computation of the fluctuating pressure field, the source term  $S(y, \omega)$  is not square integrable [3, 33]. Consequently, we will be working with auto-correlations of the fluctuating components of pressure which decay to zero for large delays. Using power-spectral densities (PSDs) and cross-spectral densities (CSDs), which are the Fourier transform of the autocorrelation and cross-correlation functions respectively, we express the far-field sound pressure level using second order statistics

$$\langle p(\mathbf{x}, \omega) p^*(\mathbf{x}, \omega) \rangle \approx \int_V \int_V \langle S(\mathbf{y}_1, \omega) S^*(\mathbf{y}_2, \omega) \rangle G(\mathbf{x}, \mathbf{y}_1, \omega) G^*(\mathbf{x}, \mathbf{y}_2, \omega) d\mathbf{y}_1 d\mathbf{y}_2, \quad (9)$$

where both PSDs and CSDs are obtained by multiplying by the complex conjugate and the hats have been dropped for convenience. The free-field Green's function is

$$G(\mathbf{x}, \mathbf{y}, \omega) = \frac{1}{4\pi} \frac{e^{ik|\mathbf{x}-\mathbf{y}|}}{|\mathbf{x}-\mathbf{y}|}. \quad (10)$$

We now define the coherence function between the points  $y_1$  and  $y_2$  as

$$\gamma^2(y_1, y_2, \omega) = \frac{|\langle S(y_1, \omega) S^*(y_2, \omega) \rangle|^2}{\langle |S(y_1, \omega)|^2 \rangle \langle |S(y_2, \omega)|^2 \rangle}. \quad (11)$$

To obtain the two-point source term with unit coherence ( $\gamma^2(y_1, y_2, \omega) = 1$ ), we multiply equation 8 by its complex conjugate at position  $y_2$

$$\begin{aligned} S(y_1, \omega) S^*(y_2, \omega) &= A^2(\omega) e^{-(\frac{y_1}{L})^2} e^{-(\frac{y_2}{L})^2} \{ e^{ik_h(y_1-y_2)} \} \times \\ &\quad \sum_n c_{s_n}^2 \{ e^{ik_{s_n}y_1} + e^{-ik_{s_n}y_1} \} \{ e^{ik_{s_n}y_2} + e^{-ik_{s_n}y_2} \}. \end{aligned} \quad (12)$$

In order to capture coherence decay, we modelled  $\gamma^2(y_1, y_2, \omega)$  as a Gaussian distribution following Cavalieri and Agarwal [3],

$$\gamma^2(y_1, y_2, \omega) = \exp\left(-2\frac{(y_1 - y_2)^2}{L_c^2}\right). \quad (13)$$

The coherence decay between points  $y_1$  and  $y_2$  is now defined by the characteristic coherence length scale  $L_c$ . Introducing this effect by substituting equation (13) into (12), we arrive at the CSD of the two-point source model for broadband shock associated noise

$$\begin{aligned} S(y_1, \omega)S^*(y_2, \omega) &= A^2(\omega)e^{-(\frac{y_1}{L})^2}e^{-(\frac{y_2}{L})^2}\left\{e^{ik_h(y_1 - y_2)}\right\}e^{\left(\frac{(y_1 - y_2)^2}{L_c^2}\right)} \times \\ &\quad \sum_n c_{sn}^2 \left\{e^{ik_{sn}y_1} + e^{-ik_{sn}y_1}\right\} \left\{e^{ik_{sn}y_2} + e^{-ik_{sn}y_2}\right\}. \end{aligned} \quad (14)$$

For a given pair of points  $(y_1, y_2)$ , the source term is described by two wavepacket envelope terms  $\exp(-y_1/L)^2$  and  $\exp(-y_2/L)^2$  at the two points respectively. The term  $\exp[ik_h(y_1 - y_2)]$  describes the phase difference between  $y_1$  and  $y_2$  while the coherence decay is modelled by  $\exp[(y_1 - y_2)^2/L_c^2]$ . Finally this is multiplied by the shock-cell modes at point  $y_1$  and  $y_2$  by the expression  $[\exp(ik_s y_1) + \exp(-ik_s y_1)][\exp(ik_s y_2) + \exp(-ik_s y_2)]$ .

Similar to Cavalieri and Agarwal [3], the model is now governed by two characteristic length scales. The first length scale,  $L$ , characterises the wavepacket amplitude envelope. The second,  $L_c$ , is the coherence length scale which characterises the decay of coherence between two points along the axial direction. It should be noted that as  $L_c \rightarrow \infty$ , the two-point model (14) reduces to the perfectly coherent model (12).

The far-field sound pressure for both models can now be found by inserting equation (14) and equation (12) into equation (9). Using the usual far-field approximation, we arrive at the expression

$$\langle p(\mathbf{x}, \omega)p^*(\mathbf{x}, \omega) \rangle \approx \frac{A^2(\omega)}{4\pi x^2} \int \int \langle S(y_1, \omega)S^*(y_2, \omega) \rangle e^{ik \cos \theta (y_1 - y_2)} dy_1 dy_2. \quad (15)$$

Due to the line-source approximation for this model, the double volume integral reduces to a double integral in the streamwise direction.

### III. Acoustic efficiency & directivity

The far-field sound is obtained by numerical evaluation of equation (15). Fig. 1 shows the variation of far-field sound pressure level as a function of directivity and frequency for an underexpanded jet operating at  $NPR = 3.4$ . It is clear from Fig. 1 that coherence decay does have a significant effect on the predicted BBSAN spectrum. Consistent with experimental observations, both plots demonstrate the peak frequency increasing as observation angle moves downstream of the jet axis; though the effect is more evident in the unit coherence case.

The first step of our analysis considers cases where the pressure fluctuations are represented by a single shock-cell mode ( $n = 1$ ); the centreline pressure fluctuations in a moderately underexpanded jet are well represented by a single mode [29, 34]. Fig. 2 shows the directivity for far-field sound pressure levels at a specified frequency for the jet operating at the same conditions as Fig. 1. Models with unit coherence and coherence decay are plotted on the same figure for comparison. At  $St = 0.5$ , both models predict the highest amplitude of radiation in the upstream direction, consistent with previous findings. At a higher value of  $St = 1.0$ , the BBSAN peaks in a more downstream direction but with a smaller sound amplitude. With all other terms equal, the introduction of coherence decay broadens the peak. Contrary to the subsonic jet case [35, 36, amongst others], however, the introduction of coherence decay reduces the peak amplitude by approximately 5dB. Moreover, coherence decay significantly alters the directivity, increasing the sound pressure level in the downstream direction (low  $\theta$  values). The reason for this behaviour will be further explored in § IV.

Fig. 3 shows a comparison of the noise spectra between the two models and experimental data of an underexpanded jet operating at  $NPR = 3.4$  [37]. The theoretical peak amplitudes are adjusted by a certain  $\Delta dB$  amount to match experimental data. Amplitude prediction is beyond the scope of this model and study. As can be seen, there is a reasonable agreement between the two models and the measured data at the peak frequency. Both the unit coherence and two-point models predict that as observation angle moves upstream, peak frequency decreases and the spectral peak width narrows. This is consistent with the observed directivity behaviour of BBSAN. For angles above  $\theta = 75^\circ$ , the



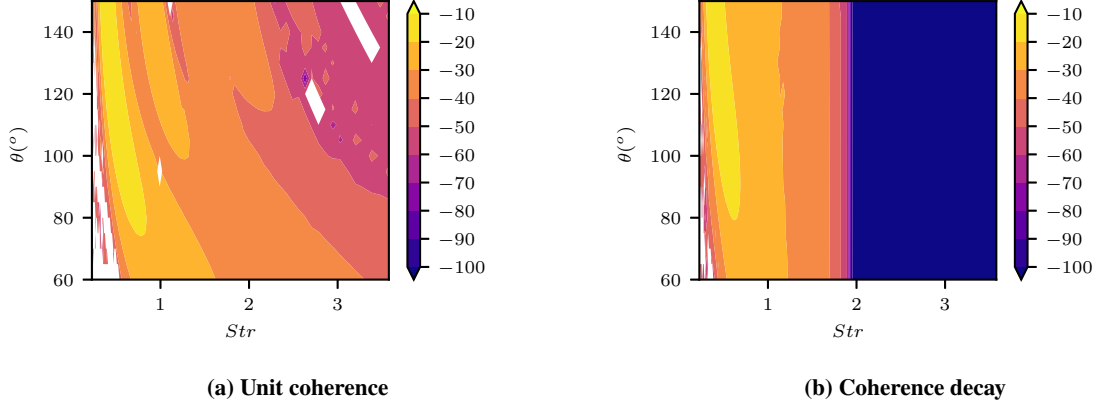


**Fig. 1** Contours of sound pressure level (arbitrary dB) as a function of frequency ( $Str$ ) and directivity ( $\theta$ ) between single and two-point model. The jet is issuing at a nozzle pressure ratio of  $NPR = 3.4$  which corresponds to a fully expanded jet Mach number of  $M_j = 1.49$ .

wavepacket models are able to capture the peak frequency with reasonable accuracy. With the inclusion of coherence decay, the spectral peak is broadened by  $0.1 \sim 0.2$  Strouhal and a more favourable agreement is obtained for frequencies greater than the peak. Below  $\theta = 75^\circ$ , both models incorrectly predict the peak.

It is evident from Fig. 3 that the jitter of wavepackets, modelled by coherence decay, broadens the wavespectrum. The current kinematic BBSAN model, however, suggests that coherence decay does not have a major impact on the sound amplitude. Unlike in subsonic flows, it provides little contribution to the peak sound pressure level. This is also consistent with the results presented by Sinha et al. [27] for isothermal fully expanded supersonic jets, where it was found that the far-field noise spectrum is well captured even without considering the jitter of wavepackets.

In all cases, using a single shock-cell waveguide mode, both wavepacket models show a reasonable agreement with the peak shape from experimental data. However, it suffers the same downfall found by Ray and Lele [29] where the high frequency sound at upstream angles is ‘missing’. In their study, the frequency range of interest was restricted to below  $St \approx 1$  due to the assumed breakdown of linear theory at high frequencies. More recently, however, it has been shown by Sasaki et al. [38] that linear theory still yields good agreement for frequencies up to  $St = 4$ . We will see later that this issue is associated with the use of only a single shock-cell mode.

#### IV. Interpretation of sound radiation characteristics

In order to explore how coherence affects the source structure and sound radiation characteristics, the CSD of the models with and without coherence decay are transformed into wavenumber space. This transformation is achieved with a double Fourier transform defined as per equation (16)

$$\mathcal{F}(k_{y1}, k_{y2}) = \frac{1}{(\sqrt{2\pi})^2} \int_{-\infty}^{\infty} \int_{-\infty}^{\infty} F(y_1, y_2) e^{ik_{y1}y_1} e^{ik_{y2}y_2} dy_1 dy_2. \quad (16)$$

If we take coherence as unity ( $\gamma^2(y_1, y_2, \omega) = 1$ ) for the entire domain by inserting equation (12) into equation (16), the Fourier transform for the perfectly coherent model for a single shock-cell mode is

$$\begin{aligned} \mathcal{F}(k_{y1}, k_{y2}) = & \frac{1}{(\sqrt{2\pi})^2} \int_{-\infty}^{\infty} \int_{-\infty}^{\infty} A_{n=1}^2(\omega) e^{-(\frac{y_1}{L})^2} e^{-(\frac{y_2}{L})^2} \{e^{ik_s y_1} + e^{-ik_s y_1}\} \times \\ & \{e^{ik_s y_2} + e^{-ik_s y_2}\} \{e^{ik_h(y_1 - y_2)}\} e^{ik_{y1}y_1} e^{ik_{y2}y_2} dy_1 dy_2. \end{aligned} \quad (17)$$

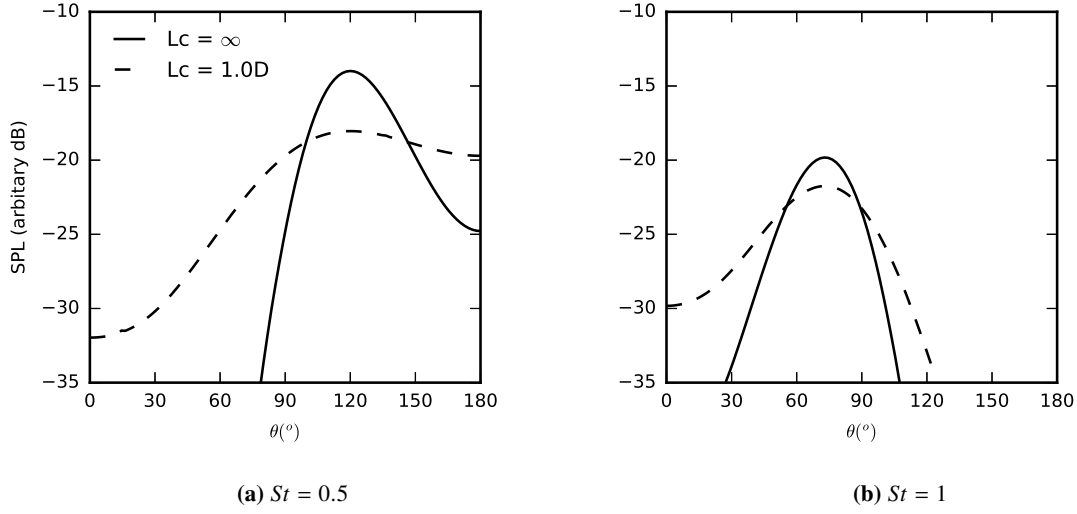


**Fig. 2** Sound pressure level at a distance of  $100D$  as a function of observation angle  $\theta$  for a wavepacket with  $k_h L = 5$ .

Evaluating the above integral gives

$$\mathcal{F}(k_{y1}, k_{y2}) = \frac{A_{n=1}^2(\omega)}{8} \left( e^{-\frac{1}{4}(k_h - k_s + k_{y1})^2 L^2} + e^{-\frac{1}{4}(k_h + k_s + k_{y1})^2 L^2} \right) \times \left( e^{-\frac{1}{4}(k_h + k_s - k_{y2})^2 L^2} + e^{-\frac{1}{4}(-k_h + k_s + k_{y2})^2 L^2} \right) L^2, \quad (18)$$

which is the Fourier transform of the perfectly coherent source CSD. Likewise, by inserting equation (14) into equation (16) and evaluating the resulting integral, the Fourier transformed CSD of the coherence decay model can also be obtained

$$\mathcal{F}(k_{y1}, k_{y2}) = \frac{A_{n=1}^2(\omega)}{8 \sqrt{\frac{1}{L^2} + \frac{1}{L_c^2}} \sqrt{\frac{2L^2 + L_c^2}{L^4 + L^2 L_c^2}}} \left( e^{-\frac{L^2(k_{y2}^2 L^2 + 2k_h^2 L_c^2 - 2k_h k_{y2} L_c^2 + k_{y2}^2 L_c^2 + k_{y1}^2 (L^2 + L_c^2) + 2k_s^2 (2L^2 + L_c^2) - 2k_s(k_{y1} + k_{y2})(2L^2 + L_c^2) + 2k_{y1}(k_{y2} L^2 + k_h L_c^2))}{4(2L^2 + L_c^2)}}} + e^{-\frac{L^2(k_{y2}^2 L^2 + 2k_h^2 L_c^2 - 2k_h k_{y2} L_c^2 + k_{y2}^2 L_c^2 + k_{y1}^2 (L^2 + L_c^2) + 2k_s^2 (2L^2 + L_c^2) + 2k_s(k_{y1} + k_{y2})(2L^2 + L_c^2) + 2k_{y1}(k_{y2} L^2 + k_h L_c^2))}{4(2L^2 + L_c^2)}}} + e^{-\frac{L^2(2(k_h - k_s)^2 L_c^2 + 2(-k_h + k_s)k_{y2} L_c^2 + k_{y1}^2 (L^2 + L_c^2) + k_{y2}^2 (L^2 + L_c^2) + 2k_{y1}(k_{y2} L^2 + (k_h - k_s)L_c^2))}{4(2L^2 + L_c^2)}}} + e^{-\frac{L^2(2(k_h + k_s)^2 L_c^2 - 2(k_h + k_s)k_{y2} L_c^2 + k_{y1}^2 (L^2 + L_c^2) + k_{y2}^2 (L^2 + L_c^2) + 2k_{y1}(k_{y2} L^2 + (k_h + k_s)L_c^2))}{4(2L^2 + L_c^2)}}} \right). \quad (19)$$

Equation (18) is obtained from equation (19) by taking the limit  $L_c \rightarrow \infty$ .

Both source CSD models in physical space are first shown in Fig. 4a and Fig. 4b. In this model problem, the jet nozzle is not present and the sources are simply centred at the origin and extended in both positive and negative directions along the jet axis. The peaks in the contour map is similar to the freckled appearance seen in the pressure two-point correlations obtained by Suzuki [39]. The introduction of coherence decay seems to concentrate the sources in space; along the axis  $y_1 = y_2$ . This behaviour is also seen in the non-shock containing case as found by Cavalieri and Agarwal [3].

A comparison of the models' Fourier transformed CSD as given by equation (18) and (19) is shown in Fig. 4c and Fig. 4d respectively. The contour scale is logarithmic and both axes are normalised by the hydrodynamic wavenumber

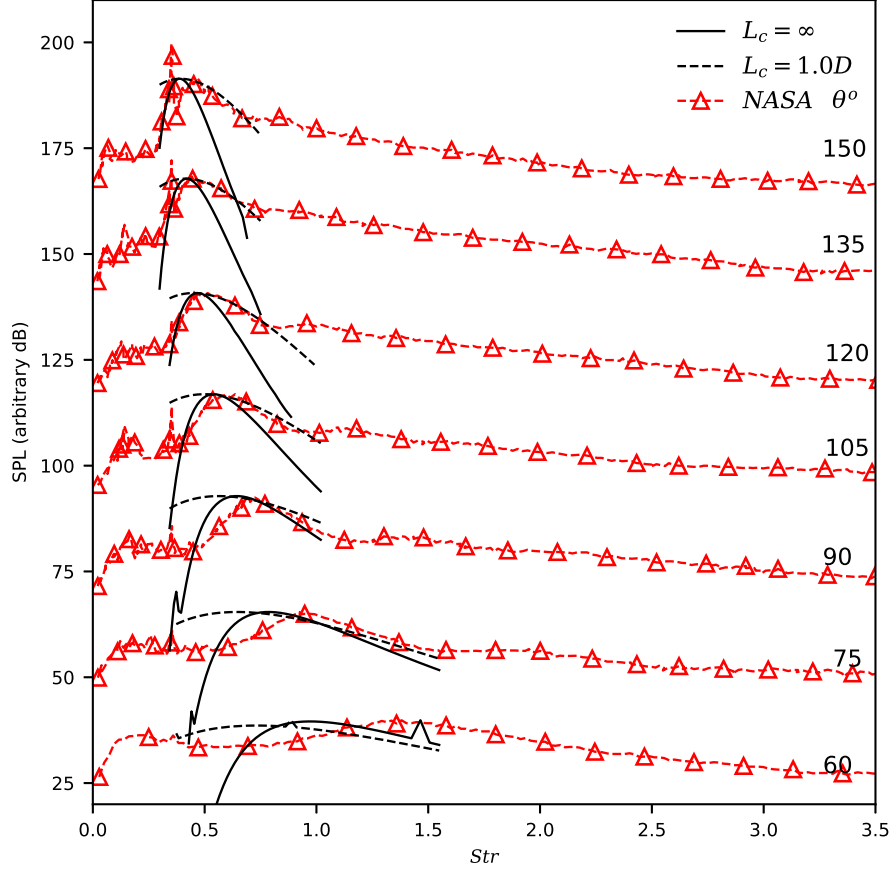


**Fig. 3** Power spectrum at a distance of  $100D$  through a range of observation angles between  $\theta = 60^\circ$  to  $\theta = 120^\circ$  measured from the downstream jet axis for a wavepacket with  $k_h L = 5$ . Each measurement angle is offset by  $\Delta dB = 15$ . NASA experimental data from Norum and Seiner [37].

of the wavepacket  $k_h$ . The source term in both cases produces four distinct lobes. The introduction of coherence decay stretches the lobes parallel to the  $k_{y1} = -k_{y2}$  axis. This is consistent with what has been observed in subsonic jets [3, 16].

As noted by Crighton [26], only certain spectral components of the source term corresponding to supersonic phase speeds can contribute to far-field noise. In order to isolate only the radiating wavenumbers of the source term, the following conditions need to be met

$$\frac{|k_{y1}|}{k_h} \leq M_c \quad (20a)$$

$$\frac{|k_{y2}|}{k_h} \leq M_c, \quad (20b)$$

where  $M_c = \omega/(k_h c_0)$  is the convective Mach number. These conditions in wavenumber space are represented by the white circles in Fig. 4c and 4d. Source energy which lies outside the circle do not contribute to the far-field sound generation. Unlike the subsonic jet case, where the unit coherence source lies completely outside the radiation circle, the supersonic shock-containing case already has a source lobe satisfying the radiation criterion. This is similar to what is observed in ideally expanded supersonic jets [3, 27]. The other three lobes are silent as they lie outside the radiation circle.

When coherence decay is introduced we see that the stretching of the radiation lobe actually removes part of the source energy from the radiating circle. Unlike the subsonic case, where jittering of the wavepacket causes the source

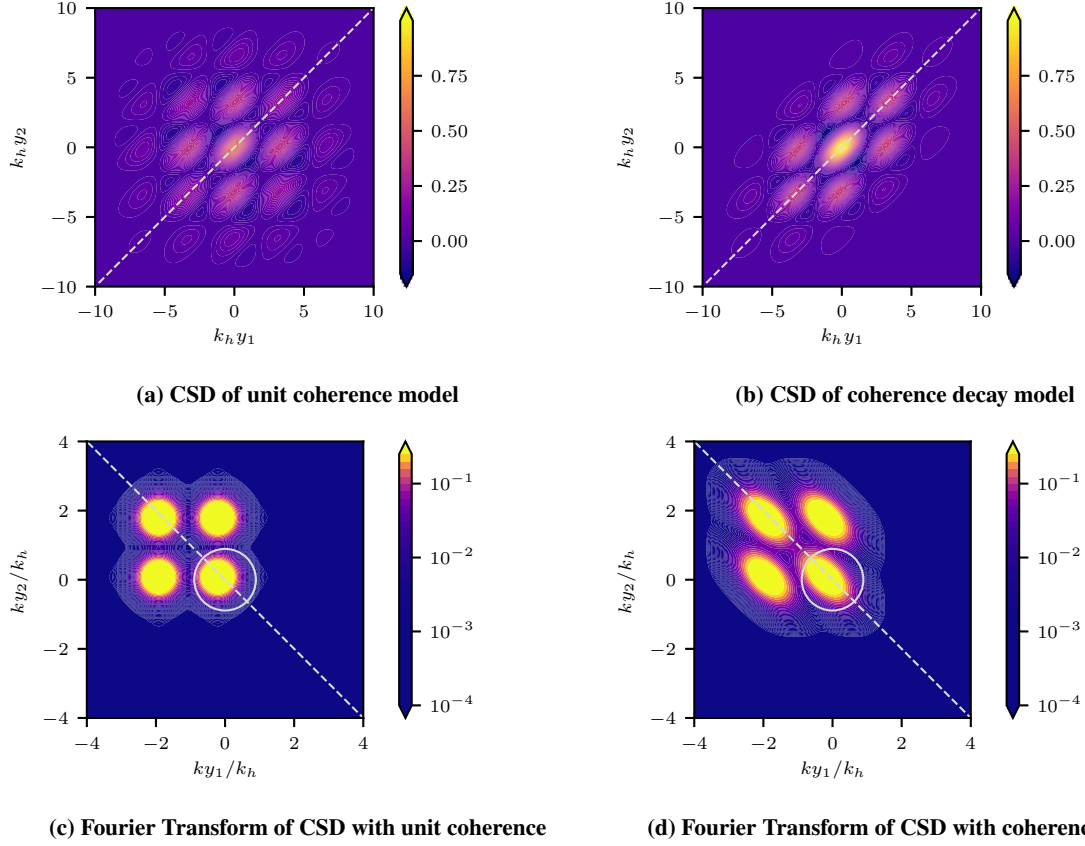


**Fig. 4** The real part of the CSD without a) and with b) coherence decay is shown for  $L_c = 1.0D$ . The diagonal line represents  $y_1 = y_2$ . The corresponding Fourier transformed CSD in wavenumber space for models without a) and with b) coherence decay. Diagonal line corresponds to  $k_{y1} = -k_{y2}$ . The white circle represents the acoustic matching criterion  $|k|/k_h = 0.6M_j$ . The amplitude of both models have been normalised to highlight the effect of coherence decay. The wavepacket frequency is  $St = 0.8$  for a jet operating at  $\beta = 1.1$ .

energy to be stretched into the radiation circle, coherence decay removes energy in the BBSAN case. This explains why the introduction of coherence decay decreases the peak sound pressure level compared to the unit coherence case as seen in Fig. 2.

The Fourier transform contour plots can also be used to explain the directivity behaviour observed in Fig. 2. For a given value of  $\theta$ , the Fourier transformed wavenumbers  $k_{y1}$  and  $k_{y2}$  are given by

$$(k_{y1}, k_{y2}) = (-M_c \cos \theta, M_c \cos \theta). \quad (21)$$

Therefore, for  $\theta$  values corresponding to the perpendicular direction, the relevant part of the Fourier transform is close to the origin. Moving away from the origin along this axis will correspond to angles upstream and downstream of the jet axis respectively. Hence, the stretching of the source lobe along the  $k_{y1} = -k_{y2}$  axis also broadens the directivity of the jet as depicted in Fig. 2. This broadening is due to the source energy being stretched in both directions from the origin within the radiation circle. To summarise, coherence decay is not a sound amplifier as found in the subsonic case but rather broadens the directivity of BBSAN. This broadening will be seen to be even more important when we consider higher-order shock-cell modes in § V.

## V. Coherence decay and higher-order shock-cell modes

### A. Far-field sound prediction

We now focus on the more general model where higher-order shock-cell modes are included. It has been argued these additional shock-cell modes do make significant contributions to high frequency sound in upstream directions [29, 34]. The inclusion of these higher-order modes will hopefully rectify the high frequency drop-off seen in Fig. 3.

Tam et al. [34] have argued that it should only be necessary to include the first four shock-cell modes and any higher modes are unnecessary to describe the shock-cell structure. Ray and Lele, on the other hand, justified the use of only the fundamental shock-cell mode as source activity associated with higher-order modes lie outside the range of radiating wavenumbers. This is true when coherence decay is not accounted for.

By including higher order modes (up to 10 for this study), as shown by Fig. 5, an improvement in sound pressure level prediction is observed for all observation angles. Higher waveguide modes are required to describe the acoustic spectra for frequencies greater than the broadband peak, consistent with Tam et al. [34]. While there are still discrepancies for the downstream angle at  $\theta = 60^\circ$ , both models with and without coherence decay predict the peak frequency within reasonable accuracy. The spectral peak shape predicted when coherence decay is included is more accurate than the case with perfect coherence. For the perfectly coherent wavepacket, oscillations start to occur at higher Strouhal numbers resulting in ‘narrow-banded’ secondary peaks which are consistent with predictions from linear models (unit coherence by construction) [29].

Conversely, the two-point model with coherence decay ‘smooths’ out these narrow-banded peaks. This observation is consistent with Ray and Lele’s (2007) assertion that non-linear effects, such as stochastic turbulent forcing, can rectify these artificial peaks introduced from the instability wave interacting with the higher-order shock-cell modes. We turn to the Fourier transformed CSD maps to gain a better insight into this behaviour.

### B. Interpreting sound radiation characteristics

The Fourier transformed CSD maps are computed for two frequencies,  $St = 0.8$  (Fig. 6a and 6b) and  $St = 1.0$  (Fig. 6c and 6d) where we have now included the first ten shock-cell waveguide modes. Compared to the previous single-mode ( $n = 1$ ) case, the additional lobes are now arranged on top of and perpendicular to the  $k_{y1} = -k_{y2}$  line. The additional source energy lobes are due to the wavepackets now interacting with the higher Fourier modes of the shock-cells.

For the unit coherence case (Fig. 6a and 6c), the far-field sound radiation is still dominated by the wavepacket interaction with the  $n = 1$  waveguide mode. For the frequency  $St = 0.8$ , interaction with the second mode does not contribute to the far-field radiation as the source energy from this interaction lies outside the radiation circle. This was observed by Ray and Lele [29] and the reason that modes higher than the fundamental were not considered further in their study. At a higher frequency ( $St = 1.0$ ), however, the Fourier lobes become more compact and the  $n = 2$  mode migrates into the radiation circle as seen in Fig. 6c. This is consistent with the behaviour seen in the far-field acoustic spectrum of Fig. 3 and 5. For frequencies below the broadband peak, we do not see an increase in sound pressure level when higher order shock modes are added.

For the model where coherence decay is taken into account (Fig. 6b and 6d), we observe once again a stretching of the source lobes along the  $k_{y1} = -k_{y2}$  line. The stretching causes the fundamental ( $n = 1$ ) mode to merge with the second mode and spreads the source energy within the radiating circle. This means that coherence decay, which accounts for stochastic effects, can rectify the ‘missing sound’ at higher frequencies in the upstream direction seen in Fig. 3. It is clear, when compared to the perfectly coherent wavepacket, coherence decay ‘smooths’ the source energy in wavenumber space. This levelling effect in both directivity and frequency is evident when comparing the sound pressure level contour plots in Fig. 1a and Fig. 1b. Nevertheless, the overprediction in sound pressure level for frequencies below the spectral peak is still present for all observation angles. The overprediction at low frequencies is most likely a result of the non-physical constant coherence length assumption which was used for this present study.

## VI. Conclusions

In this work, we have demonstrated that coherence decay is an important parameter for the modelling of broadband shock associated noise in the wavepacket framework. By transforming the single point model first suggested by Lele [2] into a two-point framework, we show here that coherence decay may be crucial in predicting higher frequency noise in the upstream direction.

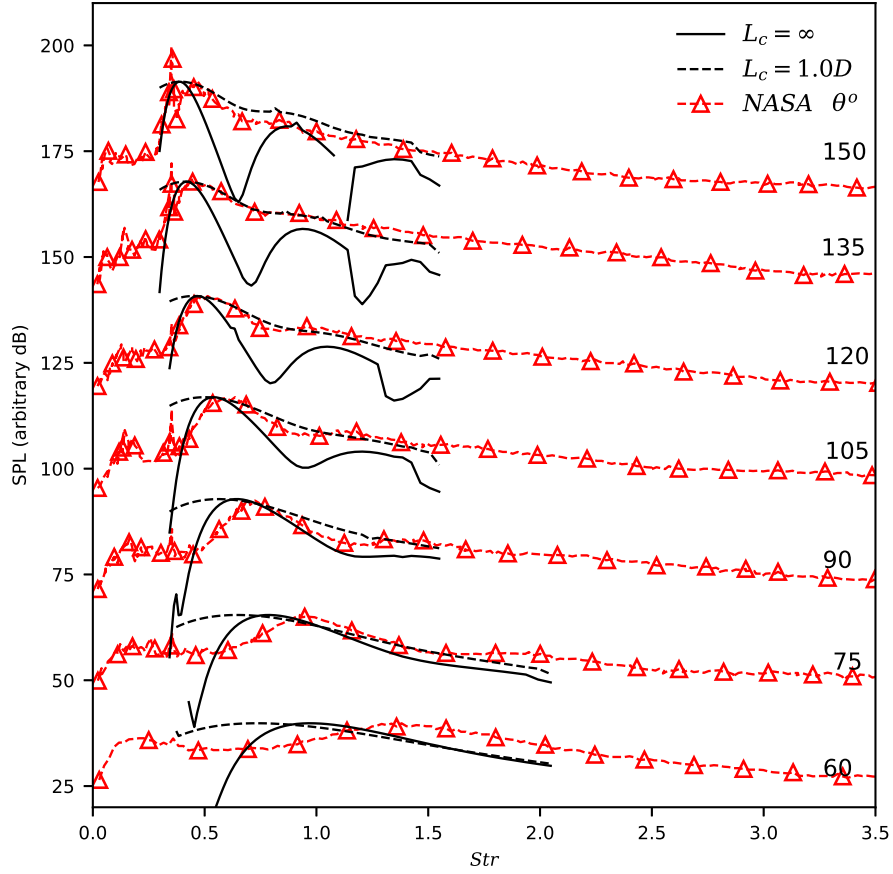


**Fig. 5** Power spectrum at a distance of  $100D$  through a range of observation angles between  $\theta = 60^\circ$  to  $\theta = 120^\circ$  measured from the downstream jet axis for a wavepacket with  $k_h L = 5$  for multiple shock-cell waveguide modes. Each measurement angle is offset by  $15\text{dB}$ . NASA experimental data from Norum and Seiner [37].

When coherence decay is considered, the acoustic efficiency of wavepackets at peak frequency is largely unaltered but source energy is spread over a greater directivity range. The overprediction in sound pressure level at frequencies below the peak suggests that a constant coherence length is not appropriate and its dependency on frequency would need to be known. By comparing with experimental spectra, it is clear that coherence decay in shock-containing supersonic flows does not amplify the amplitude of the sound.

Wavepacket jitter, however, seems to come into play for acoustic frequencies which are greater than the peak amplitude. By capturing this coherence decay, clear improvements are made, especially in the upstream and sideline directions where BBSAN dominates. Moreover, we show the importance of including higher order shock modes along with coherence decay to model higher frequency sound. In contrast with the subsonic case, coherence decay impacts the directivity of higher frequency sound rather than its amplitude.

Future works will focus on extracting the relevant flow variables to build the prediction kinematic model from the ‘inside-out’ from experimental measurements or numerical simulations. Determining the exact flow features and mechanisms involved is beyond the scope of this model problem. A follow up study would be to look at the degree shocks has on the jittering of a wavepacket and how different this non-linear behaviour is compared to the subsonic case. Results from the kinematic model suggests that an improved dynamic stability model for BBSAN would have to include some sort of forcing term to include jitter.

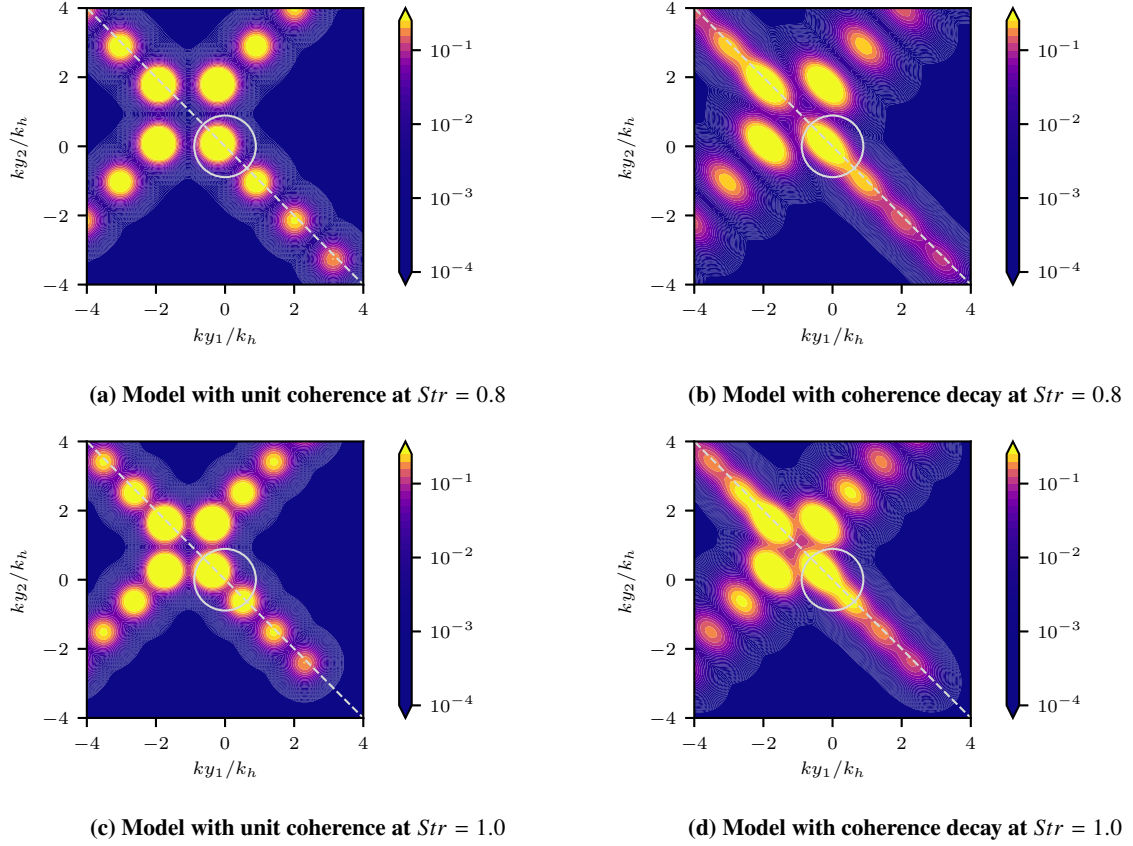


**Fig. 6** The corresponding Fourier transformed CSD in wavenumber space for  $St = 0.8$  and  $St = 1.0$ . Left-hand side frames ((a) and (c)) correspond to the unit coherence model while the right-hand side ((b) and (d)) are for the two-point model with a coherence decay length  $L_c = 1.0D$ . Diagonal line corresponds to  $k_{y1} = -k_{y2}$ . The white circle represents the acoustic matching criterion  $|k|/k_h = 0.6M_j$ . The amplitude of both models have been normalised to highlight the effect of coherence decay. The jet is operating at  $\beta = 1.1$ .

### Acknowledgements

This work was supported by the Australian Government via a Research Training Program (RTP) Scholarship and the Australian Research Council through the Discovery Projects scheme.

### References

- [1] Savarese, A., Jordan, P., Girard, S., Royer, A., Fourment, C., Collin, E., Gervais, Y., and Porta, M., “Experimental study of shock-cell noise in underexpanded supersonic jets,” *AIAA Paper*, Vol. 2080, 2013, p. 2013.
- [2] Lele, S. K., “Phased array models of shock-cell noise sources,” *AIAA Paper*, Vol. 2841, 2005, p. 2005.
- [3] Cavalieri, A. V., and Agarwal, A., “Coherence decay and its impact on sound radiation by wavepackets,” *Journal of Fluid Mechanics*, Vol. 748, 2014, pp. 399–415.
- [4] Harper-Bourne, M., and Fisher, M. J., “The noise from shock waves in supersonic jets,” *AGARD-CP-131*, Vol. 11, 1973, pp. 1–13.
- [5] Tam, C. K., “Supersonic jet noise,” *Annual Review of Fluid Mechanics*, Vol. 27, No. 1, 1995, pp. 17–43.
- [6] Lighthill, M. J., “On sound generated aerodynamically. I. General theory,” *Proceedings of the Royal Society of London A: Mathematical, Physical and Engineering Sciences*, Vol. 211, The Royal Society, 1952, pp. 564–587.

- [7] Jordan, P., and Colonius, T., “Wave packets and turbulent jet noise,” *Annual Review of Fluid Mechanics*, Vol. 45, 2013, pp. 173–195.
- [8] Tam, C., “Stochastic model theory of broadband shock associated noise from supersonic jets,” *Journal of Sound and Vibration*, Vol. 116, No. 2, 1987, pp. 265–302.
- [9] Morris, P. J., and Miller, S. A., “The prediction of broadband shock-associated noise using RANS CFD,” *15th AIAA Aeroacoustics Conference*, Vol. 15, 2009, pp. 49–56.
- [10] Kalyan, A., and Karabasov, S. A., “Broad band shock associated noise predictions in axisymmetric and asymmetric jets using an improved turbulence scale model,” *Journal of Sound and Vibration*, Vol. 394, 2017, pp. 392–417.
- [11] Crow, S. C., and Champagne, F., “Orderly structure in jet turbulence,” *Journal of Fluid Mechanics*, Vol. 48, No. 3, 1971, pp. 547–591.
- [12] Mollo-Christensen, E., “Jet noise and shear flow instability seen from an experimenter’s viewpoint,” *Journal of Applied Mechanics*, Vol. 34, No. 1, 1967, pp. 1–7.
- [13] Gudmundsson, K., and Colonius, T., “Instability wave models for the near-field fluctuations of turbulent jets,” *Journal of Fluid Mechanics*, Vol. 689, 2011, pp. 97–128.
- [14] Tam, C. K., and Tanna, H., “Shock associated noise of supersonic jets from convergent-divergent nozzles,” *Journal of Sound and Vibration*, Vol. 81, No. 3, 1982, pp. 337–358.
- [15] Tam, C., Seiner, J., and Yu, J., “Proposed relationship between broadband shock associated noise and screech tones,” *Journal of sound and vibration*, Vol. 110, No. 2, 1986, pp. 309–321.
- [16] Jaunet, V., Jordan, P., and Cavalieri, A., “Two-point coherence of wave packets in turbulent jets,” *Physical Review Fluids*, Vol. 2, No. 2, 2017, p. 024604.
- [17] Maia, I. A., Jordan, P., Jaunet, V., and Cavalieri, A. V., “Two-point wavepacket modelling of jet noise,” *23rd AIAA/CEAS Aeroacoustics Conference*, 2017, p. 3380.
- [18] Tam, C., Seiner, J., and Yu, J., “Proposed relationship between broadband shock associated noise and screech tones,” *Journal of sound and vibration*, Vol. 110, No. 2, 1986, pp. 309–321.
- [19] Pack, D., “A note on Prandtl’s formula for the wave-length of a supersonic gas jet,” *The Quarterly Journal of Mechanics and Applied Mathematics*, Vol. 3, No. 2, 1950, pp. 173–181.
- [20] Towne, A., Colonius, T., Jordan, P., Cavalieri, A., and Bres, G. A., “Stochastic and nonlinear forcing of wavepackets in a Mach 0.9 jet,” *AIAA paper*, Vol. 2217, 2015, p. 2015.
- [21] Semeraro, O., Jaunet, V., Jordan, P., Cavalieri, A. V., and Lesshafft, L., “Stochastic and harmonic optimal forcing in subsonic jets,” 2016, p. 2935.
- [22] Tissot, G., Zhang, M., Lajús, F. C., Cavalieri, A. V., and Jordan, P., “Sensitivity of wavepackets in jets to nonlinear effects: the role of the critical layer,” *Journal of Fluid Mechanics*, Vol. 811, 2017, pp. 95–137.
- [23] Cavalieri, A. V., Rodríguez, D., Jordan, P., Colonius, T., and Gervais, Y., “Wavepackets in the velocity field of turbulent jets,” *Journal of fluid mechanics*, Vol. 730, 2013, pp. 559–592.
- [24] Baqui, Y., Agarwal, A., Cavalieri, A. V., and Sinayoko, S., “Nonlinear and linear noise source mechanisms in subsonic jets,” *19th AIAA/CEAS Aeroacoustics Conference, AIAA Paper*, Vol. 2087, 2013.
- [25] Suzuki, T., “Coherent noise sources of a subsonic round jet investigated using hydrodynamic and acoustic phased-microphone arrays,” *Journal of Fluid Mechanics*, Vol. 730, 2013, p. 659.
- [26] Crighton, D., “Basic principles of aerodynamic noise generation,” *Progress in Aerospace Sciences*, Vol. 16, No. 1, 1975, pp. 31–96.
- [27] Sinha, A., Rodríguez, D., Brès, G. A., and Colonius, T., “Wavepacket models for supersonic jet noise,” *Journal of Fluid Mechanics*, Vol. 742, 2014, pp. 71–95.
- [28] Cavalieri, A. V., Jordan, P., Wolf, W. R., and Gervais, Y., “Scattering of wavepackets by a flat plate in the vicinity of a turbulent jet,” *Journal of sound and Vibration*, Vol. 333, No. 24, 2014, pp. 6516–6531.



- [29] Ray, P. K., and Lele, S. K., “Sound generated by instability wave/shock-cell interaction in supersonic jets,” *Journal of fluid mechanics*, Vol. 587, 2007, pp. 173–215.
- [30] Tam, C., “Broadband shock-associated noise of moderately imperfectly expanded supersonic jets,” *Journal of Sound and Vibration*, Vol. 140, No. 1, 1990, pp. 55–71.
- [31] Cavalieri, A. V., Jordan, P., Colonius, T., and Gervais, Y., “Axisymmetric superdirectivity in subsonic jets,” *Journal of fluid Mechanics*, Vol. 704, 2012, pp. 388–420.
- [32] Prandtl, L., *Über die stationären Wellen in einem Gasstrahl*, Hirzel, 1904.
- [33] Landahl, M. T., and Mollo-Christensen, E., *Turbulence and random processes in fluid mechanics*, Cambridge University Press, 1992.
- [34] Tam, C. K., Jackson, J. A., and Seiner, J., “A multiple-scales model of the shock-cell structure of imperfectly expanded supersonic jets,” *Journal of Fluid Mechanics*, Vol. 153, 1985, pp. 123–149.
- [35] Cavalieri, A. V., Jordan, P., Agarwal, A., and Gervais, Y., “Jittering wave-packet models for subsonic jet noise,” *Journal of Sound and Vibration*, Vol. 330, No. 18, 2011, pp. 4474–4492.
- [36] Baqui, Y. B., Agarwal, A., Cavalieri, A. V., and Sinayoko, S., “A coherence-matched linear source mechanism for subsonic jet noise,” *Journal of Fluid Mechanics*, Vol. 776, 2015, pp. 235–267.
- [37] Norum, T. D., and Seiner, J. M., “Measurements of mean static pressure and far field acoustics of shock containing supersonic jets,” 1982.
- [38] Sasaki, K., Cavalieri, A. V., Jordan, P., Schmidt, O. T., Colonius, T., and Brès, G. A., “High-frequency wavepackets in turbulent jets,” *Journal of Fluid Mechanics*, Vol. 830, 2017.
- [39] Suzuki, T., “Wave-Packet Representation of Shock-Cell Noise for a Single Round Jet,” *AIAA Journal*, 2016.

## Appendix B

# A Parabolised Stability Equation Based Broadband Shock-Associated Noise Model

### B.1 Introductory Statement

Following the results from Chapter 6, a more realistic description of the wavepackets was desired. To this end, parabolised stability equations were used to obtain the wavepacket structure. With the availability of LES data [216], two-point coherence information from an ideally-expanded supersonic jet was obtained and substituted into the source description. Unlike the final model, this paper uses a line-source model where the PSE solutions were integrated radially before propagation to the far-field. The encouraging preliminary results confirmed conclusions from the simple line source model [203] and motivated the refinement of the source model which ultimately led to the final version presented in Chapter 7. This conference paper [204] was prepared for and presented at the *25th AIAA/CEAS Aeroacoustics Conference*.

### B.2 Conference Paper

## A Parabolised Stability Equation based Broadband Shock-Associated Noise Model

Marcus H. Wong<sup>\*</sup>, Daniel Edgington-Mitchell<sup>†</sup> and Damon Honnery<sup>‡</sup>

*Laboratory for Turbulence Research in Aerospace and Combustion (LTRAC), Department of Mechanical and Aerospace Engineering, Monash University, Melbourne, VIC 3800, Australia*

André V. G. Cavalieri<sup>§</sup>

*Instituto Tecnológico de Aeronáutica, São José dos Campos, SP, 12228-900, Brazil*

Peter Jordan<sup>¶</sup>

*Institut PPrime CNRS - Université de Poitiers - ENSMA, Poitiers, 86036, France*

Wavepacket models have been used extensively to predict the noise produced from turbulent subsonic and supersonic jets. Such wavepackets, which represent the organised structures of the flow, are solutions to the linearised Navier-Stokes equations. Using a kinematic two-point model, Wong et al. [1] have indicated the importance of incorporating coherence decay in modelling broadband shock-associated noise (BBSAN) in supersonic jets. In this work, we aim to improve the model by using solutions from linear parabolised stability equations (PSE) to model the wavepacket part of the BBSAN source. The two-point coherence of the wavepackets is obtained from large-eddy simulation (LES) data of a  $M_j = 1.5$  fully-expanded isothermal supersonic jet [2]. The aim is to build a dynamic sound-source model for BBSAN that would improve on the simplified line-source model proposed by Wong et al. [3]. We find that a frequency dependent coherence decay length scale is important in order to suppress the higher-order harmonic peaks [4] and to obtain the correct BBSAN peak shape. Moderate agreement up to  $St = 1$  was found between the current noise predictions and those from experimental data.

### I. Nomenclature

$\omega$	=	wavepacket frequency
$\theta$	=	azimuthal co-ordinate
$c_{s_n}$	=	amplitude coefficient of the shock cells
$G$	=	Green's function
$k_s$	=	shock-cell wavenumber
$k_h$	=	hydrodynamic wavenumber
$L$	=	longitudinal extent of wavepacket
$L_c$	=	coherence length of wavepacket
$m$	=	azimuthal mode number
$M_j$	=	ideally-expanded Mach number
$r$	=	radial co-ordinate
$u_s$	=	shock cell velocity fluctuation
$u_t$	=	wavepacket fluctuations
$\hat{u}_\omega^*$	=	velocity fluctuations at a frequency $\omega$
$x$	=	axial co-ordinate

<sup>\*</sup>PhD Student, Laboratory for Turbulence Research in Aerospace and Combustion (LTRAC), Department of Mechanical and Aerospace Engineering, Monash University, Melbourne, VIC 3800, Australia

<sup>†</sup>Senior Lecturer, Laboratory for Turbulence Research in Aerospace and Combustion (LTRAC), Department of Mechanical and Aerospace Engineering, Monash University, Melbourne, VIC 3800, Australia

<sup>‡</sup>Professor, Laboratory for Turbulence Research in Aerospace and Combustion (LTRAC), Department of Mechanical and Aerospace Engineering, Monash University, Melbourne, VIC 3800, Australia

<sup>§</sup>Assistant Professor, Divisão de Engenharia Aeronáutica, Instituto Tecnológico de Aeronáutica

<sup>¶</sup>Research-Scientist, Institute PPrime, CNRS - Université de Poitiers - ENSMA, UPR 3346, 43 Rue de l'Aérodrome, 86036 Poitiers, France

## II. Introduction

**B**ROADBAND shock-associated noise (BBSAN) in supersonic jets is generated when there is a ‘mismatch’ in pressure between the exiting jet flow and the ambient conditions. While other types of noise exist such as mixing noise [5] and screech [6, 7], BBSAN remains important for many modern aircraft [8]. The generation of noise is due to the weak interaction of shock-cells with the downstream-convecting turbulent structures of the jet. The study and modelling of BBSAN has been well documented in literature [9–13]. A review of supersonic jet noise is provided by Tam [14]. Although progress has been made in understanding this form of jet noise, a reduced-order model that links the radiated sound field to the acoustically important part of the flow field over a broad frequency range remains elusive.

BBSAN is characterised by a broad, high frequency peak that is dependent on observer location. The most intense noise is towards the sideline and upstream directions. As the observer location moves downstream, the broad peak shifts to higher frequencies and the spectral peak width increases. This directional dependence of the peak frequency  $f_p$  is predicted by

$$f_p = \frac{U_c}{L(1 - M_c \cos(\theta))}, \quad (1)$$

where  $U_c$  is the convection velocity,  $L$  is the shock-cell spacing,  $M_c$  is the convection Mach number and  $\theta$  is the observer angle measured from the downstream jet axis.

As proposed by Lele [15], the non-linear acoustic source ( $S$ ) for BBSAN in terms of frequency is modelled by the interaction between fluctuations due to turbulence ( $u_t$ ) and modulations due to the quasi-periodic shock-cells ( $u_s$ )

$$S(\mathbf{x}, \omega) = u_s(\mathbf{x}) \times u_t(\mathbf{x}, \omega). \quad (2)$$

To obtain the sound pressure field, the acoustic source term can be propagated using Lighthill’s [16] acoustic analogy

$$\frac{\partial^2 \rho'}{\partial t^2} - c_\infty^2 \nabla^2 \rho' = \frac{\partial^2}{\partial x_i \partial x_j} S, \quad (3)$$

where  $\rho'$  is the fluctuating density,  $c_\infty^2$  is the far-field speed of sound and  $S$  is the source term. The double spatial derivative can be passed onto the Green’s function [17]. The source term, which encapsulates the non-linearities of the flow, drives the fluctuations in the far-field. The utilisation of the acoustic analogy to predict BBSAN has also been performed by Kalyan and Karabasov [12], Morris and Miller [18] amongst others. The far-field pressure can be obtained analytically using a free-field Green’s function

$$p(\mathbf{x}, \omega) = \frac{1}{4\pi} \int S(\mathbf{y}, \omega) e^{i|\mathbf{x}-\mathbf{y}|} \frac{dV}{|\mathbf{x}-\mathbf{y}|}. \quad (4)$$

Recently, wavepacket models have been proposed in the modelling of subsonic jet noise [19, 20]. Pioneered by the seminal findings of Mollo-Christensen [21] and Crow and Champagne [22], wavepacket descriptions provide a direct link between the instabilities of the flow with the radiated sound field. Wavepackets, or instability waves, represent the coherent structures of a turbulent flow; they grow from the initial instabilities near the nozzle exit, become neutrally stable some distance downstream and then decay. The signature of wavepackets, which can be obtained via azimuthal decomposition of the turbulent jet [23], shows these to have different length scales compared to the energy-containing eddies [24]. For a given frequency, their non-compact shapes can also be clearly seen in the leading spectral proper orthogonal decomposition (SPOD) modes [25]. The non-compact nature of the resulting convected wave gives rise to the distinctive directivity of jet noise [26]. The detection of wavepackets has been supported by numerous near-field pressure measurement studies [27–30]. Their results are further supported in the comparisons made between velocity fields and stability calculations by Cavalieri et al. [31] and recent resolvent analysis studies by Schmidt et al. [25], Lesshafft et al. [32]. Sasaki et al. [33] have also found that the evolution of the lower-order azimuthal modes can be predicted using linear wavepackets up to a Strouhal value of  $St = 4$ . More recently, wavepacket models have also been developed and applied to non free-field cases such as jets in the vicinity of a flat plate [34].

While linear wavepacket models have been successful in modelling the large-scale structures in subsonic turbulent jets, the predicted sound pressure level is several orders of magnitude less than those obtained from experiments [35–37].

The aforementioned shortcomings can be resolved when we include wavepacket ‘jitter’ [38]; the desynchronisation of wavepackets due to the action of background turbulence [35, 36, 39]. Using two-point statistics of a turbulent jet, the jittering behaviour is represented as coherence decay. The decay of coherence can be seen in both numerical and experimental PIV data [24]. The two-point coherence function  $\gamma^2$ , extracted from the magnitude square coherence (MSC) of axial velocity between points  $x_1$  and  $x_2$ , can be modelled using a simple Gaussian function

$$\gamma^2(x_1, x_2, \omega) = \exp\left(-2\frac{(x_1 - x_2)^2}{L_c^2(\omega)}\right), \quad (5)$$

where  $L_c(\omega)$  is given as the characteristic length scale for coherence decay. Cavalieri and Agarwal [35] found that for a given sound source, the average amplitude, phase and also its coherence function  $\gamma^2$  need to be modelled correctly to match the original source. Hence, for a given frequency  $\omega$ , the power spectral density of the far-field sound  $\langle p(\mathbf{r}, \omega)p^*(\mathbf{r}, \omega) \rangle$  at an observer location position  $\mathbf{r}$  can now be obtained using the following expression

$$\langle p(\mathbf{r}, \omega)p^*(\mathbf{r}, \omega) \rangle \approx \int_V \int_V \langle \tilde{S}(x_1, \omega)\tilde{S}^*(x_2, \omega)\gamma(x_1, x_2, \omega) \rangle G(\mathbf{r}, x_1, \omega)G^*(\mathbf{r}, x_2, \omega)dx_1dx_2. \quad (6)$$

The linear two-point description of the source  $S(x_1, \omega)S^*(x_2, \omega)$  is multiplied by the coherence decay term  $\gamma(x_1, x_2, \omega)$  to form the full cross-spectral density (CSD)  $\tilde{S}(x_1, \omega)\tilde{S}^*(x_2, \omega)$  of the original source found in the integral of equation 6. The relationship between the linear and full statistical source is given as

$$\tilde{S}(x_1, \omega)\tilde{S}^*(x_2, \omega) = S(x_1, \omega)S^*(x_2, \omega)\gamma(x_1, x_2, \omega). \quad (7)$$

Instability wave models have also been used in perfectly-expanded [40] and imperfectly-expanded supersonic flows [10, 15, 41, 42]. In perfectly-expanded flows characterised by supersonic convection velocity, the results of Sinha et al. [40] show that coherence decay is here less important to obtain the sound radiation at peak polar angles due to the phase speeds of the wavepackets being supersonic and thus capable of radiating to the far-field efficiently. To study the influence of coherence decay in shock-containing flows, Wong et al. [1] used a line-source wavepacket model containing only the  $m = 0$  axisymmetric mode. It was found that coherence decay, rather than increasing acoustic efficiency as in the subsonic case, suppressed artificial higher-order harmonic peaks when additional shock-cell modes are included. The peaks occur due to the higher order shock-cell modes interacting with the instability waves of the mean flow. These spurious peaks were also previously predicted by both Tam et al. [10] and Lele [15]; both these models have perfectly-coherent sources. Using the source description in equation 2, the CSD for BBSAN found in equation 6 is now modelled as a two-point line source [1] expressed as

$$\begin{aligned} \tilde{S}(x_1, \omega)\tilde{S}^*(x_2, \omega) &= A^2(\omega)e^{-\left(\frac{x_1-x_0}{L(\omega)}\right)^2}e^{-\left(\frac{x_2-x_0}{L(\omega)}\right)^2}\left\{e^{ik_h(\omega)(x_1-x_2)}\right\}e^{-\left(\frac{(x_1-x_2)^2}{L_c^2(\omega)}\right)}\times \\ &\sum_{n_1} c_{s_{n_1}}\left\{e^{ik_{s_{n_1}}x_1} + e^{-ik_{s_{n_1}}x_1}\right\}\sum_{n_2} c_{s_{n_2}}\left\{e^{ik_{s_{n_2}}x_2} + e^{-ik_{s_{n_2}}x_2}\right\}, \end{aligned} \quad (8)$$

where a wavepacket at a given frequency is characterised by its hydrodynamic wavenumber  $k_h$  and two length scales  $L$  and  $L_c$ , which are the wavepacket amplitude envelope and coherence lengths respectively. The shock-cell component is modelled using the Pack & Prandtl model, where  $k_{s_n}$  and  $c_{s_n}$  are the wavelength and amplitude of the  $n^{th}$  shock-cell mode respectively. Wong et al. [3] found that the inclusion of coherence decay, while able to suppress higher-order peaks, led to poor agreement at frequencies lower than the peak frequency. It was assumed that this was due to the use of ad-hoc constant values of  $k_h$ ,  $L$  and  $L_c$ . Moreover, the 1D line source assumption may be overly restrictive due to the distributed nature of the acoustic sources for BBSAN [42, 43]. In order to assess these issues, a more realistic representation of the wavepacket parameters as a function of frequency is necessary.

The current work aims to extend the model proposed by Wong et al. [1], by obtaining a volumetric description of  $u_t$  from stability theory and large-eddy simulation (LES) data. In order to develop a more realistic two-point model and to establish a link to linear stability theory, the axisymmetric part of the turbulent fluctuations are approximated via solutions to the parabolised stability equations (hereinafter PSE). The modulations due to the shocks  $u_s$  are obtained from the Pack & Prandtl model [44, 45]. The methodology is similar to Ray and Lele [42] who used PSE solutions coupled with shock-cell solutions, but differs in so far we incorporate two-point coherence in the source model. The

mean flow used for the PSE analysis will be extracted from the LES data of Brès et al. [2]. To compare with the original line source model (equation 8), both the  $u_s$  and  $u_t$  fluctuations are integrated radially [39]. The two-point coherence behaviour is extracted from the MSC of the decomposed streamwise velocity originating from the same LES data set. The BBSAN predictions are compared to experimental data [18] and the analytical wavepacket BBSAN model of Wong et al. [1].

The paper is organised as follows. The LES dataset of Brès et al. [2] is briefly discussed in section III. In section IV we present the proposed methodology to model BBSAN and the construction of the source terms. Emphasis is placed on the approach used to solve the linear PSE and the extraction of coherence information from the LES data. In section V we present preliminary results from the PSE and compare them to LES data in section VI. Results for coherence decay length scales are shown in section VII and the resulting far-field BBSAN predictions are presented in section VIII.

### III. LES Database

A large-eddy simulation database of a  $M_j = 1.5$  supersonic ideally-expanded isothermal jet is used in this present study. The simulation was performed using the compressible flow solver “Charles” developed at Cascade Technologies [2], on an unstructured adapted grid with 40 million cells. This database is an extension of the previous work by Brès et al. [46], with the flow conditions and nozzle geometry (convergent-diverging) matching those of the experiment carried out at the United Technologies Research Center (UTRC) anechoic jet facility [47]. The main differences with the previous simulations are that wall modelling and near-wall adaptive mesh refinement are now employed on the internal nozzle surface, and that the simulated Reynolds number is now  $Re = \rho_j U_j D / \mu_j = 1.78 \times 10^6$ , matching the experimental value. This is done to better capture/model the state of the boundary layer inside the nozzle, which has been shown to be important for flow field and noise predictions [48]. This modelling leads to (nominally) turbulent boundary layer profiles at the nozzle exit. The rest of the numerical setup is identical to Brès et al. [2]. A slow co-flow of  $M_{co} = 0.1$  is also included in the simulation to match the experimental conditions. The nozzle exit is centered at  $(x, y, z) = (0, 0, 0)$  and the axisymmetric computation domain extends to  $45D$  and  $20D$  in the streamwise and radial direction respectively. To facilitate post-processing and analysis, the LES data is interpolated from the original unstructured LES grid onto a structured cylindrical grid with uniform spacing in azimuth. The three-dimensional cylindrical grid extends to  $0 \leq x/D \leq 30$ ,  $0 \leq r/D \leq 6$ , with  $(n_x, n_r, n_\theta) = (698, 136, 128)$ , where  $n_x$ ,  $n_r$  and  $n_\theta$  are the number of points in the streamwise, radial and azimuthal direction, respectively. The database is sampled every delta  $tc_\infty/D = 0.1$  acoustic time units, resulting in a cutoff (Nyquist) frequency of  $St = \Delta f D / U_j = 3.33$ . The jet operating conditions and simulation parameters are summarised in table 1.

In order to extract the coherence decay information, post-processing of the velocity data is required. The LES data is Fourier transformed in the azimuthal direction in order to extract the  $m = 0$  axisymmetric mode. Prior to the temporal Fourier transform used to extract frequency-dependent information, a Hann window is used to divide the signal into data blocks of 178 time samples with 50% overlap.

**Table 1 Jet Operating Conditions**

Case	$M_j$	$T_j/T_\infty$	$M_a$	$Re$	Sim. Duration	Sampling Period	Nyquist Freq.	Nom. Snapshots
B118	1.5	1.0	1.5	$3 \times 10^5$	215	0.1	3.33	5000

## IV. Methodology & Theory

### A. BBSAN Source Model

We adopt the previous nonlinear source description for BBSAN [1, 10, 15, 42] as shown in equation 2. The far-field sound is obtained using a convolution of the source CSD with the free-field Green’s function (equation 6). By describing the source in such a manner, the turbulent fluctuations ( $u_t$ ) and the modulations due to the shock-cells ( $u_s$ ) are obtained independently. In order to construct the source term, we need to define both the axial and radial structure of  $u_s$  and  $u_t$ . We will only be studying the axisymmetric mode ( $m = 0$ ) and hence a two-dimensional description of the source is sufficient. After arriving at the two-dimensional, axisymmetric description of the source term, it is integrated radially to

form an equivalent line source.

We deduce the wavepacket behaviour from Brès et al. [2] high fidelity LES database of an ideally expanded  $M_j = 1.5$  jet. The database has been validated and we use it to inform the wavepacket parameters ( $k_h, L_c$ ) via results of linear PSE. Due to the slow-varying assumption of the base flow in the PSE formulation, we decided not to use a base flow with shocks but rather the ideally-expanded jet with the same perfectly-expanded jet velocity  $M_j$ . While this is consistent with the methodology of previous BBSAN studies [42], it is not possible to study the effects that the shock cells might have on the instability waves [49]. The two-point behaviour of the wavepacket is also probed from the azimuthally decomposed velocity field of the jet, allowing the CSD to be computed to recover the MSC.

The shock-cells are represented by zero-frequency eigenmodes of a locally parallel jet, modelled as a vortex sheet, as proposed by Pack & Prandtl, ensuring that the model remains grounded in stability theory. The fluctuations  $u_t$  and  $u_s$  are then combined to form the BBSAN source term. An overview of the method is shown in figure 1 and details of each  $u_s$  and  $u_t$  component are discussed in the following sections.

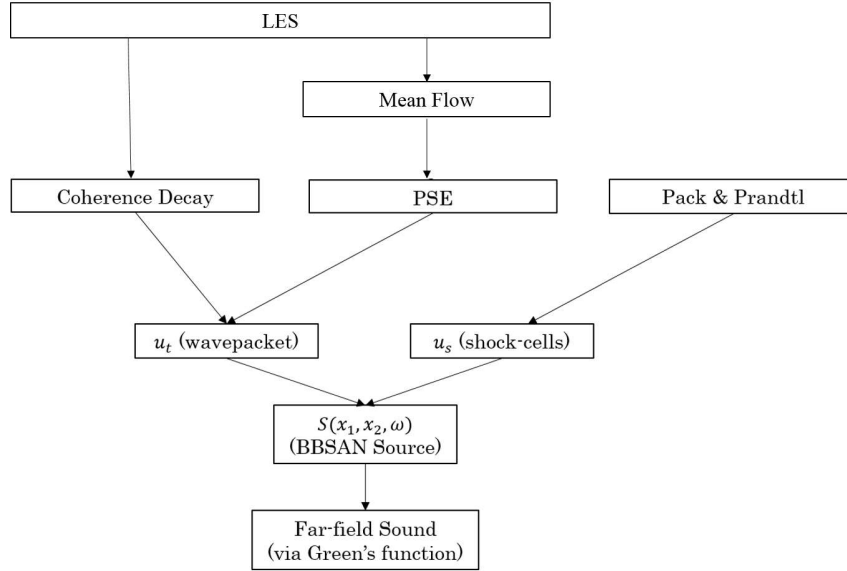


**Fig. 1 Overview of the proposed methodology.**

### B. Pack & Prandtl Shock-cell Model

The shock-cell disturbances are treated as stationary waveguide modes of the jet flow as proposed by Prandtl [44], Pack [45], where the shear layer is modelled as a vortex sheet. For small disturbances, the linearised flow equations can be solved and the velocity fluctuations due to shock-cells  $u_s$  is given by

$$u_s(x, r) = \sum_n c_{s_n} \Phi(r) \frac{1}{2} \{ e^{ik_{s_n} x} + e^{-ik_{s_n} x} \}. \quad (9)$$

The radial profile  $\Phi(r)$  is described by the Bessel functions of order 0 and 1. The shock-cell waveguide modes  $n$  are described by the wavenumbers  $k_{s_n}$  and the amplitude terms  $c_{s_n}$ . While the fundamental mode ( $n = 1$ ) predicts the BBSAN peak frequency lobe well, higher-order shock-cell modes are required for frequencies greater than the peak and in the upstream direction [3, 42].

### C. Parabolised Stability Equations

The wavepackets are based on linear stability theory. Since the jet mean flow is slowly diverging, we use parabolised stability equations (PSE) to describe the velocity fluctuations of the jet. PSE have been extensively used [40, 42, 50] to

model turbulent jets.

The flow quantities are first non-dimensionalised. Length quantities are normalised by the jet diameter  $D$  while velocities by the ambient speed of sound  $c_\infty$ . Pressure  $p$  and temperature  $T$  are normalised by  $\rho_\infty c_\infty^2$  and  $c_\infty^2/c_p$ , where  $c_p$  is the heat capacity ratio for air [51]. Density  $\rho$  can be obtained via the perfect gas law and the Prandtl number is fixed at 0.7 for air. By working in cylindrical co-ordinates, the non-dimensionalised fluid properties of a jet can be described by the vector  $\mathbf{q}$  and can be decomposed into a mean component  $\bar{\mathbf{q}}(x, r)$  and a fluctuating component  $\mathbf{q}'(x, r, \theta, t)$

$$\mathbf{q}(x, r, \theta, t) = \bar{\mathbf{q}}(x, r) + \mathbf{q}'(x, r, \theta, t). \quad (10)$$

The vector  $\mathbf{q}$  refers to the dependent flow variables of interest,  $\mathbf{q} = (u_x, u_r, u_\theta, T, \rho)$ , where  $u_x$ ,  $u_r$  and  $u_\theta$  are the axial, radial and azimuthal velocity components respectively. The thermodynamic variables include  $T$  and  $\rho$ , which are the temperature the density of the fluid respectively. The problem is formulated in cylindrical coordinates. For stability calculations, an appropriate ansatz to model the velocity fluctuations for a compressible jet is given as

$$\mathbf{q}'(x, r, \theta, t) = \hat{\mathbf{q}}(x, r) e^{-i\omega t} e^{im\theta}. \quad (11)$$

The term  $\hat{\mathbf{q}}$  is the Fourier coefficient in space,  $m$  is the azimuthal wavenumber and  $\omega = 2\pi St M_a$  is the angular frequency of the fluctuations. In the PSE framework, it is assumed that  $q'(x, r, \theta, t)$  can be further decomposed into a slow and fast varying component. Hence, the appropriate multiple-scales ansatz as first proposed by Crighton and Gaster [52] can be written as

$$\mathbf{q}'(x, r, \theta, t) = \hat{\mathbf{q}}(x, r) e^{i \int \alpha(x') dx'} e^{-i\omega t} e^{im\theta}, \quad (12)$$

where the slowly-varying part is described by the  $\hat{\mathbf{q}}$  shape function and the fast part  $e^{i \int \alpha(x') dx'}$ . The term  $\alpha(x')$  is the complex-valued hydrodynamic wavenumber that varies with axial direction.

The ansatz as described in equation 12 can be substituted into the governing linearised equations where viscosity is not accounted for. The resultant matrix system can be recast into the following compact form (exact terms can be found in Gudmundsson and Colonius [30])

$$[\mathbf{A}(\bar{\mathbf{q}}, \alpha, \omega) + \mathbf{B}(\bar{\mathbf{q}})]\hat{\mathbf{q}} + \mathbf{C}(\bar{\mathbf{q}})\frac{\partial \hat{\mathbf{q}}}{\partial x} + \mathbf{D}(\bar{\mathbf{q}})\frac{\partial \hat{\mathbf{q}}}{\partial x} = 0. \quad (13)$$

To find  $\alpha_{m,\omega}(x)$  and  $q(x, r)$ , the system is discretised and solved by streamwise spatial marching. We used Chebyshev polynomials to discretise in the radial direction and first-order finite differences is used to approximate the axial derivatives. The axial step-size  $\Delta x$  is limited by the numerical stability condition as specified by Li and Malik [53]

$$\Delta x \geq \frac{1}{|Re\{\alpha_{m,\omega}(x)\}|}. \quad (14)$$

A complete description of the procedure is provided by Gudmundsson and Colonius [30] and a good summary is provided by Sasaki et al. [54]. To initiate the marching problem, initial flow conditions at the nozzle exit plane are provided by using the eigenfunction corresponding to the most dominant Kelvin-Helmholtz instability mode from solving the locally-parallel stability problem of the base flow which is the mean flow from the LES data.

In the pre-processing of the LES mean flow, no smoothing of the base flow was used, though analytical fits can be implemented to avoid non-smoothness problems [55]. The LES grid was interpolated onto the PSE grid via linear interpolation and for each frequency solved on its own axial grid given the condition specified in equation 14. The amplitude of the wavepackets is undefined since PSE is a linear problem and we have just multiplied it by a constant to match experimental data. A more rigorous approach, which we have not pursued for this study, will be to compute an alignment metric across a range of frequencies with experimental data [40, 56]. The  $\alpha_{m,\omega}(x)$  and  $q(x, r)$  terms are used to identify the  $k_h$  and  $L$  parameters for the wavepacket at a given frequency as shown in equation 8.



#### D. Coherence Decay

We model the two-point coherence using the same Gaussian envelope as Cavalieri and Agarwal [35] as shown in equation 5. The model is used to fit the computed magnitude square coherence (MSC) from the azimuthally decomposed Fourier transformed LES data. The CSD of streamwise velocities at two axial points,  $\langle u_x(x_1, r, \omega) u_x^*(x_2, r, \omega) \rangle$ , and their corresponding power spectral density (PSD), are used to compute the MSC  $\gamma^2(x_1, x_2, \omega, m)$  as

$$\gamma^2(x_1, x_2, \omega, m) = \frac{|\langle \hat{u}_{\omega, m}(x_1) \hat{u}_{\omega, m}^*(x_2) \rangle|^2}{\langle |\hat{u}_{\omega, m}(x_1)|^2 \rangle \langle |\hat{u}_{\omega, m}(x_2)|^2 \rangle}. \quad (15)$$

Due to the axisymmetry of the jet, the MSC does not depend on  $\theta$  [24]. The MSC is calculated for all axial separations for a given reference position. The fitted coherence model is then used in the sound-source model in equation 8.

#### V. Wavepacket Solutions from PSE

In this section, we present solutions from linear PSE for a  $M_j = 1.5$  jet. Results shown below are for the axisymmetric mode ( $m = 0$ ). The same PSE code has also been used in both subsonic [33] and supersonic [55] flows.

Figure 2 depicts the real parts of the pressure component of the PSE solution for a range of frequencies. The contour plots show features consistent with solutions from stability analysis of supersonic jets in the literature [40, 42]. The PSE solutions capture both the near-field fluctuations as well as the propagating acoustic far-field noise. The wavelength of the sound field matches those of the most energetic wavepacket; the wavepacket is ‘acoustically matched’ to the sound field that it radiates [17]. This condition is also seen in wavenumber space [35, 40] and the propagating sound waves are described by Tam [14] as Mach wave radiation. The wavepacket envelope shape is recovered. As frequency increases, the axial location of the wavepacket peak ( $x_0$ ) shifts further upstream and the spatial wavelength decreases.

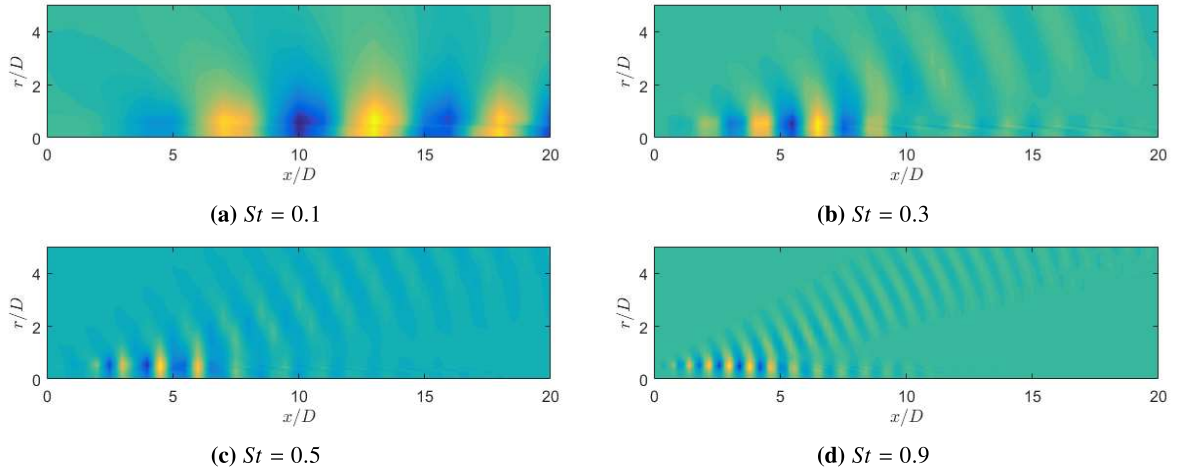


**Fig. 2** Pressure component contour profiles from PSE solution for a  $M_j = 1.5$  isothermal jet for a range of frequencies.

Radial profiles of PSE solutions are shown in figure 3. One can observe the phase shift between two sides of the mixing layer. This is consistent with the findings of Cavalieri et al. [50] and Ray and Lele [42] in subsonic jets.

Lastly, we show the power spectral density of the axial velocity fluctuations integrated radially for a range of frequencies in figure 4. The fluctuation energy of the axial velocity component forms the classical wavepacket envelope shape. The PSE results confirm the extended nature of wavepackets for lower-order azimuthal modes. While symmetric Gaussian functions have been used in previous studies to fit the PSD of the velocity fluctuations [35, 36], it can be seen from figure 4 that at higher frequencies the envelope has an asymmetric shape. Nevertheless, to be consistent with the current model, a symmetric Gaussian fit was used. Future attempts to model wavepacket PSD shapes should capture

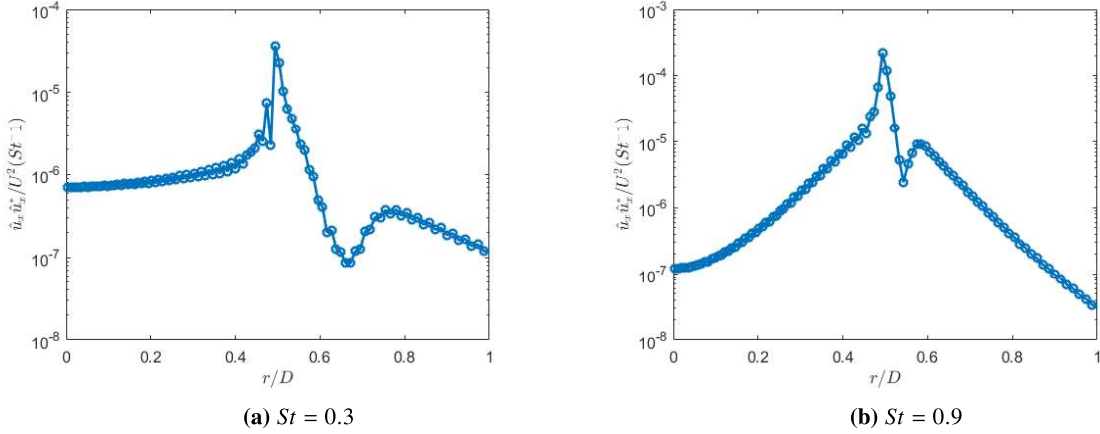


**Fig. 3** Instability radial profiles for a  $M_j = 1.5$  isothermal jet at axial station  $x/D = 2.0$ .

this asymmetry. Along with the real part of the complex wavenumber  $\alpha_{m,\omega}(x)$  (results not shown here), we extracted the wavepacket wavenumber  $k_h$  and characteristic length  $L$  which form the turbulent fluctuation component  $u_t$  of the source term (equation 6).

## VI. Large-Eddy Simulation Results

We compare the velocity fluctuations along the jet centerline between the LES data and the  $m = 0$  mode solution of the PSE in figure 5. The PSE solutions have been multiplied by a constant to match the magnitudes from the LES data.

Figure 5 shows an increase in fluctuation energy of approximately four orders of magnitude. This is also observed in hot wire measurements in subsonic jets [50]. Within the potential core of the jet ( $x/D \leq 6$ ), the maximum fluctuation energy ranges from  $10^{-8} - 10^{-4}$ , which is an order of magnitude smaller ( $10^{-4} - 10^{-3}$ ) than those found by Cavalieri et al. [50] of a subsonic  $M = 0.4$  jet. This is consistent with the notion that the growth rates of the instabilities are suppressed as Mach number increases due to compressibility effects.

We note that in figure 5, while the PSE solutions are able to capture the increase in fluctuation energy in regions close to the nozzle exit, the LES PSD data increases more rapidly for the region  $x/D \leq 2$ . At positions further downstream, the LES data diverges from the PSE solution. This divergence is consistent with previous work by Suzuki and Colonius [27], Gudmundsson and Colonius [30] and Cavalieri et al. [50]. It is attributed to wavepacket growth via non-modal mechanisms caused by non-linear forcing [57].

## VII. Coherence Decay Length

The coherence decay length of the azimuthally decomposed  $m = 0$  instability wave, while previously modelled [35, 36], had only been previously measured experimentally by Jaunet et al. [24] via twin synchronised time-resolved stereo PIV systems. The coherence lengths were obtained by computing the MSC between two points in the flow. To capture coherence decay, Jaunet et. al measured it at a fixed axial location of  $x/D = 3.0$  and a radial position of  $r/D = 0.42$ . In this present study, however, we have chosen to have the reference position  $x_0$  where the wavepacket peaks and the fixed radial position of  $r/D = 0.5$ . Jaunet et al. [24] did show that difference in coherence decay behaviour between the two radial positions remain minimal.

While we find that the coherence decay function is asymmetric [24, 39] and an improved fit can be obtained by using a two-sided convolution of a Gaussian and exponential [39, 58], a simple Gaussian function was used to model coherence decay (equation 5). This is consistent with the proposed source model in equation 2 and will allow a comparison between the present findings with the constant coherence length used by Wong et al. [1].

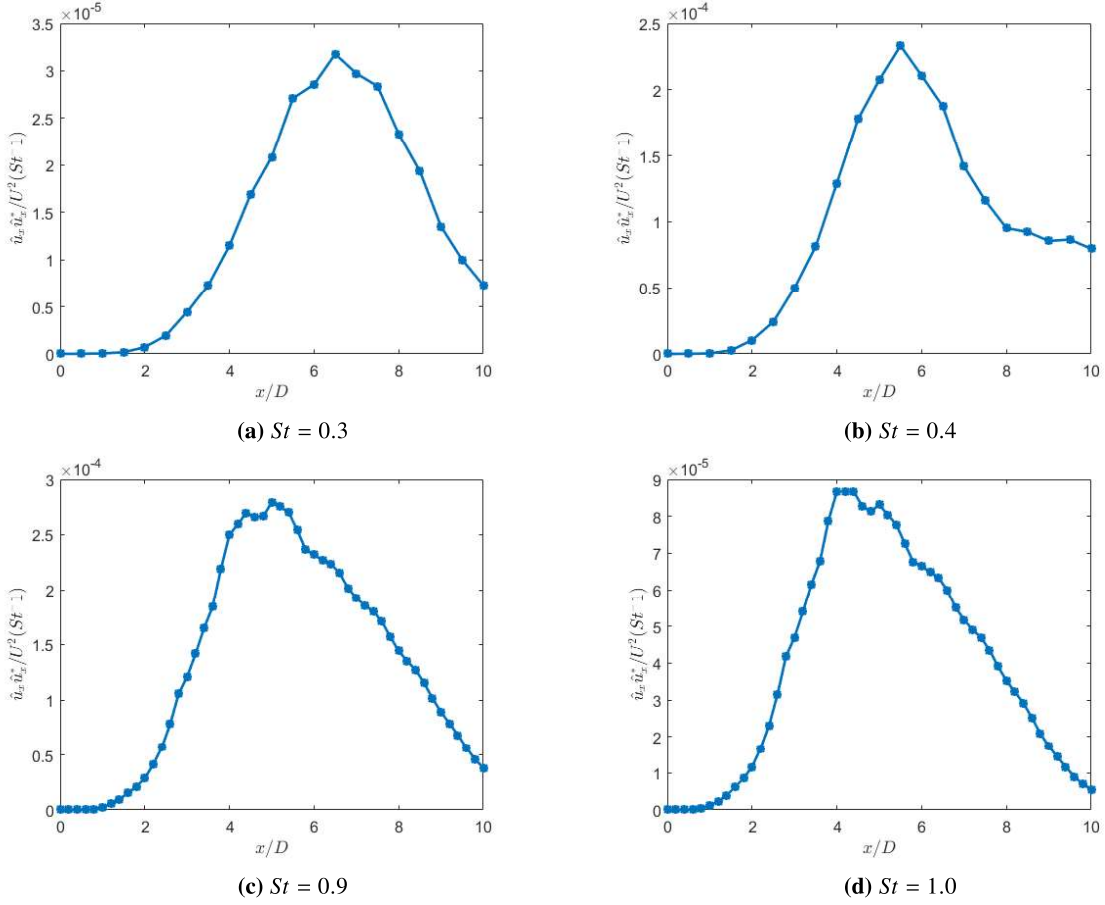


**Fig. 4** PSE solutions of the integrated PSD of the axial velocity fluctuations  $u_x$  for a  $M_j = 1.5$  isothermal jet.

The one-sided MSC is shown in figure 6 showing a clear decay as a function of downstream axial separation distance. Moreover, the decay rate is a function of frequency, with a quicker decay rate as frequency increases. By fitting the MSC with a Gaussian function, the characteristic length scale  $L_c$  in equation 15 can be obtained. The frequency dependence of  $L_c$  can be seen in figure 7 and shows that the ad-hoc assumption of the constant coherence length used by Wong et al. [1] of  $1.0D$  is not realistic. It should be noted that compared to the subsonic  $M = 0.4$  jet [24, 39], the coherence lengths obtained for the current supersonic jet  $M_j = 1.5$  are much smaller. This suggests that wavepackets in supersonic jets desynchronise over a shorter distance compared to its subsonic counterpart. The coherence length trend seen in figure 7 is similar to the decay in the ‘cross-coherence’ of the sources found by Lele [15].

### VIII. Far-field BBSAN Sound Prediction

By using the source description in equation 2 and combining the Pack & Prandtl shock-cell model with the outputs from the PSE analysis and LES database, we can obtain a two-dimensional source description for BBSAN. To aide the analysis, solutions from PSE and the MSC results have been smoothed by fitting the appropriate analytical functions as shown in equation 2. Similar to Wong et al. [1], a total of ten ( $n = 10$ ) shock-cell modes have been used. The far-field sound behaviour can be obtained by using the appropriate free-field Green’s function. The line source integration region extends from  $0 \leq x/D \leq 20D$  corresponding to 1000 grid points. A Hann-windowing technique is used in order to make the downstream source amplitude decay to remove artificial errors from an abrupt discontinuity of the source [59].

Figure 8 shows the comparison between model predictions and experimental data from NASA’s Small Hot Jet acoustic Rig (SHJAR) for a supersonic jet operating at  $M_j = 1.5$  and  $M_d = 1.0$  at three observer angles ( $80^\circ$ ,  $90^\circ$  and  $130^\circ$ ) relative to the downstream jet axis [18]. The degree of underexpansion, captured by the off-design parameter

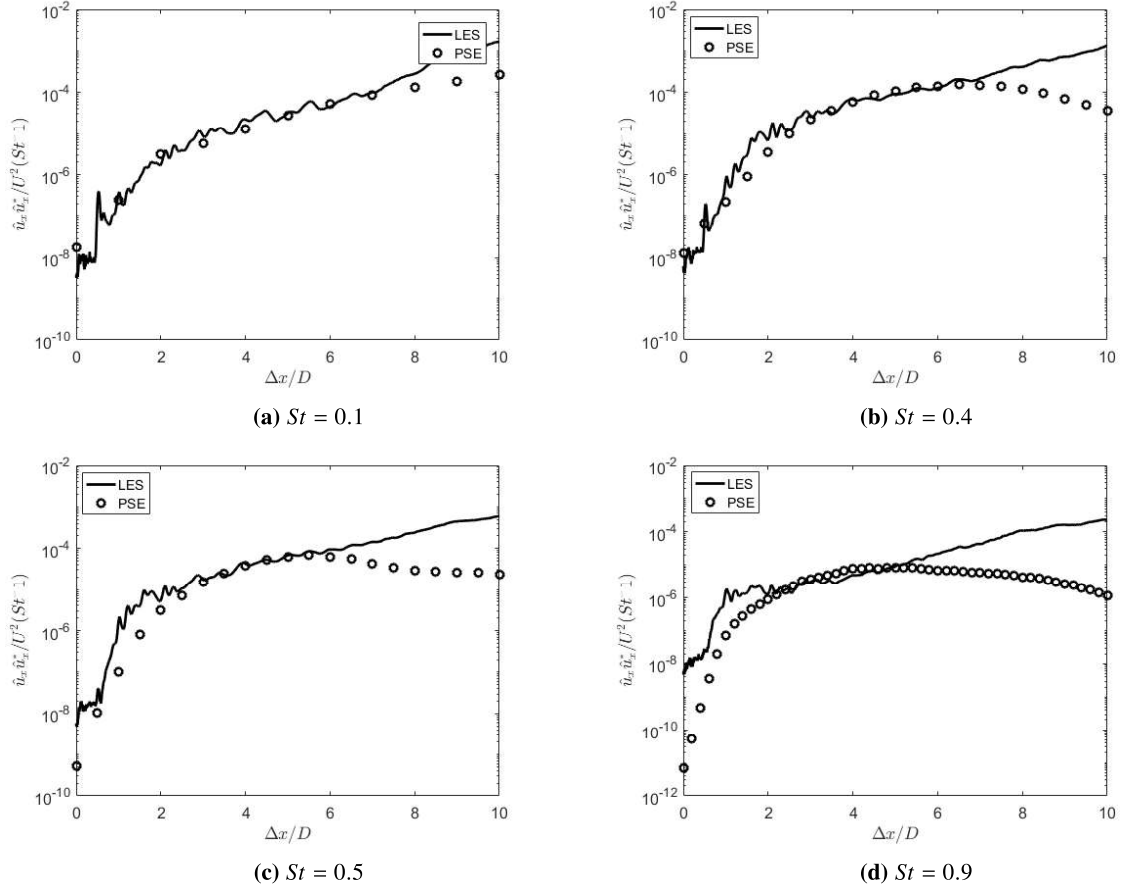


**Fig. 5** Comparison between PSE solutions and LES PSD of velocity fluctuations  $u_x$  along the jet centerline for a  $M_j = 1.5$  isothermal jet.

$\beta = \sqrt{M_j^2 - M_d^2}$ , is matched. The observer location is located at  $R = 100D$ . The peak maximum amplitudes are matched by scaling it with a constant factor. There is a fair agreement between the two models. As the angle to the jet downstream axis increases, the movement of the BBSAN peak to lower Strouhal numbers is reproduced. The agreement in the roll-off at low frequencies is well captured at all angles. However, there is a small under-prediction of the peak frequency at  $80^\circ$ . Moreover, the predictions begin to diverge at higher Strouhal frequencies ( $St \geq 1$ ). Below  $St = 0.2 - 0.3$ , the dominance of turbulent mixing noise rather than BBSAN at low frequencies results in an underprediction in SPL, which is expected.

When compared to the far-field noise prediction of Wong et al. [1] (dashed lines in figure 8), the importance of capturing the correct coherence length is seen in the shape of the predicted peak. The suppression of higher-order peaks is evident in both cases with the inclusion of coherence decay. Wong et al. [1] used a constant coherence length to establish the impact of coherence decay but obtained an overprediction at low frequencies. Contrastingly, using a coherence length with frequency dependence was found to obtain the correct low frequency roll-off as observed in figure 8. The current results further confirm the importance of coherence decay in supersonic shock-containing flows as found by [1].

Nevertheless, there remain differences between the current predictive model and those from literature and experiments. The underprediction of high frequency sound could be due to the incorrect scaling of the free amplitude of the linear PSE solution. By projecting the leading mode from SPOD of LES data onto the PSE solutions, Antonialli et al. [56] found an exponential dependence of wavepacket amplitude with Strouhal. No such dependence has been implemented

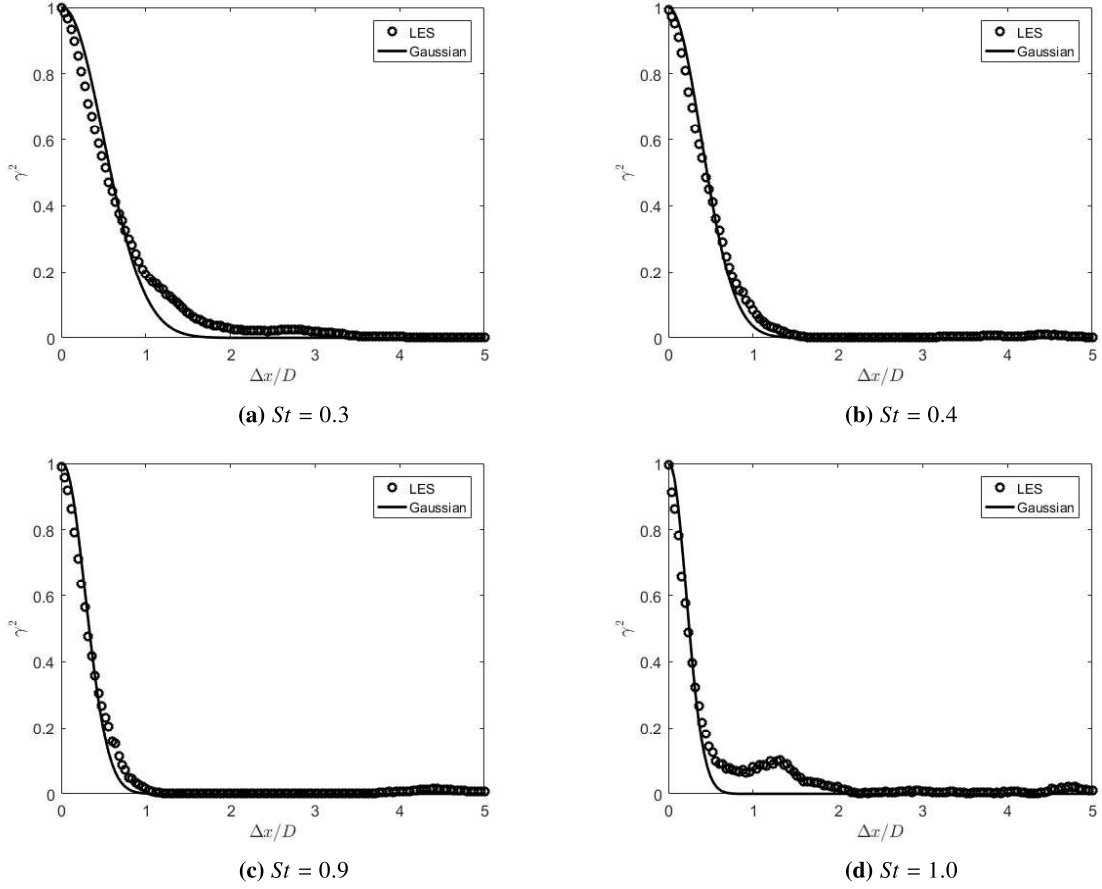


**Fig. 6** Magnitude-squared coherence function (MSC) as a function of axial separation distance  $\Delta x$  for the  $m = 0$  mode. Reference axial position  $x_0$  is the peak of the wavepacket and radial position at  $r/D = 0.5$ .

in the current results. The negligence of higher-order azimuthal wavepacket modes [60] could have also affected sound prediction at upstream angles. Moreover, there remains an underprediction in the peak Strouhal frequency at low downstream angles ( $80^\circ$ ). This was also observed in the previous analytical model of Wong et al. [1]. This could be due to the increase in interference of the line source at downstream directions for extended sources Cavalieri et al. [20], though further investigation is required.

## IX. Conclusion

Motivated by the results of the two-point BBSAN source model developed by Wong et al. [3], flow properties based on stability theory were obtained as inputs into the model. The LES data of a  $M_j = 1.5$  ideally-expanded supersonic turbulent jet [2] was used as the base flow for obtaining the linear PSE solutions of the flow. The ‘jittering’ non-linear behaviour of the flow was modelled as coherence decay between two points of the jet and the relevant length scale was extracted.

The PSE solutions at different frequencies are presented and the average wavepacket characteristics were obtained including its spatial envelope size and wavenumber. The radial structure and growth in the initial region close to the nozzle exit have similar behaviour to wavepackets in subsonic jets [39, 50]. The coherence decay length scale was found to be much shorter than its subsonic counterpart.

Using the results from the LES and PSE solutions, coupled with the Pack & Prandtl representation of the shock cells,

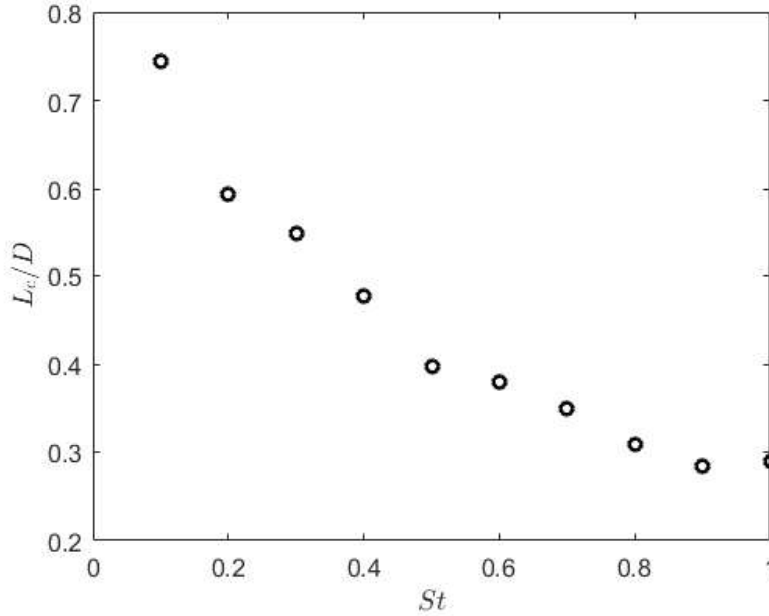


**Fig. 7** Normalised coherence length as a function of Strouhal number. Reference position  $x_0$  is the peak of the wavepacket.

far-field BBSAN spectra are presented for multiple radiation angles. The far-field predictions re-affirm the importance of coherence decay in supersonic shock-containing flows. The higher-order peaks are suppressed and a frequency dependant length scale improved the low-frequency roll-off of the BBSAN peak compared to the predictions made by Wong et al. [1].

Future works will focus on refining the methodology, which includes using appropriate analytical functions to fit the data. An analytical fit to the LES mean flow should be used to avoid non-smoothness problems [55] as well as new non-Gaussian functions to fit the asymmetric behaviour of the wavepacket envelope and the magnitude square coherence of the jet [39]. In order to improve noise predictions at higher frequencies, a more rigorous scaling of the free-amplitude PSE solutions is required. These refinements should improve the current BBSAN predictions and provide a better indication of the robustness of the current model.

### Acknowledgements

This work was supported by the Australian Government via a Research Training Program (RTP) Scholarship and the Endeavour Leadership Program (ELP). The project is also funded by the Australian Research Council through the Discovery Projects scheme. The authors would like to thank Dr. Guillaume Brès at Cascade Technologies for providing the simulation database. The LES work was supported by ONR, with computational resources provided by DoD HPCMP. M.H.W would also like to thank Mr. I. Maia and Ms. R. Kirby for their insightful advice and recommendations.

### References

- [1] Wong, M. H., Jordan, P., Honnery, D. R., and Edgington-Mitchell, D., “Impact of coherence decay on wavepacket models for broadband shock-associated noise in supersonic jets,” *Journal of Fluid Mechanics*, Vol. 863, 2019, pp. 969–993.
- [2] Brès, G., Ham, F., Nichols, J., and Lele, S., “Unstructured large-eddy simulations of supersonic jets,” *AIAA Journal*, 2017, pp. 1164–1184.
- [3] Wong, M. H., Edgington-Mitchell, D. M., Honnery, D. R., Jordan, P., and Savarese, A., “Kinematic wavepacket model for

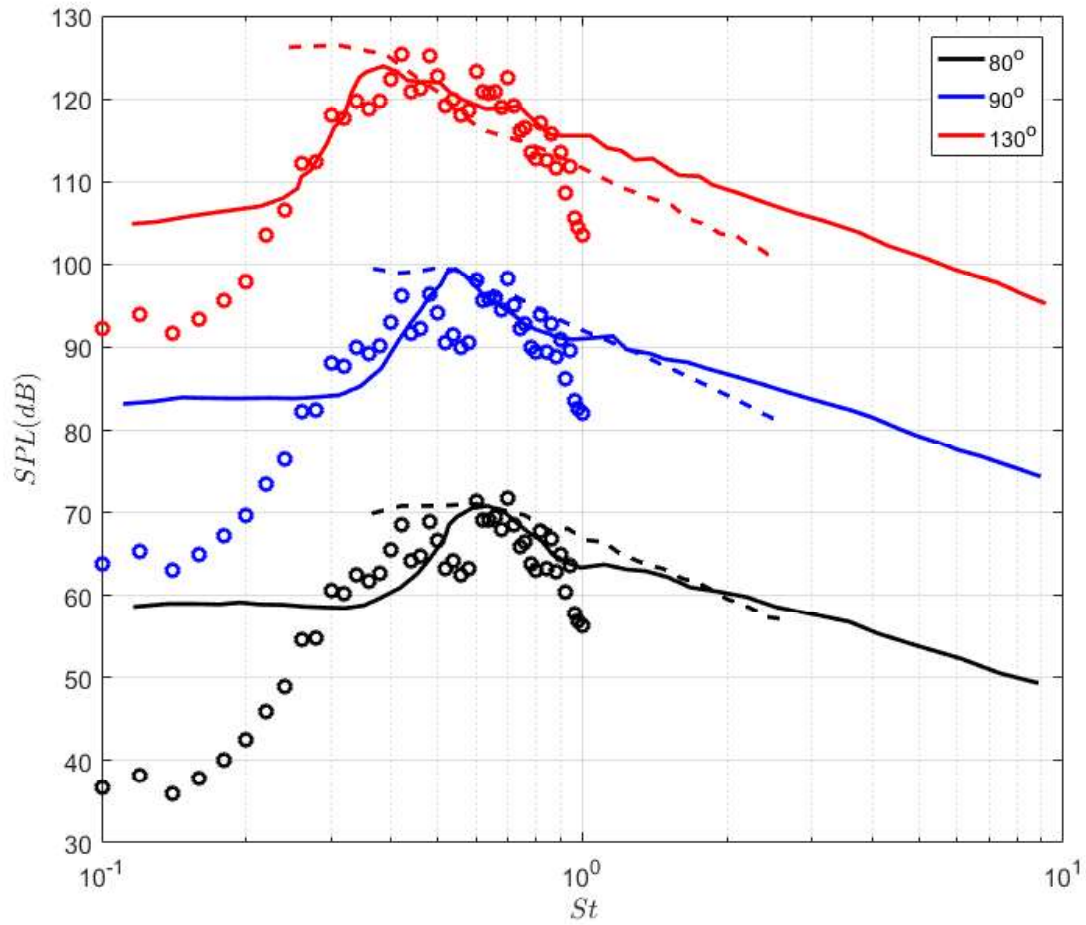


**Fig. 8 Comparison of far-field sound pressure level (arbitrary) as a function of frequency at 80° (black), 90° (blue) and 130° (red) observation angles. ‘o’ represent predicted spectrum from model, ‘- -’ is obtained from Wong et al. [1] BBSAN model and ‘-’ from NASA experimental data.**

broadband shock associated noise in underexpanded supersonic jets,” *2018 AIAA/CEAS Aeroacoustics Conference*, 2018, p. 3465.

- [4] Tam, C., “Broadband shock-associated noise of moderately imperfectly expanded supersonic jets,” *Journal of Sound and Vibration*, Vol. 140, No. 1, 1990, pp. 55–71.
- [5] Lighthill, M., “On sound generated aerodynamically. I. General theory,” *Proceedings of the Royal Society of London A: Mathematical, Physical and Engineering Sciences*, Vol. 211, The Royal Society, 1952, pp. 564–587.
- [6] Edgington-Mitchell, D., Oberleithner, K., Honnery, D., and Soria, J., “Coherent structure and sound production in the helical mode of a screeching axisymmetric jet,” *Journal of Fluid Mechanics*, Vol. 748, 2014, pp. 822–847.
- [7] Raman, G., “Supersonic jet screech: half-century from Powell to the present,” *Journal of Sound and Vibration*, Vol. 225, No. 3, 1999, pp. 543–571.
- [8] Vaughn, A. B., Neilsen, T. B., Gee, K. L., Wall, A. T., Micah Downing, J., and James, M. M., “Broadband shock-associated noise from a high-performance military aircraft,” *The Journal of the Acoustical Society of America*, Vol. 144, No. 3, 2018, pp. EL242–EL247.

- [9] Harper-Bourne, M., and Fisher, M., "The noise from shock waves in supersonic jets," *AGARD-CP-131*, Vol. 11, 1973, pp. 1–13.
- [10] Tam, C., Seiner, J., and Yu, J., "Proposed relationship between broadband shock associated noise and screech tones," *Journal of sound and vibration*, Vol. 110, No. 2, 1986, pp. 309–321.
- [11] Morris, P., and Zaman, K., "Velocity measurements in jets with application to noise source modeling," *Journal of sound and vibration*, Vol. 329, No. 4, 2010, pp. 394–414.
- [12] Kalyan, A., and Karabasov, S., "Broad band shock associated noise predictions in axisymmetric and asymmetric jets using an improved turbulence scale model," *Journal of Sound and Vibration*, Vol. 394, 2017, pp. 392–417.
- [13] Tan, D., Kalyan, A., Gryazev, V., Wong, M., Honnery, D., Edgington-Mitchell, D., and Karabasov, S., "On the Application of Shock-Associated Noise Models to PIV Measurements of Screeching Axisymmetric Cold Jets," *23rd AIAA/CEAS Aeroacoustics Conference*, 2017, p. 3028.
- [14] Tam, C., "Supersonic jet noise," *Annual Review of Fluid Mechanics*, Vol. 27, No. 1, 1995, pp. 17–43.
- [15] Lele, S., "Phased array models of shock-cell noise sources," *AIAA Paper*, Vol. 2841, 2005, p. 2005.
- [16] Lighthill, M., "On sound generated aerodynamically. I. General theory," *Proceedings of the Royal Society of London A: Mathematical, Physical and Engineering Sciences*, Vol. 211, The Royal Society, 1952, pp. 564–587.
- [17] Crighton, D., "Basic principles of aerodynamic noise generation," *Progress in Aerospace Sciences*, Vol. 16, No. 1, 1975, pp. 31–96.
- [18] Morris, P., and Miller, S., "Prediction of broadband shock-associated noise using Reynolds-averaged Navier-Stokes computational fluid dynamics," *AIAA Journal*, Vol. 48, No. 12, 2010, p. 2931.
- [19] Jordan, P., and Colonius, T., "Wave packets and turbulent jet noise," *Annual Review of Fluid Mechanics*, Vol. 45, 2013, pp. 173–195.
- [20] Cavalieri, A. V., Jordan, P., and Lesshafft, L., "Wave-packet models for jet dynamics and sound radiation," *Applied Mechanics Reviews*, Vol. 71, No. 2, 2019, p. 020802.
- [21] Mollo-Christensen, E., "Jet noise and shear flow instability seen from an experimenter's viewpoint," *Journal of Applied Mechanics*, Vol. 34, No. 1, 1967, pp. 1–7.
- [22] Crow, S., and Champagne, F., "Orderly structure in jet turbulence," *Journal of Fluid Mechanics*, Vol. 48, No. 3, 1971, pp. 547–591.
- [23] Michalke, A., "A wave model for sound generation in circular jets," 1970.
- [24] Jaunet, V., Jordan, P., and Cavalieri, A., "Two-point coherence of wave packets in turbulent jets," *Physical Review Fluids*, Vol. 2, No. 2, 2017, p. 024604.
- [25] Schmidt, O. T., Towne, A., Rigas, G., Colonius, T., and Brès, G. A., "Spectral analysis of jet turbulence," *Journal of Fluid Mechanics*, Vol. 855, 2018, pp. 953–982.
- [26] Cavalieri, A., Jordan, P., Colonius, T., and Gervais, Y., "Axisymmetric superdirectivity in subsonic jets," *Journal of fluid Mechanics*, Vol. 704, 2012, pp. 388–420.
- [27] Suzuki, T., and Colonius, T., "Instability waves in a subsonic round jet detected using a near-field phased microphone array," *Journal of Fluid Mechanics*, Vol. 565, 2006, pp. 197–226.
- [28] Breakey, D., Jordan, P., Cavalieri, A., and Léon, O., "Near-field wavepackets and the far-field sound of a subsonic jet," *19th AIAA/CEAS aeroacoustics conference*, 2013, p. 2083.
- [29] Tinney, C., and Jordan, P., "The near pressure field of co-axial subsonic jets," *Journal of Fluid Mechanics*, Vol. 611, 2008, pp. 175–204.
- [30] Gudmundsson, K., and Colonius, T., "Instability wave models for the near-field fluctuations of turbulent jets," *Journal of Fluid Mechanics*, Vol. 689, 2011, pp. 97–128.
- [31] Cavalieri, A., Jordan, P., Wolf, W., and Gervais, Y., "Scattering of wavepackets by a flat plate in the vicinity of a turbulent jet," *Journal of sound and Vibration*, Vol. 333, No. 24, 2014, pp. 6516–6531.



- [32] Lesshafft, L., Semeraro, O., Jaunet, V., Cavalieri, A. V., and Jordan, P., “Resolvent-based modelling of coherent wavepackets in a turbulent jet,” *arXiv preprint arXiv:1810.09340*, 2018.
- [33] Sasaki, K., Cavalieri, A., Jordan, P., Schmidt, O., Colonius, T., and Brès, G., “High-frequency wavepackets in turbulent jets,” *Journal of Fluid Mechanics*, Vol. 830, 2017.
- [34] Piantanida, S., Jaunet, V., Huber, J., Wolf, W. R., Jordan, P., and Cavalieri, A. V., “Scattering of turbulent-jet wavepackets by a swept trailing edge,” *The Journal of the Acoustical Society of America*, Vol. 140, No. 6, 2016, pp. 4350–4359.
- [35] Cavalieri, A., and Agarwal, A., “Coherence decay and its impact on sound radiation by wavepackets,” *Journal of Fluid Mechanics*, Vol. 748, 2014, pp. 399–415.
- [36] Baqui, Y., Agarwal, A., Cavalieri, A., and Sinayoko, S., “A coherence-matched linear source mechanism for subsonic jet noise,” *Journal of Fluid Mechanics*, Vol. 776, 2015, pp. 235–267.
- [37] Zhang, M., Jordan, P., Lehnasch, G., Cavalieri, A., and Agarwal, A., “Just enough jitter for jet noise?” *20th AIAA/CEAS Aeroacoustics Conference*, 2014, p. 3061.
- [38] Cavalieri, A., Jordan, P., Agarwal, A., and Gervais, Y., “Jittering wave-packet models for subsonic jet noise,” *Journal of Sound and Vibration*, Vol. 330, No. 18, 2011, pp. 4474–4492.
- [39] Maia, I., Jordan, P., Jaunet, V., and Cavalieri, A., “Two-point wavepacket modelling of jet noise,” *23rd AIAA/CEAS Aeroacoustics Conference*, 2017, p. 3380.
- [40] Sinha, A., Rodríguez, D., Brès, G., and Colonius, T., “Wavepacket models for supersonic jet noise,” *Journal of Fluid Mechanics*, Vol. 742, 2014, pp. 71–95.
- [41] Suzuki, T., “Wave-Packet Representation of Shock-Cell Noise for a Single Round Jet,” *AIAA Journal*, 2016.
- [42] Ray, P., and Lele, S., “Sound generated by instability wave/shock-cell interaction in supersonic jets,” *Journal of fluid mechanics*, Vol. 587, 2007, pp. 173–215.
- [43] Tan, D., Honnery, D., Kalyan, A., Gryazev, V., Karabasov, S., and Edgington-Mitchell, D., “Equivalent shock-associated noise source reconstruction of screeching underexpanded unheated round jets,” *AIAA Journal*, Vol. 57, No. 3, 2018, pp. 1200–1214.
- [44] Prandtl, L., *Über die stationären Wellen in einem Gasstrahl*, Hirzel, 1904.
- [45] Pack, D., “A note on Prandtl’s formula for the wave-length of a supersonic gas jet,” *The Quarterly Journal of Mechanics and Applied Mathematics*, Vol. 3, No. 2, 1950, pp. 173–181.
- [46] Brès, G., Nichols, J., Lele, S., and Ham, F., “Towards best practices for jet noise predictions with unstructured large eddy simulations,” *42nd AIAA Fluid Dynamics Conference and Exhibit*, 2012, p. 2965.
- [47] Schlinker, R., Simonich, J., Shannon, D., Reba, R., Colonius, T., Gudmundsson, K., and Ladeinde, F., “Supersonic jet noise from round and chevron nozzles: experimental studies,” *15th AIAA/CEAS Aeroacoustics Conference (30th AIAA Aeroacoustics Conference)*, 2009, p. 3257.
- [48] Brès, G. A., Jordan, P., Jaunet, V., Le Rallic, M., Cavalieri, A. V., Towne, A., Lele, S. K., Colonius, T., and Schmidt, O. T., “Importance of the nozzle-exit boundary-layer state in subsonic turbulent jets,” *Journal of Fluid Mechanics*, Vol. 851, 2018, pp. 83–124.
- [49] Ansaldi, T., Airiau, C., Pérez Arroyo, C., and Puigt, G., “PSE-based sensitivity analysis of turbulent and supersonic single stream jet,” *22nd AIAA/CEAS Aeroacoustics Conference*, 2016, p. 3052.
- [50] Cavalieri, A., Rodríguez, D., Jordan, P., Colonius, T., and Gervais, Y., “Wavepackets in the velocity field of turbulent jets,” *Journal of fluid mechanics*, Vol. 730, 2013, pp. 559–592.
- [51] AERONÁUTICA, M. P. E. E., and SASAKI, K., “ESTUDO E CONTROLE DE PACOTES DE ONDA EM JATOS UTILIZANDO AS EQUAÇÕES DE ESTABILIDADE PARABOLIZADAS,” 2014.
- [52] Crighton, D., and Gaster, M., “Stability of slowly diverging jet flow,” *Journal of Fluid Mechanics*, Vol. 77, No. 2, 1976, pp. 397–413.
- [53] Li, F., and Malik, M. R., “Spectral analysis of parabolized stability equations,” *Computers & fluids*, Vol. 26, No. 3, 1997, pp. 279–297.

- [54] Sasaki, K., Piantanida, S., Cavalieri, A., and Jordan, P., “Real-time modelling of wavepackets in turbulent jets,” *Journal of Fluid Mechanics*, Vol. 821, 2017, pp. 458–481.
- [55] Kleine, V. G., Sasaki, K., Cavalieri, A. V., Brès, G. A., and Colonius, T., “Evaluation of PSE as a model for supersonic jet using transfer functions,” *23rd AIAA/CEAS Aeroacoustics Conference*, 2017, p. 4194.
- [56] Antonialli, L., Cavalieri, A., Schmidt, O., Colonius, T., Jordan, P., Towne, A., Brès, G., , and Agarwal, A., “Amplitude scaling of turbulent-jet wavepackets,” *23rd AIAA/CEAS Aeroacoustics Conference*, 2018, p. under review.
- [57] Jordan, P., Zhang, M., Lehnasch, G., and Cavalieri, A. V., “Modal and non-modal linear wavepacket dynamics in turbulent jets,” *23rd AIAA/CEAS Aeroacoustics Conference*, 2017, p. 3379.
- [58] Jordan, P., Wells, R., Gervais, Y., and Delville, J., “Optimisation of correlation function models for statistical aeroacoustic noise prediction,” *CFA/DAGA 2004 Acoustics conference, Strasbourg*, 2004.
- [59] Martínez-Lera, P., and Schram, C., “Correction techniques for the truncation of the source field in acoustic analogies,” *The Journal of the Acoustical Society of America*, Vol. 124, No. 6, 2008, pp. 3421–3429.
- [60] Arroyo, C. P., and Moreau, S., “Azimuthal mode analysis of broadband shock-associated noise in an under-expanded axisymmetric jet,” *Journal of Sound and Vibration*, Vol. 449, 2019, pp. 64–83.

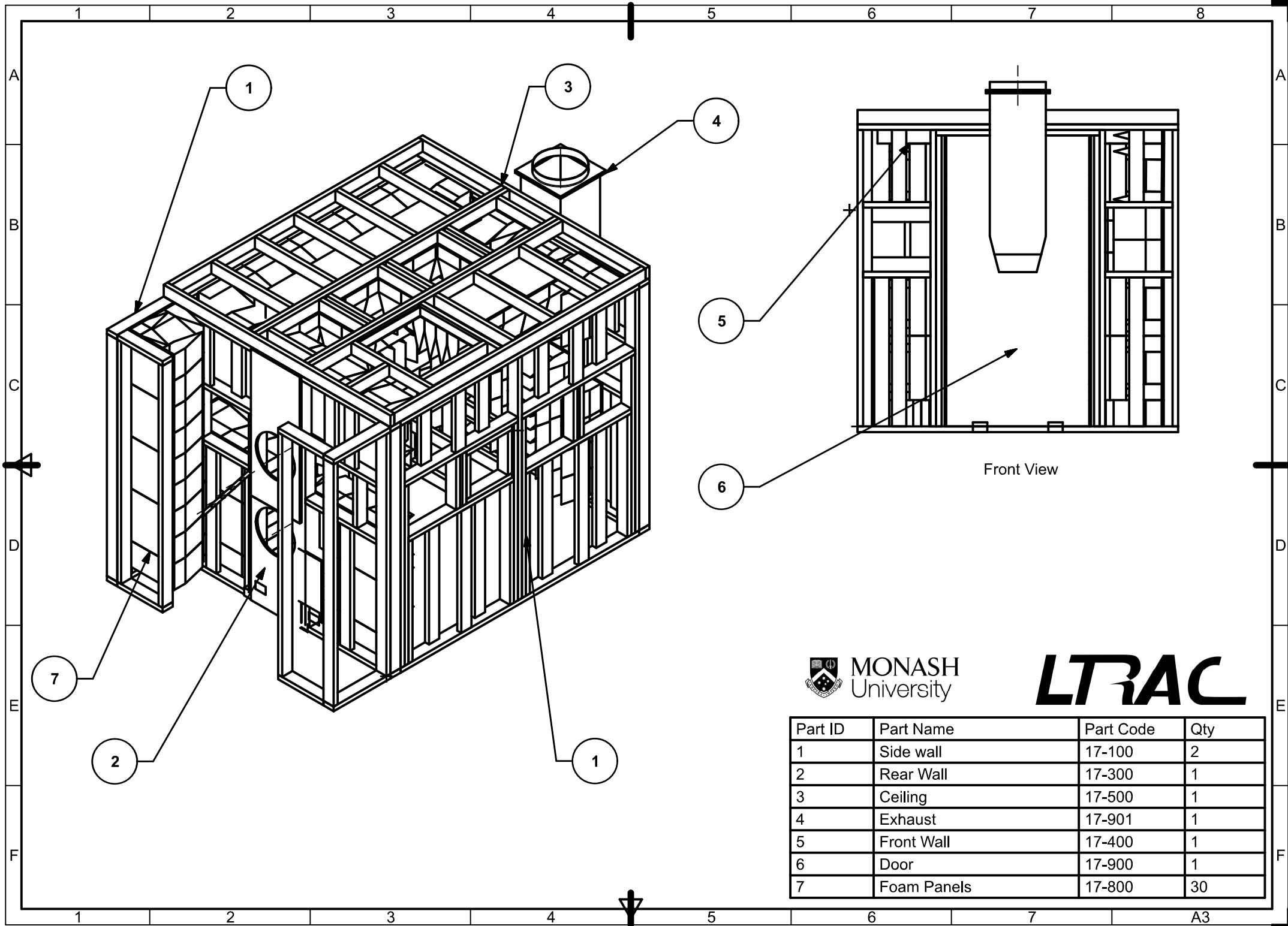
## **Appendix C**

# **Supersonic Jet Anechoic Facility Design Drawings**

### **C.1 Introductory Statement**

The design of the Supersonic Jet Anechoic Facility is described in Chapter 3. A set of engineering design drawings for the anechoic chamber and jet rig is presented here.

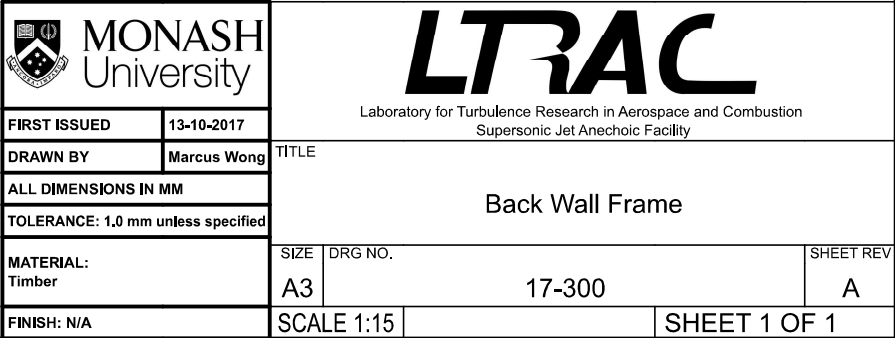
### **C.2 Anechoic Chamber Drawings**

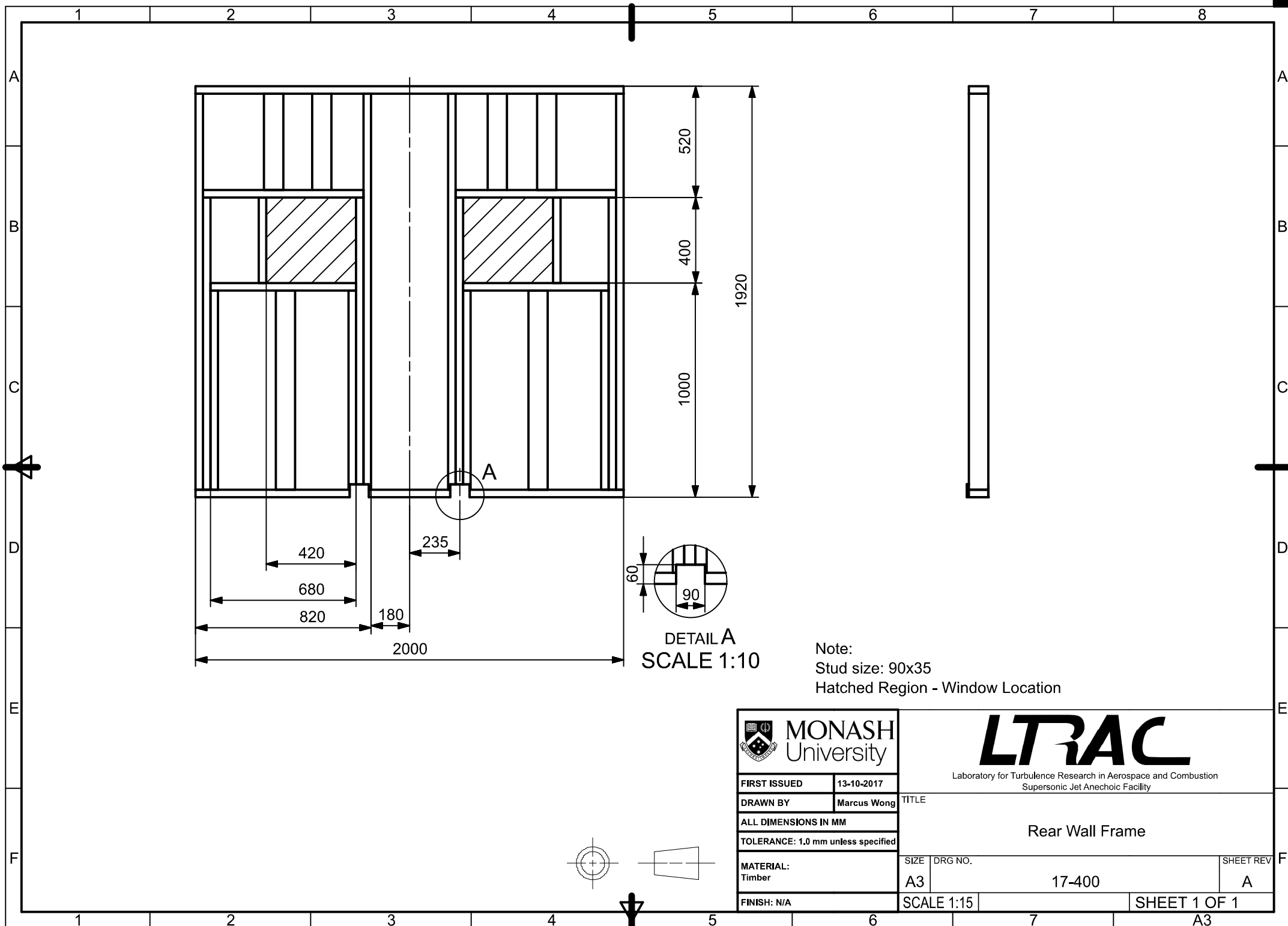


MONASH  
University

**LTRAC**

Part ID	Part Name	Part Code	Qty
1	Side wall	17-100	2
2	Rear Wall	17-300	1
3	Ceiling	17-500	1
4	Exhaust	17-901	1
5	Front Wall	17-400	1
6	Door	17-900	1
7	Foam Panels	17-800	30



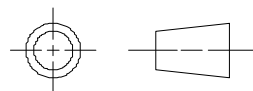


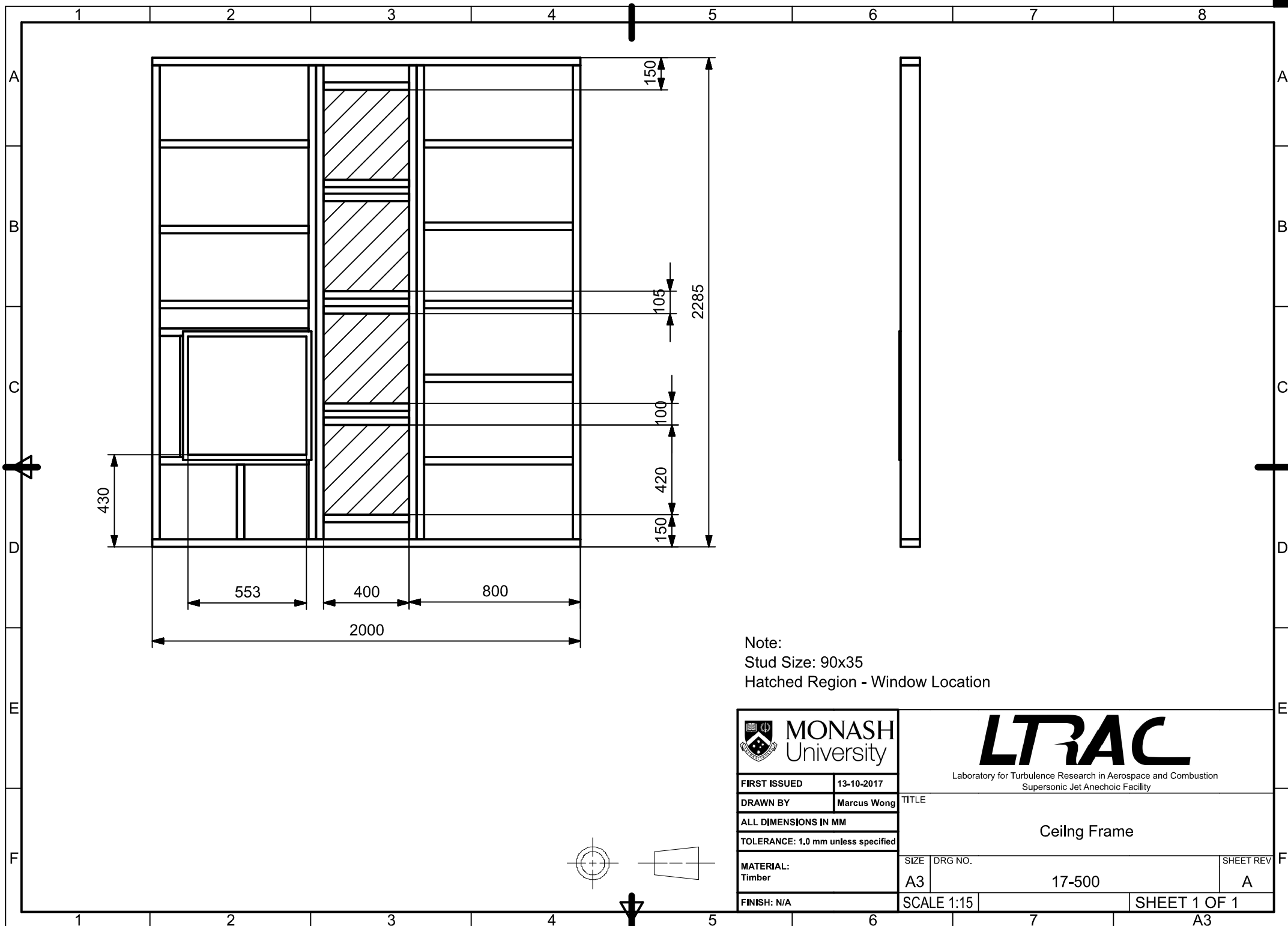
FIRST ISSUED	13-10-2017
DRAWN BY	Marcus Wong
ALL DIMENSIONS IN MM	
TOLERANCE: 1.0 mm unless specified	
MATERIAL: Timber	
FINISH: N/A	

**LTRAC**

Laboratory for Turbulence Research in Aerospace and Combustion  
Supersonic Jet Anechoic Facility

TITLE			Rear Wall Frame	
SIZE	DRG NO.	SHEET REV		
A3	17-400	A		
SCALE 1:15		SHEET 1 OF 1		



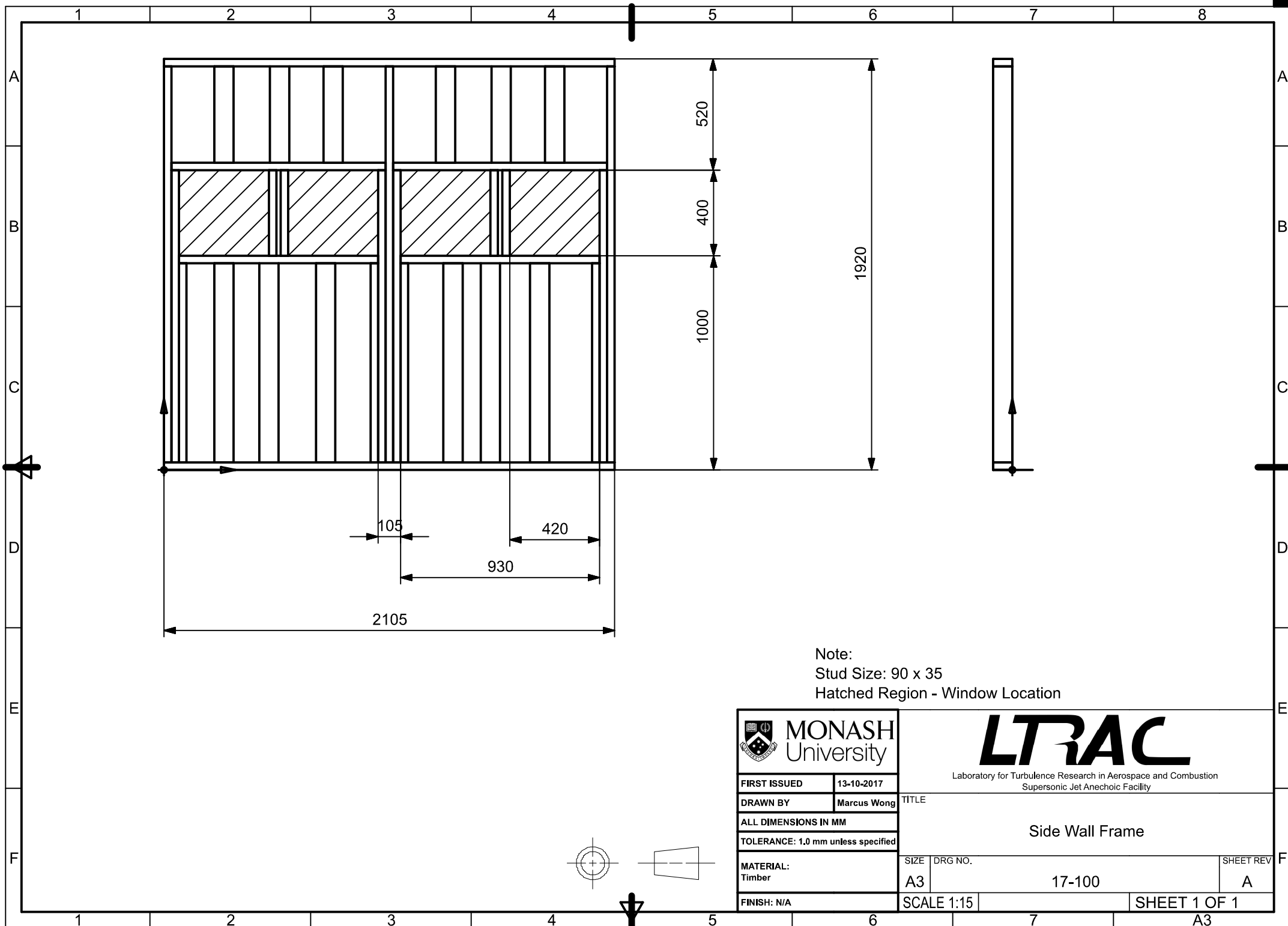


FIRST ISSUED	13-10-2017
DRAWN BY	Marcus Wong
ALL DIMENSIONS IN MM	
TOLERANCE: 1.0 mm unless specified	
MATERIAL: Timber	
FINISH: N/A	



Laboratory for Turbulence Research in Aerospace and Combustion  
Supersonic Jet Anechoic Facility

TITLE		SHEET REV	
Ceiling Frame		A	
SIZE	DRG NO.		
A3	17-500		
SCALE 1:15		SHEET 1 OF 1	



FIRST ISSUED 13-10-2017

DRAWN BY Marcus Wong

ALL DIMENSIONS IN MM

TOLERANCE: 1.0 mm unless specified

MATERIAL: Timber

FINISH: N/A

**LTRAC**

Laboratory for Turbulence Research in Aerospace and Combustion  
Supersonic Jet Anechoic Facility

TITLE

Side Wall Frame

SIZE DRG NO. SHEET REV

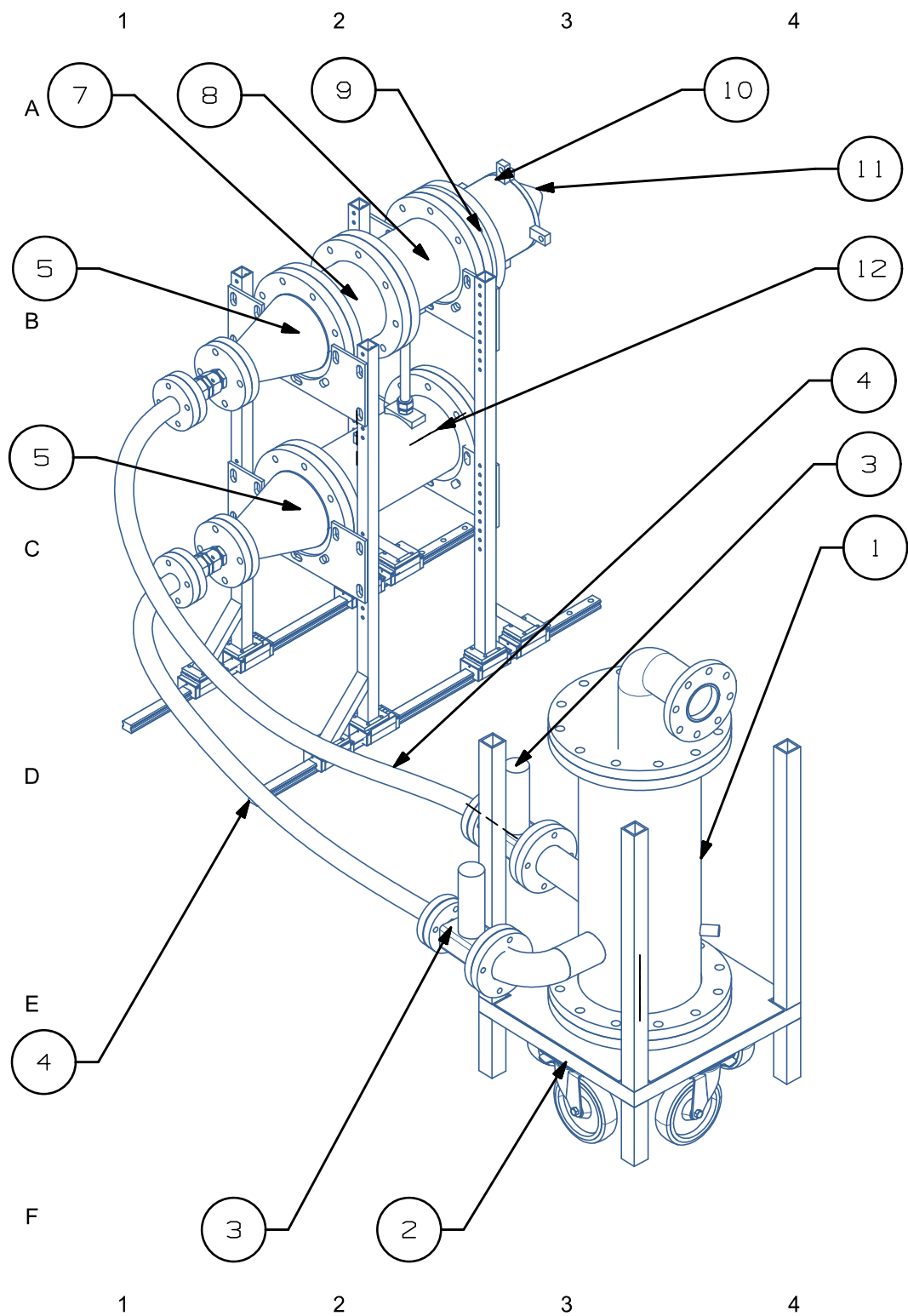
A3 17-100 A

SCALE 1:15 SHEET 1 OF 1

A3

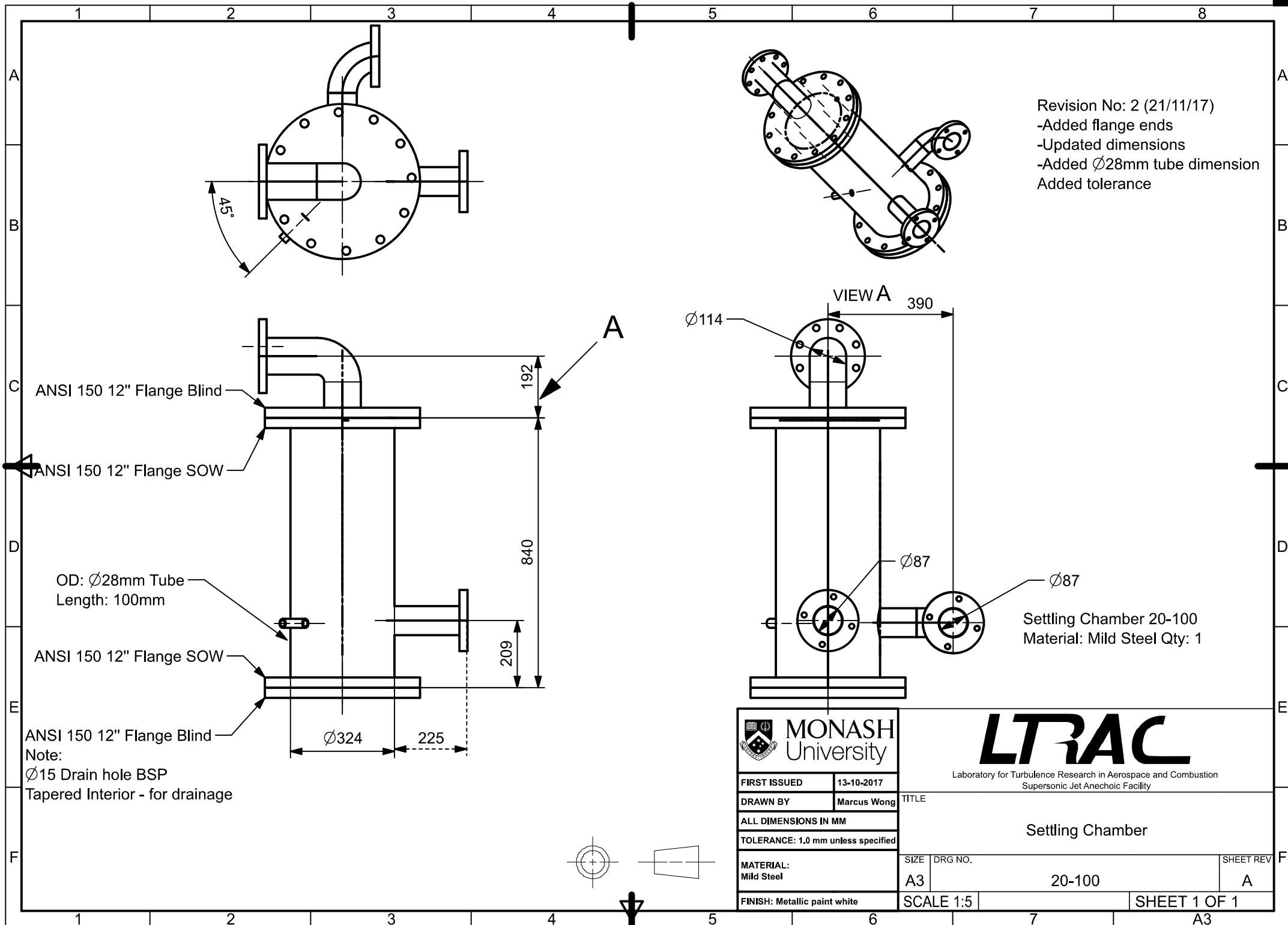


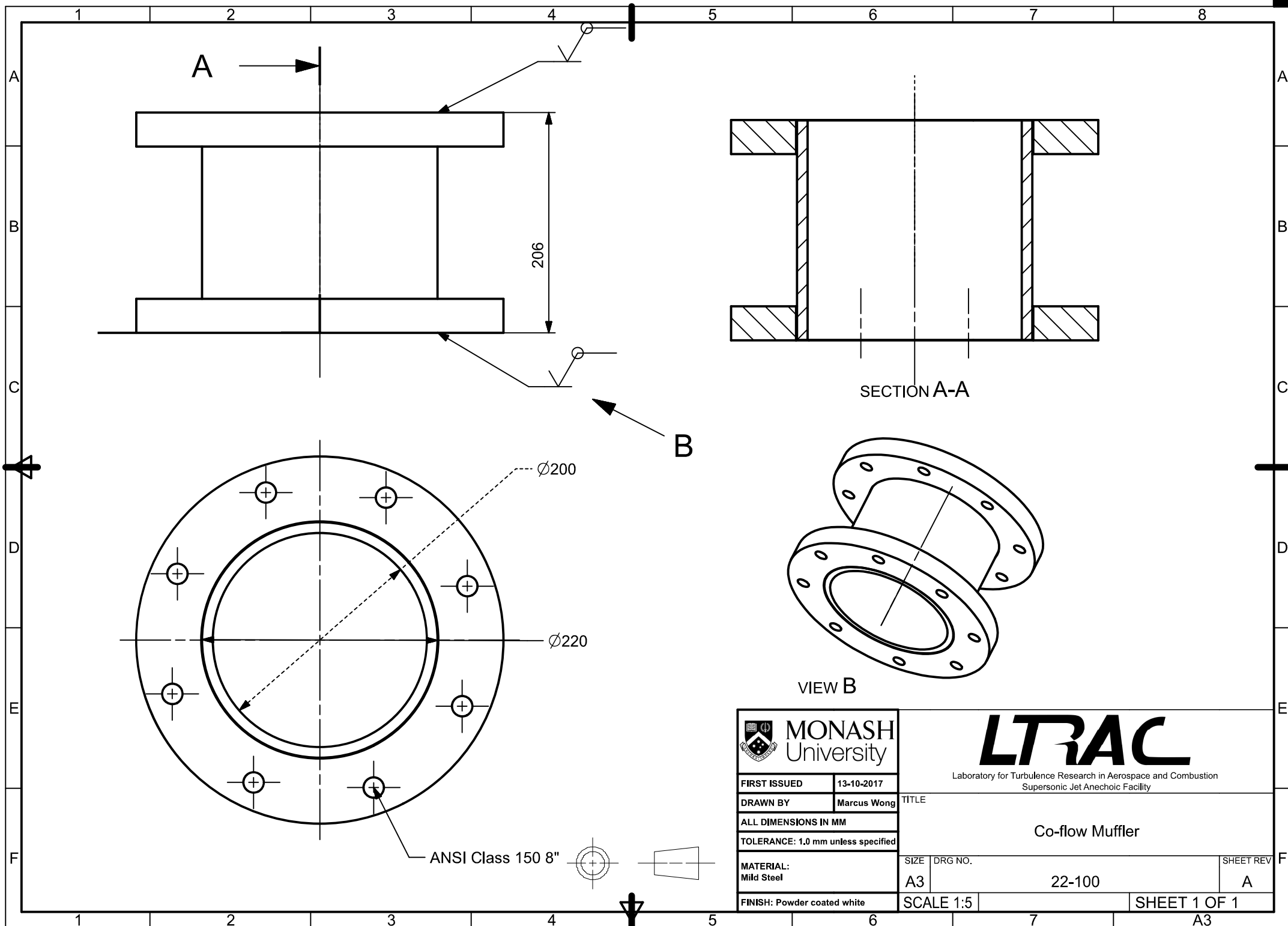
### **C.3 Jet Rig Drawings**



# LTRAC

Part ID	Part Name	Part Code	Qty
1	Settling chamber	20-100	1
2	Settling chamber stand	22-110	1
3	Fairchild regulators	-	2
4	PTFE hose	-	2
5	Wide angle diffuser	22-520	2
6	Jet rig stand	22-300	1
7	Coflow muffler	22-100	1
8	Connector piece	22-700	1
9	Spider (support flange)	22-930	1
10	Coflow plenum	22-900	1
11	Co-flow nozzle	25-300	1
12	Core jet plenum	22-510	1





FIRST ISSUED 13-10-2017

DRAWN BY Marcus Wong

ALL DIMENSIONS IN MM

TOLERANCE: 1.0 mm unless specified

MATERIAL: Mild Steel

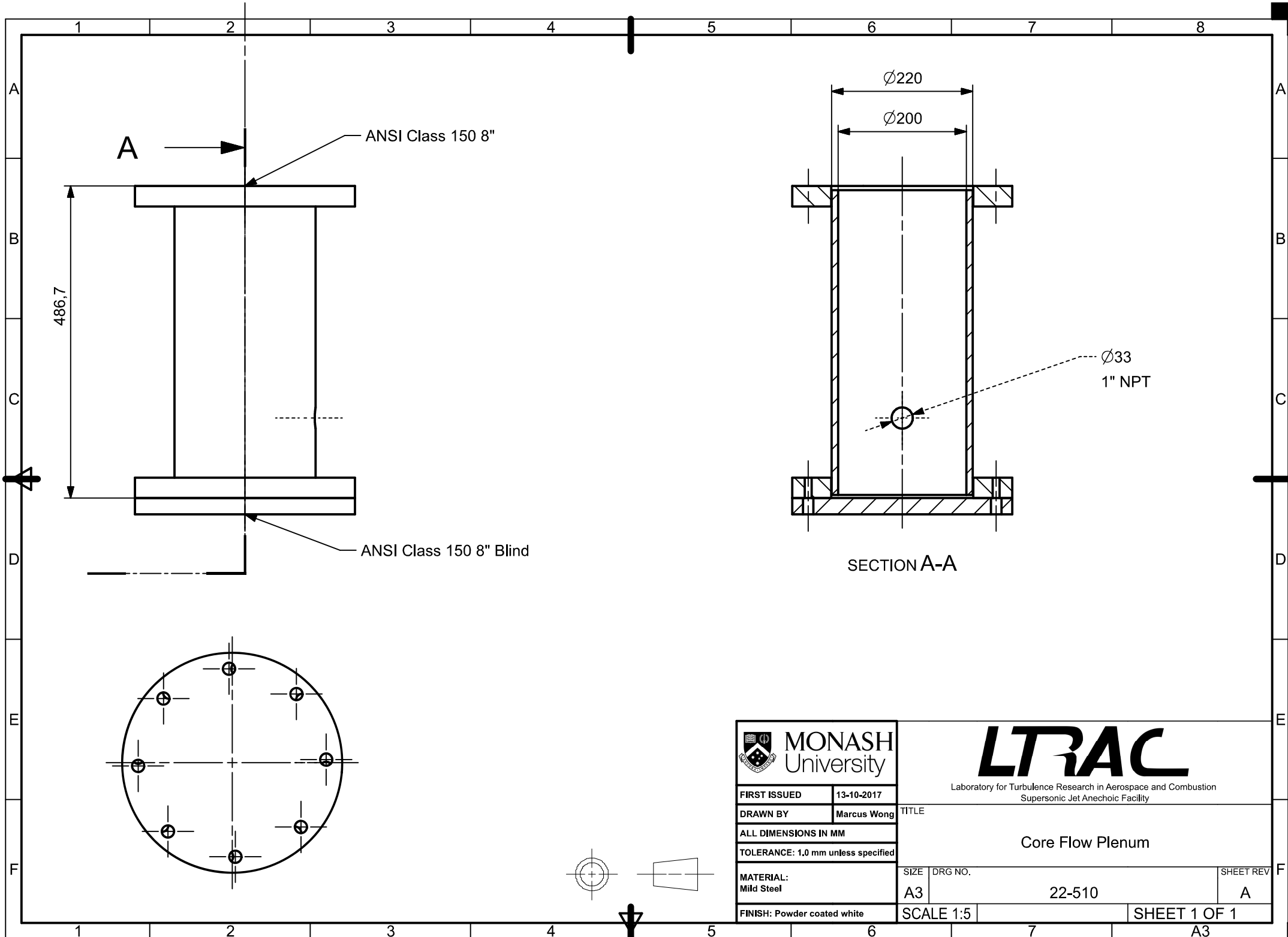
FINISH: Powder coated white

**LTRAC**

Laboratory for Turbulence Research in Aerospace and Combustion  
Supersonic Jet Anechoic Facility

TITLE				
Co-flow Muffler				
SIZE	DRG NO.			SHEET REV
A3	22-100			A
SCALE 1:5		SHEET 1 OF 1		

A3



FIRST ISSUED 13-10-2017

DRAWN BY Marcus Wong

ALL DIMENSIONS IN MM

TOLERANCE: 1.0 mm unless specified

MATERIAL: Mild Steel

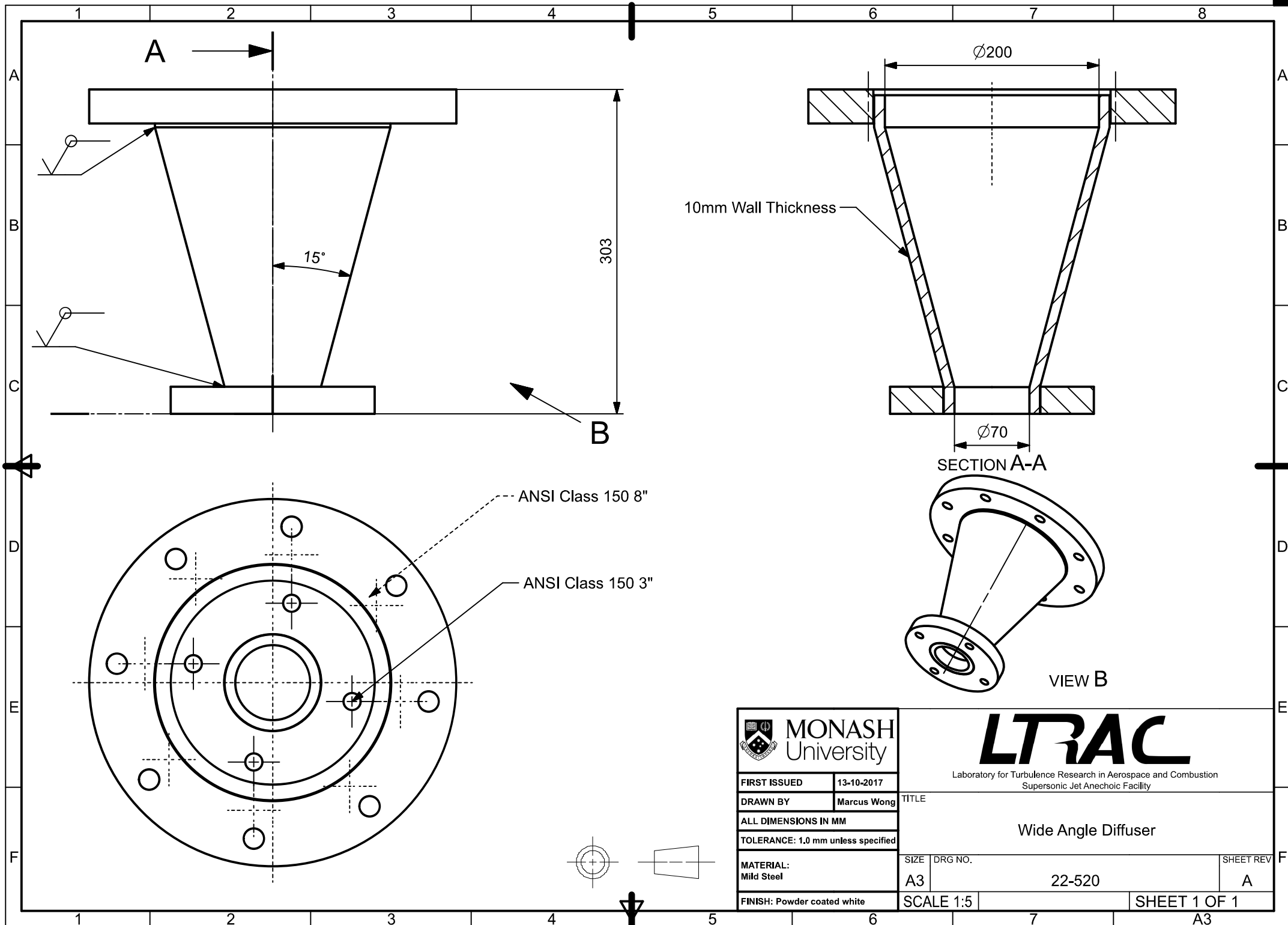
FINISH: Powder coated white


**LTRAC**


Laboratory for Turbulence Research in Aerospace and Combustion  
Supersonic Jet Anechoic Facility

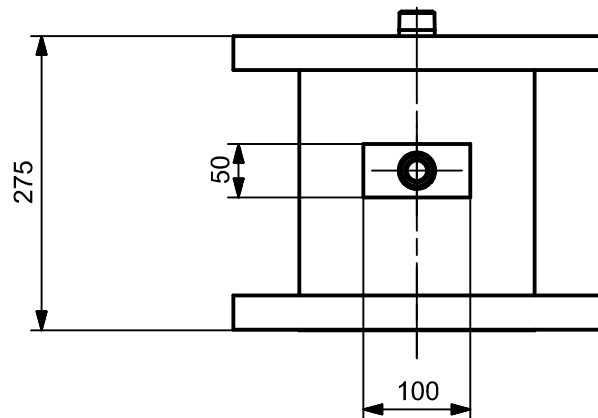
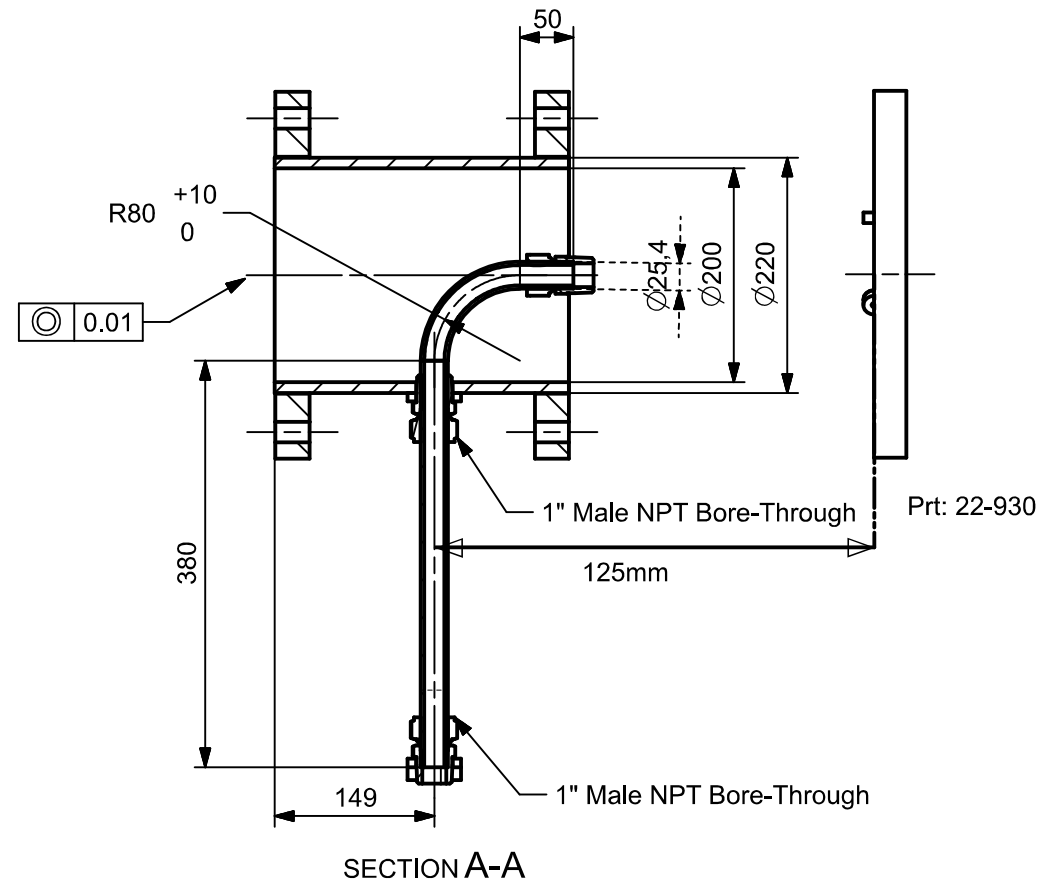
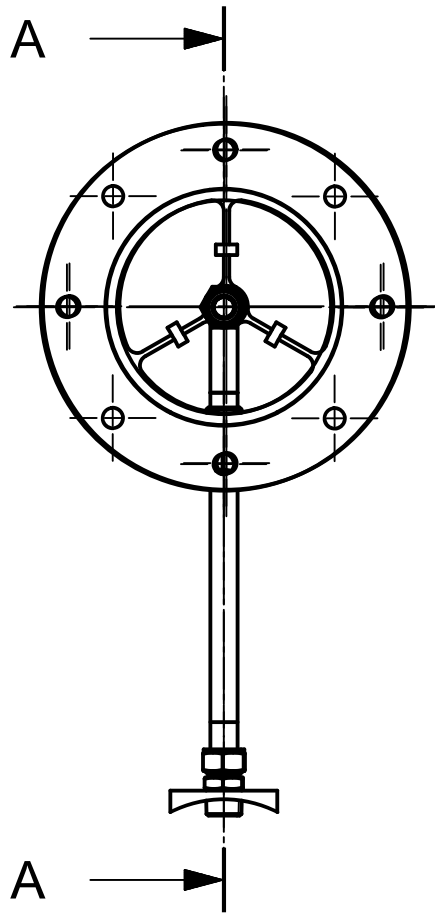
g  ed	TITLE			
	Core Flow Plenum			
	SIZE	DRG NO.		SHEET REV
	A3	22-510		A
	SCALE 1:5		SHEET 1 OF 1	

A3



 <b>MONASH</b> University	
FIRST ISSUED	13-10-2017
DRAWN BY	Marcus Wong
ALL DIMENSIONS IN MM	
TOLERANCE: 1.0 mm unless specified	
MATERIAL: Mild Steel	
FINISH: Powder coated white	

 Laboratory for Turbulence Research in Aerospace and Combustion Supersonic Jet Anechoic Facility		
TITLE  Wide Angle Diffuser		
SIZE A3	DRG NO. 22-520	SHEET REV A
SCALE 1:5		SHEET 1 OF 1



Revision No: 4 (7/08/18)  
Inserted new dimensions for copper pipe



FIRST ISSUED 13-10-2017

DRAWN BY Marcus Wong

ALL DIMENSIONS IN MM

TOLERANCE: 1.0 mm unless specified

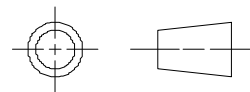
MATERIAL: Mild Steel

FINISH: Powder coat white

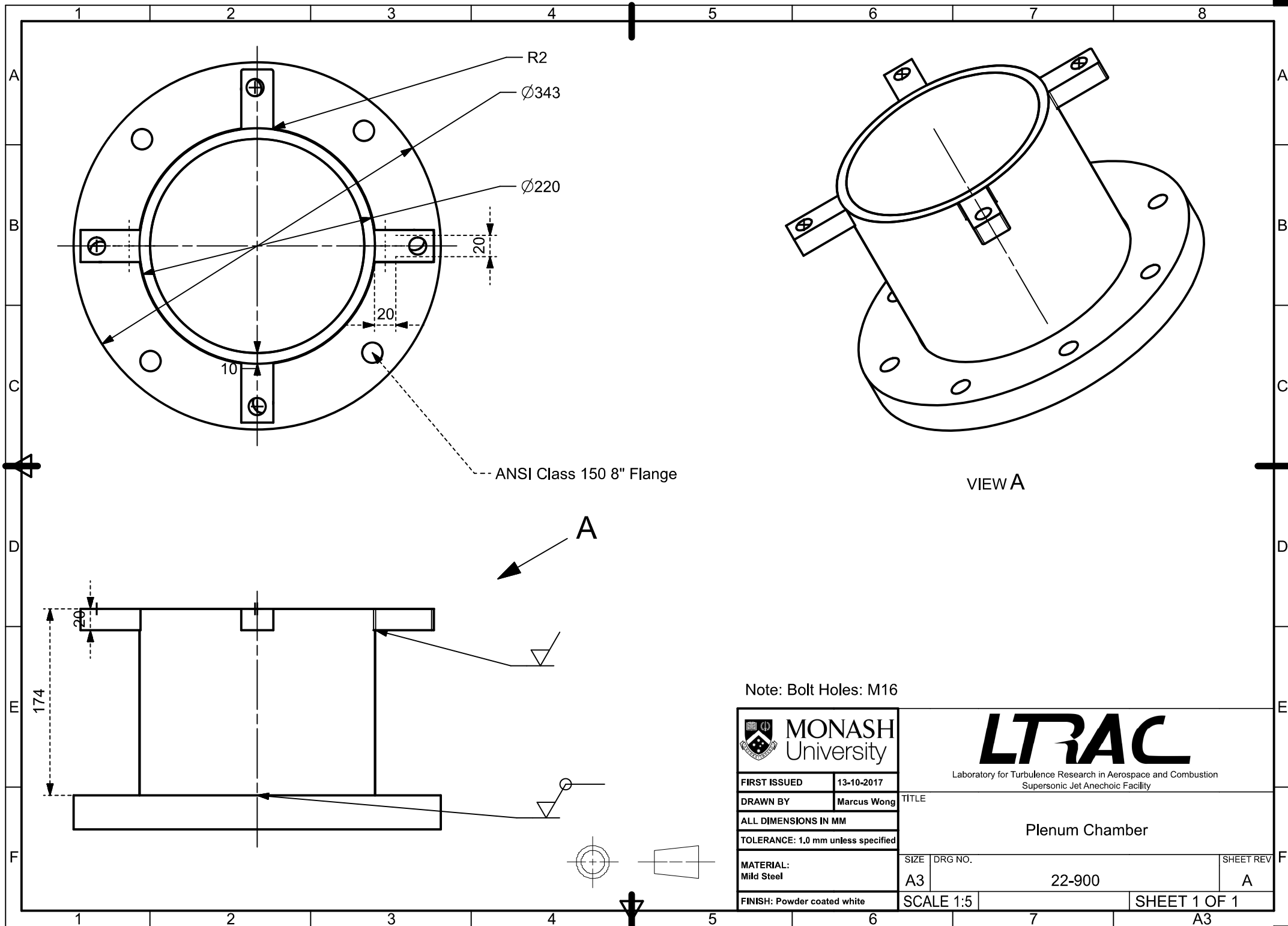
**LTRAC**

Laboratory for Turbulence Research in Aerospace and Combustion  
Supersonic Jet Anechoic Facility

TITLE		Connector Piece	
SIZE	DRG NO.	SHEET REV	
A3	22-700	A	
SCALE 1:5		SHEET 1 OF 1	



A3



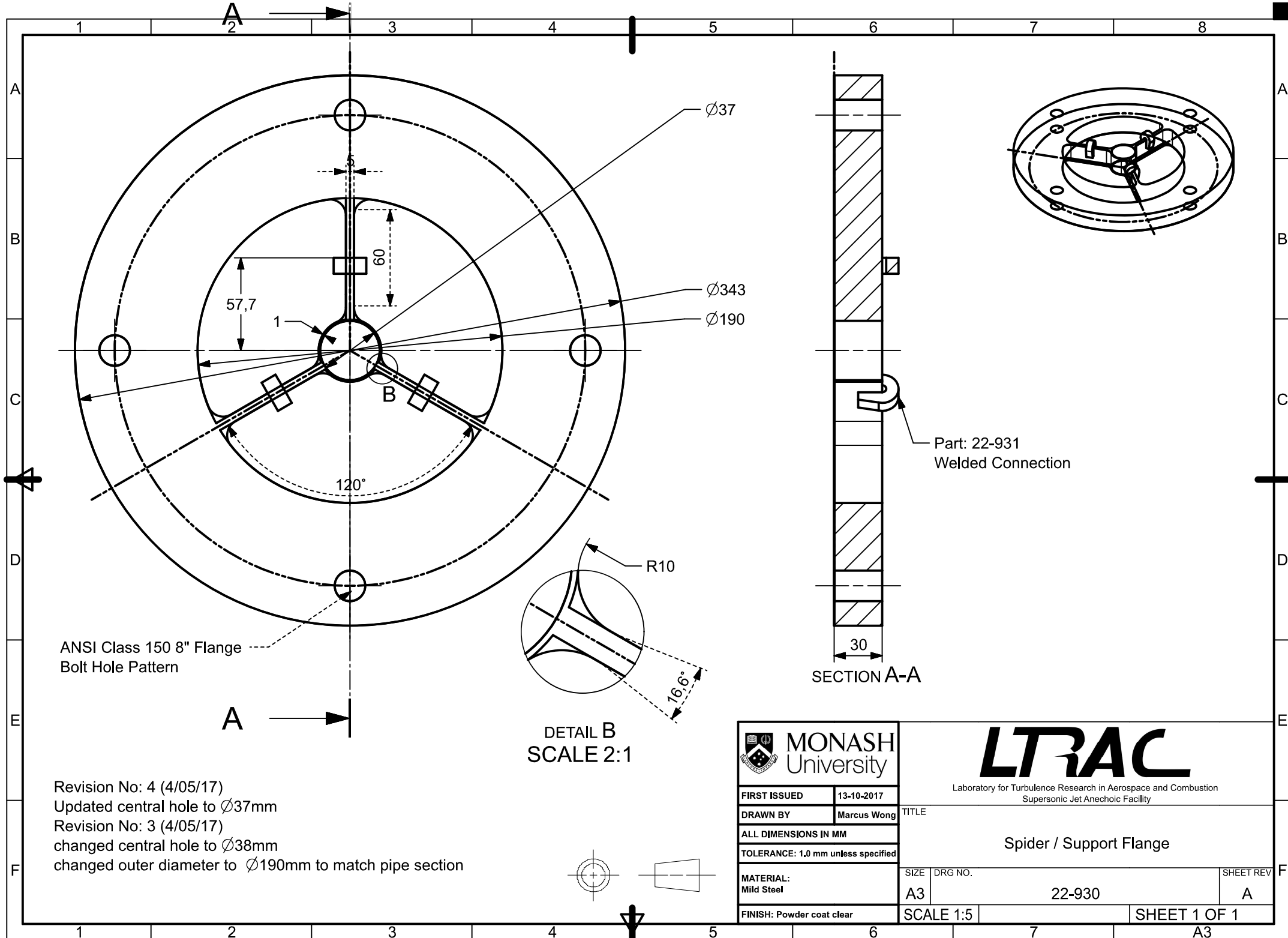
FIRST ISSUED	13-10-2017
DRAWN BY	Marcus Wong
ALL DIMENSIONS IN MM	
TOLERANCE: 1.0 mm unless specified	
MATERIAL: Mild Steel	
FINISH: Powder coated white	

**LTRAC**

Laboratory for Turbulence Research in Aerospace and Combustion  
Supersonic Jet Anechoic Facility

TITLE		SHEET REV	
Plenum Chamber		A	
SIZE	DRG NO.		
A3	22-900		
SCALE 1:5	SHEET 1 OF 1		A3





Revision No: 4 (4/05/17)  
 Updated central hole to  $\varnothing 37$  mm  
 Revision No: 3 (4/05/17)  
 changed central hole to  $\varnothing 38$  mm  
 changed outer diameter to  $\varnothing 190$  mm to match pipe section

DETAIL B  
 SCALE 2:1



FIRST ISSUED 13-10-2017

DRAWN BY Marcus Wong

ALL DIMENSIONS IN MM

TOLERANCE: 1.0 mm unless specified

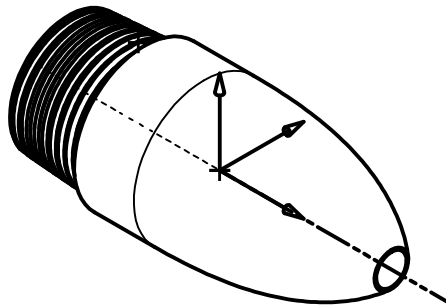
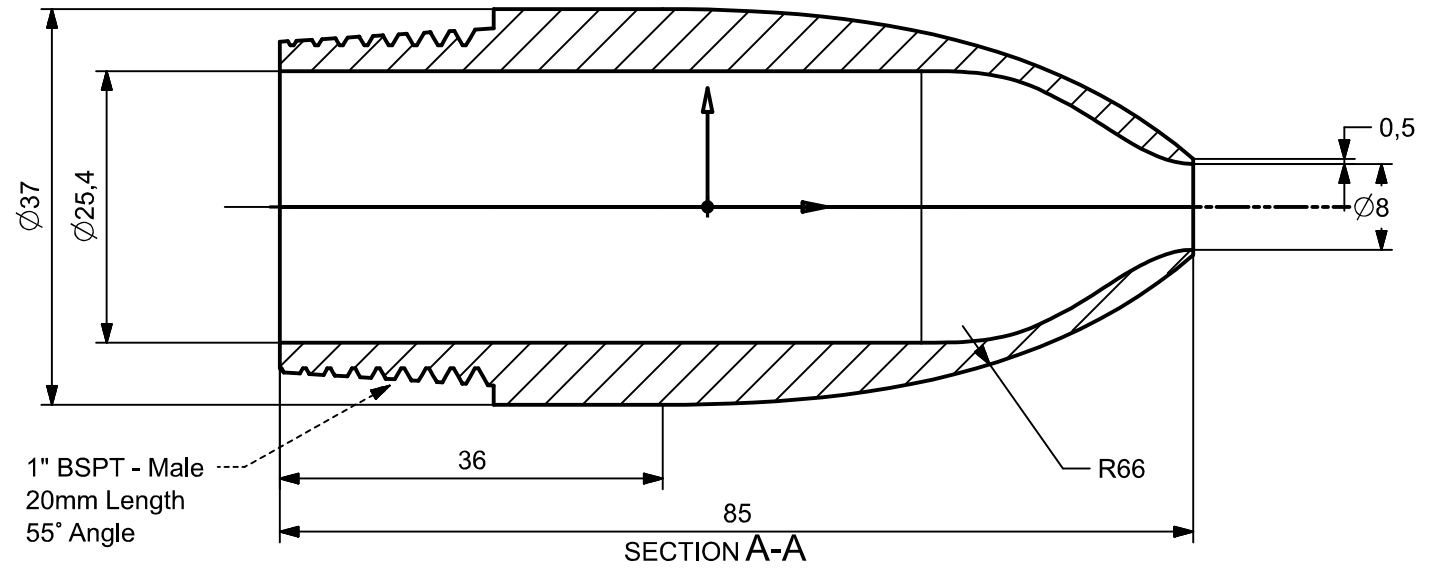
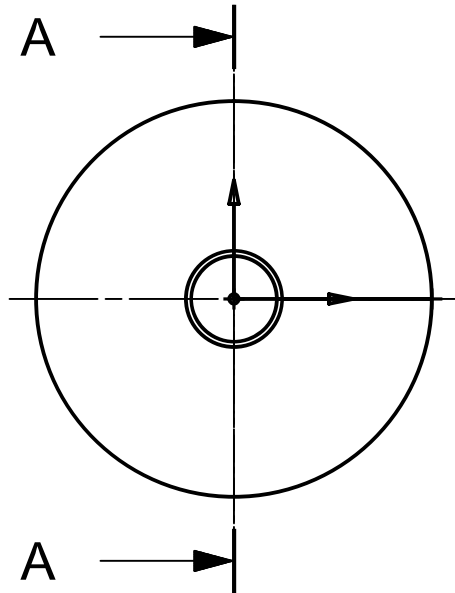
MATERIAL:  
 Mild Steel

FINISH: Powder coat clear

**LTRAC**

Laboratory for Turbulence Research in Aerospace and Combustion  
 Supersonic Jet Anechoic Facility

TITLE				SHEET REV	
Spider / Support Flange				A	
SIZE	DRG NO.				
A3	22-930				
SCALE 1:5		SHEET 1 OF 1		A3	



Revision No: 4a (8/05/18)  
Updated outer diameter to 37mm

Revision No: 4 (8/05/18)  
Updated Dimensions  
Revision No: 3 (8/05/18)  
Updated Pipe and nozzle radius  
Indication of thread type

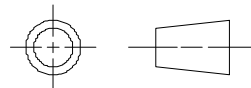


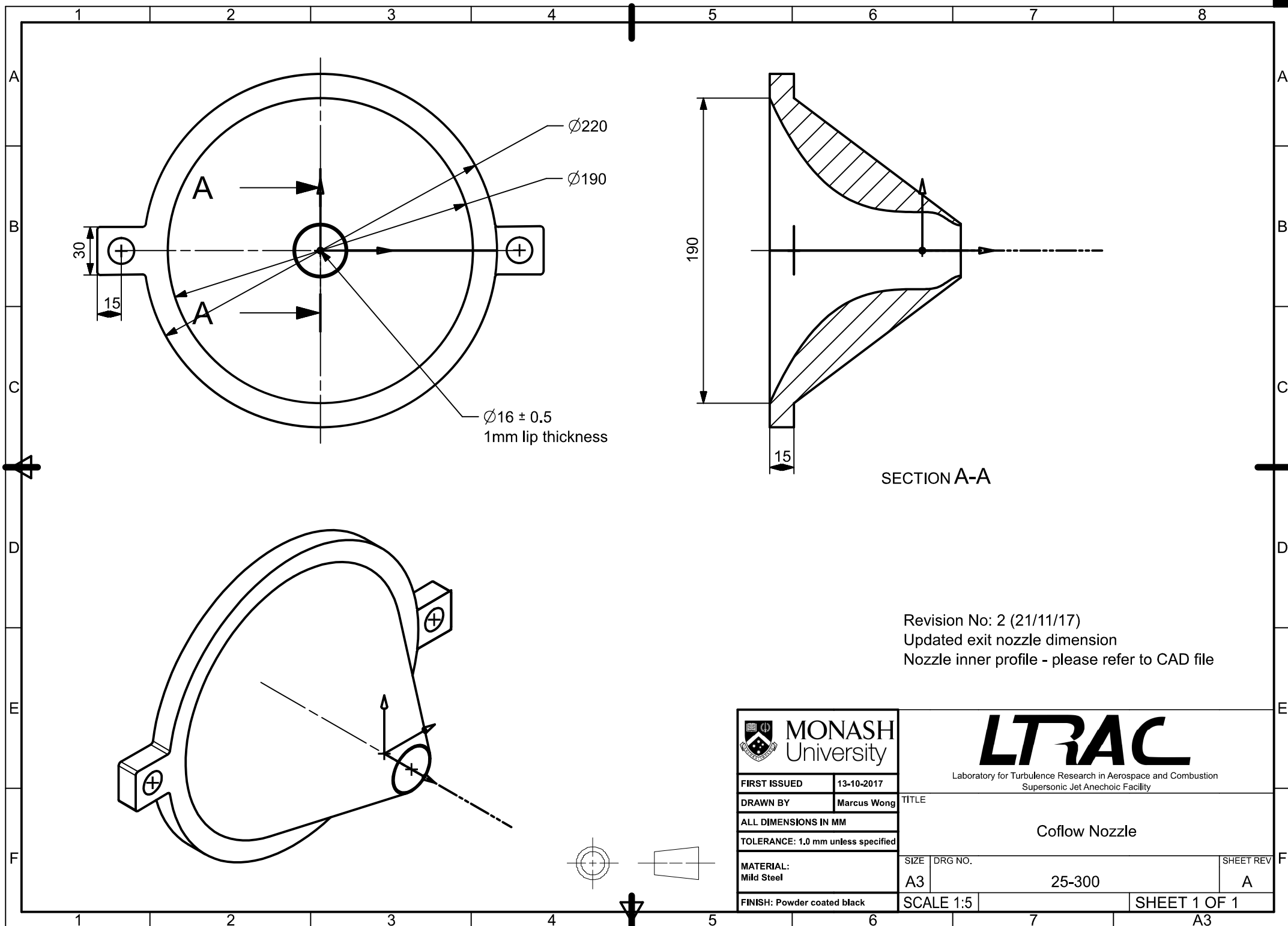
FIRST ISSUED	13-10-2017
DRAWN BY	Marcus Wong
ALL DIMENSIONS IN MM	
TOLERANCE: 1.0 mm unless specified	
MATERIAL:	
Stainless Steel	
FINISH: N/A	

**LTRAC**


Laboratory for Turbulence Research in Aerospace and Combustion  
Supersonic Jet Anechoic Facility

TITLE	Core Jet Nozzle			SHEET REV	A
SIZE	DRG NO.	25-101		SHEET 1 OF 1	
A3		SCALE 1:5		A3	





Revision No: 2 (21/11/17)  
Updated exit nozzle dimension  
Nozzle inner profile - please refer to CAD file

 <div>MONASH University</div>		<div>LTRAC</div> <div>Laboratory for Turbulence Research in Aerospace and Combustion Supersonic Jet Anechoic Facility</div>	
FIRST ISSUED	13-10-2017	TITLE  Coflow Nozzle	
DRAWN BY	Marcus Wong		
ALL DIMENSIONS IN MM			
TOLERANCE: 1.0 mm unless specified		SIZE   DRG NO.   SHEET REV A3   25-300   A	
MATERIAL: Mild Steel			
FINISH: Powder coated black		SCALE 1:5	SHEET 1 OF 1